Universitat Politècnica de València
Departamento de Máquinas y Motores Térmicos

UNIVERSITAT
POLITÈCNICA
DE VALÈNCIA

Development of a computational model for a simultaneous simulation of internal flow and spray break-up of the Diesel injection process

Ph. D. Thesis

Presented by:
Mr. Pedro Martí Gómez-Aldaraví
Supervised by:
Dr. Jaime Gimeno García

Valencia, October, 13$^{\text{th}}$, 2014

Ph. D. Thesis

DEVELOPMENT OF A COMPUTATIONAL MODEL FOR A SIMULTANEOUS SIMULATION OF INTERNAL FLOW AND SPRAY BREAK - UP OF THE DIESEL INJECTION PROCESS

presented by:
Pedro Martí Gómez-Aldaraví

and directed by:
Dr. Jaime Gimeno García

at
Departamento de Máquinas y Motores Térmicos
Universitat Politècnica de València

Thesis submitted for the
Degree of Doctor of Philosophy in Aerospace Engineering

Valencia, October, 13th, 2014

Ph. D. Thesis

DEVELOPMENT OF A COMPUTATIONAL MODEL FOR A SIMULTANEOUS SIMULATION OF INTERNAL FLOW AND SPRAY BREAK - UP OF THE DIESEL INJECTION PROCESS

Written by: Mr. Pedro Martí Gómez-Aldaraví
Directed by: Dr. Jaime Gimeno García

Examining board:

President: Dr. Jose Maria Desantes
Secretary: Dr. Francisco Tinaut Fluixa
Vocals: Dr. Tommaso Lucchini

Reserve board:

President: Dr. Antonio Torregrosa
Secretary: Dr. Magin Lapuerta
Vocals: Dr. Angelo Onorati

Valencia, October, 13th, 2014

Abstract

The purpose of the injection system in Diesel engines, and in general, of any Direct Injection engine, is the delivery of a high-quality air-fuel mixture, in such a way that an efficient combustion is achieved whilst pollutant and noise emissions are minimized. Computational Fluid Mechanics (CFD) techniques have been one of the key tools that helped fastest development of injection system over the last decades.

Among all processes that need to be included in computational models of sprays (cavitation, flow detachment, boundary layer development, etc.), the atomization or break-up of the liquid vein is probably the most complicated one. This is because physical phenomena that governs that process are not fully understood yet. Furthermore, the strong link existing between the flow inside the injector nozzle and the spray behavior is, in general, poorly simulated. The present Thesis has focused on these two aspects of the injection process: the atomization of the fuel, and seamlessly simulating the internal flow and the spray.

A new model, called Eulerian Spray Atomization (ESA), has been developed and implemented in the open source CFD software OpenFOAM ® to simulate the whole injection process. ESA model is based on a homogeneous flow description under an Eulerian framework; in other words, the air-fuel mixture is considered as a single fluid and the mixing process is modeled by means of two new transport properties: the liquid mass fraction and the interfacial surface density. The ESA model has been verified by comparison with Direct Numerical Simulations of Diesel sprays and with analytical solutions of simplified problems. It has also been validated with a large experimental database.

Thus, this work provides a new and valuable tool, the ESA model, that allows improving the understanding of direct injection processes. One of the outcomes obtained by using it is that, as a result of fuel being considered as a compressible fluid, the expansion process taking place inside the injector has a cooling effect, however the viscous friction at walls heats up the liquid. Another interesting finding is that lighter fuels atomize faster, therefore increasing the fuel temperature inside the injector is recommended in order to improve the atomization and so the combustion efficiency.

Resumen

El objetivo del sistema de inyección en los motores diésel (en general en cualquier motor de inyección directa) es la formación de una mezcla aire-combustible de calidad, de manera que se logre una combustión eficiente a la vez que se minimicen las emisiones contaminantes. Los sistemas de inyección han evolucionado rápidamente en los últimos años, y las técnicas de Mecánica de Fluidos Computacional (CFD, de sus siglas en inglés) han sido una de las herramientas claves para ello.

De todos los procesos que se han de incluir en los modelos computacionales (cavitación, desprendimientos de flujo, crecimiento de la capa límite, etc.), la atomización o ruptura de la vena líquida de combustible es, quizás, el más complicado ya que los fenómenos físicos detrás de dicho proceso no son totalmente conocidos. Además, la fuerte influencia del flujo dentro del inyector sobre el chorro, generalmente, no se simula de manera adecuada. La presente Tesis trata sobre estos dos aspectos de la inyección: la atomización del combustible, y la simulación simultánea del flujo en la tobera y en el chorro.

Un nuevo modelo, denominado en inglés "Eulerian Spray Atomization" ESA, ha sido desarrollado e implementado en el software CFD de código abierto OpenFOAM ®. Este modelo está basado en estudiar la mezcla como un medio homogéneo, utilizando para ello una descripción Euleriana del flujo; es decir, la mezcla aire-combustible se considera como un único fluido y el proceso de mezcla se modela mediante el transporte de dos nuevas variables: la fracción másica de combustible y la densidad de superficie de contacto entre las fases. La verificación del modelo ESA se ha llevado a cabo por comparación con casos de Simulación Numerérica Directa (DNS, de sus siglas en inglés) y con soluciones analíticas de problemas simplificados. Dicho modelo también ha sido validado frente a una extensa base de datos experimental.

Así pues, esta tesis aporta una nueva y valiosa herramienta, el modelo ESA, la cual ha permitido y permitirá mejorar la comprensión sobre los procesos de inyección directa. Uno de los frutos obtenidos gracias a su uso es que, debido a que se ha considerado el combustible como un fluido compresible, el proceso de expansión que se produce en la tobera enfría el propio combustible, mientras que los efectos de fricción en las paredes lo calientan. Otro resultado interesante es que los combustibles más ligeros se atomizan más rápido, es por ello que se recomienda aumentar la temperatura del combustible en el inyector para mejorar la atomización y por tanto la eficiencia de la combustión.

Resum

L'objectiu del sistema d'injecció en els motors dièsel (en general en qualsevol motor d'injecció directa) és la formació d'una barreja aire-combustible de qualitat, de manera que s'aconseguisca una combustió eficient alhora que es minimitzen les emissions contaminants. Els sistemes d'injecció han evolucionat ràpidament en els últims anys, i les tècniques de Mecànica de Fluids Computacional (CFD, de les sigles en anglès) han sigut una de les eines claus per tal d'aconseguir-ho.

De tots els processos que s'han d'incloure en els models computacionals (cavitació, despreniments de flux, creixement de la capa límit, etc.), l'atomització o ruptura de la vena líquida de combustible és, potser, el més complicat, ja que els fenòmens físics darrere de l'esmentat procés no són totalment coneguts. A més, la forta influència del flux dins l'injector sobre l'esprai, generalment, no se simula de manera adequada. La present Tesi tracta sobre estos dos aspectes de la injecció: l'atomització del combustible, i la simulació simultània del flux en la tobera i l'esprai.

Un nou model, denominat en anglés "Eulerian Spray Atomization" ESA, ha sigut desenvolupat i implementat en el software CFD de codi obert OpenFOAM (R). Este model està basat en estudiar la barreja com un medi homogeni, utilitzant per a això una descripció Euleriana del flux; és a dir, la barreja aire-combustible es considera com un únic fluid i el procés de barreja es modela mitjançant el transport de dos noves variables: la fracció màssica de combustible i la densitat de superfície de contacte entre les fases. La verificació del model ESA s'ha dut a terme per comparació amb casos de Simulació Numèrica Directa (DNS, de les seues sigles en anglés) i amb solucions analítiques de problemes simplificats. L'esmentat model també ha sigut validat front a una extensa base de dades experimental.

Doncs, aquesta tesis aporta una novedosa i valuosa eina, el model ESA, que va permetre i pemetrà millorar l'enteniment dels procesos d'injecció directa. Un dels fruits obtinguts gràcies al seu ús és que, degut a que s'ha considerat el combustible com un fluid compressible, el procés d'expansió que es produïx en la tobera refreda el propi combustible, mentre que els efectes de fricció a les parets el calenten. Altre resultat interessant és que els combustibles més lleugers s'atomitzen més ràpid, per la qual cosa es recomana augmentar la temperatura del combustible en l'injector per a millorar l'atomització i, per tant, l'eficiència de la combustió.

To my parents, Estrella and Pedro, and siblings, María and Carlos.

Once upon a time I started my formation as a researcher at CMT. First thing I did was my Final Degree Project. I liked it, and then I became Ph. D. student there. I was crazy, and I still am. Nevertheless, I like to think that now I am a wiser and better person. What I am sure about is that I am different than I was four years and half ago. This personal growth has been made possible by my surroundings and people that I met and worked with.

First of all, I would like to acknowledge my advisor Jaime Gimeno. His patient, calm and wise guidance has been of inestimable value for the development of this Thesis and my formation as a researcher. Thank you Jaime.

Secondly, I have to also acknowledge my boss and coworker Raúl Payri and F. Javier Salvador. Their advices and support have been outstanding regardless the issue I proposed in the last four years. Thank you Raúl and Javi.

Thirdly, I need to shout out to my injection (underground) research line colleges and Ph. D. students Julien, Gabriela, Joaquín, Jorge, Michele, Óscar, Juan Pablo, Marcos, David and Daniel. Some of them already graduated, some of them started his research less than one year ago, but all of them are great, clever and hardworking people. Thank you all, I am in debt with you. José Enrique, injection lab technician, deserves a special mention. His expertize and skills in the lab in combination with his good mood in general make life easier for everyone else. Thank you José Enrique.

Fourthly, I take time to thank other colleges who did not directly work with me but helped me quite a lot. Roberto Navarro and David Blanco, who shared with me a common timing in our careers. José Pedro and, again, Marcos Carreres, who started their degree with me and kept working next to me after it. Andrés Tiseira, old professor of mine, now college and friend. José Manuel Pastor, CFD expert who helped me when it was required. And many others (Vicente, Pau, Xandra, José María García. . .). Thank you, really.

Fifthly, thanks to the students who worked with me during these years. I cannot name them all because there are many, but they know who they are. I know working with me as a "boss" is not an easy task. Thank you all.

Sixthly, I cannot forget about those people who welcomed me abroad in my first year as a Ph. D. student and gave me the opportunity to work and live in Sweden for three months. Thanks to Mark Linne, Peter Dhalander, Stina Hemdal, Tom Rogers and Eugenio de Benito.

I also want to express my thanks to the Departamento de Máquinas y Motores Térmicos, and in particular to Professor Francisco Payri and Professor José María Desantes for giving me the privilege of working in this world wide

recognized research institute. Administration staff of the department also deserves a commend. Thank you for making all paperwork to seem piece of cake.

Finally, there is a nice world outside CMT. My most special gratitude to my friends Román (now Panchito Román), Raúl, Paco, Javi H., Diego (Bio), Javi V., and Sergio. Thank you for getting me out for partying, day trips, doing sport, or simply having a 7.5 beer. I am not so thankful for those nights that they kept me awake when I had to work next morning. Nonetheless, the DotA and other distractions that they brought to me helped to clear my mind. There are many other people who collaborated with them and dragged me out for all sort of plans during these last four years (Malu, Cecilia, Denitsa, Naian, Marina, Carlos, Aina, María, etc. -and there are several persons that I shall not name-).

Sorry if I missed someone. That does not mean he or she was not relevant to me and my career. All the people I met, even if it was just for a while, have had and impact on my personality.

Contents

i

List of Figures

List of Tables

Nomenclature

Acronyms

AIAA American Institute of Aeronautics and Astronautics.

ANOVA Analysis of Variance.

aSOI After start of injection.

CDM Continuum Droplets Model.

CDV Converging-diverging verification.

CFD Computational Fluid Dynamics.

CPU Central processing unit.

DBI Diffused Back-light Illumination.

DDM Discrete Droplets Model.

DI Direct injection.

DNS Direct Numerical Simulation.

DQMOM Direct quadrature method of moments.

ECN Engine Combustion Network.

ECU Electronic Control Unit.

ELSA Eulerian-Lagrangian Spray Atomization.

ESA Eulerian Spray Atomization.

FEM Finite-element method.

FOAM Field operation and manipulation.

FVM Finite-volume method.

FWHM Full Width Half Maximum.

GDI Gasoline direct injection.

GFM   Ghost fluid method.

HEG   Hydro-erosive grinding.

HEM   Homogeneous equilibrium modeling.

IDI   Indirect injection.

LDV   Laser Doppler Velocimetry.

LES   Large-Eddy Simulation.

MAC   Marker-and-Cell scheme.

MOM   Method of moments.

MPI   Message passing interface.

NIST   National Institute of Standards and Technology.

PDF   Probability Density Function.

PDI   Phase Doppler Interferometry.

PDPA   Phase Doppler Particle Analyzer.

PIMPLE Combination of PISO plus SIMPLE.

PISO   Pressure Implicit with Splitting of Operators.

PIV   Particle Image Velocimetry.

PLIC   Piecewise linear interface calculation.

PLIF   Planar Laser Induced Fluorescence.

QMOM   Quadrature method of moments.

RANS   Reynolds-Averaged Navier-Stokes.

RNG   Re-Normalization Group.

SIMPLE Semi-Implicit Method for Pressure-Linked Equations.

SOI   Start of injection.

SST   Shear Stress Transport.

TIM   Transverse Integrated Mass.

VCO   Valve closed orifice.

VOF   Volume-of-Fluid scheme.

Dimensionless quantities

φ Level-set function.

γ Heat capacity ratio.

AR Area reduction of the orifice.

Bo Bond number.

B Impact parameter.

CN Cavitation number.

Ec   Eckert number.

Eo   Eötvös number.

$k - factor$ Conic shape factor of the orifice.

Nu   Nusselt number.

Oh   Ohnesorge number.

Pr   Prandtl number.

Pr_t Turbulent Prandtl number.

Re   Reynolds number.

Sc   Schmidt number.

Sc_t Turbulent Schmidt number.

Stk   Stokes number.

Ta   Taylor number.

We   Webber number.

We_{cr} Critical Webber number.

Σ Inter-facial area per unit volume, m^{-1}.

CFL   Courant-Friedrichs-Lewy number.

C_a Area coefficient.

C_c Contraction coefficient.

C_d Discharge coefficient.

C_v Velocity coefficient.

K   Cavitation number.

K_{crit} Critical cavitation number.

M   Mach number.

X   Volume fraction or void fraction.

Y   Mass fraction.

y^+ Non-dimensional wall distance.

Y_f Fuel (liquid) mass fraction.

Y_g Gas mass fraction.

Greek symbols

α Coefficient of (cubic) thermal expansion, K^{-1}.

β Oblique shock angle, rad.

$\boldsymbol{\tau}$ Viscous shear stress, Pa.

ϵ Turbulent dissipation, m^2/s^3.

κ Thermal diffusivity, $\text{kg}/(\text{m s})$.

κ_t Turbulent thermal diffusivity, $\mathrm{kg}/(\mathrm{m\,s})$.

μ Dynamic viscosity, $\mathrm{kg}/(\mathrm{m\,s})$.

μ_f Fuel dynamic viscosity, $\mathrm{kg}/(\mathrm{m\,s})$.

μ_t Turbulent (eddy) viscosity, $\mathrm{kg}/(\mathrm{m\,s})$.

μ_{JT} Joule-Thomson (Kelvin) coefficient, $\mathrm{K/Pa}$.

ν Kinematic viscosity, $\mathrm{m^2/s}$.

ν_t Turbulent (eddy) kinematic viscosity, $\mathrm{m^2/s}$.

ω Specific turbulent dissipation, $\mathrm{s^{-1}}$.

Φ Mass flux, $\mathrm{kg/s}$.

Φ_U Volumetric flux, $\mathrm{m^3/s}$.

Φ_{visc} Head viscous dissipation, m.

Ψ Compressibility, $\mathrm{s^2/m^2}$.

Ψ_f Fuel (liquid) compressibility, $\mathrm{s^2/m^2}$.

Ψ_g Gas compressibility, $\mathrm{s^2/m^2}$.

ρ Density, $\mathrm{kg/m^3}$.

ρ_g Gas density, $\mathrm{kg/m^3}$.

ρ_l Fuel (liquid) density, $\mathrm{kg/m^3}$.

σ Surface tension, $\mathrm{kg}/(\mathrm{m^2})$.

τ_k Kolmogorov time-scale, s.

τ_p Time of dynamic relaxation of particles, s.

θ Spray spreading angle, rad.

θ_m Spray spreading micro-angle, rad.

ξ Thermal conductivity, $\mathrm{W}/(\mathrm{m\,K})$.

Latin symbols

$\boldsymbol{n}$ Normal unity vector to the surface, $-$.

$\boldsymbol{U}$ Velocity vector, $\mathrm{m/s}$.

$\dot{M}$ Spray momentum flux, N.

$\dot{m}_f$ Fuel mass flow, $\mathrm{kg/s}$.

$\dot{M}_{th}$ Theoretical spray momentum flux, N.

$\dot{m}_{f,th}$ Theoretical fuel mass flow, $\mathrm{kg/s}$.

BL Break-up length, m.

IL Intact core length, m.

LL Liquid length, m.

nl Needle lift, $\mathrm{m/s}$.

NPL	Non-perturbed length, m.
$R-parameter$	Time derivative of the penetration respect to the squared root of time, $m/\sqrt{s}$.
SMD	Sauter Mean Diameter, m.
A	Area, surface, m^2.
a	Sound (sonic) speed, m/s.
a_f	Fuel (liquid) sound (sonic) speed, m/s.
a_g	Air (gas) sound (sonic) speed, m/s.
A_i	Inlet orifice area, m^2.
A_o	Outlet orifice area, m^2.
c_p	Specific heat capacity at constant pressure, $m^2/(s^2\,K)$.
D	Diameter, m.
D_{coeff}	Diffusion coefficient, $kg/(m\,s)$.
D_{eff}	Effective orifice diameter, m.
D_d	Droplet diameter, m.
D_i	Inlet orifice diameter, m.
D_o	Outlet orifice diameter, m.
D_s	Nozzle sac diameter, m.
D_{eq}	Equivalent diameter, m.
e	Specific internal energy, m^2/s^2.
e_r	Absolute wall roughness, m.
g	Gravitational acceleration, m/s^2.
h	Specific enthalpy, m^2/s^2.
K	Specific kinetic energy, m^2/s^2.
k	Turbulent kinetic energy, m^2/s^2.
L	Length, m.
L_m	Origin in length of the micro-angle, m.
L_s	Origin in length of the spreading angle, m.
l_t	Turbulent length scale, m.
n	Droplet number density, m^{-3}.
p	Pressure, MPa.
p_0	Total pressure, MPa.
p_b	Back (discharge, chamber, ambient) pressure, MPa.
p_i	Injection pressure, MPa.
p_v	Fuel vapor pressure, MPa.

R	Gas constant, $m^2/(s^2\,K)$.
r_e	Fillet or entrance radius, m.
r_{eq}	Equilibrium droplet radius, small-scale characteristic length, m.
R_{Y_k}	Mass fraction of phase k diffusion flux, $kg/(m^2\,s)$.
S	Spray penetration, m.
T	Temperature, K.
t	Time, s.
T_b	Back (discharge, chamber, ambient) temperature, K.
T_i	Injection temperature, K.
u	Velocity component in axial direction, m/s.
u_{eff}	Effective velocity, m/s.
u_{rel}	Relative velocity, m/s.
u_r	Small-scale characteristic velocity, m/s.
u_{th}	Theoretical (Bernoulli) velocity, m/s.
z	Elevation, m.

Chapter 1

Introduction

1.1 General context

Diesel engines demonstrated indubitable strong points in terms of efficiency, reliability and adaptability. Despite the applications of this kind of engine spread over many fields (naval, electric generator, agriculture, etc.), the automotive industry is one of the sector which boosted the most its development. The competitive market, together with the stringent emissions regulations imposed by the governments (i.e Euro VI [1]), led Diesel engines to continuous improvements being nowadays one of the most efficient combustion engines [2]. Imposed regulations are a reflex of the society, its growing concerns about emissions and fuel consumption because of environmental and economical reasons in the past years.

Fuel direct injection represents one of the key aspects in the development of the Diesel engines, the idea of controlling the auto-ignition and the consequent combustion of a liquid spray injected in a reacting atmosphere during a time scale of few milliseconds has been a challenging task for the engine community and pushed forward to a massive research in this field. The quality of the air-fuel mixture defines the combustion efficiency, and therefore the engine efficiency.

In this sense, the technological advancement reached in the hardware and software employed made available systems capable of performing fast and accurate fuel (multiple) injections using very high injection pressures, higher than 200 MPa. On the other hand, the many studies performed in the last

decades allowed to gain a deep knowledge of the spray formation and combustion process. Despite, it is still difficult to assess with accuracy how a modification in the geometry affects the whole process. The small time- and length-scales involved in the phenomena, the difficulty in controlling with accuracy the relevant boundary conditions and the intrinsic complexity of the atomization process that is at the basis of the spray formation are only a few of the difficulties that characterize this study.

Currently, the primary and long term objective for researchers is to develop accurate predictive models capable of describing the injection/combustion event, with the aim of replacing (or at least reducing) the experimental practice with numerical simulation or analytical models [3]. The complexity of these tasks moved the engine community to investigate each time in more detail the phenomena involved in the injection process in order to provide modelers quantitative data to compare results of their simulations and also to gain understanding of the mechanism involved. To this end, in the last decade, several new specific diagnostics have been introduced thanks to new available technology [4], for example, X-ray measurements [5].

In the research applied to direct injection Diesel engines, two main approaches can be identified:

- engine research, oriented to the understanding of the injection and combustion within the engine;
- fundamental study, oriented to the understanding of the spray and the flame in simplified environments.

In the first approach, tests are performed in real Diesel engines with only slight modifications to gain optical access or to introduce specific probes. Results have immediate impact on the decisions to take during the engine calibration, since all the relevant phenomena are considered. However, in this approach, boundary conditions that remain unknown and somehow uncontrolled are many, for example, turbulence levels of incoming air.

Fundamental studies aim at investigating separate single processes in order to gain knowledge and control on them, for example studying the spray development avoiding the combustion, or the fuel atomization avoiding the opening and closing transients. To this end, specific test chambers capable of finely controlling all boundary conditions are built. The work developed in the present Thesis follows this second approach.

All the same, performing fundamental experiments on the flow inside Diesel nozzles and in the near-field region of the spray under real operating conditions turns out to be extremely difficult, if not impossible nowadays. This high complexity is due to the following factors:

- Small dimensions of the nozzle orifices.
- High velocity of the flow, due to high injection pressure.
- Transient phenomenon, influenced by the dynamic behavior of the injector.
- High operating pressure and temperature, that may damage the experimental equipment.
- Large density ratio (and differences in other properties) between air and liquid.

The most common experimental techniques employed in the study of nozzle flow are injection rate [6] and momentum flux measurements [7], which allow (together with some other techniques) fully hydraulic characterization [8]. All of them give integral parameters. Transparent nozzles and visualization techniques have also been used for years in order to obtain local values and profiles inside nozzles [9, 10]. However, simplified geometries and non-realistic injection conditions are used every time. A famous example of that is the work of Winklhofer et al. [11], who used a two-dimensional and rectangular transparent channel to study cavitation regimes.

Regarding the spray, Mie scattering [12, 13], Diffused Back-light Illumination (DBI) [14] and Schlieren and shadowgraph optical techniques [15] are widely employed by the engine community to study the spray macroscopic characteristics (such penetration, angle or liquid-length). Experimental assembly and light path uncertainties, limited image and time resolutions, and post-processing criteria limit the capabilities of these techniques, specially in the dense part of the spray. Tomography and X-ray measurements [5, 16] overcome some of the difficulties and are able to give some reliable information inside the nozzle and in the near-field. In terms of microscopic characteristics, such droplet size or velocity profile, Phase Doppler Interferometry (PDI) [17] and Particle Image Velocimetry (PIV) [18] are the most used techniques, though they are limited in the range of size and velocity which are able to measure.

Therefore, computational techniques are extremely useful to study the fundamental processes taking place inside the nozzle and right at the exit of

the orifice. And this is why Computational Fluid Dynamics (CFD) techniques have grown that much in the engine field for the last 20 to 30 years.

This Thesis is part of that trend. A new CFD model is used to study the flow inside the nozzle and its relation with the first millimeters of the spray. The main advantage of the developed model is that allows to simulate internal and external flows, which have very different time- and length-scales, seamlessly, thus reducing uncertainties on boundary conditions. Furthermore, the use of a free and open source software with multiphase models still under development is an additional challenge to the objectives of this Thesis and a great opportunity to obtain a model that, one day, can be quite useful for the engine industry.

The Departamento de Máquinas y Motores Térmicos at Universitat Politècnica de Valéncia, where the present investigation was carried out, has a long research history in the field of fuel injection and combustion [7, 10, 19–26], despite other topics. From the computational point of view, Salvador [8] used a commercial CFD software together with experimental tools to study the influence of cavitation phenomenon on the development of the Diesel spray. Martínez-López [27] continued Salvador work and used an open source code to study the influence of partial needle lifts on the internal flow and cavitation process. Concerning the fuel spray, Pinzello [28] combined CFD with phenomenological models to analyze fuel injection and combustion processes. His work was improved by Chávez Cobo [29], who added a combination also with one-dimensional models. Additionally, Laborda [30] moved a step forward and used engineering Large Eddy Simulations to simulate Diesel sprays. Finally, there are other two investigations which are directly related to the present one. First one, carried out by Dung [31], consists of an evaluation and validation of an Eulerian-Lagrangian Spray Atomization (ELSA) model by comparison of CFD results with experimental data. The second research has been developed at the same time than this one by A. Pandal, and his Ph. D. Thesis is going to be published soon (an example of his work is given in the work of García-Oliver et al. [32]). It deals with the evaporation process of the liquid spray under an Eulerian framework.

1.2   Objectives and methodology

Understanding and being able to predict fuel break-up during the injection process is a key step in order to improve air-fuel mixing and hence reduce the fuel consumption of an internal combustion engine. Many experimental and computational studies have been carried out for decades with this objective.

Liquid atomization or break-up is usually modeled through a Discrete Droplets Model (DDM) under a Lagrangian framework. This approach, though commonly used nowadays [33, 34], only works accurately in absence of liquid ligaments, and if droplets are dispersed.

However, Vallet et al. [35] developed an Eulerian model able to use the advantages of an Eulerian framework for the dense part. Some authors modified that model by adding a switch to a Lagrangian framework when liquid droplets are dispersed enough, creating what is called the Eulerian-Lagrangian Spray Atomization (ELSA) model [36, 37]. On the other hand, some other authors kept the Eulerian approach and improved some of the aspects of the original version, creating the $\Sigma - Y$ model [32, 38–40].

From another point of view, it is well known that the nozzle geometric parameters have a great influence on the spray behavior [41, 42]. Thus, coupling internal and external flow simulations of the Diesel injection process leads to a better representation of reality and therefore better understanding of the physics involved. Coupling is usually done by a two-step methodology [33, 43], transferring spatial and temporal distributions of all fields (velocity, turbulent kinetic energy, dissipation rate, void fraction...) from the internal flow simulation to a primary break-up model which uses them to initialize droplet properties (size, velocity, etc.). Some information is lost in this coupling procedure, as well as the effect of the discharge vessel conditions on the nozzle flow.

Then, a model capable of seamlessly simulating internal and external flows seems necessary. Thus, internal flow parameters, which are key to determine the atomization at high Webber numbers, could be somehow considered. Its development is the main objective of this Thesis. Nonetheless, that is a very ambitious objective and some simplifications are required. For this first attempt, the most important simplification is that only two-phases, liquid fuel and ambient gas, are modeled. Then, phase changes processes such cavitation or evaporation are not considered. Second simplification is assumed mainly to reduce as much as possible the complexity of the computational model: needle movement is not modeled, the needle position is kept fixed in every simulation. Therefore, this work presents an Eulerian model, which is the best approach to study dense mixtures. That model is capable of simulating the internal nozzle flow and the liquid vein atomization in the same domain (at the same time). Liquid atomization is modeled through a diffusion law, and phenomena such liquid compressibility and heat transfer are also included in the model.

Many challenges are associated with simulating realistic turbulent atomization, such as the multiplicity of length and time scales of the turbulent flow field and gas-liquid interface, discontinuous fluid properties and pressure at the phase interface, high density ratios that degrade numerical robustness, and complex shapes of spray injectors [44]. Previous progresses in Eulerian spray models made the development of this Thesis possible. Until now, there was no existing computational tool which could be applied to both types of flows, internal and external. Furthermore, no one else before attempted to simulate the whole spray at once. The relatively short experience of CMT-Motores Térmicos, where the present Thesis is carried out, with this type of spray models was also essential to ensure the success of the present work [32, 45].

The skeleton to build the new model, so called Eulerian Spray Atomization (ESA) model, is OpenFOAM ®, an object-oriented, free, open source CFD software package developed by OpenCFD Ltd. It has a large user base across most areas of engineering and science, from both commercial and academic organizations. By being open, OpenFOAM offers users complete freedom to customize and extend its existing functionality. It follows a highly modular code design in which collections of functionality (e.g. numerical methods, meshing, physical models...) are each compiled into their own shared library. Executable applications are then created that are simply linked to the library functionality.

With the brand new developed ESA model it is possible to obtain some unique results, such the influence of a single internal nozzle geometrical parameter into the spray formation or the effect of changing one of the properties of the fuel. Spray near-nozzle field is the focus of this Thesis, just because that is the area where DDM Lagrangian models lack of accuracy.

1.3   Thesis outline

This Thesis deals with the development of a model which is able to predict the internal flow pattern together with the spray structure, in other words, the spray break-up. To do so, it is required the combination of some existing tools and libraries with a few new sub-models. CFD software OpenFOAM, which is free and open source, is the base where all equations are assembled. The development process and details of the final model are presented in this document.

After this brief introduction (Chapter 1), the injection process is discussed in the context of Diesel engine and the critical requirement presented together

with trends and technological development. This forms Chapter 2. It starts describing the key aspects of the Diesel engine and the common-rail system, but focuses on the flow characteristics inside the nozzle (internal flow) and outside the injector (Diesel spray). Phenomena that take place during an injection, such cavitation of liquid break-up, are also described, at least what is known at the time this Thesis is being written.

Following this fundamental chapter, a deep review of techniques available to model the spray formation and evolution is given in Chapter 3. Methodologies that have been employed by other authors for years are described and analyzed, so advantages and drawbacks are known. The main intention of this review is to select the approach to study the full injection process, from upstream the needle to the air-liquid mixture formation. Homogeneous flow model turns out to be the best way of study the different time- and length-scales that occur in the Diesel injection process.

However, some sub-models are required to calculate the flow behavior, for example, the dependency of the liquid properties on the thermodynamic variables (pressure and temperature). This and the rest of the sub-models that have been used or developed are explained in Chapter 4. Not only the equations and sub-models are studied in this chapter, also the structure of the solver: order of the equations, loops to solve them, updates positions, etc.

Every new model needs validation. Chapter 5 attends this requirement. In first place, verification assessment is done by comparing results obtained by the model with analytical and high accurate solutions of simplified problems. Secondly, the model is used to replicate a large experimental database with the aim of completing the validation assessment. Thus, strengths and flaws of the model are highlighted. All experimental trends are well reproduced by the model but the transients, concretely, the opening of the injector.

Chapter 6 presents the first set of results. They are related to the numerics and parameters of the code. The objective of this chapter is to improve the accuracy and the computational cost of the model. Then, results are compared with high accurate DNS results to check the effect of numerical schemes. Those DNS results are also used to adjust some constants of the atomization model. At the end of the chapter, a D-optimal design of experiments is carried out to minimize the differences between the model and the experiments in spray penetration at short times after start of injection.

Up to that point, the model can be used to obtain some unique results. Chapter 7 displays the spray metrics, i.e. discharge coefficient or spray penetration, for different geometries and injection conditions. Though the analysis

is performed following the classical approach of splitting the injection process into internal and external flows, it is important to keep in mind that the solution is only one. Then, effects of changing internal parameters can be easily seen in the spray. This model also allows to study the influence of fluid properties one by one, for example, changing only its density or its viscosity.

The last chapter, Chapter 8, draws the main conclusions of this Thesis contrasting all the new information brought indicating the possible directions in which to orient to future studies.

References

[1]   *On type-approval of motor vehicles and engines with respect to emissions from heavy duty vehicles (Euro VI) and on access to vehicle repair and maintenance information and amending Regulation (EC) No 715/2007 and Directive 2007/46/EC and repealing Directives 80/1269/EEC and 2005/78/EC.* English. Official Journal of the European Union. Regulation. Eurpoean Union, 2009 (*cit. on p. 1*).

[2]   Payri, F., J. M. Desantes, and et al. *Motores de combusitión interna alternativos.* Ed. by F. Payri and J. M. Desantes. First edition. Loreto 13-15, Local B, 08029 Barcelona, Spain: Editorial Reverté, 2011 (*cit. on p. 1*).

[3]   Pickett, L. M. *Engine Combustion Network.* English. Sandia National Laboratories. 2014. URL: http://www.sandia.gov/ecn/ (*cit. on p. 2*).

[4]   Linne, M. "Imaging in the optically dense regions of a spray: A review of developing techniques". *Progress in Energy and Combustion Science*, vol. 39.5 (2013), pp. 403–440. DOI: 10.1016/j.pecs.2013.06.001 (*cit. on p. 2*).

[5]   Kastengren, A. L. and C. F. Powell. "Spray density measurements using X-ray radiography". *Proceedings of the Institution of Mechanical Engineers, Part D: Journal of Automobile Engineering*, vol. 221.6 (2007), pp. 653–662. DOI: 10.1243/09544070JAUTO392 (*cit. on pp. 2, 3*).

[6]   Bosch, W. "The Fuel Rate Indicator: A New Measuring Instrument For Display of the Characteristics of Individual Injection". *SAE Technical Paper 660749* (1966). DOI: 10.4271/660749 (*cit. on p. 3*).

[7]   Gimeno, J. "Desarrollo y aplicación de la medida de flujo de cantidad de movimiento de un chorro Diésel". PhD thesis. Camino de Vera, s/n, 46022, Valencia, Spain: Departamento de Máquinas y Motores Térmicos, Universitat Politècnica de València, 2008 (*cit. on pp. 3, 4*).

[8]   Salvador, F. J. "Estudio teórico experimental de la influencia de la geometría de toberas de inyección Diésel sobre las características del flujo interno y del chorro". PhD thesis. Camino de Vera, s/n, 46022, Valencia, Spain: Departamento de Máquinas y Motores Térmicos, Universitat Politècnica de València, 2003 (*cit. on pp. 3, 4*).

[9]   Walther, J. "Quantitative Untersuchungen der Innenströmung in kavitierenden Dieseleinspritzdüse". PhD thesis. Karolinenplatz 5, 64289 Darmstadt, Germany: TU Darmstadt, 2002 (*cit. on p. 3*).

[10] Pereira, H̃. V. "Estudio del fenómeno de la cavitación en la inyección diésel mediante la visualización del flujo interno en orificios transparentes". PhD thesis. Camino de Vera, s/n, 46022, Valencia, Spain: Departamento de Máquinas y Motores Térmicos, Universitat Politècnica de València, 2014 (*cit. on pp. 3, 4*).

[11] Winklhofer, E., E. Kull, E. Kelz, and A. Morozov. "Comprehensive hydraulic and flow field documentation in model throttle experiments under cavitation conditions". *23rd Annual Conference on Liquid Atomization & Spray Systems (ILASS Europe)*. Ed. by B. Ineichen. Zurich, Switzerland, 2001, pp. 574–579 (*cit. on p. 3*).

[12] Siebers, D. L. "Liquid-Phase Fuel Penetration in Diesel Sprays". *SAE Technical Paper 980809* (1998). DOI: 10.4271/980809 (*cit. on p. 3*).

[13] Payri, R., F. J. Salvador, J. Gimeno, and L. D. Zapata. "Diesel nozzle geometry influence on spray liquid-phase fuel penetration in evaporative conditions". *Fuel*, vol. 87.7 (2008), pp. 1165–1176. DOI: 10.1016/j.fuel.2007.05.058 (*cit. on p. 3*).

[14] Ghandhi, J. B. and D. M. Heim. "An optimized optical system for backlit imaging". *Review of Scientific Instruments*, vol. 80.5 (2009), pp. 1–3. DOI: 10.1063/1.3128728 (*cit. on p. 3*).

[15] Settles, G. S. *Schlieren and shadowgraph techniques: visualizing phenomena in transparent media*. Ed. by Springer. First edition. Heidelberg, Germany: Springer, 2001 (*cit. on p. 3*).

[16] Yue, Y., C. F. Powell, R. B. Poola, J. Wang, and J. K. Schaller. "Quantitative measurements of diesel fuel spray characteristics in the near-nozzle region using X-ray absorption". *Atomization and Sprays*, vol. 11.4 (2001), pp. 471–490 (*cit. on p. 3*).

[17] Payri, R., L. Araneo, J. S. Shakal, and V. Soare. "Phase doppler measurements: System set-up optimization for characterization of a diesel nozzle". *Journal of Mechanical Science and Technology*, vol. 22.8 (2008), pp. 1620–1632. DOI: `10.1007/S12206-008-0432-7` (*cit. on p. 3*).

[18] Hillamo, H., O. Kaario, and M. Larmi. "Particle Image Velocimetry Measurements of a Diesel Spray". *SAE Technical Paper 2008-01-0942* (2008). DOI: `10.4271/2008-01-0942` (*cit. on p. 3*).

[19] Arrègle, J. "Análisis de la estructura y dinámica interna de chorros diésel". PhD thesis. Camino de Vera, s/n, 46022, Valencia, Spain: Departamento de Máquinas y Motores Térmicos, Universitat Politècnica de València, 1998 (*cit. on p. 4*).

[20] Correas, D. "Estudio teórico-experimental del chorro libre diésel isotermo". PhD thesis. Camino de Vera, s/n, 46022, Valencia, Spain: Departamento de Máquinas y Motores Térmicos, Universitat Politècnica de València, 1998 (*cit. on p. 4*).

[21] Ruiz, S. "Estudio teórico-experimental de los procesos de atomización y de mezcla en los chorros diésel D.I." PhD thesis. Camino de Vera, s/n, 46022, Valencia, Spain: Departamento de Máquinas y Motores Térmicos, Universitat Politècnica de València, 2003 (*cit. on p. 4*).

[22] López, J. J. "Estudio teórico-experimental del chorro libre diésel no evaporativo y de su interacción con el movimiento del aire". PhD thesis. Camino de Vera, s/n, 46022, Valencia, Spain: Departamento de Máquinas y Motores Térmicos, Universitat Politècnica de València, 2003 (*cit. on p. 4*).

[23] García-Oliver, J. M. "Aportaciones al estudio del proceso de combustión turbulenta de chorros en motores de inyección directa". PhD thesis. Camino de Vera, s/n, 46022, Valencia, Spain: Escuela Técnica Superior de Ingenieros Industriales, Universitat Politècnica de València, 2004 (*cit. on p. 4*).

[24] Morena, J. de la. "Estudio de la influencia de las características del flujo interno en toberas sobre el proceso de inyección Diésel en campo próximo". PhD thesis. Camino de Vera, s/n, 46022, Valencia, Spain: Departamento de Máquinas y Motores Térmicos, Universitat Politècnica de València, 2011 (*cit. on p. 4*).

[25]   León, G. C. B. "Experimental and theoretical study of the direct Diesel injection process at low temperatures". PhD thesis. Camino de Vera, s/n, 46022, Valencia, Spain: Departamento de Máquinas y Motores Térmicos, Universitat Politècnica de València, 2011 (*cit. on p. 4*).

[26]   Bardi, M. "Partial needle lift and injection rate shape effect on the formation and combustion of the Diesel spray". PhD thesis. Camino de Vera, s/n, 46022, Valencia, Spain: Departamento de Máquinas y Motores Térmicos, Universitat Politècnica de València, 2014 (*cit. on p. 4*).

[27]   Martínez-López, J. "Estudio computacional de la influencia del levantamiento de aguja sobre el flujo interno y el fenómeno de la cavitación en toberas de injección Diésel". PhD thesis. Camino de Vera, s/n, 46022, Valencia, Spain: Departamento de Máquinas y Motores Térmicos, Universitat Politècnica de València, 2013 (*cit. on p. 4*).

[28]   Pinzello, A. "Analysis of fuel sprays and combustion processes in Diesel engines with a combined approach of CFD and phenomenological models." PhD thesis. Camino de Vera, s/n, 46022, Valencia, Spain: Departamento de Máquinas y Motores Térmicos, Universitat Politècnica de València and Dipartamento di Energetica, Politecnico di Torino, 2008 (*cit. on p. 4*).

[29]   Chávez Cobo, M. d. J. "Modelado CFD Euleriano-Lagrangiano del chorro diésel y evaluación de su combinación con modelos fenomenológicos y unidimensionales." PhD thesis. Camino de Vera, s/n, 46022, Valencia, Spain: Departamento de Máquinas y Motores Térmicos, Universitat Politècnica de València, 2013 (*cit. on p. 4*).

[30]   Laborda, J. M. M. "Engineering Large Eddy Simulation of Diesel sprays". PhD thesis. Camino de Vera, s/n, 46022, Valencia, Spain: Departamento de Máquinas y Motores Térmicos, Universitat Politècnica de València, 2014 (*cit. on p. 4*).

[31]   Dung, K.-A. "The Eulerian-Lagrangian Spray Atomization (ELSA) model of the jet atomization in CFD simulations: evaluation and validation". PhD thesis. Camino de Vera, s/n, 46022, Valencia, Spain: Departamento de Máquinas y Motores Térmicos, Universitat Politècnica de València, 2012 (*cit. on p. 4*).

[32]   García-Oliver, J. et al. "Diesel spray CFD simulations based on the $\Sigma - Y$ eulerian atomization model". *Atomization and Sprays*, vol. 23.1 (2013), pp. 71–95. DOI: 10.1615/AtomizSpr.2013007198 (*cit. on pp. 4–6*).

[33]   Battistoni, M., C. N. Grimaldi, and F. Marianni. "Coupled Simulation of Nozzle Flow and Spray Formation Using Diesel and Biodiesel for CI Engine Applications". *SAE Technical Paper 2012-01-1267* (2012). DOI: `10.4271/2012-01-1267` (*cit. on p. 5*).

[34]   Lee, C. H. and R. D. Reitz. "CFD simulations of diesel spray tip penetration with multiple injections and with engine compression ratios up to 100:1". *Fuel*, vol. 111 (2013), pp. 289–297. DOI: `10.1016/j.fuel.2013.04.058` (*cit. on p. 5*).

[35]   Vallet, A., A. A. Burluka, and R. Borghi. "Development of a Eulerian model for the "Atomization" of a liquid jet". *Atomization and Sprays*, vol. 11.6 (2001), pp. 619–642 (*cit. on p. 5*).

[36]   Blokkel, G., B. Barbeau, and R. Borghi. "A 3D Eulerian Model to Improve the Primary Breakup of Atomizing Jet". *SAE Technical Paper 2003-01-0005* (2003). DOI: `10.4271/2003-01-0005` (*cit. on p. 5*).

[37]   Lebas, R., G. Blokkel, P. A. Beau, and F. X. Demoulin. "Coupling Vaporization Model With the Eulerian-Lagrangian Spray Atomization (ELSA) Model in Diesel Engine Conditions". *SAE Technical Paper 2005-01-0213* (2005). DOI: `10.4271/2005-01-0213` (*cit. on p. 5*).

[38]   Beheshti, N., A. A. Burluka, and M. Fairweather. "Assessment of $\Sigma - Y_{liq}$ model predictions for air-assisted atomisation". *Theoretical and Computational Fluid Dynamics*, vol. 21.5 (2007), pp. 381–397. DOI: `10.1007/s00162-007-0052-3` (*cit. on p. 5*).

[39]   Ning, W., R. D. Reitz, R. Diwakar, and A. M. Lippert. "An Eulerian-Lagrangian Spray and Atomization model with improved turbulence modeling". *Atomization and Sprays*, vol. 19.8 (2009), pp. 727–739. DOI: `10.1615/AtomizSpr.v19.i8.20` (*cit. on p. 5*).

[40]   Lebas, R., T. Ménard, P. A. Beau, A. Berlemont, and F. X. Demoulin. "Numerical simulation of primary break-up and atomization: DNS and modelling study". *International Journal of Multiphase Flow*, vol. 35.3 (2009), pp. 247–260. DOI: `10.1016/j.ijmultiphaseflow.2008.11.005` (*cit. on p. 5*).

[41]   Desantes, J. M., R. Payri, F. J. Salvador, and V. Soare. "Study of the Influence of Geometrical and Injection Parameters on Diesel Sprays Characteristics in Isothermal Conditions". *SAE Technical Paper 2005-01-0913* (2005). DOI: `10.4271/2005-01-0913` (*cit. on p. 5*).

[42] Bermúdez, V., R. Payri, F. J. Salvador, and A. H. Plazas. "Study of the influence of nozzle seat type on injection rate and spray behaviour". *Proceedings of the Institution of Mechanical Engineers, Part D: Journal of Automobile Engineering*, vol. 219.5 (2005), pp. 677–689. DOI: 10.1243/095440705X28303 (*cit. on p. 5*).

[43] Som, S. and S. K. Aggarwal. "Effects of primary breakup modeling on spray and combustion characteristics of compression ignition engines". *Combustion and Flame*, vol. 157.6 (2010), pp. 1179–1193. DOI: 10.1016/j.combustflame.2010.02.018 (*cit. on p. 5*).

[44] Desjardins, O., J. O. McCaslin, M. Owkes, and P. T. Brady. "Direct numerical and large-eddy simulation of primary atomization in complex geometries". *Atomization and Sprays*, vol. 23.11 (2013), pp. 1001–1048. DOI: 10.1615/AtomizSpr.2013007679 (*cit. on p. 6*).

[45] Hoyas, S., A. Gil, X. Margot, D. Khuong-Anh, and F. Ravet. "Evaluation of the Eulerian-Lagrangian Spray Atomization (ELSA) model in spray simulations: 2D cases". *Mathematical and Computer Modelling*, vol. 57.7-8 (2013), pp. 1686–1693. DOI: 10.1016/j.mcm.2011.11.006 (*cit. on p. 6*).

Chapter 2

Fundamentals of direct injection in Diesel engines

2.1 Introduction

Direct injection in the Diesel engine is, from many years ago, the most employed way to introduce the fuel in the combustion chamber [1]. This method imposed itself as the dominant technology in diesel engines thanks to the substantial increase in efficiency and reduction in size of the engine head, consequent to the elimination of the pre-chamber. However, by definition, the fuel has to mix and ignite directly within the combustion chamber: this fact has represented the main drawback of this system pushing to a continuous innovation in the technology as well as strategies.

In this chapter, the fundamentals of the direct injection are described highlighting the critical achievements that led to more performing injection systems. The short summary presented refers to a global understanding result of decades of research and well-established results obtained in the field of Diesel engines [1]. As the most important element of the Diesel injection system, the performance of the injector is explained in detail. The accuracy in the control of the injection parameters (e.g. injection pressure) and the flexibility of the injection system oriented to the extension of the available injection strategies are the key points in that topic.

Furthermore, in order to improve the quality of the air-fuel mixture and then the combustion efficiency, the dynamics of the spray formation should

be completely understood. Due to the implicit turbulent nature of the atom-
ization process and to the transient character of the spray formation (small
length- and time-scales), the spray formation is a very complex phenomenon
that still remains the real cornerstone of the success of the Diesel injection. A
summary of the physics involved in the this complex process is given also in this
chapter, dividing the study in two: phenomena associated to the flow inside
the injector nozzle (internal flow); and phenomena associated to the breaking
of the liquid core, droplet formation and evaporation (external flow).

2.2 Diesel injection systems

The fuel delivery system of an engine must accomplish the following general
tasks or goals:

- Deliver the required amount of fuel into the combustion chamber at the
  appropriate time, synchronized with the movement of the piston engine.
  These aspects determine the development of the different phases of the
  combustion process [2].

- Mix the fuel with the compressed air in a fast and efficient way.

- Enhance the atomization phenomenon in order to increase the air-fuel
  interface surface and then accelerate the fuel evaporation process.

(a) Indirect injection   (b) Direct injection
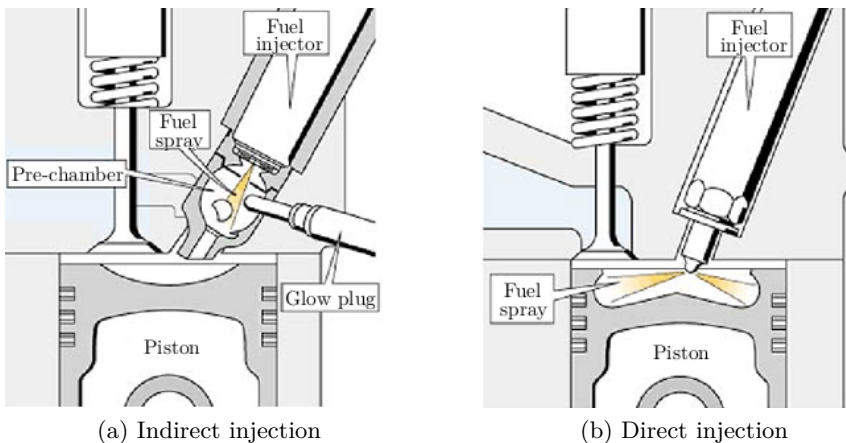
Figure 2.1: Sketch of an indirect and a direct injection Diesel engine.

According to how the fuel is delivered into the combustion chamber, injection systems can be classified in two categories: indirect injection (IDI) and direct injection systems (DI). An indirect injection engine, sketched in Figure 2.1a, delivers fuel into a chamber off the combustion chamber (placed at some point before the intake valve), called a pre-chamber, where the combustion begins and the spreads into the main combustion chamber. In direct-injection engines, sketched in Figure 2.1b, the fuel is directly injected into the combustion chamber, and this fact creates a tide link between the injection event (air-fuel mixing) and the heat released during the combustion. Therefore, the performance of the fuel delivery system in general and more concretely of the injector is one of the key aspects in a DI engine design.

Figure 2.1 also shows main differences in the piston head for this two type of engines. Low turbulence levels are found inside DI engine cylinders due to low air velocities through the intake valve (about 25 m/s). Thus, the shape of the piston head for DI engines plays an important role in the air-fuel mixing by increasing the swirl of the air flow inside the cylinder. Nonetheless, the convective field of the fuel and not the air is the main responsible of the mixing, and this leads towards more advanced injections systems to enhance the fuel atomization by the use of, for example, multi-hole nozzles with orifice diameters around 0.1 mm and very high injection pressure, even greater than 200 MPa. On the other hand, in IDI engines, the air moves from the cylinder to the pre-chamber during the compression stroke, forming a turbulent vortex due to the geometry of the chamber, which stimulates the air-fuel mixing. Injection conditions (fuel inlet velocity, liquid distribution, exit orifice diameter...) are not as relevant in IDI engines as in DI engines, and therefore single-hole nozzles with orifice diameters around 1 mm and low injection pressures $(20 - 40$ MPa$)$ are used.

Lower surface/volume ratio, then lower heat losses, and absence of air pressure losses when it moves through orifices lead the DI systems to a higher efficiency. And because of this, IDI systems fell into obsolescence [1].

2.2.1 Diesel direct injection systems

Among the Diesel DI systems nowadays available in the market, the most employed ones and their main characteristics are listed below:

- Rotary pump: first in history combustion-ignition DI systems, they are compound by a high-pressure pump which delivers the fuel to an injector, whose only purpose is the atomization of the fuel. The main drawback

of this type of injection is the lack of regulation of the injection pressure, which depends only on the engine speed. Thus, keep a constant injection pressure for a certain period of time is not possible.

- Unit injector: the pump and the injector are included in the same device, placed at the cylinder head. The pump plunger is driven directly by the camshaft. The start of injection (SOI) and the injection duration are controlled by a solenoid valve located inside each injector. Being able to electronically control the system by the Electronic Control Unit (ECU) together with the high injection pressures reached in this system are the main advantages.

- Unit pump: is an alternative to the previous system in which the pump and the injector are connected through a short high-pressure pipe. This system also allows obtaining high injection pressures and control the SOI and the injection duration with a solenoid valve located at each pump of each cylinder.

- Accumulation system (common-rail): is based on accumulating fuel at high pressure in a volume located between the pump and the injector, where it is stored until injected. The pump, driven by the crankshaft, just delivers the required mass flow meanwhile the injector manages the air-fuel ratio and atomization of the fuel.

The common-rail is currently the most employed injection system in Diesel engines, nearly in the totality of the automotive applications and in most of the Diesel engine in general. In fact, at the current state of maturity, it is the system that matches the most the requirements of the automotive market [3] that, due to the variability of the working conditions typical of this applications, requires an extreme flexibility of the injection system.

2.2.2   Common-rail Diesel injection system

Figure 2.2 represents the main components and layout of a typical common-rail system [4]. A low pressure pump, generally placed in the fuel tank, feeds the fuel to the high-pressure pump. This second pump, mechanically connected to the engine (the crankshaft), provides a certain fuel mass flow rate abundantly higher than the average one required by the engine. The fuel is directed to the rail, which is connected to the injectors. A flow valve combined with a pressure sensor control the pressure of the fuel in the rail, diverting part of the fuel that is not injected to the fuel tank.
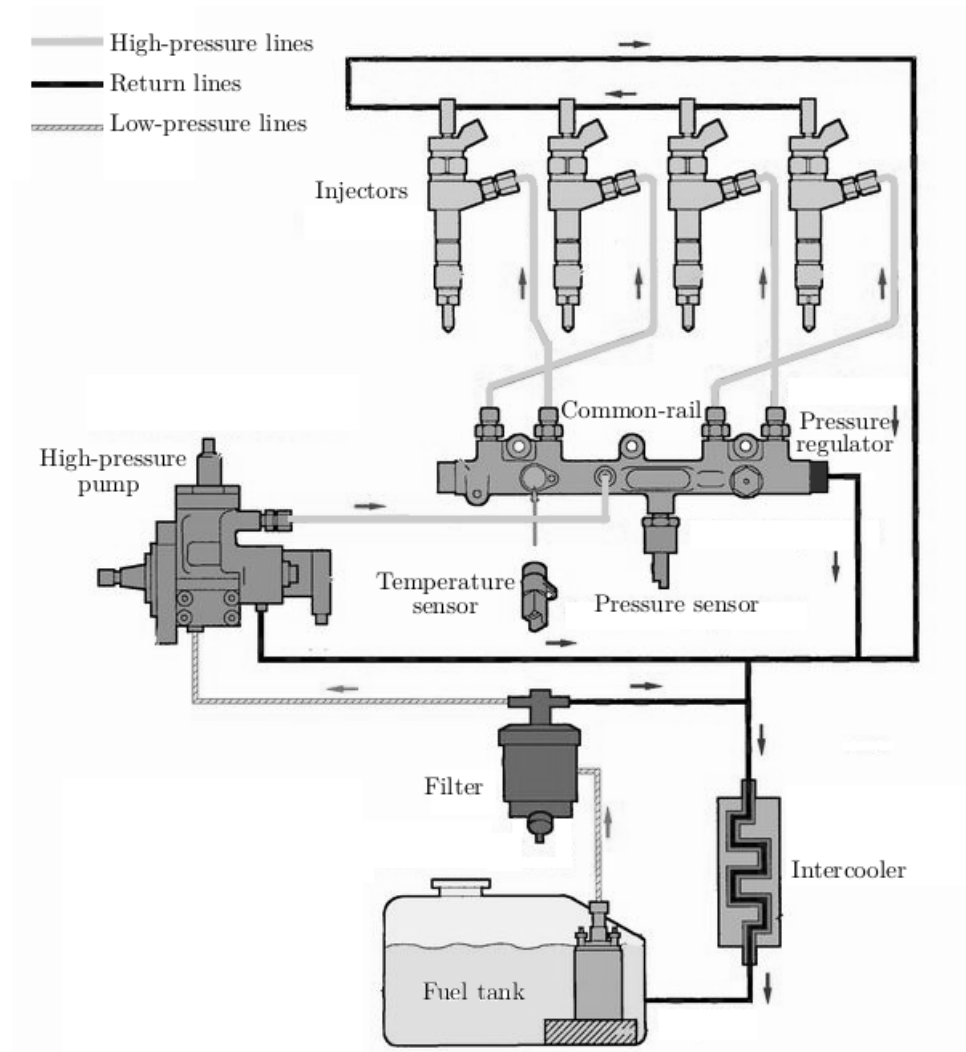
Figure 2.2: Components and layout of a typical common-rail system.

In this way, a relatively high fuel volume (rail and high-pressure pipes) is maintained at high and constant pressure. The rail acts like an accumulator limiting on the one hand, the fluctuations related to the high pressure pump and, on the other hand, the pressure drop occurring at the opening of one of the injectors [4]. The injectors, connected to the rail through short high pressure lines (typically $100 - 200$ mm long), are actuated independently by the

ECU. Third generation common-rail Diesel engines now feature piezoelectric injectors for increased precision, with fuel pressures up to 300 MPa [5].

The fundamental advantage of this injection system is the fact that the rail pressure and the timing of the injectors opening and closing are completely released by the engine operating conditions and it is controlled electronically. In fact, a part from the rail pressure, the ECU is connected to a wide number of sensors (i.e. engine speed, throttle position...), providing information needed to understand the particular working condition of the engine. Additionally, the possibility of controlling independently the pressure of the fuel and the injection timing allows to adapt the most suitable injection strategy for each condition, topic which is still an ongoing research [6, 7].

Therefore, the common-rail system, with respect to other technologies described in previous sections, presents the following benefits:

- more control on the start and duration of the injection;
- accuracy on the injected mass;
- release the injection system from the engine operating condition;
- maximize the control on the mass flow rate.

2.2.3   The common-rail Diesel injector

Among all elements mentioned in previous Section §2.2.2 and represented in Figure 2.2, the injector is certainly the most complex organ of the common-rail system. Main elements composing a common-rail injector are shown later in Figures 2.4 and 2.5 and can be branched in the following main components:

- Injector nozzle. The injector nozzle generally has several orifices (typically from 5 to 10 in automotive applications). In this branch, the needle is also included, which has the function of controlling the fuel through the nozzle orifices.

- Connecting rod. The connecting rod transmits the movement from the servo-actuated circuit to the nozzle needle. The top of the needle pushes against the bottom of this component.

- Servo actuated system. This mechanism is composed by an actuator (solenoid or piezoelectric), a fuel valve and a control volume. This is the core of the injector and allows to generate the forces needed to move the needle effectively during the injection.

The schematic presented in Figure 2.3 [8] illustrates the working principle of the servo actuated injector highlighting the different phases of the injector. The fuel, coming from the rail through the high pressure line, is divided into two channels right after the entrance: one goes down toward the nozzle and the other goes to the control volume. The control volume, located at the top of the connecting rod, is endowed with two calibrated orifices: one connected to the injector entrance and the other to the low pressure return line; the fuel flow through this second channel is controlled by the solenoid/piezoelectric valve. When the solenoid/piezoelectric crystal is not activated (rest condition), the valve is closed and no flow can exit from the control volume. Consequently, the fuel pressure in the control volume is equivalent to the fuel pressure in the feeding line, and since the area at the top of the connecting rod is higher than that of needle, the resultant force pushes the connecting rod and then the needle toward the nozzle, closing all orifices. Even without pressure, this position is maintained by a preloaded spring.
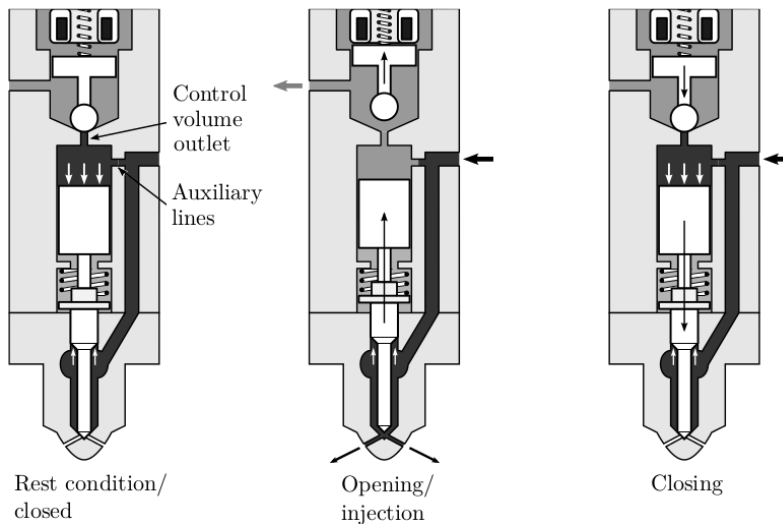
Figure 2.3: Working principle of a typical common-rail injector.

Once the solenoid/piezoelectric crystal is activated, the valve opens and the fuel flows through the outlet of the control volume. Due to the specific design of the calibrated orifices, the fuel flow generated causes a significant decrease of pressure in this region of the injector. As a consequence of that, the pressure at the top of the connecting rod is lower and the high pressure at the bottom of the needle makes the connecting rod and the needle go up. Once the

needle is lifted, the fuel can flow through the orifices and the injection starts. When the solenoid/piezoelectric crystal is deactivated, the flow through the control volume stops, causing the fuel pressure to rise again and leading the forces acting on the connecting rod and the needle to the initial conditions. This pushes the needle down until its seat, blocking the fuel flow through the orifices and thus ending the injection.

Different solutions have been implemented during the last years, improving the accuracy and the rapidity of the injector actuation. In particular, the reduction of the inertia of the connecting rod (even dispense with it) and needle system and the effectiveness of the actuator allowed to reduce significantly the time lag between the electric signal and the injection event, allowing the implementation of a higher number of injections during each cycle.

Solenoid driven injectors

Main components of a solenoid injector are shown in Figure 2.4: the electro-magnetic valve, the injector holder (which includes the high pressure fitting, the fuel return line, the filter, the body, the spring and the rod) and the nozzle.
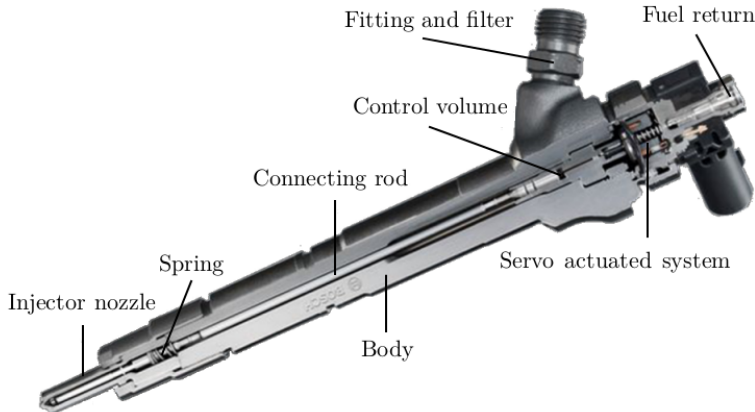
Figure 2.4: Main components of a solenoid driven injector. Image of a Bosch CRI2-20 injector.

By the time an injection is required, the ECU sends an electric pulse whose width defines the injection duration and then the injected mass. That pulse excites a coil, generating an electromagnetic field which induces an upward force over the servo actuator rod (see Figure 2.3, rod-ball assembly over the control volume outlet), then opening the valve. When the electric pulse ends,

the rod of the servo actuator goes back to its resting position, closing the valve.

Piezoelectric driven injectors

Figure 2.5 shows the internal components of this kind of injector: the piezoelectric valve (which consists of the piezoelectric actuator, the hydraulic amplifier and the control valve), the injector holder (which includes the high pressure fitting, the fuel return line, the filter, the body and the spring) and the nozzle.
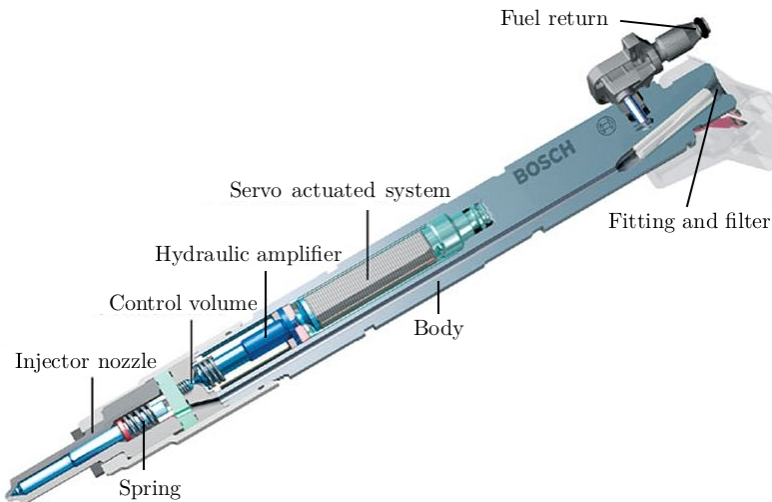
Figure 2.5: Main components of a piezoelectric driven injector. Image of a Bosch injector family.

The piezoelectric effect allows to replace some of the mobile elements and the connecting rod by a piezoelectric crystal which is compressed or expanded in function of the applied electric field. The working principle is the same, but it is the piezoelectric crystal, and not the solenoid valve, which opens or closes the outlet orifice of the control volume. Then, the main advantages of this type of injector are:

- Fast response to opening and closing signals. This allows multiple injections strategies which are associated to a reduction in noise and emissions.

- High accuracy. The piezoelectric crystal allows needle displacements of the order of magnitude of nanometers just by changing the electric tension applied to it.

- Absence of attrition after millions of cycles.

There are other mechanical differences. Unlike the typical solenoid injector whose control volume has two active orifices, one inlet and one outlet, the piezoelectric injector control volume has three, one outlet and two inlet, and the outlet orifice also works as an inlet. Furthermore, the control volume is placed directly over the needle, which improves the dynamic response of the injector and facilitates the introduction of multiple injection (up to eight consecutive injections).

When the actuator is activated, it expands, displacing the amplifier piston, which compresses the fuel located between the lower part of the amplifier piston and the upper part of the command piston. The shape of the volume between the piezoelectric-actuator and the amplifier piston amplifies the vertical displacement of the system, opening the upper seat of the control valve and closing the lower one. At these conditions, the decrease in pressure in the control volume causes the movement of the needle and the consequent start of injection.

Further improvements in Diesel injectors

Despite the injector performance improved considerably, previously described injectors can work only in on/off mode, allowing a high control on the injection timing and duration, but leaving the shape of the mass flow rate profile a dependent parameter, related above all to the injection pressure. Even if the pressure in the rail is a well controlled parameter, it is difficult to adjust this quantity in cycle-to-cycle timing, and even more, to have a control on it capable of modifying accurately the shape of the injection rate profile.

The hydraulic amplifier or piston amplifier system allows a partial modulation of the mass flow rate during the injection. This solution, called from Bosch Hydraulic Amplifier Diesel Injection System (HADIS) [9, 10] has been adopted by different manufacturers (e.g. Bosch, Delphi) and allows to inject fuel at two different pressure levels: the rail pressure and a higher pressure obtained thanks to the action of a piston amplifier. However, the complication of the system, together with the limited flexibility generated, limit the appeal of this solution [10].

A similar system has been adopted by Caterpillar in the so called HEUI system (hydraulically acutated, electronically controlled unit injector) [11]. In

this system, a fuel high-pressure pump is combined to the availability of high-pressure oil. As in the previous system, the injector can work in non-amplified mode at the line fuel pressure, and in an amplified mode, in which case the amplifier piston is activated by the oil and its movement can be modulated thanks to the actuation valve. The implementation of this system is limited by the need of high pressure oil, that is normally not available in automotive vehicles.

In comparison to conventional servo hydraulic actuated technology, the direct acting system proposed by Delphi in their DFI3 generation eliminates the usual four step servo hydraulic actuated concept down to a single step: the direct actuation of the needle through a hydraulic amplifier by a piezoelectric-ceramic actuator [12]. Unlike a servo actuated injector, the force change needed for the needle opening is provided by a piezoelectric-actuator that is decoupled from the rail pressure supply. It is therefore possible to adapt the force change delivered by the actuator electronically as required. Moreover, this injector contains an internal volume of fuel and does not have any back-leak, which simplifies the installation and eliminates the need for fuel return lines and inter-coolers even when operating at 200 MPa. Thanks to this configuration, the maximum needle speed is increased from 1 m/s to 3 m/s. Besides, the needle speed is not dependent on rail pressure and so it is maintained even at very low rail pressure [12].

The Continental direct-acting (CDA) injector has the outstanding feature to set into motion the nozzle needle by the direct coupling between the piezoelectric actuator and the nozzle needle itself. Opposite to the solution presented by Delphi, the CDA provides a mechanical coupling between the piezoelectric crystal and the nozzle needle through the introduction of a leverage system. The leverage system has the function to overcome the limited deformations of piezoelectric actuator, amplifying them and causing a larger displacement of the needle. Thereby, the limiting open-close working mode is extended to a variety of controlled needle movements. Both the intrinsic fast time-response of the piezoelectric crystal actuator and the capability of the ECU to generate complex electric signals, promise to control accurately the needle position and to throttle the fuel flow through changes of the electronic signal to the injector [13]. However, if the injection pressure varies, the voltage applied to the piezoelectric crystal needs to be adjusted to obtain the same lift; and when the temperature of the crystal increases the related deformation of the actuator lowers, so the injector temperature control has to be accurate [14].

2.3   Internal flow

In order to fully understand the air-fuel mixing process in Diesel engines, it is necessary to know the flow conditions inside the nozzle because they define the behavior of the spray. The fuel hydrostatic energy stored in the rail forces the fuel to flow through the injector and eventually enter in the combustion chamber through the nozzle orifices. Processes taking place in this phase fall in the forced internal flow category since the fuel is forced to move through the injector channels and valves by a pressure difference. The transformations involved are mainly variation in pressure and velocity, energy dissipation and is some cases the formation of fuel vapor due to the presence of regions at very low pressure (cavitation).

2.3.1   Forced internal flow

The Bernoulli equation (Equation (2.1)), that can be considered as a statement of the energy transport equation applied to the non-viscous flow of incompressible fluids, is generally presented as a starting point to face forced internal flow problems:

$$\frac{p}{\rho} + \frac{u^2}{2} + gz = \text{const.} \tag{2.1}$$

Three characteristic terms can be distinguished in Equation (2.1): the elevation gz, normally neglected in automotive applications since the elevation differences are modest; the pressure p/ρ; and the dynamic pressure $0.5u^2/g$. Nonetheless, the transformation from potential to kinetic energy is incomplete without any viscous dissipation Φ_{visc}, a term which cannot be neglected in real applications. The term Φ_{visc} accounts the total viscous losses of the flow and is the responsible of the pressure losses observed when a real fluid flows in a pipe. The determination of this term is always complex and many studies in the past were and are carried out to characterize it [15–17]. The quantity Φ_{visc} is the result of the sum of two terms: the minor losses $\Phi_{visc,m}$ and the major losses $\Phi_{visc,M}$. The minor losses, also called singular pressure losses, are related to sudden changes in the shape or in the direction of the channel driving the flow. In these cases, the fluid cannot completely follow the internal shape of the channel and a separation of the boundary layer may occur. This separation results in the apparition of a recirculation zone that restrains the flow in a smaller section, commonly called *vena contracta*. This restriction makes the flow speed up and then slow down around the *vena contracta* causing energy dissipation and eventually pressure losses. These

minor losses can actually be significant due to the complex geometry of the injector channels [17]. The pressure drop related to a minor loss is normally expressed as in Equation (2.2), where ξ is the minor loss coefficient and ranges from 0, when there is no loss, to usually 1, which means that the pressure drop is equal to the dynamics pressure. Note that the minor loss coefficient can also be greater than 1 for some specific case.

$$\Delta p_{visc,m} = \xi \rho \frac{u^2}{2} \tag{2.2}$$

In order to predict accurately the pressure losses, the flow regime has to be identified to know which theory has to be applied in the studied case [15, 16]. Two flow regimes are commonly identified: laminar and turbulent, which are distinguished for specific values of the Reynolds number. The Reynolds number, defined in Equation (2.3) where L is a typical length scale in the system, is a dimensionless parameter that gives a measure of the ratio between inertial and viscous forces.

$$Re = \frac{\rho u L}{\mu} = \frac{u L}{\nu} \tag{2.3}$$

For cylindrical straight ducts, internal experimental observations show that the flow is laminar for values of Reynolds number below $Re \approx 2300$ and turbulent values above $Re \approx 4000$. The interval $Re \in [2300, 4000]$ is considered as a transition regime where both laminar and turbulent regimes are possible and occur intermittently, depending on the pipe roughness. Nonetheless, care must be taken with respect to this definition because it appears to be valid only for fully developed flows. In fact, when there are changes in the pipe section, the perturbations in the flow are generated and protracted for a certain length (several diameters) called flow development length. This distance needed to get stabilized flow also depends on the regime (laminar or turbulent) and needs different equations or coefficients to be studied for each specific perturbation.

On the other hand, the major losses are induced by the friction of the fuel on walls and they depend on the length of the considered channel. The pressure drop related to the major loss is defined by Equation (2.4), where k_{fric} is the friction coefficient and in this case L is the length of the pipe, that depends on the Reynolds number and wall relative roughness.

$$\Delta p_{visc,M} = k_{fric} \frac{L}{D} \rho \frac{u^2}{2} \tag{2.4}$$

To evaluate k_{fric}, the flow regime again must be known. In the case of fully developed flow in laminar regime and neglected surface roughness, Equation (2.5) is used. In turbulent regime, the interaction between the fluid and the wall changes, as well as the velocity profile, so the surface roughness effect has to be taken into account.

$$k_{fric} = \frac{64}{Re} \tag{2.5}$$

The Colebrooke's Equation (2.6) [15] presents an analytical solution of the friction coefficient, where e_r/D is generally referred as the relative roughness.

$$\frac{1}{\sqrt{k_{fric}}} = -2\log\left(\frac{2.51}{Re\sqrt{k_{fric}}}\right) + \frac{e_r/D}{3.72} \tag{2.6}$$

The theory presented for circular sections can be extended to other shapes using the equivalent diameter D_{eq} concept.

2.3.2   Upstream the injector nozzle

Before reaching the injector nozzle, the fuel stored in the rail has to pass through the high pressure feeding line and then the hydraulic circuit within the injector (see Sections §2.2.2 and §2.2.3). In these transformations from potential to kinematic energy, the fuel normally does not experiences important pressure losses, but the accurate design of this part has important consequences on the dynamic of the system [17]. Normally, the feeding line internal diameter is about 3 mm, ant its length depends on the injection system arrangement (typical values in passenger cars from 300 to 700 mm). The velocity of the flow in the feeding pipe is about $5-8$ m/s, corresponding to a $Re \approx 10^4$. Calculating the pressure drop with the methodology described in previous Section §2.3.1, the pressure drop is expected to be less than 0.3 MPa. This value, compared with the total available pressure drop, typically in Diesel engines ranging from 30 MPa to 300 MPa, is negligible. However, the correct design of the feeding pipe is important, for example, the time required for a pressure wave to travel through the line is around 0.4 ms, that is of the same order of magnitude of the injection duration [18]; moreover, the propagation of pressure waves could have repercussions on the injection process as well as on the following injection in the case of multiple injections [17].

Normally the fuel flow within the injector is estimated performing simulation with 1D models [4, 17–20]. The characterization of the flow within the

injector becomes important in the phase of injector design when, for example, the size of the apertures of the control volume has to be decided. The correct design of the hydraulic circuit of the injector together with the reduction of the moving components are the keys for a fast response of the injector. Moreover, the design of the injector internal channels can generate pressure waves that are eventually reflected by oscillation of the mass flow rate [18].

2.3.3 Geometry of the injector nozzle

Needle seat

The needle interference with the flow is traditionally considered limited or negligible since in the steady conditions the needle lift is sufficiently high to neglect its interference with the flow. In conventional injectors, save the transient phases at start and end of the injection, the needle is fully lifted and the relatively wide cross-section area at the needle seat makes the restriction caused by the needle very low. However, due to the tendency in reducing the injection duration by separating the event in several pilot, main and post injections, the transient at intermediate needle lift are catching the attention of the engine community. In this sense, specific studies have been performed to asses the effect of the needle seat type on the spray development [21], the needle position [22] and even the three-dimensional needle movement [23–25] during the last years.

Nowadays, there are two main typologies of needle seat types employed in commercial injectors: valve closed orifice (VCO) and micro-sac. As shown in Figure 2.6, VCO orifices inlet lay on the needle-nozzle contact surface, while in micro-sac nozzles the sealing of the needle is performed upstream of the orifices, in other words, the orifices inlet is placed in a specific volume called sac.
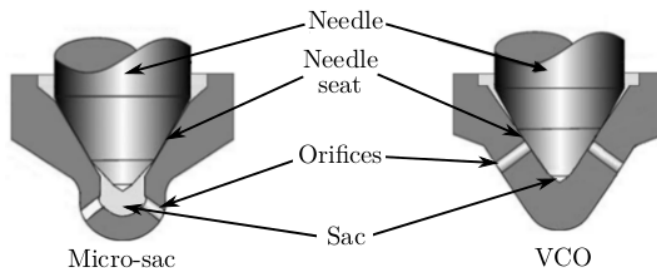
Figure 2.6: Example of two different needle set types.

The VCO nozzle has a faster response and higher accuracy in the amount of fuel delivered. Once the needle is lifted the fuel flow directly through the orifices. However, during opening/closing transients, the position or the eccentricity of the needle strongly influences the fuel flow and it often results in asymmetric fuel flow and uneven distribution of the mass around the nozzle [26].

The sac nozzle is designed to avoid that problem of asymmetry, however the residual fuel that, after the needle closing, remains into the sac can result in fuel dripping and consequent increase of unburned hydrocarbons and soot. For that reason, the volume of the sac is strongly limited and the current tendency is to reduce it to a micro-sac.

Nozzle orifice

The nozzle orifices are the part of the nozzle where the fuel potential energy due to the pressure is transformed in kinetic energy, accelerating the flow before entering into the combustion chamber. Microscopic features of the orifices are strictly related to the Diesel spray characteristics [27, 28] and therefore to the air-fuel mixing process.

Figure 2.7 schematically defines the main features of a typical orifice that can be found in a modern direct injection nozzle: inlet and outlet diameters, D_i and D_o respectively, orifice length L, and entrance radius r_e. From these dimensions, some dimensionless parameters can be defined, which characterize the shape of the orifice:

- length to outlet diameter ratio: L/D_o;
- entrance radius to inlet diameter ratio: r_e/D_i;
- inlet to outlet diameter ratio: D_i/D_o.
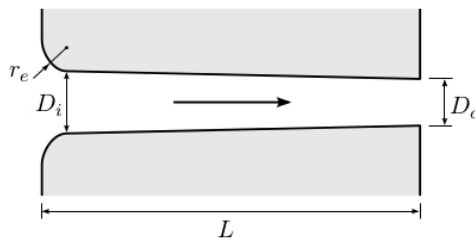
Figure 2.7: Geometric parameters to define the nozzle orifice.

The last ratio gives the conic shape or convergence (or divergence) of the orifice, and it is equal to unity for cylindrical nozzle. Though, the common parameter to determine the convergence of an orifice found in the literature is the $k - factor$ defined in Equation (2.7) [29]. Nevertheless, this parameter presents the disadvantage of not taking into account the absolute outlet orifice diameter.

$$k - factor = \frac{D_i - D_o}{10 \ [\,\mu m]}$$ (2.7)

Another parameter sometimes used to measure the convergence of the orifice is the area reduction AR, defined in Equation (2.8) [30].

$$AR = \frac{A_i - A_o}{A_i} = \frac{D_i^2 - D_o^2}{D_i^2}$$ (2.8)

As it is explained in next sections, these and more geometric parameters, i.e. the number of orifices, have a strong effect on the characteristics of the internal flow. Notwithstanding, the study of the flow inside the nozzle presents great difficulties due to its very small size and to the highly transient nature of the injection process. Therefore, uncertainties/defects inherent of manufacturing and hydro-erosive grinding[1] (HEG) processes might be relevant. An effort has been made by the research community in order to develop nondestructive experimental techniques to accurately obtain the nozzle geometry. On one hand, Macián et al. [30] use a silicone mold of the nozzle together with a Scanning Electron Microscope to obtain the images and a CAD software to measure the geometric parameters from the images. The errors with this technique are between 0.5% and 1%. On the other hand, Lee et al. [31] use phase-enhanced high-energy x-rays to visualize the internal structure of the nozzle, allowing to observe irregular features which cannot be visualized by any other nondestructive technique, i.e. the wall roughness. X-ray tomography technique can also be used to measure the needle movement inside the injector [32].

Influence of nozzle geometry on the internal flow

Length to outlet diameter ratio: L/D_o

If there is not cavitation, an increase of the L/D_o ratio induces higher losses due to wall friction. Lichtarowicz et al. [33] compared several results under

---

[1]Hydro-erosive grinding is a process for increasing the radius of an edge by flowing an abrasive fluid through. This process can calibrate the holes to flow a certain static flow rate.

non-cavitating conditions and confirmed that the maximum discharge coefficient obtained at high Reynolds number (see next Section §2.3.4) decreases as the L/D_o ratio increases. On the other hand, an excessive reduction of the L/D_o ratio ($L/D_o < 2$) causes a reduction of the discharge coefficient due to flow detachment at the entrance. Moreover, an increase in this ratio reduces the possibility of the appearance of cavitation. In fact, a higher major pressure loss due to an increase of L/D_o brings as a consequence that, for similar discharge pressure and mass flow, the pressure at the orifice entrance is higher, thus leading to a lower probability of reaching the vapor pressure.

Entrance radius to inlet diameter ratio: r_e/D_i

The main case of pressure losses at the orifice is the separation of the boundary layer produced by the high velocity of the fuel combined with a sudden change in the flow direction. The introduction of a curvature at the entrance of the orifice helps mitigating the detachment of the boundary layer. This reduction of the pressure losses leads to higher values of the discharge coefficient but also a decrease of the possibility of cavitation (higher pressure at the orifice entrance). The introduction of a rounding to the orifice inlet edge reaches its maximum effect for $r_e/D_i \geq 0.2$; from that point the pressure loss generated is considered negligible [34].

Convergence of the orifice

The convergence of the orifice is the relation between both inlet and outlet sectional areas. A convergent orifice has the outlet diameter smaller than the inlet one. A reduction in area produces an increase in velocity for subsonic flows [35], so in this kind of orifices the acceleration of the flow is not concentrated at the orifice inlet as in a cylindrical orifice, but it is distributed along the orifice length. For this reason, the mean velocity of the flow at the entrance section is lower than the outlet mean velocity. Therefore, convergence induces a higher pressure at the orifice entrance, leading to several consequences. Firstly, apparition of cavitation is delayed or even canceled for all operating conditions [30, 36]. Secondly, a higher pressure at the orifice entrance means a lower pressure difference with upstream pressure and thus minor pressure losses. Finally, and as a result from these two consequences, there is a direct effect on the injected mass. If the pressure loss is lower through the orifice, the mass flow rate is higher so it is the discharge coefficient. For these reasons, almost all nozzles implemented nowadays in Diesel engines use convergent nozzles.

2.3.4 Hydraulic characterization of the nozzle

In the case of axially centered single-hole nozzles with an axisymmetric orifice, such the one commonly used for research [8, 37, 38], the flow enters equally from all directions, but as a consequence of the abrupt change in the direction the flow detaches at the orifice inlet and form recirculation regions between the walls and the flow lines (*vena contracta*), as sketched in Figure 2.8a.

(a) Axisymmetric nozzle (b) Multi-hole nozzle
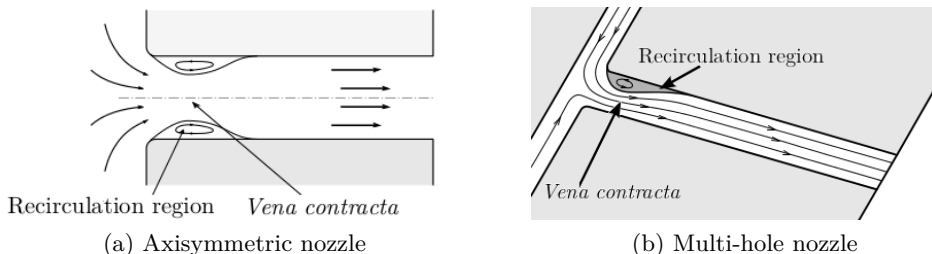
Figure 2.8: Main features of the fuel flow through the nozzle orifice.

In the case of multi-hole nozzles, the common ones in commercial applications, the axis of the orifices form an angle respect to the symmetry axis of the nozzle [39], so the change in direction is greater but only in the upper part of the orifice, as shown in Figure 2.8b. However, Salvador et al. [22] proved that for low needle lift that recirculation region may appear in the lower part of the orifice.

The detachment is the main cause of pressure losses characterizing the flow through the orifice. The wall friction of the liquid causes a further pressure loss that also contributes to the viscous dissipation. Nonetheless, care must be taken when attempting to calculate these losses. When a fluid is traveling into a pipe, a sudden change of direction can produce local perturbations and it takes time (distance) for the boundary layer to be stabilized again. It is generally considered that it takes several diameters for the flow to be stable. The exact distance depends, among other parameters, on the regime (laminar or turbulent), in other words, on the Reynolds number. Equation (2.9) [40] estimates the stabilization distance in case of laminar flow, where other values for the coefficient can be found in the literature ranging from 0.03 to 0.06 [41]. If $Re = 2000$, for example, the length should be around 60 time the (inlet or outlet) diameter to consider the flow fully developed.

$$\frac{L}{D} = 0.03Re \text{ if } Re < 2300 \tag{2.9}$$

When the regime is turbulent, the mixing intensity induced by the turbulence itself makes shorter the length needed to get a developed flow. Equation (2.10) [41] can be used in this case. As an example, for Reynolds numbers about $10^4 - 10^5$, the length should be between 20 and 30 times the orifice diameter to get a fully developed turbulent flow.

$$\frac{L}{D} = 4.4 Re^{\frac{1}{6}} \text{ if } Re > 4000 \tag{2.10}$$

It is clear orifices used in Diesel injectors are not long enough (typically $L/D \approx 4 - 10$) to get fully developed flow in neither laminar nor turbulent regime. Thus, the following aspects should be taken into account for the internal flow analysis:

- the behavior of the flow is directly related to the geometry of the entrance of the orifice and will affect the flow characteristics, e.g thickness of the boundary layer (or separation), local pressure losses, etc.;

- since the flow is not completely developed, the limits usually given to determine if the regime is laminar or turbulent are not valid [42]; as a consequence, the Reynolds number is not enough to characterize the flow regime and therefore the intensity of the turbulence;

- fluid mechanics theories based on fully developed flow cannot be applied in this case, for example, the velocity profiles at the orifice outlet are not almost constant in the whole section as it would be if flow were stabilized in turbulent regime, but neither they follow Hagen-Poiseuille law for laminar regime [35].

Hence, the most common way to analyze the internal flow consists of mean parameters at the orifice exit and dimensionless coefficients such the discharge coefficient C_d [21, 32]. This coefficient is defined as the real mass flow to theoretical mass flow ratio. Theoretically, the mass flow through the orifice exit can be computed by Equation (2.11), if density and velocity profiles are known.

$$\dot{m}_f = \int_A \rho \left(\boldsymbol{U} \cdot \boldsymbol{n} \right) dA \tag{2.11}$$

Considering the velocity component perpendicular to the orifice exit area Equation (2.11) can be rewritten as Equation (2.12).

$$\dot{m}_f = \int_A \rho u \, dA \qquad (2.12)$$

As discussed earlier in this chapter, it is not possible to know with accuracy the axial velocity and the density profiles due to the small length- and time-scales of the problem [43]. Nevertheless, if the fluid is considered incompressible and inviscid (consequently with no boundary layer), the integral simplifies into Equation (2.13), where u_{th} (Equation (2.14)) is the theoretical velocity obtained from Bernoulli's Equation (2.1).

$$\dot{m}_{f,th} = \rho u_{th} A_o \qquad (2.13)$$

$$u_{th} = \sqrt{\frac{2\Delta p}{\rho_f}} \qquad (2.14)$$

Once the theoretical mass flow ratio is obtained for a particular condition, the discharge coefficient can be calculated by Equation (2.15).

$$C_d = \frac{\dot{m}_f}{\dot{m}_{f,th}} = \frac{\dot{m}_f}{A_o\sqrt{2\rho_f\Delta p}} \qquad (2.15)$$

This equation highlights the dependence between the mass flow rate and the pressure difference inside the nozzle. Moreover, it underlines that the discharge coefficient is an evaluator of the efficiency of the nozzle in delivering fuel. When cavitation (see Section §2.3.5) is avoided, the mass flow rate dependence on $\sqrt{\Delta p}$ is linear, while when cavitation appears the mass flow stops growing, remains at constant value, and then the discharge coefficient decreases.

Actually, the behavior of the discharge coefficient in orifices has been deeply studied for the last decades [28, 33, 44–46]. Its evolution with the Reynolds number is asymptotic, as shown in Figure 2.9. This figure also proves that the flow regime can also be determined by the shape of the discharge coefficient curve: laminar regime if the dependence with Reynolds number is linear, turbulent if there is not dependence, and transition regime otherwise.

The shape of the curve in Figure 2.9 mainly depends on the geometry of the orifice. Some empirical expressions have been developed in order to correlate
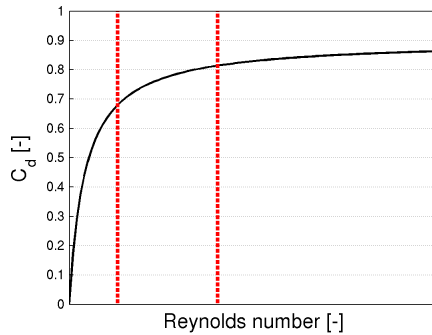
Figure 2.9: Example of a typical discharge coefficient evolution as function of Reynolds number for non-cavitating orifices.

the discharge coefficient with the main geometric parameters described in Section §2.3.3. Hall [47] proposes Equation (2.16) and discusses the effects of chamfered and radiused entry.

$$C_d = 1 - 0.184 \left(\frac{L}{D_o} - 1 + 1.11 Re^{0.25} \right)^{0.8} Re^{-0.2} \qquad (2.16)$$

Nakayama [48] proposes a different equation fitted to experimental results obtained with rounded and cylindrical nozzles, Reynolds number ranging between 550 and 10000 and L/D ration between 0.799 and 16.520 (Equation (2.17)). He also analyzes the pressure drop and recovery downstream the orifice.

$$C_d = \frac{Re^{\frac{5}{6}}}{17.11 \frac{L}{D_o} + 1.65 Re^{0.8}} \qquad (2.17)$$

Lichtarowicz et al. [33] added the asymptotic value, called $C_{d,max}$, as an input of the equation which depends only on the diameter and not on L/D ratio (Equation (2.18)).

$$\frac{1}{C_d} = \frac{1}{C_{d,max}} + \frac{20}{Re} \left(1 + 2.25 D_o^{-1} \right) - \frac{0.0015 D_o^{-1}}{1 + 7.5 \log^2 (0.00015 Re)} \qquad (2.18)$$

In the development of their Eulerian-Lagrangian spray model, Arcoumanis et al. [49] use a simplification of Lichtarowicz et al. proposal where the last

term of Equation (2.18) is neglected. There are other computational models and softwares which also use simplified equations for the discharge coefficient of an orifice, i.e. AMESim® [50].

Finally, Salvador [46] gives an expression correlating the discharge coefficient directly with the geometric parameters of a Diesel injector nozzle for Reynolds number ranging from 5000 to 30000 (Equation (2.19)).

$$C_d = 0.98 - 0.07 \left(r_e^{-0.49} nl^{-1.14} D_o^{1.2} AR^{-0.088} \right) - \frac{10.7}{Re^{0.5}} \qquad (2.19)$$

As mentioned earlier, the discharge coefficient measures the efficiency of an orifice in delivering certain fluid, and this includes the wall friction pressure losses but also losses due to non-uniform velocity profile at the orifice exit and the cavitation phenomenon when it appears (see Figure 2.10a). Nonetheless, this complex configuration of losses can be simplified (see Figure 2.10b) considering that all the fluid is in liquid phase and flows through an effective area A_{eff} with a constant effective velocity u_{eff} so the mass flow rate is the real one [43], given by Equation (2.20).

$$\dot{m}_f = \rho_f A_{eff} u_{eff} \qquad (2.20)$$

(a) Axisymmetric nozzle   (b) Multi-hole nozzle
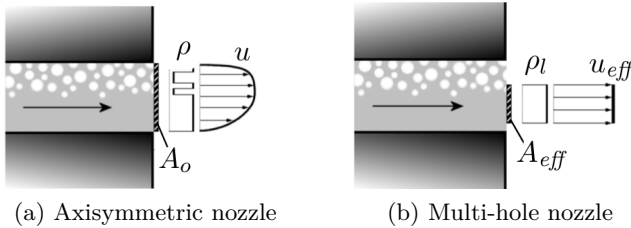
Figure 2.10: Effective area and effective velocity definition sketch.

Therefore, losses included in the discharge coefficient can be divided into two parts, as Equation (2.21) shows: the velocity coefficient C_v takes into account the energy or pressure loss, whilst the area coefficient C_a incorporate the loss of section due to non-uniform velocity profile, cavitation bubbles reaching the exit area and flow separation from the wall (hydraulic flip). Accordingly, the velocity coefficient is defined as the relationship between effective velocity and theoretical velocity, Equation (2.22), whereas the area coefficient is

defined as the effective area divided by the geometrical area, Equation (2.23) [43, 51].

$$C_d = C_v C_a \tag{2.21}$$

$$C_v = \frac{u_{eff}}{u_{th}} \tag{2.22}$$

$$C_a = \frac{A_{eff}}{A_o} = \frac{D_{eff}^2}{D_o^2} \tag{2.23}$$

A Diesel spray is composed by a number of droplets of different sizes moving at different velocities, and the momentum of a moving object is the product of its mass and its velocity, so Equation (2.24) gives the momentum flux.

$$\dot{\boldsymbol{M}} = \int_A \rho \boldsymbol{U} \left(\boldsymbol{U} \cdot \boldsymbol{n} \right) dA \tag{2.24}$$

Again, considering the velocity component perpendicular to the orifice exit area Equation (2.24) can be rewritten as Equation (2.25).

$$\dot{M}_x = \int_A \rho u^2 dA \tag{2.25}$$

If the fluid is considered incompressible and inviscid, the integral simplifies into Equation (2.26) and the momentum coefficient C_M (Equation (2.27)) is introduced to compare the theoretical momentum obtained using the Bernoulli velocity to the measured momentum. Furthermore, effective area and effective velocity are defined to ensure that the momentum flux is also the real one [43], given by Equation (2.28).

$$\dot{M}_{th} = \rho_f u_{th}^2 A_o \tag{2.26}$$

$$C_M = \frac{\dot{M}}{\dot{M}_{th}} = \frac{\dot{M}}{2 A_o \Delta p} \tag{2.27}$$

$$\dot{M} = \rho_f u_{eff}^2 A_{eff} \tag{2.28}$$

The momentum flux is a fundamental measurement since it is strictly related to the spray development [52]. For example, Naber and Siebers [53] carried out a comprehensive experimental study linking this parameter with the spray penetration at different ambient conditions. Gimeno [8] performed a vast experimental characterization of the momentum flux of different injectors; he stressed the relationship between momentum flux and spray penetration together and analyzed the cavitation phenomenon effects on the spray.

If the momentum flux is measured together with the mass flow rate, Equations (2.20) and (2.28) can be used to obtain the effective velocity (Equation (2.29)) and the effective area (Equation (2.30)). Therefore, velocity, area and discharge coefficients can be obtained without knowing the internal nozzle geometry parameters (i.e. orifice exit area); and this is one of the advantages of this methodology [8].

$$u_{eff} = \frac{\dot{M}}{\dot{m}_f} \tag{2.29}$$

$$A_{eff} = \frac{\dot{m}_f^2}{\rho_f \dot{M}} \tag{2.30}$$

2.3.5 Cavitation phenomenon

As explained in previous Section §2.3.4, a recirculation zone near the entrance between the *vena contracta* and the orifice wall (see Figure 2.8). In this zone there is a pressure depression due to the acceleration of the fluid. This reduced pressure can drop to the valve of the vapor pressure for the existing temperature, causing a partial vaporization of the liquid, generating small bubbles of vapor cavities, which is called cavitation. The first time vapor bubbles appear inside the nozzle is called incipient cavitation.

The formation of cavitation bubbles depends mainly on the fluid velocity (in other words, injection and chamber pressures) and the nozzle geometry. Bergwerk [54] studied the influence of the nozzle geometry on the flow behavior through visualization of the internal flow in transparent nozzles. Cavitation phenomenon was obtained under certain conditions, but also another phenomenon, called hydraulic flip, was visualized. The hydraulic flip phenomenon consists on the introduction of gas from the combustion chamber into the orifice when the detached flow extends until the orifice exit; then the gas tends to occupy the space between the wall and the *vena contracta* [46]. Soteriou et al. [55] observed that orifices under hydraulic flip conditions lead to large spray

penetration and low liquid atomization. Nonetheless, this phenomenon has been never observed in real size Diesel nozzle under real operating conditions. In order to be able to predict the cavitation appearance, Bergwerk defined the cavitation number CN as in Equation (2.31), where subscript "i" refers to injection pressure and also the upstream point in Figure 2.12, "b" represents the discharge pressure and the downstream point in the figure, but p_v just means vapor pressure of the fuel.

$$CN = \frac{p_i - p_b}{p_b - p_v} \qquad (2.31)$$

Chaves et al. [56] defined the term "supercavitation" as the cavitation that extends along the full length of the orifice and reaches the exit. The "supercavitation" increases the spray angle [46, 56, 57]. However, cavitation may not extend until the orifice exit. In fact, the spray angle also increases under incipient cavitation [55]. Chaves et al. [56] also proved that wall surface irregularities or high wall roughness may also cause cavitation. Therefore, it is necessary to know the extension of the orifice occupied by cavitation bubbles. Figure 2.11 [56, 58, 59] represents that distance as function of the cavitation number. Four types of cativation are defined: incipient cavitation, "subcavitation", unsteady cavitation and "supercavitation". "Subcavitation" and unsteady cavitation may be grouped as cavitation under development.
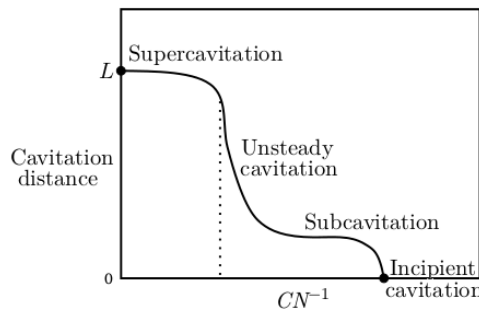
Figure 2.11: Evolution of the extension occupied by cavitation bubbles as function of cavitation number CN.

Despite the inherent difficulties, there are two possibilities to experimentally study the cavitation phenomenon: the hydraulic characterization of the cavitating flow and its direct visualization. The first option, the hydraulic characterization, allows studying real size nozzles in a non-intrusive way obtaining the discharge coefficient together with other dimensionless parameters

that characterize the flow. The second option requires transparent nozzles, with usually simpler geometries than real nozzles due to complexity of the flow (high velocities and pressures, small diameters, two-phase flow).

Bergwerk [54] demonstrated a decrease in the discharge coefficient under cavitating operation, together with a weak link with the Reynolds number. On the contrary, the cavitating discharge coefficient strongly depends on the pressure ratio defined as $(p_i - p_b)/p_b$. Spikes and Pennington [60] corroborated these trends and related the cavitation phenomenon to the nozzle geometry, i.e. larger L/D ratios lead to higher discharge coefficient of the orifice. Nurick [59] proposed and validated a one-dimensional model to explain the behavior of the discharge coefficient. Based on the simplification made on Figure 2.12, Nurick defines three characteristic points: one upstream the orifice inlet where the velocity is negligible compared to those inside the orifice (point i); another one placed at the minimum cross-sectional area of the *vena contracta*, with the highest velocity and lowest pressure (point c); and a third point at the exit of the orifice (point b).
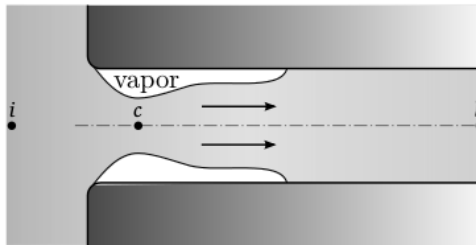
Figure 2.12: Sketch of the cavitation phenomenon in an axisymmetric nozzle according to Nurick one-dimensional model.

Assuming that the area occupied by the vapor remains constant, starting at the inlet and not reaching the exit, the percentage of area available for the fluid to flow inside the *vena contracta* (point c) is defined as the contraction coefficient C_c (Equation (2.32)). The liquid mass flow rate at that point, assuming constant density and constant velocity profile is given in Equation (2.33).

$$A_c = C_c A \tag{2.32}$$

$$\dot{m}_f = \rho_f A_c u_c \tag{2.33}$$

From Bernoulli's Equation (2.1) and assuming that there are no pressure losses between points i and c and that the pressure at the *vena contracta* is the vapor pressure, Equation (2.34) can be used to compute the velocity at point c. Therefore, Equation (2.33) becomes Equation (2.35), and the mass flow rate turns out to be not dependent on the discharge pressure, fact that is also experimentally observed [8, 46, 55, 57] and is called mass flow rate collapse.

$$p_i = p_v + \frac{1}{2}\rho_f u_c^2 \tag{2.34}$$

$$\dot{m}_f = AC_c\sqrt{2\rho_f\left(p_i - p_v\right)} \tag{2.35}$$

Combining Equations (2.15) and (2.35), Equation (2.36) gives the discharge coefficient as function of injection and discharge pressures. This expression allows a definition of a new cavitation number, given in Equation (2.37).

$$C_d = C_c\sqrt{\frac{p_i - p_v}{p_i - p_b}} \tag{2.36}$$

$$K = \frac{p_i - p_v}{p_i - p_b} \tag{2.37}$$

Equation (2.36) points out the linear relationship between the discharge coefficient and the square root of cavitation number K. As K increases, it means the discharge pressure increases or the injection pressure decreases, injection conditions are less favorable for cavitation to appear and this linear trend breaks down; vapor phase disappears from the orifice and the discharge coefficient depends again on the Reynolds number and not the cavitation number K. The value of the cavitation number K at which the break down happens is called critical cavitation number K_{crit}.

Payri et al. [43] experimentally proved that, despite the mass flow rate collapses under cavitating operation, the momentum flux does not, and it still increases when Reynolds number does. This happens because of the reduction of wall friction losses due to the presence of vapor phase next to the walls. Another interesting result of this study is the demonstration that the cavitation increases the exit velocity and decreases the effective area of the liquid core. These results are confirmed by other authors who employed visualization techniques (LDV, PDPA) to obtain the velocity at the orifice exit [61, 62].

Regarding the visualization of the internal flow, using transparent rectangular orifices is one of the most common solutions adopted. In this kind of geometries, in addition to facilitate the optical access, the light can enter through the planar faces that form the nozzle, avoiding refraction effects. Then, the apparition of the first bubbles can be observed, what occurs at different conditions than the mass flow collapse, for higher values of back pressure [63]. The hysteresis phenomenon of the discharge coefficient associated to the cavitation, a larger measured discharge coefficient from cavitating operation to non-cavitating operation, can be explained by the resistance of the bubbles to collapse once they are generated [64].

These visualization studies in transparent nozzles can also be combined with spray near-field visualization to correlate the presence of cavitation with modifications in the spray structure [65]. For example, Sou et al. [66] observed an increment in the spray angle when cavitation appears. They also confirmed that the distance occupied by vapor phase depends mainly on the cavitation number (see Figure 2.11). Also, Park et al. [67] obtained a decrease on the droplet mean diameter of the spray when cavitation appears.

Even though using rectangular real size transparent orifices is a difficult task [65], it gets even harder when real geometries with cylindrical or conical orifices are desired. Such geometries are necessary to study, for example, the effect of the orifice inclination angle on the cavitation formation. Therefore, it is common to use large scale transparent models to do so. Andriotis et al. [68] observed cavitation generated by vortices placed in the sac of multi-hole injector nozzles, what the called string cavitation. This string cavitation may appear between two orifices or between one orifice and the needle, and strongly depends on the needle position. Arcoumanis et al. [69] studied the asymmetry of the cavitation (specially for VCO nozzles) due to the orifice inclination angle that, in addition to the fluid preference to enter into the upper part, generates a stronger cavitation in the upper half of the orifice (see Figure 2.8b). They also related this asymmetry with the needle position, which alters the flow pattern inside the nozzle. This asymmetry of the cavitation is related with an asymmetry in the spray structure [70], which shows a wider angle in the upper part.

It is clear that scales models are useful to study the cavitation phenomenon, but it is necessary to work on real size geometries to take into account scale effects. Meanwhile in large scale models the cavitation appears as a bubble distribution [55], in real size nozzle it forms films [56], so the cavitation phenomenon has its own scale which depends on the collapse time and the flow velocity.

2.4 Diesel spray formation

The spray formation is the pillar of the direct injection in Diesel engines: the mixing of the fuel with the surrounding air takes place suddenly in a very small volume. The correct prediction of its development and the understanding of its internal structure are the base for the improvement of the injection strategies. Although the effort of the engine community in this sense has been strong and constant along the last decades, the atomization process still has many aspects to be understood and its prediction is strongly linked to empirical data.
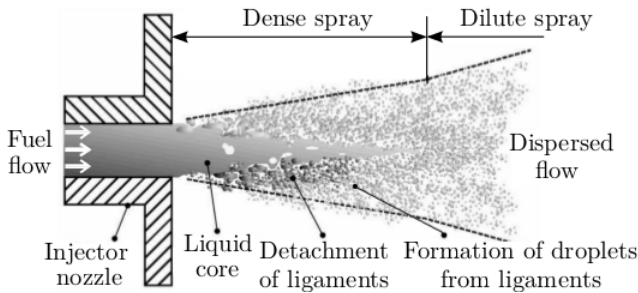
Figure 2.13: Structure of the Diesel spray [71].

The Diesel spray is the complex result of the fuel atomization process, which is the segregation of the liquid core into droplets. The area normally considered spray starts from the orifice outlet, as shown in Figure 2.13. This sketch also describes the Diesel spray structure. The first millimeters from the orifice outlet are characterized from an intact liquid core. Depending on the injection condition, it can be also observed the so called intact surface, a region of the spray (not longer than $1-1.5$ mm) where the liquid vein proceeds intact without forming any droplet nor ligament. The aerodynamic instabilities at the liquid-gas interface, combined with the perturbations deriving from the turbulent flow, causes the segregation of the liquid core with the formation of relatively large liquid structures called ligaments. These structures do not have a specific shape and are characterized by their direct origin from the liquid core. This process is called primary atomization. Once detached from the liquid core, their relative velocity to the surrounding gas and the related viscous interaction lead the ligaments to a further aerodynamic instability that breaks them in smaller formations. This process is repeated until the surface tension of the fluid is enough to compensate the aerodynamic forces. This second part of the process is called secondary atomization.

The regions of the spray are also classified as dense and dilute region. This defines the optical depth and experimental approach that can be used for its study. The first one, also called near-field, is the area close to the orifice outlet including the liquid core and ligaments. Although it is possible [57], the spray is optically too dense to be studied using conventional optics: many studies related to this part have been performed using x-ray techniques [72, 73] or ballistic imaging [37]. However, the study of this region remains very difficult and the results obtained are sometimes controversial [74]. The dilute region, also called far-field, is normally referred to as the area where the atomization process is completed. In this region the optical depth of the spray allows the implementation of conventional techniques [38, 75, 76]. It is important to remind that this is not a strict definition but it is rather used for descriptive purposes.

2.4.1 Atomization process

The disintegration of the liquid vein exiting from the orifice outlet is the result of interaction occurring at microscopic scale, involving inertial forces, surface instabilities, aerodynamic interactions and surface tension.

- The liquid surface tension: the resulting force causes the liquid vein to remain compact or to form droplets.

- Surface instabilities: passing from forced to free-flow, the liquid vein is in unstable condition. This means that the surface tension resulting force is in equilibrium only if the cylindrical shape of the liquid vein is maintained. A minimum perturbation is amplified and causes the initial shape to disappear.

- The turbulence within the orifice: depending on the flow regime within the orifice (see Section §2.3.4), the fuel may have a different level of radial velocities. The resulting inertial forces tend to spread the liquid in the chamber.

- Aerodynamic interaction: the relative movement between the liquid and the surrounding gas causes friction forces that, among other things, are strongly dependent on the shape of the liquid vein.

Atomization regimes

It is important to realize that different forces control the break-up of jets from cylindrical orifices and their relative weight changes depending on the

conditions. As a consequence of that, different regimes can be identified. Following the work presented by Reitz [77, 78], the break-up regimes can be classified as follows (see also Figure 2.14):
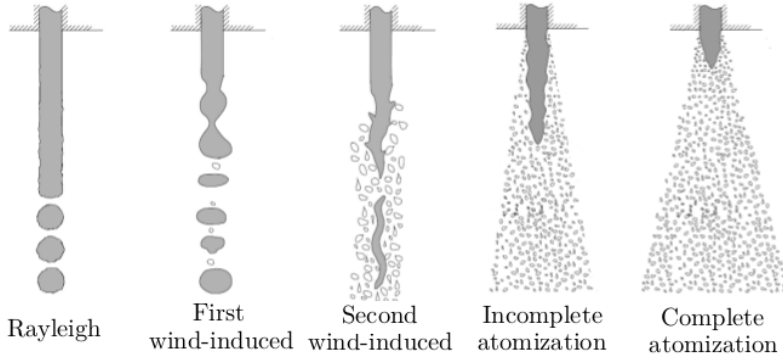
Figure 2.14: Schematic representation of the different atomization regimes.

- Rayleigh regime. This regime is observed at the lowest jet velocities. In this case the perturbations at the surface of the jet cause small deformations on the liquid surface. The surface tension amplifies these deformations until the liquid vein is separated in droplets, whose sizes are uniform and similar to the outlet orifice diameter.

- First wind-induced regime. The effect of the first perturbation is amplified by the relative velocities between the jet and the surrounding ambient. In this way, the friction forces effect plays the same role of the surface tension and ease droplet formation. In this regime the aerodynamic forces can be observed also in a helical oscillation of the jet around its symmetry axis. In these first two regimes the droplets are pinched off from the end of the jet and again their size is comparable to that of the orifice diameter.

- Second wind-induced regime. Increasing again the jet velocity, the initial perturbations are amplified by the aerodynamic forces and grow exponentially with time. This growth results in the formation of droplets of a size comparable to the wavelength of the initial perturbations. The formation of the droplet is, in this regime, closer to the orifice but still a certain distance is needed for the droplets to be formed.

- Atomization regime. The initial perturbations, combined with the aerodynamic forces, cause the droplets to form in the immediate proximity

of th orifice and their size is, as in the second wind-induced regime, much smaller than the orifice diameter. In this case, the intact surface length is zero, which means that the surface is broken right at the orifice outlet. However, in the atomization regime the intact core can still be present. For this reason, two atomization regimes are commonly defined: incomplete and complete, whereas the intact core can be observed or not.

Grant and Middleman [79] characterized the break-up regimes basing on the measured intact core length. They noticed that the predominance of one force or the other is reflected on the behavior of this quantity (see Figure 2.15). In the Rayleigh regime, after the first region of dripping, the intact core length increases gradually, since the jet velocity goes along with the gravitational forces and helps the liquid vein to extend farther from the outlet. The aerodynamic forces gain relevance contrasting the aforesaid effect, and when these two effects are balanced the intact core length reaches its maximum and this maximum is indicated to define the onset of the first-wind induced break-up. Therefore, the intact core length decreases until a local minimum is reached. At this point the droplets formed are strongly reduced in size since they are direct consequence of the initial perturbation, and therefore more disintegration is needed to reach the jet core. Finally, this effect is balanced again by the increasing of aerodynamic forces, causing a final reduction of the intact core length. The last part of the curve in Figure 2.15 is dashed above certain value of velocity because the intact core length becomes difficult to measure especially at Diesel injection conditions. Nonetheless, Lefebvre [80] associates these variations in the intact core length to the turbulence level at the orifice exit.

Dimensional analysis of the atomization process

Based on the information available in the literature, the parameters mainly affecting the atomization process are the following:

- Gas density, ρ_g.
- Fuel density, ρ_f.
- Jet velocity (or relative velocity between fuel and gas), u_{eff}.
- Effective orifice diameter, D_{eff}.
- Fuel viscosity, μ_f.
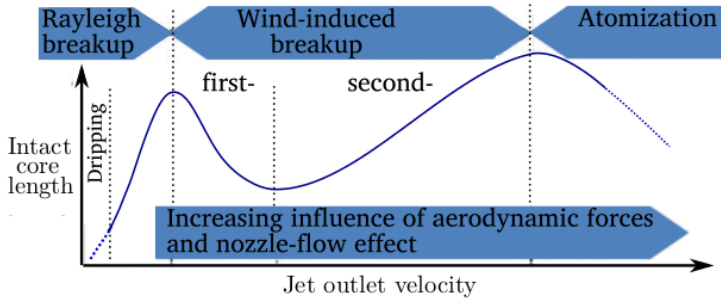
Figure 2.15: Qualitative relationship between velocity at the orifice outlet and intact core length.

- Surface tension, σ.

There are six parameters affecting the atomization process, and they contain three fundamental quantities (length, mass and time), so following Buckingham's π-theorem [81], three dimensionless groups of parameters can be used to analyze the influence of the six parameters described above. In general, the dimensionless groups most employed in the literature are the density ratio ρ_g/ρ_f, the Reynolds number (Equation (2.3)) and one of the three following:

$$\text{Ohnesorge number: } Oh = \frac{\mu_f}{\sqrt{\rho_f \sigma D_{eff}}} \tag{2.38}$$

$$\text{Weber number: } We = \frac{\rho u_{eff}^2 D_{eff}}{\sigma} \tag{2.39}$$

$$\text{Taylor number: } Ta = \frac{\rho_f}{\rho_g}\left(\frac{Re}{We_g}\right)^2 \tag{2.40}$$

Reitz and Bracco [78] established the borders between the different atomization regimes by using Ohnesorge number, as sketched in Figure 2.16. It is clear that the density ratio affects the atomization only at its low values. For that reason, it is common to represent the atomization regimes separation as function of only Reynolds and Ohnesorge number for high density ratios, as done in Figure 2.17.

The quantification of the atomization regimes borders has been studied for decades. Table 2.1 shows some of the existing criteria to define them,
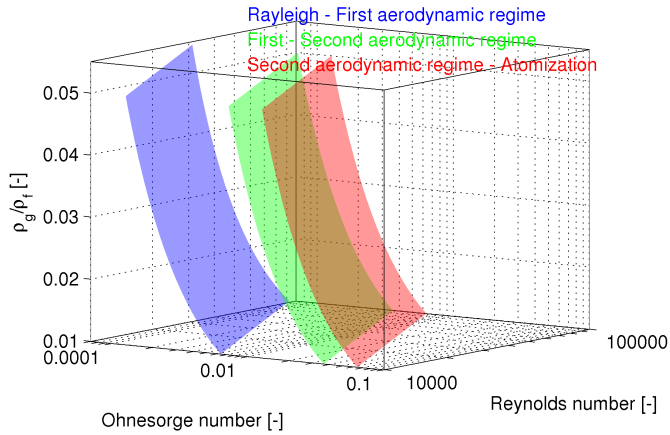
Figure 2.16: Qualitative separation of atomization regimes using the three dimensionless parameters required by the Buckingham's π-theorem.
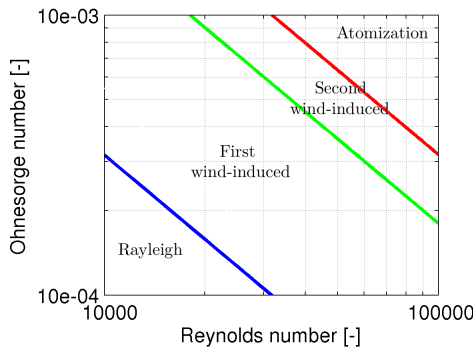
Figure 2.17: Qualitative separation of atomization regimes for high values of ρ_g/ρ_f ratio.

where We_g is the gas Weber number (Equation (2.39) with the gas density). In the expression proposed by Reitz [77], the constant C is calculated from the spray angle, which has to be experimentally measured. Thus, internal flow parameters, which are key to determine the atomization at high Weber numbers [78], are somehow considered.

Regime	Expression	Ref.
Rayleigh to	$We_g = 0.4$	[82]
First wind-induced	$We_g = 1.2 + 3.41\,Oh^{0.9}$	[83]
First wind-induced to Second wind-induced	$We_g = 13$	[82]
Second wind-induced	$We_g = 40.3$	[84]
to Atomization	$\frac{\rho_g}{\rho_f} = \frac{\sqrt{C}-1.15}{744}\left(\frac{\sqrt{3}}{6}\left(1 - e^{-10\,Ta}\right)\right)^{-2}$	[77]

Table 2.1: Definition of the transition between atomization regimes.

Atomization mechanisms

Although Rayleigh and first wind-induced atomization regimes (low Weber numbers) are well known and characterized, still an established theory about atomization at high Weber numbers does not exist. It is believed that, for those conditions, the break-up is caused by a sum of several effects (which are described next), whose each one's level of influence is unknown.

Aerodynamic instabilities

Once unstable perturbations are generated at the liquid-gas interface, the relative velocity between them produces a shear stress which likely increases them. Then, the mechanism that controls the second wind-induced regime is reproduced: high frequency instabilities of the vein surface, caused by the local variations in pressure, form thin ligaments, which break due to surface tension and/or aerodynamic forces.

This mechanism has been studied by several authors [78, 85] based on the Taylor's linear analysis [86, 87]. For low jet velocities, this analysis matches experimental results. However, as the jet velocity increases, the atomization rate and spray angle theoretically obtained are lower than those experimentally observed, and this fact clearly indicates that there are other relevant atomization mechanisms. Additionally, the aerodynamic theory does not consider the influence of the nozzle geometry.

Turbulence

Other authors, such Lefebvre [80], purpose the turbulence as one on the main causes of atomization. This turbulence is generated inside the nozzle orifices, where the radial component of the perturbation velocity is contained by the walls, but outside the injector this fluctuating component pushes the liquid outward the vein, generating the atomization. This mechanism allows

explaining the atomization in void atmospheres where aerodynamic interaction is not possible. On the other hand, this mechanism does not explain the large changes in spray behavior when the gas density varies.

Reorganization of the velocity profile

Another mechanism that provokes the atomization of the liquid vein is the modification of the velocity profile just after the orifice exit. Viscous effects (due to the presence of the orifice wall) disappear and the fluid near the vein surface accelerates. According to this theory proposed by Brennen [88], this modification in the velocity generates instabilities at the vein surface which favor atomization. In the case of laminar flow inside the orifice the velocity profile corresponds to Poiseuille flow, but it is transformed into a uniform profile outside the nozzle. If the momentum is conserved, this reorganization of the velocity profiles entails a decrease in the kinetic energy of the liquid vein, which in turn entails a generation of a radial velocity component, then favoring the atomization.

Cavitation

Cavitation phenomenon is the last relevant atomization mechanism. Its influence can be divided in two different types. On one hand, fuel vapor separates the flow from the wall, which eventually can be attached to it again, and this increases turbulence levels due to an increase in the fluctuations and implosion or disintegration of the bubbles, which at the same time favors the atomization resulting in shorter and wider sprays [46, 55, 57].

On the other hand, cavitation bubbles presence at the orifice exit means discontinuities in the fluid, which ease the separation of ligaments and droplets from the vein. In the case of high ambient temperatures, the expansion of these vapor bubbles generates radial stresses which also lead to atomization of the liquid vein. Furthermore, bubbles located at the orifice exit decrease the effective area, increasing the average velocity and modifying the velocity profile. Nonetheless, bubbles do not need to reach the orifice exit to modify the velocity profile.

Secondary atomization

Droplets formed by the liquid jet break-up (primary atomization) are still moving at high speed in a gaseous atmosphere. The fate of the droplets is also decided by the same balance of forces already described, causing the so called secondary break-up. Due to the difference is shape (spherical droplet instead of cylindrical jet), the modality in which this process occurs is different.

Aerodynamic forces due to the relative velocity between the droplets and the gas tend to break them into smaller droplets. On the opposite side, forces associated to the surface tension tend to maintain the original spherical shape of the droplet. Therefore, it is harder, in other words, requires higher relative velocity to break smaller droplets because their curvature and so their surface tension is higher.

Like the primary break-up, secondary atomization can be studied through the dimensionless Weber number [89], but in this case defined with the gas density and the relative velocity between droplets and the surrounding gas, as done in Equation (2.41).

$$We_g = \frac{\rho_g u_{rel}^2 D_{eff}}{\sigma} \qquad (2.41)$$

According to Wierzba [90], five different regimes depicted in Figure 2.18 of secondary atomization can be distinguished. For Weber numbers lower than $We_g = 12$, aerodynamic forces are not able to break the droplet, generating only small deformations on its shape. However, a small increment in the relative velocity can propitiate the first regime, known as vibrational, in which the surface deformation progressively grows up to provoke its division. In the second regime, which corresponds to Weber numbers from $We_g = 12$ to $We_g = 20$, the droplet break-up initiates with a deformation into a sac or bag shape and ends up with a disintegration in many small droplets. Third regime is similar, the only difference is that the droplet initially forms also a stamen oriented anti-parallel to the direction of the drop motion which breaks into relatively large droplets. In the fourth sheet stripping regime, for Weber numbers lower than $We_g = 100$, a film is continuously eroded from the droplet surface ends and disintegrates rapidly resulting of small droplets and, in some cases, a cores whose size is comparable to that of the parent droplet. Fifth and last regimes, known as catastrophic break-up, occurs for Weber number greater than $We_g = 1000$. The droplet surface is corrugated by waves of large amplitude and long wavelengths forming a small number of large fragments that in turn break up into even smaller units.

These regimes were also studied by Arcoumanis et al. [49], who found the same five but did not agree in the limits between them especially at high Weber numbers, as shown in Table 2.2; and by Pilch and Erdman [91] who differ primarily by the names assigned to each mode.

Han and Tryggvason [92] focused their study in the sac or bag regime at different density ratios. They used, instead of the Weber number, other
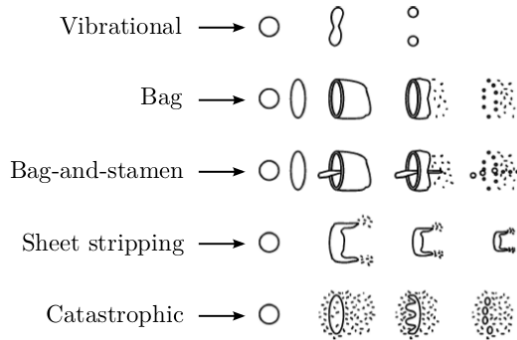
Figure 2.18: Sketch of secondary atomization regimes.

Regime	Wierzba [90]	Arcoumanis et al. [49]
Vibrational	$We_g \approx 12$	$12 \leq We_g \leq 18$
Bag	$We_g < 20$	$We_g \leq 45$
Bag-and-stamen	$We_g < 50$	$We_g \leq 350$
Sheet stripping	$We_g < 100$	$We_g \leq 2670$
Catastrophic	$We_g > 100$	$We_g > 2670$

Table 2.2: Definition of the transition between secondary atomization regimes.

two dimensionless parameters: Ohnesorge number base on the droplet (Equation (2.38) where the length is the droplet diameter and not D_{eff}); and Eötvös number (interchangeably called the Bond number) defined in Equation (2.42), where $\Delta\rho$ is the density difference between the droplet and the surrounding gas. They found out that for low Ohnesorge numbers and low density ratios, the droplet does not break for Eötvös numbers less than about $Eo = 18$, for Eötvös numbers between $Eo = 18$ and $Eo = 36$ the droplet breaks-up by the formation of a backward facing bag, a transient break-up is observed for Eötvös nubers around $Eo = 48$, and for values larger than about $Eo = 60$, the droplet evolves into a forward facing bag. As the Ohnesorge number increases, the effect of the viscosity reduces the rate of deformation. At high density ratios and large Eötvös numbers, the sac regime is replaced by the sheet stripping break-up where the edge of the drop is pulled in the downstream direction.

$$Eo = \frac{g\Delta\rho D_d}{\sigma} \tag{2.42}$$

Coalescence of droplets

At the same time and location that the atomization takes place, the coalescence phenomenon and bouncing of droplets also do (droplet-droplet interactions) [49]. It is known that especially in the case of low ambient temperatures (non-evaporating sprays), spray droplet size is the outcome of a competition between droplet break-up and droplet coalescence phenomena. The coalescence is defined as the process by which two or more droplets merge during contact to form a single droplet. The contact or collision probability depends on the relative velocity between the droplets, the relative direction and the local fuel concentration. Therefore, collision is more frequent in the near-field and the axis of the spray, in other words, in the dense part [87, 93].

While the collision frequency may be estimated from kinetic theory considerations, the outcome depends on the impact energy, the ratio of droplet sizes, and ambient conditions like gas density, gas viscosity, and the air-fuel ratio of the gas surrounding the droplets during impact. There are four important dimensionless parameters governing the collision phenomenon [94]: the Reynolds number (Equation (2.43), where $D_{d,1}$ is the diameter of the larger drop), the Weber number (Equation (2.44)), the droplet diameter ratio $D_{d,2}/D_{d,1}$, and the impact parameter B. The dimensionless factor B value varies from 1 to 0. In the case of head-on collision ($B = 0$), the relative velocity vector coincides with the center-to-center line. If $B > 0$ the collision is off-axis, and $B = 1$ is called a tangential of grazing collision.

$$Re_{coll} = \frac{\rho_f D_{d,1} u_{rel}}{\mu_f} \tag{2.43}$$

$$We_{coll} = \frac{\rho_f D_{d,2} u_{rel}^2}{\sigma} \tag{2.44}$$

Collision may result in bouncing, coalescence, reflexive separation, stretching separation or shattering collision, and a criterion has to be specified to determine which one occurs [95, 96] (see Figure 2.19 for a graphical representation). Qian and Law [95] defined the transition between these five collision regimes in terms of the collision Weber number and the impact parameter, qualitatively described in Figure 2.20. They also proved that an increase of gas density promotes bouncing, while a gas atmosphere with a high content of evaporated fuel promotes coalescence. In addition, the numbers and size of the new droplets resulting from a collision event strongly depend on the diameter ratio of the parent droplets.
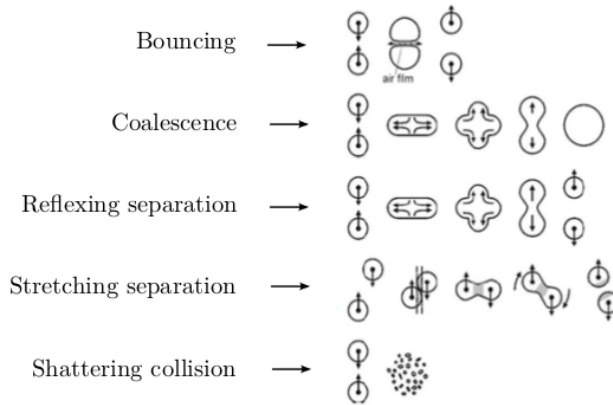
Figure 2.19: Sketch of coalescence regimes, droplet-droplet interactions.
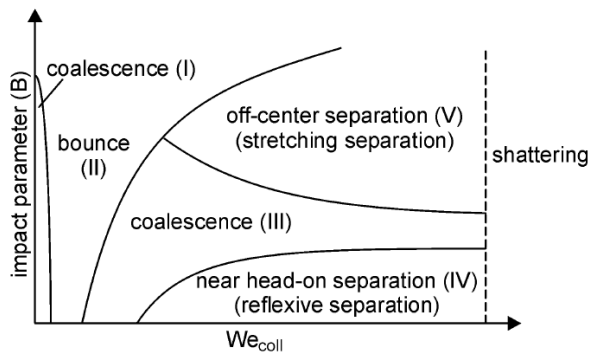
Figure 2.20: Schematic of droplet collision regimes borders.

2.4.2   Evaporation process

In addition to the break-up of the spray and mixing processes of air and fuel droplets, the evaporation of liquid droplets also has a significant influence on ignition, combustion, and formation of pollutants (it is a prerequisite for the subsequent chemical reactions) [94].

The energy for evaporation is transferred from the combustion chamber gas to the colder droplet due to conductive, convective, and radiative heat transfer, resulting in diffuse and convective mass transfer of fuel vapor from its surface into the gas. Hence, there is a strong linking of evaporation rate and gas conditions: pressure, temperature and transport properties (such the

boiling point, heat of evaporation, critical temperature, volatility, droplet size and relative velocity between the droplets and the surrounding gas).

The study of the evaporation process from the microscopic point of view is complex and multidisciplinary, it involves heat and mass transport, fluid dynamics and chemical kinetics problems. It gets more even complex under real engine conditions. That is why many researchers prefer a macroscopic study of the evaporation process, i.e. in terms of liquid length (see Section §2.4.3). Furthermore, phase equilibrium is usually assumed, it is presume that the phase transition (liquid to vapor) is much faster than the vapor transport from the surface into the surrounding gas. Further on it is assumed that even if the conditions in the gas phase or inside the droplet change (e.g. temperature rise), phase equilibrium is always immediately reached. Notwithstanding, it is proved that the hypothesis of phase equilibrium is not correct [97, 98]. A boundary layer where fuel vapor accumulates is formed around the droplet, this produces over-heating of the droplet and a saturation of the boundary layer, then slowing down the evaporation process. Additionally, Ayoub and Reitz [98] comment that for high injection pressure and ambient conditions close to the critical point: the diffusion characteristic time scales of both phases, ambient gas and vapor, are similar, so the common hypothesis of quasi-steady surrounding gas is not longer correct; and the thermodynamic properties vary with the pressure, temperature and fuel concentration, so equations of state for all properties must be calculated and used.

Although real fuels consist of a multitude of different components that influence the evaporation process (more volatile and less ignitable components evaporate first, components with higher molecular weight evaporate later), the standard approach is to use a single-component model fuel because of its simplicity and low consumption of computational time. Usually tetradecane or dodecane is used to represent the relevant properties of Diesel, and octane is used for Gasoline [94].

Nevertheless, research work today concentrates on more sophisticated evaporation models, especially with respect to modeling more realistic component fuels and to replace the single-component fuel calculations. For example, Diesel fuel consists of more than 300 different components, and it is obvious that a single reference fuel cannot predict all of the relevant sub-processes during evaporation, ignition and combustion with sufficient accuracy. Jin and Borman [99] showed that the overall mixture formation process, and thus also ignition and combustion, may be significantly influenced by the composition of the fuel vapor, and that it may be important to describe the multicomponent character of fuels more accurately. However, the computational effort describ-

ing mixtures of ten and more components is enormous. Tamim and Hallett [100] have shown the possibility of introducing the multicomponent character based on so-called continuous thermodynamics, which provides a relatively simple and elegant description of mixtures consisting of a multitude of different components. The main idea of the continuous thermodynamics approach is the description of the relevant fuel properties needed to determine the evaporation process like boiling and critical temperatures, heat conductivity, heat of evaporation, etc. as a function of a distribution variable. If the distribution of the different components inside the droplet changes during the evaporation process (the more volatile component evaporate first), the distribution function and thus the fuel properties also change. This kind of approach, although requires a larger modeling effort to a discrete two-component model, ensures that the effect of the different fuel components on the time-dependent evaporation process is accounted for with lower computational cost.

2.4.3 Spray characterization

Until now, the spray has been described from a physical point of view, trying to underline the processes behind the atomization and spray formation. Conventionally, the spray characterization is divided into two groups: macroscopic and microscopic, depending on the scale of the parameter observed. The macroscopic characterization investigates the global shape of the spray, while the microscopic characterization is focused on local parameters.

Macroscopic characterization

The macroscopic characterization of the spray aims at the understanding of the global interaction of the spray with the surrounding gas. The following parameters are widely studied due to their fundamental importance for the understanding of the spray dynamics and because, from the experimental point of view, their measurements are robust and relatively easy.

As shown in Figure 2.21, there are two parts clearly differentiated: a first steady part of the spray which extends up to 60% or 70% of the spray length and has conical shape; and a second transient part at the spray tip which has a semi-elliptical shape due to the aerodynamic interaction with the surrounding gas.

Spray penetration

The spray penetration S is the distance traveled by the spray tip into the combustion chamber (see Figure 2.21). This is a fundamental parameter not only because it measures the air-fuel mixing but also because it determines the
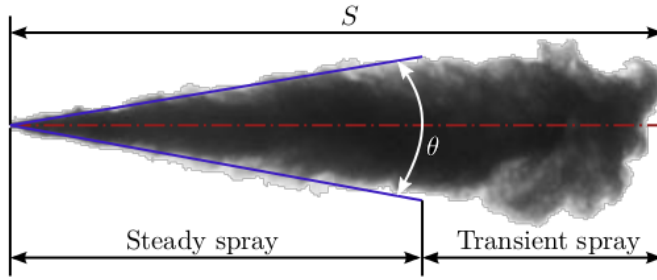
Figure 2.21: Macroscopic description of the spray: penetration and angle.

wall impingement, a key factor for the combustion and emissions [101]. Even if conceptually it is very easy to understand the meaning of this parameter, its definition is not easy.

From the wide number of studies that can be found in the literature, many correlations have been proposed to link the spray penetration to the injection conditions such as injection pressure, ambient density, orifice diameter, etc. The spray penetration depends mainly on the spray momentum, the ambient density and the spray spreading angle. Hay and Jones [102] made a review of the correlations available in the literature at the time and highlighted as the best correlations the ones presented by Dent [103] and Wakuri et al. [104]. Apart from the proportional constant applied to the relationship and other minor details, all the equations, even those presented in more recent works [21, 53], are in the form of Equation (2.45), where the value of each exponent is obtained by simple application of the dimensional analysis, except for the dimensionless term that includes the spray angle. The value of 1/2 for the exponent of this term is obtained through an analytical analysis of the spray evolution by assuming it has conical shape [53].

$$S\left(t\right) \propto \rho_g^{-\frac{1}{4}} \Delta p^{\frac{1}{4}} \tan^{-\frac{1}{2}}\left(\frac{\theta}{2}\right) D_o^{\frac{1}{2}} t^{\frac{1}{2}} = \rho_g^{-\frac{1}{4}} \dot{M}^{\frac{1}{4}} \tan^{-\frac{1}{2}}\left(\frac{\theta}{2}\right) t^{\frac{1}{2}} \qquad (2.45)$$

Wakuri et al. [104] were the first including the spray spreading angle into the equation; on the other hand Dent [103] included the effect of the ambient temperature, or more precisely, the difference between the ambient and the nozzle tip temperature with the factor $(T_{nozzle}/T_g)^{\frac{1}{4}}$.

Hiroyasu and Arai [105] presented a penetration law split into two parts (see Equation (2.46)) because the spray penetration shows a different, lin-

ear proportionality with time in the first millimeters. The time t_b in Equation (2.46) represents the time needed to reach the penetration at which the break-up is completed, and it is defined by Equation (2.47).

$$
\begin{aligned}
S\left(t\right) &= 0.39\sqrt{\frac{2\Delta p}{\rho_f}}t; \text{ if } t < t_b \\
S\left(t\right) &= 2.95\rho_g^{-\frac{1}{4}}\Delta p^{\frac{1}{4}}D_o^{\frac{1}{2}}t^{\frac{1}{2}}; \text{ if } t \geq t_b
\end{aligned}
\tag{2.46}
$$

$$
t_b = 28.65\frac{\rho_f D_o}{\left(\rho_g\Delta p\right)^{\frac{1}{2}}}
\tag{2.47}
$$

More recently, Naber and Siebers [53] developed a penetration law based on their experimental measurements under evaporative conditions, also showing two different behaviors of the spray penetration (Equation (2.48)). Moreover, they inserted other flow parameters related to the internal flow in the expression, concretely velocity C_v and area C_a coefficients, and included the spray spreading angle θ. In this case, the time t_b is defined as the time when the spray is controlled by air entrainment, given in Equation (2.49). Desantes et al. [106] identify this time t_b with the transient period at which the mass flow rate (and so the momentum flux) is still increasing due to the dynamic of the injector and the variation of the nozzle's effective section as a function of needle position. Instead of 0.66 as a constant of Equation (2.49), they use 0.36.

$$
\begin{aligned}
S\left(t\right) &= C_v\sqrt{\frac{2\Delta p}{\rho_f}}t; \text{ if } t < t_b \\
S\left(t\right) &= C_v^{\frac{1}{2}}\left(2C_a\right)^{\frac{1}{4}}\tan^{-\frac{1}{2}}\left(\frac{\theta}{2}\right)\rho_g^{-\frac{1}{4}}\Delta p^{\frac{1}{4}}D_o^{\frac{1}{2}}t^{\frac{1}{2}}; \text{ if } t \geq t_b
\end{aligned}
\tag{2.48}
$$

$$
t_b = \frac{\left(2C_a\right)^{\frac{1}{2}}}{0.66C_v\tan\left(\frac{\theta}{2}\right)}\frac{\rho_f D_o}{\left(\rho_g\Delta p\right)^{\frac{1}{2}}}
\tag{2.49}
$$

Gimeno [8] also studied the splitting time t_b and proposed a new expression to compute it, Equation (2.50), as function of the spray momentum flux. It includes parameters related to the internal flow, such area and velocity

coefficients or pressure drop (see Equation (2.28)). This Equation (2.50) is similar to the one proposed by Naber and Siebers [53], but a new constant k_i has been added, whose value depends on the opening time of the injector, as proposed by Desantes et al. [106]. This means that Equation (2.50) considers both effects previously explained, the air entrainment and the transient period of the mass flow rate.

$$t_b = \frac{0.855}{k_i \tan\left(\frac{\theta}{2}\right)} \frac{\sqrt{\dot{M}}}{\sqrt{\rho_g u_{eff}^2}} \tag{2.50}$$

The value of the constant k_i is given by Equation (2.51), which was obtained by fitting a general correlation to experimental results. Both ambient density and injection pressure affect this constant, and so the time t_b, though the injection pressure in a much lesser way.

$$k_i = 0.1237 \left(\frac{\rho_g}{\rho_f}\right)^{-0.2624} p_i^{0.08175} \tag{2.51}$$

Other authors have obtained empirical correlation by statistical analysis of the experimental data. For example, Payri et al. [107] propose Equation (2.52) for non-evaporative conditions, and Payri et al. [108] give Equation (2.53) for the linear part of the penetration. These equations also remark a good agreement between dimensional analysis and experimental measurements.

$$S(t) \propto \rho_g^{-0.268} \dot{M}^{0.254} \tan^{-0.5}\left(\frac{\theta}{2}\right) t^{0.513} \tag{2.52}$$

$$S(t) = 0.018 \rho_g^{-0.25} \Delta p^{0.51} t^{1.04} \tag{2.53}$$

When comparing non-evaporative and evaporative conditions for the same injection conditions (injection pressure, discharge pressure, ambient density...), Naber and Siebers [53] observed that evaporation can decrease the spray penetration value up to 20%. This reduction is attributed to an increase of the gas-vapor fuel mixture density within the spray since the temperature is lower due to the evaporation process. Finally, under reactive conditions, the spray penetration increases because of the local density reduction due to combustion reactions [109].

Spray angle

The spray spreading angle θ is the angle included between the two sides of the spray cone, usually calculated as the angle included by the lines fitting the two sides, as shown in Figure 2.21. This is also a fundamental parameter driving the entrainment of air in the spray and determining the fuel evaporation and combustion processes. After a first transient short time after start of injection, this angle stabilizes at a certain value.

Again, different correlations to predict the behavior of the spreading angle can be found in the literature. One of the first, presented by Ranz [82], is given in Equation (2.54) where F_t represents an analytical expression that, in the case of typical Diesel injection conditions, reaches its limit value $F_t = 0.288$. However, this expression contains a constant, C, that needs to be tuned for the specific nozzle geometry.

$$\tan\left(\frac{\theta}{2}\right) = \frac{4\pi}{C}\left(\frac{\rho_f}{\rho_g}\right)^{\frac{1}{2}} F_t\left(\frac{\rho_g}{\rho_f}\frac{\sigma^2}{\mu_f^2 u_{th}^2}\right) \qquad (2.54)$$

Reitz and Bracco [110] carried out an extensive experimental study including several variations in the internal geometry which led them to obtain Equation (2.55) as the solution for the constant C. However, it does not take into account neither the contraction of the orifice nor the curvature of the orifice inlet. Therefore, this definition gives good predictions for geometries similar to the ones employed by Ranz [82] but loses its effectiveness when the geometry is radically changed.

$$C = 3 + \frac{1}{3.6}\frac{L}{D_o} \qquad (2.55)$$

Hiroyasu and Arai [105] assessed the impact of the variation in the size of the sac by performing a set of tests. Basing on their experimental results, they gave Equation (2.56) as the solution for the spray spreading angle. Other experimental studies propose similar results [53, 106, 111]. Naber and Siebers [53] made a review of these and more expressions proposed for the spray spreading angle and realized that the density ration exponent varied between 0.2 and 0.5, though they proposed 0.19. In all these studies the injection pressure and the fuel viscosity have been found to have a negligible effect.

$$\theta = 83.5\left(\frac{L}{D_o}\right)^{0.022}\left(\frac{D_o}{D_s}\right)^{0.15}\left(\frac{\rho_g}{\rho_f}\right)^{0.26} \qquad (2.56)$$

Kampmann et al. [112] investigated the effect of the HEG level at the orifice inlet and proved that higher the degree of HEG, the lower the spreading angle. Moreover, decreasing the HEG level, a higher statistic dispersion of the measurements was observed.

In general, research carried out agree on the main parameters that affect the spray spreading angle: density ratio, injector geometry and cavitation phenomenon. The injection pressure has some effect, but a general rule cannot be found since, probably, this effect is the result of many parameters combined together, such as the nozzle seat type, the orifice inlet radius, etc. Additionally, as commented in Sections §2.3.5 and §2.4.1, the presence of cavitation has a strong effect on the spray spreading angle due to its effect on the primary atomization [46]. However, the quantification of these effects is still an open issue, first of all, due to the complexity of the phenomenon itself (combination of turbulence and aerodynamic instabilities), but also due to the high sensitivity to many aspects of the experiments: the experimental technique employed, the details of the optical arrangement and the methodology used for the image processing [113] . Furthermore, the definition of the spreading angle is not always consistent, for example, Naber and Siebers [53] presented a definition based on the spray area calculation, while Payri et al. [28] based their definition on the fitting of two lines on the spray boundary (even how to define the fitting lines is controversial, i.e. if they should be forced to pass through the orifice exit or not). Consequently, the spray spreading angle is inaccurate and values obtained by different authors cannot be compared between them.

Liquid length

At evaporative conditions, the air entrained by the spray produces the progressive evaporation of the fuel (see Section §2.4.2) and as a consequence the liquid phase initially penetrates until it reaches a steady value, as shown in Figure 2.22.

The liquid phase penetration or liquid length LL is a measurement commonly performed to characterize the mixing process of the Diesel spray [106, 114]; a simple definition can be given as the distance that the injected fuel has to penetrate in the chamber until its complete evaporation. Again, the dependence of the liquid length upon different parameters such ambient temperature, ambient density, injection pressure, nozzle diameter and fuel type has been studied by several authors [38, 106, 114]. Its behavior is generally well described by empirical correlations obtained by different authors [115, 116]. For reference, the relationship obtained by dimensional analysis by [117] is given in Equation (2.57), where K_p is a constant depending on ambient
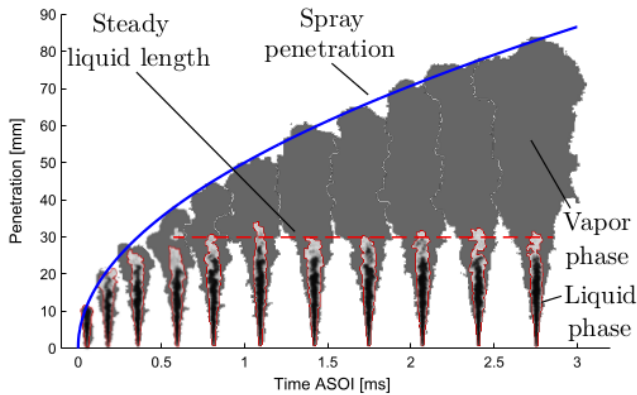
Figure 2.22: Liquid and vapor phase of the Diesel spray penetrating in a quiescent and non-reacting atmosphere.

conditions and C_{mv} is a coefficient depending on the fuel and ambient gas properties.

$$LL = K_p \frac{C_a D_o}{C_{mv} \tan\left(\frac{\theta}{2}\right)} \tag{2.57}$$

Intact and break-up lengths

The region right at the exit of the orifice is characterized by a very dense ambient and, for a certain distance, it is considered to exist an intact core length IL [77]. It is generally defined as the distance between the orifice exit and the location where the first droplets appear due to the atomization process. Even if this feature is listed in the macroscopic characteristics (undoubtedly it is a global feature of the spray) the length of the intact core can be less than 1 mm.

Chehroudi et al. [118] studied water sprays and obtained a qualitative relationship between the intact core length and the fuel velocity the the orifice outlet, already represented in Figure 2.15. Other authors demonstrate its variability depending on the air-fuel density ratio [53, 105, 114, 118], on the orifice outlet diameter and L/D_o ratio or on the fuel properties [51, 114].

The correct evaluation of this length is essential to understand the fundamental of the spray break-up: many researchers simulate the primary break-up via DNS method [119, 120], but many other focus their attention on the experimental measurement using commercial Diesel injectors. For instance,

Morena [57] performed a microscopic visualization of the spray and noticed that, at low injection pressure, the spray was characterized close to the orifice outlet by nearly zero spreading angle and he named the length of this region non-perturbed length *NPL* (length where air entrainment has not started yet, see Figure 2.23).

Even if their definition is very similar, the non-perturbed length has not to be confused with the intact core length since the last one refers to the geometry of the spray while the first to the atomization process. Furthermore, these two quantities are different than the well known break-up length *BL*, which is defined as the distance from the orifice outlet where the liquid vein disappears (see Figure 2.23). It depends, among other factors, on the jet velocity at the orifice outlet and follows the trend showed in Figure 2.15.

Spray micro-angle

Spray spreading micro-angle θ_m is the angle included between the two sides of the spray cone at first millimeters from the orifice outlet, and is smaller than the spray spreading angle θ, as shown in Figure 2.23 [105] where L_m is the origin of the micro-angle and L_s is the origin of the spreading angle. This angle together with the break-up length are reduced if conical orifices with rounded inlet are used. On the contrary, the spray angle in the first millimeters significantly increases when cavitation occurs [57, 121].
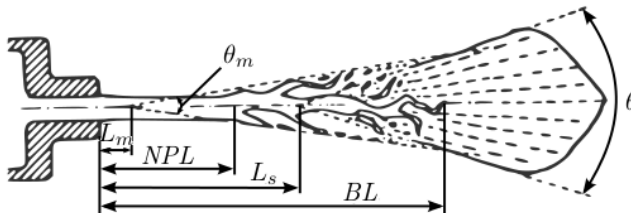
Figure 2.23: Macroscopic description of the spray: near-field spray structure.

Microscopic characterization

The microscopic characterization aims at the understanding of what is within the spray boundaries. The following parameters are fundamental for the development and validation of spray models and CFD simulations. However, the difficulties related to the Diesel spray measurements (high temperature/pressure conditions, dense spray, very short time scale, etc.) make the access to these quantities a constant scientific/technological challenge.

Droplet size

The measurement of the droplet size is important for the understanding of the atomization process and of the droplet-air momentum transfer (once combined with droplet velocity). Notwithstanding, the real droplet size involves a huge amount of information: the droplets formed span over a wide range of diameter values; and the evaporation process (occurring also at ambient temperature) reduces the size of the droplets while traveling within the combustion chamber. As a consequence of these facts, the droplet diameter cannot be treated as a deterministic measurement but a statistical approach is always employed. The droplet size is therefore characterized by mapping the spray (in time and space) and relating each point to a histogram. By representing the effective experimental measurements on the histogram, the related Probability Density Functions (PDF) are obtained. However, this characterization requires many hypothesis and lead to complex results and analysis; thus, it is addressed only to very specific studies. Moreover, the analysis of the PDF generally does not provide any crucial information except regarding spray non-uniformity.

One solution normally employed to describe the atomization quality is the definition of a characteristic diameter. This quantity can be defined in different ways depending on the application. Mugele and Evans [122] classified these definitions proposing the notation represented in Table 2.3 that nowadays is the most employed.

Notation	Factor	Physical meaning	Formulation
D_{10}	Diameter	Mean geometrical diameter	$\frac{\sum_i N_i D_i}{\sum_i N_i}$
D_{20}	Surface	Mean surface area	$\left(\frac{\sum_i N_i D_i^2}{\sum_i N_i}\right)^{\frac{1}{2}}$
D_{30}	Volume	Mean volume/mass	$\left(\frac{\sum_i N_i D_i^3}{\sum_i N_i}\right)^{\frac{1}{3}}$
D_{32}	Vol./Surf.	Volume/surface ratio	$\frac{\sum_i N_i D_i^3}{\sum_i N_i D_i^2}$

Table 2.3: Definitions of mean droplet diameters.

Among the definition given in Table 2.3, the most employed for Diesel spray studies is the D_{32}, also called Sauter Mean Diameter (*SMD*). It is in fact an effective indicator of the relationship between drag forces (related to the droplet surface) and inertia forces (related to the droplet mass). Moreover, it

can be obtained directly by the application of imaging techniques, the Planar Laser Induced Fluorescence (PLIF) [123] and its derived techniques [124], which relate the fluorescence signal, proportional to the droplet volume, to the scattering signal, that is a function of the droplet surface. Another technique normally employed for the determination of the droplet diameter is the Phase Doppler Particle Analyzer (PDPA). This technique allows to determine the size and the velocity of the droplets. When comparing the two techniques, PDPA is more accurate than PLIF methods, but it has the relevant drawback of being a punctual measurement, extending significantly the time required for the tests.

Several experimental studies have proposed correlations to link the droplet size D_{32} with the injection conditions [125, 126]. For reference, the correlation presented by Hiroyasu et al. [125] is given in Equation (2.58), which is one of the first that can be found in the literature.

$$D_{32} = SMD = 0.38 \Delta p^{-0.135} \rho_g^{0.121} \dot{m}_f^{0.131} \qquad (2.58)$$

However, care must be taken with these correlations because large variations are obtained on the predictions, in part due to the weak amount of experimental data used to build the correlation. It is then hazardous to extend an expression to other nozzle shapes, diameters or fuels. Therefore they may be used only as a starting point and adjusted to fit well the experimental data under consideration and as qualitative guidelines [127].

Velocity distribution

The characterization of the velocity field of the spray allows to evaluate and understand the process of air-fuel mixing. For this reason, many authors have investigated this parameter. Most of them based their studies on the similitude between Diesel spray and gas-jet theory proposed by Adler and Lyn [128] that is accepted to describe in an accurate way the behavior of the steady spray at a certain distance from the orifice (far-field or dilute region) [53, 129]. However, an important difference lays between the gas-jet and the Diesel spray, in the first case the spreading angle is constant and depends only on the properties of the fluids involved in the process, while in the second case the geometry of the orifice and the gas density in the chamber have a significant effect.

The radial velocity profiles can be then extended to concentration profiles [52] by means of the Schmidt number defined in Equation (2.59) as the relationship between the diffusion of momentum and mass. These models show how the concentration and velocity profiles are characterized by two different

zones: the first one, related to the intact length, where the velocity and concentration variables remain constant; and at certain distance the second one where both are proportional to $1/x$.

$$Sc = \frac{\mu}{\rho \kappa_m} \tag{2.59}$$

The experimental tools available for these measurement are different: Rayleigh scattering [130] and Particle Image Velocimetry (PIV) [131] allow to obtain entire maps of, respectively, concentration and velocity fields; PDPA technique is used to determine the velocity field and, when it is dedicated only to particle velocity, it is also called Laser Doppler Velocimetry (LDV).

References

[1] Payri, F., J. M. Desantes, and et al. *Motores de combusitión interna alternativos.* Ed. by F. Payri and J. M. Desantes. First edition. Loreto 13-15, Local B, 08029 Barcelona, Spain: Editorial Reverté, 2011 (*cit. on pp. 15, 17*).

[2] García-Oliver, J. M. "Aportaciones al estudio del proceso de combustión turbulenta de chorros en motores de inyección directa". PhD thesis. Camino de Vera, s/n, 46022, Valencia, Spain: Escuela Técnica Superior de Ingenieros Industriales, Universitat Politècnica de València, 2004 (*cit. on p. 16*).

[3] Flaig, U., W. Polach, and G. Ziegler. "Common Rail System (CR-System) for Passenger Car DI Diesel Engines, Experiences with Applications for Series Production Projects". *SAE Technical Paper 1999-01-0191* (1999). DOI: 10.4271/1999-01-0191 (*cit. on p. 18*).

[4] Payri, R., F. J. Salvador, P. Martí-Aldaraví, and J. Martínez-López. "Using one-dimensional modeling to analyse the influence of the use of biodiesels on the dynamic behavior of solenoid-operated injectors in common rail systems: Detailed injection system model". *Energy Conversion and Management*, vol. 54 (2012), pp. 90–99. DOI: 10.1016/j.enconman.2011.10.004 (*cit. on pp. 18, 19, 28*).

[5] Johnson, J. et al. "Correlations of Non-Vaporizing Spray Penetration for 3000 Bar Diesel Spray Injection". *SAE Technical Paper 2013-24-0033* (2013). DOI: 10.4271/2013-24-0033 (*cit. on p. 20*).

[6]   Macián, V., R. Payri, S. Ruiz, M. Bardi, and A. H. Plazas. "Experimental study of the relationship between injection rate shape and Diesel ignition using a novel piezo-actuated direct-acting injector". *Applied Energy*, vol. 118 (2014), pp. 100–113. DOI: 10.1016/j.apenergy.2013.12.025 (*cit. on p. 20*).

[7]   Zhuang, J., X. Qiao, J. Bai, and Z. Hu. "Effect of injection-strategy on combustion, performance and emission characteristics in a DI-diesel engine fueled with diesel from direct coal liquefaction". *Fuel*, vol. 121 (2014), pp. 141–148. DOI: 10.1016/j.fuel.2013.12.032 (*cit. on p. 20*).

[8]   Gimeno, J. "Desarrollo y aplicación de la medida de flujo de cantidad de movimiento de un chorro Diésel". PhD thesis. Camino de Vera, s/n, 46022, Valencia, Spain: Departamento de Máquinas y Motores Térmicos, Universitat Politècnica de València, 2008 (*cit. on pp. 21, 33, 39, 42, 59*).

[9]   Dohle, U., S. Kampmann, J. Hammer, T. Wintrich, and C. Hinrichsen. "Advanced Diesel Common Rail Systems for Future Emission Legislation". *International Conference on Automotive Technologies (ICAT)*. Ed. by A. M. Yildirim, C. Sorusbay, E. Tezer, B. Sanayo, and A. S. Ticaret. Hyatt Regency Hotel, Istanbul, Turkey, 2004, pp. 109–113 (*cit. on p. 24*).

[10]   Benajes, J., R. Payri, S. Molina, and V. Soare. "Investigation of the Influence of Injection Rate Shaping on the Spray Characteristics in a Diesel Common Rail System Equipped with a Piston Amplifier". *Journal of Fluids Engineering, Transactions of the ASME*, vol. 127.6 (2005), pp. 1102–1110. DOI: 10.1115/1.2062767 (*cit. on p. 24*).

[11]   Glassey, S. F., A. Stockner, and M. Flinn. "HEUI - A New Direction for Diesel Engine Fuel Systems". *International Congress & Exposition*. SAE International. Detroit, Michigan, United States of America: SAE Technical Paper, 1993. DOI: 10.4271/930270 (*cit. on p. 24*).

[12]   Schöppe, D. et al. "Delphi Common Rail System with Direct Acting Injector". *MTZ Worldwide*, vol. 69 (2008), pp. 32–38 (*cit. on p. 25*).

[13]   Payri, R., J. Gimeno, O. Venegas, and A. H. Plazas. "Experimental and computational study of the influence of partial needle lift on nozzle flowin diesel fuel injectors". *Atomization and Sprays*, vol. 22.8 (2012), pp. 687–714. DOI: 10.1615/AtomizSpr.2012005810 (*cit. on p. 25*).

[14]   Altieri, L. and A. Tonoli. "Piezoelectric Injectors for Automotive Applications: Modeling and Experimental Validation of Hysteretic Behavior and Temperature Effects". *Journal of Dynamic Systems, Measurement and Control, Transactions of the ASME*, vol. 135.1 (2013). DOI: `10.1115/1.4006627` (*cit. on p. 25*).

[15]   Colebrook, C. F. "Turbulent Flow in Pipes, with particular reference to the Transition Region between the Smooth and Rough Pipe Laws". *Journal of the Institution of Civil Engineers*, vol. 11.4 (1939), pp. 133–156 (*cit. on pp. 26–28*).

[16]   Garza de León, O. A. de la. "Estudio de los efectos de la cavitación en toberas de inyección diésel sobre el proceso de inyección y el de formación de hollín". PhD thesis. Camino de Vera, s/n, 46022, Valencia, Spain: Departamento de Máquinas y Motores Térmicos, Universitat Politècnica de València, 2012 (*cit. on pp. 26, 27*).

[17]   Salvador, F. J., A. H. Plazas, J. Gimeno, and M. Carreres. "Complete modelling of a piezo actuator last-generation injector for diesel injection systems". *International Journal of Engine Research*, vol. 15.1 (2014), pp. 3–19. DOI: `10.1177/1468087412455373` (*cit. on pp. 26–28*).

[18]   Salvador, F. J., J. Gimeno, J. de la Morena, and M. Carreres. "Using one-dimensional modeling to analyze the influence of the use of biodiesels on the dynamic behavior of solenoid-operated injectors in common rail systems: Results of the simulations and discussion". *Energy Conversion and Management*, vol. 54.1 (2012), pp. 122–132. DOI: `10.1016/j.enconman.2011.10.007` (*cit. on pp. 28, 29*).

[19]   Bianchi, G. M., S. Falfari, M. Parotto, and G. Osbat. "Advanced Modeling of Common Rail Injector Dynamics and Comparison with Experiments". *SAE Technical Paper 2003-01-0006* (2003). DOI: `10.4271/2003-01-0006` (*cit. on p. 28*).

[20]   Bianchi, G. M. et al. "Advanced Modelling of a New Diesel Fast Solenoid Injector and Comparison with Experiments". *SAE Technical Paper 2004-01-0019* (2004). DOI: `10.4271/2004-01-0019` (*cit. on p. 28*).

[21]   Payri, F., V. Bermúdez, R. Payri, and F. J. Salvador. "The influence of cavitation on the internal flow and the spray characteristics in diesel injection nozzles". *Fuel*, vol. 83 (2004), pp. 419–431. DOI: `10.1016/j.fuel.2003.09.010` (*cit. on pp. 29, 34, 58*).

[22]   Salvador, F. J., J. Martínez-López, M. Caballer, and C. de Alfonso. "Study of the influence of the needle lift on the internal flow and cavitation phenomenon in diesel injector nozzles by CFD using RANS methods". *Energy Conversion and Management*, vol. 66 (2013), pp. 246–256. DOI: `10.1016/j.enconman.2012.10.011` (*cit. on pp. 29, 33*).

[23]   Wang, Y., W. G. Lee, R. D. Reitz, and R. Diwakar. "Numerical Simulation of Diesel Sprays Using an Eulerian-Lagrangian Spray and Atomization (ELSA) Model Coupled with Nozzle Flow". *SAE Technical Paper 2011-01-0386* (2011). DOI: `10.4271/2011-01-0386` (*cit. on p. 29*).

[24]   Battistoni, M., C. N. Grimaldi, and F. Marianni. "Coupled Simulation of Nozzle Flow and Spray Formation Using Diesel and Biodiesel for CI Engine Applications". *SAE Technical Paper 2012-01-1267* (2012). DOI: `10.4271/2012-01-1267` (*cit. on p. 29*).

[25]   Xue, Q. et al. "Three-dimensional Simulations of the Transient Internal Flow in a Diesel Injector: Effects of Needle Movement". *25th Annual Conference on Liquid Atomization & Spray Systems (ILASS Americas)*. Pittsburgh, Pensilvania, United States of America, 2013 (*cit. on p. 29*).

[26]   Bae, C., J. Yu, J. Kang, J. Kong, and K. O. Lee. "Effect of Nozzle Geometry on the Common-Rail Diesel Spray". *SAE Technical Paper 2002-01-1625* (2002). DOI: `10.4271/2002-01-1625` (*cit. on p. 30*).

[27]   Benajes, J., J. V. Pastor, R. Payri, and A. H. Plazas. "Analysis of the influence of diesel nozzle geometry in the injection rate characteristic". *Journal of Fluids Engineering, Transactions of the ASME*, vol. 126 (2004), pp. 63–71. DOI: `10.1115/1.1637636` (*cit. on p. 30*).

[28]   Payri, R., S. Molina, F. J. Salvador, and J. Gimeno. "A study of the relation between nozzle geometry, internal flow and sprays characteristics in diesel fuel injection systems". *KSME International Journal*, vol. 18.7 (2004), pp. 1222–1235 (*cit. on pp. 30, 35, 62*).

[29]   Payri, R., C. Guardiola, F. J. Salvador, and J. Gimeno. "Critical cavitation number determination in diesel injection nozzles". *Experimental Techniques*, vol. 28.3 (2004), pp. 49–52 (*cit. on p. 31*).

[30]   Macián, V., V. Bermúdez, R. Payri, and J. Gimeno. "New technique for determination of internal geometry of a diesel nozzle with the use of silicone methodology". *Experimental Techniques*, vol. 27.2 (2003), pp. 39–43 (*cit. on pp. 31, 32*).

[31] Lee, W.-K., K. Fezzaa, and J. Wang. "Metrology of steel micronozzles using x-ray propagation-based phase-enhanced microimaging". *Applied Physics Letters*, vol. 87.22 (2005). DOI: `10.1063/1.2034099` (*cit. on p. 31*).

[32] Kastengren, A. L. et al. "Engine combustion network (ECN): Measurements of nozzle geometry and hydraulic behavior". *Atomization and Sprays*, vol. 22 (2012), pp. 1011–1052. DOI: `10.1615/AtomizSpr.2013006309` (*cit. on pp. 31, 34*).

[33] Lichtarowicz, A., R. K. Duggins, and E. Markland. "Discharge coefficients for incompressible non-cavitating flow through long orifices". *Journal of Mechanical Engineering Science*, vol. 7.2 (1965), pp. 210–219. DOI: `10.1243/jmes_jour_1965_007_029_02` (*cit. on pp. 31, 35, 36*).

[34] Barrero, A. and M. Pérez-Saborid. *Fundamentos y aplicaciones de la mecánica de fluidos.* Ed. by A. Barrero. First edition. New York, New York, United States of America: McGraw Hill / Interamericana de España S. A., 2005 (*cit. on p. 32*).

[35] Anderson, J. D. *Fundamentals of Aerodynamics.* Ed. by J. D. Anderson. Fourth edition. New York, New York, United States of America: McGraw Hill, 2007 (*cit. on pp. 32, 34*).

[36] Payri, R., F. J. Salvador, J. Gimeno, and J. de la Morena. "Study of cavitation phenomena based on a technique for visualizing bubbles in a liquid pressurized chamber". *International Journal of Heat and Fluid Flow*, vol. 30.4 (2009), pp. 768–777. DOI: `10.1016/j.ijheatfluidflow.2009.03.011` (*cit. on p. 32*).

[37] Linne, M., M. Paciaroni, and T. Hall. "Ballistic imaging of the near field in a diesel spray". *Experiments in Fluids*, vol. 40.6 (2006), pp. 836–846. DOI: `10.1007/s00348-006-0122-0` (*cit. on pp. 33, 45*).

[38] Bardi, M. et al. "Engine combustion network: Comparison of spray development, vaporization, and combustion in different combustion vessels". *Atomization and Sprays*, vol. 22.12 (2012), pp. 807–842. DOI: `10.1615/AtomizSpr.2013005837` (*cit. on pp. 33, 45, 62*).

[39] Payri, R., F. J. Salvador, J. Gimeno, and J. de la Morena. "Effects of nozzle geometry on direct injection diesel engine combustion process". *Applied Thermal Engineering*, vol. 29.10 (2009), pp. 2051–2060. DOI: `10.1016/j.applthermaleng.2008.10.009` (*cit. on p. 33*).

[40] Schlichting, H. and K. Gersten. *Boundary Layer Theory*. Ed. by H. Schlichting. Eighth edition. Heidelberg, Germany: Springer, 2000 (*cit. on p. 33*).

[41] White, F. M. *Fluid Mechanics*. Ed. by M. Lange. Seventh edition. New York, New York, United States of America: McGraw-Hill Companies, Inc., 2011 (*cit. on pp. 33, 34*).

[42] Gravensen, P., J. Branebjerg, and O. S. Jensen. "Microfluidics - a review". *Journal of Micromechanics and Microengineering*, vol. 3.4 (1993), pp. 168–182. DOI: 10.1088/0960-1317/3/4/002 (*cit. on p. 34*).

[43] Payri, R., J. M. García, F. J. Salvador, and J. Gimeno. "Using spray momentum flux measurements to understand the influence of diesel nozzle geometry on spray characteristics". *Fuel*, vol. 84.5 (2005), pp. 551–561. DOI: 10.1016/j.fuel.2004.10.009 (*cit. on pp. 35, 37, 38, 42*).

[44] Kent, J. C. and G. M. Brown. "Nozzle exit flow characteristics for square-edged and rounded inlet geometries". *Combustion Science and Technology*, vol. 30.1-6 (1983), pp. 121–132. DOI: 10.1080/00102208308923615 (*cit. on p. 35*).

[45] Fox, T. A. and J. Stark. "Discharge coefficients for miniature fuel injectors". *Proceedings of the Institution of Mechanical Engineers. Part G: Journal of Aerospace Engineering*, vol. 203.17 (1989), pp. 75–78. DOI: 10.1243/pime_proc_1989_203_056_01 (*cit. on p. 35*).

[46] Salvador, F. J. "Estudio teórico experimental de la influencia de la geometría de toberas de inyección Diésel sobre las características del flujo interno y del chorro". PhD thesis. Camino de Vera, s/n, 46022, Valencia, Spain: Departamento de Máquinas y Motores Térmicos, Universitat Politècnica de València, 2003 (*cit. on pp. 35, 37, 39, 40, 42, 51, 62*).

[47] Hall, G. W. "Analytical Determination of the Discharge Characteristics of Cylindrical-Tube Orifices". *Journal of Mechanical Engineering Science*, vol. 5.1 (1963), pp. 91–97. DOI: 10.1243/jmes_jour_1963_005_013_02 (*cit. on p. 36*).

[48] Nakayama, Y. "Action of the Fluid in the Air-Micrometer (1st Report, Characteristics of Small-Diameter Nozzle and Orifice No. 1, In the Case of Compressibility Being Ignored)". *The Japan Society of Mechanical Engineers*, vol. 4.15 (1961), pp. 507–515. DOI: 10.1299/jsme1958.4.507 (*cit. on p. 36*).

[49] Arcoumanis, C., M. Gavaises, and B. French. "Effect of Fuel Injection Processes on the Structure of Diesel Sprays". *SAE Technical Paper 970799* (1997). DOI: `10.4271/970799` (*cit. on pp. 36, 52–54*).

[50] Imagine.Lab, L. *AMESim v.4.2 user's manual.* 2004 (*cit. on p. 37*).

[51] Siebers, D. L. "Scaling Liquid-Phase Fuel Penetration in Diesel Sprays Based on Mixing-Limited Vaporization". *SAE Technical Paper 1999-01-0528* (1999). DOI: `10.4271/1999-01-0528` (*cit. on pp. 38, 63*).

[52] Desantes, J. M., R. Payri, J. M. García, and F. J. Salvador. "A contribution to the understanding of isothermal diesel spray dynamic". *Fuel*, vol. 86.7-8 (2007), pp. 1093–1101. DOI: `10.1016/j.fuel.2006.10.011` (*cit. on pp. 39, 66*).

[53] Naber, J. D. and D. L. Siebers. "Effects of Gas Density and Vaporization on Penetration and Dispersion of Diesel Sprays". *SAE Technical Paper 960034* (1996). DOI: `10.4271/960034` (*cit. on pp. 39, 58–63, 66*).

[54] Bergwerk, W. "Flow Pattern in Diesel Nozzle Spray Holes". *Proceedings of the Institution of Mechanical Engineers*, vol. 173.1 (1959), pp. 655–660. DOI: `10.1243/pime_proc_1959_173_054_02` (*cit. on pp. 39–41*).

[55] Soteriou, C., R. Andrews, and M. Smith. "Direct Injection Diesel Sprays and the Effect of Cavitation and Hydraulic Flip on Atomization". *SAE Technical Paper 950080* (1995). DOI: `10.4271/950080` (*cit. on pp. 39, 40, 42, 43, 51*).

[56] Chaves, H., M. Knapp, A. Kubitzek, F. Obermeier, and T. Schneider. "Experimental Study of Cavitation in the Nozzle Hole of Diesel Injectors Using Transparent Nozzles". *SAE Technical Paper 950290* (1995). DOI: `10.4271/950290` (*cit. on pp. 40, 43*).

[57] Morena, J. de la. "Estudio de la influencia de las características del flujo interno en toberas sobre el proceso de inyección Diésel en campo próximo". PhD thesis. Camino de Vera, s/n, 46022, Valencia, Spain: Departamento de Máquinas y Motores Térmicos, Universitat Politècnica de València, 2011 (*cit. on pp. 40, 42, 45, 51, 64*).

[58] Sato, K. and Y. Saito. "Unstable Cavitation Behavior in a Circular-Cylindrical Orifice Flow". *The Japan Society of Mechanical Engineers International Journal, Series B: Fluids and Thermal Engineering*, vol. 45.3 (2002), pp. 638–645. DOI: `10.1299/jsmeb.45.638` (*cit. on p. 40*).

[59] Nurick, W. H. "Orifice Cavitation and Its Effect on Spray Mixing". *Journal of Fluids Engineering*, vol. 98.4 (1976), pp. 681–687. DOI: `10.1115/1.3448452` (*cit. on pp. 40, 41*).

[60]   Spikes, R. H. and G. A. Pennington. "Discharge Coefficient of Small Submerged Orifices". *Proceedings of the Institution of Mechanical Engineers*, vol. 173.1 (1959), pp. 661–674. DOI: `10.1243/pime_proc_1959_173_055_02` (*cit. on p. 41*).

[61]   Suh, H. K. and C. S. Lee. "Effect of cavitation in nozzle orifice on the diesel fuel atomization characteristics". *International Journal of Heat and Fluid Flow*, vol. 29.4 (2008), pp. 1001–1009. DOI: `10.1016/j.ijheatfluidflow.2008.03.014` (*cit. on p. 42*).

[62]   Soteriou, C., M. Smith, and R. Andrews. "Diesel injection - laser light sheet illumination of the development of cavitation in orifices". *Institution of Mechanical Engineers Transactions*, vol. 4 (1998), pp. 137–158 (*cit. on p. 42*).

[63]   Mishra, C. and Y. P. Peles. "Flow visualization of cavitating flows through a rectangular slot micro-orifice ingrained in a microchannel". *Physics of Fluids*, vol. 17.11 (2005), pp. 1–14. DOI: `10.1063/1.2132289` (*cit. on p. 43*).

[64]   Mishra, C. and Y. P. Peles. "Cavitation in flow through a micro-orifice inside a silicon microchannel". *Physics of Fluids*, vol. 17.1 (2005), pp. 1–15. DOI: `10.1063/1.1827602` (*cit. on p. 43*).

[65]   Pereira, H̃. V. "Estudio del fenómeno de la cavitación en la inyección diésel mediante la visualización del flujo interno en orificios transparentes". PhD thesis. Camino de Vera, s/n, 46022, Valencia, Spain: Departamento de Máquinas y Motores Térmicos, Universitat Politècnica de València, 2014 (*cit. on p. 43*).

[66]   Sou, A., S. Hosokawa, and A. Tomiyama. "Effects of cavitation in a nozzle on liquid jet atomization". *International Journal of Heat and Mass Transfer*, vol. 50.17-18 (2007), pp. 3575–3582. DOI: `10.1016/j.ijheatmasstransfer.2006.12.033` (*cit. on p. 43*).

[67]   Park, S., H. K. Suh, and C. S. Lee. "Effect of cavitating flow on the flow and fuel atomization characteristics of biodiesel and diesel fuels". *Energy and Fuels*, vol. 22.1 (2008), pp. 605–613. DOI: `10.1021/ef7003305` (*cit. on p. 43*).

[68]   Andriotis, A., M. Gavaises, and C. Arcoumanis. "Vortex flow and cavitation in diesel injector nozzles". *Journal of Fluid Mechanics*, vol. 610 (2008), pp. 195–215. DOI: `10.1017/S0022112008002668` (*cit. on p. 43*).

[69] Arcoumanis, C., H. Flora, M. Gavaises, N. Kampanis, and R. Horrocks. "Investigation of Cavitation in a Vertical Multi-Hole Injector". *SAE Technical Paper 1999-01-0524* (1999). DOI: 10.4271/1999-01-0524 (*cit. on p. 43*).

[70] Blessing, M., G. König, C. Krüger, U. Michels, and V. Schwarz. "Analysis of Flow and Cavitation Phenomena in Diesel Injection Nozzles and Its Effects on Spray and Mixture Formation". *SAE Technical Paper 2003-01-1358* (2003). DOI: 10.4271/2003-01-1358 (*cit. on p. 43*).

[71] Bardi, M. "Partial needle lift and injection rate shape effect on the formation and combustion of the Diesel spray". PhD thesis. Camino de Vera, s/n, 46022, Valencia, Spain: Departamento de Máquinas y Motores Térmicos, Universitat Politècnica de València, 2014 (*cit. on p. 44*).

[72] Yue, Y., C. F. Powell, R. B. Poola, J. Wang, and J. K. Schaller. "Quantitative measurements of diesel fuel spray characteristics in the near-nozzle region using X-ray absorption". *Atomization and Sprays*, vol. 11.4 (2001), pp. 471–490 (*cit. on p. 45*).

[73] Kastengren, A. L. and C. F. Powell. "Spray density measurements using X-ray radiography". *Proceedings of the Institution of Mechanical Engineers, Part D: Journal of Automobile Engineering*, vol. 221.6 (2007), pp. 653–662. DOI: 10.1243/09544070JAUTO392 (*cit. on p. 45*).

[74] Linne, M. "Imaging in the optically dense regions of a spray: A review of developing techniques". *Progress in Energy and Combustion Science*, vol. 39.5 (2013), pp. 403–440. DOI: 10.1016/j.pecs.2013.06.001 (*cit. on p. 45*).

[75] Brunneaux, G. "Liquid and vapor spray structure in high-pressure common rail diesel injection". *Atomization and Sprays*, vol. 11.5 (2001), pp. 533–556 (*cit. on p. 45*).

[76] Pickett, L. M. et al. "Relationship Between Diesel Fuel Spray Vapor Penetration/Dispersion and Local Fuel Mixture Fraction". *SAE International Journal of Engines*, vol. 4.1 (2011), pp. 764–799. DOI: 10.4271/2011-01-0686 (*cit. on p. 45*).

[77] Reitz, R. D. "Atomization and other breakup regimes of a liquid jet". PhD thesis. 08544, Princeton, New Jersey, United States of America: Princeton University, 1978 (*cit. on pp. 46, 49, 50, 63*).

[78] Reitz, R. D. and F. V. Bracco. "Mechanism of atomization of a liquid jet". *Physics of Fluids*, vol. 25 (1982), pp. 1730–1742. DOI: 10.1063/1.863650 (*cit. on pp. 46, 48–50*).

[79] Grant, R. P. and S. Middleman. "Newtonian jet stability". *American Institute of Chemical Engineers Journal*, vol. 12.4 (1966), pp. 669–678. DOI: `10.1002/aic.690120411` (*cit. on p. 47*).

[80] Lefebvre, A. H. *Atomization and Sprays*. Ed. by S. Tamburrino and M. Prescott. 711 3rd Avenue, 10017, New York, New York, United States of America: Taylor & Francis, 1989 (*cit. on pp. 47, 50*).

[81] Buckingham, E. "Model experiments and the forms of empirical equations". *American Society of Mechanical Engineers Transcriptions*, vol. 37 (1915), pp. 263–296 (*cit. on p. 48*).

[82] Ranz, W. E. "Some experiments on orifice sprays". *The Canadian Journal of Chemical Engineering*, vol. 36.4 (1958), pp. 175–191. DOI: `10.1002/cjce.5450360405` (*cit. on pp. 50, 61*).

[83] Sterling, A. M. and C. A. Sleicher. "The instability of capillary jets". *Journal of Fluid Mechanics*, vol. 68.3 (1975), pp. 477–495. DOI: `10.1017/S0022112075001772` (*cit. on p. 50*).

[84] Miesse, C. C. "Correlation of Experimental Data on the Disintegration of Liquid Jets". *Industrial & Engineering Chemistry*, vol. 47.9 (1955), pp. 1690–1701 (*cit. on p. 50*).

[85] Ruiz, F. "Few useful relations for cavitating orifices". *Proceedings of the 5th International Conference on Liquid Atomization and Spray Systems*, vol. 813 (1991), pp. 595–602 (*cit. on p. 50*).

[86] Reitz, R. D. and R. Diwakar. "Effect of Drop Breakup on Fuel Sprays". *SAE Technical Paper 860469* (1986). DOI: `10.4271/860469` (*cit. on p. 50*).

[87] Reitz, R. D. and R. Diwakar. "Structure of High-Pressure Fuel Sprays". *SAE Technical Paper 870598* (1987). DOI: `10.4271/870598` (*cit. on pp. 50, 54*).

[88] Brennen, C. "An oscillating-boundary-layer theory for ciliary propulsion". *Journal of Fluid Mechanics*, vol. 65.4 (1974), pp. 799–824. DOI: `10.1017/S0022112074001662` (*cit. on p. 51*).

[89] Guildenbecher, D. R., C. López-Rivera, and P. E. Sojka. "Secondary atomization". *Experiments in Fluids*, vol. 46.3 (2009), pp. 371–402 (*cit. on p. 52*).

[90] Wierzba, A. "Deformation and breakup of liquid drops in a gas stream at nearly critical Weber numbers". *Experiments in Fluids*, vol. 9.1-2 (1990), pp. 59–64. DOI: `10.1007/BF00575336` (*cit. on pp. 52, 53*).

[91] Pilch, M. M. and C. A. Erdman. "Use of breakup time data and velocity history data to predict the maximum size of stable fragments for acceleration-induced breakup of a liquid drop". *International Journal of Multiphase Flow*, vol. 13.6 (1987), pp. 741–757 (*cit. on p. 52*).

[92] Han, J. H. and G. Tryggvason. "Secondary breakup of axisymmetric liquid drops. I. Acceleration by a constant body force". *Physics of Fluids*, vol. 11.12 (1999), pp. 3650–3667 (*cit. on p. 52*).

[93] Liu, A. B., D. Mather, and R. D. Reitz. "Modeling the Effects of Drop Drag and Breakup on Fuel Sprays". *SAE Technical Paper 930072* (1993). DOI: `10.4271/930072` (*cit. on p. 54*).

[94] Baumgarten, C. *Mixture Formation in Internal Combustion Engines*. Ed. by D. Mewes and F. Mayinger. First edition. Heidelberg, Germany: Springer, 2006 (*cit. on pp. 54–56*).

[95] Qian, J. and C. K. Law. "Regimes of coalescence and separation in droplet collision". *Journal of Fluid Mechanics*, vol. 331.25 (1997), pp. 59–80 (*cit. on p. 54*).

[96] Post, S. L. and J. Abraham. "Modeling the outcome of drop-drop collisions in Diesel sprays". *International Journal of Multiphase Flow*, vol. 28.6 (2002), pp. 997–1019. DOI: `10.1016/S0301-9322(02)00007-1` (*cit. on p. 54*).

[97] Abramzon, B. M. and W. A. Sirignano. "Approximate theory of a single droplet vaporization in a convective field: effects of variable properties, Stefan flow and transient liquid heat". *Proceedings of the American Society of Mechanical Engineers / Japan Society of Mechanica Engineers. Thermal Engineering Joint Conference*. Ed. by P. J. Marto and I. Tanasawa. Honolulu, Hawaii, United States of America, 1987 (*cit. on p. 56*).

[98] Ayoub, N. N. and R. D. Reitz. "Multidimensional Computation of Multicomponent Spray Vaporization and Combustion". *SAE Technical Paper 950285* (1995). DOI: `10.4271/950285` (*cit. on p. 56*).

[99] Jin, J. D. and G. L. Borman. "A Model for Multicomponent Droplet Vaporization at High Ambient Pressures". *SAE Technical Paper 850264* (1985). DOI: `10.4271/850264` (*cit. on p. 56*).

[100] Tamim, J. and W. L. H. Hallett. "A continuous thermodynamics model for multicomponent droplet vaporization". *Chemical Engineering Science*, vol. 50.18 (1995), pp. 2933–2942 (*cit. on p. 57*).

[101]   Liu, B., M. Jia, and Z. Peng. "An Investigation of Multiple-Injection
        Strategy in a Diesel PCCI Combustion Engine". *SAE Technical Paper
        2010-04-12* (2010). DOI: `10.4271/2010-01-1134` (*cit. on p. 58*).

[102]   Hay, N. and P. L. Jones. "Comparison of the Various Correlations for
        Spray Penetration". *SAE Technical Paper 720776* (1972). DOI: `10.
        4271/720776` (*cit. on p. 58*).

[103]   Dent, J. C. "A Basis for the Comparison of Various Experimental Meth-
        ods for Studying Spray Penetration". *SAE Technical Paper 710571*
        (1971). DOI: `10.4271/710571` (*cit. on p. 58*).

[104]   Wakuri, Y., M. Fujii, T. Amitani, and R. Tsuneya. "Studies on the
        Penetration of Fuel Spray in a Diesel Engine". *Bulletin of the Japan
        Society of Mechanical Engineers*, vol. 3.9 (1960), pp. 123–130 (*cit. on
        p. 58*).

[105]   Hiroyasu, H. and M. Arai. "Structures of Fuel Sprays in Diesel En-
        gines". *SAE Technical Paper 900475* (1990). DOI: `10.4271/900475`
        (*cit. on pp. 58, 61, 63, 64*).

[106]   Desantes, J. M., R. Payri, F. J. Salvador, and V. Soare. "Study of the
        Influence of Geometrical and Injection Parameters on Diesel Sprays
        Characteristics in Isothermal Conditions". *SAE Technical Paper 2005-
        01-0913* (2005). DOI: `10.4271/2005-01-0913` (*cit. on pp. 59–62*).

[107]   Payri, R., F. J. Salvador, J. Gimeno, and V. Soare. "Determination of
        diesel sprays characteristics in real engine in-cylinder air density and
        pressure conditions". *Journal of Mechanical Science and Technology*,
        vol. 19.11 (2005), pp. 2040–2052. DOI: `10.1007/BF02916497` (*cit. on
        p. 60*).

[108]   Payri, R., F. J. Salvador, J. Gimeno, and J. de la Morena. "Macroscopic
        Behavior of Diesel Sprays in the Near-Nozzle Field". *SAE Technical
        Paper 2008-01-0929* (2008). DOI: `10.4271/2008-01-0929` (*cit. on
        p. 60*).

[109]   Pastor, J. V., R. Payri, J. M. García-Oliver, and J.-G. Nerva. "Schlieren
        Measurements of the ECN-Spray A Penetration under Inert and Re-
        acting Conditions". *SAE Technical Paper 2012-01-0456* (2012). DOI:
        `10.4271/2012-01-0456` (*cit. on p. 60*).

[110]   Reitz, R. D. and F. V. Bracco. "On the Dependence of Spray Angle and
        Other Spray Parameters on Nozzle Design and Operating Conditions".
        SAE Technical Paper 790494 (1979). DOI: `10.4271/790494` (*cit. on
        p. 61*).

[111] Delacourt, E., B. Desmet, and B. Besson. "Characterisation of very high pressure diesel sprays using digital imaging techniques". *Fuel*, vol. 84.7-8 (2005), pp. 859–867. DOI: `10.1016/j.fuel.2004.12.003` (*cit. on p. 61*).

[112] Kampmann, S., B. Dittus, P. Mattes, and M. Kirner. "The Influence of Hydro Grinding at VCO Nozzles on the Mixture Preparation in a DI Diesel Engine". *SAE Technical Paper 960867* (1996). DOI: `10.4271/960867` (*cit. on p. 62*).

[113] Macián, V., R. Payri, A. García, and M. Bardi. "Experimental evaluation of the best approach for diesel spray images segmentation". *Experimental Techniques*, vol. 36.6 (2012), pp. 26–34. DOI: `10.1111/j.1747-1567.2011.00730.x` (*cit. on p. 62*).

[114] Siebers, D. L. "Liquid-Phase Fuel Penetration in Diesel Sprays". *SAE Technical Paper 980809* (1998). DOI: `10.4271/980809` (*cit. on pp. 62, 63*).

[115] Payri, R., F. J. Salvador, J. Gimeno, and L. D. Zapata. "Diesel nozzle geometry influence on spray liquid-phase fuel penetration in evaporative conditions". *Fuel*, vol. 87.7 (2008), pp. 1165–1176. DOI: `10.1016/j.fuel.2007.05.058` (*cit. on p. 62*).

[116] Payri, R., J. M. García-Oliver, M. Bardi, and J. Manin. "Fuel temperature influence on diesel sprays in inert and reacting conditions". *Applied Thermal Engineering*, vol. 35.1 (2012), pp. 185–195 (*cit. on p. 62*).

[117] Pastor, J. V., J. J. López, J. M. García, and J. M. Pastor. "A 1D model for the description of mixing-controlled inert diesel sprays". *Fuel*, vol. 87.13-14 (2008), pp. 2871–2885. DOI: `10.1016/j.fuel.2008.04.017` (*cit. on p. 62*).

[118] Chehroudi, B., S.-H. Chen, F. V. Bracco, and Y. Onuma. "On the Intact Core of Full-Cone Sprays". *SAE Technical Paper 850126* (1985). DOI: `10.4271/850126` (*cit. on p. 63*).

[119] Lebas, R., T. Ménard, P. A. Beau, A. Berlemont, and F. X. Demoulin. "Numerical simulation of primary break-up and atomization: DNS and modelling study". *International Journal of Multiphase Flow*, vol. 35.3 (2009), pp. 247–260. DOI: `10.1016/j.ijmultiphaseflow.2008.11.005` (*cit. on p. 63*).

[120]   Fuster, D. et al. "Simulation of primary atomization with an octree adaptive mesh refinement and VOF method". *International Journal of Multiphase Flow*, vol. 35.6 (2009), pp. 550–565. DOI: 10.1016/j.ijmultiphaseflow.2009.02.014 (*cit. on p. 63*).

[121]   Andriotis, A. and M. Gavaises. "Influence of vortex flow and cavitation on near-nozzle diesel spray dispersion angle". *Atomization and Sprays*, vol. 19.3 (2009), pp. 247–261. DOI: 10.1615/AtomizSpr.v19.i3.30 (*cit. on p. 64*).

[122]   Mugele, R. A. and H. D. Evans. "Droplet Size Distribution in Sprays". *Industrial & Engineering Chemistry*, vol. 43.6 (1951), pp. 1317–1324. DOI: 10.1021/ie50498a023 (*cit. on p. 65*).

[123]   Jicha, M., J. Jedelsky, J. Otahal, and J. Slama. "Influence of Some Geometrical Parameters on the Characteristics of Effervescent Atomization". *18th Annual Conference on Liqud Atomization & Spray Systems (ILASS Europe)*. Zaragoza, Spain, 2002 (*cit. on p. 66*).

[124]   Kristensson, E. et al. "Analysis of multiple scattering suppression using structured laser illumination planar imaging in scattering and fluorescing media". *Optics Express*, vol. 19.14 (2011), pp. 13647–13663. DOI: 10.1364/OE.19.013647 (*cit. on p. 66*).

[125]   Hiroyasu, H., M. Arai, and M. Tabata. "Empirical Equations for the Sauter Mean Diameter of a Diesel Spray". *SAE Technical Paper 890464* (1989). DOI: 10.4271/890464 (*cit. on p. 66*).

[126]   Arrègle, J., J. V. Pastor, and S. Ruiz. "The Influence of Injection Parameters on Diesel Spray Characteristics". *SAE Technical Paper 1999-01-0200* (1999). DOI: 10.4271/1999-01-0200 (*cit. on p. 66*).

[127]   Payri, R., L. Araneo, J. S. Shakal, and V. Soare. "Phase doppler measurements: System set-up optimization for characterization of a diesel nozzle". *Journal of Mechanical Science and Technology*, vol. 22.8 (2008), pp. 1620–1632. DOI: 10.1007/S12206-008-0432-7 (*cit. on p. 66*).

[128]   Adler, D. and W. T. Lyn. "The Evaporation and Mixing of a Liquid Fuel Spray in a Diesel Air Swirl". *Proceedings of the Institution of Mechanical Engineers*, vol. 184.10 (1969), pp. 171–180. DOI: 10.1243/pime_conf_1969_184_330_02 (*cit. on p. 66*).

[129]   Desantes, J. M., R. Payri, F. J. Salvador, and A. Gil. "Development and validation of a theoretical model for diesel spray penetration". *Fuel*, vol. 85.7-8 (2006), pp. 910–917. DOI: 10.1016/j.fuel.2005.10.023 (*cit. on p. 66*).

[130] Espey, C., J. E. Dec, T. A. Litzinger, and D. A. Santavicca. "Planar laser Rayleigh scattering for quantitative vapor-fuel imaging in a diesel jet". *Combustion and Flame*, vol. 109.1-2 (1997), pp. 65–86. DOI: 10.1016/S0010-2180(96)00126-5 (*cit. on p. 67*).

[131] Cao, Z. M., K. Nishino, S. Mizuno, and K. Torii. "PIV measurement of internal structure of diesel fuel spray". *Experiments in Fluids*, vol. 29.Suppl. (2000), pp. 211–219. DOI: 10.1007/s003480070023 (*cit. on p. 67*).

Chapter 3

State of the art

3.1 Introduction

Turbulent (and mixing) multiphase flows have been investigated by many authors since years ago. However this topic is still not fully resolved due to, first, the complex phenomena (e.g. turbulence, heat transfer, atomization...) taking place, and second, the presence of a very wide spectrum of length- and time-scales. Therefore, a review of the state of the art is required.

It has been estated in prior Section §1.2 that the main objective of this Thesis is developing a model capable of simulating internal and external flows of the Diesel injection process which are strongly linked [1–6] at the same time; likewise disadvantages and uncertainties of adding a coupling methodology are avoided. Based on the level of description, multiphase computational models can be grouped in four classes: inter-phase tracking models, Eulerian-Lagrangian models, Eulerian multi-fluid models and homogeneous flow models.

3.2 Classification of turbulent multiphase flows

The first classification of multiphase (usually named dispersed and carrier phases) flows can be according to the combination of phases: gas-solid (fluidized beds, conveying), gas-liquid (sprays, nuclear reactors), liquid-solid (sedimentation, fiber suspensions), liquid-liquid (oil-water separation), gas-liquid-liquid (catalytic cracking), etc. Depending on the type of distribution of the

dispersed phase, the flow is homogeneous (alcohol and water, coffee) or heterogeneous (clusters, sprays, flocks). And regarding the geometry of the phase interfaces, multiphase flows are classified into three main classes, separated (by a geometrically simple interface), transitional or mixed, and dispersed (inter-facial complexity), each of which can be subdivided in several regimes as shown in Table 3.1 [7]. Being the objective of this Thesis the Diesel injection process (a spray), only gas-liquid, heterogeneous and dispersed flows are considered.

If the flow is laminar, each element released from a point will follow a smooth unique trajectory. On the other hand, individual elements introduced into a turbulent carrier flow will each have their own, oscillating path due to interaction with the fluctuating turbulent velocity field. According to Elghobashi [8], different classes of interaction between phases can be distinguished depending primarily on the volume fraction, as sketched in Figure 3.1. For droplet volume fraction less than $X = 10^{-6}$, droplet motion is influenced by continuous phase properties but there is practically no feedback (momentum exchange) from the dispersed phase, in other words, the droplets have negligible effect on turbulence, and the interaction between the droplets and turbulence is termed as one-way coupling. Theoretically, the description of one-way coupling is simple because the flow field of the continuous phase in the absence of feedback mechanism can be computed as a single phase flow and droplet motion is determine in a post-processing step.

In the second regime, from $X = 10^{-6}$ to approximately $X = 10^{-3}$, the momentum exchange between the droplets and turbulence is large enough to alter the turbulence structure. This interaction is called two-way coupling. In this regime and for a given value of volume fraction X, there are two zones A and B, depending on the ratio of the time of dynamic relaxation of particles over the Kolmogorov time-scale τ_p/τ_k, where the transition from A to B occurs at about $\tau_p/\tau_k = 10$. Time of dynamic relaxation of particles τ_p is defined by Equations (3.1) and (3.2) [9], where τ_{p0} is the value for Stokes flow and Re_d is the Reynolds number of the droplet (Equation (2.3) calculated with the droplet diameter and the relative velocity). In zone A the droplet Reynolds number is $Re_d < 1$ and the effects of the droplets on the turbulence vary significantly as function of the τ_p/τ_k ratio: micro-particles ($\tau_p/\tau_k \leq 1$) cause both turbulent kinetic energy and its dissipation rate to be larger than in the single-phase flow; ghost particles ($0.1 < \tau_p/\tau_k < 0.5$) modify the turbulence energy spectrum in a way such that turbulent kinetic energy is unchanged but its dissipation rate is larger than that of the single-phase flow; critical particles ($\tau_p/\tau_k \approx 1$) reduce turbulent kinetic energy but keep its dissipation rate unchanged relative to the single-phase flow; and large particles ($\tau_p/\tau_k > 1$)

Class	Typical regimes	Geometry	Examples
Separated	Film		Film condensation, film boiling
	Annular		Film boiling, boilers
	Jet		Atomization, jet condenser
Mixed	Cap, slug or chum-turbulent		Sodium boiling in forced convection
	Bubbly annular		Evaporators with wall nucleation
	Droplet annular		Steam generator
	Bubbly droplet annular		Boiling nuclear reactor channel
Dispersed	Bubbly		Chemical reactors
	Droplet		Spray cooling
	Particulate		Transportation of powder

Table 3.1: Classification of multiphase flows based on the interfaces structures.

reduce both turbulent kinetic energy and its dissipation rate relative to their values in the single-phase flow. In zone B, as τ_p increases (e.g. by increasing the droplet diameter) for the same volume fraction, the droplet Reynolds number increases, and at values of $Re_p \geq 400$, vortex shedding takes place
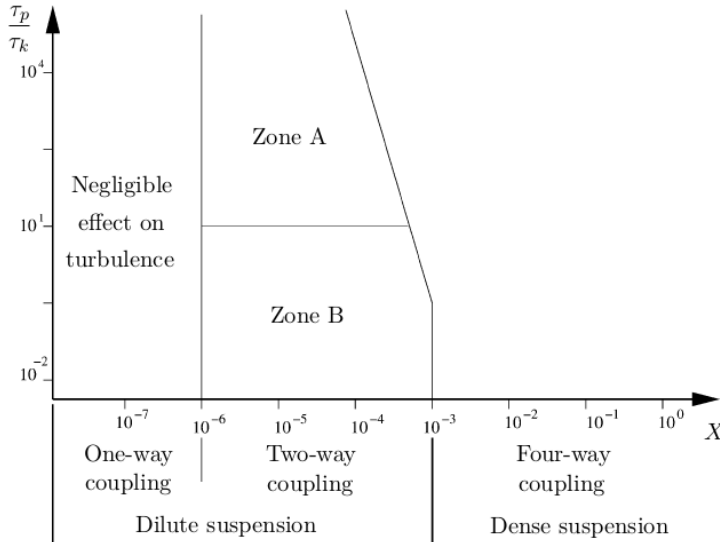
Figure 3.1: Classification map of multiphase turbulent flows.

resulting in enhanced production of turbulence energy.

$$\tau_p = \frac{\tau_{p0}}{C} = \frac{\rho_f D_d^2}{18\mu_f C} \tag{3.1}$$

$$
\begin{aligned}
C &= 1 + \frac{Re_p^{\frac{2}{3}}}{6}; \text{ if } Re_d \leq 10^3 \\
C &= 0.11\frac{Re_p}{6}; \text{ if } Re_d > 10^3
\end{aligned}
\tag{3.2}
$$

In the third regime, for droplet volume fractions higher than $X = 10^{-3}$, because of the increased droplet loading flows are referred to as dense suspensions. Here, in addition to the two-way coupling between droplets and turbulence, droplet-droplet collision takes place, hence the term four-way coupling.

A complementary classification is given by Varaksin [9] depending on the most important dimensionless parameter which characterizes the droplet inertia, namely, the Stokes number (Equation (3.3)) in the averaged motion, the large-scale fluctuation motion (Stk_l) and the small-scale fluctuation motion (Stk_k). He differentiated five different types of flow:

- equilibrium flow (type 1),

- quasi-equilibrium flow (type 2),

- non-quasi-equilibrium flow (type 3),

- flow with large particles (type 4),

- and flow past stationary "frozen" particles (type 5).

Table 3.2 gives information about mean and perturbation (turbulent) momentum and heat transfer parameters depending on the flow type. Varaksin [9] affirms that this classification is quite universal. First, it covers the entire range of droplet concentrations from the case of motion of single droplets, when their presence has no effect on the characteristics of flow of carrier gas, to the motion of dense sets of droplets, when the space taken up by the dispersed phase is comparable to the volume taken up by the carrier. Second, the classification covers the entire range of droplet inertia from minute droplets, whose size is commensurable with that of carrier molecules, to large stationary droplets.

$$Stk = \frac{\tau_p u}{L} \tag{3.3}$$

Type	Stk	Momentum transfer		Heat transfer
		Re_d	u_d	T_d
1	$Stk \to 0$	$Re_d \to 0$	$u_d \approx u$	$T_d \approx T$
	$Stk_l \to 0,\ Stk_k \to 1$	$Re_d' \to 0$	$u_d' \approx u'$	$T_d' \approx T'$
2	$Stk \to 0$	$Re_d \to 0$	$u_d \approx u$	$T_d \approx T$
	$Stk_l \to 1,\ Stk_k \to 1$	$Re_d' > 0$	$u_d' \neq u'$	$T_d' \neq T'$
3	$Stk \to 1$	$Re_d > 0$	$u_d \neq u$	$T_d \neq T$
	$Stk_l \to 1,\ Stk_k \to \infty$	$Re_d' > 0$	$u_d' \neq u'$	$T_d' \neq T'$
4	$Stk \to 1$	$Re_p > 0$	$u_d \neq u$	$T_d \neq T$
	$Stk_l \to \infty,\ Stk_k \to \infty$	$Re_d' >> 0$	$u_d' \approx 0$	$T_d' \approx 0$
5	$Stk \to \infty$	$Re_d >> 0$	$u_d \approx u$	$T_d \approx 0$
	$Stk_l \to \infty,\ Stk_k \to \infty$	$Re_d' >> 0$	$u_d' \approx 0$	$T_d' \approx 0$

Table 3.2: Classification of turbulent heterogeneous multiphase flows by values of the Stokes number.

3.3   Interface tracking and capturing models

Flows with free surfaces are an especially difficult class of flows with moving boundaries. The position of the boundary is known only at initial time; its location at later times has to be determined as part of the solution [10]. In the most common case, the free surface is an air-water boundary, i.e. simulation of a cargo ship shown in Figure 3.2, but other liquid-gas surfaces occur, as do liquid-liquid interfaces.
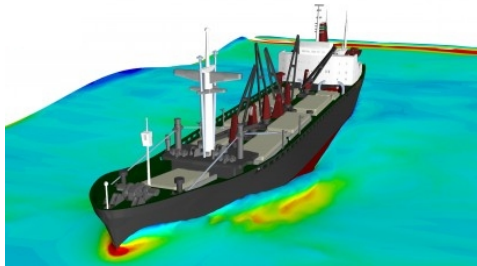
Figure 3.2: Dynamic Fluid Interaction simulation of a large cargo ship: modeling the motion of a body resulting from the forces and moments on it (STAR-CCM+ website).

If phase change at the free surface can be neglected, the following boundary conditions apply [10]: the kinematic condition requires that the free surface be a sharp boundary separating the two fluids that allows no flow through it; and the dynamic condition requires that the forces acting on the fluid at the free surface be in equilibrium (momentum conservation at the free surface), this means that the normal forces on either side of the free surface are of equal magnitude and opposite direction.

Many methods have been used to find the shape of the free surface. They can be classified into two major groups:

- Interface-tracking methods: treat the free surface as a sharp interface whose motion is followed. In this type of method, the flow field is discretized by a conservative finite difference approximation, and the interface is explicitly represented by a separate, unstructured grid that moves through the stationary grid. Since the interface deforms continuously, it is necessary to restructure its grid as the calculation proceed [11, 12]. This method stands out for its high accuracy [13], it allows

to resolve interface structures smaller than the grid size. On the contrary, the generation of the interface grid, its spatial distribution and its dependency on time, together with the high computational cost due to the high amount of data required, remain as the main drawbacks of this method.

- Interface-capturing methods: do not define interface as a sharp boundary. The computation is performed on a fixed grid, which extends beyond the free surface. The shape of the free surface is determined by computing the fraction of each near-interface cell that is partially filled. This can be achieved by introducing massless particles at the free surface at the initial time and following their motion, what is called Marker-and-Cell (MAC) scheme. Alternatively, one can solve a transport equation for the fraction of the cell occupied by the liquid phase, the Volume-of-Fluid (VOF) scheme, or define the surface as the one on which a level-set function is equal to zero (level-set formulation). Because of structures smaller in size than the mesh are not solved, the interface location, orientation and curvature cannot be accurately calculated.

There exist also hybrid methods which do not fall into either categories described above. These methods borrow elements from both interface capturing and interface-tracking methods.

3.3.1   Volume-of-Fluid method

In the VOF method, in addition to the conservation equations for mass and momentum, an equation for the filled fraction of each cell, X, is solved so that $X = 1$ in filled cells and $X = 0$ in empty cells. From the continuity equation, one can show that the evolution of X is governed by Equation (3.4). In incompressible flows this equation is invariant with respect to interchange of X and $1-X$; for this to be assured in the numerical method, mass conservation has to be strictly enforced.

$$\frac{\partial X}{\partial t} + \operatorname{div}(X\boldsymbol{U}) = 0 \qquad (3.4)$$

The critical issue in this type of method is the characterization of convective term in Equation (3.4). Low-order schemes (like the first-order accurate upwind method) smear the interface and introduce artificial mixing of the two fluids, so higher-order schemes are preferred. Since X must satisfy the condition $0 \leq X \leq 1$, it is important to ensure that the method does not generate

overshoots of undershoots. Fortunately, it is possible to derive schemes which both keep interface sharp and produce monotone profiles of X across it [14]. Actually, there are several interface reconnection algorithms: fractional [15, 16], steps [17] and piecewise linear interface calculation (PLIC) [18].

The main drawback of this methodology is that any topological change associated to break-up or coalescence of droplets or bubbles is hardly obtained except if the grid resolution is extremely fine.

Alternatively, both fluids can be treated as a single fluid whose properties vary in space according to the volume fraction of each phase [10]. In this case the interface is not treated as a boundary so no boundary conditions need to be prescribed on it. The interface is simply the location where the fluid properties change abruptly. If surface tension is significant at the free surface, it can be taken into account by treating the force as a body force [14, 16]. However, there are problems when surface tension effects become dominant, like in the case of droplets of bubbles whose diameter is of the order of 1 mm or less and which move with very low velocity. In this case, there are two very large terms in the momentum equations, the pressure term and the body force representing the surface tension effects, which have to balance each other, they are the only non-zero terms if the bubble or droplet is stationary.

Volume-of-Fluid method in Diesel engine applications

Dirke et al. [19] used a VOF method to study the cavitation zones in a ball valve, sac-hole nozzle and a single-hole nozzle geometries and obtained good agreement with experimental results. Nonetheless, they highlighted the necessity of improvement in the unsteady transient boundary conditions and mesh movement.

In that direction, Marcer et al. [20] coupled a Kinematics and Mass Transfer VOF model with a one-dimensional system AMESim® so they were able to simulate the needle movement. Though obtained results showed good agreement with the experimental data concerning the mass flow rate, further validation was required to calibrate the whole system (upstream and downstream pressure, needle forces, etc.).

Marcer et al. [21] developed an improved version so called Segment Lagrangian VOF which allowed to describe numerically the onset and development of cavitation within Diesel injectors, including its different regimes. They ensured that in a near future this type of model should give a better insight into the mechanism of fragmentation for the three phase flow (liquid, vapor and ambient gas) downstream the orifice exit.

As a recent example of the application of VOF methods in engine application, Befrui et al. [22] performed VOF LES simulations of the nozzle internal flow and near-field primary atomization of a gasoline direct injection (GDI) multi-hole injector. Their results, sampled in Figure 3.3 highlighted the potential capability of the VOF LES method for analysis of the hydrodynamics of liquid jet break-up and the influence of the nozzle geometry on the spray break-up process. This model was able to predict the deviation angle between the nozzle-hole axis and the issuing liquid jet trajectory.
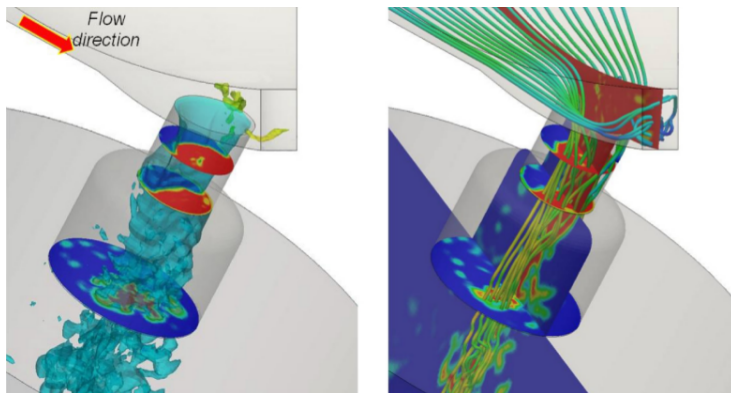
Figure 3.3: VOF LES simulation results ($p_i = 20$ MPa) [22].

3.3.2   Level-set method

Another class of interface-capturing methods is based on the level-set formulation, introduced by Osher and Sethian [23]. The surface is defined as the one on which a level-set function $\varphi = 0$. Other values of this function have no significance, and to make it a smooth function φ is typically initialized as the signed distance from the interface. This function then is allowed to evolve as a solution of a transport equation (Equation (3.5)), and if it becomes too complicated, it can be re-initialized. As in VOF methods, fluid properties are determined by the local value of φ but here, only the sign is important.

$$\frac{\partial \varphi}{\partial t} + \operatorname{div}\left(\varphi \boldsymbol{U}\right) = 0 \tag{3.5}$$

The advantage of this approach relative to the VOF scheme is that φ varies smoothly across the interface while the volume fraction is discontinuous there. However, as noted above, the computed φ need to be re-initialized. Sussman

et al. [24] proposed to do this by solving Equation (3.6) until steady state is reached. This guaranties that φ has the same sign and zero level as φ_0, and fulfills the condition that $|\mathrm{grad}\,(\varphi)| = 1$, making it similar to a signed distance function.

$$\frac{\partial \varphi}{\partial t} = \mathrm{sign}\,(\varphi_0)\,(1 - |\mathrm{grad}\,(\varphi)\,|) \tag{3.6}$$

Since φ does not explicitly occur in any of the conservation equations, the original level-set method did not exactly conserve mass. Mass conservation can be enforced by making the right-hand side of Equation (3.6) a function of the local mass imbalance [25], but also by a two step second order conservative re-initialization [26]. The more frequently this equation is solved, the fewer iterations are needed to reach steady state; of course, frequent solution of this equation increases the computational cost so there is a trade-off.

Sussman et al. [27] combined a level-set method with a variable density (large density ratios) projection method to allow for computation of a two-phase flow where the interface can merge/break and the flow can have a high Reynolds number with good agreement with expected results. They proposed to include an adaptive mesh refinement method as future work in order to save computational time.

Regarding the description of the interface discontinuities, two approaches can be used, namely the continuous force formulation ("delta" formulation), which assumes that the interface is 2 or 3 grid cells thick, and the ghost fluid method (GFM) which was derived by Fedkiw et al. [28] to capture jump conditions on the interface. The GFM approach not only avoids the introduction of a fictitious interface thickness, but it is also suitable to provide a more accurate discretization of discontinuous terms, reducing parasitic current and improving the resolution on the pressure jump condition [29].

Many other level-set methods have been proposed; they differ in the choices for various steps. The review made by Osher and Fedkiw [30] is a good summary of them. Even VOF and level-set combination methods have been developed to ensure mass conservation [31].

Level-set method in Diesel engine applications

Desjardins et al. [32] combined a GFM for handling the inter-facial forces and large density jumps while avoiding artificial spreading of the interface with a conservative level-set method [26] to simulate a liquid Diesel jet at $Re = 3000$. Their method was robust and mass conservation errors remained small.

Following the same strategy, Ménard et al. [33] developed a model in which the interface tracking is ensured by the level set method with a re-distancing algorithm and GFM is used to capture accurately sharp discontinuities for pressure, density and viscosity. The level set method is coupled with the VOF method for mass conservation. This model was used to successfully simulate the primary break-up of a turbulent liquid jet, as shown in Figure 3.4.
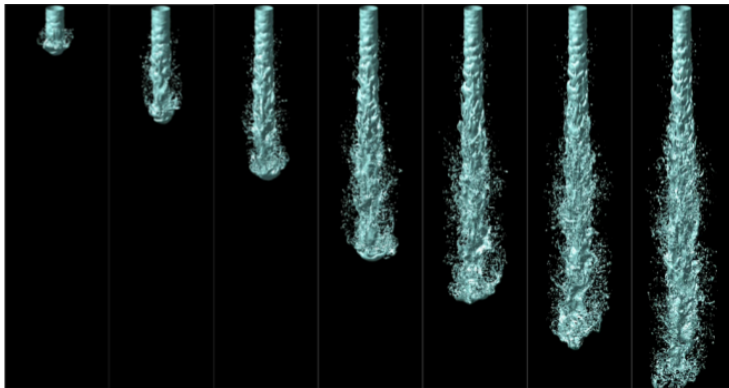
Figure 3.4: Development of the liquid jet (injection velocity of $100\,\mathrm{m/s}$, time step of 2.5 µm) [33].

Herrmann [34] used a refined level-set method grid approach to simulate the primary atomization of round turbulent liquid jets injected into stagnant high-pressure air under Diesel engine conditions. In his simulation, broken off, small-scale nearly spherical droplets were transferred into a Lagrangian point particle description allowing for full two-way coupling. All level-set related equations were evaluated on a separate, uniform Cartesian grid with aspect ratio 1, split into uniform super-grid blocks and overlaid onto the flow solver grid on which the Navier-Stokes equations were solved. Grid independence of larger scale droplets could be obtained, however it was not fully achieved for drop size number frequency. From his results, turbulence appears to the driving mechanism or at least the initiator of atomization within the fist 20 diameters downstream of the injector. As a final remark, he highlighted that although computational resources have increased manifold in past decades, those simulations still remained extremely challenging due to the range of involve time- and length-scales.

DNS and LES simulations of air-assisted break-up of both planar and coaxial liquid layers carried out by Desjardins et al. [35] showed to agree well with

theoretical and experimental results. They were able to capture important in-
stabilities for atomizing flows, such as Rayleigh-Plateau and Kelvin-Helmholtz
instabilities. A conservative level-set method was employed, improved through
the use of local re-initialization enabled by an efficient fast marching method.
A high density ratio correction algorithm was employed that led to tighter
coupling between mass and momentum transport.

Finally, Arienti and Sussman [36] combined the level-set VOF method
with the wall boundary representation using a second level-set function to
treat complex wall boundaries in two-phase, free-surface flow simulations. The
non-slip boundary condition at the walls is enforced by properly populating
the ghost cells of a narrow band inside the solid body, using a simple and nu-
merically robust treatment of the contact line. The update of the ghost region
cells and the handling of the contact angles (see Figure 3.5) were relatively
inexpensive operations, however there was a substantial extra cost when the
full reconstruction of the solid level set is carried out at every time step, as in
the moving needle.
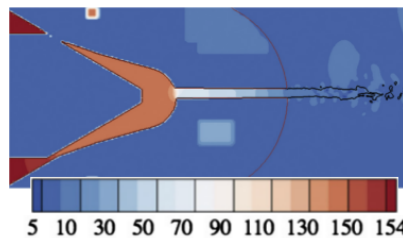
Figure 3.5: Contours of pressure (MPa) at 1710 µs after SOI [36].

3.4 Eulerian-Lagrangian models

The Eulerian-Lagrangian model is the classical approach in engine applications
not only due to its high efficiency to predict macroscopic and microscopic
parameters of the spray, but also because it suits well to all process taking place
in a combustion chamber: evaporation, combustion, emissions, heat transfer,
etc. This model was first developed for dispersed sprays (see Figure 3.1), with
a maximum limit for the volume fraction of about $X = 0.1$, however due to
its reasonable efficiency, it is also used for dense jets, such the Diesel spray
which presents an intact liquid vein nearby the injection point.

Computational particles (droplet or bubbles parcels) are released into the
main flow and their position and velocity are obtained by integrating the par-

ticle equation of motion. Therefore, two numerical approaches are used in these models: the carrier phase is resolved by an Eulerian description, while the dispersed phase in form of parcels is resolved by a Lagrangian description. Parcels represent a group of identical droplets (i.e. same radius, velocity, temperature, etc.) which do not interact between them and are used to statistically represent the entire spray field. In the statistical treatment of the droplets, originally proposed by Dukowicz [37] and named Discrete Droplets Model (DDM), equations governing the liquid part of the spray are solved by a Monte-Carlo method. This saves computational effort compared to the Continuum Droplets Model (CDM) where each single droplet is represented and calculated.

Spray droplets are subject to several processes from the time of injection until the time of vaporization. The interaction between phases is performed by addition of source terms, pondered by the void fraction, in the governing equations. Different sub-models, which play a major role in the success of the Eulerian-Lagrangian models, are used to define these source terms because the interface cannot be directly resolved due to computational limitations. The grid resolution is also a key parameter for the simulations. It must not be too coarse to avoid numerical diffusion and thus poor estimation of the evolution of the spray; but at the same time it cannot be too fine due to the limitation to the void fraction. In that sense, Abraham [38] proved that at least two cells covering the orifice exit are needed to correctly model a turbulent gaseous jet (the orifice exit diameter is the characteristic length of the problem).

3.4.1   Break-up models

Among all the sub-models employed in Eulerian-Lagrangian methods (which are the liquid injection model, the spray break-up model, the droplet drag, collision, and turbulent dispersion models, the droplet/wall interaction model, and the evaporation model) the break-up one is the most important. There are several options for this model depending on the main atomization mechanism:

- Kelvin-Helmholtz or wave break-up model: based on a liquid jet stability analysis, it is described in detail by Reitz [39]. The analysis considers the stability of a cylindrical, viscous, liquid jet issuing from a circular orifice into a stagnant, incompressible, inviscid gas. The primary break-up of the jet is then related to the Kelvin-Helmholtz instability induced by the relative velocity at the interface. Among the many wavelengths, the one which grows faster is considered as the one responsible for the break-up.

- Kelvin-Helmholtz ACT break-up model: developed by Som and Aggarwal [40], it is a modification of the Kelvin-Helmholtz model that includes the effects of aerodynamics, cavitation and turbulence on primary break-up.

- Rayleigh-Taylor break-up model: in addition to the Kelvin-Helmholtz break-up model, the Rayleigh-Taylor instability is also believed to be responsible for droplet break-up [41]. The unstable Rayleigh-Taylor waves are thought to occur due to the rapid deceleration of the droplets from the magnitude of the drag force.

- Taylor Analogy Break-up model: developed by O'Rourke and Amsden [42], it is a classic method for calculating drop distortion and break-up. This method is based on Taylor's analogy between an oscillating and distorting droplet and a spring-mass system.

- Linearized Instability Sheet Atomization model: developed by Senecal et al. [43], it includes two parts, a general liquid sheet break-up mechanism proposed by Dombrowski and Johns [44] and a liquid injection methodology specifically for pressure-swirl atomizers.

- Reitz and Diwakar model: according to this model, droplet break-up due to aerodynamic forces occurs in one of the following modes (see also Section §2.4.1), bag break-up in which the non-uniform pressure field around the droplet causes it to expand in the low-pressure wake region and eventually disintegrates when surface tension forces are overcome, and sheet stripping break-up in which liquid is sheared or stripped from the droplet surface [45].

- Pilch and Erdman model: droplet break-up is directly calculated from correlations developed by Pilch and Erdman [46] who assumed that it occurs if the droplet Weber number is greater than the critical Weber number. Five break-up regimes are distinguished (see Section §2.4.1), which define the dimensionless total break-up times.

- Hsiang and Faeth model: developed by Hsiang and Faeth [47], it is valid for droplet Weber numbers lower than 1000 and covers all types of break-up that are of interest in Diesel engine spray applications.

- Chu model: developed by Chu and Corradini [48], it is based on the Rayleigh-Taylor instabilities. Its theoretical correlation predicts droplet sizes on the basis of an exponential function.

- Kelvin-Helmholtz Rayleigh-Taylor model: described by Patterson and Reitz [49], it consists of a composite process which Kelvin-Helmholtz

aerodynamic instabilities growing on a droplet surface are simultaneously calculated with Rayleigh-Taylor instabilities resulting from the deceleration of the injected droplets. The two physical models compete with each other and the one predicting the fastest onset of an instability gives rise to break-up event.

Eulerian-Lagrangian models in Diesel engine applications

Typical Eulerian-Lagrangian spray computations are strongly mesh (size and structure) and time-step dependent because of an inadequate spatial resolution of the strong velocity and vapor concentration gradients induces numerical diffusion [50]. Thus, in Diesel sprays, the Eulerian field is not properly computed close to the nozzle exit in the vicinity of the liquid phase. The main two sources of grid-dependency are due to errors in predicting the droplet-gas relative velocity, and errors in describing droplet-droplet collision and coalescence processes. The injector position in the grid also strongly influences the results. When the injector tip is at a mesh node, the spray is split into four cells. Furthermore, there are other sources of errors [51]. In simulations where a fixed number of computational particles is used to represent the dispersed phase on a grid, the statistical error in a grid-based estimate of any mean field quantity increases with grid refinement, resulting in a non-convergent simulation. A solution to this problem is the use of grid-free kernel-base estimators. Another source of numerical errors is spatial non-uniformity in the distribution of computational particles. A computational particle number density control algorithm that employs time-evolving statistical weights ensures a near-uniform distributions to remedy this problem.

Béard et al. [52] proposed a solution to the grid-dependency problem consisting in retaining vapor and momentum along parcel trajectories as long as the mesh is insufficient to resolve the steep gradients. Vapor and momentum are gradually released on the mesh following specified laws. They reproduced properly the evaporating spray structure and penetration while having a very limited mesh sensitivity. Following the same path, Abani et al. [53] and Abani and Reitz [54] introduced a sub-grid scale gas-jet model in the unresolved regions near the injector nozzle in order to reduce grid-dependency due to the relative velocity effects. The new spray model proved to provide adequate mesh independent results in terms of spray penetration, droplet sizes, pressure traces and heat-release rates, better than the original model for high-load operation points. García-Oliver et al. [55] also obtained better agreement with experiments and grid independence following exactly the same procedure but using a one-dimensional model [56, 57] instead of the gas-theory. In addition,

Shuai et al. [58] established a radius of influence of collision methodology for each gas phase to estimate the collision probability for each parcel in the cell and greatly reduced the mesh dependence for low temperature combustion Diesel engine. A different approach was employed by Kim et al. [59], who, after reviewing the momentum equation, presented an enhanced momentum coupling and introduced the improved collision models to obtain the goal of reducing grid dependency.

Xue et al. [60–62] developed an adaptive mesh refinement methodology to, on one side, overcome the grid dependence issue, and on the other side save computational cost. They tested the new methodology in both spray and engine cases. Kolakaluri et al. [63] compared simulations carried out employing this adaptive mesh strategy with experimental data in gasoline spray structure and liquid length, and also in liquid length of a vaporizing Diesel spray and its variations with different parameters (orifice outlet diameter, injection pressure, ambient gas temperature and density). Computations showed accuracy with reasonable computational cost. Lucchini et al. [64] also employed a dynamic local grid refinement where the air-fuel mixing process takes place to drastically reduce computational time. Their methodology works also with unstructured hexahedral meshes, hence it can be applied to simulate real Diesel engine combustion chambers.

Hohmann and Renz [65] extended the evaporation model to account for the effects of non-ideal droplet vaporization and gas solubility including the diffusion of heat and species within fuel droplets. Their results showed that the differences between the various spray models are pronounced for single droplets, however the droplet diameter distribution is more influenced by secondary break-up and droplet coalescence.

Abraham and Pickett [66] tested three models, an Eulerian-Lagrangian model, a gas jet model and a virtual-liquid source model, and quantitatively compared fuel vapor concentrations with experiments. While all three were in general agreement as shown in Figure 3.6, computed and measured results did not agree along the axial centerline during transient penetration, measured values were higher. The computed spreading angle was, as expected, greater than the measured one, and radial profiles at the quasi-steady state showed better agreement far downstream from the nozzle exit than close to the orifice.

Regarding the break-up model, Hossainpour and Binsesh [67] analyzed four different models, Chu, Reitz and Diwakar, Kelvin-Helmholtz and Kelvin-Helmholtz Rayleigh-Taylor (according to the authors, models other than these have not acceptable predictions for Diesel engine simulations), for a sample case. Compared to experimental results, Chu and Reitz and Diwakar models
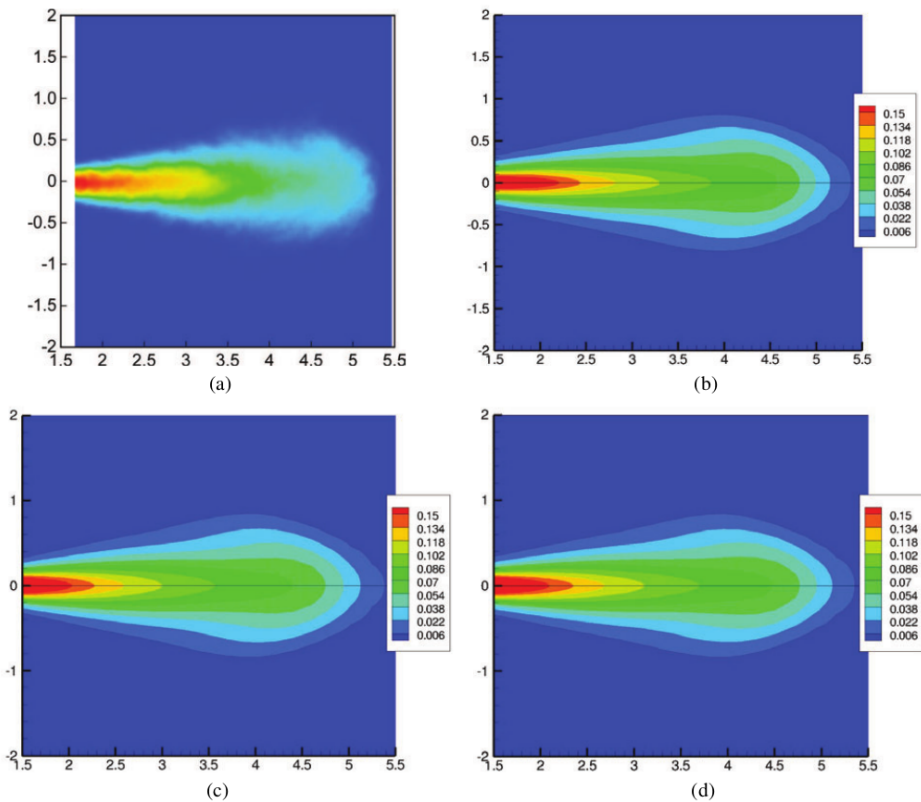
Figure 3.6: (a) Measured mixture fraction and computed mixture fraction contours at 1.13 ms after SOI with the (b) Eulerian-Lagrangian, (c) virtual-liquid source and (d) gas jet models [66].

over predicted the spray penetration. Additionally and as expected, Kelvin-Helmholtz Rayleigh-Taylor predicted faster disintegration of big droplets and higher rate of vaporization than the Kelvin-Helmholtz model.

Kösters and Karlsson [68] developed a new model where the traditional parcel was replaced by a so-called stochastic blob containing droplets with a distribution of sizes rather than a number of uniform-sized droplets. These blobs do not interact with the grid directly, but through bubbles of locally determined size (less grid dependence). In addition, they compared results obtained with both the standard $k - \epsilon$ and RNG $k - \epsilon$ turbulence models. When the RNG $k - \epsilon$ model was used with standard constants the predicted vapor penetration is too high, however with a tuned standard $k - \epsilon$ model,

the model predicts the vapor and liquid penetration very well under all tested injected conditions tested.

Contrary to Kösters and Karlsson [68], Sukumaran et al. [69] found a tendency to under-predict the vapor penetration, especially at high ambient pressure conditions, associated to the lack of momentum sources beyond the liquid spray region. To solve that problem, they implemented a gas particle model which tracks the momentum sources resulting from the evaporated spray. The imaginary gas particle continuously exchanges momentum with the gas phase until the velocity of the gas particle is comparable to that of the gas phase velocity. Good levels of agreement with experimental data and grid independence were observed.

Tonini et al. [70] tried to solve the issues of the Eulerian-Lagrangian model in the near-field, and then avoid the necessity of using other type of models, by the simultaneous employment of three numerical methodologies: distribution of source terms expressing the mass, momentum and energy coupling between the two phases through the use of weighting functions (which distribute them in a conservative way), estimation of the airflow properties at the time scale of droplet movement through the introduction of so-called virtual properties, and application of adaptive local mesh refinement in the area of liquid injection. The results obtained highlighted the significant improvements of the method compared to the standard methodology, in terms of accuracy (errors lower than 8%), numerical stability and dependency on the grid resolution.

A two-way interaction bubble tracking method was developed by Tomiyama et al. [71]. They successfully applied the model to a laminar bubbly up-flow in a vertical duct, and observed the potential of the model of predicting flow pattern transition from bubbly to slug flow. Though the original purpose of the model was a different one, it can be used to model cavitation inside the injector nozzle. In fact, and although they followed a different approach, Giannadakis et al. [72, 73] presented and validated an Eulerian-Lagrangian model which accounts for a number of primary physical processes pertinent to cavitation bubbles, integrated into the stochastic framework of the model. Figure 3.7 is an example of their results.

Senecal et al. [74] presented a state of the art modeling methodology, and described key features of it, such as adaptive mesh refinement, advanced liquid-gas momentum coupling, and improved distribution of the liquid phase. They demonstrated the ability of the Eulerian-Lagrangian approach to use cell sizes much smaller than the nozzle diameter. Continuing their work, Som et al. [75] used the same methodology and implemented a METIS multilevel partitioning (which improved the load-balancing and wall-clock time per cycle) for
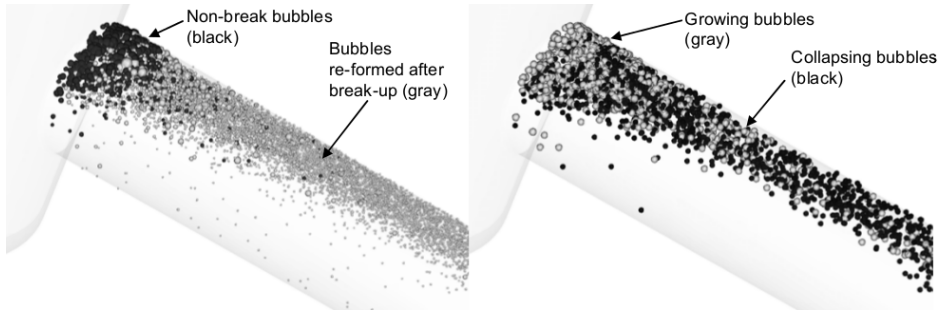
Figure 3.7: Predicted flow structure inside the nozzle, revealing the zones where the break-up, growth and collapse take place ($p_i = 60$ MPa, $p_b = 0.6$ MPa, $nl = 300\,\mu$m) [73].

simulating a single-cylinder compression ignition engine. They also performed a grid dependence study, concluding that 0.25 mm grid size may be optimum keeping in mind computational accuracy and wall-clock times.

Eulerian-Lagrangian LES models in Diesel engine applications

Bharadwaj et al. [76, 77] were one of the first in simulating high injection pressure Diesel sprays using a LES model. The sub-grid stress tensor was modeled with a non-viscosity tensor coefficient (one equation dynamic structure model) and an extra transport equation for the sub-grid kinetic energy was solved. Since the liquid droplets can be a significant source of turbulence, a spray source term for the sub-grid kinetic energy was developed to account for spray-induced gas turbulence. The model depends on the sub-grid gas velocity which is obtained using an approximate deconvolution method. Vuorinen et al. [78] also used a LES and proved that even in a low Weber number flow (*We* < 13) the droplet break-up modeling (natural resonance time according to the Poisson process) may need considerable attention in contrast to what is typically assumed. They also showed that a dispersion pattern that depends on droplet diameter is produced even without any dispersion model.

Xue et al. [79] studied the LES sub-grid scale Smagorinsky, one equation dynamic structure models and no use of it, and compared the results with the Reynolds-Averaged Navier-Stokes (RANS) approach using the RNG $k-\epsilon$ turbulence model simulations and experimental results. They also studied the grid dependence by using an adaptive mesh refinement method. At the end, they estated that nowadays LES is a viable alternative to RANS for engine

sprays, since it is more predictive in capturing flow structure and local spray characteristic with reasonable wall-clock times.

Jones and Lettieri [80] developed a probabilistic LES (based on the local Weber number) for secondary break-up able to adapt different break-up mechanisms. They also proposed a simple modification to the drag coefficient to account for droplet shapes and orientations other than spherical (balloon or parachute), but realized that the statistical nature of the model ameliorated the effects of that model. Such type of model was also employed by Irannejad and Jaberi [81], who assumed that the size and number density of the droplets generated by the break-up model are governed by a Fokker-Planck equation describing the evolution of the probability density function of droplet radii, and that the fragmentation intensity spectrum is Gaussian. The aerodynamic interactions of droplets in the dense part of the spray were modeled by correcting the relative velocity of droplets in the wake of other droplets, whose effect is shown in Figure 3.8.
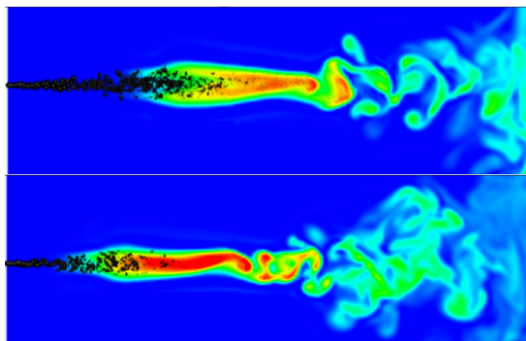
Figure 3.8: Vapor concentration contours of spray, at top without droplet wake interactions and at bottom with them (injection velocity of 90.3 m/s, $\rho_g = 14.8$ kg/m^3 and $T_b = 700$ K) [80].

3.5   Eulerian multi-fluid models

In the Eulerian multi-fluid model, gas and liquid phases are treated as interpenetrating continua in an Eulerian framework with separate velocity and temperature fields. The gas phase is considered as the primary phase, whereas the liquid phase is considered as dispersed or secondary phase. Both phases are characterized by volume fractions, and by definition, the volume fractions of all phases must sum to unity.

The governing equations of the multi-fluid model can be derived by conditionally ensemble averaging of the local instant conservation equations of single-phase flow. However, since the averaged fields of one phase are not independent of the other phase, interaction terms are needed for the mass, momentum and energy transfers to the phase from the interfaces [7, 82]

The methods used to compute these flows are similar to those used for single-phase flows, except for the addition of the interaction terms and boundary conditions (which make them far more complicated) and, of course, twice as many equations need to be solved. The transfer processes of each phase are expressed by their own balance equations, anticipating that the model can predict more detailed changes and phase interactions than the mixture or homogeneous model. Thus, it is expected that multi-fluid models can be useful to the analysis of transient phenomena, wave propagations and flow regime changes taking into account dynamic and non-equilibrium interaction between phases.

However, if the two phases are strongly coupled, the multi-fluid model brings into the system unnecessary complications for practical applications. Furthermore, no generally accepted turbulence models exist; parameter in any models are probably volume fraction dependent. Several alternatives have been suggested, divided in mixture and dispersed turbulence models: mixture models use mixture properties to calculate the viscous stress so they are applicable for stratified flows when densities of the phases are of the same order; and dispersed models use the theory of dispersion of particles by homogeneous turbulence to obtain the turbulence quantities of the dispersed phase. There is also another option, which consists of using a different turbulence model for each phase.

Eulerian multi-fluid models in Diesel engine applications

A cavitation Eulerian multi-fluid model was developed by Alajbegovic et al. [83]. The model was isothermal, so energy balances were not needed and only mass and momentum exchange terms were used. As proposed by Sato and Sekoguchi [84], a bubble induced viscosity term was added to the standard turbulent viscosity induced by shear and turbulence effect.

Zhang et al. [85] numerically studied also the cavitation phenomena in sac and VCO type nozzles. Injection pressure, back pressure, inlet rounded radius and inclination angle of the orifice were changed. As experimentally obtained [3], increasing injection pressure could easily lead cavitation, decreasing back pressure is helpful to generate fuel bubbles, and large inlet rounded radius

and inclination angle of the orifice generate less vapor bubbles and increase exit mass flow. They also found that at high injection pressure, the change in mass flow of sac type nozzles is less than that of VCO type.

Alajbegovic et al. [86] extended the common Eulerian two-fluid model to a three-phase model. Though it was applied to GDI high-pressure swirl injector, the results are also interesting for Diesel applications. The key features of the flow were predicted, the formation of a thin conical fuel sheet with an air core, and also cavitation in the depression located in the air core, as depicted in Figure 3.9. Masuda et al. [87] also used a three-fluid and a cavitation model but for a real size Diesel injector nozzle, and took into account the needle movement. They found out that unsteady change of the secondary flow (twin vortices), which splits the cavitation region in two, is caused by the needle movement.

Battistoni et al. [88, 89] used the model developed by Alajbegovic et al. [83] to investigate fuel property effects in terms of density, viscosity and vapor pressure of two fuels, Diesel and Bio-diesel, and two nozzle designs, cylindrical and conical orifices. The transient needle lift was linearized and included in the simulation. Vapor pressure revealed to be scarcely important as far as the mass flow rate and the inner nozzle flow field are concerned (see Figure 3.10). Diesel fuel seemed to provide slightly higher values than Bio-diesel when the orifice is conical. In case of strong cavitation, effects of viscosity and density were counterbalanced and mass flow rates were similar. In their works, the internal flow simulation results were coupled with spray simulations, but this aspect is analyzed in a posterior section.

Iyer and Abraham [90] presented an Eulerian multi-fluid model for Diesel sprays and carried out computations under a wide range of injection conditions. Adequate agreement according to the authors was obtained quantitatively, within 30%, when simulations are compared with experiments, and qualitatively as parameters were changed.

High order Eulerian moment methods in Diesel engine applications

However, for spray simulations where the flow is dispersed, Eulerian multi-fluid models are computationally expensive and simulation of real cases of practical interest requires intractable computing times. Nonetheless, there are another approaches for the particle size distribution calculation, the method of moments (MOM) or quadrature method of moments (QMOM) [91], which are computationally affordable but have proven to be inaccurate [92]. Marchisio and Fox [93] formulated and validated a direct quadrature method of moments
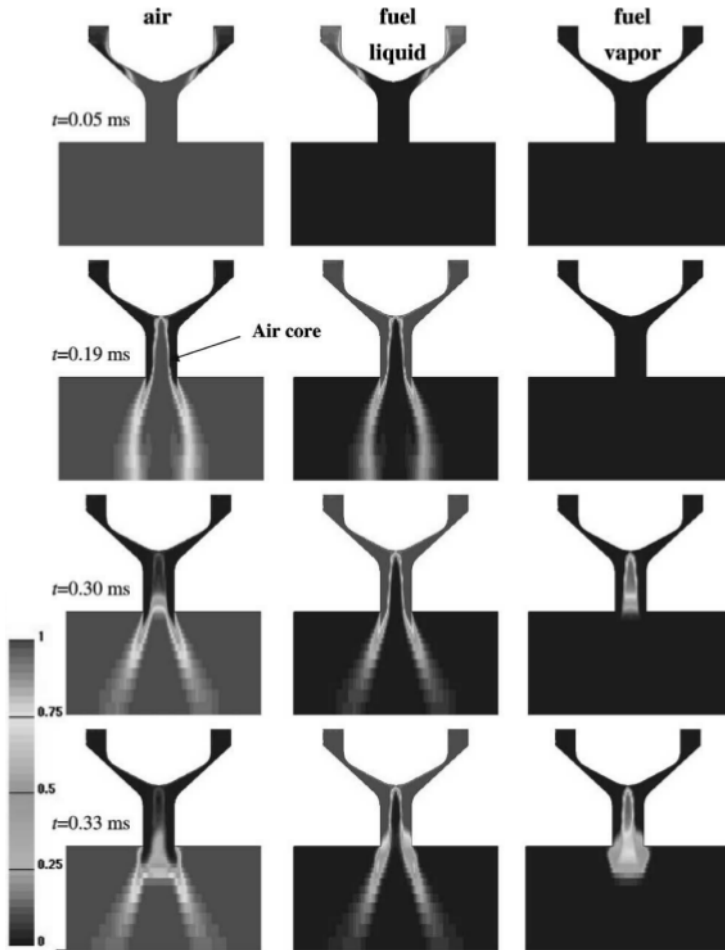
Figure 3.9: Volume fraction field for air, fuel liquid and vapor phase as a function of simulation time [86].

(DQMOM) based on the idea of tracking directly the variables appearing in the quadrature approximation rather than tracking the moments of the particle size distribution. This model was successfully applied to Diesel engine conditions by Friedrich and Weigand [94]; results showed good agreement with experimental data such as spray penetration, local droplet sized and local droplet velocities.
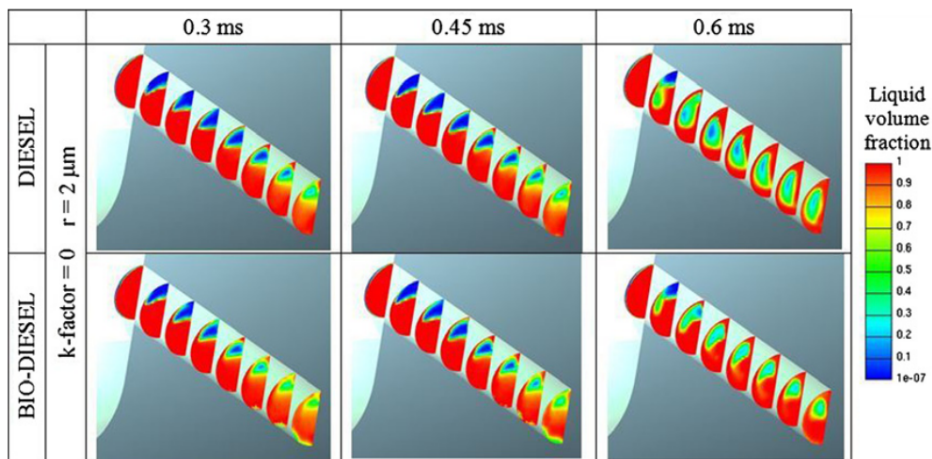
Figure 3.10: Liquid volume fraction at three different times after SOI [89].

3.6 Homogeneous flow models

A computational particle is not a real physical particle, i.e. Lagrangian parcels. Alike, a computational phase in multiphase CFD is not the same as a phase in the physical sense, computational phase represents a mass moving at a single velocity.

Homogeneous flow approach is the simplest multiphase CFD model. The basic concept of this model is to consider the mixture as a whole, therefore the field equations should be written for the balance of mixture mass, momentum and energy in terms of the mixture properties. These three macroscopic mixture conservation equations are then supplemented by a diffusion equation that takes account for the concentration changes. A local equilibrium between the continuous, carrier, and dispersed phases is assumed (all phases share the same pressure), i.e. at every point the particles move with the terminal slip velocity relative to the continuous phase, this allows velocity components for dispersed phases to be calculated from algebraic formulas. Other hypothesis, which could be also applied to previous models, are [95]: each of the phases may consist of the same pure substance, both phases are chemically inert, polar and electromagnetic effects are neglected, and all interfaces between the phases are devoid of any physical property such as mass, surface tension, surface energy, etc.

This model is also called in the literature by algebraic slip (mixture) model, diffusion model, suspension model, local-equilibrium model and drift-

flux model. Its main advantages are: fast because there are significantly less equations to be solved; describes well particle size and other distributions; and describes well the effect of turbulence on mixing of the dispersed phase. Its main drawbacks are: numerical problems such long computing times due to small time steps; difficulties in convergence; only a few secondary phases are possible; and more difficulties if mass transfer (evaporation) and chemical reactions are considered. Additionally, when applied to high-to-low pressure transients, these models may cause significant discrepancies, artificial discontinuities and numerical instability [7].

The essential approximation of this model is the local equilibrium assumption, in other words, particle are accelerated instantaneously to the terminal velocity. Therefore, a requirement for the applicability of this model is that the characteristic length of particle acceleration is much smaller than the characteristic length of the system. So generally, homogeneous flow models are not suitable for gas-particle flows or clustering flows, but can be used for liquid-solid flows and bubbly flows if bubbles are not big.

Homogeneous flow models in Diesel nozzle flow applications

As pointed out by Delannoy and Kueny [96], the pulsation of an attached vapor cavity in a cavitating flow is hard to describe with classical interface tracking methods. So they proposed a homogeneous model with a barotropic equation of state able to treat supersonic zones, incompressible zones and discontinuities. In that equation, the density was a continuous function which took the value of the incompressible liquid or incompressible vapor depending on the zone and varied with a sine function of the local pressure in the mixture zone. The growth, detachment and collapse phases were well represented, though the experimental Strouhal number was not predicted. Furthermore, due to instability issues the density ratio could not be large.

Kubota et al. [97] presented a bubbly two-phase flow model which could explain the interaction between viscous effects including vortices and cavitation bubbles where the growth and collapse of a bubble cluster is given by a modified Rayleigh's equation. Their model treated the inside and outside of a cavity as one continuum by regarding the cavity as a compressible viscous flow whose density changes greatly. They showed the mechanism of cavitation cloud generation and large-scale vortices, the boundary layer separates at the cavity leading edge, then it rolls up and produces the cavitation cloud.

Posteriorly, Chen and Heister [98] implemented a cavitation model via solution of the two-phase Navier-Stokes equations formulated with the use

of a pseudo-density which varies between vapor and liquid densities and it
is calculated from an analytical correlation based on the Rayleigh's bubble
collapse. Results for sharp-edged orifices indicated that partial cavitation
flows are typically periodic, with a period of the order of the orifice transit
time. Reducing orifice diameter tended to inhibit cavitation, even a slight
rounding of the orifice inlet lip had dramatic effects on both cavitation and
orifice discharge characteristics. This model assumed that the flow contained
certain number of small spherical bubbles, in agreement with experimental
images obtained by Soteriou et al. [99] in large scale nozzles, but not with the
ones published by Chaves et al. [100] in real size Diesel nozzles, who observed
a continuous vapor cloud.

In order to model extremely high pressures, Schmidt et al. [101] presented
a numerical model that treats liquid and vapor as a continuum where the com-
pressibility of both phases was included through a barotropic Wallis model,
and a third-order shock-capturing technique was applied to the continuity
equation to capture sharp jumps in density. The model successfully predicted
discharge coefficient and exit velocity for a variety of nozzle geometries. Kär-
rholm et al. [102] validated this type of model against calibrated orifices, and
Habchi et al. [103] proved that homogeneous equilibrium modeling (HEM)
was able to reproduce different cavitation regimes observed experimentally, as
seen in Figure 3.11.
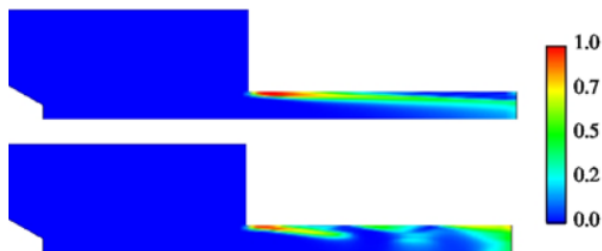
Figure 3.11: Contours of void fraction. Appearance and stabilization of cavi-
tation in a single hole injector ($p_i = 30$ MPa), bottom at 14.2 µs and top at
531 µs after SOI [103].

Giannadakis et al. [73] studied the predictive capability of an Eulerian-
Lagrangian, an Eulerian multi-fluid and a homogeneous full cavitation models
(all three assumed that cavitation is a mechanically-driven phenomenon de-
parting from thermodynamic equilibrium) for the onset and development of
cavitation for different cavitation numbers (regimes). Results indicated that

the two Eulerian models predicted a large void area inside the injection hole while the Lagrangian model predicted a more diffused and gradual vapor distribution. The collapse of the cavitation zone was not captured properly from the Eulerian models in the case of transition from the incipient to the fully cavitating flow regimes. This trend was better captured by the Lagrangian model. However, all models predicted similarly the velocity increase inside the injection hole caused by the presence of vapor, and a similar reduction in the nozzle discharge coefficient.

Liquid turbulence was significantly underestimated by the Eulerian models in the cavitation zone showing decreasing trends in contradiction with experimental observations while this was better simulated by the Lagrangian model [73]. However, it was found by Bicer et al. [104] that SST $k-\omega$ turbulence model gives good prediction for the cavitation region while the traditional $k-\epsilon$ model underestimated vapor mass fraction in terms of cavity length and thickness due to and over prediction of turbulent viscosity. They also estated that HEM with a barotropic closure cannot predict the transient cavitation may be due to the assumption of perfectly mixed liquid and vapor phases in each cell.

Another comparison between models was carried out by Battistoni et al. [105]. In this case, they compared a homogeneous relaxation model with a multi-fluid non-homogeneous model which used the Rayleigh bubble-dynamics model to account for cavitation. The amount of void predicted by the multi-fluid model was in good agreement with measurements, while the mixture model over predicted the values, though qualitatively void regions looked similar.

Echouchene et al. [106] used a HEM to study the effect of wall roughness in the cavitating and turbulent flow inside a Diesel injector. They noticed that the effect of wall roughness on turbulence variables appeared mainly on the wall vicinity (see Figure 3.12). Nonetheless, for low injection pressure, the discharge coefficient decreased when increasing the roughness height (due to the modification of the velocity profile shape); and for large injection pressure, the effect of roughness height revealed to be relatively small.

Salvador et al. [107] computationally compared the internal flow behavior of a standard Diesel fuel against a Bio-diesel fuel at cavitating and non-cavitating conditions. Bio-diesel fuel gives higher mass flow (due to its higher density) and reaches later critical cavitation conditions, so cavitation intensity is lower for the same injection conditions. As a consequence of the decrease of injection velocity and cavitation intensity, the air-fuel mixing process worsen
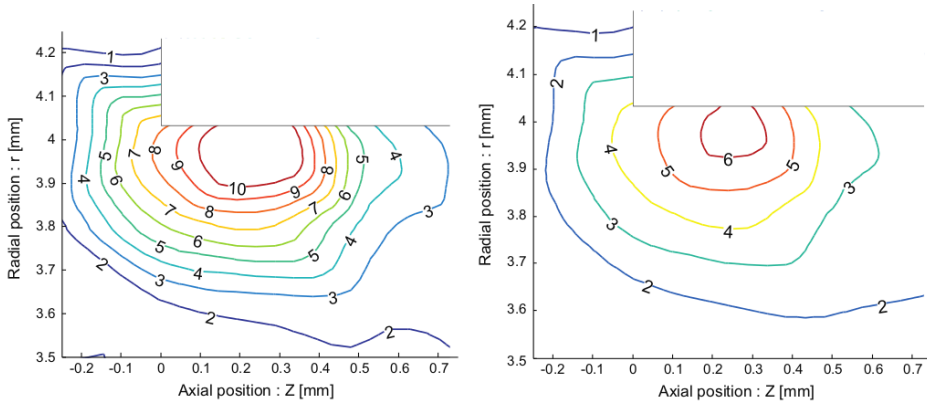
Figure 3.12: Comparison of contour lines of vapor volume fraction for smooth (left hand side) and rough (right hand side) wall [106].

for the Bio-diesel fuel. This work is similar to the one carried out by Battistoni et al. [88, 89] but results and conclusions are not exactly the same.

Some of the so far cited authors remarked the necessity of taking into account transient boundary conditions when numerically studying the cavitation. For example, Habchi et al. [103] and Lee and Reitz [108] used pressure wave transmissive inlet and outlet boundary conditions so cavitation could normally leave the domain without any numerical collapse. An arbitrary Lagrangian-Eulerian approach was used to model the needle displacement. Martínez-López [109] dug deeper in this topic and used a HEM with pressure wave transmissive boundary conditions to study the effect of the needle lift on the cavitation phenomenon. He showed that for low needle lifts, the mass flow is always chocked as a consequence of the presence of vapor in the needle seat closing. He also compared steady state simulations at different needle lifts with a moving mesh strategy, obtaining differences in mass flow rate, momentum flux and injection velocity lower than 15%.

A new criterion for cavitation inception based on the total stress was implemented in a mixture model and evaluated by Som et al. [110]. Results indicated that under realistic diesel engine conditions, cavitation patterns inside the orifice are influenced by the new cavitation criterion. The computational model was then used to characterize the effects of the injection pressure, the needle lift position and the fuel type on the internal nozzle flow and cavitation behavior. They observed, for example, that cavitation patterns shifted dramatically as the needle lift position was changed during an injection event.

Saha et al. [111] developed a model based on the mixture approach with newly derived expressions for the phase change rate and local mean effective pressure, the two key components of a cavitation model. The effects of fuel type, turbulence, compressibility and wall roughness were accounted for. Their results showed agreement with already commented ones: RNG $k-\epsilon$ turbulence model was comparable in performance with realizable $k-\epsilon$ and SST $k-\omega$ models, the wall roughness was not an important factor, cavitation inception for Bio-diesel occurred at a higher injection pressure compared to Diesel due to its higher viscosity, and the effect of liquid phase compressibility becomes considerable for high injection pressures.

Homogeneous flow models in Diesel spray applications

So far, homogeneous flow models have been used to simulate the multi-phase flow of cavitating nozzles, but the same principle can be applied for a Diesel sprays. Vallet et al. [112] developed an Eulerian model for the atomization of a liquid jet, considered as turbulent mixing in a homogeneous flow with variable density in the limit of large Reynolds and Weber numbers. In this model, large-scale features of the flow are supposed to be independent of viscosity and surface tension; while small-scale features do depend on viscosity and surface tension. Dispersion of the liquid in the gas phase is computed by a classical equation for the turbulent diffusion flux of the liquid. The mean size of the liquid fragments is obtained with a new equation for the mean surface area of the liquid-gas interface per unit of volume. Their results were encouraging when compared to experiments, though clear imperfections showed up in the range $x/D_o < 20$.

Blokkel et al. [113] combined for the first time an Eulerian model for the dense part of the spray, concretely the model developed by Vallet et al. [112], with a Lagrangian DDM model. The switch criteria they used was that the average free space between two droplets is twice the size of the mean droplet diameter. A comparison with an experimental case and several qualitative validations demonstrated the good trends of the model and its ability to accurately reproduce the evolution of the spray angle as the gas density in the combustion chamber increased. However, authors pointed out some improvements left: a new generalized turbulence model to take into account flows with very high density ratio, and add the vaporization process to carry out complete combustion calculation.

Beau et al. [114] used the same procedure and named it Eulerian-Lagrangian Spray Atomization (ELSA) model. They tested three different turbulent flux closure laws: gradient, single-phase and drag law. The gradient

closure did not appear to be efficient for modeling the cases where the liquid and the gas phases were not in dynamic equilibrium (drift between the two phases), so the exact transport equation of the diffusion flux was considered as well. The criteria of the switch to Lagrangian approach was that the liquid volume fraction becomes smaller than 0.1. It was not possible to validate the new models or decide which one was the best because of the lack of precise experimental data near the injector nozzle, nevertheless, a better behavior of the model based on turbulent transfer in the dense part of the spray and on the drag law when the spray can be considered as a set of liquid droplets was shown.

In the same framework, Lebas et al. [115] validated the ELSA model with a gradient closure law for the turbulent flux under several evaporating conditions, changing the ambient gas density (from 12 to 30 kg/m^3), the ambient temperature (from 800 to 1100 K), the injection pressure (from 80 to 150 MPa) and the fuel type (heptane and dodecane). Figure 3.13 is a sample of their results. They concluded that more work was still needed: take into account evaporation in the dense spray region, a secondary order closure term, and apply a combustion model.
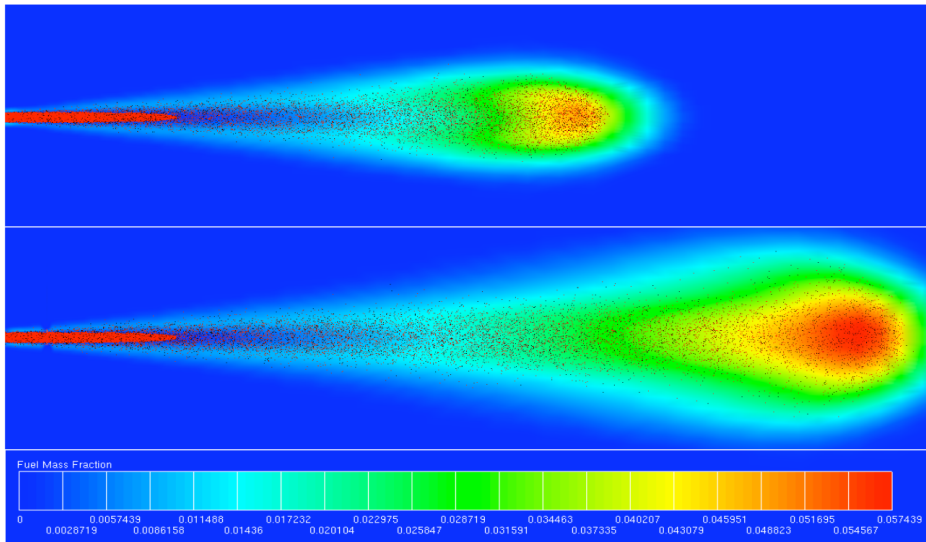
Figure 3.13: An example of spray evolution in the transient time, top at 100 µs and bottom at 200 µs [115].

Following the recommendations given by Blokkel et al. [113] and Lebas et al. [115], Demoulin et al. [116] developed a new turbulence model describing

the increase in turbulent flux due to Rayleigh-Taylor instability induced by density fluctuations and turbulence. This improved the predictions of the model. They also proposed a different closure term for the turbulent diffusion flux of the liquid which takes into account the large density variation effect. Additionally, Ning et al. [117] implemented an equilibrium evaporation model for the Eulerian part of the spray, and corrected the standard $k - \epsilon$ turbulence model to include the effects of compressibility and stretching of vortex tube by the mean flow (which led to greater scale reduction and dissipation, less kinetic energy and a lower effective viscosity). They also successfully developed a HEM for cavitation able to predict well experimental trends [118]. As a final remark, they ask for further improvements on the source terms in the transport equation for the liquid surface density, which is used to determine primary atomization.

Beheshti et al. [119] forgot about switching to Lagrangian description and assessed the ability of a simple Eulerian model based on the use of a transport equation for the average liquid surface, what they called $\Sigma - Y_{liq}$ model, on modeling air-assisted jet atomization. They used a standard $k - \epsilon$ turbulence model justified by the self-similar state of the air-assisted atomization. The model was able to represent quantitatively the effects of injector geometry, liquid and gas velocities and densities and the liquid surface tension.

Lebas et al. [120] compared the results of a new version of the ELSA model in the dense zone of the spray to a DNS based on a coupled level-set/VOF/ghost fluid method [33] in order to establish values of constants and parameters of the model. Figure 3.14 summarizes their results. The new version included an Eulerian evaporation model, the turbulent diffusion flux developed by Demoulin et al. [116] with a standard $k - \epsilon$ turbulence model, and a new, more complete, expression for the mean interface area density which accounts for the production by turbulent mixing, the mean shear stress, break-up, coalescence and vaporization. After validation, they included a combustion model for computing premixed/diffusion combustion, which was able to represent well the influence of initial gas temperature on the flame lift-off found experimentally.

A slight modification on production and destruction terms of the original mean interface area density equation of the $\Sigma - Y_{liq}$ model was proposed and tested on pressure-swirl atomizers by Belhadef et al. [121], who used two-dimensional axisymmetric swirl calculations using three-dimensional results as boundary conditions in order to reduce the computational time. They obtained good agreement in Sauter Mean Diameter when compared the simulation results to experiments, however proposed that the closure term for the
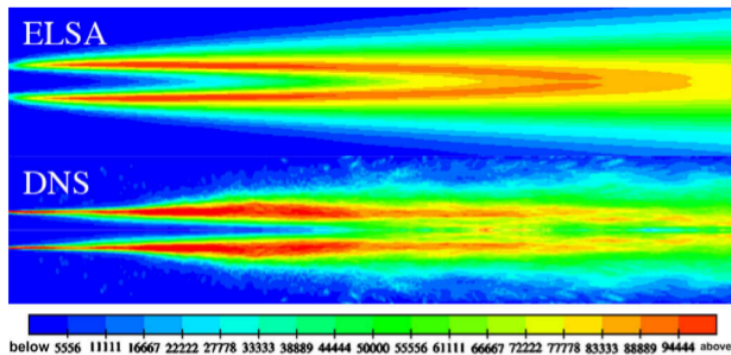
Figure 3.14: Cut of the liquid-gas surface density field obtained by using the ELSA model and DNS [120].

liquid turbulent flux could be calculated using a transport equation in order to take into account the gradients of the mean velocity and pressure.

Already introduced ELSA and $\Sigma - Y_{liq}$ models used to simulate Diesel sprays encountered difficulty in matching film profiles at large mass flow rates. Trask et al. [122] solved this problem by including compressibility effects in the $\Sigma - Y_{liq}$ model, which allowed, for example, to calculate the sudden expansion occurring following the injector lip of gas-centered swirl-coaxial injectors. They assumed an isentropic relationship between density and pressure and then split the compressible effects between turbulent mixing, thermal expansion and Mach effects by applying the chain rule to the continuity equation. By limiting the rate at which entrainment occurs via the Schmidt number, the film profile was accurately predicted over a wide range of momentum flux ratios.

Hoyas et al. [123] evaluated and validated the ELSA model by performing a grid independence study for a two-dimensional case and adjusting one of the constants of the dissipation rate transport equation of the standard $k - \epsilon$ turbulence model. At the end, they proved that the ELSA model could provide an accurate description of the droplet generation, spray angle and spray shape; however, a broader range of injection conditions needed to be tested.

In the same way, García-Oliver et al. [124] evaluated and validated the compressible $\Sigma - Y_{liq}$ model for Diesel sprays under non-vaporizing and vaporizing conditions. Accurate predictions of liquid and vapor spray penetration, as well as axial velocity and mixture fraction profiles, could be simultaneously achieved for a wide range of injection pressure and ambient conditions

if one of the constants of the dissipation rate transport equation of the standard $k - \epsilon$ turbulence model was changed (as done by Hoyas et al. [123]). Nonetheless, model accuracy was better for high ambient density and injection pressure conditions. It was proposed that under low ambient density and injection pressure conditions, inter-facial dynamics become more important and the single velocity field assumption of the homogeneous model is less appropriate.

3.7 Coupling methodology

The study of jets is classically divided in two different fields, internal (Section §2.3) and external (Section §2.4) flows, not only due to the different phenomenon taking place, but also the different time- and length-scales of the problems and the easiness of access which defines the experimental technique to be used. However, they are strongly linked, the flow properties at the exit of the nozzle orifice define the structure and the behavior of the spray, therefore the efficiency of the combustion process.

Lot of experimental research has been done for the last decades to know the influence of the nozzle geometry and internal flow parameters on the spray behavior [5, 125–128], so computational effort had to be also dedicated to this topic.

Coupling methodology in Diesel engine applications

The common way to couple internal and external flows is, first, performing an internal flow simulation, second, extracting the values of certain variables at the orifice exit (i.e. velocity, turbulent kinetic energy, dissipation rate or area coefficient), and third, using those values as input boundary and initial conditions for the external flow simulation. Examples of this methodology are the works of Chen et al. [129], Arcoumanis and Gavaises [130], Qin et al. [131] and Masuda et al. [87] (each one selected different variables to use as inlet boundary conditions). It has certain drawbacks related to its decoupled nature. One issue is limited temporal resolution of the transient nozzle flow phenomena, computational time steps are generally much different (on the order of 10^{-8} s for nozzle flow and 10^{-6} s for spray) and can be incompatible, thus time interpolation is used. In addition, the procedure does not take into account feedback between the regions (e.g. recirculation) and furthermore does not solve the full set of conservation equations for the bulk liquid phase during the primary break-up process.

Alajbegovic et al. [132] used an Eulerian multi-fluid model for modeling a cavitating nozzle and the primary break-up. The model provided the initial droplet size and velocity distribution for the droplet parcels released from the surface of a coherent liquid core, and then switched to an Eulerian-Lagrangian DDM model for the secondary break-up (the model used turbulent length scale to determine the atomization length scale and also the droplet diameter, assumed constant but depended on the radial position). Nonetheless, the turbulence was resolved with a homogeneous model, ignoring then inter-facial exchange terms. The injector and spray regions were represented within a single calculation domain, represented in Figure 3.15. In this way there was no need for the implementation of artificial boundary conditions, though a mapping procedure was needed due to the mesh resolution of the internal flow part of the domain was finer than the external flow part. The transition from nozzle flow to spray was established by a continuous primary break-up process, which caused disintegration of the continuous liquid phase over a certain distance. The major advantage of the coupled approach was the natural link between the cavitating nozzle flow and the downstream spray break-up behavior. This allowed detailed and robust modeling of the overall injection process.
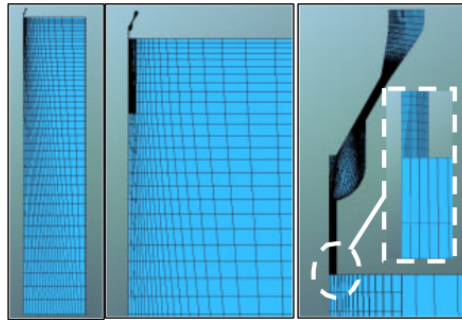
Figure 3.15: Computational grid of the single-hole Diesel injector [132].

The development of the ELSA model allowed a different coupling approach, the radial profile of the variables could be employed. Ning et al. [118, 133] used a HEM for simulating a cavitating nozzle and introduced the liquid or liquid-vapor mixture fraction, together with all the steady state flow quantities obtained from the nozzle flow simulations, into the computational domain through an inflow velocity boundary, whose diameter is the same as the nozzle exit diameter. The number of cells across the inflow velocity boundary in the ELSA simulations was equal to the number of cells across the nozzle

exit diameter in the corresponding nozzle flow simulations. However, if a different number of cells is desired, the inflow boundary conditions for ELSA simulations can be interpolated from the nozzle flow simulation results instead of using direct coupling.

Wang et al. [134] modeled the nozzle flow also with a HEM. A special rezoning method was made for needle lift motion [103] to replace the snapping algorithm previously used [108]. After the nozzle flow was finished, the outflow velocity and mixture density at each grid vertex of the nozzle exit were saved. These data were then read into the ELSA external flow simulation as inflow boundary conditions. Due to the large dimension of the solution domain, the number of cells at the nozzle exit had to be smaller than that of a nozzle flow simulation to ensure a reasonable computational time. Therefore, when the physical quantities at the nozzle flow outlet are interpolated onto the inlet of the spray chamber, the accuracy of the profiles is reduced by the coarse resolution of the grid. To solve this issue, interpolated mixture density and inflow velocity were corrected with factors to ensure the corresponding mass and momentum flow rates were consistent with those from the nozzle flow results.

In the simulation of Battistoni et al. [88] the domain comprised the injector, the nozzle region and extends beyond the hole exit including and outlet chamber, as shown in Figure 3.16. Then, unphysical boundary conditions at the nozzle exit, e.g. a constant pressure boundary which would influence the results of cavitation patterns, were avoided. Spray calculations were carried out by a DDM with blob injection model using the common coupling to initialize the parcels of droplets, but, at each time step, blobs were released from random locations within the exit cross section area (a suitable number of blobs was required, they used 64 per time step). Thus, depending on the release position, each parcel inherited the appropriate local value for each physical quantity (velocity, turbulent kinetic energy and dissipation rate, density, volume fraction and temperature). Thus a sort of mapping procedure was implemented. Using this approach radial distributions of momentum or radial distributions of liquid mass fraction could be accurately predicted. Also asymmetries originating from cavitation areas or due to uneven flow distributions inside the nozzle hole, were transferred to the spray computation, which may reflect these effects.

Finally and though it is not a proper coupling methodology neither a Diesel engine application, Befrui et al. [22, 135] used a VOF LES methodology capable of simultaneous analysis (a single domain) of the injector nozzle internal flow and the near-field jet breakup process to study the influence of nozzle
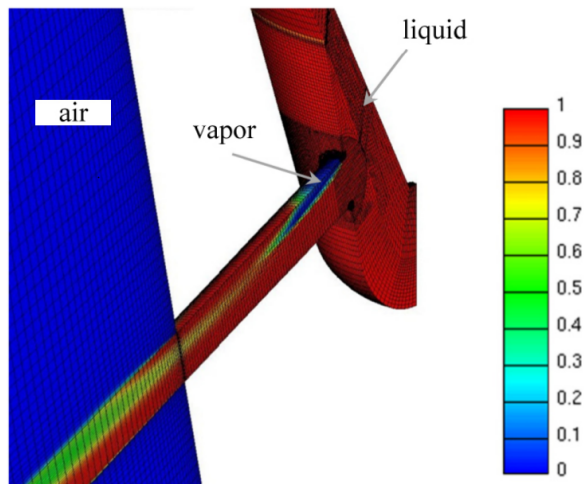
Figure 3.16: Contours of liquid volume fraction. Cavitation pattern inside the nozzle orifice [88].

design and geometric parameters of a single-hole GDI injector on the spray structure (see Figure 3.3). In the field of Diesel injection, Arienti and Sussman [36] also took profit of a level-set VOF method and injected the liquid (cavitation was not modeled) directly into air at standard conditions, all in the same domain (see Figure 3.17). This setting could affect the exit velocity of the jet, but had the advantage of showing the direct link between spray characteristics and nozzle internal flow. Xue et al. [136] also used a single domain in their spray simulations; they employed a VOF cavitation model for the nozzle though cavitation was not expected, and coupled it with the homogeneous model developed by Vallet et al. [112]. Simulations were validated against liquid distributions obtained through X-ray techniques with very good agreement for distances lower than $2\,\mathrm{mm}$. They conclude that the coupled approach can directly incorporate the in-nozzle feature such as turbulence, cavitation and geometrical effects (i.e. orifice eccentricity) into spray simulations.

3.8 Summary and conclusions

An extensive review of the state of art of simulating the Diesel injection process has been done. First thing to notice is that the most suitable model depends mainly on the flow type, which can be defined from several points of view.
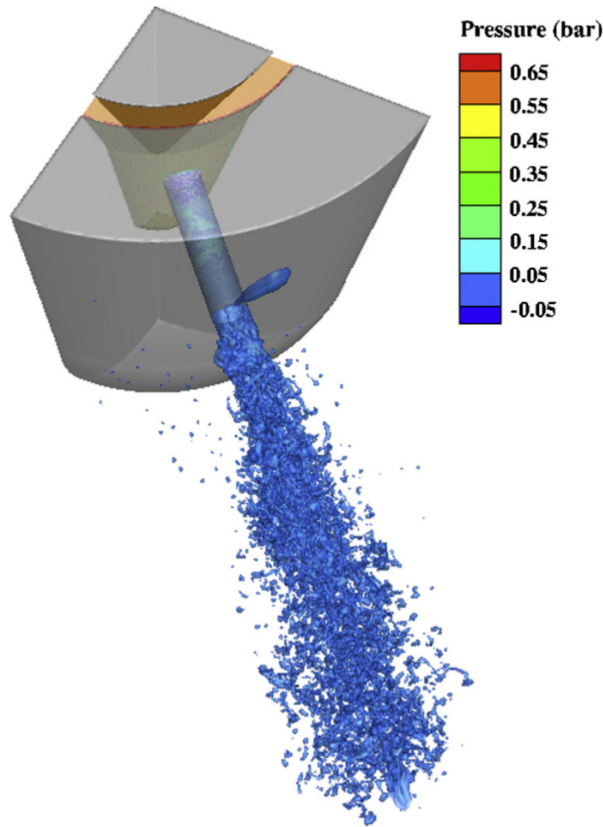
Figure 3.17: Terminal tip of the injector. Simulation snapshot of the full domain at 35 ms after SOI [22].

Dispersed phase (particle) volume fraction is generally high in technical applications. Consequently, turbulence modification (or another approach) has to be taken into account and included in a proper mathematical description of turbulent multiphase flows to consider at least a two-way coupling, for example, assuming that turbulence production is due to detachment of eddies created in the wake of the droplets (vortex shedding). Concretely, during a Diesel injection process the three couplings are found: droplet volume fraction is close to 1 near the orifice exit (four-way coupling), but it decreases as the atomization process takes place (two-way coupling), until finally, far from the nozzle and under some conditions (i.e. non-evaporative conditions), the volume fraction falls below $X = 10^{-6}$ (one-way coupling).

As commented in the introduction of this chapter, the injection process modeling is clearly split in two separate but dependent fields: internal and external flows. Coupling both fields has been investigated for more than a decade, however simulating the internal flow and the near-field seamlessly was attempted just a couple years ago, and no one has tried to simulate the whole injection process with the same model.

Eulerian-Lagrangian approach is definitely the most used one for simulating sprays despite its drawbacks. Main efforts of the research community are dedicated to reduce grid dependence (by adding new source terms and the use of adaptive mesh refinement) and enhance sub-models since more physical approach (available in the literature) to model droplets phenomena cannot be used due to high computational cost of CDM. With the proper selection and tuning of sub-models and mesh strategy, computational results are quite accurate compared to experimental ones. Nonetheless, new ELSA and $\Sigma - Y_{liq}$ models have proved to be a rising alternative to DDM, but they are still under development.

There is not such agreement of the community regarding the internal flow. HEM seems to be the most used model to predict cavitation and study the turbulence inside the nozzle, though multi-fluid models are also commonly employed. Both are capable of capturing all cavitation regimes and transient phenomena.

Interface tracking methods (level-set/VOF) are the natural approach when performing LES and DNS of the spray but also the cavitation. High computational cost when the interface shape is complicated make them unsuitable for RANS simulations. Nowadays, these kind of simulations are still computationally expensive for industrial applications, however LES is a viable alternative in combination with an Eulerian-Lagrangian model to perform engine simulations. Some techniques have been developed to reduce that computational cost, being the adaptive mesh refinement the most promising one.

As the objective of this Thesis is to simulate the flow inside the nozzle and its relation with the spray development with a single model and a single domain, a homogeneous flow model widely used for internal flow simulations and lately employed for spray studies by the ELSA and $\Sigma - Y$ models is the best option; it has lower computational cost than interface tracking models. Nevertheless, main drawbacks of this type of models have been also exposed, and they need to be solved or minimized.

References

[1] Bae, C., J. Yu, J. Kang, J. Kong, and K. O. Lee. "Effect of Nozzle Geometry on the Common-Rail Diesel Spray". *SAE Technical Paper 2002-01-1625* (2002). DOI: `10.4271/2002-01-1625` (*cit. on p. 83*).

[2] Blessing, M., G. König, C. Krüger, U. Michels, and V. Schwarz. "Analysis of Flow and Cavitation Phenomena in Diesel Injection Nozzles and Its Effects on Spray and Mixture Formation". *SAE Technical Paper 2003-01-1358* (2003). DOI: `10.4271/2003-01-1358` (*cit. on p. 83*).

[3] Payri, F., V. Bermúdez, R. Payri, and F. J. Salvador. "The influence of cavitation on the internal flow and the spray characteristics in diesel injection nozzles". *Fuel*, vol. 83 (2004), pp. 419–431. DOI: `10.1016/j.fuel.2003.09.010` (*cit. on pp. 83, 103*).

[4] Payri, R., S. Molina, F. J. Salvador, and J. Gimeno. "A study of the relation between nozzle geometry, internal flow and sprays characteristics in diesel fuel injection systems". *KSME International Journal*, vol. 18.7 (2004), pp. 1222–1235 (*cit. on p. 83*).

[5] Payri, R., J. M. García, F. J. Salvador, and J. Gimeno. "Using spray momentum flux measurements to understand the influence of diesel nozzle geometry on spray characteristics". *Fuel*, vol. 84.5 (2005), pp. 551–561. DOI: `10.1016/j.fuel.2004.10.009` (*cit. on pp. 83, 115*).

[6] Payri, R., F. J. Salvador, J. Gimeno, and L. D. Zapata. "Diesel nozzle geometry influence on spray liquid-phase fuel penetration in evaporative conditions". *Fuel*, vol. 87.7 (2008), pp. 1165–1176. DOI: `10.1016/j.fuel.2007.05.058` (*cit. on p. 83*).

[7] Ishii, M. and T. Hinbiki. *Thermo-Fluid Dynamics of Two-Phase Flow*. Ed. by M. Ishii and T. Hinbiki. Second edition. Heidelberg, Germany: Springer, 1975. DOI: `0.1007/978-1-4419-7985-8_11` (*cit. on pp. 84, 103, 107*).

[8] Elghobashi, S. "On predicting particle-laden turbulent flows". *Applied Scientific Research*, vol. 52.4 (1994), pp. 309–329. DOI: `10.1007/BF00936835` (*cit. on p. 84*).

[9] Varaksin, A. Y. *Turbulent Particle-Laden Gas Flows*. Ed. by A. Y. Varaksin. First edition. Heidelberg, Germany: Springer, 2007 (*cit. on pp. 84, 86, 87*).

[10] Ferziger, J. H. and M. Perić. *Computational Methods for Fluid Dynamics*. Ed. by J. H. Ferziger. Third edition. Heidelberg, Germany: Springer, 2002 (*cit. on pp. 88, 90*).

[11]   Unverdi, S. O. and G. Tryggvason. "A front-tracking method for
       viscous, incompressible, multi-fluid flows". *Journal of Computational
       Physics*, vol. 100.1 (1992), pp. 25–37. DOI: 10.1016/0021-9991(92)
       90307-K (*cit. on p. 88*).

[12]   Hayashi, K. and A. Tomiyama. "Interface tracking simulation of mass
       transfer from a dissolving bubble". *Journal of Computational Multi-
       phase Flows*, vol. 3.4 (2011), pp. 247–262. DOI: 10.1260/1757-482X.
       3.4.247 (*cit. on p. 88*).

[13]   Hayashi, K., S. Hosoda, G. Tryggvason, and A. Tomiyama. "Effects of
       shape oscillation on mass transfer from a Taylor bubble". *International
       Journal of Multiphase Flow*, vol. 58 (2014), pp. 236–254. DOI: 10.1016/
       j.ijmultiphaseflow.2013.09.009 (*cit. on p. 88*).

[14]   Sames, P. C., T. E. Schellin, S. Muzaferija, and M. Perić. "Application
       of a two-fluid finite volume method to ship slamming". *Journal of Off-
       shore Mechanics and Arctic Engineering*, vol. 121.1 (1999), pp. 47–52.
       DOI: 10.1115/1.2829554 (*cit. on p. 90*).

[15]   Hirt, C. W. and B. D. Nichols. "Volume of fluid (VOF) method for the
       dynamics of free boundaries". *Journal of Computational Physics*, vol.
       39.1 (1981), pp. 201–225 (*cit. on p. 90*).

[16]   Lafaurie, B., C. Nardone, R. Scardovelli, S. Zaleski, and G. Zanetti.
       "Modelling Merging and Fragmentation in Multiphase Flows with
       SURFER". *Journal of Computational Physics*, vol. 113.1 (1994),
       pp. 134–147. DOI: 10.1006/jcph.1994.1123 (*cit. on p. 90*).

[17]   Chorin, A. J. "Flame advection and propagation algorithms". *Journal
       of Computational Physics*, vol. 35.1 (1980), pp. 1–11 (*cit. on p. 90*).

[18]   Gueyffier, D., J. Li, A. Nadim, R. Scardovelli, and S. Zaleski. "Volume-
       of-Fluid Interface Tracking with Smoothed Surface Stress Methods
       for Three-Dimensional Flows". *Journal of Computational Physics*, vol.
       152.2 (1999), pp. 423–456. DOI: 10.1006/jcph.1998.6168 (*cit. on
       p. 90*).

[19]   Dirke, M. von, A. Krautter, J. P. Ostertag, M. Mennicken, and C.
       Badock. "Simulation of cavitating flows in diesel injectors". *Oil and
       Gas Science and Technology*, vol. 54.2 (1999), pp. 223–223 (*cit. on
       p. 90*).

[20]   Marcer, R. et al. "Coupling 1D System AMESim and 3D CFD EOLE
       models for Diesel Injection Simulation". *23rd Annual Conference on
       Liqud Atomization & Spray Systems (ILASS Europe)*. Brno, Czech Re-
       public, 2010 (*cit. on p. 90*).

[21] Marcer, R. et al. "A Validated Numerical Simulation of Diesel Injector Flow Using a VOF Method". *SAE Technical Paper 2000-01-2932* (2000). DOI: 10.4271/2000-01-2932 (*cit. on p. 90*).

[22] Befrui, B., G. Corbinelly, M. D'Onofrio, and D. Varble. "GDI Multi-Hole Injector Internal Flow and Spray Analysis". *SAE Technical Paper 2011-01-1211* (2011). DOI: 10.4271/2011-01-1211 (*cit. on pp. 91, 117, 119*).

[23] Osher, S. J. and J. A. Sethian. "Fronts propagating with curvature-dependent speed: Algorithms based on Hamilton-Jacobi formulations". *Journal of Computational Physics*, vol. 79.1 (1988), pp. 12–49 (*cit. on p. 91*).

[24] Sussman, M., P. Smereka, and S. J. Osher. "A Level Set Approach for Computing Solutions to Incompressible Two-Phase Flow". *Journal of Computational Physics*, vol. 114.1 (1994), pp. 146–159. DOI: 10.1006/jcph.1994.1155 (*cit. on pp. 91, 92*).

[25] Zhang, H., L. Zheng, V. R. Prasad, and T. Hou. "A curvilinear level set formulation for highly deformable free surface problems with application to solidification". *Numerical Heat Transfer, Part B: Fundamentals*, vol. 34.1 (1998), pp. 1–20 (*cit. on p. 92*).

[26] Olsson, E. and G. Kreiss. "A conservative level set method for two phase flow". *Journal of Computational Physics*, vol. 210.1 (2005), pp. 225–246. DOI: 10.1016/j.jcp.2005.04.007 (*cit. on p. 92*).

[27] Sussman, M., E. Fatemi, P. Smereka, and S. J. Osher. "An improved level set method for incompressible two-phase flows". *Computers and Fluids*, vol. 27.5-6 (1998), pp. 663–680. DOI: 10.1016/S0045-7930(97)00053-4 (*cit. on p. 92*).

[28] Fedkiw, R. P., T. Aslam, B. Merriman, and S. J. Osher. "A Non-oscillatory Eulerian Approach to Interfaces in Multimaterial Flows (the Ghost Fluid Method)". *Journal of Computational Physics*, vol. 152.2 (1999), pp. 457–492. DOI: 10.1006/jcph.1999.6236 (*cit. on p. 92*).

[29] Tanguy, S. and A. Berlemont. "Application of a level set method for simulation of droplet collisions". *International Journal of Multiphase Flow*, vol. 31.9 (2005), pp. 1015–1035. DOI: 10.1016/j.ijmultiphaseflow.2005.05.010 (*cit. on p. 92*).

[30] Osher, S. J. and R. P. Fedkiw. "Level Set Methods: An Overview and Some Recent Results". *Journal of Computational Physics*, vol. 169.2 (2001), pp. 463–502. DOI: 10.1006/jcph.2000.6636 (*cit. on p. 92*).

[31] Sussman, M. and E. G. Puckett. "A Coupled Level Set and Volume-of-Fluid Method for Computing 3D and Axisymmetric Incompressible Two-Phase Flows". *Journal of Computational Physics*, vol. 162.2 (2000), pp. 301–337. DOI: `10.1006/jcph.2000.6537` (*cit. on p. 92*).

[32] Desjardins, O., V. Moureau, and H. G. Pictsch. "An accurate conservative level set/ghost fluid method for simulating turbulent atomization". *Journal of Computational Physics*, vol. 227.18 (2008), pp. 8395–8416. DOI: `10.1016/j.jcp.2008.05.027` (*cit. on p. 92*).

[33] Ménard, T., S. Tanguy, and A. Berlemont. "Coupling level set/VOF/ghost fluid methods: Validation and application to 3D simulation of the primary break-up of a liquid jet". *International Journal of Multiphase Flow*, vol. 33.5 (2007), pp. 510–524. DOI: `10.1016/j.ijmultiphaseflow.2006.11.001` (*cit. on pp. 93, 113*).

[34] Herrmann, M. A. "On simulating primary atomization using the refined level set grid method". *Atomization and Sprays*, vol. 21.4 (2011), pp. 283–301. DOI: `10.1615/AtomizSpr.2011002760Doc` (*cit. on p. 93*).

[35] Desjardins, O., J. O. McCaslin, M. Owkes, and P. T. Brady. "Direct numerical and large-eddy simulation of primary atomization in complex geometries". *Atomization and Sprays*, vol. 23.11 (2013), pp. 1001–1048. DOI: `10.1615/AtomizSpr.2013007679` (*cit. on p. 93*).

[36] Arienti, M. and M. Sussman. "An embedded level set method for sharp-interface multiphase simulations of Diesel injectors". *International Journal of Multiphase Flow*, vol. 59 (2014), pp. 1–14. DOI: `10.1016/j.ijmultiphaseflow.2013.10.005` (*cit. on pp. 94, 118*).

[37] Dukowicz, J. K. "A particle-fluid numerical model for liquid sprays". *Journal of Computational Physics*, vol. 35.2 (1980), pp. 229–253. DOI: `10.1016/0021-9991(80)90087-X` (*cit. on p. 95*).

[38] Abraham, J. "What is Adequate Resolution in the Numerical Computations of Transient Jets". *SAE Technical Paper 970051* (1997). DOI: `10.4271/970051` (*cit. on p. 95*).

[39] Reitz, R. D. "Atomization and other breakup regimes of a liquid jet". PhD thesis. 08544, Princeton, New Jersey, United States of America: Princeton University, 1978 (*cit. on p. 95*).

[40] Som, S. and S. K. Aggarwal. "Effects of primary breakup modeling on spray and combustion characteristics of compression ignition engines". *Combustion and Flame*, vol. 157.6 (2010), pp. 1179–1193. DOI: `10.1016/j.combustflame.2010.02.018` (*cit. on p. 96*).

[41] Su, T. F., M. A. Patterson, R. D. Reitz, and P. V. Farrell. "Experimental and Numerical Studies of High Pressure Multiple Injection Sprays". *SAE Technical Paper 960861* (1996). DOI: `10.4271/960861` (*cit. on p. 96*).

[42] O'Rourke, P. J. and A. A. Amsden. "The Tab Method for Numerical Calculation of Spray Droplet Breakup". *SAE Technical Paper 872089* (1987). DOI: `10.4271/872089` (*cit. on p. 96*).

[43] Senecal, P. K. et al. "Modeling high-speed viscous liquid sheet atomization". *International Journal of Multiphase Flow*, vol. 25.6-7 (1999), pp. 1073–1097. DOI: `10.1016/S0301-9322(99)00057-9` (*cit. on p. 96*).

[44] Dombrowski, N. and W. R. Johns. "The aerodynamic instability and disintegration of viscous liquid sheets". *Chemical Engineering Science*, vol. 18.3 (1963), pp. 203–214 (*cit. on p. 96*).

[45] Reitz, R. D. and R. Diwakar. "Effect of Drop Breakup on Fuel Sprays". *SAE Technical Paper 860469* (1986). DOI: `10.4271/860469` (*cit. on p. 96*).

[46] Pilch, M. M. and C. A. Erdman. "Use of breakup time data and velocity history data to predict the maximum size of stable fragments for acceleration-induced breakup of a liquid drop". *International Journal of Multiphase Flow*, vol. 13.6 (1987), pp. 741–757 (*cit. on p. 96*).

[47] Hsiang, L.-P. and G. M. Faeth. "Near-limit drop deformation and secondary breakup". *International Journal of Multiphase Flow*, vol. 18.5 (1992), pp. 635–652 (*cit. on p. 96*).

[48] Chu, C. C. and M. L. Corradini. "One-dimensional transient fluid model for fuel/coolant interaction analysis". *Nuclear Science and Engineering*, vol. 101.1 (1989), pp. 48–71 (*cit. on p. 96*).

[49] Patterson, M. A. and R. D. Reitz. "Modeling the Effects of Fuel Spray Characteristics on Diesel Engine Combustion and Emission". *SAE Technical Paper 980131* (1998). DOI: `10.4271/980131` (*cit. on p. 96*).

[50] Barroso, G., B. Schneider, and K. Boulouchos. "An Extensive Parametric Study on Diesel Spray Simulation and Verification with Experimental Data". *SAE Technical Paper 2003-01-3230* (2003). DOI: `10.4271/2003-01-3230` (*cit. on p. 97*).

[51] Subramaniam, S. "Lagrangian-Eulerian methods for multiphase flows". *Progress in Energy and Combustion Science*, vol. 39.2-3 (2013), pp. 215–245. DOI: `10.1016/j.pecs.2012.10.003` (*cit. on p. 97*).

[52] Béard, P. et al. "Extension of Lagrangian-Eulerian Spray Modeling: Application to High Pressure Evaporating Diesel Sprays". *SAE Technical Paper 2000-01-1893* (2000). DOI: `10.4271/2000-01-1893` (*cit. on p. 97*).

[53] Abani, N. et al. "An Improved Spray Model for Reducing Numerical Parameter Dependencies in Diesel Engine CFD Simulations". *SAE Technical Paper 2008-01-0970* (2008). DOI: `10.4271/2008-01-0970` (*cit. on p. 97*).

[54] Abani, N. and R. D. Reitz. "Modeling subgrid-scale mixing of vapor in diesel sprays using jet theory". *Atomization and Sprays*, vol. 20.1 (2010), pp. 71–83. DOI: `10.1615/AtomizSpr.v20.i1.60` (*cit. on p. 97*).

[55] García-Oliver, J. M., X. Margot, M. L. Chávez, and A. Karlsson. "A combined 1D3D-CFD approach for reducing mesh dependency in Diesel spray calculations". *Mathematical and Computer Modelling*, vol. 54.7-8 (2011), pp. 1732–1737. DOI: `10.1016/j.mcm.2011.01.041` (*cit. on p. 97*).

[56] Pastor, J. V., J. J. López, J. M. García, and J. M. Pastor. "A 1D model for the description of mixing-controlled inert diesel sprays". *Fuel*, vol. 87.13-14 (2008), pp. 2871–2885. DOI: `10.1016/j.fuel.2008.04.017` (*cit. on p. 97*).

[57] Desantes, J. M., J. V. Pastor, J. M. García-Oliver, and J. M. Pastor. "A 1D model for the description of mixing-controlled reacting diesel sprays". *Combustion and Flame*, vol. 156.1 (2009), pp. 234–249. DOI: `10.1016/j.combustflame.2008.10.008` (*cit. on p. 97*).

[58] Shuai, S., N. Abani, T. Yoshikawa, R. D. Reitz, and S. W. Park. "Simulating low temperature diesel combustion with improved spray models". *International Journal of Thermal Sciences*, vol. 48.9 (2009), pp. 1786–1799. DOI: `10.1016/j.ijthermalsci.2009.01.011` (*cit. on p. 98*).

[59] Kim, S., S. W. Park, and C. S. Lee. "Improved Eulerian-Lagrangian spray simulation by using an enhanced momentum coupling model". *Proceedings of the American Society of Mechanical Engineerss. Internal Combustion Engine Division Fall Technical Conference*. Lucerne, Switzerland, 2009, pp. 433–442. DOI: `10.1115/ICEF2009-14079` (*cit. on p. 98*).

[60] Xue, Q., S.-C. Kong, D. J. Torres, Z. Hu, and J. Yi. "DISI Spray Modeling Using Local Mesh Refinement". *SAE Technical Paper 2008-01-0967* (2008). DOI: `10.4271/2008-01-0967` (*cit. on p. 98*).

[61] Xue, Q. and S.-C. Kong. "Development of adaptive mesh refinement scheme for engine spray simulations". *Computers and Fluids*, vol. 38.4 (2009), pp. 939–949. DOI: 10.1016/j.compfluid.2008.10.004 (*cit. on p. 98*).

[62] Xue, Q. and S.-C. Kong. "Multilevel dynamic mesh refinement for modeling transient spray and mixture formation". *Atomization and Sprays*, vol. 19.8 (2009), pp. 755–769. DOI: 10.1615/AtomizSpr.v19.i8.40 (*cit. on p. 98*).

[63] Kolakaluri, R., Y. Li, and S.-C. Kong. "A unified spray model for engine spray simulation using dynamic mesh refinement". *International Journal of Multiphase Flow*, vol. 36.11-12 (2010), pp. 858–869. DOI: 10.1016/j.ijmultiphaseflow.2010.08.001 (*cit. on p. 98*).

[64] Lucchini, T., G. D'Errico, and D. Ettorre. "Numerical investigation of the spray-mesh-turbulence interactions for high-pressure, evaporating sprays at engine conditions". *International Journal of Heat and Fluid Flow*, vol. 32.1 (2011), pp. 285–297. DOI: 10.1016/j.ijheatfluidflow.2010.07.006 (*cit. on p. 98*).

[65] Hohmann, S. and U. Renz. "Numerical simulation of fuel sprays at high ambient pressure: The influence of real gas effects and gas solubility on droplet vaporisation". *International Journal of Heat and Mass Transfer*, vol. 46.16 (2003), pp. 3017–3028. DOI: 10.1016/S0017-9310(03)00077-2 (*cit. on p. 98*).

[66] Abraham, J. and L. M. Pickett. "Computed and measured fuel vapor distribution in a diesel spray". *Atomization and Sprays*, vol. 20.3 (2010), pp. 241–250. DOI: 10.1615/AtomizSpr.v20.i3.50 (*cit. on pp. 98, 99*).

[67] Hossainpour, S. and A. R. Binsesh. "Investigation of fuel spray atomization in a DI heavy-duty diesel engine and comparison of various spray breakup models". *Fuel*, vol. 88.5 (2009), pp. 799–508. DOI: 10.1016/j.fuel.2008.10.036 (*cit. on p. 98*).

[68] Kösters, A. and A. Karlsson. "A Comprehensive Numerical Study of Diesel Fuel Spray Formation with OpenFOAM". *SAE Technical Paper 2011-01-0842* (2011). DOI: 10.4271/2011-01-0842 (*cit. on pp. 99, 100*).

[69] Sukumaran, S., S.-C. Kong, and N. H. Cho. "Modeling Evaporating Diesel Sprays Using an Improved Gas Particle Model". *SAE Technical Paper 2013-01-1598* (2013). DOI: 10.4271/2013-01-1598 (*cit. on p. 100*).

[70] Tonini, S., M. Gavaises, and A. Theodorakakos. "Modelling of high-pressure dense diesel sprays with adaptive local grid refinement". *International Journal of Heat and Fluid Flow*, vol. 29.2 (2008), pp. 427–448 (*cit. on p. 100*).

[71] Tomiyama, A., I. Zun, H. Higaki, Y. Makino, and T. Sakaguchi. "A three-dimensional particle tracking method for bubbly flow simulation". *Nuclear Engineering and Design*, vol. 175.1-2 (1997), pp. 77–86. DOI: 10.1016/S0029-5493(97)00164-7 (*cit. on p. 100*).

[72] Giannadakis, E., M. Gavaises, and C. Arcoumanis. "Modelling of cavitation in diesel injector nozzles". *Journal of Fluid Mechanics*, vol. 616 (2008), pp. 153–193. DOI: 10.1017/S0022112008003777 (*cit. on p. 100*).

[73] Giannadakis, E., D. Papoulias, M. Gavaises, C. Arcoumanis, and C. Soteriou. "Evaluation of the Predictive Capability of Diesel Nozzle Cavitation Models". *SAE Technical Paper 2007-01-0245* (2007). DOI: 10.4271/2007-01-0245 (*cit. on pp. 100, 101, 108, 109*).

[74] Senecal, P. K., E. Pomraning, K. J. Richards, and S. Som. "Grid-convergent spray models for internal combustion engine CFD simulations". *Proceedings of the American Society of Mechanical Engineerss. Internal Combustion Engine Division Fall Technical Conference*. Vancouver, Canada, 2012, pp. 697–710. DOI: 10.1115/ICEF2012-92043 (*cit. on p. 100*).

[75] Som, S. et al. "A Numerical Investigation on Scalability and Grid Convergence of Internal Combustion Engine Simulations". *SAE Technical Paper 2013-01-1095* (2013). DOI: 10.4271/2013-01-1095 (*cit. on p. 100*).

[76] Bharadwaj, N., C. J. Rutland, and S. Chang. "Large eddy simulation modelling of spray-induced turbulence effects". *International Journal of Engine Research*, vol. 10.2 (2009), pp. 97–119. DOI: 10.1243/14680874JER02309 (*cit. on p. 101*).

[77] Bharadwaj, N. and C. J. Rutland. "A large-eddy simulation study of sub-grid two-phase interaction in particle-laden flows and diesel engine sprays". *Atomization and Sprays*, vol. 20.8 (2010), pp. 673–695. DOI: 10.1615/AtomizSpr.v20.i8.20 (*cit. on p. 101*).

[78] Vuorinen, V. A. et al. "Effect of droplet size and atomization on spray formation: A priori study using large-eddy simulation". *Flow, Turbulence and Combustion*, vol. 86.3-4 (2011), pp. 533–561. DOI: 10.1007/s10494-010-9266-3 (*cit. on p. 101*).

[79]   Xue, Q., S. Som, P. K. Senecal, and E. Pomraning. "Large eddy simulation of fuel-spray under non-reacting IC engine conditions". *Atomization and Sprays*, vol. 23.10 (2013), pp. 925–955. DOI: 10.1615/AtomizSpr.2013008320 (*cit. on p. 101*).

[80]   Jones, W. P. and C. Lettieri. "Large eddy simulation of spray atomization with stochastic modeling of breakup". *Physics of Fluids*, vol. 22.11 (2010), pp. 1–12. DOI: 10.1063/1.3508353 (*cit. on p. 102*).

[81]   Irannejad, A. and F. Jaberi. "Large Eddy Simulation of Evaporating Spray with a Stochastic Breakup Model". *SAE Technical Paper 2013-01-1101* (2013). DOI: 10.4271/2013-01-1101 (*cit. on p. 102*).

[82]   Crowe, C. T., J. D. Schwarzkopf, M. Sommerfeld, and Y. Tsuji. *Multiphase Flows with Droplets and Particles*. Ed. by C. T. Crowe. Second edition. 711 3rd Avenue, 10017, New York, New York, United States of America: CRC Press, Taylor & Francis Group, 1998 (*cit. on p. 103*).

[83]   Alajbegovic, A., H. A. Grogger, and H. Philipp. "Calculation of Transient Cavitation in Nozzle Using the Two Fluid Model". *12th Annual Conference on Liquid Atomization & Spray Systems (ILASS Americas)*. Indianapolis, Indiana, United States of America, 1999 (*cit. on pp. 103, 104*).

[84]   Sato, Y. and K. Sekoguchi. "Liquid velocity distribution in two-phase bubble flow". *International Journal of Multiphase Flow*, vol. 2.1 (1975), pp. 79–95. DOI: 10.1016/0301-9322(75)90030-0 (*cit. on p. 103*).

[85]   Zhang, J., Q. Du, Y.-X. Yang, and J. Sun. "Study on cavitating flow in different types of diesel nozzle orifice". *Transactions of Chinese Society for Internal Combustion Engines*, vol. 28.2 (2010), pp. 133–140 (*cit. on p. 103*).

[86]   Alajbegovic, A., G. Meister, D. Greif, and B. Basara. "Three phase cavitating flows in high-pressure swirl injectors". *Experimental Thermal and Fluid Science*, vol. 26.6-7 (2002), pp. 677–681. DOI: 10.1016/S0894-1777(02)00179-6 (*cit. on pp. 104, 105*).

[87]   Masuda, R., T. Fuyuto, M. Nagaoka, E. von Berg, and R. Tatschi. "Validation of Diesel Fuel Spray and Mixture Formation from Nozzle Internal Flow Calculation". *SAE Technical Paper 2005-01-2098* (2005). DOI: 10.4271/2005-01-2098 (*cit. on pp. 104, 115*).

[88]   Battistoni, M., C. N. Grimaldi, and F. Marianni. "Coupled Simulation of Nozzle Flow and Spray Formation Using Diesel and Biodiesel for CI Engine Applications". *SAE Technical Paper 2012-01-1267* (2012). DOI: 10.4271/2012-01-1267 (*cit. on pp. 104, 110, 117, 118*).

[89]   Battistoni, M. and C. N. Grimaldi. "Numerical analysis of injector flow and spray characteristics from diesel injectors using fossil and biodiesel fuels". *Applied Energy*, vol. 97 (2012), pp. 656–666. DOI: 10.1016/j.apenergy.2011.11.080 (*cit. on pp. 104, 106, 110*).

[90]   Iyer, V. and J. Abraham. "An Evaluation of a Two-Fluid Eulerian-Liquid Eulerian-Gas Model for Diesel Sprays". *Journal of Fluids Engineering*, vol. 125.4 (2003), pp. 660–669. DOI: 10.1115/1.1593708 (*cit. on p. 104*).

[91]   Beck, J. C. and A. P. Watkins. "On the development of a spray model based on drop-size moments". *Proceedings of the Royal Society A: Mathematical, Physical and Engineering Sciences*, vol. 459.2034 (2003), pp. 1365–1394. DOI: 10.1098/rspa.2002.1052 (*cit. on p. 104*).

[92]   Marchisio, D. L., R. D. Vigil, and R. O. Fox. "Implementation of the quadrature method of moments in CFD codes for aggregation-breakage problems". *Chemical Engineering Science*, vol. 58.15 (2003), pp. 3337–3351 (*cit. on p. 104*).

[93]   Marchisio, D. L. and R. O. Fox. "Solution of population balance equations using the direct quadrature method of moments". *Journal of Aerosol Science*, vol. 36.1 (2005), pp. 43–73. DOI: 10.1016/j.jaerosci.2004.07.009 (*cit. on p. 104*).

[94]   Friedrich, M. and B. Weigand. "Eulerian multi-fluid simulation of polydisperse dense liquid sprays by the direct quadrature method of moments". *10th International Conference on Liquid Atomization and Spray Systems (ICLASS)*. Kyoto, Japan, 2006 (*cit. on p. 105*).

[95]   Bataille, J. and J. Kesting. *Continuum modeling of two-phase flows*. Technical Report LA-UR-81-3325. Washington, District of Columbia, Washington, United States of America: Los Alamos National Laboratory, 1981 (*cit. on p. 106*).

[96]   Delannoy, Y. and J. L. Kueny. "Two phase flow approach in unsteady cavitation modelling". *Proceedings of the American Society of Mechanical Engineerss. Fluids Engineering Division*. Vol. 98. Toronto, Canada, 1990, pp. 153–158 (*cit. on p. 107*).

[97]   Kubota, A., H. Kato, and H. Yamaguichi. "A new modelling of cavitating flows: a numerical study of unsteady cavitation on a hydrofoil section". *Journal of Fluid Mechanics*, vol. 240 (1992), pp. 59–96 (*cit. on p. 107*).

[98] Chen, Y. and S. D. Heister. "Modeling cavitating flows in diesel injectors". *Atomization and Sprays*, vol. 6.6 (1996), pp. 709–726 (*cit. on p. 107*).

[99] Soteriou, C., R. Andrews, and M. Smith. "Direct Injection Diesel Sprays and the Effect of Cavitation and Hydraulic Flip on Atomization". *SAE Technical Paper 950080* (1995). DOI: `10.4271/950080` (*cit. on p. 108*).

[100] Chaves, H., M. Knapp, A. Kubitzek, F. Obermeier, and T. Schneider. "Experimental Study of Cavitation in the Nozzle Hole of Diesel Injectors Using Transparent Nozzles". *SAE Technical Paper 950290* (1995). DOI: `10.4271/950290` (*cit. on p. 108*).

[101] Schmidt, D. P., C. J. Rutland, and M. L. Corradini. "A fully compressible, two-dimensional model of small, high-speed, cavitating nozzles". *Atomization and Sprays*, vol. 9.3 (1999), pp. 255–276 (*cit. on p. 108*).

[102] Kärrholm, F. P., H. Weller, and N. Nordin. "Modelling Injector Flow Including Cavitation Effects for Diesel Applications". *Proceedings of the American Society of Mechanical Engineers / Japan Society of Mechanica Engineers. Fluids Engineering Summer Conference*. Vol. 2. San Diego, California, United States of America, 2007, pp. 465–474. DOI: `10.1115/FEDSM2007-37518` (*cit. on p. 108*).

[103] Habchi, C., N. Dumont, and O. Simonin. "Multidimensional simulation of cavitating flows in Diesel injectors by a homogeneous mixture modeling approach". *Atomization and Sprays*, vol. 18.2 (2008), pp. 129–162. DOI: `10.1615/AtomizSpr.v18.i2.20` (*cit. on pp. 108, 110, 117*).

[104] Bicer, B., A. Tanaka, T. Fukuda, and A. Sou. "Numerical Simulation of Cavitating Phenomena in Diesel Injector Nozzles". *12th Annual Conference on Liquid Atomization & Spray Systems (ILASS Asia)*. Osaka, Japan, 2013 (*cit. on p. 109*).

[105] Battistoni, M., S. Som, and D. Longman. "Comparison of Mixture and Multifluid Models for In-Nozzle Cavitation Prediction". *Journal of Engineering for Gas Turbines and Power*, vol. 136.6 (2014). DOI: `10.1115/1.4026369` (*cit. on p. 109*).

[106] Echouchene, F., H. Belmabrouk, L. L. Penven, and M. Buffat. "Numerical simulation of wall roughness effects in cavitating flow". *International Journal of Heat and Fluid Flow*, vol. 35.5 (2011), pp. 1068–1075. DOI: `10.1016/j.ijheatfluidflow.2011.05.010` (*cit. on pp. 109, 110*).

[107] Salvador, F. J., J. Martínez-López, J. V. Romero, and M. D. Roselló. "Influence of biofuels on the internal flow in diesel injector nozzles". *Mathematical and Computer Modelling*, vol. 54.7-8 (2011), pp. 1699–1705. DOI: 10.1016/j.mcm.2010.12.010 (*cit. on p. 109*).

[108] Lee, W. G. and R. D. Reitz. "A numerical investigation of transient flow and cavitation within minisac and valve-covered orifice diesel injector nozzles". *Journal of Engineering for Gas Turbines and Power*, vol. 132.5 (2010), pp. 1–8. DOI: 10.1115/1.4000145 (*cit. on pp. 110, 117*).

[109] Martínez-López, J. "Estudio computacional de la influencia del levantamiento de aguja sobre el flujo interno y el fenómeno de la cavitación en toberas de injección Diésel". PhD thesis. Camino de Vera, s/n, 46022, Valencia, Spain: Departamento de Máquinas y Motores Térmicos, Universitat Politècnica de València, 2013 (*cit. on p. 110*).

[110] Som, S., S. K. Aggarwal, E. M. El-Hannouny, and D. Longman. "Investigation of Nozzle Flow and Cavitation Characteristics in a Diesel Injector". *Journal of Engineering for Gas Turbines and Power*, vol. 134.4 (2010), pp. 1–12. DOI: 10.1115/1.3203146 (*cit. on p. 110*).

[111] Saha, K., E. Abu-Ramadan, and X. Li. "Modified Single-Fluid Cavitation Model for Pure Diesel and Biodiesel Fuels in Direct Injection Fuel Injectors". *Journal of Engineering for Gas Turbines and Power*, vol. 135.6 (2013), pp. 1–8. DOI: 10.1115/1.4023464 (*cit. on p. 111*).

[112] Vallet, A., A. A. Burluka, and R. Borghi. "Development of a Eulerian model for the "Atomization" of a liquid jet". *Atomization and Sprays*, vol. 11.6 (2001), pp. 619–642 (*cit. on pp. 111, 118*).

[113] Blokkel, G., B. Barbeau, and R. Borghi. "A 3D Eulerian Model to Improve the Primary Breakup of Atomizing Jet". *SAE Technical Paper 2003-01-0005* (2003). DOI: 10.4271/2003-01-0005 (*cit. on pp. 111, 112*).

[114] Beau, P. A., M. Funk, R. Lebas, and F. X. Demoulin. "Applying Quasi-Multiphase Model to Simulate Atomization Processes in Diesel Engines: Modeling of the Slip Velocity". *SAE Technical Paper 2005-01-0220* (2005). DOI: 10.4271/2005-01-0220 (*cit. on p. 111*).

[115] Lebas, R., G. Blokkel, P. A. Beau, and F. X. Demoulin. "Coupling Vaporization Model With the Eulerian-Lagrangian Spray Atomization (ELSA) Model in Diesel Engine Conditions". *SAE Technical Paper 2005-01-0213* (2005). DOI: 10.4271/2005-01-0213 (*cit. on p. 112*).

[116] Demoulin, F. X., P. A. Beau, G. Blokkel, and R. Borghi. "A new model for turbulent flows with large density fluctuations: Application to liquid atomization". *Atomization and Sprays*, vol. 17.4 (2007), pp. 315–345. DOI: `10.1615/AtomizSpr.v17.i4.20` (*cit. on pp. 112, 113*).

[117] Ning, W., R. D. Reitz, A. M. Lippert, and R. Diwakar. "Development of a Next-generation Spray and Atomization Model Using an Eulerian-Lagrangian Methodology". *20th Annual Conference on Liquid Atomization & Spray Systems (ILASS Americas)*. Chicago, Illinois, United States of America, 2007 (*cit. on p. 113*).

[118] Ning, W., R. D. Reitz, A. M. Lippert, and R. Diwakar. "A Numerical Investigation of Nozzle Geometry and Injection Condition Effects on Diesel Fuel Injector Flow Physics". *SAE Technical Paper 2008-01-0936* (2008). DOI: `10.4271/2008-01-0936` (*cit. on pp. 113, 116*).

[119] Beheshti, N., A. A. Burluka, and M. Fairweather. "Assessment of $\Sigma - Y_{liq}$ model predictions for air-assisted atomisation". *Theoretical and Computational Fluid Dynamics*, vol. 21.5 (2007), pp. 381–397. DOI: `10.1007/s00162-007-0052-3` (*cit. on p. 113*).

[120] Lebas, R., T. Ménard, P. A. Beau, A. Berlemont, and F. X. Demoulin. "Numerical simulation of primary break-up and atomization: DNS and modelling study". *International Journal of Multiphase Flow*, vol. 35.3 (2009), pp. 247–260. DOI: `10.1016/j.ijmultiphaseflow.2008.11.005` (*cit. on pp. 113, 114*).

[121] Belhadef, A., A. Vallet, M. Amielh, and F. Anselmet. "Pressure-swirl atomization: Modeling and experimental approaches". *International Journal of Multiphase Flow*, vol. 39 (2012), pp. 13–20. DOI: `10.1016/j.ijmultiphaseflow.2011.09.009` (*cit. on p. 113*).

[122] Trask, N., D. P. Schmidt, M. Lightfoot, and S. Danczyk. "Compressible modeling of the internal flow in a gas-centered swirl-coaxial fuel injector". *Journal of Propulsion and Power*, vol. 28.4 (2012), pp. 685–693. DOI: `10.2514/1.B34102` (*cit. on p. 114*).

[123] Hoyas, S., A. Gil, X. Margot, D. Khuong-Anh, and F. Ravet. "Evaluation of the Eulerian-Lagrangian Spray Atomization (ELSA) model in spray simulations: 2D cases". *Mathematical and Computer Modelling*, vol. 57.7-8 (2013), pp. 1686–1693. DOI: `10.1016/j.mcm.2011.11.006` (*cit. on pp. 114, 115*).

[124]   García-Oliver, J. et al. "Diesel spray CFD simulations based on the $\Sigma - Y$ eulerian atomization model". *Atomization and Sprays*, vol. 23.1 (2013), pp. 71–95. DOI: 10.1615/AtomizSpr.2013007198 (*cit. on p. 114*).

[125]   Kampmann, S., B. Dittus, P. Mattes, and M. Kirner. "The Influence of Hydro Grinding at VCO Nozzles on the Mixture Preparation in a DI Diesel Engine". *SAE Technical Paper 960867* (1996). DOI: 10.4271/960867 (*cit. on p. 115*).

[126]   Jicha, M., J. Jedelsky, J. Otahal, and J. Slama. "Influence of Some Geometrical Parameters on the Characteristics of Effervescent Atomization". *18th Annual Conference on Liqud Atomization & Spray Systems (ILASS Europe)*. Zaragoza, Spain, 2002 (*cit. on p. 115*).

[127]   Desantes, J. M., R. Payri, F. J. Salvador, and V. Soare. "Study of the Influence of Geometrical and Injection Parameters on Diesel Sprays Characteristics in Isothermal Conditions". *SAE Technical Paper 2005-01-0913* (2005). DOI: 10.4271/2005-01-0913 (*cit. on p. 115*).

[128]   Payri, R., J. Gimeno, O. Venegas, and A. H. Plazas. "Experimental and computational study of the influence of partial needle lift on nozzle flowin diesel fuel injectors". *Atomization and Sprays*, vol. 22.8 (2012), pp. 687–714. DOI: 10.1615/AtomizSpr.2012005810 (*cit. on p. 115*).

[129]   Chen, J. L., M. R. Wells, and J. L. Creehan. "Primary Atomization and Spray Analysis of Compound Nozzle Gasoline Injectors". *Journal of Engineering for Gas Turbines and Power*, vol. 120.1 (1998), pp. 237–243. DOI: 10.1115/1.2818082 (*cit. on p. 115*).

[130]   Arcoumanis, C. and M. Gavaises. "Linking nozzle flow with spray characteristics in a diesel fuel injection system". *Atomization and Sprays*, vol. 8.3 (1998), pp. 307–347 (*cit. on p. 115*).

[131]   Qin, J. R. et al. "Correlating the Diesel Spray Behavior to Nozzle Design". *SAE Technical Paper 1999-01-3555* (1999). DOI: 10.4271/1999-01-3555 (*cit. on p. 115*).

[132]   Alajbegovic, A. et al. "Coupled Simulations of Nozzle Flow, Primary Fuel Jet Breakup, and Spray Formation". *Journal of Engineering for Gas Turbines and Power*, vol. 127.4 (2004), pp. 897–908. DOI: 10.1115/1.1914803 (*cit. on p. 116*).

[133]   Ning, W., R. D. Reitz, R. Diwakar, and A. M. Lippert. "An Eulerian-Lagrangian Spray and Atomization model with improved turbulence modeling". *Atomization and Sprays*, vol. 19.8 (2009), pp. 727–739. DOI: 10.1615/AtomizSpr.v19.i8.20 (*cit. on p. 116*).

[134] Wang, Y., W. G. Lee, R. D. Reitz, and R. Diwakar. "Numerical Simulation of Diesel Sprays Using an Eulerian-Lagrangian Spray and Atomization (ELSA) Model Coupled with Nozzle Flow". *SAE Technical Paper 2011-01-0386* (2011). DOI: 10.4271/2011-01-0386 (*cit. on p. 117*).

[135] Befrui, B., G. Corbinelly, P. Spiekermann, M. Shost, and M. C. Lai. "Large Eddy Simulation of GDI Single-Hole Flow and Near-Field Spray". *SAE Technical Paper 2012-01-0392* (2012). DOI: 10.4271/2012-01-0392 (*cit. on p. 117*).

[136] Xue, Q. et al. "Eulerian CFD Modelling of Coupled Nozzle Flow and Spray with Validation Against X-Ray Radiography Data". *SAE International Journal of Engines*, vol. 7.2 (2014), pp. 1061–1072. DOI: 10.4271/2014-01-1425 (*cit. on p. 118*).

Chapter 4

Computational methodology. Description of the model

4.1 Introduction

As done in Chapter 2, it is common to divide the problem in two parts depending on the area of interest and composition of the fluid: internal flow and external flow. Internal flow studies deal with the influence of the injector geometry on the flow pattern, the cavitation phenomena, the needle lift and eccentricity and other manufacturing issues. External flow studies, on the other hand, deal with fuel break-up, atomization, air-fuel mixing, evaporation and combustion processes. This division is made because of the different flow nature: in the internal part the flow is *continuous*, mono-phase liquid (or multiphase if cavitation is considered); and in the external part, far from the nozzle exit, the flow is *dispersed* multiphase.

It is well known that coupling internal and external flow experiments and simulations leads to a better representation of reality [1–3]. However, common coupling methodologies have several issues to be solved. For example, a sort of mapping procedure has to be implemented to spatially distribute blobs and its physical quantities of the primary break-up model inside the nozzle area. Also, computational time-steps are much different (on the order of 10^{-8} s for nozzle flow and 10^{-6} s for spray [3]), thus a time interpolation is required.

If the whole injection process (internal and external flows) is going to be simulated at the same time, an Eulerian approach seems to be the best option

(see Chapter 3). A mixture model with a liquid mass fraction that defines the percentage of liquid in the cell is desired rather than a VOF model. This is due to, far downstream from the nozzle exit, the fuel droplets are very small ($5-20$ µm in diameter [4]) and then tracking the interface becomes very expensive in computational cost.

A new Eulerian two-phase model (which in the future could be extended to include more phases, i.e. fuel vapor) is developed with the aim of simulating internal and external flows seamlessly, with a single domain. The governing equations are solved using the finite-volume Computational Fluid Dynamics (CFD) software OpenFOAM 2.1.0 ®, which employs temporal and spatial discretization schemes that are bounded and preserve the proper physical limits on the fluid dynamics variables. The main advantages of OpenFOAM are:

- Open-source, freely available, licensed under the GNU General Public License.
- Includes a wide range of solvers, model libraries, meshing and post-processing tools
- Allows easy customization, extensions and modifications by the user.
- Represents partial differential equations in their natural language.

However, since the code is relatively young, it lacks some capabilities and some existing ones have not been thoroughly validated. For instance, there are no adaptive mesh refinement tools, and moving mesh approaches are quite limited. Nonetheless, developers and the research community are making a serious effort in solving this issues and completing the code.

4.2   Model description

4.2.1   Transport equations

All kind of fluid flows can be described by systems of linked partial differential equations of the form of Equation (4.1) [5, 6], where $\boldsymbol{Q}$ is any tensor-valued property of the flow, such as species concentration. These equations involve time derivatives, convective terms, diffusive terms, and source (production and destruction) terms $S\boldsymbol{Q}$ and S_q.

$$\frac{\partial \left(\rho \boldsymbol{Q} \right)}{\partial t} + \nabla \cdot \left(\rho \boldsymbol{U} \boldsymbol{Q} \right) - \nabla^2 \left(D_{coeff} \boldsymbol{Q} \right) = S\boldsymbol{Q} + S_p \qquad (4.1)$$

The effect of the nonlinearity embodied in these equations is significant; only in special cases can algebraic solutions be found. The vast majority of fluid flow problems, at least until now, can only be properly studied by using computational methods involving discretization of the domain and equations, followed by numerical solution of the resulting system of equations. The complexity of the problem is increased if effects such as turbulence, compressibility, multiphase, free surface, chemical reactions, and electromagnetism are included. The two predominant solution techniques are the finite-element method (FEM), in which the functional form of the solution of these equations is expanded in terms of predetermined basis set and its residual minimized, and the finite-volume method (FVM) [7]. In the latter technique, which is used in this Thesis, the computational domain is divided into a set of discrete volumes which fill the computational domain without overlap. The fluid flow equations are then volume integrated over each individual finite volume. Gauss's theorem, also known as divergence or Ostrogradsky's theorem[1], is used to convert the divergence terms in Equation (4.1) into surface integrated flux terms, reducing the problem of discretization of these terms to one of finding difference approximations for the fluxes at the surface of the control volume based on the know cell-center values. Other spatial derivatives are dealt with a similar manner. This converts the equations into a set of ordinary differential equations including temporal derivatives, which can be discretized in a straightforward manner using finite-difference approximations. This results in a set of equations that, when linearized by fixing the flux $\Phi = \rho \boldsymbol{U}$, can be described in matrix form of Equation (4.2), where $\boldsymbol{M}$ is a sparse block matrix, which can be inverted to solve the equation.

$$\boldsymbol{M}Q = \boldsymbol{B} \qquad (4.2)$$

The nonlinear term in Equation (4.1) requires an iterative solution technique, one in which the linearized system specified above is solved several times, with the fluxes being updated each time (see a more detailed description of that in Section §4.3), until it has converged sufficiently.

Coupling between equations is treated in a field operation and manipulation (FOAM) using a segregated approach, in which equations are formulated for each dependent variable and solved sequentially, with the possibility of iteration over the system of equations until convergence is achieved.

---

[1]Gauss's theorem states that the outward flux of a vector field through a closed surface is equal to the volume integral of the divergence over the region inside the surface. Intuitively, it states that the sum of all sources minus the sum of all sinks gives the net flow out of a region.

Solving this type of transport equations with in micro-level description[2] is a formidable task, especially for multiphase flows since there are two deformable materials, occupying distinct regions of physical space and separated from each other by a large number of definite interfaces. In order to appreciate the difficulties in deriving the balance equations for structured, namely, inhomogeneous media with inter-facial discontinuities, recall that in continuum mechanics the field theories are constructed on integral balances of mass, momentum and energy. Thus if the variables in the region of integration are continuously differentiable and the Jacobian transformation between material and spatial coordinates exists, the Eulerian differential balance can be obtained by using the Leibnitz's rule [5]. In multiphase flows, the presence of inter-facial surfaces introduces great difficulties in the mathematical and physical formulation of the problem:

- existence of the multiple deformable moving interfaces with their motions being unknown;
- existence of the fluctuations of variables due to turbulences and to the motion of the interfaces;
- significant discontinuities of properties at interface.

The first effect causes complicated coupling between the field equations of each phase and the inter-facial conditions, whereas the second effect inevitably introduces a statistical characteristic originated from the instability of the Navier-Stokes equations and of the inter-facial waves. The third effect introduces huge local jumps in various variables in space and time.

Intuition, however, suggests that if the observer accepts a macro-level description[3] of the multiphase medium, it may be viewed as a mixture of overlapping equivalent continua, each of them undergoing its own process (diffusion, mixture or homogeneous model, described in Section §3.6). When this point of view is adopted, the interfaces are smeared out across the equivalent continua and the real thermal and mechanical interactions across the interfaces become average volumetrically distributed interactions. Then, in order to

---

[2]A level of description whose time- and length-scales are much larger than the largest of the time- and length-scales associated with discrete processes taking place on a molecular or micro-structural level in either phase, and at the same time much smaller than the smallest time- and length-scales which characterize the space-time heterogeneity of the system [8].

[3]A level of description whose time- and length-scales are much larger than the microlevel ones.

determine the collective interaction of particles and the dynamics of the interface, it is necessary to describe first the local properties of the flow and then to obtain a macroscopic description by means of appropriate averaging procedures. For dispersed flows, for example, it is necessary to determine ranges of nucleation, evaporation or condensation, motion and disintegration of single droplets (or gas bubbles) as well as the collisions and coalescence processes of several droplets (bubbles). The averaging procedure can be considered as low-pass filtering, excluding unwanted high frequency signals from local instant fluctuations. However, it is important to note that the statistical properties of these fluctuations influencing the macroscopic phenomena should be taken into account in a formulation based on averaging.

There exist various methods of averaging that can be applied to thermo-fluid dynamics in general and to multiphase flow in particular. According to Ishii and Hinbiki [5], depending on the basic physical concepts used to formulate thermal-hydraulic problems, averaging procedures can be classified into three main groups: the Eulerian averaging; the Lagrangian averaging; and the Boltzmann statistical averaging. They can be further divided into subgroups based on a variable with which a mathematical operator of averaging is defined. Additionally, according to Hinze [9], the following three averaging methods can be distinguished: time averaging in a fixed point of space, for stationary turbulence; space averaging for a fixed moment in time in the case of homogeneous turbulence; and ensemble averaging for a series of identical experiments (this is the most general form of averaging). All these methods can appear in two versions, unweighted (Reynolds) and weighted (e.g. density-weighted Favre averaging). In the case of compressible flows, Favre averaging is usually applied, also in this Thesis. The description of all averaging procedures (including Favre averaging) can be easily found in the literature, so it is not included in this document. Because of that, all equations in this and following chapters are written in their final form after performing the averaging procedure. Therefore, ρ, $\boldsymbol{U}$... represent average density, velocity... values and not instantanous ones.

Hypothesis and highlights of the model

Before proceeding to present the averaged transport equations, it is important to remark that the model described here for atomization and mixing, proposed by Vallet et al. [10], is based on four basic principles:

- Because surface tension and viscosity act essentially at small length-scales (micro-scales, associated with high curvature of the liquid-gas

interface and large velocity gradients), the large scale features of the multiphase flow must become independent of surface tension and viscosity at infinite Weber and Reynolds numbers. Then the modeling of the large scale features should not depend on the capillarity surface tension or the dynamic viscosity nor on the small scale features. They may depend on the density ratio only. On the contrary, the small scale features, and in particular the mean size of liquid droplets of parcels extracted from the liquid jet, will be linked directly to the surface tension and dynamic viscosity, and, of course to the large scale features. This basic hypothesis is nothing but the generalization of the Kolmogorov hypothesis for turbulence. Some atomization regimes studies considered the liquid viscosity as one of the variables determining atomization quality, however, flow visualization of liquid jets used in such studies indicate that those jets are, in all likelihood, laminar, and therefore the mechanism of their atomization may be very different from that of practically important turbulent sprays [11].

- The random velocity field of a two-phase flow, which is not predictable at each time, can be studied in terms of mean values as well as for single-phase turbulent flows. These mean values can be calculated within the framework of a two equation model (see Section §4.4.4). The definition of the turbulent variables does not distinguish between liquid and gaseous fluid particles, but a difference between mean velocities does exist, and can eventually be calculated.

- The dispersion of the liquid phase into the gas can be computed by a balance equation through the definition and modeling of a "turbulent diffusion liquid flux", similar to the turbulent diffusion flux defined classically for single-phase flows. Thus the need to postulate a balance equation for the liquid diffusion flux is needed, together with equations for mean velocity and mean density medium.

- The mean size of the liquid fragments can be calculated through the definition and modeling of the mean surface area of the liquid-gas interface per unit volume.

Therefore, this new model described in this chapter is similar to the one developed by Vallet et al. [10] except for three important matters:

- The common pressure-equation [6] is used instead of a the equation of state [10] or an isentropic relationship [12].
- The new model is compressible so the energy equation is required.

- A PIMPLE algorithm is preferred rather than the common PISO algorithm.

Continuity equation

From the general balance Equation (4.1), the mixture continuity equation, Equation (4.3), can be obtained if $Q = 1$, $S = 0$ and $S_p = 0$. This equation has exactly the same form as that for a continuum without internal discontinuities.

$$\frac{\partial \rho}{\partial t} + \nabla \cdot (\rho \boldsymbol{U}) = 0 \tag{4.3}$$

Liquid mass fraction transport equation

The diffusion equation, which expresses the change in concentration (volume fraction), can be derived from a mass balance of a chemically inert mixture. By setting $Q = 1$ and $S = 0$, the continuity equation for one of the phases can be obtained, Equation (4.4), where the mass source term $X_{p,k}$ appears due to phase changes. Equation ((4.5)) expresses the conservation of mass at interfaces.

$$\frac{\partial \left(X_k \rho_k\right)}{\partial t} + \nabla \cdot (X_k \rho_k \boldsymbol{U}_k) = X_{p,k} \tag{4.4}$$

$$\sum_{k=1}^{n} X_{p,k} = 0 \tag{4.5}$$

The diffusion velocity of each phase, namely, the relative velocity with respect to the mass center of the mixture, is defined by Equation (4.6).

$$\boldsymbol{U}_{k,rel} = \boldsymbol{U}_k - \boldsymbol{U} \tag{4.6}$$

Combining Equations (4.4) and (4.6), Equation (4.7) is obtained as a concentration transport equation. It has a diffusion term on the right-hand side which carries the information that the liquid and gas mean velocities are not the same. The relation between volume and mass fractions of Equation (4.8) can be used to express the transport equation in terms of mixture density and mass fraction, as shown in Equation (4.9).

$$\frac{\partial \left(X_k \rho_k\right)}{\partial t} + \nabla \cdot (X_k \rho_k \boldsymbol{U}) = X_{p,k} - \nabla \cdot (X_k \rho_k \boldsymbol{U}_{k,rel}) \tag{4.7}$$

$$X_k = \frac{\rho}{\rho_k} Y_k \tag{4.8}$$

$$\frac{\partial (Y_k \rho)}{\partial t} + \nabla \cdot (Y_k \rho \boldsymbol{U}) = Y_{p,k} - \nabla \cdot (Y_k \rho \boldsymbol{U}_{k,rel}) \tag{4.9}$$

Though Equation (4.9) is written in a general way so it is valid for n species, the present model only uses it once for the liquid mass fraction. Nonetheless, if more species were used, for example, fuel vapor was included through cavitation of evaporation, a decision had to be taken on whether one diffusivity value is used for all species or different diffusivity values for different species. Due to the hypothesis of high Reynolds number, turbulent diffusivity dominates over molecular one, therefore a single turbulent diffusivity value for all species should be used. Additionally, that helps to improve the numerical stability and solution convergence.

Momentum equation

By applying the general balance Equation (4.1) to the conservation of momentum, Equation (4.10) is obtained, where M_σ is an inter-facial momentum source due to the surface tension effect. The diffusivity coefficient $D_{U,coeff}$ models shear stresses, accounting for the average viscous stress, the turbulent stress and the diffusion stress. It is evident that if the surface tension term is neglected, then there are no direct inter-facial terms in the mixture momentum equation.

$$\frac{\partial (\rho \boldsymbol{U})}{\partial t} + \nabla \cdot (\rho \boldsymbol{U} \boldsymbol{U}) - \nabla^2 (D_{U,coeff} \boldsymbol{U}) = -\nabla p + \rho \boldsymbol{g} + \boldsymbol{M}_\sigma \tag{4.10}$$

Energy equation

The mixture energy equation can be obtained also from Equation (4.1) applied to the balance of the total energy, as shown in Equation (4.11) where $\boldsymbol{q}$ is the energy source term, E_σ is the inter-facial energy source term, K is the specific kinetic energy given by Equation (4.12) and the term $\nabla \cdot (\boldsymbol{\tau} \cdot \boldsymbol{U})$ is the viscous dissipation. Viscous sub-grid/turbulent dissipation term is missing, as usually, it is neglected.

$$\frac{\partial (\rho (e + K))}{\partial t} + \nabla \cdot (\rho \boldsymbol{U} (e + K)) - \nabla^2 (D_{e,coeff} (e + K)) =$$
$$= -\nabla \cdot \boldsymbol{q} - \nabla \cdot (p \boldsymbol{U}) + \nabla \cdot (\boldsymbol{\tau} \cdot \boldsymbol{U}) + \rho \boldsymbol{g} \cdot \boldsymbol{U} + E_\sigma \tag{4.11}$$

$$K = \frac{\boldsymbol{U}^2}{2} + \frac{\sum_{k=1}^{n} X_k \rho_k \frac{\boldsymbol{U}_{k,rel}^2}{2}}{\rho} \tag{4.12}$$

It can be seen that the form of Equation (4.11) is quite similar to the single-phase flow energy equation. The differences appear as additional heat fluxes, namely the turbulent flux, the diffusion flux and the inter-facial source. However, the most interesting characteristic of the mixture can be found in the kinetic energy term, Equation (4.12). The total mixture kinetic energy consists of the kinetic energy of mean flow plus the diffusion kinetic energies of all phases. Again, if the surface tension is neglected, the inter-facial term does not appear in the mixture total energy equation.

In a single-phase flow, the separation of the mechanical and thermal energy can be carried out quite easily by subtracting the mechanical energy equation from the total energy balance. Exactly the same method could be used in the multi-fluid model formulation. In the diffusion model formulation, however, it is further complicated by the existence of the diffusion kinetic energy transport. Consequently, there is no clear cut method to obtain a corresponding thermal energy equation for the mixture [5]. First option is to subtract the kinetic energy of both phases from the total energy equation. Same result is obtained by adding the enthalpy equation of each phase. In this way, the diffusion kinetic energy can be eliminated. Nonetheless, the inter-facial term involves complicated exchanges between the total and the mechanical energies. Second option is using the mixture kinetic energy equation in terms of the mean velocity, which avoids the difficulty in the inter-facial terms but has additional terms from the diffusion kinetic energy. By subtracting the mixture mechanical energy equation, namely, the momentum equation (Equation (4.10)) dotted by $\boldsymbol{U}$, from Equation (4.11), Equation (4.13) is obtained.

$$\frac{\partial (\rho h)}{\partial t} + \nabla \cdot (\rho \boldsymbol{U} h) - \nabla^2 (D_{h,coeff} h) =$$

$$= -\nabla \cdot \boldsymbol{q} + \frac{Dp}{Dt} - \frac{\partial (\rho K)}{\partial t} - \nabla \cdot (\rho \boldsymbol{U} K) + \boldsymbol{\tau} \cdot \nabla \boldsymbol{U} + (E_\sigma - \boldsymbol{M}_\sigma \boldsymbol{U}) \tag{4.13}$$

It can be concluded that the mixture energy transfer is highly complicated due to the diffusion of each phase. The form of the right hand side of Equations (4.11) and (4.13) suggests that if the effects of the mechanical terms originated from the diffusion are important, then the constitutive laws for the diffusion (or mixture) cannot be simple. Thus, in such case, the Eulerian

multi-fluid model may be more suitable. However, in most multiphase problems with large heat additions, these mechanical effects from the diffusions are insignificant. The only important effect to be taken into account is the diffusion of the transport of thermal energy because of the large difference on the phase enthalpies, namely, the latent heat.

Pressure equation

In the original model of Vallet et al. [10], the continuity equation (Equation (4.3)) did not allow the calculation of the mean density, which was obtained directly from Equations (4.9) and (4.63), but allowed the calculation of the mean pressure. In the case where there are only two phases, liquid and gas, and the gas is a compressible perfect gas, the assumption that the pressure is the same in neighboring gas liquid and fluid particles (thus neglecting the mean energetic contribution of surface tension) allows to simply obtain Equation (4.14) for the mean pressure. Then it is necessary to know the mean gas temperature in order to close the set of equations. This could be done with a classical balance equation for the gas internal energy (Equation (4.11)), including heat exchange between gas and liquid phase, or just by prescribing the gas temperature by an isentropic law when these exchanges are not important.

$$p = \frac{\rho\,(1 - Y_f)\,RT}{1 - \frac{\rho Y_f}{\rho_f}} \tag{4.14}$$

There are other approaches in the literature. Ning et al. [12] assumed isentropic flow, which led to the relationship of Equation (4.15) where the sound speed a varied from the gas sonic to the liquid sonic speed depending on the void fraction. Combination of this equation with the continuity equation (Equation (4.3)) gives Equation (4.16) as a pressure equation.

$$\frac{D\rho}{Dt} = \frac{1}{a^2}\frac{Dp}{Dt} \tag{4.15}$$

$$\frac{1}{a^2}\frac{\partial p}{\partial t} + \frac{1}{a^2}\boldsymbol{U}\cdot\nabla p + \rho\nabla\cdot\boldsymbol{U} = 0 \tag{4.16}$$

Trask et al. [13] extended the single-phase, incompressible algorithm outlined by Jasak [14] (see next Section §4.2.2) to account for the compressible,

multiphase, variable temperature flow. By manipulation of momentum equation, the form of Equation (4.17) can be obtained, which in combination with continuity equation, results in the pressure equation.

$$\nabla \cdot \boldsymbol{U} = \nabla \cdot \left(\frac{\boldsymbol{H}}{A} \right) - \nabla \cdot \left(\frac{1}{A} \nabla p \right) \tag{4.17}$$

For the case of multiphase, compressible flow the velocity divergence is nonzero and could be split between the effects of the turbulent mixing, Mach (compressibility) and thermal expansion by applying the chain rule to the continuity equation, as shown in Equation (4.18). In order to obtain a fully closed transport equation for pressure, each of those terms must be treated in a numerically stable manner. At the end, Equation (4.19) is obtained.

$$\nabla \cdot \boldsymbol{U} = -\frac{D\rho}{Dt} = -\frac{1}{\rho}\frac{\partial \rho}{\partial Y_f}\frac{DY_f}{Dt} - \frac{1}{\rho}\frac{\partial \rho}{\partial p}\frac{Dp}{Dt} - \frac{1}{\rho}\frac{\partial \rho}{\partial T}\frac{DT}{Dt} \tag{4.18}$$

$$\nabla \cdot \left(\frac{\boldsymbol{H}}{A} \right) - \nabla \cdot \left(\frac{1}{A} \nabla p \right) = -\left(\frac{Y_f \Psi_l}{\rho_f} + \frac{1 - Y_f}{p} \right) \frac{Dp}{Dt} +$$
$$+ \frac{1 - Y_f}{T}\frac{DT}{Dt} - \left(\frac{1}{\rho_f} - \frac{1}{\rho_g} \right) \nabla^2 \left(D_{Y,coeff} Y \right) \tag{4.19}$$

However, the implementation of Trask et al. [13] did not guarantee consistency of the mass fraction equation with the definition of density, as found out by García-Oliver et al. [15]. To solve this issue, they created a small penalty function in the pressure projection step. The function relaxes the density calculated from the continuity equation toward the value stipulated by Equation (4.63), as shown by Equation (4.20) where the constant multiplier C_r represents the approximate number of time steps for relaxation to the correct density and Δt is the time-step. This approach successfully maintained consistency without iterative solutions of the continuity and mass transfer equations.

$$\nabla \cdot \left(\frac{\boldsymbol{H}}{A} \right) - \nabla \cdot \left(\frac{1}{A} \nabla p \right) = -\left(\frac{Y_f \Psi_f}{\rho_f} + \frac{1 - Y_f}{p} \right) \frac{Dp}{Dt} +$$
$$+ \frac{1 - Y_f}{T}\frac{DT}{Dt} - \left(\frac{1}{\rho_f} - \frac{1}{\rho_g} \right) \nabla^2 \left(D_{Y,coeff} Y \right) - \frac{\rho_{EOS} - \rho}{\Delta t C_r \rho} \tag{4.20}$$

In the present model, in order to avoid drawbacks of previous methods, the single-phase compressible pressure equation, Equation (4.21), is used. It is obtained as a combination of continuity and momentum equations [7], where the compressibility Ψ accounts for the effects of the turbulent mixing, Mach (compressibility) and thermal expansion.

$$\frac{\partial \left(\Psi p\right)}{\partial t} + \nabla \cdot \left(\frac{\boldsymbol{H}}{A}\right) - \nabla \cdot \left(\frac{1}{A}\nabla p\right) = 0 \tag{4.21}$$

Inter-facial surface density transport equation

The mean size of the liquid droplets, liquid parcels or ligaments, is calculated through the quantity Σ, the mean inter-facial area per unit volume. When the flow is composed by only droplets with identical diameters in a gas phase, knowledge of inter-facial surface density and liquid mass fraction allows computing the diameter of the droplets and droplet number density simply by Equations (4.22) and (4.23), correspondingly. When the droplets have different diameters but are all spherical, the previous formula gives the *SMD* (defined in Section §2.4.3).

$$D_{32} = SMD = \frac{6\rho Y_f}{\rho_f \Sigma} \tag{4.22}$$

$$n = \frac{\rho_f^2 \Sigma^3}{36\pi \rho^2 Y_f^2} \tag{4.23}$$

The most general method to include the inter-facial surface density in the multiphase, two-fluid in this case, formulation would be to introduce one more transport equation. From Equation (4.1), Equation (4.24) is obtained [10], where $D_{\Sigma,coeff}$ is an appropriate diffusion coefficient to consider that the interface is also dispersed by turbulence, $1/A$ and $1/a$ are two different production time scales and V_s is a destruction coefficient with the dimension of velocity, all of them to take into account the physical phenomena responsible for droplet expansions, collapses, coalescences, stretching, disintegration and inter-facial instabilities. Descriptions of $D_{\Sigma,coeff}$, A, a and V_s as well as other approaches are given in Section §4.4.1.

$$\frac{\partial \left(\rho\Sigma\right)}{\partial t} + \nabla \cdot \left(\rho\boldsymbol{U}\Sigma\right) - \nabla^2 \left(D_{\Sigma,coeff}\Sigma\right) = \left(A + a\right)\Sigma - V_s\Sigma^2 \tag{4.24}$$

In some cases the balance Equation (4.24) may be replaced by a simpler algebraic constitutive relation such as Equation (4.25), but this is not the case.

$$\Sigma = \Sigma\left(\boldsymbol{U}_{k,rel}, \rho_k, \mu_k, X_k, |\nabla X_k|, \sigma, g\right) \tag{4.25}$$

4.2.2 Code algorithm

The sequence and methodology (in other words, the algorithm) of solving previously described equations needs to be also decided. In this case, a PIMPLE approach is used. This algorithm combines the loop structures of Pressure Implicit with Splitting of Operators (PISO, developed by Issa [16, 17]) and Semi-Implicit Method for Pressure-Linked Equations (SIMPLE developed by Patankar and Spalding [18]), including $\partial/\partial t$ terms in equations, so it can run transient simulations, but it is not limited by Courant number, unlike PISO. Table 4.1 shows the advantages and disadvantages of PISO and SIMPLE algorithms, particularly construction of the momentum matrix. Combining both it is possible to take profit of the advantages and avoid some disadvantages. Although a higher Courant number (CFL) can be used and so higher time-step, the main drawback of PIMPLE algorithms is its high computational cost.

Algorithm	PISO	SIMPLE
Efficiency	Fast: [$\boldsymbol{U}$ Eqn] created once	Slower: under-relaxation
Stability	Typically unstable for CFL > 1	Stable for CFL > 1
Accuracy	Potential $\partial/\partial t$ error	-

Table 4.1: Advantages and disadvantages of PISO and SIMPLE algorithms.

PISO algorithm

Figure 4.1 shows the sequence of equations used in the PISO algorithm. The sketch represents the whole time step loop for incompressible problems. For compressible ones, the other equations (continuity, energy...) can be added after the pressure corrector [14], however, most of the solvers solve those equations just before assembling the momentum matrix [6].

The "trick" in PISO
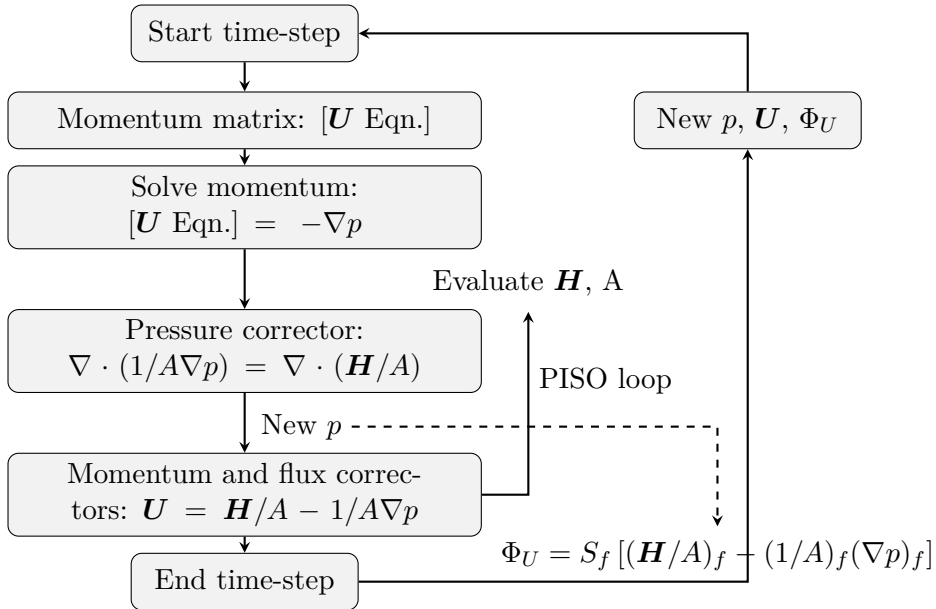
Figure 4.1: Sketch of the PISO algorithm for incompressible cases.

- Manipulation of [U Eqn]:

$$
\begin{bmatrix}
+ & & \circ & \\
& + & \circ & \circ \\
\circ & \circ & + & \\
& \circ & & +
\end{bmatrix} \cdot [U] = B
$$

$$
\begin{bmatrix}
+ & & & \\
& + & & \\
& & + & \\
& & & +
\end{bmatrix} \cdot [U] = B -
\begin{bmatrix}
& & \circ & \\
& & \circ & \circ \\
\circ & \circ & & \\
& & \circ &
\end{bmatrix} \cdot [U] \Rightarrow A\,[U] = H
$$

- A and H are evaluated in OpenFOAM by functions "UEqn.A()" and "UEqn.H()":

  - A contains 1 value per cell, it is a volumetric scalar field.
  - H is calculated using latest values of U, it is a volumetric vector field.

- Explicit momentum equation:

$$\frac{\partial \boldsymbol{U}}{\partial t} + \nabla \cdot (\boldsymbol{U}\boldsymbol{U}) - \nabla \cdot \nu \nabla \boldsymbol{U} \;=\; -\nabla p$$

$$[\boldsymbol{U}] \;=\; -\nabla p$$

$$A\boldsymbol{U} \;=\; -\nabla p + \boldsymbol{H}$$

- From the expression for momentum, a momentum corrector equation can be written:

$$\boldsymbol{U} = \frac{\boldsymbol{H}}{A} - \frac{1}{A}\nabla p$$

- Applying continuity ($\nabla \cdot \boldsymbol{U} = 0$) for an incompressible flow, a pressure corrector equation is derived:

$$\nabla \cdot \left(\frac{1}{A}\nabla p\right) = \nabla \cdot \left(\frac{\boldsymbol{H}}{A}\right)$$

- A flux corrector equation can be written (subindex f refers to a magnitude normal to cell faces):

$$\Phi_U = \boldsymbol{U_f} \cdot \boldsymbol{S_f} = \boldsymbol{S_f} \cdot \left[\left(\frac{\boldsymbol{H}}{A}\right)_f - \left(\frac{1}{A}\right)_f (\nabla p)_f\right]$$

Some comments on the algorithm

- $\boldsymbol{U}$ field temporally stores $\boldsymbol{H}/A$, rather than creating a new field.
- Similarly, Φ_U field temporally stores the flux of $\boldsymbol{H}/A$.
- Recovering $\boldsymbol{U}$ with the momentum corrector is simple, in OpenFOAM:

$$- = \mathrm{rUA} * \mathrm{fvc::grad(p)}$$

- A "flux()" function of OpenFOAM returns the flux field from the matrix.
- Loop over the pressure, momentum and flux correctors in OpenFOAM:

$$\mathrm{for\ (int\ corr=0;\ corr<nCorr;\ corr++)}$$

- Correct fluxes to conserve globally in badly-posed cases in OpenFOAM:

$$\mathrm{adjust(phi,U,p);}$$

- Loop over the pressure to correct non-orthogonality in OpenFOAM:

$$\mathrm{for\ (int\ nonOrth=0;\ nonOrth<=nNonOrthCorr;\ nonOrth++)}$$

SIMPLE algorithm

Figure 4.2 shows the sequence of equations used in the SIMPLE algorithm. The sketch represents again the whole time step loop for incompressible problems.
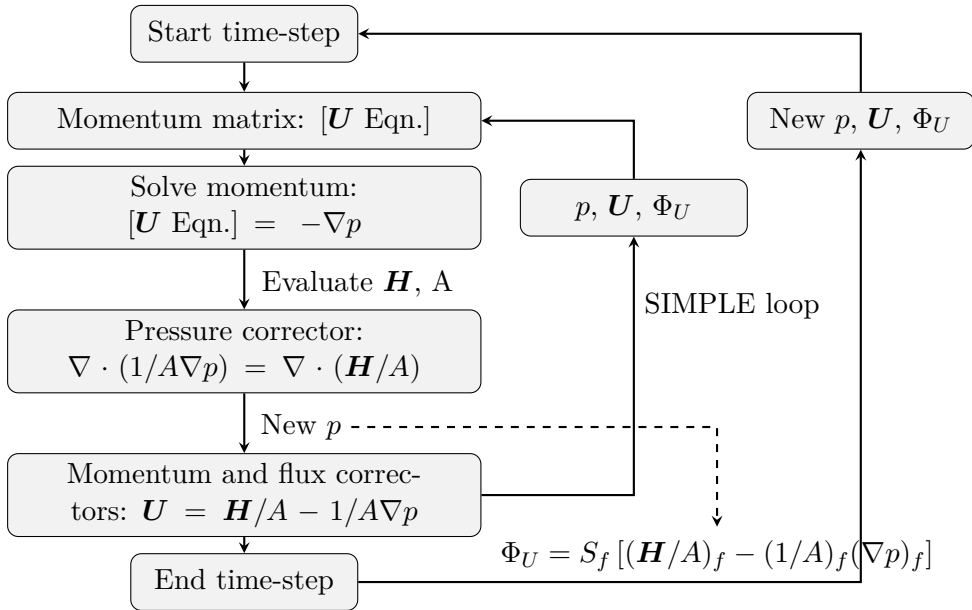
Figure 4.2: Sketch of the SIMPLE algorithm for incompressible cases.

Some comments on the algorithm

- SIMPLE is the algorithm generally used in steady-state solvers.
- Under-relaxation is performed using the "relax()" function of Open-FOAM:
    - An equation can be under-relaxed by increasing the diagonal and adding equivalent contribution to source based on existing values.

        UEqn().relax();

    - A field can be explicitly under-relaxed using values from the previous iteration.

        p.relax();

PIMPLE algorithm for the ESA model

Figure 4.3 shows the sequence of equations (previously described in detail in Section §4.2.1) used in the PIMPLE algorithm used by the ESA model. The sketch represents again the whole time step loop.

Figure 4.3: Sketch of the compressible PIMPLE algorithm used by the model.

All equations inside the outer/SIMPLE loop are solved as many times as required to reach convergence of each time-step, or until the maximum

number of outer iterations, fixed by the user, is reached. The liquid mass fraction transport equation is solved first. After it, fluxes are updated because the density has changed (see Section §4.3). The common sequence of solving continuity, momentum, energy and pressure equations, including the PISO loop, follows next. Then turbulence transport equations, which depend on the turbulence model selected, are solved. The last equation is the interfacial surface density transport equation, which is decoupled from the rest. Between time-steps, the density is computed from the equation of state to ensure consistency of the solution.

4.2.3   Numerical schemes

In this section, discretization schemes and linear solvers available in Open-FOAM ® are generally described. The ones used for simulations are written in corresponding case set-up sections. However, as the objective of this Thesis is to simulate Diesel sprays, a study of different numerical schemes is performed specifically for that. This study is presented in Section §6.3, where the best schemes are highlighted.

Discretization schemes

Numerical schemes for solving temporal, convection and diffusive terms of the transport equations presented in Section §4.2.1 have a major influence over convergence and accuracy of the simulation. Previous studies have shown that the same numerical scheme gives different convergence and accuracy with different geometries and boundary conditions [19], then the real domain has to be used; and this is very expensive in computational time. The set of terms for which numerical schemes must be specified in OpenFOAM are subdivided into the categories listed in Table 4.2. Some of the schemes listed in this Section are described in detail by Ferziger and Perić [7].

The interpolation schemes category contains terms that are interpolations of values typically from cell centers to face centers. A selection of interpolation schemes in OpenFOAM are listed in Table 4.3, being divided into four categories: one of general schemes and three of schemes used primarily in conjunction with Gaussian discretization of convection (divergence) terms in fluid flow. Note that additional schemes such as "UMIST" are available in OpenFOAM but only schemes which are generally recommended are listed in Table 4.3.

The convection-specific interpolation schemes calculate the interpolation based on the flux of the flow velocity. The specification of these schemes re-

Keyword	Category of mathematical terms
interpolationSchemes	Point-to-point interpolation of values
snGradSchemes	Component of gradient normal to a cell face
gradSchemes	Gradient ∇
divSchemes	Divergence $\nabla\cdot$
laplacianSchemes	Laplacian ∇^2
ddtScheme	First and second time derivatives $\partial/\partial t$, $\partial^2/\partial t^2$

Table 4.2: Categories for which numerical schemes are defined in OpenFOAM.

Centered schemes	
linear	Linear interpolation (central differencing)
cubic	Cubic scheme
midPoint	Linear interpolation with symmetric weighting
Upwinded convection schemes	
upwind	Upwind differencing
linearUpwind	Linear upwind differencing
skewLinear	Linear with skewness correction
filteredLinear2	Linear with filtering for high-frequency ringing
TVD schemes	
limitedLinear	Limited linear differencing
vanLeer	van Leer limiter
MUSCL	MUSCL limiter
limitedCubic	Cubic limiter
NV schemes	
SFCD	Self-filtered central differencing
Gamma	Gamma differencing

Table 4.3: Some interpolation schemes available in OpenFOAM.

quires the name of the flux field on which the interpolation is based; in most OpenFOAM applications this is Φ, the name commonly adopted for the surface scalar field mass/velocity flux. The three categories of convection-specific interpolation schemes are referred to as: general convection; normalized variable (NV); and total variation diminishing (TVD). Some TVD/NV schemes require a coefficient ψ, $0 \leq \psi \leq 1$, where $\psi = 1$ corresponds to TVD con-

formance, usually giving best convergence, and $\psi = 0$ corresponds to best accuracy. Running with $\psi = 1$ is generally recommended.

There are enhanced versions of some of the limited interpolation schemes for scalars that need to be strictly bounded. To bound between user-specified limits, the scheme name should be preceded by the word limited and followed by the lower and upper limits respectively. There are also specialized versions of these schemes for scalar fields that are commonly bounded between 0 and 1. These are selected by adding 01 to the name of the scheme. Strictly bounded versions are available for the following schemes: "limitedLinear", "vanLeer", "Gamma", "limitedCubic", "MUSCL" and "SuperBee". Improved versions of some of the limited schemes are currently available for vector fields in which the limiter is formulated to take into account the direction of the field. These schemes are selected by adding V to the name of the general scheme. "V" versions are available for the following schemes: "limitedLinearV", "vanLeerV", "GammaV", "limitedCubicV" and "SFCDV".

A surface normal gradient ("snGrad") is evaluated at a cell face; it is the component, normal to the face, of the gradient of values at the centers of the two cells that the face connects. A surface normal gradient may be specified in its own right and is also required to evaluate a Laplacian terms using Gaussian integration. The available schemes are listed in Table 4.4 and are specified by simply quoting the keyword and entry, with the exception of "limited" which requires a coefficient ψ, $0 \leq \psi \leq 1$ where $\psi = 0$ corresponds to "uncorrected", $\psi = 0.333$ to non-orthogonal correction lower than 0.5 times orthogonal part, $\psi = 0.5$ to non-orthogonal correction lower than orthogonal part, and $\psi = 1$ corresponds to "corrected".

Scheme	Description
corrected	Explicit non-orthogonal correction
uncorrected	No non-orthogonal correction
limited ψ	Limited non-orthogonal correction
bounded	Bounded correction for positive scalars
fourth	Fourth order

Table 4.4: Surface normal gradient schemes available in OpenFOAM.

The discretization scheme for the gradient of each term can be selected from those listed in Table 4.5. It is sufficient to specify the scheme completely. The Gauss keyword specifies the standard finite volume discretization

of Gaussian integration which requires the interpolation of values from cell centers to face centers. Therefore, the Gauss entry must be followed by the choice of interpolation scheme from Table 4.3. It would be extremely unusual to select anything other than general interpolation schemes and in most cases the linear scheme is an effective choice.

Discretization scheme	Description
Gauss <interpolationScheme>	Second order, Gaussian integration
leastSquares	Second order, least squares
fourth	Fourth order, least squares
cellLimited <gradScheme>	Cell limited version of one of the above
faceLimited <gradScheme>	Face limited version of one of the above

Table 4.5: Gradient discretization schemes available in OpenFOAM.

For the discretization of Laplacian terms in the form of $\nabla \cdot (D_{coeff} \nabla \boldsymbol{Q})$, the Gauss scheme is the only choice, and it requires a selection of both an interpolation scheme for the diffusion coefficient and a surface normal gradient scheme. The interpolation scheme is selected from Table 4.3, the typical choices being from the general schemes and, in most cases, linear. The surface normal gradient scheme is selected from Table 4.4; the choice of scheme determines numerical behavior as described in Table 4.6.

Scheme	Numerical behavior
corrected	Unbounded, second order, conservative
uncorrected	Bounded, first order, non-conservative
limited ψ	Blend of 'corrected' and 'uncorrected'
bounded	First order for bounded scalars
fourth	Unbounded, fourth order, conservative

Table 4.6: Behavior of surface normal schemes available in OpenFOAM selected for Laplacian terms discretization.

For the discretization of divergence terms in the form of $\nabla \cdot (\rho \boldsymbol{U} \boldsymbol{Q})$, the Gauss scheme is again the only choice, and it requires a selection of the interpolation scheme for the dependent field $\boldsymbol{Q}$. The interpolation scheme is selected from the full range of schemes in Table 4.3, both general and convection-specific. The choice critically determines numerical behavior as described in Table 4.7.

Scheme	Numerical behavior
linear	Second order, unbounded
skewLinear	Second order, (more) unbounded, skewness correction
cubic	Fourth order, unbounded
linearUpwind	First/second order, bounded
QUICK	First/second order, bounded
TVD schemes	First/second order, bounded
SFCDV	Second order, bounded
NV schemes	First/second order, bounded

Table 4.7: Behavior of interpolation schemes available in OpenFOAM selected for divergence terms discretization.

Finally, the discretization scheme for time derivative terms can be selected from those listed in Table 4.8. There is an off-centering coefficient Ψ with the Crank-Nicholson scheme that blends it with the Euler scheme. A coefficient of $\psi = 1$ corresponds to pure Crank-Nicholson and $\psi = 0$ corresponds to pure Euler. The blending coefficient can help to improve stability in cases where pure Crank-Nicholson is unstable. Only the Euler scheme is available for second time derivative terms.

Scheme	Description
Euler	First order, bounded, implicit
localEuler	Local-time step, first order, bounded, implicit
CrankNicholson ψ	Second order, bounded, implicit
backward	Second order, implicit
steadyState	Does not solve for time derivatives

Table 4.8: Time derivative discretization schemes available in OpenFOAM.

Linear solvers

It is necessary to specify each linear solver that is used for each discretized equation. It is emphasized that the term linear solver refers to the method of number-crunching to solve the set of linear equations, as opposed to application solver which describes the set of equations and algorithms to solve a particular problem (previously described in Sections §4.2.1 and §4.2.2).

The sparse matrix solvers are iterative, i.e. they are based on reducing the equation residual over a succession of solutions. The residual is ostensibly a measure of the error in the solution so that the smaller it is, the more accurate the solution. More precisely, the residual is evaluated by substituting the current solution into the equation and taking the magnitude of the difference between the left and right hand sides; it is also normalized to make it independent of the scale of the problem being analyzed.

Before solving an equation for a particular field, the initial residual is evaluated based on the current values of the field. After each solver iteration the residual is re-evaluated. The solver stops if either of the following conditions are reached:

- the residual falls below the solver tolerance;
- the ratio of current to initial residuals falls below the solver relative tolerance;
- the number of iterations exceeds a maximum number of iterations.

The solver tolerance should represent the level at which the residual is small enough that the solution can be deemed sufficiently accurate. The solver relative tolerance limits the relative improvement from initial to final solution. In transient simulations, it is usual to set the solver relative tolerance to 0 to force the solution to converge to the solver tolerance in each time step.

The linear solver of each transport equation can be selected from those listed on Table 4.9. Solvers distinguish between symmetric matrices and asymmetric matrices, i.e. PCG is used for symmetric matrices, and PBiCG for asymmetric ones. There are multiple options for preconditioning of matrices in the conjugate gradient solvers listed in Table 4.10.

Solver	Keyword
Preconditioned (bi-)conjugate gradient	PCG/PBiCG
Solver using a smoother	smoothSolver
Generalized geometric-algebraic multi-grid	GAMG
Diagonal solvers for explicit systems	diagonal

Table 4.9: Linear solvers available in OpenFOAM.

Most of the solvers are described in detail by Ferziger and Perić [7] but not GAMG. The generalized method of geometric-algebraic multi-grid uses the

principle of: generating a quick solution on a mesh with a small number of cells; mapping this solution onto a finer mesh; using it as an initial guess to obtain an accurate solution on the fine mesh. GAMG is faster than standard methods when the increase in speed by solving first on coarser meshes outweighs the additional costs of mesh refinement and mapping of field data. In practice, GAMG starts with the mesh specified by the user and coarsens/refines the mesh in stages.

Preconditioner	Keyword
Diagonal incomplete-Cholesky (symmetric)	DIC
Faster diagonal incomplete-Cholesky (DIC with caching)	FDIC
Diagonal incomplete-LU (asymmetric)	DILU
Diagonal	diagonal
No preconditioning	none

Table 4.10: Preconditioner options available in OpenFOAM.

Some solvers requires a smoother, selected from Table 4.11. Generally Gauss-Seidel is the most reliable option, but for bad matrices DIC can offer better convergence. In some cases, additional post-smoothing using Gauss-Seidel is further beneficial, i.e. the method denoted as "DICGaussSeidel".

Smoother	Keyword
Gauss-Seidel	GaussSeidel
Diagonal incomplete-Cholesky	DIC
Diagonal incomplete-Cholesky with Gauss-Seidel	DICGaussSeidel

Table 4.11: Smoother options available in OpenFOAM.

4.3   Flux updates-equations sequence

Available solvers update the mass (or volumetric) flux Φ (or Φ_U) through the cell faces twice: before (corrected flux) and after (conservative flux) solving the pressure equation, as shown in Figures 4.1 and 4.2. However, correcting the fluxes at different positions inside the equations sequence could improve the solver performance.

4.3.1 Flux updates description

The mass flux, a magnitude normal to cell faces (subindex f), is calculated as the inner product of the velocity times the density (Equations (4.26) and (4.27)). The approximation of Equation (4.26), although not true in general, is commonly found in compressible solvers because it is acceptable when fields are not strongly non-uniform (no-shocks).

$$\Phi = (\rho \boldsymbol{U})_f \approx \rho_f \boldsymbol{U}_f \qquad (4.26)$$

$$\Phi = \rho_f \Phi_U \qquad (4.27)$$

It is clear that, if the mesh and cell size are fixed, the flux changes with the density and/or the velocity. Thus, skipping the pressure equation where fluxes are already updated in a conservative way, fluxes can be updated in three different positions along the sequence of equations, as shown in Figure 4.4: (1) after mass fraction transport equation where the density changes because the amount of liquid inside cell changes or, if not, because the density has been updated in the previous time-step; (2) after continuity equation; and (3) after velocity equation. In the first two possibilities, Equation (4.27) can be used, where Φ_U is calculated inside the PISO loop at the previous time-step. But after the velocity equation the volumetric flux has also to be updated and then Equation (4.26) is used. Notwithstanding, updating fluxes using the velocity field does not enforce the mass conservation principle because conservation is not enforced on $\boldsymbol{U}$ exactly, but on Φ (the flux is the conservative variable, not the velocity). Thus, conservation errors could be introduced by this way.

Thus, it is necessary to study the effect of these three different updates and their possible combinations on the solution of the solver. Results and the final selection for the present model are given in the next sections. All possible combinations of three different variables (three updates) with two levels, "yes" if the update is activated and "no" if it is not, lead to $2^3 = 8$ cases of interest, as depicted in Table 4.12. Note that the first four cases include the non conservative update 3.

4.3.2 Case set-up

Instead of a Diesel spray problem, the converging-diverging verification (CDV) nozzle case described in Section §5.2.4 is used to perform the flux updates-equations sequence study. As the solution of this problem is exact, errors of the simulations are better analyzed and the code can be more easily improved
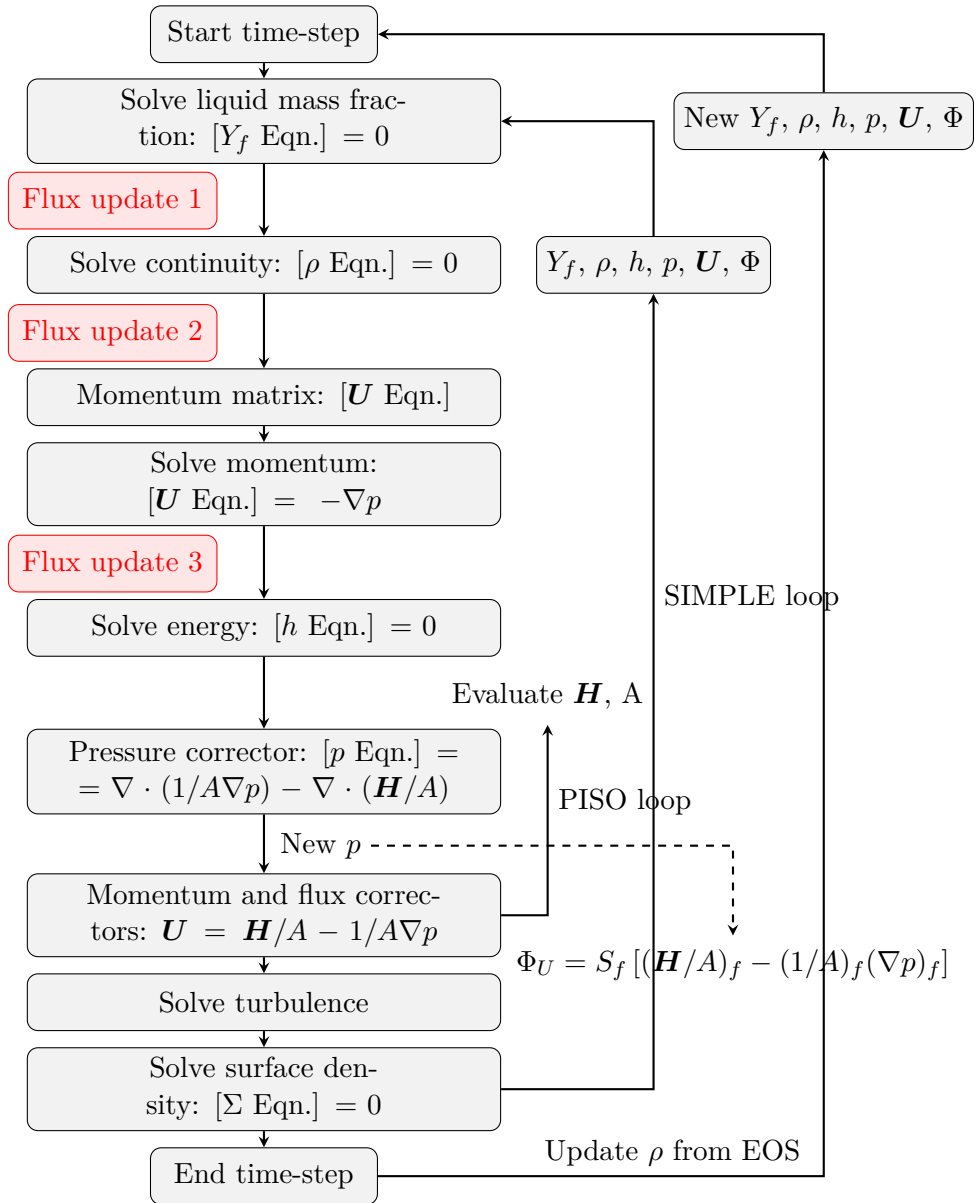
Figure 4.4: Flux updates-equations sequences possibilities for the ESA model.

Case	Update 1[a]	Update 2[b]	Update 3[c]
1	yes	yes	yes
2	no	yes	yes
3	yes	no	yes
4	no	no	yes
5	yes	yes	no
6	no	yes	no
7	yes	no	no
8	no	no	no

[a] Update after mass fraction equation.
[b] Update after continuity equation.
[c] Update after velocity or momentum equation.

Table 4.12: Test matrix for updated fluxes test.

than if experimental data is used as reference. Two fluids are employed: incompressible liquid (water) and compressible gas (air).

As the solver includes time derivative terms in the transport equations, a criterion to determine when the simulation reaches the steady state is needed. The criterion used in this Thesis is that the difference between two following time-steps is below 10^{-6} in all variables. The time-step which satisfies this criterion is called convergence time.

Simulations are carried out with a fixed time-step of $5 \ 10^{-5}$ s, which gives a maximum Courant-Friedrichs-Lewy (CFL) number of approximately 0.2 for incompressible calculations and 1 for compressible ones. The computational cost is usually measured with the physical runtime, which however depends on the computer characteristics and load. In order to skip this dependency, the average number of iterations of U_x variable per time-step is taken as measurement of the computational cost.

4.3.3   Results and conclusions

Incompressible flow problem

Table 4.13 shows the average error and the computational cost of each case of Table 4.12. Errors, convergence time and number of iterations per time-step are the same regardless the case, meaning that any flux updates affect neither the accuracy nor the computational cost for incompressible problems.

Case	Avg. Error [%]	Conv. time [µs]	Avg. U_x #Iters.
1	3.31	230	1.0
2	3.31	230	1.0
3	3.31	230	1.0
4	3.31	230	1.0
5	3.31	230	1.0
6	3.31	230	1.0
7	3.31	230	1.0
8	3.31	230	1.0

Table 4.13: Accuracy and computational cost results for the incompressible CDV problem of the flux updates-equations sequence study.

Figure 4.5 shows the evolution of velocity, pressure and temperature along the axis of the nozzle. The analytical solution is well represented by the 8 cases, the maximum error is placed at the throat. However, a difference of around 6 K between the first four and the other cases can be observed in Figure 4.5c because update 3 creates an artificial coupling between velocity and temperature fields.

Compressible flow problem

Table 4.14 summarizes accuracy and computational cost results, as before. First thing to notice is that updating fluxes with the velocity (non-conservative way) leads to divergence. This means that mass conservation must be ensured along the loop for applications with density gradients. For the other four cases, errors are quite similar regardless the case. Average error is around 6%, so there is a general agreement with the theoretical solution. Nonetheless, update 2 increases the number of iterations per time-step probably because the flux used in continuity equation is not the same than in the rest of transport equations, and then more SIMPLE loops (see Figure 4.4) are required to reach convergence. Update 1 decreases the convergence time with approximately the same number of iterations per time-step, then it reduces computational cost. This happens because the flux is recalculated with the updated density from the previous time-step, then reducing differences between time-steps.

Figure 4.6 shows the evolution of velocity, pressure and temperature along the axis of the nozzle. All 4 cases that converge predict well the analytical solution. Small differences which can be seen in the figures for both, incompressible and compressible problems, are due to two-dimensional effects in the

(a) Velocity distribution.

(b) Pressure distribution.

(c) Temperature distribution.
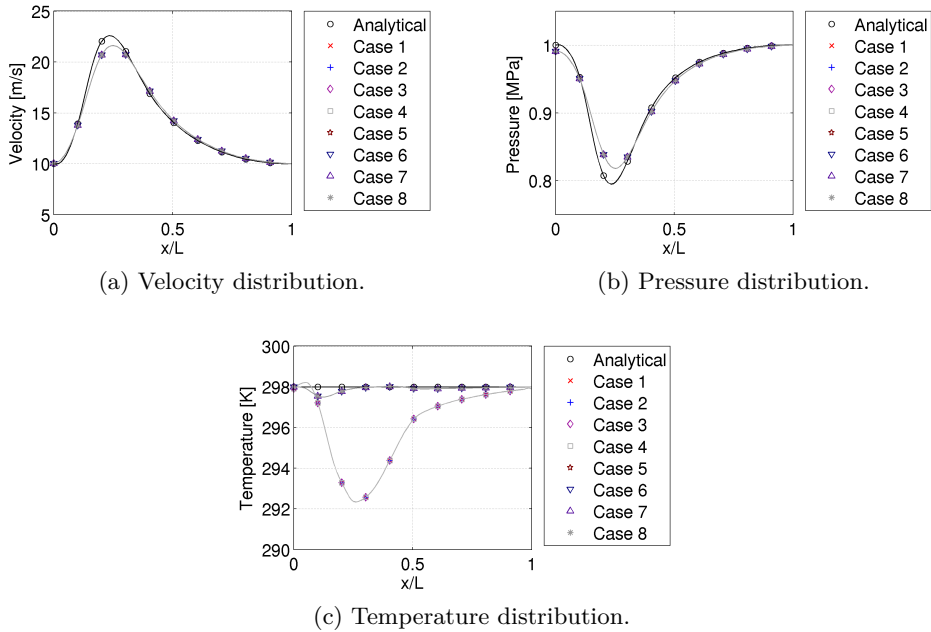
Figure 4.5: Variables axial distributions for the incompressible CDV problem of the flux updates-equations sequence study.

Case	Avg. Error [%]	Conv. time [µs]	Avg. U_x #Iters.
5	6.21	5480	3.6
6	6.14	5500	3.7
7	6.38	5470	3.0
8	6.27	5530	2.8

Table 4.14: Accuracy and computational cost results of the compressible CDV problem of the flux updates-equations sequence study.

simulations. A pressure gradient is obtained in the radial direction of the nozzle, meanwhile the analytical solution assumes that fluid properties and variables are constant in every section, in other words, assumes one-dimensional flow field in the axial direction.

(a) Velocity distribution.

(b) Pressure distribution.

(c) Temperature distribution.
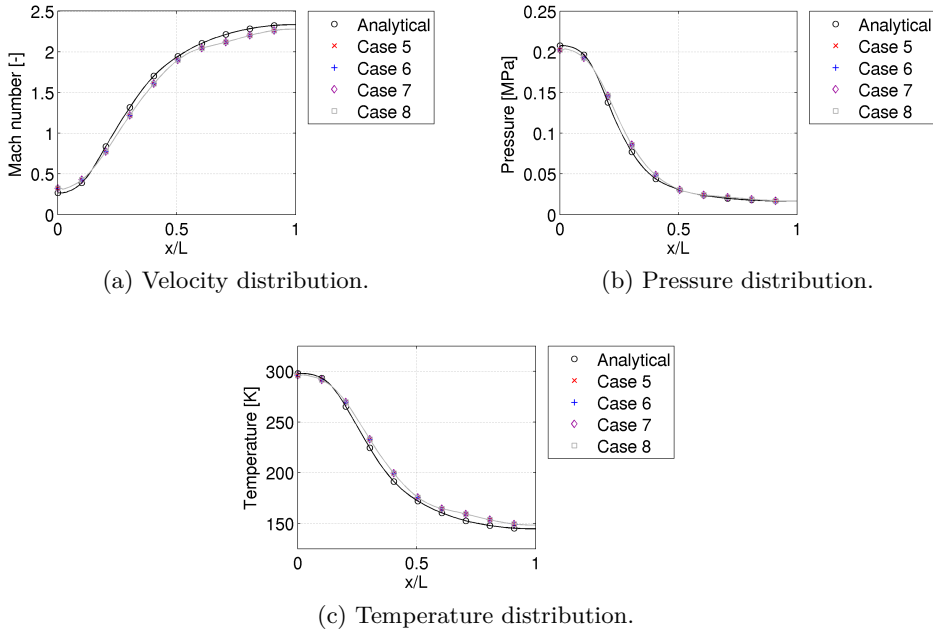
Figure 4.6: Variables axial distributions for the compressible CDV problem of the flux updates-equations sequence study.

Conclusions

Up to 8 updates-equations sequences have been calculated for incompressible and compressible problems. It is seen that updating fluxes in a non-conservative way leads to divergence when compressible fluids are used, so this option can only be used inside the PISO loop where the internal corrector loop ensures convergence and the flux is calculated at the end in a conservative way from the pressure corrector.

For incompressible solvers, none of the sequences changes the accuracy of the solution neither the computational cost, though the temperature drop is bigger with non-conservative updates. For the compressible problem the

accuracy is the same in all cases that converge, but sequences with no updates or only update 1 are slightly faster.

The final proposal for this model is updating the fluxes after the mass fraction equation (update 1, case 7) because of its slightly lower computational cost. Furthermore, this way ensures that mass fraction and density fields are consistent in every iteration of every time-step for multi-phase simulations.

4.4 Sub-models description

Two different approaches to the problem of closure can be taken, one which deliberate ignores what happens on the microlevel (continuum theory of mixtures), and one which calculates the different statistical contributions to the macro-level quantities. The particular choice to be made depends on:

- the applicability of each of them to the physical situation under consideration;

- the amount of information which is needed in practice as well as the required degree of precision;

- the number of closure equations which are necessary and, accordingly, the mathematical complexity of the resulting equations.

For practical purposes, both second and third conditions suggest the diffusion theory to be selected. Indeed, for obvious reasons, it is the diffusion theory equations, or rather simplified versions of them, which are favored most of the time. But, as indicated, its physical relevance should be discussed. As the matter of fact, it is known from the classical theory of fluid mixtures that the diffusion theory, although it applies to the great majority of cases and is very accurate, requires that the two fluids be in thermal equilibrium and that the diffusion velocities be sufficiently small for the kinetic energy of diffusion to be negligible [8].

Whether the average temperatures of the continuum phases may be assumed equal and their velocities to be close to another (in other words, if the hypothesis of the model are fulfilled) should be examined in each specific case. This depends on the width of the space-time windows, on the external actions imposed on the medium and on the intensity of the momentum and energy transfer between the two original phases on the microlevel, which, in particular, implies that the time-scales characterizing such interactions be small compared to the macro-level time-scaled associated with the phenomenon under

consideration. Vallet et al. [10] use Reynolds and Weber numbers to measure this. Such a condition is not likely to be satisfied when high-frequency instabilities exist or high-frequency waves are propagated. Local average thermal equilibrium is certainly achieved when the process undergone by two different substances is isothermal. Also, when the two phases of the same pure substance flow across a pipe, the preceding condition is probably satisfied with a good approximation, if the classical thermodynamic phase-equilibrium conditions hold on the microlevel (i.e. for modeling cavitation). On the other hand, such a theory is expected to break down when, for example, a hot fluid flows inside a cold, adiabatic atmosphere.

As pointed out by Bataille and Kesting [8], there is not a systematic method to provide general forms of closure equations valid for any type of multiphase flow, therefore foregoing several options presented in the literature are summarized.

4.4.1 Atomization and mixing

Mass fraction diffusion flux

According to Vallet et al. [10], by analogy with Fick's law of diffusion, Equation (4.28) [5] can be used, where the diffusion coefficient is defined through the turbulent Schmidt number of Equation (4.29) (option widely employed in the literature [15, 20–23]). Fick's law postulates that the flux goes from regions of high concentration to regions of low concentration with a magnitude that is proportional to the concentration gradient.

$$R_{Y_k} = Y_k \rho \boldsymbol{U}_{k,rel} = -D_{Y,coeff} \nabla Y_k \tag{4.28}$$

$$Sc_t = \frac{\mu_t}{D_{Y,coeff}} \tag{4.29}$$

A much more physical approach can be followed. Applying the general transport equation, Equation (4.1), on R_{Y_k} Equation (4.30) is obtained. This way, density variations effects (i.e. segregation that occurs between the heavy and the light phases because of the acceleration difference under a mean pressure gradient) are considered. However, the definition of source, production and destruction, terms is far more complicated and add three arbitrary constants to the model [10, 24]. If those production and destruction terms are supposed to be dominating, an algebraic expression for the turbulent flux can

be obtained from the former transport equation [10]. Physically, one can expect that those more complicated expressions may provide better accuracy in the presence of a strong mean pressure gradient such as would exist, e.g. in a pressure-assisted Diesel engine injector [11].

$$\frac{\partial \left(\rho R_{Y_k}\right)}{\partial t} + \nabla \cdot \left(\rho \boldsymbol{U} R_{Y_k}\right) - \nabla^2 \left(D_{R_{Y_k} coeff} R_{Y_k}\right) =$$
$$= -\rho \boldsymbol{\tau} \nabla Y_k - \rho R_{Y_k} \nabla \boldsymbol{U} + S_{R_{Y_k},p} - S_{R_{Y_k},d} \tag{4.30}$$

Given the relevance of the mass fraction diffusion flux, Demoulin et al. [25] first considered closure terms similar to the ones used by Vallet et al. [10], shown in Equations (4.31), (4.32) and (4.33) for a two phase flow: fuel and air. They did not obtain sufficiently good results.

$$D_{R_{Y_f} coeff} = -\frac{\mu_t}{Sc_{R_{Y_f}}} \nabla R_{Y_f}; \ \ Sc_{R_{Y_f}} = 0.9 \tag{4.31}$$

$$S_{R_{Y_f},p} = -C_1 \rho \frac{\epsilon}{k} R_{Y_f} + C_2 \rho R_{Y_f} \nabla \boldsymbol{U} +$$
$$+ C_3 \rho Y_f \left(1 - Y_f\right) \left(\frac{1}{\rho_f} - \frac{1}{\rho_g}\right) \nabla p + C_4 \rho Y_f \left(1 - Y_f\right) \left(\frac{1}{\rho_g} - \frac{1}{\rho_f}\right) \boldsymbol{g}$$
$$C_1 = 5, \ C_2 = 0.5, \ C_3 = 0.5, \ C_4 = \frac{1}{3} \tag{4.32}$$

$$S_{R_{Y_f},d} = \rho Y_f \left(1 - Y_f\right) \left(\frac{1}{\rho_f} - \frac{1}{\rho_g}\right) \nabla p \tag{4.33}$$

For flow with density stratification, gravity can act either as a destabilizing of a stabilizing force. This phenomenon was modeled by Lumley [26] and Launder [27] by adding a new contribution to the equation for the turbulent flux, already included in Equation (4.32). However, the gravity is usually not taken into account because of the large value of the Froude number.

The flow is also accelerated randomly by the fluctuating acceleration induced by turbulent motions. The turbulent acceleration can be chosen proportional to the turbulent kinetic energy divided by a characteristic length-scale. If the length-scale is chosen to be the inverse of the mean scalar gradient, the additional contribution on Equation (4.32) takes the form of Equation (4.34).

$$C_\rho Y_f \left(1 - Y_f\right) \frac{k^2}{\epsilon} \rho \left(\frac{1}{\rho_g} - \frac{1}{\rho_f}\right) \nabla Y_f; \ C_\rho = 1.8 \tag{4.34}$$

The mass fraction diffusion flux can be calculated through the algebraic expression of Equation (4.35) by assuming an equilibrium situation between the dissipation term, the classical (and usually dominant) production term of Equation (4.30) and this last additional term. The first term between brackets corresponds to the usual modeling of turbulent mass flux within a gradient law hypothesis and the second term is a correction term that only plays a role for high density ratio situations.

$$R_{Y_f} = -D_{Y,coeff}\nabla Y_f = -\left[\frac{\mu_t}{Sc_t} + C_\rho Y_f \left(1 - Y_f\right)\frac{k^2}{\epsilon}\rho^2\left(\frac{1}{\rho_g} - \frac{1}{\rho_f}\right)\right]\nabla Y_f$$

(4.35)

Demoulin et al. [25] were able to reproduce experimental results by employing Equation (4.35) for the liquid mass fraction diffusion flux. The physical interpretation of Equation (4.35) can be described as the acceleration fluctuations due to turbulence-induced Rayleigh-Taylor instabilities. Such instabilities are characterized by the production of liquid ligaments. The effect is important since fluctuations throw those liquid ligaments out, far away from the dense part of the liquid jet. Hence, they drastically increase the liquid turbulent mass transfer. Note that the effect is damped if scalar dissipation takes place. In this case, the high density gradients vanish as the molecular diffusion smooths the density profile.

Equation (4.35) is the one used in the present model due to its simplicity and capability of reproducing experimental results.

Inter-facial area density equation closure terms

There exist several ways of obtaining closure terms for inter-facial surface density transport equation (Equation (4.24)). Ishii and Hinbiki [5] even ensure that Equation (4.24) is too detailed to be employed in practice, and therefore they use a more macroscopic formulation by integrating over the volume to obtain a particle number density transport equation. Nonetheless, Vallet et al. [10] first developed and validated the required closure terms.

For a two-phase turbulent flow, the assumption of equilibrium of the convective forces and the viscous forces (Kolmogorov hypothesis for small scale features) leads to a definition of an equilibrium length-scale for the liquid droplets, say r_{eq}, in such way that the small scale Weber number, Equation (4.36), has a critical value about unity.

$$We_{cr} = \rho_g \frac{u_r r_{eq}}{\sigma} \approx 1$$

(4.36)

The estimation of the small scale velocity u_r depends on whether it belongs to the inertial range (Equation (4.37)) or to the viscous range of the velocity spectrum (Equation (4.38)).

$$r_{eq} = \left(\frac{\sigma}{\rho_g} \right)^{\frac{3}{5}} \frac{l_t^{\frac{2}{5}}}{k^{\frac{3}{5}}} \, We_{cr}^{\frac{3}{5}} \tag{4.37}$$

$$r_{eq} = \left(\frac{\sigma l_t \nu}{\rho_g k^{\frac{3}{2}}} \right)^{\frac{1}{3}} \, We_{cr}^{\frac{1}{3}} \tag{4.38}$$

The direct consideration of an equilibrium Weber number means that there is an equilibrium between break-up of too large droplets due to the difference of velocity with the surrounding gas, and the coalescence of too small ones, stirred by the turbulence at their own scale. Of course, this equilibrium radius is to be understood as a mean radius, because variations of droplet sizes are always present.

Another phenomenon that can be expected to occur is the break-up of the droplets because of collisions of two droplets stirred by the turbulence. In order to estimate the influence of this second effect, consider that after collision the minimum radius of droplets (equilibrium radius) produced is such that all the kinetic energy due to an initial velocity difference is transformed in surface energy. Equation (4.39) is then obtained. The constant C appears finally to be of order unity.

$$r_{eq} = C \frac{\sigma^{\frac{3}{5}} l_t^{\frac{2}{5}}}{k^{\frac{3}{5}}} \frac{(\rho Y_f)^{\frac{2}{15}}}{\rho_f^{\frac{11}{15}}} \tag{4.39}$$

It should be stressed, however, that this equilibrium may take a very long time to establish, for example, because of greater inertia of the heavier liquid phase. This means, for example, that it is unreasonable to assume that this equilibrium is established instantaneously just near the nozzle orifice exit, but there is a relaxation time for this equilibrium to be reached. It is necessary now to make precise the modeling of A, a, V_s and the diffusion coefficient $D_{\Sigma,coeff}$ of Equation (4.24).

The physical phenomenon linked with A is considered to be the stretching of the interface by the mean velocity gradients. A^{-1} is considered as a single characteristic time-scale related to this stretching. There are several possibilities for building such a time-scale, the simplest one uses the curl of the mean

velocity vector. It is more common, however, to use the same time-scale as in the production term for turbulent kinetic energy (see Section §4.4.4), in other words, to use Equation (4.40), where α_0 is a modeling constant with a default value of $\alpha_0 = 1$.

$$A = \alpha_0 C_\mu \frac{k}{\epsilon} \nabla \boldsymbol{U} \cdot \nabla \boldsymbol{U} \qquad (4.40)$$

The turbulent flow field, even in the case of homogeneous and isotropic turbulence, is also expected to stretch the interface, and this is taken into account through the time-scale a^{-1}. Here, again, there are several possibilities. The simplest one is to consider the integral characteristic time-scale of turbulence itself, leading to Equation (4.42) with a proportionality constant α_1 of order unity. The collision of droplets that has been shown important for breaking the droplets has its own characteristic time, leading to Equation (4.42) which takes implicitly into account the liquid content because the density ratio depends on it.

$$a \;=\; \alpha_1 \frac{\epsilon}{k} \qquad (4.41)$$

$$a_{col} \;=\; \frac{\alpha_1}{(36\pi)^{\frac{2}{9}}} \left(l_t \Sigma\right)^{\frac{2}{3}} \left(\frac{\rho_f}{\rho}\right)^{\frac{4}{9}} \frac{\epsilon}{k} Y^{-\frac{4}{9}} \qquad (4.42)$$

Equation (4.24) has to satisfy the assumption of equilibrium. This implies an equilibrium value for Σ given by Equation (4.43). Combining this last equation with Equation (4.22), Equation (4.44) is obtained, with a given by Equation (4.42) and r_{eq} given by Equation (4.39).

$$a\Sigma_{eq} = V_s \Sigma_{eq}^2 \qquad (4.43)$$

$$V_s = \frac{a\rho_f r_{eq}}{3\rho Y} \qquad (4.44)$$

Concerning the diffusion coefficient $D_{\Sigma,coeff}$, the simplest way is to use the classical assumption and, by analogy with Fick's law, to use Equation (4.45), where the value of Schmidt number Sc_Σ has a value very similar to that of Equation (4.31) in the main part of the atomization region (in most cases the exact same value is taken [28]). This approach is valid if there is no mean slip velocity between the liquid and the gas, but if a phase velocity difference still

exists. This can be also the case in the very dense part of the spray, where the amount of liquid is so important that motion of gas fluid particles is controlled by the liquid motion. If there is any reason to assume that the slip velocity between phases may be important, this model would have to be improved.

$$D_{\Sigma,coeff} = \frac{\mu_t}{Sc_{\Sigma}} \qquad (4.45)$$

This original approach is the one used in the present model. However and as commented by Vallet et al. [10], there are several alternative ways of obtaining closure terms of Equation (4.24). For example, Beheshti et al. [11] use Equation (4.46) where again Σ_{eq} is given by Equation (4.22) and τ_c is the characteristic time of surface production. This characteristic time-scale is a weighted sum of rates determined by the bulk turbulence and the droplet collision, that is Equation (4.47), where C_t and C_{col} are constants and τ_{col} is the inverse of the droplet collision frequency, estimated by Equation (4.48).

$$\frac{\partial (\rho\Sigma)}{\partial t} + \nabla \cdot (\rho \boldsymbol{U}\Sigma) - \nabla^2 (D_{\Sigma,coeff}\Sigma) = \frac{\rho\Sigma}{\tau_c} \left[1 - \frac{\Sigma}{\Sigma_{eq}} \right] \qquad (4.46)$$

$$\frac{1}{\tau_c} = C_t \frac{\epsilon}{k} + C_{col} \frac{1}{\tau_{col}} \qquad (4.47)$$

$$\tau_{col} = \frac{X^{\frac{4}{9}}}{\epsilon^{\frac{1}{3}} (\rho\Sigma)^{\frac{2}{3}}} \qquad (4.48)$$

Lebas et al. [28] also use a different approach to solve the inter-facial surface density, shown in Equation (4.49). A repartition function F is introduced to take into account the two different mechanisms of generating/destructing inter-facial surface: a first one for the dense part of the spray where no droplets can be defined (primary break-up) and a second one far away from the injector where droplets are already formed (secondary break-up). F is chosen in order to return a value of 1 in the dense region ($X_f > 0.5$) and a value of 0 in the dilute region ($X_f < 0.1$). The transition between these two cases is made via a linear regression.

$$\frac{\partial (\rho\Sigma)}{\partial t} + \nabla \cdot (\rho \boldsymbol{U}\Sigma) - \nabla^2 (D_{\Sigma,coeff}\Sigma) =$$
$$= F (S_{init} + S_{turb}) + (1 - F) (S_{col} + S_{2b}) + S_{vap} \qquad (4.49)$$

S_{init}, given by Equation (4.50), can be considered as an initialization term, taking high values near the injector nozzle and becoming negligible by comparison with the other source terms once initial surface density is created. This term is derived to obtain surface density greater than a minimum value defined by Equation (4.51), which represents the probability to have both liquid and gas divided by a characteristic scale. First wrinkles of the surface are supposed to have a characteristic size equal to the integral turbulent length-scale.

$$S_{init} = \frac{12\rho\mu_t}{\rho_f\rho_g Sc_t l_t}\nabla Y \cdot \nabla Y \qquad (4.50)$$

$$\Sigma_{min} = \frac{X_f\left(1 - X_l\right)}{l_t} \qquad (4.51)$$

S_{turb} corresponds to the production/destruction of interface density due to the turbulent flow stretching and the effects of collision and coalescence in the dense part of the spray. It is exactly the right hand side of Equation (4.46), but in this case τ_c is the turbulent time-scale and the equilibrium value of Σ is given by Equation (4.52).

$$\Sigma_{eq} = \frac{\rho X_f k}{\sigma\, We_{dense}};\ \ We_{dense} = 1 \qquad (4.52)$$

Duret et al. [29] use DNS to improve the predictability of this turbulent source term. They redefine the equilibrium Weber number as Equation (4.53) and add a proportionality constant to the source term of $C = 0.4$.

$$We_{eq} = 4\frac{0.5\left(\rho_f - \rho_g\right)X_f\left(1 - X_f\right)k}{\sigma\Sigma_{eq}} \qquad (4.53)$$

The collision-coalescence source term for the dilute part of the spray S_{col} is again identical to the right hand side of Equation (4.46). The collision time-scale in this case is estimated by Equation (4.54) and the equilibrium surface density calculated from Equations (4.55)-(4.57).

$$\tau_{col} = \frac{1}{\Sigma\sqrt{\frac{2}{3}k}} \qquad (4.54)$$

$$We_{col} = \frac{4Y_f\rho k}{\sigma\Sigma} \qquad (4.55)$$

$$D_{32,eq} = D_{32}\frac{1 + \frac{We_{col}^N}{6}}{1 + \frac{We_{col}}{6}}; \ \ We_{col}^N = 12 \tag{4.56}$$

$$We_{col,eq} = \frac{\rho_f\frac{2}{3}kD_{32,eq}}{\sigma} \tag{4.57}$$

The source term S_{2b} deals with the production of liquid-gas interface surface density due to effects of secondary break-up in the dilute region. This source term comes from the model first proposed by Pilch and Erdman [30] and is given in Equation (4.58). Only positive values of this source terms are taken into account because the break-up process increases the surface density.

$$S_{2b} = \max\left[\frac{\Sigma}{\tau_{2b}}\left(1 - \frac{\rho\Sigma}{\Sigma_{eq}}\right), 0\right] \tag{4.58}$$

The estimation of the break-up time-scale is given in Equation (4.59), where the parameter T is given as a function of the Weber number of Equation (4.60) [30] and the relative velocity between phases can be calculated from Equation (4.28). The equilibrium value of surface density in this case is obtained from Equation (4.60) considering that the equilibrium Weber number is $We_{2b,eq} = 12$ for small Ohnesorge numbers.

$$\tau_{2b} = T\frac{D_{32}}{u_{rel}}\sqrt{\frac{\rho_f}{\rho_g}} \tag{4.59}$$

$$We_{2b} = \frac{6\rho_g u_{rel}Y_f\rho}{\rho_f\sigma\Sigma} \tag{4.60}$$

The last source term, S_{vap} represents the production/destruction of surface density by vaporization. A simple model, Equation (4.61), is used in which the reduction of surface density depends on the mass evaporation rate. Though, it should not be valid in the dense zone of the spray and it is not sure that the vaporization term decreases surface density. As the present model does not consider evaporation, this term could be neglected.

$$S_{vap} = -\frac{2\Sigma^2}{3\rho Y_f}\frac{\dot{m}_{vap}}{\pi D_{32}^2} \tag{4.61}$$

4.4.2 Mixture transport/thermal properties

Equation of state

The density of a mixture is calculated by Equation (4.62) [5]. For a two-phase flow, fuel and gas, it can be easily transformed into Equation (4.63) [10].

$$\rho = \sum_{k=1}^{n} X_k \rho_k \tag{4.62}$$

$$\rho = \frac{1}{\frac{Y_f}{\rho_f} + \frac{1-Y_f}{\rho_g}} \tag{4.63}$$

Gas phase is considered as an ideal gas, so its density is calculated from Equation (4.64). Liquid phase (fuel) can be considered compressible with density depending on both pressure and temperature. As there is no common equation of state for liquids, a polynomial fit to experimental data is taken, following the procedure developed by Payri et al. [31]. Hence, general Equation (4.65) is used, with reference values of $p_{ref} = 0.1\,\mathrm{MPa}$ and $T_{ref} = 298\,\mathrm{K}$; and its respective coefficients for several fuels are shown in Table 4.15.

$$\rho_g = \frac{p}{RT} \tag{4.64}$$

$$\rho_f = C_1 + C_2 \left(T - T_{ref}\right) + C_3 \left(p - p_{ref}\right) + C_4 \left(p - p_{ref}\right)^2 +$$
$$+ C_5 \left(T - T_{ref}\right)^2 + C_6 \left(p - p_{ref}\right)\left(T - T_{ref}\right) \tag{4.65}$$

Compressibility and speed of sound

Together with the density, the compressibility of the mixture needs to be defined. Some authors, i.e. Dumont et al. [34], have studied both experimentally and computationally the compressibility of a mixture and they use a definition such Equation (4.66), based on the isothermal acoustic speed of the two-phase flow formulated by Wallis [35].

$$\Psi = \frac{1}{a^2} = \rho \left[\frac{X_f}{\rho_f a_f^2} + \frac{1 - X_f}{\rho_g a_g^2} \right] \tag{4.66}$$

The isothermal sound speed in the homogeneous mixture decreases dramatically as soon as the fluid is not composed of a single phase, as it is shown

	C_1	C_2	$C_3(10^6)$
Diesel Elite$^+$ [31]	835.70	-0.6280	0.4914
Winter Diesel [31]	821.47	-0.5615	0.4951
Rape Methyl Ester [31]	874.58	-0.6991	0.4790
n-Dodecane [32]	744.83	-0.7079	0.7324
n-Hexadecane [33]	771.51	-07406	0.6880
	$C_4(10^{15})$	$C_5(10^3)$	$C_6(10^9)$
Diesel Elite$^+$ [31]	-0.705	0.7374	1.036
Winter Diesel [31]	-0.728	0.1839	1.035
Rape Methyl Ester [31]	-0.364	0.9704	0.919
n-Dodecane [32]	-2.074	0.1078	2.227
n-Hexadecane [33]	-2.069	0.4573	2.171

Table 4.15: Density polynomial coefficients for Equation (4.65) of several fuels.

later in Figure 4.7. This can be explained by the multiple reflexions of the waves between mixture components interfaces. As the matter of fact, it can be almost considered that the flow becomes locally supersonic as soon as mixing begins [34]. This effect leads to numerical instabilities and early divergence of the solution. For that reason, physical definition of Equation (4.66) cannot be used for the present model.

Therefore, a linear compressibility model is taken, generally given by Equation (4.67). For a two-phase flow, fuel and gas, it can be easily transformed into Equation (4.68). This model is widely employed in computational multiphase solvers.

$$\Psi = \frac{\partial \rho}{\partial p} = \sum_{k=1}^{n} X_k \Psi_k \tag{4.67}$$

$$\Psi = \frac{\partial \rho}{\partial p} = Y_f \frac{\rho}{\rho_f} \Psi_f + \left(1 - Y_f \frac{\rho}{\rho_f}\right) \Psi_g \tag{4.68}$$

Gas compressibility, Equation (4.69), is easy to obtain from Equation (4.64). For the liquid phase (fuel) compressibility there is not, again, a common definition, so Equation (4.70) in terms of speed of sound is used.

$$\Psi_g = \frac{1}{RT} \tag{4.69}$$

$$\Psi_f = \frac{1}{a_f^2} \qquad (4.70)$$

For the liquid speed of sound, a polynomial fit to experimental data is taken, following the procedure developed by Payri et al. [31]. Hence, general Equation (4.71) is used, with reference values of $p_{ref} = 0.1\,\text{MPa}$ and $T_{ref} = 298\,\text{K}$; and its respective coefficients for several fuels are shown in Table 4.16.

$$a_f = C_1 + C_2\,(T - T_{ref}) + C_3\,(p - p_{ref}) +$$
$$+ C_4\,(p - p_{ref})^2 + C_5\,(p - p_{ref})\,(T - T_{ref}) \qquad (4.71)$$

	C_1	C_2	$C_3(10^6)$
Diesel Elite$^+$ [31]	1363.05	-3.1135	4.1751
Winter Diesel [31]	1355.84	-3.3272	4.3013
Rape Methyl Ester [31]	1385.70	-3.0688	3.8373
n-Dodecane [32]	1268.01	-3.2284	5.8711
n-Hexadecane [33]	1316.90	-3.0012	5.5249
	$C_4(10^{15})$	$C_5(10^9)$	
Diesel Elite$^+$ [31]	-6.9676	9.4014	
Winter Diesel [31]	-7.1465	11.743	
Rape Methyl Ester [31]	-6.5078	11.634	
n-Dodecane [32]	-14.704	10.047	
n-Hexadecane [33]	-13.905	9.521	

Table 4.16: Speed of sound polynomial coefficients for Equation (4.71) of several fuels.

Figure 4.7 shows the differences between the isothermal definition of compressibility (Equation (4.66)) and the linear model (Equation (4.68)). Numerical values are taken at reference conditions $p_{ref} = 0.1\,\text{MPa}$ and $T_{ref} = 298\,\text{K}$ for Diesel Elite$^+$. It is proved that both definitions are not similar at all. Thus, this topic is an interesting future work to improve the quality and the accuracy of simulations.

Momentum diffusion coefficient

As stated by the Newton's law of viscosity, the diffusion coefficient of momentum is the viscosity [36, 37]. In the case of turbulent flows, the effective

(a) Depending on mass fraction.

(b) Depending on volume fraction.
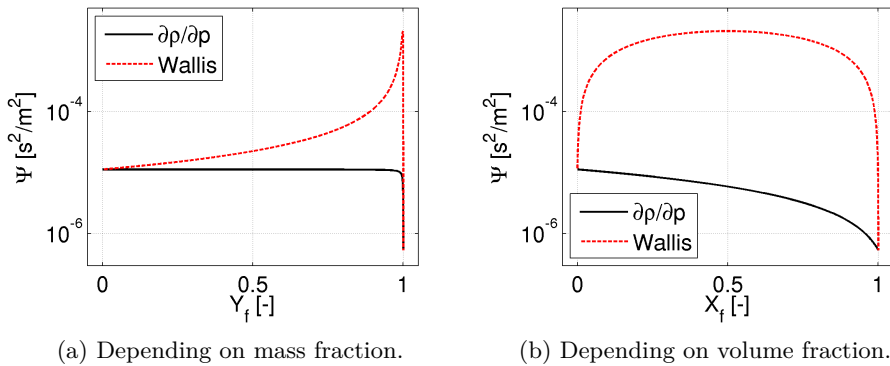
Figure 4.7: Comparison of both definitions of mixture compressibility.

viscosity of Equation (4.72) is used [7]. See Section §4.4.4 for the definition of the turbulent viscosity. It is expected that the mixture viscosity is a function of concentration and viscosity of phases, given by Equation (4.73) [5].

$$D_{U,coeff} = \mu_{eff} = \mu + \mu_t \tag{4.72}$$

$$\mu = \sum_{k=1}^{n} X_k \mu_k \tag{4.73}$$

Thermal energy diffusion coefficient

As stated by the Fourier's law of thermal conduction, the thermal flux is proportional to the material's thermal conductivity. The conductivity of a fluid can be defined and related to the diffusivity by the Prandtl number, defined in Equation (4.74). In the case of turbulent flows, the effective diffusivity of Equation (4.75) is used. It is expected that the mixture conductivity is a function of concentration and conductivity of phases, given by Equation (4.76).

$$Pr = \frac{\mu}{D_{h,coeff}} \tag{4.74}$$

$$D_{h,coeff} = \kappa + \kappa_t = \kappa + \frac{\mu_t}{Pr_t} \tag{4.75}$$

$$\kappa = \sum_{k=1}^{n} X_k \kappa_k = \sum_{k=1}^{n} X_k \frac{\mu_k}{Pr_k} \tag{4.76}$$

4.4.3   Temperature calculation

It is expected to obtain the temperature field from the energy equation, in this case conservation of the specific enthalpy of Equation (4.13). The specific enthalpy is a defined thermodynamic potential that consists of the specific internal energy of the system e plus the product of pressure and specific volume (inverse of density) of the system (see Equation (4.77)), which are all function of the state of the thermodynamic system.

$$h = e + \frac{p}{\rho} \tag{4.77}$$

The enthalpy is an extensive property. This means that, for homogeneous systems, it is proportional to the size of the system. For multiphase or inhomogeneous systems the enthalpy is the sum of enthalpies of the composing phases, as shown in Equation (4.78).

$$h = \sum_{k=1}^{n} Y_k h_k \tag{4.78}$$

As any other thermodynamic potential, enthalpy can be expressed as a characteristic function of any other independent thermodynamic properties. Equation (4.79) shows it as function of temperature and pressure, where c_p is the specific heat capacity at constant pressure and α is the coefficient of thermal expansion. Both of them are function of pressure and temperature.

$$dh = c_p dT + (1 - \alpha T) \frac{dp}{\rho} \tag{4.79}$$

Notice that for an ideal gas, $\alpha T = 1$, and for perfect gas the heat capacity is constant [38]. Therefore, for gas phases the relationship between enthalpy and temperature, given in Equation (4.80), is straightforward.

$$dh_g = c_{p,g} dT \tag{4.80}$$

For a two-phase flow, fuel and gas, Equation (4.78) can be easily transformed into Equation (4.81). The specific enthalpy of the liquid h_f is the only

unknown of that equation, though it can be computed from Equation (4.79) if c_p, α and ρ are known as function of pressure and temperature.

$$dh = Y_f dh_f + (1 - Y_f)\, c_{p,g} dT \tag{4.81}$$

The dependency of density on pressure and temperature has been already discussed in previous Section §4.4.2. The same methodology could be applied for the specific heat capacity at constant pressure and thermal expansion coefficient.

Liquid heat capacity and thermal expansion

A polynomial fit to experimental data is taken. For the specific heat capacity at constant pressure, general Equation (4.82) is used, with reference values of $p_{ref} = 0.1\,\text{MPa}$ and $T_{ref} = 298\,\text{K}$; and its respective coefficients for several fuels are shown in Table 4.17.

$$
\begin{aligned}
c_{p,f} = {} & C_1 + C_2\,(T - T_{ref}) + C_3\,(T - T_{ref})^2 + C_4\,(p - p_{ref}) + \\
& + C_5\,(p - p_{ref})^2 + C_6\,(T - T_{ref})\,(p - p_{ref})
\end{aligned} \tag{4.82}
$$

	C_1	C_2	$C_3(10^3)$
n-Hexane [39]	2268.1934	4.6103	1.1466
n-Heptane [39]	2252.18	4.1887	1.2484
n-Dodecane [39]	2201.55	3.0076	0.9598
n-Hexadecane [33]	2221.8	2.5356	3.8670
	$C_4(10^6)$	$C_5(10^{15})$	$C_6(10^9)$
n-Hexane [39]	-3.7734	33.7896	-15.1809
n-Heptane [39]	-2.7297	24.7024	-11.4765
n-Dodecane [39]	0.6977	5.3590	-4.4538
n-Hexadecane [33]	-0.6804	4.0012	-2.1190

Table 4.17: Specific heat capacity polynomial coefficients for Equation (4.82) of several fuels.

There is not direct measurement of the thermal expansion coefficient in the literature for any fluid. However, the rate of change of temperature with respect to pressure in a Joule-Thomson process (that is, at constant enthalpy)

is the Joule-Thomson (Kelvin) coefficient μ_{JT}; which can be measured and expressed in terms of known variables as shown in Equation (4.83) [38].

$$\mu_{JT} = \frac{1}{\rho c_p} \left(\alpha T - 1 \right) \tag{4.83}$$

Nonetheless, measurement of Joule-Thomson (Kelvin) coefficient is not necessary because, if the density as function of pressure and temperature is known, the thermal expansion coefficient can be calculated though its definition of Equation (4.84).

$$\alpha_f = \rho_f \frac{\partial \left(\frac{1}{\rho_f} \right)}{\partial T} \tag{4.84}$$

Combination of Equations (4.79), (4.82) and (4.84) gives the enthalpy of the liquid h_f, the only unknown of Equation (4.81). The temperature can be obtained as a function of specific enthalpy and pressure from that equation. However, this procedure is complicated and requires a numerical solution for the Equation (4.81). This adds unnecessary computational cost to the model. A simpler methodology is employed.

Mixture temperature

From the literature, i.e. NIST database [39], the specific enthalpy of the liquid as direct function of pressure and temperature can be obtained. Again, a polynomial fit to the experimental data such Equation (4.85) is taken, with reference values of $p_{ref} = 0.1\,\mathrm{MPa}$ and $T_{ref} = 298\,\mathrm{K}$. Its respective coefficients for several fuels are shown in Table 4.18.

$$\begin{aligned} h_f = C_1 + C_2 \left(T - T_{ref} \right) + C_3 \left(T - T_{ref} \right)^2 + C_4 \left(p - p_{ref} \right) + \\ + C_5 \left(p - p_{ref} \right)^2 + C_6 \left(T - T_{ref} \right) \left(p - p_{ref} \right) \end{aligned} \tag{4.85}$$

As thermal equilibrium (same temperature for both phases) is assumed, the temperature can be easily calculated from Equations (4.81) and (4.85).

4.4.4 Turbulence modeling

Most fluid flows occurring in the industry are turbulent, including Diesel sprays. Turbulence can be described as a three-dimensional and time dependent state of continuous instability in the flow, where it is still possible to

	C_1	C_2	C_3
n-Hexane [39]	0	2274.52	2.0136
n-Heptane [39]	0	2257.37	1.9244
n-Dodecane [39]	0	2206.46	1.8352
	$C_4(10^4)$	$C_5(10^{12})$	$C_6(10^6)$
n-Hexane [39]	7.7976	2.5732	-1.6148
n-Heptane [39]	8.4011	1.9670	-1.2403
n-Dodecane [39]	9.3984	0.6401	-0.5107

Table 4.18: Specific enthalpy polynomial coefficients for Equation (4.85) of several fuels.

separate the fluctuations from the mean flow properties. It is characterized by irregularity in the flow, increased diffusivity and energy dissipation. The range of scales in such flows is very large, from the smallest turbulent eddies characterized by Kolmogorov micro-scales, to the flow features comparable with the size of the geometry.

There are several possible approaches for the simulation of turbulent flows. In general, they can be classified in terms of degree of modeling (from largest to lowest):

1. Direct Numerical Simulation (DNS) numerically integrates the governing equations over the whole range of turbulent scales. The requirements on mesh resolution and time-step size put very high demands on the computer resources, rendering it unsuitable for engineering applications (high Reynolds numbers) nowadays.

2. Large Eddy Simulation (LES) uses a spatial filter in order to separate different length-scales in a turbulent flow field. Large scale structures that can be resolved by the numerical method on a given mesh are called the super-grid scales. The influence of all behind (sub-grid) scales to the super-grid behavior is modeled. The rationale behind this principle lies in the fact that the small scales of turbulence are more homogeneous and isotropic and therefore easier to model. As the mesh gets finer, the number of scales that require modeling becomes smaller, thus approaching the DNS.

3. Reynolds-Averaged Navier-Stokes (RANS) uses an averaging procedure (see Section §4.2.1) to separate all scales fluctuations from the mean

flow, which is resolved. The effect of the fluctuations in the mean flow is then modeled. It is the approach selected for this Thesis mainly due to its lowest computational cost.

RANS models can be also classified in three categories: linear eddy viscosity models, nonlinear eddy viscosity models, and Reynolds stress models. Discussions about which one is the best in every case can be easily found in the literature. The employed transport model (see Section §4.2.1) requires an eddy viscosity model, and a linear constitutive relationship between the Reynolds stresses and the mean flow straining field is taken with the aim of simplifying the model. This linear relationship is also known as Boussinesq hypothesis.

At the same time, linear eddy viscosity models are classified according to the number of equations: algebraic equations or zero-equation models, where eddy viscosity is calculated directly from the flow variables; one equation models, which usually solve the turbulent kinetic energy; two equation models, which include two extra transport equations to represent the turbulent properties of the flow such turbulent kinetic energy and turbulent dissipation or specific dissipation; etc. Two equation turbulence models are one of the most common type of turbulence models. Models like $k - \epsilon$ and $k - \omega$ models have become industry standard models and are commonly used for most types of engineering problems.

The physics of turbulence in the vicinity of impermeable non-slip walls is considerably different from the other parts of the flow [37]. It is therefore necessary to use appropriate turbulence models in the near-wall region. For most general and detailed treatment, low-Re versions should be used. However, in order to resolve the near-wall details well, the computational mesh needs to be very fine in this region. It is possible to compensate for the existence of the wall without resolving the near-wall region, albeit at he expense of considerable approximation with adverse effects on numerical resolution [14]. Wall-functions represent a simplified model of turbulence, which mimics the near-wall behavior of the velocity, turbulent kinetic energy k and turbulent dissipation ϵ. It assumes that the flow near the solid wall behaves like a fully developed turbulent boundary layer. In numerical simulations, this model is used to bridge the regions of high gradients near the wall and couples with the high-Re models in the rest of the domain.

In comparison to single-phase flows, the number or terms to be modeled in multiphase flows is large, and this makes the modeling of turbulence in multiphase simulations extremely complex [40]. Three methods are commonly

considered depending on the simulation approach: mixture turbulence model for homogeneous models, dispersed turbulence model for Eulerian-Lagrangian models, and turbulence for each phase for Eulerian multi-fluid models. As already said by one of the basic hypothesis of the model (see Section §4.2.1), only mixture turbulence models are considered.

This section generally describes some of the turbulence models available in OpenFOAM ®. The one used for simulations of Diesel sprays need to be selected among them. That selections is tough because turbulence models designed for wall-bounded (nozzle) flows do not give accurate results in the spray region and the other way around. The turbulence model study and the final selection are depicted in Section §5.3.5.

Standard compressible $k - \epsilon$

This two equation turbulence model, developed by Launder and Sharma [41], solves an equation for the turbulent kinetic energy k (Equation (4.86)) and an equation for the turbulent dissipation ϵ (Equation (4.87)). Both equations include temporal, convection and diffusion terms, together with different source terms. Its compressible version is a 6-constants model whose default values are depicted in Table 4.19.

$$\frac{\partial (\rho k)}{\partial t} + \nabla \cdot (\rho \boldsymbol{U} k) - k \left(\frac{\partial \rho}{\partial t} + \nabla \cdot (\rho \boldsymbol{U}) \right) - \nabla^2 (D_{kEff} k) =$$
$$= G - k \frac{2}{3} \rho \nabla \cdot \boldsymbol{U} - k \frac{\rho \epsilon}{k} \qquad (4.86)$$

$$\frac{\partial (\rho \epsilon)}{\partial t} + \nabla \cdot (\rho \boldsymbol{U} \epsilon) - \epsilon \left(\frac{\partial \rho}{\partial t} + \nabla \cdot (\rho \boldsymbol{U}) \right) - \nabla^2 (D_{\epsilon Eff} \epsilon) =$$
$$= C_1 G \frac{\epsilon}{k} - \epsilon \left(\frac{2}{3} C_1 + C_3 \right) \rho \nabla \cdot \boldsymbol{U} - C_2 \frac{\rho \epsilon^2}{k} \qquad (4.87)$$

Turbulent kinetic energy diffusivity coefficient D_{kEff} is calculated from Equation (4.88) and turbulent dissipation diffusivity $D_{\epsilon Eff}$ coefficient from Equation (4.89). Both are effective coefficients, meaning that they take into account molecular and turbulent diffusivity. The turbulence production source term G follows Equation (4.90).

$$D_{kEff} = \rho \left(\nu + \frac{\nu_t}{\sigma_k} \right) \qquad (4.88)$$

Constant	Default value
C_μ	0.09
C_1	1.44
C_2	1.92
C_3	-0.33
σ_k	1.0
σ_ϵ	1.3

Table 4.19: Default values of constants of the standard compressible $k - \epsilon$ turbulence model in OpenFOAM.

$$D_{\epsilon Eff} = \rho \left(\nu + \frac{\nu_t}{\sigma_\epsilon} \right) \tag{4.89}$$

$$G = 2\rho\nu_t \left(\nabla \boldsymbol{U} : \mathrm{dev}\left(\mathrm{symm}\left(\nabla \boldsymbol{U} \right) \right) \right) \tag{4.90}$$

At the end, the eddy viscosity, also called in this document turbulent viscosity, is computed from Equation (4.91).

$$\nu_t = C_\mu \frac{k^2}{\epsilon} \tag{4.91}$$

RNG compressible $k - \epsilon$

The RNG model was developed by Yakhot et al. [42, 43] using Re-Normalization Group (RNG) methods to re-normalize the Navier-Stokes equations, to account for the effects of smaller scales of motion. In the standard $k - \epsilon$ model the eddy viscosity is determined from a single turbulence length-scale, so the calculated turbulent diffusion is that which occurs only at the specified scale, whereas in reality all scales of motion will contribute to the turbulent diffusion. The RNG approach results in a modified form of the ϵ equation (Equation (4.92)) which attempts to account for the different scales of motion through changes to the production term. Its compressible version is a 8-constants model whose default values are depicted in Table 4.20.

$$\frac{\partial\left(\rho\epsilon\right)}{\partial t} + \nabla \cdot (\rho \boldsymbol{U} \epsilon) - \epsilon \left(\frac{\partial\rho}{\partial t} + \nabla \cdot (\rho \boldsymbol{U})\right) - \nabla^2\left(D_{\epsilon Eff}\epsilon\right) =$$

$$= (C_1 - R)\, G \frac{\epsilon}{k} - \epsilon \left(\frac{2}{3}C_1 + C_3\right) \rho \nabla \cdot \boldsymbol{U} - C_2 \frac{\rho \epsilon^2}{k} \qquad (4.92)$$

Constant	Default value
C_μ	0.0845
C_1	1.42
C_2	1.68
C_3	-0.33
σ_k	0.71942
σ_ϵ	0.71942
η_0	4.38
β	0.012

Table 4.20: Default values of constants of the RNG compressible $k - \epsilon$ turbulence model in OpenFOAM.

The additional term R substracted to the constant C_1 is the one that takes into account the smaller scales of turbulence. It is computed from Equation (4.93), where η follows Equation (4.94).

$$R = \frac{\eta\left(1 - \frac{\eta}{\eta_0}\right)}{1 + \beta\eta^3} \qquad (4.93)$$

$$\eta = \frac{k}{\epsilon}\sqrt{2|\left(\nabla \boldsymbol{U} : \text{dev}\left(\text{symm}\left(\nabla \boldsymbol{U}\right)\right)\right)|} \qquad (4.94)$$

High density ratio $k - \epsilon$

Demoulin et al. [25] made a review of turbulent models which can be applied to the Eulerian-Lagrangian Spray Atomization (ELSA) model. They also developed a new $k - \epsilon$ model that deals with the limitations of other models: first, the density ratio can be of the order of 1000 and second, at small scales there is no dissipation of the density gradient by molecular diffusion.

The transport equation for the turbulent kinetic energy k is Equation (4.95), completed by an equation for turbulent dissipation ϵ such Equation (4.96). When the high density ratio $k - \epsilon$ model is used, the Boussinesq

relation is used as in Equations (4.90) and (4.91). A term to account for the shift of acceleration between the heavy fluid particles and the light particles under the effect of the same pressure gradient is added to the production source term G. This is a 7-constants model whose default values are depicted in Table 4.21.

$$\frac{\partial(\rho k)}{\partial t} + \nabla \cdot (\rho \boldsymbol{U} k) - k \left(\frac{\partial \rho}{\partial t} + \nabla \cdot (\rho \boldsymbol{U}) \right) - \nabla^2 (D_{kEff} k) =$$
$$= G + \rho \frac{k^2}{\epsilon} \left(\frac{1}{\rho_f} - \frac{1}{\rho_g} \right) \frac{C_\mu}{Sc} (\nabla Y_l \cdot \nabla p) - k \frac{2}{3} \rho \nabla \cdot \boldsymbol{U} - k \frac{\rho \epsilon}{k} \qquad (4.95)$$

$$\frac{\partial(\rho \epsilon)}{\partial t} + \nabla \cdot (\rho \boldsymbol{U} \epsilon) - \epsilon \left(\frac{\partial \rho}{\partial t} + \nabla \cdot (\rho \boldsymbol{U}) \right) - \nabla^2 (D_{\epsilon Eff} \epsilon) =$$
$$= C_1 \left(G + \rho \frac{k^2}{\epsilon} \left(\frac{1}{\rho_f} - \frac{1}{\rho_g} \right) \frac{C_\mu}{Sc} (\nabla Y_l \cdot \nabla p) \right) \frac{\epsilon}{k} -$$
$$- \epsilon \left(\frac{2}{3} C_1 + C_3 \right) \rho \nabla \cdot \boldsymbol{U} - C_2 \frac{\rho \epsilon^2}{k} \qquad (4.96)$$

Constant	Default value
C_μ	0.09
C_1	1.44
C_2	1.92
C_3	-0.33
σ_k	1.0
σ_ϵ	1.3
Sc	0.9

Table 4.21: Default values of constants of the high density ratio $k-\epsilon$ turbulence model [25].

The effect of molecular viscosity is neglected here (Equations (4.97) and (4.98)) since high Reynolds numbers flows are considered.

$$D_{kEff} = \rho \frac{\nu_t}{\sigma_k} \qquad (4.97)$$

$$D_{\epsilon Eff} = \rho \frac{\nu_t}{\sigma_\epsilon} \qquad (4.98)$$

Compressible SST $k - \omega$

The first transported variable is the turbulent kinetic energy k (Equation (4.99)). The second transported variable in this case is the specific dissipation ω (Equation (4.100)), which determines the scale of the turbulence. The Shear Stress Transport (SST) formulation was designed, by Menter [44, 45], to overcome deficiencies in the $k - \omega$ model by the inclusion of transport effects into the formulation of the eddy-viscosity. Then, it gives a highly accurate predictions of the onset and the amount of flow separation under adverse pressure gradients. The use of a $k - \omega$ formulation in the inner parts of the boundary layer makes the model directly usable all the way down to the wall through the viscous sub-layer, hence the SST $k - \omega$ model can be used as a low-Re turbulence model without any extra damping functions. The SST formulation switches to a $k - \epsilon$ behavior in the free-stream and thereby avoids the common $k - \omega$ problem that is too sensitive to the inlet free-stream turbulence properties. This results in a major improvement in terms of flow separation predictions. However, the SST $k - \omega$ model produces a bit too large turbulence levels in regions with large normal strain, like stagnation regions and regions with strong acceleration. This tendency is much less pronounced that with a normal $k - \epsilon$ model though. Its compressible version is a 11-constants model whose default values are depicted in Table 4.22.

$$\frac{\partial (\rho k)}{\partial t} + \nabla \cdot (\rho \boldsymbol{U} k) - k \left(\frac{\partial \rho}{\partial t} + \nabla \cdot (\rho \boldsymbol{U}) \right) - \nabla^2 \left(D_{kEff} \left(F_1 \right) k \right) =$$
$$= \min \left(G, c_1 \beta^* \rho k \omega \right) - k \frac{2}{3} \rho \nabla \cdot \boldsymbol{U} - \rho \beta^* \omega k \quad (4.99)$$

$$\frac{\partial (\rho \omega)}{\partial t} + \nabla \cdot (\rho \boldsymbol{U} \omega) - \omega \left(\frac{\partial \rho}{\partial t} + \nabla \cdot (\rho \boldsymbol{U}) \right) - \nabla^2 \left(D_{\omega Eff} \left(F_1 \right) \omega \right) =$$
$$= \rho \gamma \left(F_1 \right) * G_\mu - \omega \frac{2}{3} \rho \gamma \left(F_1 \right) \nabla \cdot \boldsymbol{U} - \rho \beta \left(F_1 \right) \omega^2 - \omega \rho \frac{\left(F_1 - 1 \right) CD_{k\omega}}{\omega} \, (4.100)$$

In this case, turbulent kinetic energy diffusivity coefficient is calculated with Equation (4.101) and turbulent specific dissipation diffusivity coefficient with Equation (4.102). Notice that both terms use a blending function depending on the auxiliary relation F_1. The turbulence production source term G follows Equation (4.103), basically it is the same than for the standard compressible $k - \epsilon$ model divided by the viscosity.

$$D_{kEff} \left(F_1 \right) = \rho \left(\nu + \left[F_1 \left(\alpha_{k1} - \alpha_{k2} \right) + \alpha_{k2} \right] \nu_t \right) \quad (4.101)$$

Constant	Default value
α_{k1}	0.85034
α_{k2}	1.0
$\alpha_{\omega 1}$	0.5
$\alpha_{\omega 2}$	0.85616
β_1	0.075
β_2	0.0828
β^*	0.09
γ_1	0.5532
γ_2	0.4403
a_1	0.31
c_1	10.0

Table 4.22: Default values of constants of the compressible SST $k - \omega$ turbulence model in OpenFOAM.

$$D_{\epsilon Eff}(F_1) = \rho \left(\nu + \left[F_1 \left(\alpha_{\omega 1} - \alpha_{\omega 2} \right) + \alpha_{\omega 2} \right] \nu_t \right) \tag{4.102}$$

$$G_\mu = 2 \left(\nabla U : \text{dev} \left(\text{symm} \left(\nabla U \right) \right) \right) \tag{4.103}$$

One of the closure coefficients used in Equation (4.100) also uses a blending function, concretely Equation (4.104).

$$\gamma(F_1) = F_1 \left(\gamma_1 - \gamma_2 \right) + \gamma_2 \tag{4.104}$$

As already shown, in this model there are two different auxiliary coefficients F_1 and F_2, given by Equations (4.105) and (4.106) correspondingly. They use the mesh coordinates y and a new coefficient $CD_{k\omega}^+$ defined by Equations (4.107) and (4.108).

$$F_1(CD_{k\omega}) = \tanh \left[\left(\min \left(\min \left(\max \left(\frac{\sqrt{k}}{\beta^* \omega y}, \frac{500\nu}{y^2 \omega} \right), \frac{4\alpha_{\omega 2} k}{CD_{k\omega}^+ y^2} \right), 10 \right) \right)^4 \right] \tag{4.105}$$

$$F_2 = \tanh \left[\left(\min \left(\max \left(\frac{2\sqrt{k}}{\beta^* \omega y}, \frac{500\nu}{y^2 \omega} \right), 100 \right) \right)^2 \right] \tag{4.106}$$

$$CD_{k\omega} = 2\alpha_{\omega 2}\frac{\nabla k \cdot \nabla \omega}{\omega} \tag{4.107}$$

$$CD_{k\omega}^+ = \max\left(CD_{k\omega}, 10^{-10}\right) \tag{4.108}$$

At the end, the eddy viscosity is computed from Equation (4.109). In order to fully close the model, the turbulent dissipation is also calculated from the turbulent energy and the specific dissipation in Equation (4.110).

$$\nu_t = \frac{a_1 k}{\max\left(a_1\omega, \sqrt{2}F_2|\text{symm}\left(\nabla U\right)|\right)} \tag{4.109}$$

$$\epsilon = \beta^* k\omega \tag{4.110}$$

4.5 Summary

The model developed for this Thesis, capable of simulating internal and external flows of the Diesel injection problem seamlessly, has been described in detail in this chapter. Several alternatives found in the literature have been also commented.

Six transport equations (liquid mass fraction, continuity, momentum, energy, pressure and inter-facial surface density) together with turbulence modeling are solved within a PIMPLE algorithm. Most of the equations are the ones traditionally used [6, 10], including the pressure-velocity coupling. This is an important difference with the original model, which uses an equation of state to compute the pressure [10], that allows including the nozzle flow in the simulation.

The model is compressible, so an equation of state and a compressibility value are required not only for the mixture, also for all single phases. Gas thermodynamic behavior is more or less well known. Nonetheless, the variation of the liquid properties (density, compressibility and enthalpy) with the thermodynamic variables had to be searched in the literature and added to the model.

Closure sub-models, i.e. previously cited equation of state, are needed in order to solve all transport equation. Some of them, including the atomization and mixing sub-model developed by Demoulin et al. [25], have been described.

Others (i.e. turbulence model), however, have been generally discussed and left to be finally selected in future sections.

An original study presented in this chapter is the modification of the flux updates-equations sequence. After testing up to eight different combinations, a flux update has been added after the liquid mass fraction transport equation because it reduces the computational cost and ensures that mass fraction and density fields are consistent.

References

[1] Desantes, J. M., R. Payri, F. J. Salvador, and V. Soare. "Study of the Influence of Geometrical and Injection Parameters on Diesel Sprays Characteristics in Isothermal Conditions". *SAE Technical Paper 2005-01-0913* (2005). DOI: 10.4271/2005-01-0913 (*cit. on p. 137*).

[2] Som, S. and S. K. Aggarwal. "Effects of primary breakup modeling on spray and combustion characteristics of compression ignition engines". *Combustion and Flame*, vol. 157.6 (2010), pp. 1179–1193. DOI: 10.1016/j.combustflame.2010.02.018 (*cit. on p. 137*).

[3] Battistoni, M., C. N. Grimaldi, and F. Marianni. "Coupled Simulation of Nozzle Flow and Spray Formation Using Diesel and Biodiesel for CI Engine Applications". *SAE Technical Paper 2012-01-1267* (2012). DOI: 10.4271/2012-01-1267 (*cit. on p. 137*).

[4] Pastor, J. V., R. Payri, J. M. Salavert, and J. Manin. "Evaluation of natural and tracer fluorescent emission methods for droplet size measurements in a diesel spray". *International Journal of Automotive Technology*, vol. 13.5 (2012), pp. 713–724. DOI: 10.1007/s12239-012-0070-z (*cit. on p. 138*).

[5] Ishii, M. and T. Hinbiki. *Thermo-Fluid Dynamics of Two-Phase Flow*. Ed. by M. Ishii and T. Hinbiki. Second edition. Heidelberg, Germany: Springer, 1975. DOI: 0.1007/978-1-4419-7985-8_11 (*cit. on pp. 138, 140, 141, 145, 168, 170, 176, 179*).

[6] Weller, H. G., G. Tabor, H. Jasak, and C. Fureby. "A Tensorial Approach to Computational Continuum Mechanics using Object Orientated Techniques". *Computers in Physics*, vol. 12.6 (1998), pp. 620–631. DOI: 10.1063/1.168744 (*cit. on pp. 138, 142, 149, 191*).

[7] Ferziger, J. H. and M. Perić. *Computational Methods for Fluid Dynamics*. Ed. by J. H. Ferziger. Third edition. Heidelberg, Germany: Springer, 2002 (*cit. on pp. 139, 148, 154, 159, 179*).

[8] Bataille, J. and J. Kesting. *Continuum modeling of two-phase flows.* Technical Report LA-UR-81-3325. Washington, District of Columbia, Washington, United States of America: Los Alamos National Laboratory, 1981 (*cit. on pp. 140, 167, 168*).

[9] Hinze, J. O. *Turbulence.* Ed. by J. O. Hinze. Second edition. New York, New York, United States of America: McGraw Hill, 1975 (*cit. on p. 141*).

[10] Vallet, A., A. A. Burluka, and R. Borghi. "Development of a Eulerian model for the "Atomization" of a liquid jet". *Atomization and Sprays*, vol. 11.6 (2001), pp. 619–642 (*cit. on pp. 141, 142, 146, 148, 168–170, 173, 176, 191*).

[11] Beheshti, N., A. A. Burluka, and M. Fairweather. "Assessment of $\Sigma - Y_{liq}$ model predictions for air-assisted atomisation". *Theoretical and Computational Fluid Dynamics*, vol. 21.5 (2007), pp. 381–397. DOI: `10.1007/s00162-007-0052-3` (*cit. on pp. 142, 169, 173*).

[12] Ning, W., R. D. Reitz, A. M. Lippert, and R. Diwakar. "Development of a Next-generation Spray and Atomization Model Using an Eulerian-Lagrangian Methodology". *20th Annual Conference on Liquid Atomization & Spray Systems (ILASS Americas)*. Chicago, Illinois, United States of America, 2007 (*cit. on pp. 142, 146*).

[13] Trask, N., D. P. Schmidt, M. Lightfoot, and S. Danczyk. "Compressible modeling of the internal flow in a gas-centered swirl-coaxial fuel injector". *Journal of Propulsion and Power*, vol. 28.4 (2012), pp. 685–693. DOI: `10.2514/1.B34102` (*cit. on pp. 146, 147*).

[14] Jasak, H. "Error Analysis and Estimation for the Finite Volume Method with Applications to Fluid Flows". PhD thesis. South Kensington Campus, SW7 2AZ, London, United Kingdom: Department of Mechanical Engineering, Imperial College of Science, Technology and Medicine, 1996 (*cit. on pp. 146, 149, 184*).

[15] García-Oliver, J. et al. "Diesel spray CFD simulations based on the $\Sigma - Y$ eulerian atomization model". *Atomization and Sprays*, vol. 23.1 (2013), pp. 71–95. DOI: `10.1615/AtomizSpr.2013007198` (*cit. on pp. 147, 168*).

[16] Issa, R. I. "Solution of the implicitly discretised fluid flow equations by operator-splitting". *Journal of Computational Physics*, vol. 62.1 (1986), pp. 40–65. DOI: `16/0021-9991(86)90099-9` (*cit. on p. 149*).

[17] Issa, R. I., B. Ahmadi-Befrui, K. R. Beshay, and A. D. Gosman. "Solution of the implicitly discretised reacting flow equations by operator-splitting". *Journal of Computational Physics*, vol. 93.2 (1991), pp. 388–410. DOI: 10.1016/0021-9991(91)90191-M (*cit. on p. 149*).

[18] Patankar, S. V. and D. B. Spalding. "A calculation procedure for heat, mass and momentum transfer in three-dimensional parabolic flows". *International Journal of Heat and Mass Transfer*, vol. 15.10 (1972), pp. 1787–1806. DOI: 10.1016/0017-9310(72)90054-3 (*cit. on p. 149*).

[19] Salvador, F. J., J. Martínez-López, M. Caballer, and C. de Alfonso. "Study of the influence of the needle lift on the internal flow and cavitation phenomenon in diesel injector nozzles by CFD using RANS methods". *Energy Conversion and Management*, vol. 66 (2013), pp. 246–256. DOI: 10.1016/j.enconman.2012.10.011 (*cit. on p. 154*).

[20] Lebas, R., G. Blokkel, P. A. Beau, and F. X. Demoulin. "Coupling Vaporization Model With the Eulerian-Lagrangian Spray Atomization (ELSA) Model in Diesel Engine Conditions". *SAE Technical Paper 2005-01-0213* (2005). DOI: 10.4271/2005-01-0213 (*cit. on p. 168*).

[21] Ning, W., R. D. Reitz, R. Diwakar, and A. M. Lippert. "An Eulerian-Lagrangian Spray and Atomization model with improved turbulence modeling". *Atomization and Sprays*, vol. 19.8 (2009), pp. 727–739. DOI: 10.1615/AtomizSpr.v19.i8.20 (*cit. on p. 168*).

[22] Wang, Y., W. G. Lee, R. D. Reitz, and R. Diwakar. "Numerical Simulation of Diesel Sprays Using an Eulerian-Lagrangian Spray and Atomization (ELSA) Model Coupled with Nozzle Flow". *SAE Technical Paper 2011-01-0386* (2011). DOI: 10.4271/2011-01-0386 (*cit. on p. 168*).

[23] Hoyas, S., A. Gil, X. Margot, D. Khuong-Anh, and F. Ravet. "Evaluation of the Eulerian-Lagrangian Spray Atomization (ELSA) model in spray simulations: 2D cases". *Mathematical and Computer Modelling*, vol. 57.7-8 (2013), pp. 1686–1693. DOI: 10.1016/j.mcm.2011.11.006 (*cit. on p. 168*).

[24] Blokkel, G., B. Barbeau, and R. Borghi. "A 3D Eulerian Model to Improve the Primary Breakup of Atomizing Jet". *SAE Technical Paper 2003-01-0005* (2003). DOI: 10.4271/2003-01-0005 (*cit. on p. 168*).

[25] Demoulin, F. X., P. A. Beau, G. Blokkel, and R. Borghi. "A new model for turbulent flows with large density fluctuations: Application to liquid atomization". *Atomization and Sprays*, vol. 17.4 (2007), pp. 315–345. DOI: `10.1615/AtomizSpr.v17.i4.20` (*cit. on pp. 169, 170, 187, 188, 191*).

[26] Lumley, J. L. "Modeling turbulent flux of passive scalar quantities in inhomogeneous flows". *Physics of Fluids*, vol. 18.6 (1975), pp. 619–621. DOI: `10.1063/1.861200` (*cit. on p. 169*).

[27] Launder, B. E. "On the effects of a gravitational field on the turbulent transport of heat and momentum". *Journal of Fluid Mechanics*, vol. 67.3 (1975), pp. 569–581. DOI: `10.1017/S002211207500047X` (*cit. on p. 169*).

[28] Lebas, R., T. Ménard, P. A. Beau, A. Berlemont, and F. X. Demoulin. "Numerical simulation of primary break-up and atomization: DNS and modelling study". *International Journal of Multiphase Flow*, vol. 35.3 (2009), pp. 247–260. DOI: `10.1016/j.ijmultiphaseflow.2008.11.005` (*cit. on pp. 172, 173*).

[29] Duret, B., J. Réveillon, T. Ménard, and F. X. Demoulin. "Improving primary atomization modeling through DNS of two-phase flows". *International Journal of Multiphase Flow*, vol. 55 (2013), pp. 130–137. DOI: `10.1016/j.ijmultiphaseflow.2013.05.004` (*cit. on p. 174*).

[30] Pilch, M. M. and C. A. Erdman. "Use of breakup time data and velocity history data to predict the maximum size of stable fragments for acceleration-induced breakup of a liquid drop". *International Journal of Multiphase Flow*, vol. 13.6 (1987), pp. 741–757 (*cit. on p. 175*).

[31] Payri, R., F. J. Salvador, J. Gimeno, and G. Bracho. "The effect of temperature and pressure on thermodynamic properties of diesel and biodiesel fuels". *Fuel*, vol. 90.3 (2011), pp. 1172–1180. DOI: `10.1016/j.fuel.2010.11.015` (*cit. on pp. 176–178*).

[32] Khasanshin, T. S., A. P. Shchamialiou, and O. G. Puddobskij. "Thermodynamic Properties of Heavy n-Alkanes in the Liquid State: n-Dodecane". *International Journal of Thermophysics*, vol. 24.5 (2005), pp. 1277–1289 (*cit. on pp. 177, 178*).

[33] Khasanshin, T. S., V. S. Samuilov, and A. P. Shchemelev. "Determination of the thermodynamic properties of liquid n-hexadecane from the measurements of the velocity of sound". *Journal of Engineering Physics and Thermophysics*, vol. 82.1 (2009), pp. 149–156. DOI: `10.1007/s10891-009-0156-2` (*cit. on pp. 177, 178, 181*).

[34] Dumont, N., O. Simonin, and C. Habchi. "Numerical Simulation of Cavitating Flows in Diesel Injectors by a Homogeneous Equilibrium Modeling Approach". *CAV 2001: Fourth International Symposium on Cavitation.* California Institute of Technolog. Pasadena, California, United States of America, 2001 (*cit. on pp. 176, 177*).

[35] Wallis, G. B. *One-dimensional Two-phase Flow.* New York, New York, United States of America: Mcgraw-Hill, 1969 (*cit. on p. 176*).

[36] White, F. M. *Fluid Mechanics.* Ed. by M. Lange. Seventh edition. New York, New York, United States of America: McGraw-Hill Companies, Inc., 2011 (*cit. on p. 178*).

[37] Anderson, J. D. *Fundamentals of Aerodynamics.* Ed. by J. D. Anderson. Fourth edition. New York, New York, United States of America: McGraw Hill, 2007 (*cit. on pp. 178, 184*).

[38] Çengel, Y. A. and M. A. Boles. *Thermodynamics: an engineering approach.* Ed. by Y. A. Çengel. Seventh edition. McGraw Hill Higher Education, 2011 (*cit. on pp. 180, 182*).

[39] Secretary of Commerce on behalf of the U. S. A., U. S. *Dodecane.* English. National Institute of Standards and Technology. 2013. URL: http://www.nist.gov/ (*cit. on pp. 181–183*).

[40] Crowe, C. T., J. D. Schwarzkopf, M. Sommerfeld, and Y. Tsuji. *Multiphase Flows with Droplets and Particles.* Ed. by C. T. Crowe. Second edition. 711 3rd Avenue, 10017, New York, New York, United States of America: CRC Press, Taylor & Francis Group, 1998 (*cit. on p. 184*).

[41] Launder, B. E. and B. I. Sharma. "Application of the energy-dissipation model of turbulence to the calculation of flow near a spinning disc". *Letters in Heat and Mass Transfer*, vol. 1.2 (1974), pp. 131–137 (*cit. on p. 185*).

[42] Yakhot, V., S. A. Orszag, S. Thangam, T. B. Gatski, and C. G. Speziale. "Development of turbulence models for shear flows by a double expansion technique". *Physics of Fluids A: Fluid Dynamics*, vol. 4.7 (1992), pp. 1510–1520. DOI: 10.1063/1.858424 (*cit. on p. 186*).

[43] Yakhot, V. and S. A. Orszag. "Renormalization group analysis of turbulence. I. Basic theory". *Journal of Scientific Computing*, vol. 1.1 (1986), pp. 3–51. DOI: 10.1007/BF01061452 (*cit. on p. 186*).

[44] Menter, F. R. *Improved Two-Equation $k - \omega$ Turbulence Models for Aerodynamic Flows.* Technical Report N93-22809. Ames Research Center, Moffett Field, California, United States of America: National Aeronautics and Space Administration, 1992 (*cit. on p. 189*).

[45]   Menter, F. R. "Two-equation eddy-viscosity turbulence models for engineering applications". *American Institute of Aeronautics and Astronautics Journal*, vol. 32.8 (1994), pp. 1598–1605. DOI: 10.2514/3.12149 (*cit. on p. 189*).

Chapter 5

Verification and validation

5.1 Introduction

For every new model, verification and validation are the primary means to assess accuracy and reliability in computational simulations [1]. Basically, verification consists of determining that a model implementation accurately represents the developer's conceptual description and the solution of the model. Hence verification does not address whether the model itself is a good representation of the physics of the problem at hand, it is not a physical issue but a mathematical or computational issue. Validation consists of determining the degree to which a model is an accurate representation of the real world from the perspective of the intended uses of the model. The fundamental strategy of validation involves identification and quantification of the error and uncertainty in the conceptual model and computational models, quantification of the numerical error in the computational solution, estimation of the experimental uncertainty, and finally, comparison between the computational results and the experimental data.

According to Oberkampf and Trucano [1], the American Institute of Aeronautics and Astronautics (AIAA) suggests the following logical organization of testing CFD codes: (1) test with analytical solutions, (2) test with semi-analytical solutions, and (3) benchmark solutions that may be representative of application complexity. Their work is a useful guide about how to assess accuracy and reliability in computational simulations. Verification and validation assessments are clearly described and a brief guide of "how to" is provided.

5.2   Verification assessment

Ghia et al. [2] present a collection of fluid mechanics problems with exact solutions which can be used to verify the numerical accuracy of solutions obtained by CFD codes. Additionally, Slater [3] supplies extra verification cases. Both works are used to verify the present model.

Unfortunately any proper multiphase problems with analytical or high accurate solutions have been found in the literature. Even Grace and Taghipour [4] say that verification is virtually impossible in dense multiphase systems, except for trivial cases. Verification of multiphase solvers is often carried out by problems with single bubbles [5, 6] or cases with propagation of one phase into the other [6], for example, the water faucet problem [7]. The Riemann problem is also a common verification case for multiphase solvers [8]. However, none of these benchmark cases deal with the mixing between phases nor the break-up of one of them.

The method of manufactured solutions is a general and very powerful approach to code verification [2]. Instead of trying to find an exact solution to a system of partial differential equations, the goal is to manufacture an exact solution to a slightly modified set of equations. The general concept behind method of manufactured solutions is to choose the solution a priori, then operate the governing partial differential equations onto the chosen solution, thereby generating analytical source terms. The chosen solution is then the exact solution to the modified governing equations plus the analytical source terms. However, as the governing equations get more complex, this method of manufactured solutions also does. Thus, it has not been used.

Other high accurate solutions commonly used for verification are DNS. Usually, Reynolds number of this type of simulations are low, then not fulfilling the basic hypothesis of the model (see Section §4.2.1). Moreover, available works with this type of simulations assume incompressible flow, so the compressibility effects cannot be checked. Nonetheless, Lebas et al. [9] compare their results obtained by an ELSA model with the DNS carried out by Ménard et al. [10] ($Re = 5800$). Additionally to verification, this procedure allows fixing the modeling parameters and constants. The same is done by Demoulin et al. [11], who in addition to validation of the ELSA model, develop a large eddy simulation formulation of the liquid atomization.

5.2.1   Prandtl-Meyer expansion fan

This verification case is chosen because during an injection event two expansion processes take place. The first one occurs inside the nozzle, fuel accel-

erates due to the pressure difference upstream and downstream. The second expansion process is found right at the exit of the nozzle due to an abrupt change in cross-sectional area.

Problem description

As described by Ghia et al. [2], a uniform supersonic flows along a sudden divergence, turning around the corner through a smooth isentropic expansion fan, to assume its rotated direction. The gas is assumed to satisfy the ideal gas relation, Equation (4.64). The gas is also assumed to have a constant ratio of specific heats ($\gamma = 1.4$). With this equation of state, the analytical solution is independent of any other properties.

The variation of properties across the fan are taken as comparison metrics, including the final Mach number. In particular, the velocity after the expansion should be parallel to the inclined wall, and the isentropic relations for pressure, density and temperature are expected to be satisfied within no more than 5-10% error, even on a relatively coarse grid (the quality of the computational solution may be highly sensitive to the local grid refinement in the vicinity of the corner, and slightly dependent on the grid alignment).

Figure 5.1 shows the expansion fan domain and boundaries. Three different mesh refinements, 30x15, 120x60 and 960x480, are used just because the only way asymptotic convergence can be demonstrated is to compute three solutions [1]. All pressure distributions are obtained for a line 5 mm over the wall. The isentropic ratios are obtained with the values at the beginning and at the end of this line.
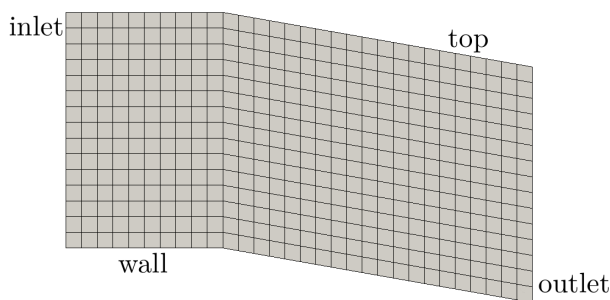
Figure 5.1: Expansion fan domain, 30x15 mesh elements. Overall domain bounding box: (0 0 -0.003473) (0.029696 0.001 0.015) m.

For an inlet Mach number of $M_1 = 2.0$ and expansion angle of $\delta = -10°$ the following should result: $M_2 = 2.383$, $p_2/p_1 = 0.5471$, $\rho_2/\rho_1 = 0.6500$ and $T_2/T_1 = 0.8417$.

Case set-up

Tables 5.1-5.4 present the boundary conditions used for Y_f, $\boldsymbol{U}$, T and p variables. k, ϵ and Σ are not required because turbulence is switched off. Temperature and velocity at the inlet are calculated to obtain a Mach number $M_1 = 2.0$.

Patch	Type	Value
inlet	fixedValue	0
outlet	zeroGradient	-
wall	zeroGradient	-
top	zeroGradient	-

Table 5.1: Y_f boundary conditions for the Prandtl-Meyer expansion fan case.

Patch	Type	Value
inlet	fixedValue	(600 0 0)
outlet	zeroGradient	-
wall	slip	-
top	zeroGradient	-

Table 5.2: $\boldsymbol{U}$ boundary conditions for the Prandtl-Meyer expansion fan case.

Patch	Type	Value
inlet	fixedValue	224
outlet	zeroGradient	-
wall	zeroGradient	-
top	zeroGradient	-

Table 5.3: T boundary conditions for the Prandtl-Meyer expansion fan case.

Patch	Type	Value
inlet	fixedValue	1e05
outlet	zeroGradient	-
wall	zeroGradient	-
top	zeroGradient	-

Table 5.4: p boundary conditions for the Prandtl-Meyer expansion fan case.

Gas properties such constant $R = 287$ m^2/(s^2 K) and heat capacity at constant pressure $c_p = 1039$ m^2/(s^2 K) are introduced to the model. The rest of required parameters do not matter because they are not used in this simulation.

It is important to specify the right schemes to get a stable and consistent solution [1]. The temporal resolution is limited by setting a maximum

Courant number of CFL = 0.2. Table 5.5 summarizes the low and high order numerical schemes used for the spatial resolution. Time scheme does not change due to this is a steady problem. Note that divergence scheme does not vary either; many other options were tested and all of them led to divergence of the calculation.

ddtSchemes		
Euler	-	Euler
gradSchemes		
Gauss linear	-	fourth
divSchemes		
Gauss upwind	-	Gauss upwind
laplacianSchemes		
Gauss linear uncorrected	-	Gauss cubic uncorrected
interpolationSchemes		
linear	-	linear
snGradSchemes		
uncorrected	-	uncorrected

Table 5.5: Schemes used for the spatial resolution for the Prandtl-Meyer expansion fan case.

Linear solvers for partial differential equations are the same in all the verification cases, PBiCG with DILU as preconditioner for all variables but for the pressure, where PCG is used with DIC as preconditioner. The absolute tolerance is always 10^{-15}.

Results

Figure 5.2 shows the pressure distributions along the line 5 mm over the wall. It shows how the pressure variation across the expansion fan is correctly predicted, even on coarse meshes, and how the quality and accuracy of the solution monotonically improves with increasing grid refinement. Ghia et al. [2] point out that these profiles are not precisely centered about the exact solution profile probably because of the computational diffusion being unequal in the upstream and downstream directions. Although it cannot be appreciated in the figure, higher discretization order schemes lead to a very slightly sharper pressure profiles.

(a) Low order discretization.   (b) High order discretization.
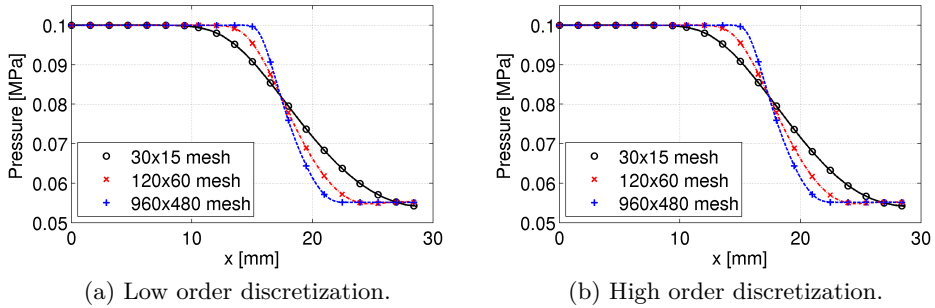
Figure 5.2: Line plot of the pressure distribution along a line 5 mm over the wall for the Prandtl-Meyer expansion fan case.

Regarding the comparison metrics, Table 5.6 shows all the information. Mach number and all ratios are predicted with an error lower than 5%.

	M_2	p_2/p_1	ρ_2/ρ_1	T_2/T_1	Error [%]
Analytical	2.383	0.5471	0.6500	0.8417	–
30x15 low order	2.370	0.5418	0.6373	0.8500	1.95
120x60 low order	2.368	0.5522	0.6491	0.8508	0.93
960x480 low order	2.373	0.5514	0.6495	0.8490	0.79
30x15 high order	2.370	0.5519	0.6373	0.8501	1.95
120x60 high order	2.369	0.5519	0.6489	0.8507	0.93
960x480 high order	2.373	0.5514	0.6495	0.8490	0.79

Table 5.6: Comparison metrics for the Prandtl-Meyer expansion fan case.

Following, Mach number contours are shown in Figures 5.3 and 5.4. There is a similarity between the ones obtained by Ghia et al. [2] and current simulations. These figures show how, as expected, increasing the mesh resolution gives a narrower and better defined expansion fan.

Finally, for the present solver the same trends than in the test case of Ghia et al. [2] are observed, as well for the grid resolution as for the solution itself. Furthermore, errors in all the comparison metrics are below the limits. According to this test case, the solver is verified.

(a) Low order discretization.

(b) High order discretization.
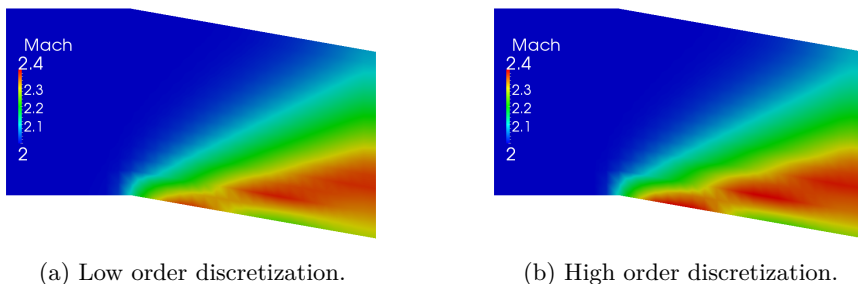
Figure 5.3: Mach number contours with a mesh resolution of 30x15 for the Prandtl-Meyer expansion fan case.

(a) Low order discretization.

(b) High order discretization.
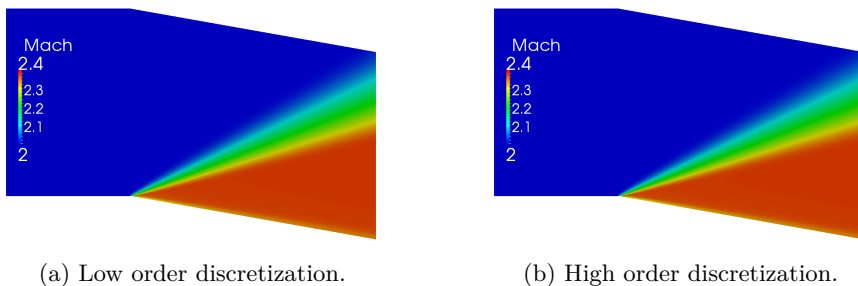
Figure 5.4: Mach number contours with a mesh resolution of 960x480 for the Prandtl-Meyer expansion fan case.

5.2.2   Steady-state oblique shock wave

This verification case is chosen because during an injection event, pressure waves travel along the domain. One inside the nozzle, at speeds much lower than the liquid speed of sound, which bounces up and down until the steady state is reached. The other one is generated at the tip of the spray. An injection supersonic velocity has a potential to generate a shock wave which may affect the penetration and break-up of Diesel sprays [12]. This depends on ambient conditions, high ambient temperature increases the speed of sound and therefore hinders potential shock wave generation, and high ambient density decelerates the spray such that it may never reach sonic velocities.

Problem description

As described by Ghia et al. [2], a uniform supersonic stream impinges on a
wedge, resulting in a stationary, oblique shock wave, separating two regions
of uniform flow. The gas is assumed to satisfy the ideal gas relation, Equa-
tion (4.64). The gas is also assumed to have a constant ratio of specific heats
($\gamma = 1.4$). With this equation of state, the analytical solution is independent
of any other properties.

The variation of properties across the shock are taken as comparison met-
rics, including the final Mach number. In particular, the velocity after the
expansion should be parallel to the inclined wall, a specific shock angle should
result, and the jump conditions for pressure, density and temperature are ex-
pected to be satisfied within no more than 10-20% error (the quality of the
computational solution may be highly sensitive to the local grid refinement in
the vicinity of the corner, and slightly dependent on the grid alignment).

Figure 5.5 shows the oblique shock geometry and boundaries. As in the
previous verification case, three different mesh refinements, 20x10, 80x40 and
640x320, are used just to demonstrate asymptotic convergence [1]. All pressure
distributions are obtained for a line 2 mm over the wall. The jump ratios are
obtained with the values at the beginning and at the end of this line.
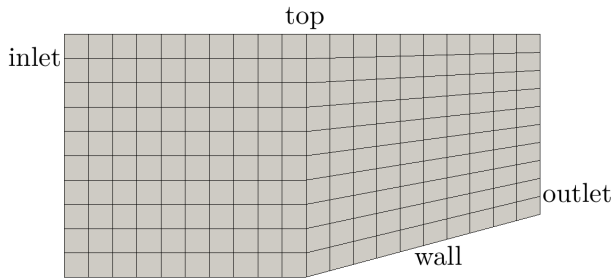
Figure 5.5: Oblique shock wave domain, 20x10 mesh elements. Overall domain
bounding box: (0 0 0) (0.019659 0.001 0.01) m.

For the specific example with an inlet Mach number of $M_1 = 3.0$ and
wall angle of $\delta = 15°$ the following should result: $M_2 = 2.255$, $\beta = 32.24°$,
$p_2/p_1 = 2.822$, $\rho_2/\rho_1 = 2.0342$ and $T_2/T_1 = 1.345$.

Case set-up

Tables 5.7-5.10 present the boundary conditions used for Y_f, U, T and p variables. k, ϵ and Σ are not required because turbulence is switched off. Temperature and velocity at the inlet are calculated to obtain a Mach number $M_1 = 3.0$.

Patch	Type	Value
inlet	fixedValue	0
outlet	zeroGradient	-
wall	zeroGradient	-
top	zeroGradient	-

Table 5.7: Y_f boundary conditions for the Oblique shock case.

Patch	Type	Value
inlet	fixedValue	(900 0 0)
outlet	zeroGradient	-
wall	slip	-
top	zeroGradient	-

Table 5.8: U boundary conditions for the Oblique shock case.

Patch	Type	Value
inlet	fixedValue	224
outlet	zeroGradient	-
wall	zeroGradient	-
top	zeroGradient	-

Table 5.9: T boundary conditions for the Oblique shock case.

Patch	Type	Value
inlet	fixedValue	1e05
outlet	zeroGradient	-
wall	zeroGradient	-
top	zeroGradient	-

Table 5.10: p boundary conditions for the Oblique shock fan case.

Gas properties such constant $R = 287$ m^2/(s^2 K) and heat capacity at constant pressure $c_p = 1039$ m^2/(s^2 K) are introduced to the model. The rest of required parameters do not matter because they are not used in this simulation.

It is important to specify the right schemes to get a stable and consistent solution [1]. The temporal resolution has been limited by setting a maximum Courant number of CFL = 0.2. Table 5.5 summarizes the low and high order numerical schemes used for the spatial resolution, which are the same then for the Prandtl-Meyer expansion fan case.

Results

Figure 5.6 shows the pressure distributions along the line 2 mm over the wall. It shows how the pressure variation across the oblique shock is correctly predicted, and how the quality and accuracy of the solution monotonically improves with increasing grid refinement. Higher order discretization schemes significantly improve the solution for coarser meshes. As for the Prandtl-Meyer expansion fan case, these profiles are not precisely centered about the exact-solution profile because of the different computational diffusion in upstream and downstream directions.

(a) Low order discretization.   (b) High order discretization.
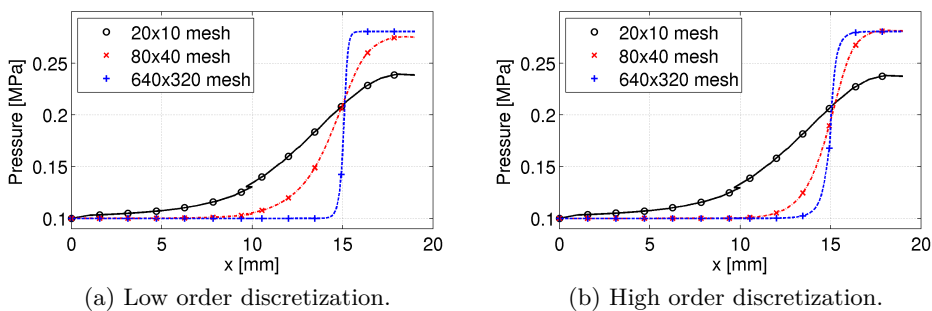
Figure 5.6: Line plot of the pressure distribution along a line 2 mm over the wall for the Oblique shock case.

Regarding the comparison metrics, Table 5.11 shows all the information. Errors in Mach number and all ratios (last column) are quite below 20% and only errors for the coarsest mesh are greater than 5%. The oblique shock angle β is analyzed separately. The shock line is defined by the points where the pressure start rising (5% higher than the upstream pressure). The slope of this line is β. As it can be seen in Figure 5.6, with the lowest mesh resolution the pressure rises from the start, and then a negative shock angle is obtained. Increasing the mesh resolution makes the pressure rise sharper and reduces the error up to 8.56% for low discretization order and 0.93% for high discretization order.

Following, Mach number contours are shown in Figures 5.7 and 5.8. There is similarity between the ones obtained by Ghia et al. [2] and the current simulations. These figures show how, as expected, increasing the mesh resolution gives a narrower and better defined oblique shock.

	M_2	β [°]	p_2/p_1	ρ_2/ρ_1	T_2/T_1	Error [%]
Analytical	2.255	32.24	2.822	2.0342	1.345	-
20x10 low order	2.328	-13.56	2.386	1.7799	1.338	15.45
80x40 low order	2.266	69.89	2.750	2.0002	1.375	2.55
640x320 low order	2.262	29.48	2.806	2.0336	1.380	2.60
20x10 high order	2.337	-13.21	2.374	1.7778	1.332	15.87
80x40 high order	2.261	43.15	2.812	2.0403	1.378	2.45
640x320 high order	2.266	31.94	2.806	2.0387	1.376	2.30

Table 5.11: Comparison metrics for the Oblique shock case.

(a) Low order discretization.

(b) High order discretization.
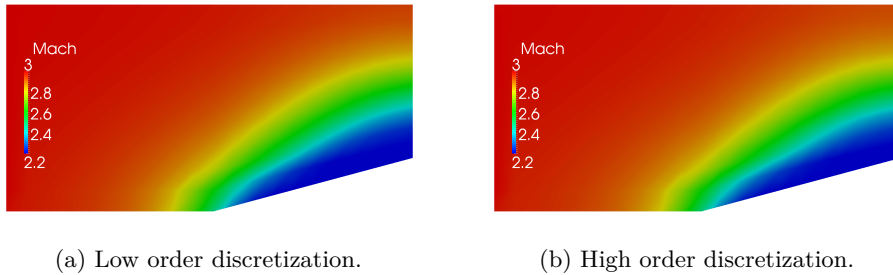
Figure 5.7: Mach number contours with a mesh resolution of 20x10 for the Oblique shock case.

Finally, for the present solver the same trends than in the test case of Ghia et al. [2] are observed, as well for the grid resolution as for the solution itself. Furthermore, errors in all the comparison metrics are below the limits. According to this test case, the solver is verified.

5.2.3 Couette thermal flow

Temperature field inside the nozzle was commonly assumed constant [13, 14]. However, pressurization of Diesel fuel in modern common-rail injectors in excess of 200 MPa can result to increased temperatures and significant variation of the fuel thermo-physical properties relative to those under atmospheric pressure and room temperature conditions. Furthermore, fuel acceleration at velocities reaching 600 m/s is also inducing further wall friction and thus heating. This is why this verification case is chosen.

(a) Low order discretization.

(b) High order discretization.
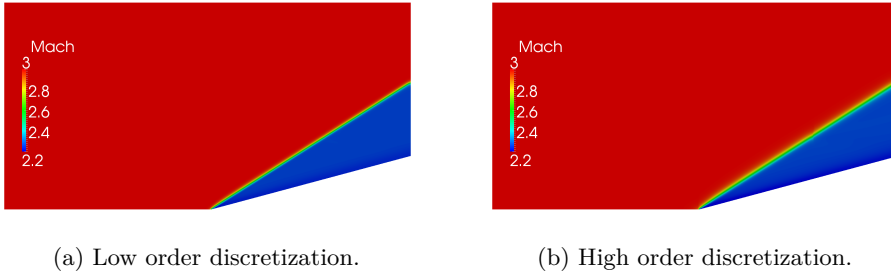
Figure 5.8: Mach number contours with a mesh resolution of 640x320 for the Oblique shock case.

Problem description

As described by Ghia et al. [2], this case presents one of the simplest cases to verify the discretization of viscous terms in the Navier-Stokes equations: laminar flow between two infinite parallel walls - a fixed wall and a moving wall at a distance L, with the moving wall having a velocity U. In order to include the computation of the thermal fluxes, both walls are considered as isothermal, but at different temperatures. Low compressible conditions, with a Mach number around 0.1, are considered. Since the non-dimensional solution depends only on the product $PrEc$ (Equation (5.1), being Pr the Prandtl number and Ec the Eckert number), this parameter defines completely the numerical solution. The fluid is a perfect gas with the following properties:

- Gas constant: $R = 287 \ \mathrm{m^2/(s^2\,K)}$
- Specific heat: $c_p = 1006 \ \mathrm{m^2/(s^2\,K)}$.
- Gamma: $\gamma = 1.4$.
- Kinematic viscosity: $\nu = 1.57 \ 10^{-5} \ \mathrm{m^2/s}$.
- Prandtl number: $Pr = 0.708$.

$$PrEc = \frac{\mu c_p}{\xi} \frac{U^2}{c_p \Delta T} = \frac{\mu U^2}{\xi \Delta T} \tag{5.1}$$

The Reynolds number based on the velocity of the moving wall is 4000. The physiscal conditions of this Couette flow are chosen such that $PrEc = 4$, with the following variables set according to:

- $L = 0.83$ mm
- $T_0 = 293$ K
- $T_1 = 294$ K
- $U = 75.4$ m/s

Figure 5.9 shows the Couette flow domain and boundaries. Four different mesh refinements, 9x9, 9x17, 9x33 and 9x65, are used just because the only way asymptotic convergence can be demonstrated is to compute three solutions [1]. All velocity and temperature distributions presented are obtained for a vertical line just in the middle of the domain. Nusselt number values are obtained at the center of the walls (ends of the middle line).
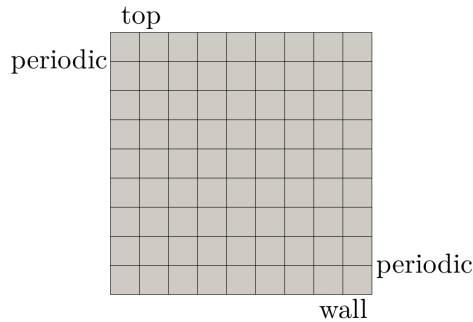
Figure 5.9: Couette Thermal flow domain, 9x9 mesh elements. Overall domain bounding box: (0 0 0) (0.00083 0.0001 0.00083) m.

In this case, instead of using comparison metrics, the velocity and temperature distributions along the vertical direction y are compared directly to the analytical solution, given by Equations (5.3) and (5.4). The wall heat transfer coefficient is an important quantity in engineering applications, and is generally expressed by the non-dimensional Nusselt number, which takes the following values (Equation (5.2)) at walls:

$$Nu = 1 + \frac{PrEc}{2} \quad \text{at} \quad y = 0$$
$$Nu = 1 - \frac{PrEc}{2} \quad \text{at} \quad y = L \tag{5.2}$$

$$u(y) = \frac{y}{L}U \tag{5.3}$$

$$T\left(y\right) = \left[1 + \frac{PrEc}{2}\left(1 - \frac{y}{L}\right)\right]\frac{y}{L}\left(T_1 - T_0\right) + T_0 \tag{5.4}$$

Case setup

Tables 5.12-5.15 present the boundary conditions used for Y_f, $\boldsymbol{U}$, T and p variables. k, ϵ and Σ are not required because fluid is considered as laminar.

Patch	Type	Value
wall	zeroGradient	-
top	zeroGradient	-

Table 5.12: Y_f boundary conditions for the Couette Thermal flow case.

Patch	Type	Value
wall	fixedValue	(0 0 0)
top	fixedValue	(75.4 0 0)

Table 5.13: $\boldsymbol{U}$ boundary conditions for the Couette Thermal flow case.

Patch	Type	Value
wall	fixedValue	293
top	fixedValue	294

Table 5.14: T boundary conditions for the Couette Thermal flow case.

Patch	Type	Value
wall	fixedValue	1e05
top	fixedValue	1e05

Table 5.15: p boundary conditions for the Couette Thermal flow case.

It is important to specify the right schemes to get a stable and consistent solution [1]. The temporal resolution has been limited by setting a maximum Courant number of CFL = 0.5. However, for this verification case only low order schemes of Table 5.5 are used.

Results

Figure 5.10 shows the velocity distributions in the wall-normal direction. It shows a perfect agreement with the analytical solution, even on coarse meshes. Figure 5.11 shows the temperature distributions in the wall-normal direction. The general agreement is also outstanding.

Although a set of comparison metrics is not given, the error in the maximum temperature and in the predicted Nusselt numbers can be provided as prove of the wealthiness of the solver. Table 5.16 shows all the information. As expected, the error is reduced if the mesh is refined, and an error lower
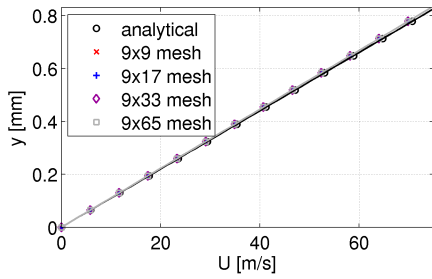
Figure 5.10: Line plot of the velocity vertical distribution for the Couette Thermal flow case.
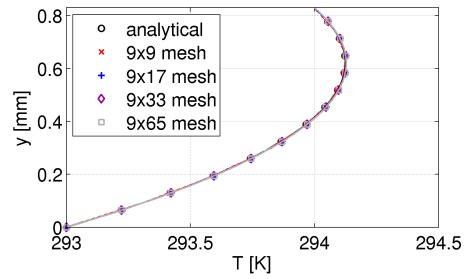
Figure 5.11: Line plot of the temperature vertical distribution for the Couette Thermal flow case.

than 5% can be obtained with a mesh having at least 33 grid cells in the wall-normal direction.

	Max. T [K]	Nu_{low}	Nu_{up}	Max. error [%]
Analytical	294.125	3	-1	-
9x9	294.125	2.816	-0.76799	23.20
9x17	294.128	2.880	-0.89598	10.40
9x33	294.128	2.944	-0.95998	4.00
9x65	294.128	3.008	-1.024	2.40

Table 5.16: Comparison metrics for the Couette Thermal flow case.

Finally, for the present solver, the same trends than in the test case of Ghia et al. [2] are observed in velocity and temperature profiles. Furthermore, errors in non-dimensional numbers and maximum temperature are lower than 5%. Thus, according to this test case, the solver is verified.

5.2.4 Converging-diverging verification (CDV) nozzle

This verification case is chosen simply because it is similar to a Diesel injector nozzle: flow moves forced by a pressure gradient inside a duct of variable cross-sectional area.

Problem description

As described by Slater [3], the converging-diverging verification (CDV) nozzle is a verification case involving the flow of inviscid, non-heat-conducting gas through a converging-diverging nozzle. The gas is assumed to satisfy the ideal gas relation, Equation (4.64). The gas is also assumed to have a constant ratio of specific heats ($\gamma = 1.4$). This is a classic one-dimensional, steady, compressible flow problem discussed in most compressible flow textbooks [15]. This case allows the verification of a CFD code in the following manner:

- verify through comparison with analytic solutions;
- verify mass conservation through a duct;
- verify of constancy of total pressure through a duct (isentropic flow);
- verify consistency of axisymetric and three-dimensional flow domains.

In this case, plenum total pressure and total temperature are assumed constant. The values used in this case are 6894.75 Pa of total pressure and 55.56 K of total temperature with the assumption of an inflow Mach number of 0.2. Two different values are used for the outlet pressure:

- $p_{out}/p_0 = 0.89$, subsonic, isentropic flow.
- $p_{out}/p_0 = 0.75$, supersonic normal shock in the diffusing section.

The geometry is an axisymetric converging-diverging duct. Figure 5.12 shows the CDV nozzle domain and boundaries. It has an area of 0.001613 m^2 at the inflow ($x = 0$ m), an area of 0.000645 m^2 at the throat ($x = 0.127$ m), and an area of 0.000968 m^2 at the outlet ($x = 0.254$ m). The nozzle area variation uses the cosine function of Equation (5.6). Three different mesh refinements, 51x31, 101x61 and 201x121 cells, are used.

$$
\begin{aligned}
A &= 0.001129 - 0.000484 \cos\left((0.0508x - 1)\,\pi\right), \ 0 \leq x < 0.127 \qquad (5.5)\\
A &= 0.000806 - 0.000161 \cos\left((0.0508x - 1)\,\pi\right), \ 0.127 \leq x \leq 0.254
\end{aligned}
$$

The comparison metrics consist of static pressure and Mach number distributions along the centerline (axis) of the nozzle as computed from one-dimensional, steady, inviscid, compressible flow theory [15].

inlet
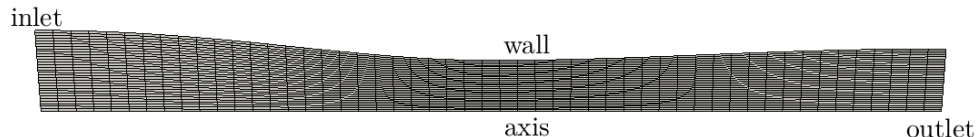
Figure 5.12: CDV nozzle domain, 51x31 mesh elements. Overall domain bounding box: (0 -0.000988 0) (0.254 0.000988 0.0226368) m.

Case setup

Tables 5.17-5.20 present the boundary conditions used for Y_f, $\boldsymbol{U}$, T and p variables[1]. The pressure value at the outlet depends on the case. k, ϵ and Σ are not required because turbulence is switched off. Temperature and velocity at the inlet are calculated to obtain a Mach number $M = 0.2$.

Patch	Type	Value
inlet	fixedValue	0
outlet	zeroGradient	-
wall	zeroGradient	-

Table 5.17: Y boundary conditions for the CDV nozzle case.

Patch	Type	Value
inlet	p.InletVelocity	(29.82 0 0)
outlet	zeroGradient	-
wall	slip	-

Table 5.18: $\boldsymbol{U}$ boundary conditions for the CDV nozzle case.

Patch	Type	Value
inlet	fixedValue	55.33
outlet	zeroGradient	-
wall	zeroGradient	-

Table 5.19: T boundary conditions for the CDV nozzle case.

Patch	Type	Value
inlet	fixedValue	6618.96
outlet	fixedValue	p_{out}
wall	zeroGradient	-

Table 5.20: p boundary conditions for the CDV nozzle case.

Gas properties such constant $R = 287$ m^2/(s$^2 \cdot$ K) or $c_p = 1039$ m^2/(s$^2 \cdot$ K) are introduced to the model. The rest of required parameters do not matter because they are not used in the simulation.

---

[1]The full name of the inlet boundary condition for the velocity is "pressureInletVelocity".

It is important to specify the right schemes to get a stable and consistent solution [1]. The temporal resolution has been limited by setting a maximum Courant number of CFL = 1.0. However and as done in the Couette thermal flow case, for this verification case only low order schemes of Table 5.5 are used.

Results

Figure 5.13 shows the pressure distribution along the centerline. The pressure variation along the CDV nozzles is well predicted, even on coarse meshes. Figure 5.14 shows the Mach number distribution, which is also well predicted. The maximum difference with the analytical solution is found at the throat in Figures 5.13a and 5.14a; and around the shock wave in Figures 5.13b and 5.14b. In this last case, the shock in the simulations is slightly moved toward the exit of the nozzle. Also observed in Sections §5.2.1 and §5.2.2, the shock becomes thinner as grid refinement increases. In general, there is a similarity between simulation results obtained by Slater [3] and current simulations.

(a) $p_{out}/p_0 = 0.89$.   (b) $p_{out}/p_0 = 0.75$.
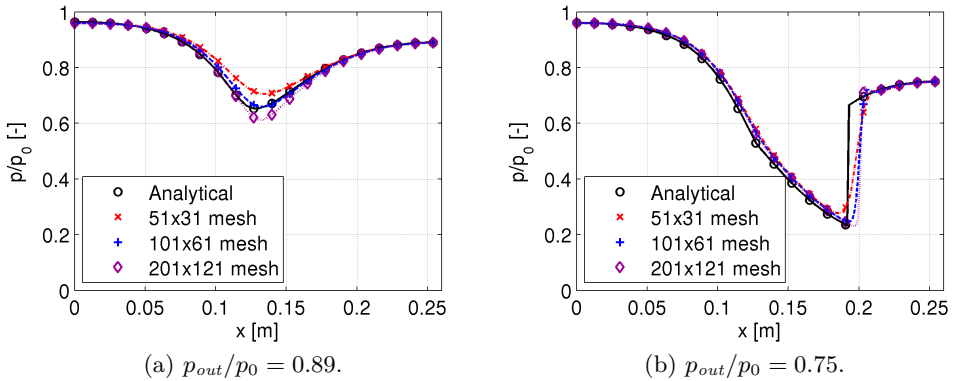
Figure 5.13: Pressure distribution along the axis of the CDV nozzle case.

Average and maximum errors of pressure and Mach number distributions are depicted in Table 5.21. The average error for the pressure remains always below 5%, and its maximum value for the subsonic, isentropic flow ($p_{out}/p_0 = 0.89$) is about 10% even on the coarsest mesh. The maximum error for the supersonic normal shock case ($p_{out}/p_0 = 0.75$) goes up to 65% but simply because the position of the shock it is not well captured, as seen

(a) $p_{out}/p_0 = 0.89$.

(b) $p_{out}/p_0 = 0.75$.
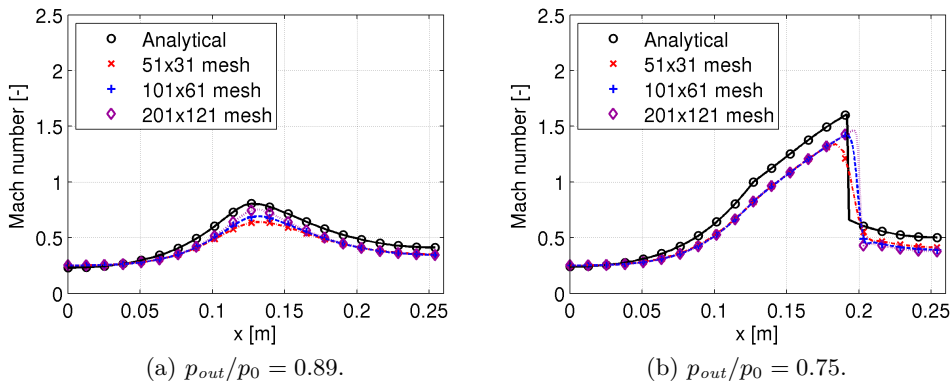
Figure 5.14: Mach number distribution along the axis of the CDV nozzle case.

in Figure 5.13b. Errors in Mach number are much larger, about 10% in average for the subsonic, isentropic flow case, and 17% for the supersonic normal shock case. The large values found for the maximum error in Mach number are again due to the incorrect position of the normal shock wave.

	p_{out}/p_0	Pressure error [%]		Mach number error [%]	
		Max.	Avg.	Max.	Avg.
51x31		10.21	2.05	21.98	13.76
101x61	0.89	3.66	0.78	16.85	12.58
201x121		6.92	1.17	16.19	11.20
51x31		50.16	4.55	64.66	13.48
101x61	0.75	63.07	4.15	114.11	16.05
201x121		66.10	4.19	129.33	17.90

Table 5.21: Comparison metrics for the CDV nozzle case.

Finally, for the present solver, the same trends than in the test case of Slater [3] are observed in pressure and Mach number profiles. Errors fall below the limits with a maximum average value of 10-20% (same limit than the steady-state oblique shock wave verification case described in Section §5.2.2). Thus, according to this text case, the solver is verified. Nonetheless, if this solver is used for solving normal shock waves (which is not the objective of the

present Thesis), a significant error in its position will be obtained, and then pressure and velocity distributions will not be very accurate.

5.2.5 Comparisons with DNS

DNS is a promising tool to improve the knowledge of break-up processes. It can be used to create a numerical experiment for region where no experimental data can be obtained [9]. In this case, results of Ménard et al. [10] are used as exact solution of the problem. Then, quantitative comparisons for the liquid volume fraction and the liquid surface density, which are the parameters controlling the break-up (see Section §4.4.1), are obtained.

Problem description

As described by Ménard et al. [10], incompressible liquid is injected at high speed into a quiescent atmosphere. Though in the original simulation the gas is assumed also incompressible, for the present calculation it satisfies the ideal gas relation, Equation (4.64). The gas is also assumed to have a constant ratio of specific heats ($\gamma = 1.4$).

Computational domain is a two-dimensional cylinder sector, 5° of wedge angle, with a radius of 6 mm and a length of 12 mm. It is larger than the one used by Ménard et al. [10] to ensure that boundary conditions do not affect the spray evolution. Three different mesh refinements are used just because the only way asymptotic convergence can be demonstrated is to compute three solutions [1]. The resolution is defined by the number of elements at the nozzle outlet: 5 (110x15), 10 (220x30) and 20 (440x60).

Liquid volume fraction profiles long time after start of injection, 0.5 ms, are taken as comparison metrics. In particular, profiles both in axial direction along the spray axis and in radial direction at three different positions, $x/D_o = 5, 10, 20$. Due to limitations of the gradient law closure to model the turbulent flux of the liquid ((4.35)), it is expected that the volume fraction to be underestimated along the axis until the distance form the injector reaches $8D_o$ [9]. Initial destabilization of the liquid surface is governed by linear instabilities just at the exit of the injector.

Case set-up

Tables 5.22-5.28 present the boundary conditions[2]. The turbulence model employed for this verification case is SST $k - \omega$ (see Section §5.3.5). The

---

[2]The full name of the outlet boundary condition for the velocity is "pressureInletOutletVelocity". The corresponding for the outlet pressure condition is "waveTransmissive".

turbulence intensity is equal to 5% of the mean inlet velocity, and the turbulent integral length-scale is 10 µm, 10% of the characteristic length-scale D_o.

Patch	Type	Value
inlet	fixedValue	1
outlet	zeroGradient	-
wall	zeroGradient	-
top	zeroGradient	-

Table 5.22: Y_f boundary conditions for the comparison with DNS case.

Patch	Type	Value
inlet	fixedValue	(100 0 0)
outlet	p.I.O.V.	(0 0 0)
wall	fixedValue	(0 0 0)
top	zeroGradient	-

Table 5.23: U boundary conditions for the comparison with DNS case.

Patch	Type	Value
inlet	fixedValue	298
outlet	zeroGradient	-
wall	fixedValue	298
top	zeroGradient	-

Table 5.24: T boundary conditions for the comparison with DNS case.

Patch	Type	Value
inlet	zeroGradient	-
outlet	zeroGradient	-
wall	zeroGradient	-
top	w.Transmissive	2.14e06

Table 5.25: p boundary conditions for the comparison with DNS case.

Patch	Type	Value
inlet	fixedValue	37.5
outlet	zeroGradient	-
wall	wallFunction	37.5
top	zeroGradient	-

Table 5.26: k boundary conditions for the comparison with DNS case.

Patch	Type	Value
inlet	fixedValue	1.118e06
outlet	zeroGradient	-
wall	wallFunction	1.118e06
top	zeroGradient	-

Table 5.27: ω boundary conditions for the comparison with DNS case.

The full domain is initialized with constant value for each variable matching discharge conditions: pure gas ($Y_f = 0$ and $\Sigma = 0$), zero velocity, 298 K of temperature, 2.14 MPa of pressure, and inlet turbulence levels.

Gas properties such constant $R = 287$ m^2/(s^2 K), viscosity $\nu_g = 4\,10^{-7}$ m^2/s, heat capacity at constant pressure $c_{p,g} = 1006$ m^2/(s^2 K) and

Patch	Type	Value
inlet	fixedValue	0
outlet	zeroGradient	-
wall	fixedValue	0
top	zeroGradient	-

Table 5.28: Σ boundary conditions for the comparison with DNS case.

Prandtl number $Pr_g = 0.708$ are introduced to the model. Liquid properties too, including density $\rho_f = 696$ kg/m^3, viscosity $\nu_f = 1.7241 \ 10^{-6}$ m^2/s, heat capacity at constant pressure $c_{p,f} = 2201.46$ m^2/(s^2 K), surface tension $\sigma = 0.06$ kg/m^2 and Prandtl number $Pr_f = 7$. The Schmidt number is set to $Sc = 1$.

It is important to specify the right schemes to get a stable and consistent solution [1]. The temporal resolution is limited by setting a maximum Courant number of CFL $= 1.0$. Maximum number of outer loops (SIMPLE) is set to 5 and the selected number of inner loops (PISO) is 2. However and as done in the two previous cases, for this verification case only low order schemes of Table 5.5 are used.

Results

The axial profiles of liquid volume fraction are shown in Figure 5.15. As commented by Lebas et al. [9], reference results are obtained after averaging over 0.1 ms after the stabilization of the injection, however statistical convergence is not perfectly reached yet. Nonetheless, the main trend is already well established. The decay in liquid volume fraction is well predicted by the model even on very coarse meshes. As expected, the error is reduced if the mesh is refined. Though, some oscillations are seen for the finest mesh.

Apparently, the volume fraction in not underestimated along the axis until the distance form the injector reaches $8D_o$. This means that the correction proposed by Demoulin et al. [16] (see Section §4.4.1) for the gradient law closure to model the turbulent works well at zones very close to the orifice outlet, at least better than only the gradient law closure used by Lebas et al. [9].

Figure 5.16 represents the radial profiles of the volume fraction. Quantitatively good agreement is obtained with respect to the reference data from
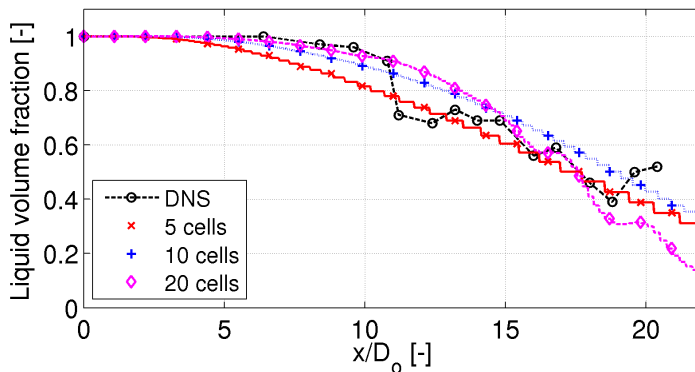
Figure 5.15: Axial profile of the liquid volume fraction for the comparison with DNS case.

DNS in near the nozzle, but the model tends to underestimate the liquid volume fraction far from the outlet. Steps formed by the lines in this figure and also in Figure 5.15 are due to values at cells are taken from the computational solution.

Liquid volume fraction fields are presented in Figure 5.17. The main behavior of the spray is well captured by the model. It shows the possibility to describe the liquid dispersion and mixing induced by complex primary breakup phenomena through a statistical approach and classical turbulence models.

Mean surface density fields are compared in Figure 5.18. As already commented in Section §4.4.1, there exist in the literature several approaches to compute the surface density Σ, and all of them have constants that need to be tuned. Though levels of surface density are clearly over-predicted by the model, results are very encouraging. Without any tuning, patterns are well predicted, and as the mesh is refined the predicted solution gets closer to DNS results. However, a closer look to the data shows a difference on the intensity in the vicinity of the injector. In Figure 5.17a the interface surface is perfectly smooth and cylindrical just at the exit of the orifice, but current simulations give a more spread contour in that area. This means that they do not predict the intact initial part of the spray, which makes sense because the mixing model estates that the liquid diffusion is proportional to the concentration gradient, higher at just at the exit of the orifice. This result is consistent with the literature [9]. Another drawback of the comparison concerns the values along the axis of the spray that do not seem similar between DNS and the

(a) $x/D_o = 5$.

(b) $x/D_o = 10$.

(c) $x/D_o = 20$.
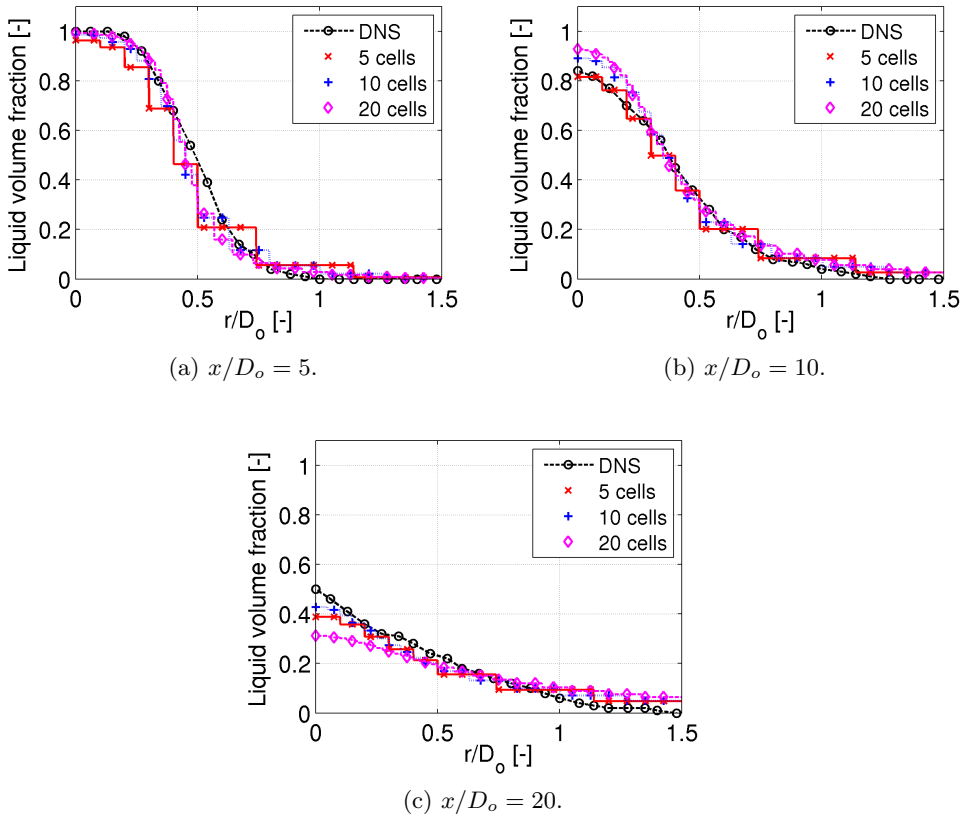
Figure 5.16: Radial profiles of the liquid volume fraction for the comparison with DNS case.

present model. For instance, the length with no presence of interface surface density is much shorter in DNS.

Nevertheless, inter-facial surface density equation is decoupled from the rest of the transport equations, meaning that results obtained for Σ do not affect the rest of fluid variables. Then, constant parameters of Equation (4.24) can be tuned to match DNS results independently from the rest of the code (done in Section §6.2).

Finally, and though some clear differences are found between the present model and DNS results, a general good agreement is achieved for the liquid volume fraction. Thus, according to this test case, the solver is verified.

(a) DNS results.

(b) Mesh with 5 cells at outlet.

(c) Mesh with 10 cells at outlet.

(d) Mesh with 20 cells at outlet.
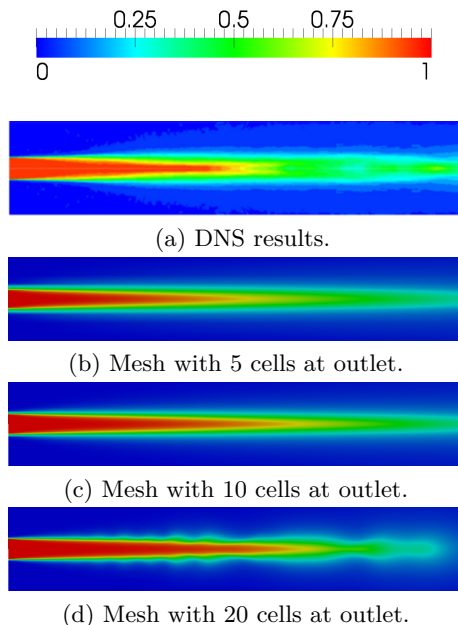
Figure 5.17: Contours of the liquid volume fraction for the comparison with DNS case.

(a) DNS results.

(b) Mesh with 5 cells at outlet.

(c) Mesh with 10 cells at outlet.

(d) Mesh with 20 cells at outlet.
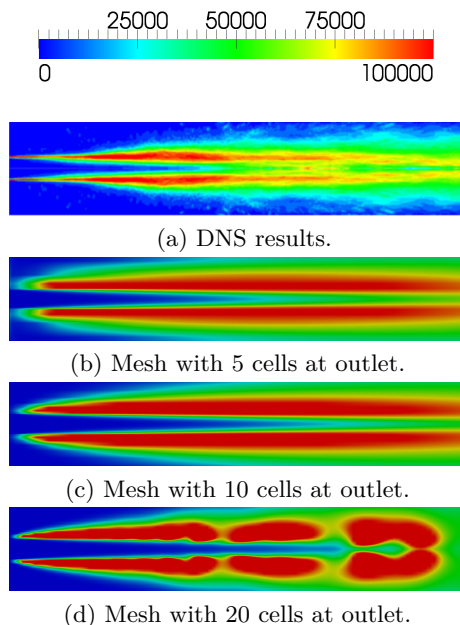
Figure 5.18: Contours of the interface surface density for the comparison with DNS case.

5.3 Validation assessment

Although individual computational outcomes of a model are validated, codes are not. Thus, a validation database (or validation experimental hierarchy) is necessary [1].

Instead of creating a new validation database, which is expensive and in most complex systems infeasible and impractical [1], an experimental database is selected from the literature. Concretely, the one created by Gimeno [17] for his Ph. D. Thesis. So all experimental results shown in this section can be found in his work.

5.3.1 Problem description and case set-up

Validation geometry

Three different micro-sac single-hole nozzle with the orifice oriented along the injector axis were selected for the experimental study. Single-hole Diesel

injectors have been used in fundamental spray research, while most DI engines use multi-hole nozzle to tailor to the combustion chamber geometry. The shape of the orifice is conic, and the nozzles were submitted to HEG processes to increase the entrance radius. Both characteristics help to avoid cavitation.

Silicone mold technique [18] was employed to obtain all values of geometric parameters of the nozzle. This methodology is based on the extraction of silicone molds of the nozzle and their visualization in either an optical or a scanning electron microscope. The images obtained by the microscope are then processed by using a computer aided design software. Results are summarized in Table 5.29. The repeatability error is 2% for the diameters and about 25% for the entrance radius.

Nozzle	L/D_o [-]	r_e [µm]	D_i [µm]	D_o [µm]	AR [%]
A	8.93	42	140	112	36.0
B	7.25	47	167	138	31.7
C	6.41	49	195	156	36.0

Table 5.29: Internal geometry parameters of single-hole nozzles used for validation.

In order to determine the geometry of the needle seat to properly generate the domain, pictures of the needle were taken with an optical microscope and overlapped to those ones of the silicone molds. The needle of the injector is a truncated cone with an angle of 60° and a base radius of 52 µm. The needle movement is not included in the model, therefore the needle is placed always at its maximum needle lift of $nl_{max} = 0.4$ mm.

Figure 5.19 shows an example of the computational domain[3] used for validation. Due to symmetry of the geometry, the mesh covers only a wedge sector of 5° and is considered two-dimensional. The external flow part of the domain is not the common rectangle found in the literature [19, 20], but a truncated cone, as done by Friedrich and Weigand [21]. The upper line has a slope of 15°. This allows obtaining very fine mesh right at the orifice outlet and large elements far from it with a reduced number of divisions in the radial direction.

---

[3]The generation of the domain and the mesh has been programmed (in a script) in such way that changing any geometric parameter, i.e. the entrance radius or number of elements, is fast and easy.
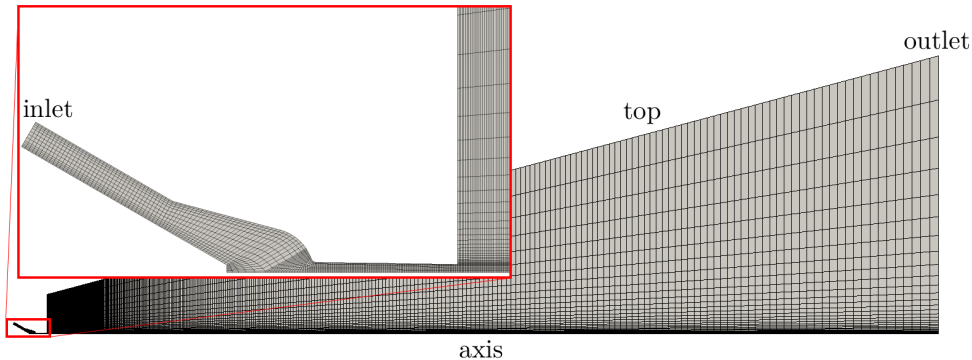
Figure 5.19: Validation single-hole domain, nozzle A, low resolution mesh. Overall domain bounding box: (0 -0.001090 0) (0.083063 0.001090 0.024976) m.

Due to the simplicity of the domain, it is possible to build a structured mesh with hexahedral elements. This type of mesh improves stability and convergence of the solution [22]. When needed (i.e. at a radial distance equal to the orifice exit diameter), the element size in the radial direction is smaller than the size in the axial direction. This allows to capture large pressure, velocity and concentration gradients with a reduced mesh size [22].

Case set-up

Boundaries of the domain are indicated in Figure 5.19. Their values must reproduce the experimental conditions, for example, the fuel temperature in the nozzle. Table 5.30 shows the test matrix. All experiments were performed under isothermal conditions, so the temperature is constant and equal to 306 K.

Injection pressure [MPa]	30 - 80 - 130
Back pressure [MPa]	2.27 - 2.95 - 3.63
Ambient gas density [kg/ m^3]	25 - 32.5 - 40
Energizing time [µs]	1000

Table 5.30: Test matrix of the validation database.

It is important to check if test points are included within the scope of the model. The main hypothesis is that Reynolds and Weber number are large

and therefore large-scale features of the flow are independent of the small-scale ones (see Section §4.2.1). Then, both dimensionless number must be high enough that the full atomization regime is reached. As explained in Section §2.4.1, borders between atomization regimes are not clear nor exact, however a limiting Weber number is a criteria commonly accepted. Figure 5.20 represents the atomization regimes borders together with the test points for the three different nozzles (note that it is the same than Figure 2.14). All points are included into fully atomization regime. For lower ambient gas densities, i.e. $\rho_g = 10\,\text{kg}/\,\text{m}^3$, points corresponding to $p_i = 30\,\text{MPa}$ for the three nozzles fall into the second wind atomization regime.
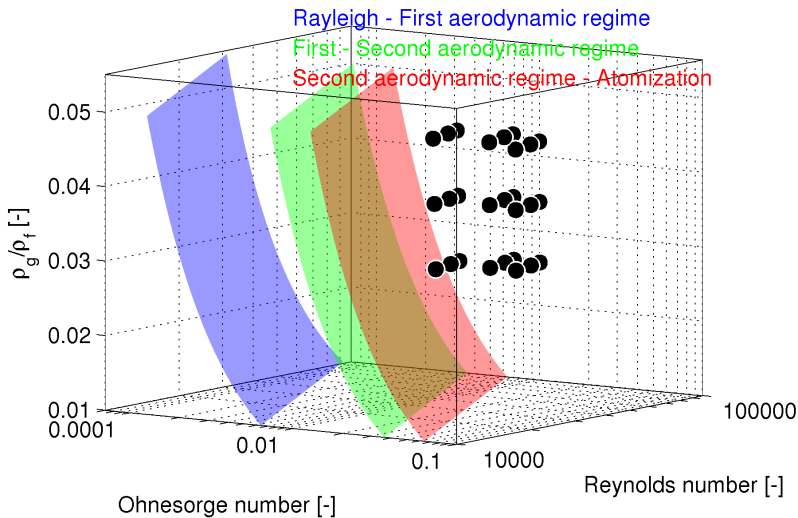
Figure 5.20: Schematic representation of the different atomization regimes including the test points of the validation database.

Lines without a name in Figure 5.19 are walls, representing the needle, the nozzle and the vessel. Non-slip condition is used for the velocity with standard wall functions for k and ϵ or ω; and "zeroGradient" or Neumann condition for the rest of variables. Tables 5.31-5.37 present the rest of boundary conditions[4]. Regardless the turbulence model selected, the turbulence intensity is equal to 5% of the mean inlet velocity, and the turbulent integral length-scale 10% of the inlet length.

---

[4]The full name of the inlet boundary condition for k and ϵ is "uniformFixedValue", which represents a time varying value.

Patch	Type	Value
inlet	fixedValue	1
outlet	zeroGradient	-
top	zeroGradient	-

Table 5.31: Y_f boundary conditions for the single-hole validation case.

Patch	Type	Value
inlet	*undefined*	*value*
outlet	p.I.O.V.	(0 0 0)
top	zeroGradient	-

Table 5.32: $\boldsymbol{U}$ boundary conditions for the single-hole validation case.

Patch	Type	Value
inlet	fixedValue	306
outlet	zeroGradient	-
top	zeroGradient	-

Table 5.33: T boundary conditions for the single-hole validation case.

Patch	Type	Value
inlet	*undefined*	*value*
outlet	w.Transmissive	p_b
top	zeroGradient	-

Table 5.34: p boundary conditions for the single-hole validation case.

Patch	Type	Value
inlet	u.fixedValue	file
outlet	zeroGradient	-
top	zeroGradient	-

Table 5.35: k boundary conditions for the single-hole validation case.

Patch	Type	Value
inlet	u.FixedValue	file
outlet	zeroGradient	-
top	zeroGradient	-

Table 5.36: ϵ boundary conditions for the single-hole validation case.

Gas (Nitrogen) properties such constant $R = 296.9\,\mathrm{m^2/(s^2\,K)}$, viscosity $\nu_g = 1.46\ 10^{-5}\,\mathrm{m^2/s}$, specific heat capacity at constant pressure $c_{p,g} = 1100.6\,\mathrm{m^2/(s^2\,K)}$ and Prandtl number $Pr_g = 0.7$ are introduced to the model. Liquid properties too. In the experiments, standard Diesel Elite$^+$ fuel was used, whose density and speed of sound were characterized by Payri et al. [23] (see Section §4.4.2). However, enthalpy as function of pressure and temperature (Equation (4.85)) is not known for a multicomponent surrogate such standard Diesel. The heat capacity at constant pressure $c_{p,f} = 2717.8\,\mathrm{m^2/(s^2\,K)}$ at reference conditions ($T_{ref} = 298\,\mathrm{K}$ and $p_{ref} = 0.1\,\mathrm{MPa}$) is used as C_2 coefficient of Equation (4.85); and values of n-Dodecane (Table 4.18) are used for the rest of coefficients. Surface tension $\sigma = 0.0289\,\mathrm{kg/m^2}$ and Prandtl number $Pr_f = 7$ are also introduced, and the Schmidt number is set to $Sc = 1$.

Patch	Type	Value
inlet	fixedValue	0
outlet	zeroGradient	-
top	zeroGradient	-

Table 5.37: Σ boundary conditions for the single-hole validation case.

The temporal resolution is limited by setting a maximum Courant number of CFL $= 0.2 - 1.0$ depending on the case, lower values for higher injection pressures. Maximum number of outer loops (SIMPLE) is set to 20 and the selected number of inner loops (PISO) is 1. For the validation cases only low order schemes of Table 5.5 are used. Linear solvers for partial differential equations are the same than for the verification cases, PBiCG with DILU as preconditioner for all variables but for the pressure, where PCG is used with DIC as preconditioner. The absolute tolerance is 10^{-15}. A relaxation factor of 0.3 is used for the pressure and a factor of 0.7 for the rest of variables but the density, which is solved without relaxation.

Many comparison metrics can be defined. In this case, dimensionless discharge, area and velocity coefficients are used in addition to spray penetration and spray angle time evolutions (see Sections §2.3.3 and §2.4.3). The spray penetration is calculated as defined by the Engine Combustion Network, the further distance along the injector axis having a liquid volume fraction higher than 0.1% [24]. The spray angle is calculated as the angle included by the lines fitting the two sides of the spray up to 60% of the spray penetration [17].

Chart of Figure 5.20 can be used to reduce the number of simulations in the validation assessment. Originally, up to 27 simulations are required, the 27 points in the figure, corresponding to 3 injection pressures, 3 ambient densities and 3 different nozzles. These points form a cubic shape. Because of spray parameter follow a monotonous trend with the ambient conditions within the selected range [17], e.g. mass flow rate and spray penetration always increase when the injection pressure does, just the most extreme points can be selected for validation. The point right in the middle of the cube is also selected as control point. Thus, the 27 points of the validation matrix are reduced to only 9.

Initialization

The internal flow in initialized fulfilled with liquid ($Y_f = 1$) with pressure equal to the back pressure p_b and zero velocity. Temperature is constant and equal to the ambient temperature T_b for the whole domain. The external flow is also stagnated (zero velocity, no cross-flow) at the beginning [25, 26].

The turbulent variables k and ϵ are initialized with the same values for the whole domain, defined by the conditions at the inlet. It is assumed that the inlet turbulence is isentropic and estimate fluctuations to be 5% of the inlet velocity. The turbulent length scale l_t is estimated to be 10% of the width of the inlet.

This way of initialization is the most similar to the real conditions found when the needle of the injector reaches its maximum lift, which is the simulated situation. Probably, the velocity field is the one that differs most from the real field due to transients effects during the opening, where the liquid is accelerated and fills the sac and the orifice.

However, recent studies have proved the presence of both gas and fuel in the sac before start of injection [27], though the amount of each one could not be estimated. Tests on a single-hole nozzle showed that bubbles are promoted by: larger orifice size, higher injection pressure and lower back pressure. Therefore, the best initialization would include both phases inside the nozzle; and this helps to obtain a more realistic velocity field once the nozzle is filled with liquid.

5.3.2 External flow simplified case

Before simulating the full case described in previous Section §5.3.1, an external flow case is studied. In other words, only a spray case is calculated and analyzed in this section. In this direction, García-Oliver et al. [20] also used Gimeno's [17] experimental database to carry out the validation of an Eulerian model, called in the literature $\Sigma - Y$ model (see Section §3.6). Their work is exactly reproduced employing the ESA model. This is very useful to check the capability of the model in simulating Diesel sprays.

Case set-up

A two-dimensional axisymmetric computational domain with 80x25 mm extent in axial and radial directions is considered. The mesh is structured with non-uniform grid resolution. There are 10 cells along the orifice diameter, keeping an aspect ratio close to 1 in the near nozzle region, as depicted in Figure 5.21. A mesh size convergence study was performed in order to achieve

grid-independent results. The mesh used in the calculations has 450x80 cells, with a cell expansion ratio of 1.01 and 1.06 in the axial and radial directions, respectively.
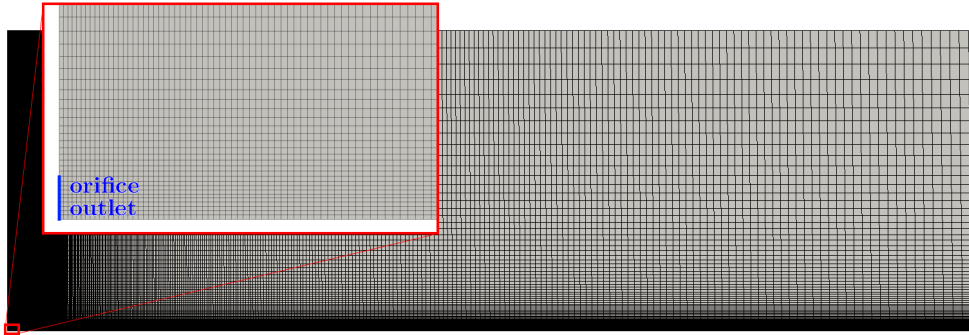
Figure 5.21: External flow validation domain, nozzle A. Overall domain bounding box: (0 0 -0.002171) (0.079812 0.024824 0.002172) m.

A Gamma NVD scheme is used for discretization of divergence terms and a first order Euler scheme is applied for time derivative terms. The inlet velocity boundary condition is obtained from mass flow rate measurements, and a constant radial profile of axial velocity and density are assumed at the orifice outlet. The turbulent intensity was set to 5% and the length scale to 10% of the nozzle diameter.

The high density ratio $k - \epsilon$ turbulence model is used. Due to the well know round jet spreading over-prediction of $k - \epsilon$ type models [28], a different value of constant C_1 than the one on Table 4.21 is used, concretely $C_1 = 1.60$. A turbulent Schmidt number $Sc_t = 0.9$ is used for the liquid mass fraction transport equation closure term.

Simulated injection conditions correspond to nozzle A, an injection pressure of $p_i = 80\,\mathrm{MPa}$, and ambient density of $\rho_g = 40\,\mathrm{kg/m^3}$. That point is included within the test matrix of Table 5.30 but not among the 9 cases that are simulated for the validation assessment.

The rest of the numerical configuration of the case, i.e. liquid and gas thermodynamic properties, is the same than the one explained in the previous sub-section.

Results

External flow parameters, spray penetration and spray angle, are shown in Figure 5.22. Very good agreement with experimental results is obtained in terms of spray penetration, the largest difference of about 5% is found at long time aSOI. This difference is explained by the evolution of the spray angle shown in Figure 5.22b, the experimental value slightly grows whilst the computational one $\theta = 15°$ remains constant.

(a) Spray penetration.

(b) Spray angle.
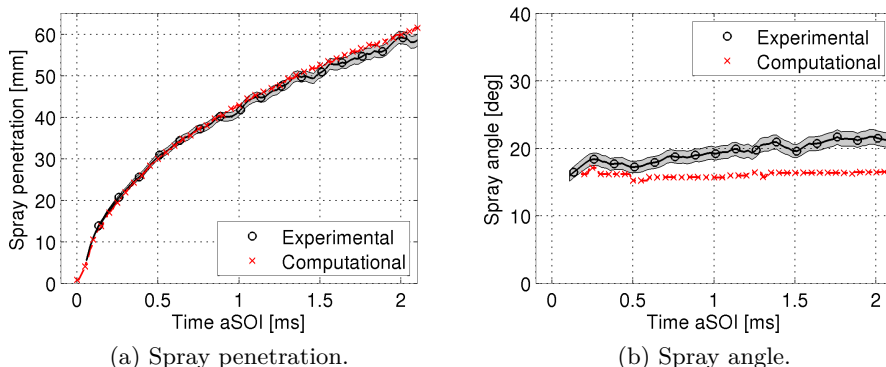
Figure 5.22: Spray penetration and angle of the external flow study compared with experimental data.

Though any other comparison metric has been defined, further analysis can be done. As in the work of García-Oliver et al. [20], the agreement shown in Figure 5.23 between the computational axial velocity and the experimental values indicates very low slip between phases, at least for the simulated conditions and measurement locations. Experimental data used for this and the following couple of figures was obtained by Payri et al. [29] applying the phase-Doppler anemometry technique.

Radial profiles of axial velocity plotted in Figure 5.24 prove that the model is able to reproduce not only the axial evolution but also the radial one. It is also observed in this figure that self-similar velocity profiles are obtained for both measurements and calculations at different axial positions, though some differences can be observed for radial positions larger than $r/x = 0.1$, both in the experiments and in the simulations.

So far, only large-scale parameters of the spray have been shown. Small-scale atomization characteristics, given by the inter-facial surface density Σ
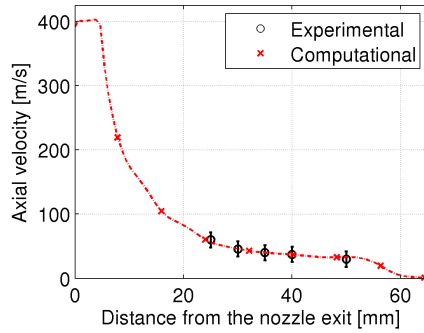
Figure 5.23: Axial velocity along the spray axis of the external flow study compared with experimental data.
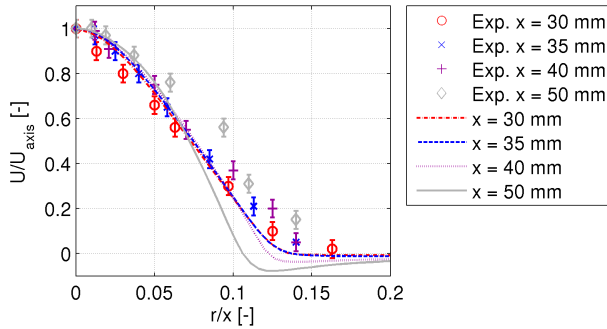
Figure 5.24: Radial profiles of axial velocity of the external flow study compared with experimental data.

and so the droplet size derived from this variable, should be analyzed. However, the optimization of inter-facial surface density transport equation (Equation (4.24)) constants has not been done yet, so high differences with experimental values are expected.

Figure 5.25 shows the predicted spray SMD contour, where smaller droplet sizes appear just downstream the liquid core, and after that SMD increases progressively with axial distance. Such droplet size increase, which has been experimentally observed in non-evaporating sprays [30, 31], is usually attributed to coalescence.

That increase in droplet size is compared with experiments in Figure 5.26.
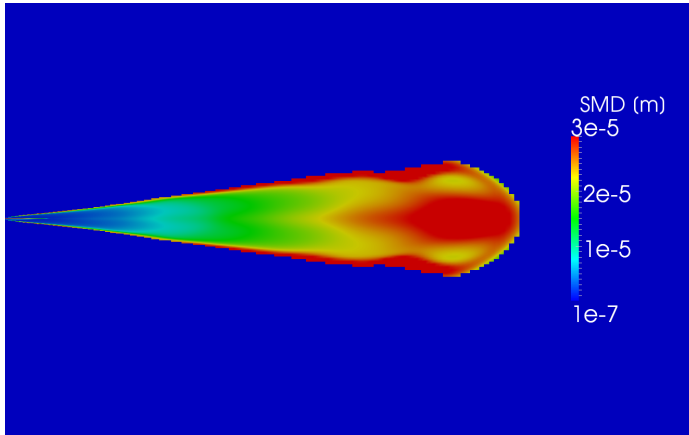
Figure 5.25: Calculated SMD contours of the external flow study. Only the spray ($Y_f < 0.001$) has been coloured.

As observed, the real increase in droplet size is smaller than in the simulations, which emphasizes the necessity of an optimization of inter-facial surface density transport equation constants. Despite that, overall values and trends are well predicted by the model.
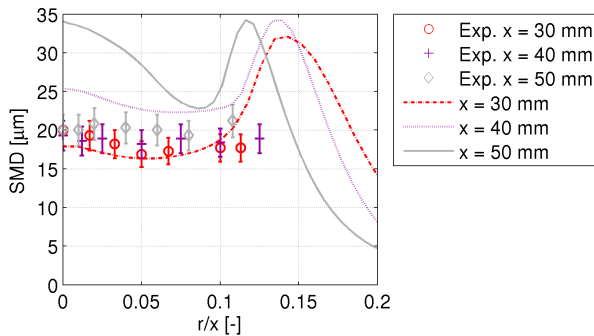
Figure 5.26: Radial profiles of SMD of the external flow study compared with experimental data.

In general, very good agreement with experiments in all studied parameters is found. Therefore, this preliminary validation case considering only the spray (external flow) encourages further validation and extent use of the developed ESA model.

5.3.3 Mesh sensitivity: nozzle flow and spray

Prior to any further analysis, mesh sensitivity of the full domain (the nozzle plus the discharge volume) has to be studied to ensure that the solution is not dependent on grid structure and resolution. The mesh sensitivity study has been divided in two parts: first, the number of elements inside the nozzle is increased; and once this study is finished, the number of elements in the discharge volume is varied.

As the turbulence is taken into account through a RANS model, it is important to have at least a few cells inside the boundary layer. The non-dimensional wall distance for a wall-bounded flow y^+ needs to be checked out. Medium and outlet sections of the orifice are selected to compute the y^+ value. According to the literature, for standard or non-equilibrium wall functions, y^+ values should fall between 30 and 300 next to the wall [32]. Definitely, the mesh should be made either coarse or fine enough to prevent the wall adjacent cells from being placed in the buffer layer ($y^+ = 5$ to 30). The best turbulence model has not been selected yet. Nonetheless standard $k - \epsilon$ is used for this study.

Nozzle A is selected to perform this analysis. Only one injection condition is taken; one which gives large velocities and large concentration gradients, in other words, the worst numerical condition: injection pressure of $p_i = 130\,\mathrm{MPa}$ and ambient density of $\rho_g = 10\,\mathrm{kg/m^3}$ (back pressure $p_b = 0.9\,\mathrm{MPa}$). The best inlet boundary condition has not been selected yet. Nonetheless, non-reflexive constant pressure ("waveTransmisive") boundary condition is applied at both inlet and outlet, with the velocity calculated from the flux normal to the patch.

A criteria for the mesh independence is required. In this case, the difference in comparison metrics previously defined between two following mesh resolutions must be lower than 1%.

Nozzle mesh

Typically, the internal geometry mesh is characterized by the number of elements at the orifice exit section (in radial direction), and the axial number of elements is defined in such way that squared elements are obtained around the injector axis. Table 5.38 depicts all meshes that have been tested, named with the number of elements at the orifice exit and the total number of elements of the mesh.

Figure 5.27 shows steady state dimensionless coefficients for all the meshes tested. They are calculated as an average for the last 0.5 ms of the simulation.

	Elements at orifice exit	Total elements
mesh_9_18k	9	18828
mesh_18_24k	18	24541
mesh_36_36k	36	36068
mesh_72_59k	72	59230
mesh_72_72k	72	73802
mesh_72_88k	72	88374
mesh_108_125k	108	125790

Table 5.38: Internal mesh resolutions tested in the mesh sensitivity study.

Red dashed lines represent a variation of 1% of the value of the finest mesh. The difference between meshes "mesh_72_88k" and "mesh_108_125k" is within the accepted limit, but computational cost of mesh "mesh_72_88k" is much lower, so this is the one selected for the nozzle discretization.

Values of the non-dimensional wall distance y^+ of the first element next to the wall are depicted in Table 5.39. They are obtained at the orifice exit section, where velocities are higher. Only the coarsest mesh gives a y^+ value in the must avoid range, the rest of them fulfill the requirement of having at least a few cells inside the boundary layer preventing the wall adjacent cells being in the buffer layer.

	y^+ [-]
mesh_9_18k	14.04
mesh_18_24k	4.54
mesh_36_36k	2.63
mesh_72_59k	3.02
mesh_72_72k	3.81
mesh_72_88k	3.41
mesh_108_125k	2.85

Table 5.39: y^+ values next to the wall at orifice exit section for all mesh resolutions tested in the nozzle mesh sensitivity study.

(a) Area coefficient.

(b) Velocity coefficient

(c) Discharge coefficient.
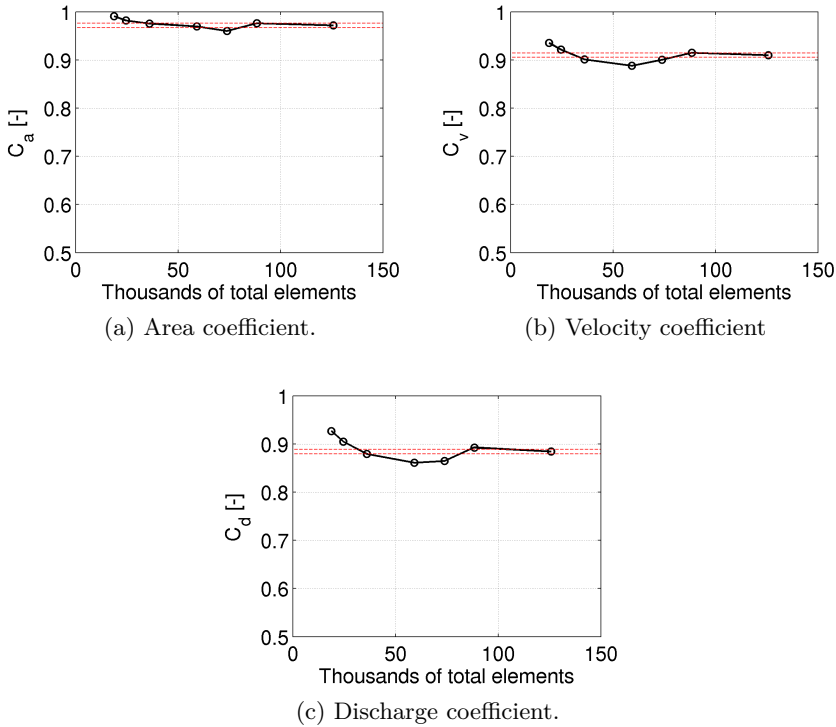
Figure 5.27: Dimensionless coefficients versus the total number of elements of the internal mesh sensitivity study. Dashed lines represent acceptable limits.

External mesh

External flow meshes are characterized by the number of elements in axial and radial directions. Mesh used by García-Oliver et al. [20], described in Section §5.3.2, is the starting point. Meshes shown in Table 5.40 are tested. They are named with the number of elements in both directions. Note that, firstly, the number of elements in the axial direction is increased, and later the number of elements in the radial direction is; so both directions can be analyzed independently.

Comparison metrics of the external flow, spray penetration and angle, are time dependent. Thus, for comparison purposes, differences between meshes are averaged for the whole simulation duration. Results are summarized in Table 5.41. Regardless that the differences in spray angle do not fall below the established limit of 1%, further increase in mesh resolution leads to an exces-

	Axial elements	Radial elements	Total elements
mesh_335_30	335	30	78174
mesh_435_30	435	30	88374
mesh_500_30	500	30	95004
mesh_435_60	435	60	101424
mesh_435_90	435	90	114474

Table 5.40: External mesh resolutions tested in the mesh sensitivity study.

sive increase in computational cost. Furthermore, no clear trend of reducing the error in the spray angle is observed. Then, mesh resolution of 435x60 is selected because it presents an averaged difference in penetration with the finest mesh below 1%.

	Averaged difference [%]	
	Penetration	Angle
mesh_335_30	-	-
mesh_435_30	8.89	23.92
mesh_500_30	0.63	5.75
mesh_435_30	-	-
mesh_435_60	6.27	5.80
mesh_435_90	0.79	8.92

Table 5.41: Averaged differences in comparison metrics between mesh resolutions of the external mesh sensitivity study.

In order to further ensure grid convergence, various other quantities are investigated, as done by Som et al. [33]. In particular, spray centerline turbulent kinetic energy k, turbulent viscosity ν_t, turbulent length-scale l_t, and turbulent time-scales τ_k, which are presented as functions of spray axis (since most of the turbulence inside the discharge chamber is generated due to the spray injection) in Figure 5.28. The turbulent length-scale l_t and time-scale τ_k are given by Equations (5.6) and (5.7), correspondingly, where C_μ is one of the turbulence model constants, usually $C_\mu = 0.09$. Note that meshes 435x30 and 500x30 are quite similar in all parameters, and meshes 435x60 and 435x90 are identical, prove of grid convergence of the solution. For all the meshes, tur-

bulent length-scales predicted are larger than cell sizes used, so the smallest, or at least the most important, scales are resolved in all cases.

$$l_t = C_\mu \frac{k^{\frac{3}{2}}}{\epsilon} \tag{5.6}$$

$$\tau_k = \frac{k}{\epsilon} \tag{5.7}$$

(a) Turbulent kinetic energy.

(b) Turbulent viscosity.

(c) Turbulent length scale.

(d) Turbulent time scale.
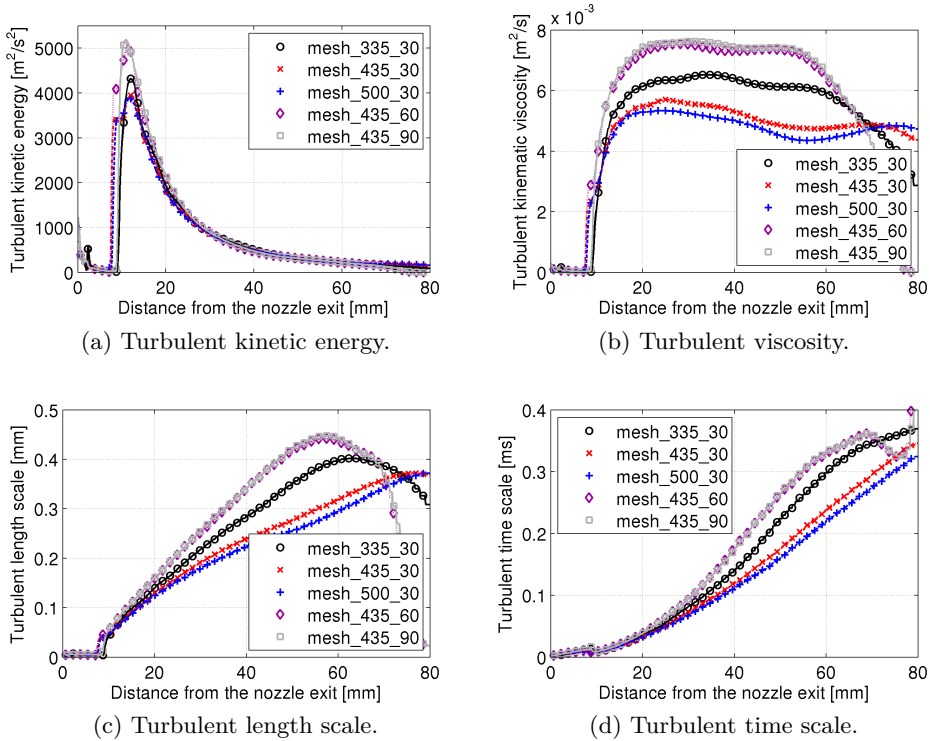
Figure 5.28: Various quantities related to turbulence distributions along the spray axis of injection at 1 ms after SOI of the external mesh sensitivity study.

Turbulent length-scale of Figure 5.28c follows the same trend than the one obtained by Som et al. [33], reaching approximately the same maximum values, taking into account that the injection conditions are not exactly the same. The main difference is found in the first millimeters of the spray; the present model predicts much lower length-scale. The intact core maintains the turbulent

length-scale from the internal flow, which is an order of magnitude lower. This behavior is not captured by the Eulerian-Lagrangian model employed by Som et al. [33]. Turbulent time-scale of Figure 5.28d also follows the same trend than the one obtained by Som et al. [33] but maximum values are two orders of magnitude larger. Regarding the turbulent viscosity, profiles are completely different. Figure 5.28b presents a more or less constant value meanwhile Som et al. [33] obtain a raising curve, similar to that of turbulent length-scale. Also the values are quite different, two orders of magnitude lower in Figure 5.28b. Finally, comparing turbulent kinetic energy profiles an interesting result is obtained. In Figure 5.28a, the maximum value is found right after the intact core length, where the break-up is completed, and from there a decrease in turbulence level is obtained. That is not the case for Som et al. [33], who obtain a quick raise in the first millimeters and then the value is more or less constant. Even so, maximum values in both cases are in the same order of magnitude. All of these differences can be attributed to the different approach used to model the two-phase flow, but also to the different turbulence model.

Decomposition for running in parallel

The method of parallel computing used by OpenFOAM is known as domain decomposition, in which the geometry and associated fields are broken into pieces and allocated to separate processors for solution. Application can then run in parallel on separate sub-domains. The parallel running uses the public domain openMPI implementation of the standard message passing interface (MPI). Apparently, OpenFOAM scales well (linear trend) up to at least 1000 CPUs.

There are several methods of decomposition, some of them are listed below:

- Simple: simple geometric decomposition in which the domain is split into pieces by direction, e.g. 2 pieces in the x-direction, 1 in y.

- Hierarchical: is the same as simple except that the order in which the directional split is done, e.g. first in the y-direction, then the y-direction.

- Scotch: requires no geometric input and attempts to minimize the number of processor boundaries. A weighting for the decomposition between processors can be specified. There is also a strategy (bi-partitioning, mapping, ordering) that controls the decomposition through a complex string supplied to Scotch.

The selection of one method or another is based in the following partitioning constraints:

- Load balance: all processing units should have approximately the same amount of work between communication and synchronization points.

- Minimum communication, relative to local work. Performing local computations is orders of magnitude faster than communicating the data.

Comparison in load balance between Simple and Scotch methods is presented in Figure 5.29. Figure 5.29a shows the cell count of each processing unit as function of the number of decompositions. It is observed that using more than 20 processing units does not give a relevant drop in the amount of work for each one, e.g. the difference between 21 and 24 CPUs is only 600 cells. The difference between the two models is seen better in Figure 5.29b. Simple method gives exactly the same number of cells for each processing unit meanwhile with Scotch method differences of about 2-8% are obtained to minimize the number of processor boundaries.

(a) Cell count.   (b) Cell count differences.
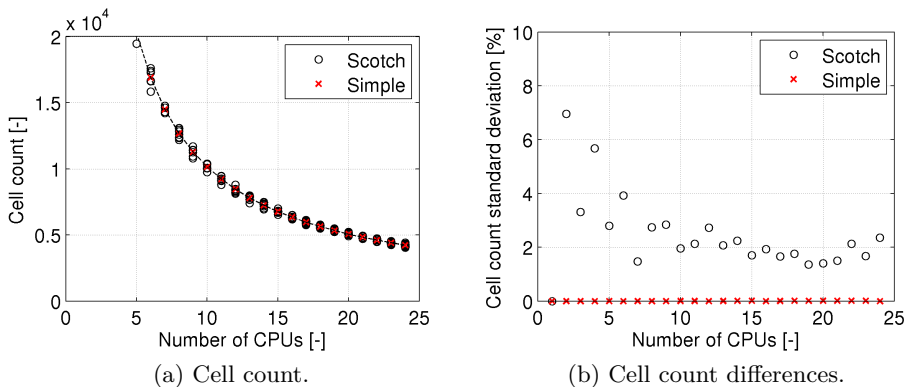
Figure 5.29: Cell count of different methods for decomposing the mesh and the domain in OpenFOAM.

Then, if a low number (less than 6-8) of processing units is used, where local computations take much longer than the communication time, Simple method is recommended. Otherwise, Scotch method should be employed despite its small load disequilibrium.

5.3.4 Selection of inlet boundary condition

When simulating internal flows of Diesel injectors, the common choice for the inlet boundary condition is to fix the injection pressure [25, 34, 35]. An

alternative to avoid pressure wave reflections that take place in compressible fluids and still being able to fix the pressure is to use a non-reflective constant pressure boundary condition, often found as outlet boundary.

When simulating external flow, in other words, the spray, the most employed inlet boundary condition is specifying the velocity, which varies with time in order to reproduce the experimental mass flow rate shape [25, 34, 36]. If it is available, the spatial distribution is used, but if not, same velocity value is imposed for the whole inlet section. The value of the velocity is obtained experimentally by means of the mass flow rate with Equation (2.20), where ρ_f is assumed constant and A_{eff} is taken as the geometrical exit section area [37, 38].

Summarizing, three types of inlet boundary condition are tested:

- Constant pressure.
- Non-reflective constant pressure (with different grades of reflection).
- Time varying velocity.

Non-reflective condition deserves extra attention. It performs some basic thermodynamic calculations and tries to create a tendency toward the preset value. The larger the grade of reflection, the further the boundary condition will deviate form the specified value. However, the smaller the grade of reflection, the more reflective the boundary tends to be. Thus, 0.01, 0.05 and 0.50 have been tested as values of grade of reflection.

Nozzle A is selected to perform also this analysis. Again, only one injection condition is taken; in this case an injection pressure of $p_i = 30\,\text{MPa}$ and ambient density of $\rho_g = 40\,\text{kg}/\,\text{m}^3$ (back pressure $p_b = 3.6\,\text{MPa}$), which is the point in the test matrix with the lowest injection velocity and therefore lowest computational cost (for the same CFL number, it gives the highest time-step value). The best turbulence model was not selected by the time this study was performed, therefore standard $k - \epsilon$ is used.

Nozzle flow

Table 5.42 shows values of the dimensionless coefficients compared to experiments. All conditions predict experimental values with an error lower than 10% except the non-reflective one with a grade of reflection of 0.50. This high grade of reflection is dismissed because it gives values for the coefficients higher than the unity, what has no physical sense. As shown next, the pressure at the

inlet continuously increases, beyond the experimental value, then increasing the velocities inside the nozzle, so mass flow rate and momentum flux. The reflection factor of 0.50 is too large. Among the rest of the boundaries, time varying velocity and non-reflective with grade of reflection 0.05 have values closer to experimental ones than the other two.

Inlet boundary	C_a [-]	C_v [-]	C_d [-]
Experimental	0.95	0.89	0.85
Constant pressure	0.94	0.84	0.79
Varying velocity	0.94	0.87	0.82
Non-reflective 0.01	0.94	0.85	0.80
Non-reflective 0.05	0.94	0.87	0.82
Non-reflective 0.50	0.95	1.07	1.02

Table 5.42: Steady state dimensionless internal flow comparison metrics of the inlet boundary condition study.

In this case, not only steady state values are relevant, also the time evolution of mass flow rate should be predicted. Figure 5.30 represents the mass flow rate of all inlet conditions together with the experimental value. From now on, the standard deviation of the experiments is represented as a shadow region; though in this case it cannot be clearly seen because it is only $\pm 0.5\%$ of the measurement [39]. Two observations can be drawn. First one concerns the oscillations at the inlet of for the constant pressure condition, which are damped inside the nozzle and disappear with time. They are generated by the wave that bounces and travels up and down from the inlet (fixed pressure) to the orifice outlet. Regardless the physical sense of these oscillations, such gradients could lead to numerical divergence of the solution. Obviously, these oscillations are not present with the non-reflective condition because pressure waves can travel through the inlet (no bouncing).

The second observation corresponds to the rising slope of the mass flow rate. Pressure boundaries do not predict this rising at all because the needle movement is not taken into account. Mass flow rate is not limited by the area inside the nozzle and then it reaches its steady value immediately. By imposing the velocity, the mass flow rate obtained is slightly shifted, delayed, compared to the experimental curve. This is associated to compressibility effects that take place inside the nozzle. As the liquid is compressible, pressure waves travel up and down, accelerating the fluid, and it takes some time until the right velocity in every section of the nozzle is reached. In future studies, these
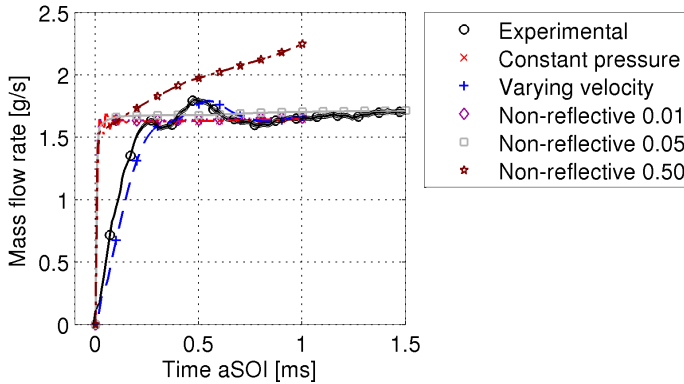
Figure 5.30: Mass flow rate of inlet boundary condition study compared with experimental data.

effects can be taken into account before starting the simulation and set the mass flow rate and the nozzle inlet that gives exactly the experimental curve at the orifice outlet.

External flow

So far, only the internal flow has been analyzed. However a change on the inlet boundary condition also affects external flow parameters such spray penetration or spray angle, plotted in Figure 5.31. All pressure conditions, constant value and non-reflective, present the same penetration and spray angle. Time varying conditions gives similar values but shifted in time.

When compared with experiments, penetration curve slope is almost the same, but the value of the spray angle is over-predicted by about $3 - 4°$ (nonetheless, if a different experimental definition of spray angle is used, a similar difference can be obtained). As commented in Section §2.4.3, the penetration law is split in two, following a linear trend with time in the first millimeters. The time t_b at which the break-up is completed is about $t_b = 0.13$ ms for both experiments and simulations, whilst Equation (2.47) gives a value of $t_b = 0.0834$ ms and Equation (2.49) a value of $t_b = 0.0903$ ms (dashed line in Figure 5.31a).

A very interesting result is the behavior of the penetration given by the time varying velocity for very short time after start of injection. In the simulation, a parabolic shape is obtained first, then a linear trend, and after certain
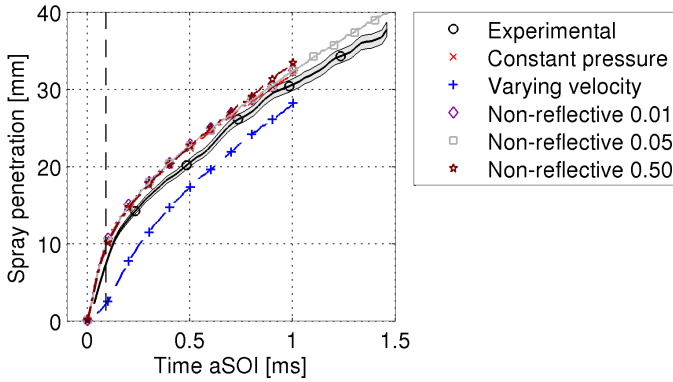
(a) Spray penetration.
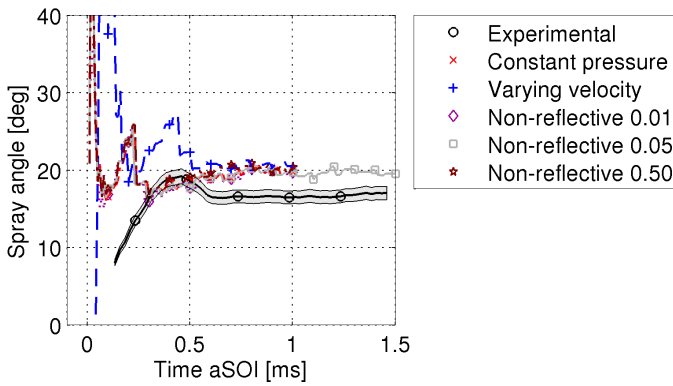
(b) Spray angle.

Figure 5.31: Spray penetration and angle of inlet boundary condition study compared with experimental data.

time t_b the penetration becomes proportional to the square root of time. This change in the slope is not present in the experimental curve because no measurements in the near field were made by Gimeno [17], notwithstanding other authors, for example Morena [40], have experimentally observed that behavior, but with a much faster transient between the parabolic and the linear trends.

Conclusion

Taking into account all the results previously explained, the time varying velocity boundary condition for fixing the mass flow rate at the inlet of the domain is the most suitable boundary condition for the inlet among the ones tested. This conditions estimates well the mass flow rate and spray tip penetration without oscillations which could lead to divergence. Furthermore, the pressure in the sac cannot be experimentally measured, it could be estimated from the pressure in the common-rail through a model of the injector losses [41]. The main drawback of this boundary condition is that the mass flow rate has to be previously experimentally measured and, in the future, corrected to exactly match the experimental value.

With this boundary condition, experimental curve shows a faster penetration than computational ones earlier than about 0.4 ms after start of injection. This is due to the initialization procedure; the nozzle is initialized with zero velocity but filled with liquid notwithstanding in reality, when the sac and orifice are filled with fuel there is non-zero velocity. If the model is used to simulate only external flow, with the right time varying inlet velocity boundary condition, the obtained penetration curve matches exactly the experimental one for short and long time after start of injection, as proved in Section §5.3.2.

5.3.5   Selection of turbulence model

Turbulence modeling has been already explained in Section §4.4.4. Although those models are still in active area of research, all four are selected for being tested in the present model. Additionally, Realizable $k - \epsilon$ model, available in OpenFOAM libraries is also tested. Summarizing:

- Standard compressible $k - \epsilon$ model.
- High density ratio $k - \epsilon$ model.
- Re-Normalization Group (RNG) $k - \epsilon$ model.
- Realizable $k - \epsilon$ model.
- Shear Stress Transport (SST) $k - \omega$ model.

Nozzle A is selected to perform also this analysis. As for the selection of the inlet boundary condition, only one injection condition is taken; an injection pressure of $p_i = 30$ MPa and ambient density of $\rho_g = 40$ kg/ m^3 (back pressure $p_b = 3.6$ MPa), which is the point in the test matrix with the lowest injection velocity and therefore lowest computational cost. The best inlet boundary

condition was not selected by the time this study was performed, therefore non-reflective constant pressure with a grade of reflection of 0.05 is used.

Nozzle flow

First parameters to be analyzed are the dimensionless coefficients that define the nature of the flow of the nozzle. Table 5.43 shows their steady state values compared with experimental ones. SST $k - \omega$ and Realizable $k - \epsilon$ models clearly overestimate all parameters. The reason of that is commented later. RNG $k - \epsilon$ model slightly over-predicts the velocity coefficient and under-predicts the area coefficient. The other two $k - \epsilon$ models predict well all coefficients, with a maximum deviation of 3%.

Turbulence model	C_a [-]	C_v [-]	C_d [-]
Experimental	0.95	0.89	0.85
Standard $k - \epsilon$	0.94	0.87	0.82
High density ratio $k - \epsilon$	0.94	0.87	0.82
RNG $k - \epsilon$	0.94	0.90	0.85
Realizable $k - \epsilon$	0.97	1.00	0.97
SST $k - \omega$	0.97	0.98	0.96

Table 5.43: Steady state dimensionless internal flow comparison metrics of the turbulence model study.

Figure 5.32 shows the velocity profile at the exit of the orifice. Standard and high density ratio $k - \epsilon$ models have the same profile, small area at the center of the orifice with constant velocity and large area with a parabolic shape. This is characteristic of laminar/low Reynolds number flow. With the RNG $k - \epsilon$ the parabolic region is reduced, and even further reduced with the SST $k - \omega$ or Realizable $k - \epsilon$ models, which shows a typical profile of turbulent/high Reynolds number flow [38, 42]. These two last models seem better than the rest because the model assumes very high Reynolds number, although they overestimate all dimensionless coefficients.

Velocity profiles of Figure 5.32 explain why SST $k - \omega$ and Realizable $k - \epsilon$ models give higher mass flow rate and momentum flux for the same value of the inlet pressure, therefore higher values of area, velocity and discharge coefficients. At this point it is worthy to mention that LES could improve the accuracy on the prediction of the velocity up to an error of 0.6% [35], with a steeper velocity profile nest to walls.
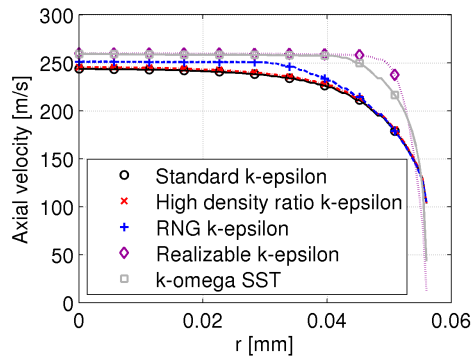
Figure 5.32: Velocity profile at the exit of the orifice of the turbulence model study.

Figure 5.33 proves that, as expected, standard and high density ratio $k - \epsilon$ models generate the same turbulence levels inside the nozzle. There is not large density change, so both models should be the same. RNG $k - \epsilon$ and SST $k - \omega$ models, which are generally recommended for simulating wall-bounded flows, produce a completely different turbulent viscosity contour, with values of at least one order of magnitude lower. The maximum value, though not seen in Figures 5.33c and 5.33e because of the scale, is reached towards the nozzle inlet due to the imposed value and also next to the orifice walls, where the boundary layer grows. In the other models, the maximum value is reached at the orifice entrance. The distribution obtained by LES [35] looks like Figures 5.33c and 5.33e. The fifth model, Realizable $k - \epsilon$, generates a turbulent viscosity pattern which is a mixture of the others, intermediate values with maximum at the nozzle and orifice inlets. Thus, according these results, RNG $k - \epsilon$ and SST $k - \omega$ turbulence models seem better than the rest once again.

External flow

Turbulent viscosity contours of the external flow are plotted in Figure 5.34. Notice that the scale is not the same than in Figure 5.33, turbulence levels in the spray are higher than in the nozzle. The turbulent intensity generated by standard and high density ratio $k - \epsilon$ models is lower than the other three models. Since the turbulent viscosity is directly related to the air-fuel mixing (Equation (4.35)) this figure can also be used to analyze the spray structure. First thing to notice is that Realizable $k - \epsilon$ model does not show the typical

(a) Standard $k - \epsilon$.

(b) High density ratio $k - \epsilon$.

(c) RNG $k - \epsilon$.

(d) Realizable $k - \epsilon$.

(e) SST $k - \omega$.
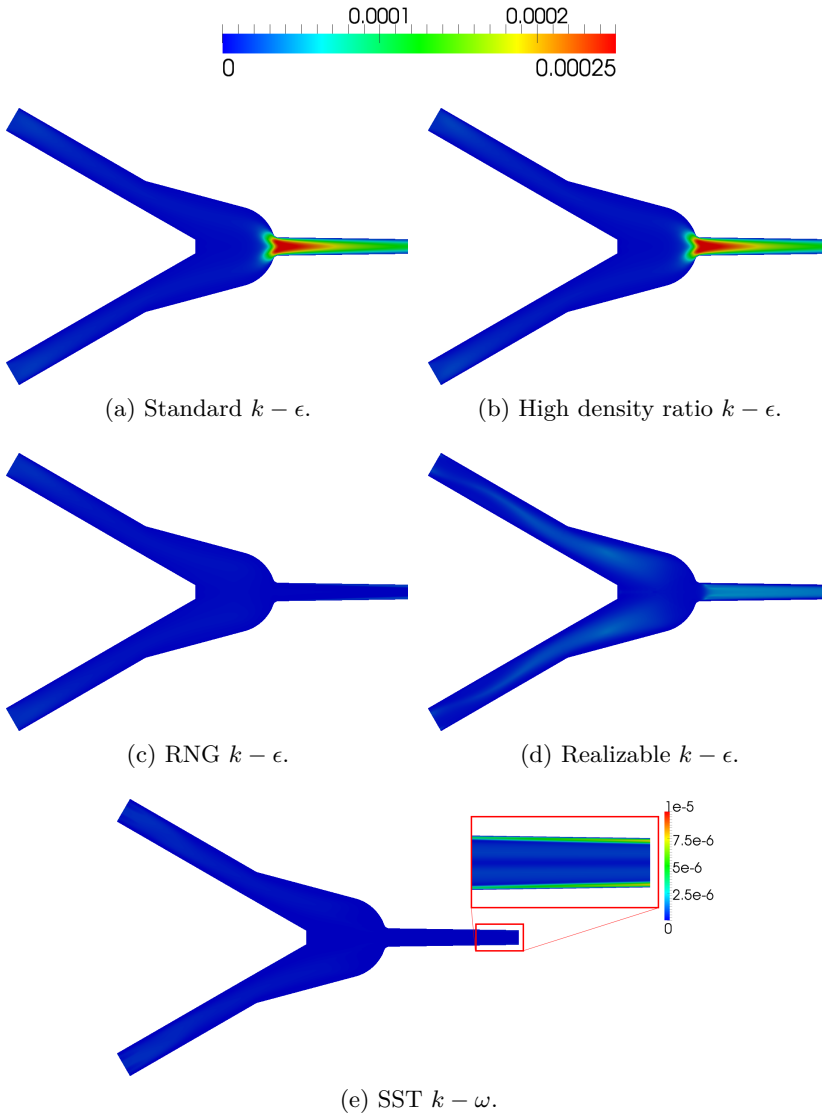
Figure 5.33: Turbulent viscosity contours inside the nozzle for the turbulence model study. Time of all images is 1 ms after start of injection.

spray contour, so it does not seem correct. RNG $k - \epsilon$ model shows wider spray and a strange spray tip structure, which is not seen in the experiments. Standard and high density ratio $k - \epsilon$ seem to correct that behavior but still a kind of mixing blob is found at the spray tip. This blob is eliminated with

SST $k - \omega$ model, which gives the typical spray structure and also the highest turbulent intensity.

(a) Standard $k - \epsilon$.

(b) High density ratio $k - \epsilon$.

(c) RNG $k - \epsilon$.

(d) Realizable $k - \epsilon$.

(e) SST $k - \omega$.
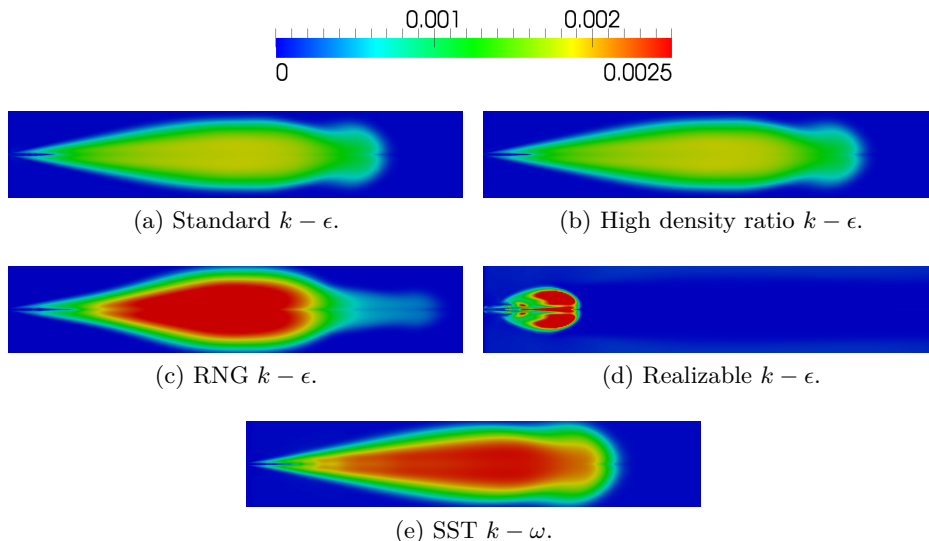
Figure 5.34: Turbulent viscosity contours on the spray for the turbulence model study. Time of all images is 1 ms after start of injection. The size of the images is 40 mm in length and 7 mm in height.

Continuing the external flow analysis, Figure 5.35 shows spray penetration and angle for the five turbulence models tested. It is seen that none of them agrees with the experimental spray angle, though this is not really important because as already commented the spray angle strongly depends on the visualization technique employed, the intensity of the light, the post-processing method of the images (i.e. the threshold), the criteria used for its definition, etc.

The spray penetration seems to be well predicted by all models but the RNG and Realizable $k - \epsilon$. The mixing blob observed in Figure 5.34c leads to a longer penetration for the RNG $k - \epsilon$. Maybe adjusting turbulence model constants could fix this discrepancy, as done by Hoyas et al. [36]. However, the Realizable $k - \epsilon$ produces, as already seen in Figure 5.34d, a completely different spray structure. The spray angle does not reach a steady state value and the penetration presents a linear trend for the whole time simulated.
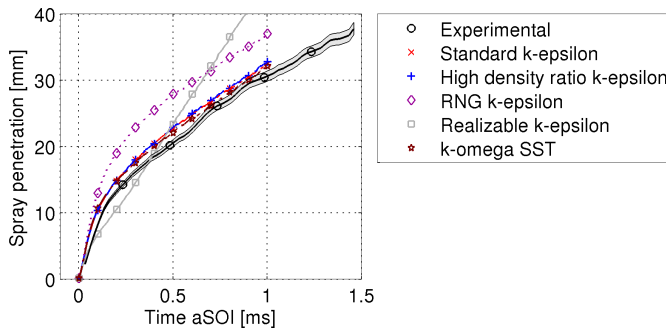
(a) Spray penetration.
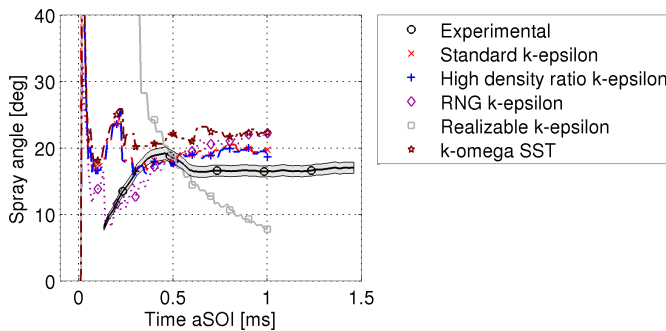
(b) Spray angle.

Figure 5.35: Spray penetration and angle of the turbulence model study compared with experimental data.

Conclusion

Taking into account all the results previously explained, the SST $k-\omega$ turbulence model is the most suitable among the ones tested for the present model. Although it clearly overestimates dimensionless area, velocity and discharge coefficients, the velocity profile at the exit of the orifice fits better the theoretical one assumed by Payri et al. [38] and also the results obtained with LES [42]. Mismatch with experiments is probably due to the pressure value at the nozzle inlet which actually has to be lower than in the common-rail, there are head losses in all conducts and volumes that connect the rail with the nozzle, including the injector.

Use of wall functions

If the flow remains attached, then generally a wall function approach can be used, which means a larger y^+ value, smaller overall mesh count and faster run times. If separation is expected, and the accurate prediction of the separation point will have an impact, then it is better to resolve the boundary layer all the way with a finer mesh.

No separation is expected in the problem which is going to be solved, but the mesh sensitivity study leads to a very fine mesh near walls (Section §5.3.3). Thus, the use of wall function may or not be correct. In order to check this, a case with standard wall functions is compared to a case without them. The case selected is one of the already presented, used in both inlet boundary condition and turbulence model studies: nozzle A, injection pressure of $p_i = 30\,\mathrm{MPa}$, ambient density of $\rho_g = 40\,\mathrm{kg/m^3}$ (back pressure $p_b = 3.6\,\mathrm{MPa}$), non-reflective pressure with a grade of reflection of 0.05 as inlet boundary, and standard $k - \epsilon$ as turbulence model.

Significant differences are found. For instance, at the medium section of the orifice it is obtained $y^+ = 2.89$ with wall function and $y^+ = 1.35$ without them. Both values are within the limits. Also, shorter penetration and lower mass flow rate is obtained without the use of wall functions. These results can be explained by the velocity profile at the orifice exit, depicted in Figure 5.36. The typical parabolic profile raising from $0\,\mathrm{m/s}$ at walls to the constant maximum velocity at the center of the section is not obtained without wall functions. Instead a strange, kind of linear, evolution is seen with values lower than the profile obtained using wall functions. These lower velocity values at the orifice exit drive to lower mass flow rate and spray penetration.

As explained in Section §2.4.1, the reorganization of the velocity profile is one of the factors accounted as atomization mechanisms of the primary atomization. Then, different velocity profiles at the orifice outlet may present different liquid mass fraction distributions in the near field. Figure 5.37 presents the contours of the liquid mass fraction near the orifice outlet. Without wall functions a longer intact length (liquid mass fraction close to unity) is obtained, with smaller oscillations of its interface. In Figure 5.37a right at the orifice outlet, some liquid sticks to the wall of the discharge volume, phenomena that is not experimentally observed [40]. This means that wall functions must be used for the present model. Nonetheless, this small test about the convenience of using wall functions should be repeated for sharp orifice inlet geometries, where flow separation is expected. This phenomena may be not well captured by, at least, the standard wall functions.
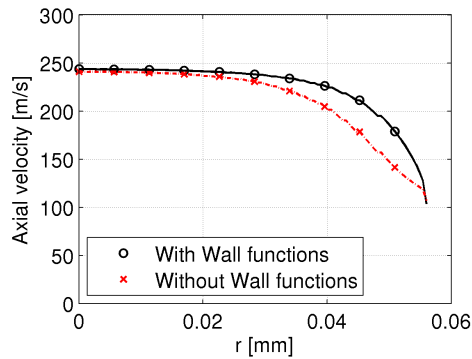
Figure 5.36: Velocity profile at the exit of the orifice of the use of wall functions study.

(a) Without wall functions.   (b) With standard wall functions.
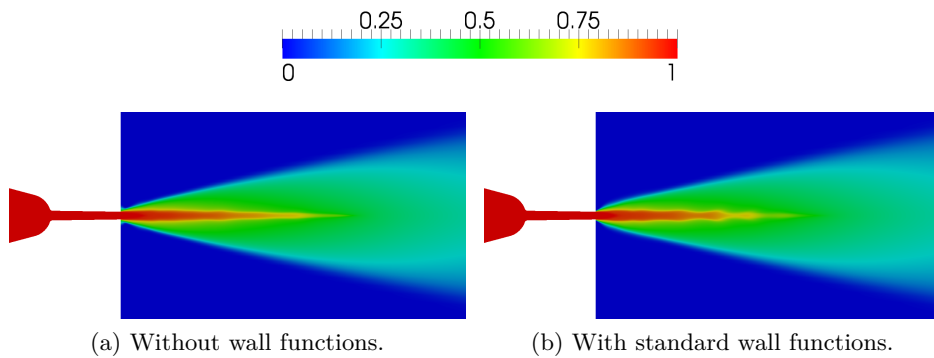
Figure 5.37: Liquid mass fraction contours of the use of wall functions study. Time of all images is 1 ms after start of injection. The size of the discharge volume is 8 mm in length and 3 mm in height.

As an additional conclusion to the necessity of using wall functions, the present model, somehow, takes into account the rearrangement of the cross-sectional velocity profile of the jet ant the boundary layer profile relaxation phenomena effects.

5.3.6   Experimental benchmark

Mesh independence is ensured, and the error is minimized by selecting the optimum inlet boundary condition and the best turbulence model. At that point, the case is ready to perform the validation itself, and compare computational solutions with the experimental benchmark of Gimeno [17].

Nozzle flow

Again, first parameters to be analyzed are the dimensionless coefficients that define the nature of the flow inside the nozzle. Table 5.44 shows their steady state values compared with experimental ones. As expected from the turbulence model selection (Section §5.3.5), the area coefficient is well predicted in all cases, with a maximum difference with experiments lower than 3%. However, the velocity coefficient is under-predicted with an error that ranges from 2% to 10%. This error is smaller for cases with higher injection pressure. This under-prediction in the velocity coefficient leads to a similar error in the discharge coefficient.

Nozzle	A	A	A	A	B	C	C	C	C
p_i [MPa]	30	30	130	130	80	30	30	130	130
ρ_g [kg/ m^3]	25	40	25	40	32.5	25	40	25	40
Exp. C_a [-]	0.95	0.95	0.98	0.98	0.98	0.96	0.96	0.99	0.98
C_a [-]	0.97	0.98	0.98	0.98	0.97	0.99	0.98	0.99	0.99
Exp. C_v [-]	0.89	0.89	0.91	0.91	0.91	0.91	0.91	0.93	0.93
C_v [-]	0.80	0.82	0.89	0.89	0.86	0.83	0.85	0.90	0.90
Exp. C_d [-]	0.85	0.85	0.89	0.89	0.90	0.87	0.87	0.91	0.91
C_d [-]	0.78	0.80	0.87	0.88	0.84	0.81	0.83	0.89	0.88

Table 5.44: Steady state dimensionless internal flow comparison metrics of all validation cases.

Underestimation of the velocity coefficient is a common result when using RANS turbulence model for simulating the internal flow of Diesel injectors [42, 43]. The velocity profile at the orifice outlet shows the typical square profile of turbulent flows but with a more parabolic shape in the viscous boundary layer, as shown in Figure 5.32. According to Payri et al. [42], LES models could improve the accuracy on the prediction of the velocity coefficient in 10% by improving the prediction in the velocity profile at the exit.

Figure 5.38 represents the mass flow rate of all injection conditions together with corresponding experimental values. Curves for the same injection pressure and different ambient densities almost overlap, both in experiments and simulations. For low injection pressure, experimental and computational results are the same except for a small initial delay, already seen in Figure 5.30 and explained in Section §5.3.4. The same should happen for high injection pressure, experimental and computational curves should almost overlap each

other, but the delay is much greater, about 0.3 ms for both nozzles A and C.
This means that the delay is not related to the geometry but to the initial and
boundary conditions. Looking at Figure 5.38, a constant pressure boundary
condition seems more appropriate when simulating high injection pressures.
Still, initial rise slope could not be generated, so most likely the best option is
to correct the inlet velocity profile to obtain the right one at the orifice exit.
If the needle movement could be simulated, all these issues would disappear
[44].
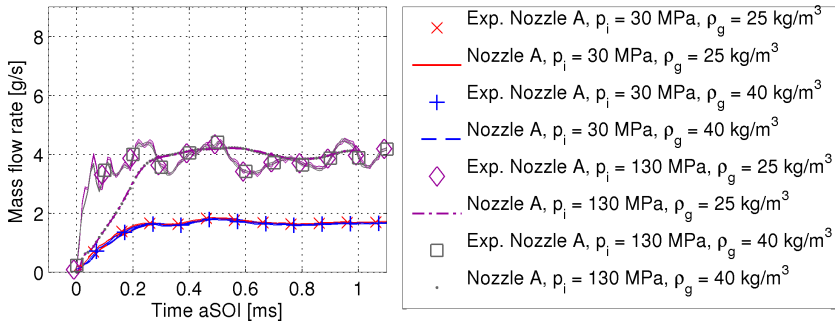
(a) Nozzle A.
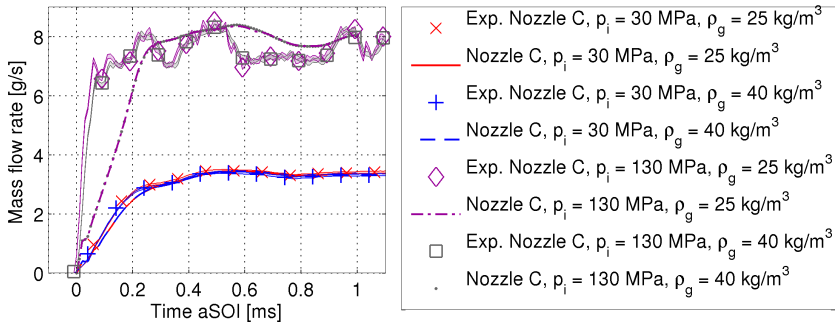
(b) Nozzle C.

Figure 5.38: Mass flow rate for two nozzles of the validation assessment.

External flow

Spray penetration for nozzles A and C under all injection conditions is plotted
in Figure 5.39. Simulations results match experiments after certain time aSOI.
The penetration slope is captured almost perfectly except for long time aSOI,
when computations predict faster spray penetration.
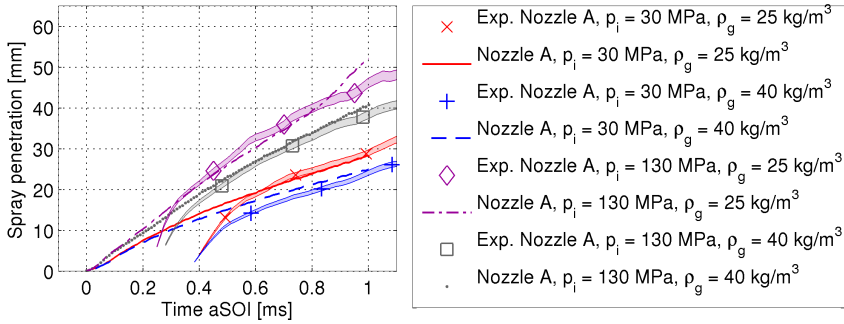
(a) Nozzle A.
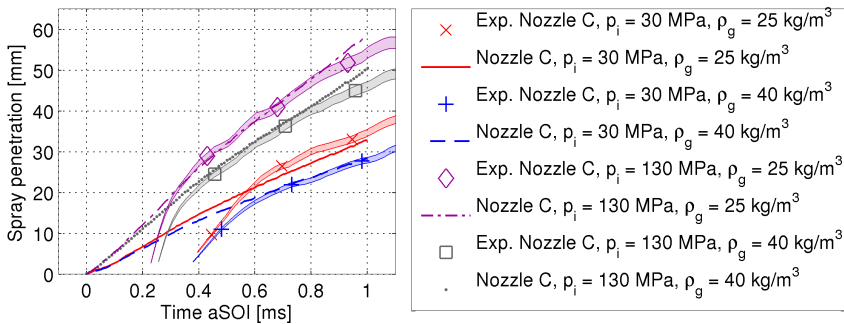
(b) Nozzle C.

Figure 5.39: Spray penetration for two nozzles of the validation assessment.

Notice that all experimental curves in Figure 5.39 have been shifted in time. Concretely for these plots, the delay is $0.35\,\mathrm{ms}$ for cases with injection pressure of $p_i = 30\,\mathrm{MPa}$ and $0.2\,\mathrm{ms}$ with $p_i = 130\,\mathrm{MPa}$. For the case of the nozzle B, though not shown, the employed delay is also $0.2\,\mathrm{ms}$. This delay comes from an under-prediction of the injection velocity in the early stages of the injection. When a pressure inlet boundary condition is used, this delay vanishes, as shown before in Figure 5.31a.

Due to this time delay, experimental and computational penetration values cannot be directly compared. Instead, a new parameter is defined and used, named $R-parameter$ and explained in detail in Appendix 5.A. This new $R-parameter$ measures the penetration curve slope, and one of its advantages is that allows parametrization (one test, one value). Table 5.45 shows the average over time value for all cases. In some cases, experiments and simulations are very close, but there is a large difference in general.

Nozzle	A	A	A	A	B	C	C	C	C
p_i [MPa]	30	30	130	130	80	30	30	130	130
ρ_g [kg/m^3]	25	40	25	40	32.5	25	40	25	40
Exp. [m/s$^{\frac{1}{2}}$]	1.34	0.98	2.29	1.86	1.67	1.94	1.37	3.57	2.67
Comp. [m/s$^{\frac{1}{2}}$]	0.84	0.65	2.55	1.73	1.69	1.13	0.85	3.52	2.59

Table 5.45: Steady state $R - parameter$ of all validation cases.

Time evolution of the $R - parameter$ is plotted in Figure 5.40 with the aim of finding the source of these differences. First thing to notice is that computational values are not constant but linear. In fact, for the highest injection pressure and the lowest ambient density, relationship between the $R - parameter$ and time is parabolic. Then, although penetration curves in Figure 5.39 are not so different, the penetration evolution for some time aSOI do not follow experimental trends.

This strange behavior may be explained through the time evolution of fuel concentration (liquid mass fraction contours) shown in Figure 5.41. Typical mushroom shape is obtained, however the liquid concentration at the tip of the spray is too high, as clearly seen in Figure 5.41c. This pushes the spray downstream faster than in reality. This high fuel concentration zones are generated by the initial and boundary conditions. Initializing the nozzle filled with stagnated liquid gives to the calculations excessive fuel mass to work with, which is thrown out increasing the spray momentum. Additionally, a time velocity boundary condition generates a small delay, larger for high injection pressure, in the mass flow rate and momentum flux when compared with experiments that extents the linear time dependency of the spray penetration (see Section §2.4.3).

Nonetheless, this mass accumulation phenomenon has been previously observed in experiments [45, 46]. Gimeno [17] explains the phenomenon as follows: at the beginning of the injection the fuel comes out from the nozzle faster each time due to an increasing mass flow; thus, fuel that exists later in time may reach the liquid that came out earlier but slower. In other words, the spray tip is composed not only by the first fuel that went out from the nozzle but also by the fuel that reaches the tip due to its higher velocity. This trend is reproduced, but as already said, the amount of fuel that reaches the tip is too high.
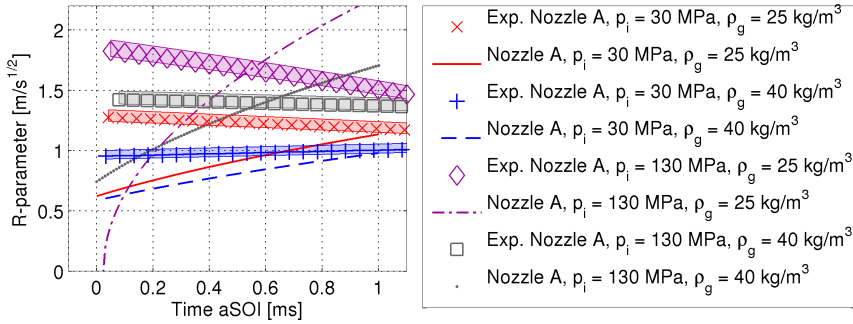
(a) Nozzle A.
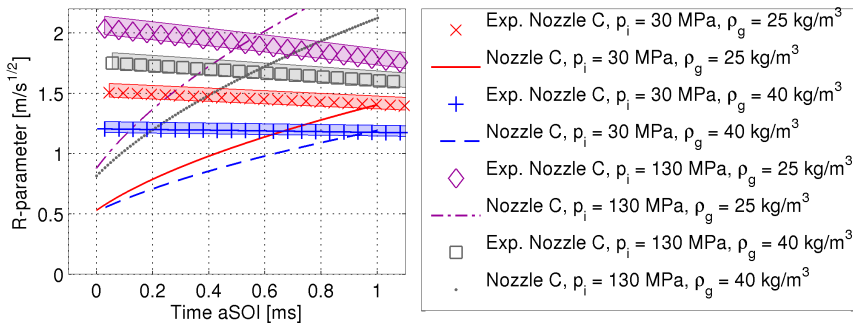
(b) Nozzle C.

Figure 5.40: $R - parameter$ time evolution for two nozzles of the validation assessment.

This result means that initial and boundary conditions selected for validation are not the best ones. Although experimental mass flow rate is properly captured, spray penetration behavior is not reproduced correctly for all injection conditions. Note that the case used for previous studies (nozzle A, $p_i = 30\,\text{MPa}$ and $\rho_g = 40\,\text{kg}/\,\text{m}^3$) is one in which the $R - parameter$ varies less with time. For future simulations, a change in the case set-up is required. Nonetheless, with the right boundaries the error in penetration can be reduced to less than 5%, as shown earlier in Section §5.3.2 and also in Figure 5.31a.

Information presented in Figure 5.39 can be rearranged to check the effect of the nozzle geometry on the spray. Low injection pressure $p_i = 30\,\text{MPa}$ condition is selected for that, but the analysis for higher injection pressure is the same. As shown in Figure 5.42, for short time aSOI, also called initial or transient zone, both nozzle penetration curves superpose. As explained by Payri

(a) 0.25 ms aSOI.

(b) 0.5 ms aSOI.

(c) 0.75 ms aSOI.

(d) 1 ms aSOI.
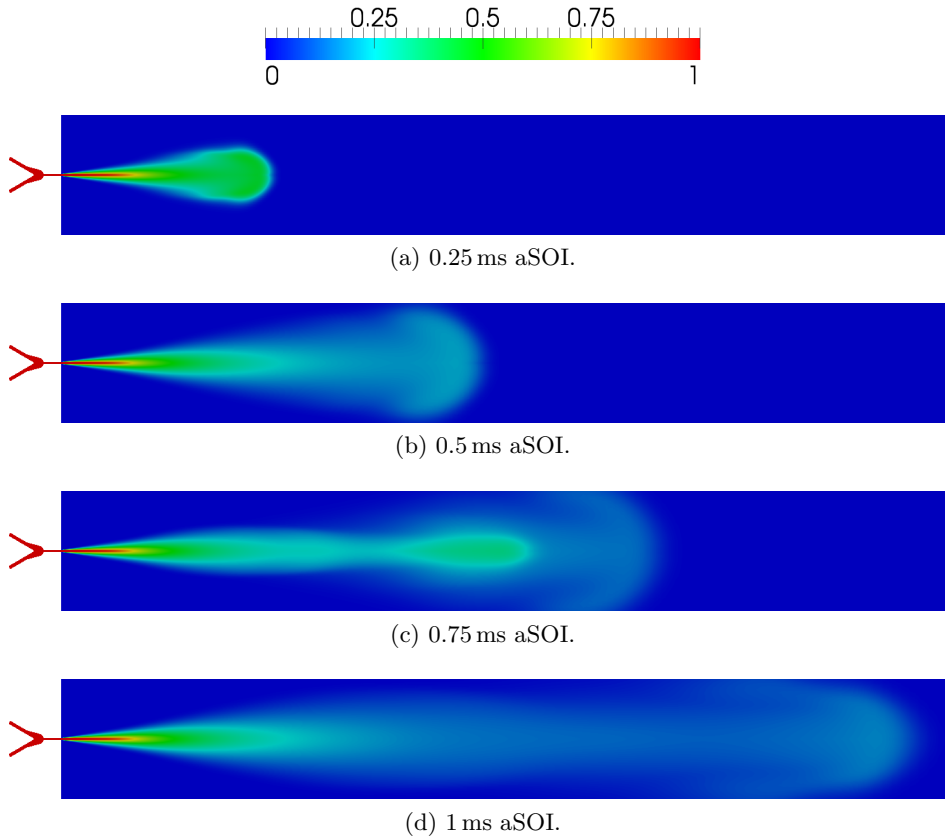
Figure 5.41: Liquid mass fraction contour of one test point of the validation assessment: nozzle A, $p_i = 130\,\mathrm{MPa}$ and $\rho_g = 25\,\mathrm{kg/\,m^3}$. Domain shown size is $55\,\mathrm{mm}$ in length (plus the nozzle) and $7\,\mathrm{mm}$ in height.

et al. [47], this zone does not depend on the orifice diameter, it only depends on the injection conditions (injection velocity and ambient density) which define the exit liquid velocity. In this zone, the penetration is proportional to time. For long time aSOI, also called spray developed zone, the greater the orifice diameter the greater the momentum flux and so the longer the spray penetration are. This trend is well captured by the model.
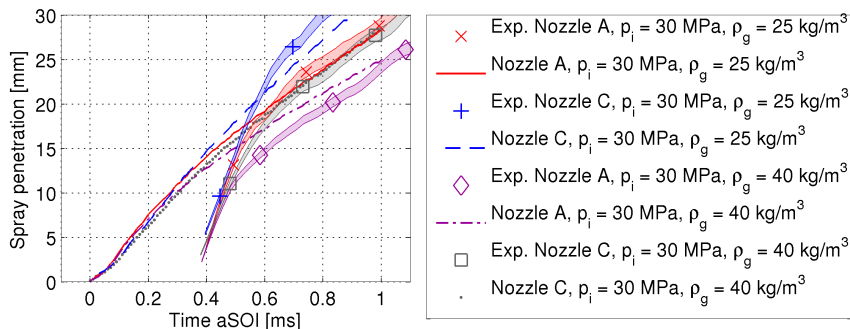
Figure 5.42: Spray penetration for low injection pressure condition and two nozzles of the external flow study compared with experimental data.

Conclusion

Taking into account all the results previously explained, two main conclusions can be drawn. First one concerns the boundary conditions selected for simulating Diesel sprays: a constant pressure boundary condition is more proper, specially when simulating high injection pressures. Spray behavior, perfectly captured by the model as proved in Section §5.3.2, is not reproduced in the simulations if time varying velocity condition is used.

The second conclusion, and also the reason why the model can be considered validated, is that all trends observed in the experimental benchmark are also obtained in the computations. For example, the effect of varying the nozzle geometry is the same in the experiments and simulations. It is important to remark that not only the trends, but the rate of variation is predicted, in other words, the model can be used to obtain how much the spray penetration grows if the orifice outlet diameter increases.

5.4   Summary

The ESA model described in Chapter 4 has been put through verification and validation assessments. For verification, solutions given by the model have been compared with analytical and high accurate (DNS) solutions of simplified problems. For validation, a real Diesel injection problem has been simulated and compared with experiments. In order to reduce the difference, best boundary conditions and turbulence model needed to be previously selected.

One of the new aspects of the model, the compressibility, has been verified against Prandtl-Meyer expansion and shock waves, but also comparing with the classical problem of the Convergent-Divergent verification nozzle. Other key point of the model, the thermal balance, has been verified by solving the Couette thermal flow. The multiphase nature of the model has been verified by comparison with DNS. In all cases, the errors felt below the prefixed limits. Therefore, the model can be considered verified. Additionally, weaknesses of the model have been identified, i.e. high computational cost and excessive spread of the fuel in the first millimeter after the nozzle outlet.

The problem used for validation consists of a single-hole axial nozzle widely used in Diesel engine research. An experimental database of the literature has been reproduced by the model. Prior to that, only the spray (external flow) has been studied under only one injection condition. Obtained results were outstanding, encouraging the use of the model.

After comparing the simulated solutions of the single-hole nozzle with the experiments, large differences were found, specially in the early stages of the injection. These differences conditioned the spray development and its behavior was not perfectly captured. Nonetheless, discrepancies are associated to the boundary conditions selected to perform the study. Time varying velocity was selected because the mass flow rate could be perfectly reproduced, and disagreement in the spray behavior could be solved by modifying the initial conditions, imposing an initial velocity for the liquid. It turned out that all of this was true only for the injection conditions used for the inlet boundary condition selection. Thus, a constant pressure boundary condition seems more proper, though the transient part of the mass flow rate is not captured. That issue can be solved by adding the needle movement to the model.

Regardless the error in the selection of the inlet boundary condition, changes in the nozzle flow pattern and spray behavior are well captured by the model, both in trends and magnitude, when injection conditions and nozzle geometry are varied. And this is the reason why the model is considered val-

idated, and so can be used for a further analysis of the Diesel spray injection process.

5.A Appendix: Calculation of squared penetration time derivative

In addition to traditional dimensionless coefficients which characterize the flow such C_a, C_v or C_d, a new parameter has been obtained from the external flow comparison metrics. The classical spray theory gives an expression for the spray penetration, Equation (2.45), depending on the momentum flux, the ambient density, the spray angle and the square root of time [39, 48].

Generally, this expression correctly predicts the spray penetration from some time after start of injection, when mass flow and spray momentum flus reach the steady part (see Section §2.4.3). From that point, momentum flux and spray angle can be taken as constants. Thus, the derivative of the spray penetration respect to the square root of time must be also constant. This derivative, theoretically given by Equation (5.8), is the new parameter and is from now on called $R - parameter$.

$$R - parameter = \frac{\partial S(t)}{\partial \sqrt{t}} \propto \rho_g^{-\frac{1}{4}} \dot{M}^{\frac{1}{4}} \tan^{-\frac{1}{2}}\left(\frac{\theta}{2}\right) \tag{5.8}$$

From the experimental (and computational) point of view, once the spray penetration is measured, the square magnitude of spray penetration should follow a linear trend with time, as shown in Figure 5.43a, with a constant slope, as pointed out by Equation (5.8) and shown in Figure 5.43b.

This $R - parameter$ is better than spray penetration $S(t)$ to analyze the spray behavior due to:

- it is independent of time for a fully developed spray;
- it is independent of the leading edge position, in other words, of the past history;
- allows parameterization (one test, one value);
- and can be correlated to other parameters, such spray momentum flux or ambient density.

(a) Square penetration.   (b) $R - parameter$.
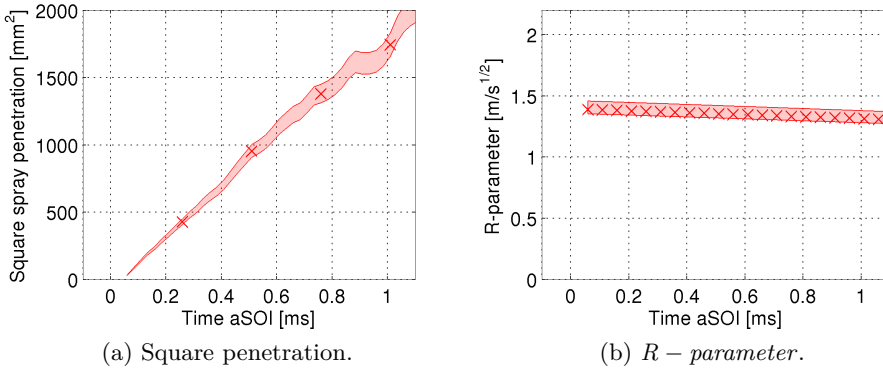
Figure 5.43: An experimental example of the calculation of $R - parameter$. Nozzle A, $p_i = 80\,\mathrm{MPa}$, $\rho_g = 32.5\,\mathrm{kg/\,m^3}$.

References

[1]   Oberkampf, W. L. and T. G. Trucano. "Verification and validation in computational fluid dynamics". *Progress in Aerospace Sciences*, vol. 38.3 (2002), pp. 209–272. DOI: `10.1016/S0376-0421(02)00005-2` (*cit. on pp. 199, 201, 202, 206, 207, 211, 212, 216, 218, 220, 223*).

[2]   Ghia, U. et al. "The AIAA Code Verification Project - Test cases for CFD Code Verification". *48th AIAA Aerospace Sciences Meeting Including the New Horizons Forum and Aerospace Exposition*. 2010-0125. Orlando, Florida, United States of America, 2010 (*cit. on pp. 200, 201, 203, 204, 206, 208–210, 213*).

[3]   Slater, J. W. *NPARC Alliance CFD Verification and Validation Web Site*. English. National Aeronautics and Space Administration. 2012. URL: `http://www.grc.nasa.gov/WWW/wind/valid/archive.html` (*cit. on pp. 200, 214, 216, 217*).

[4]   Grace, J. R. and F. Taghipour. "Verification and validation of CFD models and dynamic similarity for fluidized beds". *Powder Technology*, vol. 139.2 (2004), pp. 99–110. DOI: `10.1016/j.powtec.2003.10.006` (*cit. on p. 200*).

[5]   Premnath, K. N. and J. Abraham. "Lattice Boltzmann simulations of drop-drop interactions in two-phase flows". *International Journal of Modern Physics*, vol. 16.1 (2005), pp. 25–44. DOI: `10.1142/S0129183105006930` (*cit. on p. 200*).

[6] Tanguy, S., M. Sagan, B. Lalanne, F. Couderc, and C. Colin. "Benchmarks and numerical methods for the simulation of boiling flows". *Journal of Computational Physics*, vol. 264.1 (2014), pp. 1–22. DOI: `10.1016/j.jcp.2014.01.014` (*cit. on p. 200*).

[7] Fullmer, W. D., M. A. L. de Bertodano, and X. Zhang. "Verification of a Higher-order Finite Difference Scheme for the One-dimensional Two-fluid Model". *Journal of Computational Multiphase Flows*, vol. 5.2 (2013), pp. 139–155. DOI: `10.1260/1757-482X.5.2.139` (*cit. on p. 200*).

[8] Jung, S. K. and R. Myong. "A second-order positivity-preserving finite volume upwind scheme for air-mixed droplet flow in atmospheric icing". *Computers and Fluids*, vol. 86 (2013), pp. 459–469. DOI: `10.1016/j.compfluid.2013.08.001` (*cit. on p. 200*).

[9] Lebas, R., T. Ménard, P. A. Beau, A. Berlemont, and F. X. Demoulin. "Numerical simulation of primary break-up and atomization: DNS and modelling study". *International Journal of Multiphase Flow*, vol. 35.3 (2009), pp. 247–260. DOI: `10.1016/j.ijmultiphaseflow.2008.11.005` (*cit. on pp. 200, 218, 220, 221*).

[10] Ménard, T., S. Tanguy, and A. Berlemont. "Coupling level set/VOF/ghost fluid methods: Validation and application to 3D simulation of the primary break-up of a liquid jet". *International Journal of Multiphase Flow*, vol. 33.5 (2007), pp. 510–524. DOI: `10.1016/j.ijmultiphaseflow.2006.11.001` (*cit. on pp. 200, 218*).

[11] Demoulin, F. X. et al. "Toward using direct numerical simulationto improve primary break-up modeling". *Atomization and Sprays*, vol. 23.11 (2013), pp. 957–980. DOI: `10.1615/AtomizSpr.2013007439` (*cit. on p. 200*).

[12] Kook, S. and L. M. Pickett. "Effect of ambient temperature and density on shock wave generation in a diesel engine". *Atomization and Sprays*, vol. 20.2 (2010), pp. 163–175. DOI: `10.1615/AtomizSpr.v20.i2.50` (*cit. on p. 205*).

[13] Giannadakis, E., D. Papoulias, M. Gavaises, C. Arcoumanis, and C. Soteriou. "Evaluation of the Predictive Capability of Diesel Nozzle Cavitation Models". *SAE Technical Paper 2007-01-0245* (2007). DOI: `10.4271/2007-01-0245` (*cit. on p. 209*).

[14] Salvador, F. J., J. Martínez-López, M. Caballer, and C. de Alfonso. "Study of the influence of the needle lift on the internal flow and cavitation phenomenon in diesel injector nozzles by CFD using RANS methods". *Energy Conversion and Management*, vol. 66 (2013), pp. 246–256. DOI: 10.1016/j.enconman.2012.10.011 (*cit. on p. 209*).

[15] Anderson, J. D. *Fundamentals of Aerodynamics*. Ed. by J. D. Anderson. Fourth edition. New York, New York, United States of America: McGraw Hill, 2007 (*cit. on p. 214*).

[16] Demoulin, F. X., P. A. Beau, G. Blokkel, and R. Borghi. "A new model for turbulent flows with large density fluctuations: Application to liquid atomization". *Atomization and Sprays*, vol. 17.4 (2007), pp. 315–345. DOI: 10.1615/AtomizSpr.v17.i4.20 (*cit. on p. 220*).

[17] Gimeno, J. "Desarrollo y aplicación de la medida de flujo de cantidad de movimiento de un chorro Diésel". PhD thesis. Camino de Vera, s/n, 46022, Valencia, Spain: Departamento de Máquinas y Motores Térmicos, Universitat Politècnica de València, 2008 (*cit. on pp. 223, 228, 229, 244, 252, 256*).

[18] Macián, V., V. Bermúdez, R. Payri, and J. Gimeno. "New technique for determination of internal geometry of a diesel nozzle with the use of silicone methodology". *Experimental Techniques*, vol. 27.2 (2003), pp. 39–43 (*cit. on p. 224*).

[19] Sukumaran, S., S.-C. Kong, and N. H. Cho. "Modeling Evaporating Diesel Sprays Using an Improved Gas Particle Model". *SAE Technical Paper 2013-01-1598* (2013). DOI: 10.4271/2013-01-1598 (*cit. on p. 224*).

[20] García-Oliver, J. et al. "Diesel spray CFD simulations based on the $\Sigma - Y$ eulerian atomization model". *Atomization and Sprays*, vol. 23.1 (2013), pp. 71–95. DOI: 10.1615/AtomizSpr.2013007198 (*cit. on pp. 224, 229, 231, 236*).

[21] Friedrich, M. and B. Weigand. "Eulerian multi-fluid simulation of polydisperse dense liquid sprays by the direct quadrature method of moments". *10th International Conference on Liquid Atomization and Spray Systems (ICLASS)*. Kyoto, Japan, 2006 (*cit. on p. 224*).

[22] Salvador, F. J. "Estudio teórico experimental de la influencia de la geometría de toberas de inyección Diésel sobre las características del flujo interno y del chorro". PhD thesis. Camino de Vera, s/n, 46022, Valencia, Spain: Departamento de Máquinas y Motores Térmicos, Universitat Politècnica de València, 2003 (*cit. on p. 225*).

[23] Payri, R., F. J. Salvador, J. Gimeno, and G. Bracho. "The effect of temperature and pressure on thermodynamic properties of diesel and biodiesel fuels". *Fuel*, vol. 90.3 (2011), pp. 1172–1180. DOI: `10.1016/j.fuel.2010.11.015` (*cit. on p. 227*).

[24] Bardi, M. et al. "Engine combustion network: Comparison of spray development, vaporization, and combustion in different combustion vessels". *Atomization and Sprays*, vol. 22.12 (2012), pp. 807–842. DOI: `10.1615/AtomizSpr.2013005837` (*cit. on p. 228*).

[25] Battistoni, M., C. N. Grimaldi, and F. Marianni. "Coupled Simulation of Nozzle Flow and Spray Formation Using Diesel and Biodiesel for CI Engine Applications". *SAE Technical Paper 2012-01-1267* (2012). DOI: `10.4271/2012-01-1267` (*cit. on pp. 229, 240, 241*).

[26] Befrui, B., G. Corbinelly, P. Spiekermann, M. Shost, and M. C. Lai. "Large Eddy Simulation of GDI Single-Hole Flow and Near-Field Spray". *SAE Technical Paper 2012-01-0392* (2012). DOI: `10.4271/2012-01-0392` (*cit. on p. 229*).

[27] Duke, D. J., A. L. Kastengren, F. Z. Tilocco, A. B. Swantek, and C. F. Powell. "X-ray radiography measurements of cavitating nozzle flow". *Atomization and Sprays*, vol. 23.9 (2013), pp. 841–860. DOI: `10.1615/AtomizSpr.2013008340` (*cit. on p. 229*).

[28] Pope, S. B. "An explanation of the turbulent round-jet/plane-jet anomaly". *American Institute of Aeronautics and Astronautics Journal*, vol. 16 (1978), pp. 279–281. DOI: `10.2514/3.7521` (*cit. on p. 230*).

[29] Payri, R., L. Araneo, J. S. Shakal, and V. Soare. "Phase doppler measurements: System set-up optimization for characterization of a diesel nozzle". *Journal of Mechanical Science and Technology*, vol. 22.8 (2008), pp. 1620–1632. DOI: `10.1007/S12206-008-0432-7` (*cit. on p. 231*).

[30] Araneo, L. and C. Tropea. "Improving Phase Doppler Measurements in a Diesel Spray". *SAE Technical Paper 2000-01-2047* (2000). DOI: `10.4271/2000-01-2047` (*cit. on p. 232*).

[31] Baik, S., J. P. Blanchard, and M. L. Corradini. "Development of micro-diesel injector nozzles via MEMS technology and effects on spray characteristics". *Atomization and Sprays*, vol. 13.5-6 (2003), pp. 443–474. DOI: `10.1615/AtomizSpr.v13.i56.20` (*cit. on p. 232*).

[32] Ferziger, J. H. and M. Perić. *Computational Methods for Fluid Dynamics*. Ed. by J. H. Ferziger. Third edition. Heidelberg, Germany: Springer, 2002 (*cit. on p. 234*).

[33]   Som, S. et al. "A Numerical Investigation on Scalability and Grid Con-
       vergence of Internal Combustion Engine Simulations". *SAE Technical
       Paper 2013-01-1095* (2013). DOI: `10.4271/2013-01-1095` (*cit. on
       pp. 237–239*).

[34]   Som, S. and S. K. Aggarwal. "Effects of primary breakup modeling on
       spray and combustion characteristics of compression ignition engines".
       Combustion and Flame, vol. 157.6 (2010), pp. 1179–1193. DOI: `10.
       1016/j.combustflame.2010.02.018` (*cit. on pp. 240, 241*).

[35]   Payri, R., J. Gimeno, P. Martí-Aldaraví, and G. Bracho. "Study of the
       influence of the inlet boundary conditions in a LES simulation of inter-
       nal flow in a diesel injector". *Mathematical and Computer Modelling*,
       vol. 57.7-8 (2013), pp. 1709–1715. DOI: `10.1016/j.mcm.2011.11.019`
       (*cit. on pp. 240, 246, 247*).

[36]   Hoyas, S., A. Gil, X. Margot, D. Khuong-Anh, and F. Ravet. "Evalu-
       ation of the Eulerian-Lagrangian Spray Atomization (ELSA) model in
       spray simulations: 2D cases". *Mathematical and Computer Modelling*,
       vol. 57.7-8 (2013), pp. 1686–1693. DOI: `10.1016/j.mcm.2011.11.006`
       (*cit. on pp. 241, 249*).

[37]   Desantes, J. M., R. Payri, F. J. Salvador, and V. Soare. "Study of the
       Influence of Geometrical and Injection Parameters on Diesel Sprays
       Characteristics in Isothermal Conditions". *SAE Technical Paper 2005-
       01-0913* (2005). DOI: `10.4271/2005-01-0913` (*cit. on p. 241*).

[38]   Payri, R., F. J. Salvador, J. Gimeno, and A. García. "Flow regime
       effects over non-cavitating diesel injection nozzles". *Proceedings of
       the Institution of Mechanical Engineers, Part D: Journal of Auto-
       mobile Engineering*, vol. 226.1 (2012), pp. 133–144. DOI: `10.1177/
       0954407011413056` (*cit. on pp. 241, 246, 250*).

[39]   Payri, F., V. Bermúdez, R. Payri, and F. J. Salvador. "The influence
       of cavitation on the internal flow and the spray characteristics in diesel
       injection nozzles". *Fuel*, vol. 83 (2004), pp. 419–431. DOI: `10.1016/j.
       fuel.2003.09.010` (*cit. on pp. 242, 261*).

[40]   Morena, J. de la. "Estudio de la influencia de las características del
       flujo interno en toberas sobre el proceso de inyección Diésel en campo
       próximo". PhD thesis. Camino de Vera, s/n, 46022, Valencia, Spain:
       Departamento de Máquinas y Motores Térmicos, Universitat Politèc-
       nica de València, 2011 (*cit. on pp. 244, 251*).

[41]   Garza de León, O. A. de la. "Estudio de los efectos de la cavitación en toberas de inyección diésel sobre el proceso de inyección y el de formación de hollín". PhD thesis. Camino de Vera, s/n, 46022, Valencia, Spain: Departamento de Máquinas y Motores Térmicos, Universitat Politècnica de València, 2012 (*cit. on p. 245*).

[42]   Payri, R., B. Tormos, J. Gimeno, and G. Bracho. "The potential of Large Eddy Simulation (LES) code for the modeling of flow in diesel injectors". *Mathematical and Computer Modelling*, vol. 52.7-8 (2010), pp. 1151–1160. DOI: 10.1016/j.mcm.2010.02.033 (*cit. on pp. 246, 250, 253*).

[43]   Payri, R., B. Tormos, J. Gimeno, and Ga. "Large Eddy Simulation for high pressure flows: Model extension for compressible liquids". *Mathematical and Computer Modelling*, vol. 54.7-8 (2011), pp. 1725–1731. DOI: 10.1016/j.mcm.2010.12.001 (*cit. on p. 253*).

[44]   Xue, Q. et al. "Three-dimensional Simulations of the Transient Internal Flow in a Diesel Injector: Effects of Needle Movement". *25th Annual Conference on Liquid Atomization & Spray Systems (ILASS Americas)*. Pittsburgh, Pensilvania, United States of America, 2013 (*cit. on p. 254*).

[45]   Desantes, J. M., R. Payri, F. J. Salvador, and J. Gimeno. "Prediction of Spray Penetration by Means of Spray Momentum Flux". *SAE Technical Paper 2006-01-1387* (2006). DOI: 10.4271/2006-01-1387 (*cit. on p. 256*).

[46]   Payri, R., S. Ruiz, F. J. Salvador, and J. Gimeno. "On the dependence of spray momentum flux in spray penetration: Momentum flux packets penetration model". *Journal of Mechanical Science and Technology*, vol. 21.7 (2007), pp. 1100–1111. DOI: 10.1007/BF03027660 (*cit. on p. 256*).

[47]   Payri, R., F. J. Salvador, J. Gimeno, and R. Novella. "Flow regime effects on non-cavitating injection nozzles over spray behavior". *International Journal of Heat and Fluid Flow*, vol. 32.1 (2011), pp. 273–284. DOI: 10.1016/j.ijheatfluidflow.2010.10.001 (*cit. on pp. 257, 259*).

[48]   Naber, J. D. and D. L. Siebers. "Effects of Gas Density and Vaporization on Penetration and Dispersion of Diesel Sprays". *SAE Technical Paper 960034* (1996). DOI: 10.4271/960034 (*cit. on p. 261*).

Chapter 6

Numerical results

6.1 Introduction

Insights of the ESA model are described in detail in Chapter 4. So it is clear that there are many aspects that may affect its accuracy, i.e. numerical schemes. In order to make the model work properly, and then be able to use it as a predictive tool, those many aspects need to be studied.

In this chapter, the numerical side of the model is analyzed with the aim of finding the best set of numerical schemes and the best values of all constants and parameters included in the model. If a good solution is not found, then at least the influence of most of the model constants and parameters on the solution will be known.

The first topic is one of the key assumptions of the model, the air-liquid inter-facial surface density transport equation, described in Section §4.4.1. Concretely, the adjustment of its source terms constants to simulate Diesel spray injection conditions. DNS results are used as a reference.

The second topic is, as could not be otherwise, the selection of numerical schemes: discretization schemes and linear solvers. They are generally described in Section §4.2.3, but it is necessary to select the ones that give the best and fastest solution for problem of interest. Again, high accurate DNS results are used as a reference.

The third and last topic involves all parameters of the model except obviously those of inter-facial surface density transport equation, for example, Schmidt number or constants of the turbulence model. In the valida-

tion assessment of Section §5.3 it has been observed that the maximum error/difference with experiments if found at the first 0.4 ms aSOI, so that is the current area of interest. Parameters can be change to improve the prediction of the model for that part of the injection. As an additional objective of this section, the relationship between those values and the injection conditions is also studied and analyzed.

6.2   Inter-facial area density equation parameters

Section §4.4.1 describes the atomization sub-model, which includes the transport equation for the air-fuel inter-facial area density Σ. Assuming that droplets have different diameters but are all spherical, knowledge of Σ allows defining the *SMD* through Equation (4.22).

Nevertheless, transport Equation (4.24) includes four different modeling constants/parameters (α_0, α_1, C and $Sc_{\Sigma,coeff}$) which need to be fixed to accurately predict droplets size. The common way to give values to those constants is by comparison with experimental or DNS results [1–3]. Vallet et al. [1] perform this study, but applied on co-axial injectors where the maximum injection velocity is much lower than the one found in Diesel injectors. Beheshti et al. [2] repeats the study, also on co-axial injectors, because their source terms (see Equation (4.46)) are different than the ones used by Vallet et al. [1].

Thus, it is necessary to study the impact that those parameters have on the solution and, at the end, select the best values for them. This is done by comparing the computational solution with high accurate results coming from DNS. The same case than the verification assessment, detailed in Section §5.2.5, is used. Axial profiles and radial profiles of air-fuel surface density Σ at three different axial positions are used as comparison metrics. Contours are also used to qualitatively compare the distribution of Σ.

6.2.1   Statistical analysis: Design of Experiments

The objective of this study is to check if it is possible to reduce the error in the prediction of the inter-facial surface density. As there are four comparison metrics, the axial profile and three radial profiles, the variable of interest is the averaged error from the four distributions.

Four factors are selected for the statistical analysis: α_0, α_1, C and $Sc_{\Sigma,coeff}$. Each of them with two levels, high and low, but $Sc_{\Sigma,coeff}$, which has three levels. There is not physical explanation for the values used, they are taken

just to tune the model. For the high level, a 25% more than the value selected by Vallet et al. [1] is used, and for the low level, a 25% less. Exact values are shown in Table 6.1. The third value for $Sc_{\Sigma,coeff}$ is 1.00, the one recommended in the literature.

Factor	High level	Low level
α_0	1.25	0.75
α_1	1.25	0.75
C	3.125	1.875
$Sc_{\Sigma,coeff}$	1.25	0.75

Table 6.1: High and low values selected for the statistical study of the inter-facial surface density constants.

By selecting two levels for the constant, linear dependency is assumed between the variable of interest and each factor. Nonetheless, a parabolic dependency between the error and the diffusive coefficient $Sc_{\Sigma,coeff}$ is considered. It is expected that optimum values are close to those found by Vallet et al. [1]; so the error of assuming linearity is expected to be small because variations on the variable of interest are small too.

Commercial software Statgraphics Centurion XVI[1] ® is used to carry out the study. A multilevel factorial design [4] with first order interaction between factors is selected. This type of design leads to 24 simulations, changing the value of the four factors as depicted in Table 6.2.

Because only first order interactions between factors are considered, 11 coefficients are enough to define the mathematical model of the variable of interest. This leaves 13 degrees of freedom to estimate the error of such mathematical model, a value larger than the recommended of 10 degrees of freedom [4].

6.2.2 Results of the analysis

The analysis includes, first, substantiation that the mathematical model employed is correct, second, an analysis of variance (ANOVA) to determine the significant factors, and third and last, the analysis of effects and optimization of the system.

---

[1]This is the reason why the images presented in this chapter do not show the same format than the rest; they are obtained directly from Statgraphics software.

Case	α_0	α_1	C	$Sc_{\Sigma,coeff}$
1	0.75	1.25	1.875	0.75
2	0.75	1.25	3.125	1.25
3	0.75	1.25	1.875	1.25
4	1.25	0.75	3.125	1.00
5	1.25	0.75	3.125	0.75
6	1.25	1.25	1.875	1.00
7	1.25	0.75	1.875	1.25
8	1.25	1.25	1.875	1.25
9	1.25	0.75	1.875	0.75
10	0.75	0.75	1.875	0.75
11	1.25	1.25	3.125	0.75
12	0.75	0.75	3.125	1.25
13	1.25	1.25	3.125	1.00
14	0.75	0.75	1.875	1.00
15	0.75	0.75	3.125	1.00
16	0.75	1.25	1.875	1.00
17	1.25	1.25	1.875	0.75
18	0.75	0.75	1.875	1.25
19	1.25	1.25	3.125	1.25
20	0.75	0.75	3.125	0.75
21	0.75	1.25	3.125	1.00
22	1.25	0.75	1.875	1.00
23	1.25	0.75	3.125	1.25
24	0.75	1.25	3.125	0.75

Table 6.2: Simulations of the multilevel factorial design performed for the study of the inter-facial surface density constants.

Substantiation of the model

It is necessary to address the applicability of the hypothesis of the model (normal distribution, residual independence, homogeneity of variance and linearity) to ensure the robustness of the conclusions drawn from the study [4]. This can be done by analyzing the residuals.

Normality of the residuals

One of the most important hypothesis of the multi-factorial statistical study is the Gaussian distribution of the residuals. That means that there are only few cases in which the error deviates more than twice the standard deviation from the mean value. As shown in Figure 6.1 which represents the cumulative probability of the residuals, there is no evidence that the residuals do not fulfill this hypothesis.
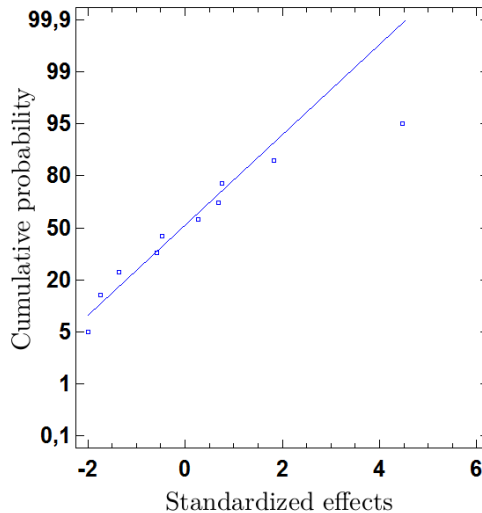
Figure 6.1: Cumulative normal probability of the residuals for the averaged error in the inter-facial surface density study.

Residuals independence

Another important hypothesis is the residual independence, in other words, there should not exist any relationship between the residuals of samples. Residuals are normally distributed in Figure 6.2, no clear trend is observed, therefore there is no evidence to reject the residual independence assumption.

Additionally, the statistic Durbin-Watson test [4] with a p-value[2] greater than 0.05 proves that there is not serial autocorrelation in the residuals with a significance level of 95%.
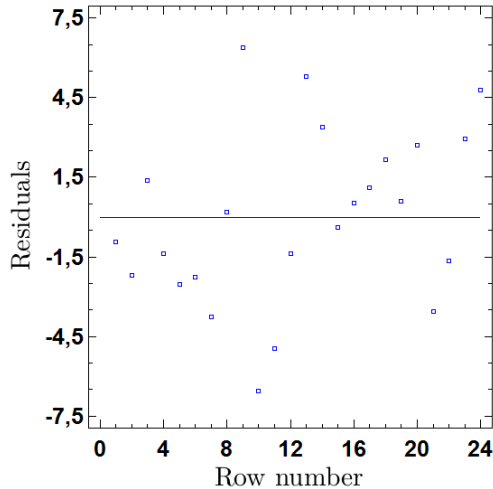
Figure 6.2: Residuals versus the number of the simulation for the averaged error in the inter-facial surface density study.

Homoscedasticity

A sequence of random variables is homoscedastic if all random variables in the sequence have the same finite variance. This is also known as homogeneity of variance. This hypothesis cannot be dismissed because, again, no trend is observe in Figure 6.3, where residuals are plotted versus their predicted values.

Linearity

As previously commented, linear dependency is assumed between the variable of interest and each factor. However, lack-of-fit test cannot be performed if replications of the study are not carried out.

In this case, replications do not add any kind of information because the system is deterministic; no matter how many times simulations are run, results are always the same. So this hypothesis is not confirmed. Nonetheless, the error of assuming linearity is expected to be small.

---

[2]The p-value is the probability of obtaining a test statistic result at least as extreme as the one that was actually observed, assuming that the null hypothesis is true. A researcher will often reject the null hypothesis when the p-value turns out to be less than a predetermined significance level, often 0.05 or 0.01.
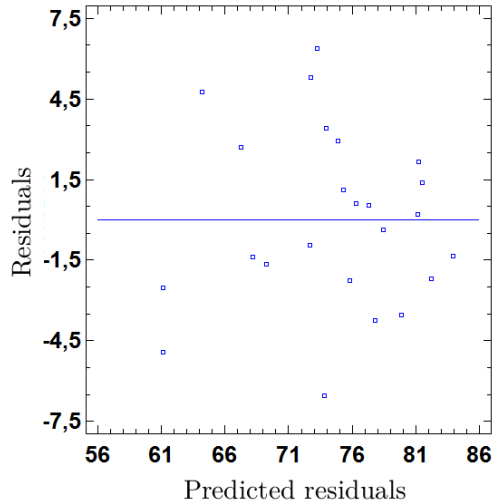
Figure 6.3: Residuals versus predicted residuals for the averaged error in the inter-facial surface density study.

Analysis of variance

The variability of the error (variable of interest) is split in different terms, each of them account for each effect. Thus, statistical significance of factors can be checked out by comparing the root mean square with an estimated experimental error.

Table 6.3 summarizes the ANOVA analysis, performed as indicated by Montgomery [4]: computing the root mean square, then performing an F-test[3], and then obtaining the p-value of each factor. In this case, only one effect (factor $Sc_{\Sigma,coeff}$) has a p-value lower than 0.05, which means that the error for this factor is statistically different with a significance level of 95%.

If factor $Sc_{\Sigma,coeff}$ is the only one considered (the rest are not included), the R^2 statistic indicates that the statistical model with only one factor explains 42.68% of the variability of the variable of interest, the averaged error in inter-facial surface density predictions. The adjusted-R^2 statistic, more suitable when comparing models with different independent variables, is 40.07%. The mean absolute error is 4.16, which at the same time is the averaged value of the residuals.

---

[3]An F-test is any statistical test in which the test statistic has an F-distribution under the null hypothesis.

Factor	Root mean square	F-test	p-value
A: α_0	101.19	3.99	0.0671
B: α_1	11.96	0.47	0.5044
C: C	76.26	3.01	0.1066
D: $Sc_{\Sigma,coeff}$	507.71	20.02	0.0006
AB	14.88	0.59	0.4573
AC	46.87	1.85	0.1971
AD	8.37	0.33	0.5755
BC	5.76	0.23	0.6415
BD	1.84	0.07	0.7917
CD	85.05	3.35	0.0901
Total error	25.36		
Total squared sum	1189.6		

Table 6.3: ANOVA of the inter-facial surface density constants.

Table 6.4 shows the estimated effect of each factor and interaction. It also shows the standard error of each of these effect, which is more or less constant. Increasing $Sc_{\Sigma,coeff}$ has an impact which is more than double the effect of any other parameter. Nonetheless, some of them, such α_0 or C, may be relevant for further reducing the error once $Sc_{\Sigma,coeff}$ is optimized.

Optimization

Finally, software Statgraphics can be used to obtain the optimum combination of parameters to minimize the averaged error. That combination is presented in Table 6.5, and corresponds to case number 5 of Table 6.2. If other mathematical model different than linear (cubic, for example) was used, a different optimization would be probably obtained; maybe with different significant variables and higher R^2 value.

The minimum averaged error is 61.18%, which is huge. However, it is necessary to remember that statistical convergence is not perfectly reached for the DNS results [5], so for sure that is an important source of errors. With the aim of digging deeper in this topic, axial profiles of inter-facial surface density are shown in Figure 6.4 for the original set of values and the optimum from Table 6.5. A great improvement is observed. The trend is not captured with the original set of values from the literature [1], meanwhile both trend and values are well predicted with optimum values.

Factor	Estimated effect	Standard error
Average	74.30	1.03
A: α_0	-4.11	2.06
B: α_1	1.41	2.06
C: C	-3.57	2.06
D: $Sc_{\Sigma,coeff}$	11.27	2.06
AB	1.58	2.52
AC	-2.80	2.06
AD	-1.45	2.52
BC	-0.98	2.06
BD	0.68	2.52
CD	4.61	2.52

Table 6.4: Estimated effects for the average error of the inter-facial surface density constants.

Factor	High level	Low level	Optimum level
α_0	1.25	0.75	1.25
α_1	1.25	0.75	0.75
C	3.125	1.875	3.125
$Sc_{\Sigma,coeff}$	1.25	0.75	0.75

Table 6.5: High, low and optimum values selected for the statistical study of the inter-facial surface density constants.

Figure 6.5 represents radial profiles of inter-facial surface density. A significant improvement in its prediction is obtained around the spray axis, for radial distances $r/D_o < 0.4$. However, the maximum value and the spray width are clearly over-predicted, which is another large source of errors. This is previously observed in the verification assessment of Section §5.2.5. The present model gives a more spread spray contour near the orifice exit. From this study it can be concluded that the solution to that problem is not tunning constants of transport equation of inter-facial surface density Σ (Equation (4.24)).
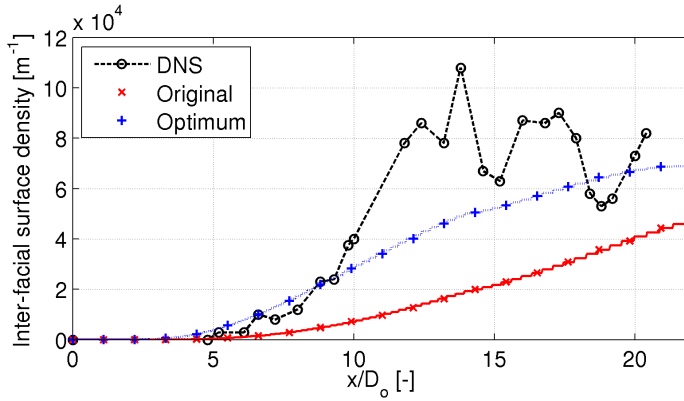
Figure 6.4: Axial profiles of the inter-facial surface density for the statistical study comparing the original case with the optimum one.

6.2.3   Conclusions and recommendations

A multilevel factorial statistical study has been performed over the four constants that appear in the inter-facial surface density transport equation. First order interaction between two factors were considered.

One constant, $Sc_{\Sigma, coeff}$, is statistically significant; however it only covers 40% of the variability of the averaged error. This means that the quality of DNS data to compare with must be improved and it is necessary to achieve statistical convergence in its post-processing.

An optimum set of values within the range of variation ($\pm 25\%$) for the four constants has been obtained. Prediction in the distribution of inter-facial surface density has been clearly improved, but the model still requires further work.

Tunning the present model does not lead to small errors when comparing with DNS results, so maybe it is recommended to change the model, as done by other authors [2, 5], and then perform a new statistical study. Still, an over-prediction in spray width is expected due to the nature of the model.

6.3   Numerical schemes

As already commented in Section §4.2.3, numerical schemes have a major influence over convergence and accuracy of the simulation. This needs to be studied for every solver, domain and set of boundary conditions. Though the

(a) $x/D_o = 5$.

(b) $x/D_o = 10$.

(c) $x/D_o = 20$.
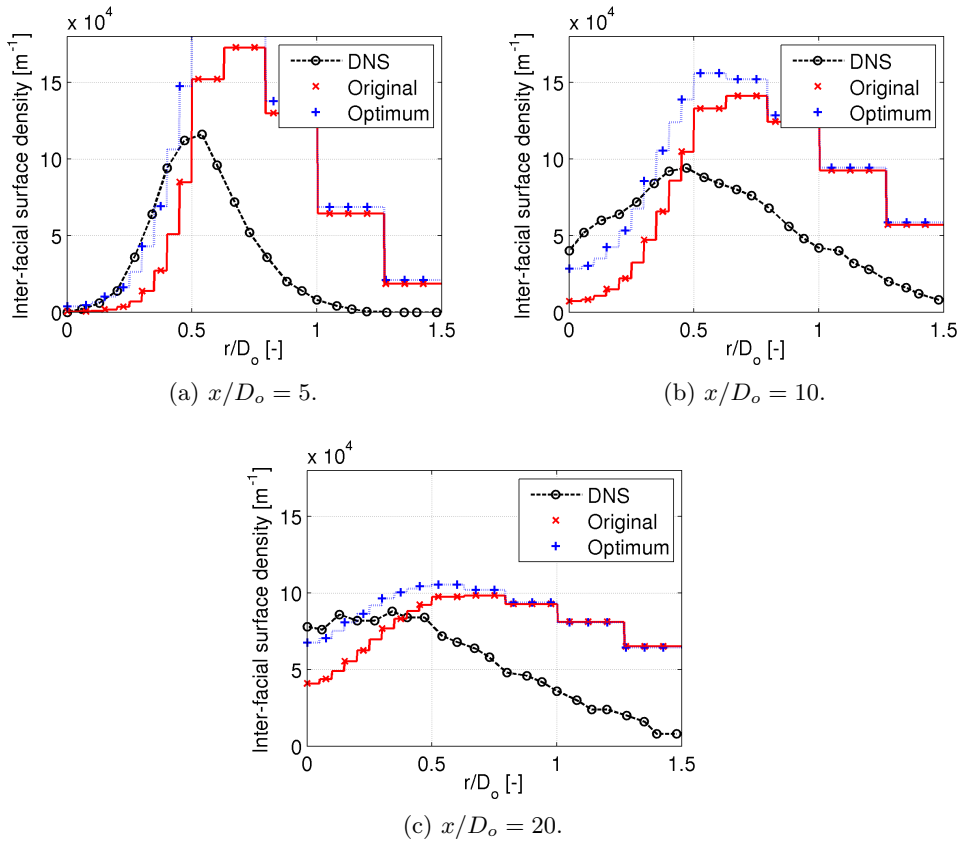
Figure 6.5: Radial profiles of the inter-facial surface density for the statistical study comparing the original case with the optimum one.

real domain should be used [6], its high computational cost, taking into account the large number of simulations to be perform, make that unreleasable.

Instead, the case used is the one employed in the verification assessment to compare with DNS results, detailed in Section §5.2.5. Since that case does not include the nozzle, the influence of numerical schemes in mass flow rate and area, velocity and discharge coefficients cannot be analyzed. Nevertheless, this case has the advantage of comparing the tested numerical schemes with a high accurate solution, not with experimental results which have some uncertainties.

6.3.1 Discretization schemes

The most common choices for terms listed in Table 4.2 are tested and compared. The first result to point out concerns the time derivative discretization schemes. Others different than Euler (first order, bounded, implicit) lead to divergence of the solution. Another interesting result is that different surface normal gradient schemes (uncorrected, corrected, bounded, fourth and limited) and different Laplacian schemes (linear uncorrected, linear corrected, linear limited, linear orthogonal, cubic uncorrected and mid point uncorrected) produce exactly the same result with the same computational cost. Linear uncorrected schemes are selected just because they are the ones used throughout Chapter 4.

Interpolation schemes

Up to 3 different schemes are tested for the discretization of interpolation terms: linear, cubic and mid point. The axial profiles of liquid volume fraction are shown in Figure 6.6. Linear and mid point interpolation generate the exact same profile with the same computational cost, whilst cubic interpolation predicts a faster decay in liquid volume fraction for distances longer than $x/D_o = 8$.

Figure 6.6: Axial profile of the liquid volume fraction for all interpolation schemes tested in comparison with DNS results.

Liquid volume fraction fields are presented in Figure 6.7. As said before, linear and mid point schemes generate the same results, both capture well the main behavior of the spray. Cubic scheme has an intact length similar

to DNS but the spray contour is not the same. Far from the orifice exit the liquid concentration is lower; and some oscillations are obtained at the air-liquid interface, which are not observed in the DNS results due to the averaging process performed by Ménard et al. [7].

(a) DNS results.   (b) Linear.

(c) Cubic.   (d) Mid point.
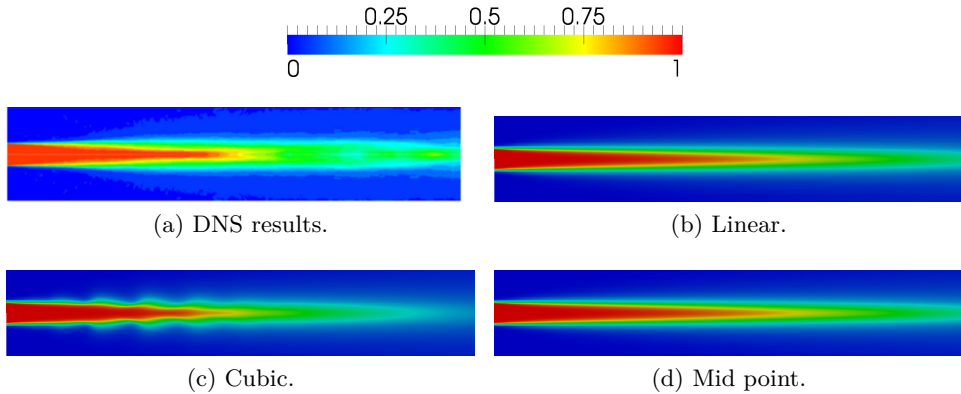
Figure 6.7: Contours of the liquid volume fraction for all interpolation schemes tested in comparison with DNS results.

Gradient schemes

Up to 5 different schemes are tested for the discretization of gradient terms: Gauss linear, fourth, least squares, Gauss cubic and Gauss mid point. The axial profiles of liquid volume fraction are shown in Figure 6.8. All schemes capture well the trend obtained with DNS but the fourth scheme, which clearly underestimates the liquid concentration for distances larger than $x/D_o = 5$. It is difficult to say which one represents better the DNS results because statistical convergence is not reached [5], nonetheless it seems that mid point scheme, the one that gives higher values for the liquid mass fraction, fits DNS evolution best.

Liquid volume fraction fields are presented in Figure 6.9. The main behavior of the spray is well captured by all schemes but fourth scheme, which obtains shorter intact core length and a spray contour very different than that from DNS. This scheme generates oscillations in the air-liquid interface, which may generate instabilities in the solution. The rest of the schemes generates almost the same contour and it is not possible to select one over the rest. Regarding the computational cost, cubic scheme is 15% more expensive than the rest, which require approximately the same CPU time.
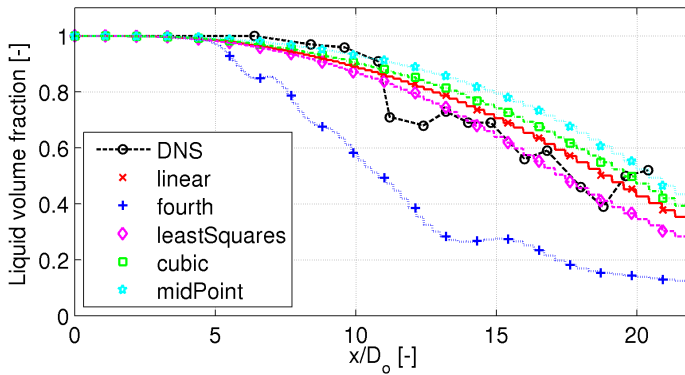
Figure 6.8: Axial profile of the liquid volume fraction for all gradient schemes tested in comparison with DNS results.

Divergence schemes

Up to 7 different schemes are tested for the discretization of divergence terms: Gauss upwind, Gauss cubic, Gauss linear, Gauss MUSCL, Gauss QUICK, Gauss SFCD and Gauss vanLeer. The axial profiles of liquid volume fraction are shown in Figure 6.10. Only upwind and SFCD schemes reproduced correctly the trend obtained with DNS. The rest of them predict a sudden drop of the volume fraction between 5 and 10 times D_o.

Liquid volume fraction fields are presented in Figure 6.11. The main behavior of the spray is well captured by only upwind scheme. SFCD scheme obtains the same intact core length, but the spray contour far from the nozzle is almost not continuum. The rest of schemes produce shorter intact core lengths and not continuous sprays. These schemes also generate oscillations in the air-liquid interface which are not observed in the averaged figure from DNS. Discontinuities and oscillations may generate instabilities in the solution, so they need to be suppressed.

Summary

OpenFOAM, unlike other CFD softwares, allows discretization of transport equations term by term. This provides an additional degree of freedom to assess accuracy and stability, but also requires and additional study.

It is shown how the discretization approaches greatly affect the solution. Just by selecting one or another scheme the spray contour is completely dif-

(a) DNS results.   (b) Linear.

(c) Fourth.   (d) Least squares.

(e) Cubic.   (f) Mid point.
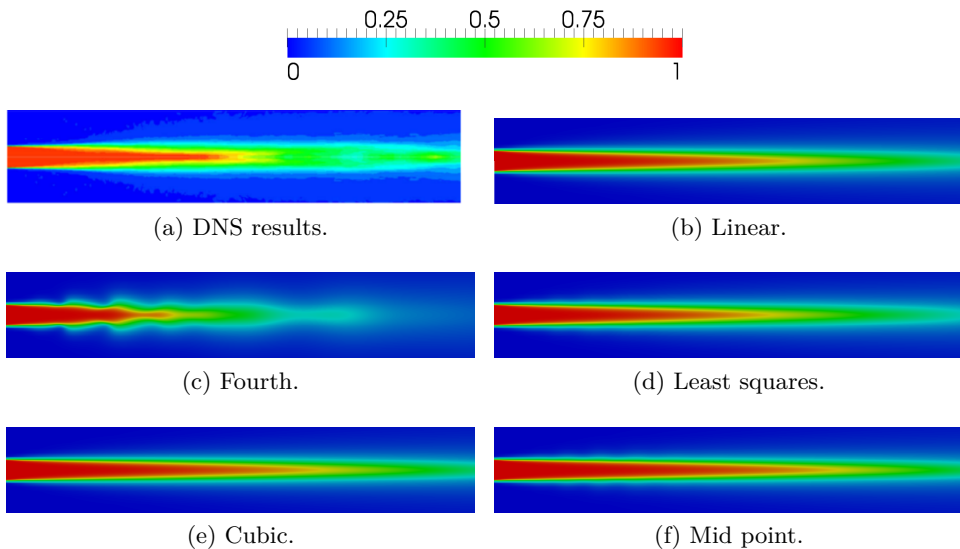
Figure 6.9: Contours of the liquid volume fraction for all gradient schemes tested in comparison with DNS results.

ferent. This may lead to wrong conclusions. Therefore, selecting the right schemes is a key step in simulating sprays.

For short distances, shorter than $x/D_o \approx 5$, the solution is similar regardless what numerical scheme is used. Nonetheless, some of them produce oscillations at the air-liquid interface, which are not observed in the high accurate solution from DNS.

Best discretization schemes for every term are depicted in Table 6.6. Except for the gradient term they are the same than the ones Martínez-López [8] selected for his RANS internal nozzle flow simulations. Then, although the schemes are tested only for the spray evolution, one can be confident that they are the best for internal and external flows at the same time.

6.3.2   Linear solvers

Linear solvers

All solvers introduced in Table 4.9 are tested. Diagonal solver only works for explicit systems, so it could not be applied to all variables, and therefore is excluded from the study. No differences in liquid volume fraction distribution are found, however smooth solver has a computational cost 6 times higher than PCG/PBiCG and GAMG solvers. It is interesting to see that GAMG,
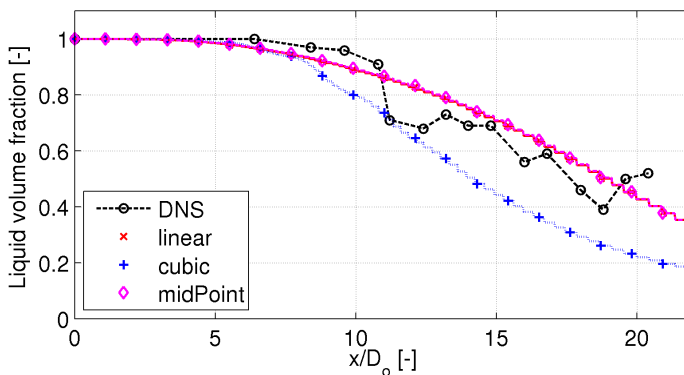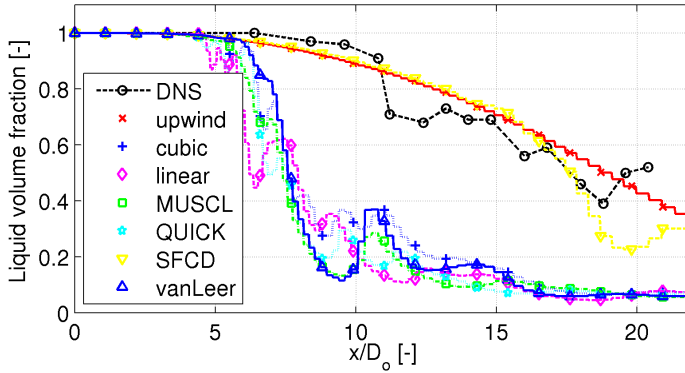
Figure 6.10: Axial profile of the liquid volume fraction for all divergence schemes tested in comparison with DNS results.

Term keyword	Best scheme
interpolationSchemes	Linear
snGradSchemes	Linear
gradSchemes	Gauss midPoint
divSchemes	Gauss upwind
laplacianSchemes	Gauss linear uncorrected
ddtScheme	Euler

Table 6.6: Numerical schemes selected for the discretization of all terms of the transport equations.

with default values for all its parameters, does not reduce the computational cost as intended.

Preconditioner

All preconditioners introduced in Table 4.10 are tested. No use of preconditioner leads to divergence of the solution. Again, no differences in liquid volume fraction distribution are found between DIC/DILU and diagonal preconditioners, however computational cost of using diagonal is more than 6 times higher than using DIC/DILU.
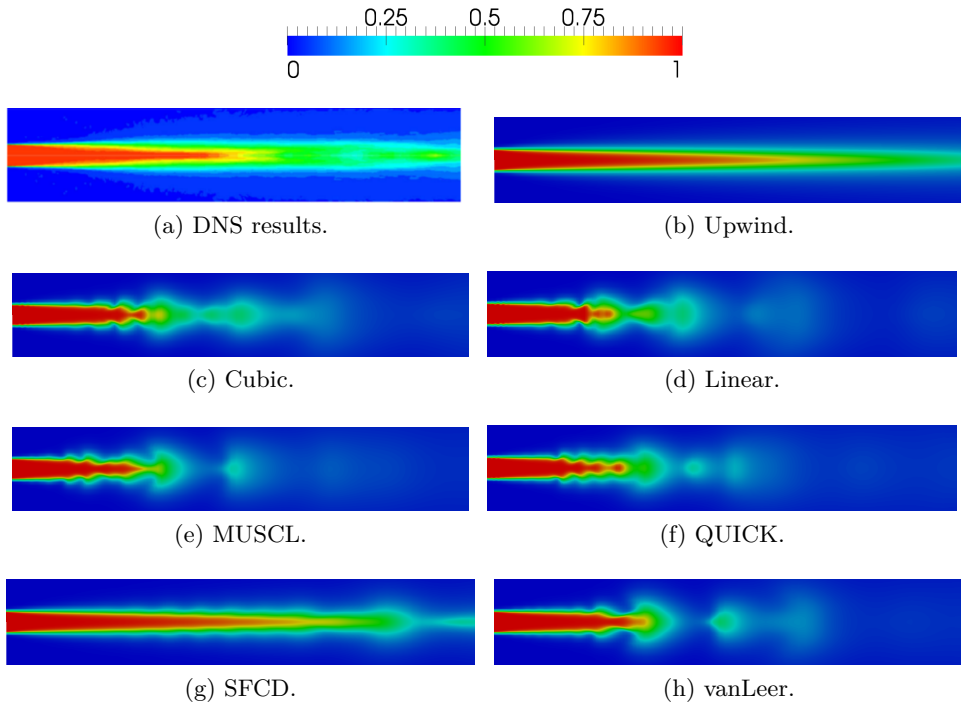
Figure 6.11: Contours of the liquid volume fraction for all divergence schemes tested in comparison with DNS results.

Smoother

All smoothers introduced in Table 4.11 are tested. The linear solver for these cases is, obviously, smooth solver and not DIC/DILU. As before, no differences in liquid volume fraction distribution are found, nonetheless the computational cost of using DIC/DILU Gauss Seidel is twice of using Gauss Seidel and 8 times of using DIC/CILU.

Summary

It is shown that, regardless the numerical solvers selected for the model, the solution is exactly the same. Only the computational cost changes. This was kind of expected. Therefore, the criteria to select one or another numerical configuration is the computational cost. Best linear solvers and their options are depicted in Table 6.7.

Keyword	Best option
Solver	PCG/PBiCG
Preconditioner	DIC/DILU
Smoother	Not required

Table 6.7: Linear solvers selected for solving all transport equations.

6.4   Parameters adjustment

In the present model there are many more parameters (additional to those previously studied) that, according to the literature, can take several values within a range. As done in Section §6.2, a design of experiments is used in order to minimize the error, but in this case results are compared with experiments. This methodology also allows obtaining the best combination of values in addition to know which are the most relevant factors of the simulation.

The problem and case set-up, boundary conditions and turbulence model are exactly the same than the ones used for the validation assessment, described in Section §5.3. The only difference is that the length of the discharge volume is reduced to 10 mm to save computational cost. Thus, this study focuses on the near-field spray development. One point of the test matrix of Table 5.30 is taken: nozzle A, injection pressure of $p_i = 30\,\mathrm{MPa}$ and ambient density of $\rho_g = 40\,\mathrm{kg/\,m^3}$ (back pressure $p_b = 3.6\,\mathrm{MPa}$), which is the lowest injection velocity and therefore lowest computational cost.

6.4.1   Statistical analysis: Design of Experiments

The objective of this study is to check if it is possible to minimize the error in spray penetration of the simulation when compared to experimental results. As the penetration is a parameter that depends on time, the averaged error for the whole injection duration is taken as the variable of interest.

The amount of parameters which influence the solution is large. It is necessary to select the most characteristics ones in order to perform the design of experiments. An Ishikawa diagram (also called fish-bone, herringbone or cause-and-effects diagram) helps out to identify potential factors causing and overall effect [4]. Each cause or reason for imperfection is a source of variation. Causes are grouped into major categories to identify these sources of variation. After a brainstorming done by experts, uncertainties on the following

parameters came out as the most relevant for causing error in the predicted penetration:

- People (mind work): domain generation and assumed hypothesis.
- Method (process): sub-models, mesh resolution, type of boundary conditions, turbulence model, atomization model constants (C_ρ, α_0, α_1, C and $Sc_{\Sigma,coeff}$), turbulence model constants (α_{k1}, α_{k2}, $\alpha_{\omega1}$, $\alpha_{\omega2}$, β_1, β_2, β^*, γ_1, γ_2, a_1 and c_1) and dimensionless parameters (turbulent Schmidt and Prandtl numbers)
- Technology (equipment): precision used in the simulation, diameter of the orifice, sac volume and needle position.
- Material (raw, parts): fluid properties such density, viscosity, specific heat capacity and compressibility, and also gas properties such viscosity.
- Measurement (quality of the data): experimental standard deviation (reproductivity, accuracy), definition of spray penetration.
- Environment (conditions): injection pressure, ambient density, ambient pressure and injection temperature.

Factors included in people primary cause are not studied simply because the hypothesis and the domain (once the solution is not domain dependent) cannot be changed. Technology and measurement categories are not related directly to the goodness of model, which is the objective of this study, so they are not considered neither. Density, compressibility and heat capacity of the fluids are well experimentally characterized [9, 10], so those secondary causes from material group are dismissed. Regarding the method causes, sub-models, mesh resolution, type of boundary conditions, turbulence model and some of the atomization model constants have been already studied in previous Sections §4.4, §5.3 and §6.2.1. And regarding the environment conditions, ambient pressure gives the ambient density because the temperature is fixed, and the injection temperature, though is one of the main concerns of the engine community, it is also fixed (in the experiments, by a temperature regulation system).

The analysis of the Ishikawa diagram gives 18 secondary causes or parameters to study. This would lead to too many simulations, so a further reduction is needed: gas viscosity is assumed known from the literature; Prandtl number is dismissed because it is expected to have a negligible effect on the spray evolution under isothermal conditions; the constant C_ρ was studied and fixed by Demoulin et al. [3]; and some turbulence model constants ($\alpha_{\omega1}$, $\alpha_{\omega2}$, β_1,

β_2, γ_1 and γ_2) are discarded because their effects it is expected to be small. At the end, 9 different factors are selected for the statistical analysis, each of them with two levels, high and low, as shown in Table 6.8. Physical meaning of the last four factors is clear, but that of turbulence model constants have not been previously discussed:

- α_{k1} and α_{k2} appear in Equation (4.101); they determine how much diffusivity the turbulent viscosity ν_t adds to the turbulent kinetic energy transport equation (Equation (4.99)).

- β^* appears in Equations (4.99) and (4.110); thus it is the constant that weights the dissipation of turbulent kinetic energy.

- a_1 only appears in Equation (4.109); it has no effect if the velocity gradient is small, but sets the turbulent viscosity value for high velocity gradient situations, such the one encountered in the Diesel injection process.

- c_1 is found also in Equation (4.109); it defines the production source term of turbulent kinetic energy.

Factor	Units	High level	Low level
α_{k1}		1.70068	0.42517
α_{k2}		1.0	0.5
β^*		0.101	0.07
a_1		0.62	0.155
c_1		20	5
Sc	-	1.5	0.5
ν_f	m^2/s	$3.5\ 10^{-6}$	$0.5\ 10^{-6}$
p_i	MPa	130	130
ρ_g	kg/m^3	40	10

Table 6.8: High and low values selected for the statistical study of the model parameters adjustment.

By selecting two levels for the constant, linear dependency is assumed between the variable of interest and each factor. It is expected that optimum values are close to those defined by default; so the error of assuming linearity is expected to be small because variations on the variable of interest are small too.

As in Section §6.2, commercial software Statgraphics Centurion XVI ® is used to carry out the study. A multilevel factorial design [4] with first order interaction between factors is selected. This type of design leads to 516 simulations. Obviously, that many simulation is not feasible. In order to reduce the number of simulation, some interactions are excluded, only interactions between environment causes (injection pressure or ambient density, one of them) and the rest of them are left. To further reduce the number of simulations, an optimal design is used [4]. Concretely, a D-optimal design, which minimizes the variance, or equivalently maximizes the differential Shannon information content of the parameter estimates. This two methodologies to reduce the number of simulations obtain a test matrix of only 25 cases, depicted in Table 6.9. Other statistical criteria were tested for the optimization, A (minimize the trace of the inverse of the information matrix) and G (minimize the maximum variance of the predicted value), but the efficiency of the D-optimal design was much higher.

Because only some first order interactions between factors are considered, 7 coefficients are enough to define the mathematical model of the variable of interest. This leaves 18 degrees of freedom to estimate the error of such mathematical model, a value larger than the recommended of 10 degrees of freedom [4].

The case set-up is the same than the one used for the validation assessment, described in detail in Section §5.3.1. Injection conditions are varied when required following Table 6.9.

6.4.2   Results of the analysis

The analysis includes, first, substantiation that the mathematical model employed is correct, second, an analysis of variance (ANOVA) to determine the significant factors, and third and last, the analysis of effects and optimization of the system.

Substantiation of the model

It is necessary to address the applicability of the hypothesis of the model (normal distribution, residual independence, homogeneity of variance and linearity) to ensure the robustness of the conclusions drawn from the study [4]. This can be done by analyzing the residuals.

Normality of the residuals

Case	α_{k1}	α_{k2}	β^*	a_1	c_1	Sc	ν_f	p_i	ρ_g
1	0.42517	0.5	0.07	0.155	5	0.5	$3.5\ 10^{-6}$	30	40
2	0.42517	0.5	0.07	0.62	20	0.5	$0.5\ 10^{-6}$	30	10
3	0.42517	0.5	0.07	0.62	20	0.5	$0.5\ 10^{-6}$	130	40
4	0.42517	0.5	0.101	0.155	20	0.5	$0.5\ 10^{-6}$	130	10
5	0.42517	0.5	0.101	0.155	20	0.5	$3.5\ 10^{-6}$	130	40
6	0.42517	2	0.07	0.155	5	0.5	$3.5\ 10^{-6}$	130	10
7	0.42517	2	0.101	0.62	5	0.5	$3.5\ 10^{-6}$	130	40
8	1.70068	0.5	0.101	0.155	5	0.5	$0.5\ 10^{-6}$	130	40
9	1.70068	0.5	0.101	0.155	20	0.5	$3.5\ 10^{-6}$	30	40
10	1.70068	0.5	0.101	0.62	20	0.5	$3.5\ 10^{-6}$	130	10
11	1.70068	2	0.07	0.155	5	0.5	$0.5\ 10^{-6}$	30	10
12	1.70068	2	0.07	0.155	20	0.5	$0.5\ 10^{-6}$	30	40
13	1.70068	2	0.07	0.62	20	0.5	$0.5\ 10^{-6}$	130	10
14	1.70068	2	0.101	0.62	20	0.5	$3.5\ 10^{-6}$	30	10
15	0.42517	0.5	0.07	0.62	20	1.5	$3.5\ 10^{-6}$	130	10
16	0.42517	0.5	0.101	0.155	20	1.5	$0.5\ 10^{-6}$	30	40
17	0.42517	2	0.07	0.155	20	1.5	$3.5\ 10^{-6}$	30	10
18	0.42517	2	0.07	0.155	20	1.5	$0.5\ 10^{-6}$	130	40
19	0.42517	2	0.101	0.62	5	1.5	$0.5\ 10^{-6}$	30	10
20	0.42517	2	0.101	0.62	5	1.5	$0.5\ 10^{-6}$	130	10
21	1.70068	0.5	0.07	0.155	5	1.5	$3.5\ 10^{-6}$	130	10
22	1.70068	0.5	0.07	0.62	5	1.5	$3.5\ 10^{-6}$	30	40
23	1.70068	0.5	0.07	0.62	5	1.5	$3.5\ 10^{-6}$	130	40
24	1.70068	0.5	0.101	0.155	20	1.5	$0.5\ 10^{-6}$	30	10
25	1.70068	2	0.101	0.155	20	1.5	$3.5\ 10^{-6}$	130	10

Table 6.9: Simulations of the multilevel factorial design performed for the model parameters adjustment.

One of the most important hypothesis of the multi-factorial statistical study is the Gaussian distribution of the residuals. That means that there are only few cases in which the error deviates more than twice the standard deviation from the mean value. As shown in Figure 6.12 which represents the cumulative probability of the residuals, there is no evidence that the residuals do not fulfill this hypothesis.

Residuals independence
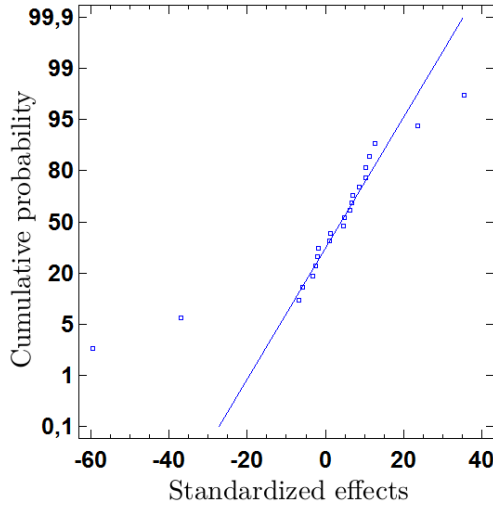
Figure 6.12: Cumulative normal probability of the residuals for the model parameters adjustment.

Another important hypothesis is the residual independence, in other words, there should not exist any relationship between the residuals of samples. Residuals are normally distributed in Figure 6.13, no clear trend is observed, therefore there is no evidence to reject the residual independence assumption. Additionally, the statistic Durbin-Watson test [4] with a p-value greater than 0.05 proves that there is not serial autocorrelation in the residuals with a significance level of 95%.

Homoscedasticity

A sequence of random variables is homoscedastic if all random variables in the sequence have the same finite variance. This is also known as homogeneity of variance. This hypothesis cannot be dismissed because, again, no trend is observe in Figure 6.14, where residuals are plotted versus their predicted values.

Linearity

As previously commented, linear dependency is assumed between the variable of interest and each factor. However, lack-of-fit test cannot be performed if replications of the study are not carried out.

In this case, replications do not add any kind of information because the system is deterministic; no matter how many times simulations are run, results
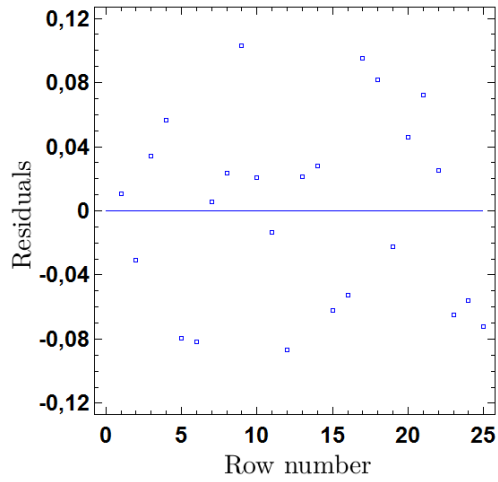
Figure 6.13: Residuals versus the number of the simulation for the model parameters adjustment.
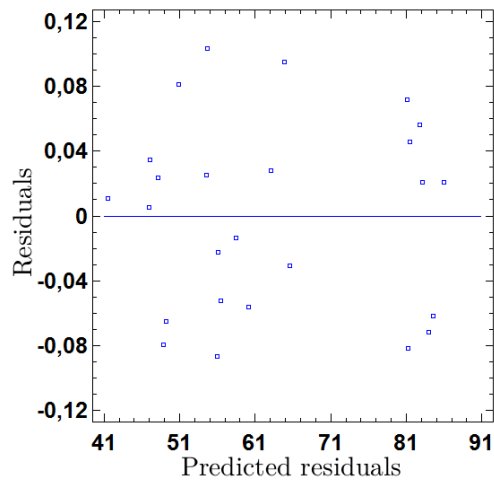
Figure 6.14: Residuals versus predicted residuals for the averaged error in the model parameters adjustment.

are always the same. So this hypothesis is not confirmed. Nonetheless, the error of assuming linearity is expected to be small.

Analysis of variance

The variability of the error (variable of interest) is split in different terms, each of them account for each effect. Thus, statistical significance of factors can be checked out by comparing the root mean square with an estimated experimental error.

Table 6.10 summarizes the ANOVA analysis, performed as indicated by Montgomery [4]. In this case, there are some factors which have a p-value lower than 0.05, which means that the error for these factors are statistically different with a significance level of 95%.

Regarding the main effects, Sc, α_{k1}, α_{k2}, a_1, c_1, p_i and ρ_g are relevant, whilst β^* and ν_f do not affect the error in predicting the penetration. Combining this results with those shown in Table 6.11, some important conclusions can be drawn. First one, the error in the prediction of the penetration depends on injection conditions: higher injection pressure leads to greater errors, and higher ambient density reduces the error. The second one involves the Schmidt number, increasing it significantly increases the error, what suggests that Schmidt number lower than unity should be used, as recommended by other authors [11]. Third and last conclusion involves the turbulence model, up to 4 of its analyzed constants may be changed to minimize the error.

Regarding the interactions between factors, it is clear that the best value of turbulence model constants do correlate to injection conditions. Just as an example, it seems that the Schmidt number should be changed as function of the ambient density, not the injection pressure, to minimize the error in predicting the penetration. This is better analyzed in the next subsection.

Next step is to consider only significant factors. This is an iterative procedure because, when factors are removed from the study, the mathematical model changes and so the significant factors. At the end the R^2 statistic indicates that the statistical model explains 99.38% of the variability of the variable of interest, the averaged error in spray penetration predictions. The adjusted-R^2 statistic, more suitable when comparing models with different independent variables, is 98.64%. Relevant factors and interactions are: Sc, α_{k1}, a_1, c_1, p_i, ρ_g, $Sc - \rho_g$, $\alpha_{k1} - \rho_g$, $\beta^* - p_i$, $\beta^* - \rho_g$, $c_1 - p_i$, $c_1 - \rho_g$ and obviously $p_i - \rho_g$. The mean absolute error is 0.91.

Factor	Root mean square	F-test	p-value
A: Sc	31.76	104.42	0.0094
B: α_{k1}	32.83	107.93	0.0091
C: α_{k2}	11.70	38.46	0.0250
D: β^*	0.51	1.66	0.3263
E: a_1	39.11	128.60	0.0077
F: c_1	169.61	557.67	0.0018
G: p_i	381.15	1253.19	0.0008
H: ρ_g	1077.95	3544.18	0.0003
I: ν_f	3.24	10.67	0.0823
AG	1.33	4.37	0.1719
AH	22.25	73.17	0.0134
BG	1.99	6.53	0.1250
BH	13.64	44.85	0.0216
CG	1.08	3.56	0.1997
CH	0.34	1.11	0.4032
DG	14.46	47.54	0.0204
DH	49.14	161.56	0.0061
EG	10.08	33.14	0.0289
EH	6.19	20.35	0.0458
FG	14.37	47.26	0.0205
FH	6.88	22.64	0.0414
GH	414.808	1363.85	0.0007
Total error	0.30		
Total squared sum	5275.53		

Table 6.10: ANOVA analysis for the model parameters adjustment.

Effects and optimization

Table 6.11 shows the estimated effect of each factor and interaction. It also shows the standard error of each of these effects, which is more or less constant. Estimated effects are also graphically represented in Figures 6.15 and 6.16.

Factor	Estimated effect	Standard error
Average	61.17	0.39
A: Sc	2.72	0.99
B: α_{k1}	3.09	0.87
D: β^*	0.10	0.83
E: a_1	2.33	0.89
F: c_1	6.55	0.90
G: p_i	10.73	0.84
H: ρ_g	-20.77	0.77
AH	2.46	0.91
BH	2.46	0.86
DG	2.11	0.94
DH	2.78	0.90
FG	-1.96	0.89
FH	2.37	0.98
GH	-11.68	0.78

Table 6.11: Estimated effects for the average error in the model parameters adjustment.

Main effects have been already commented, but interactions require further explanation. All statistically significant interactions on Figure 6.16 are analyzed one by one:

- AH, $Sc - \rho_g$: when using the low level of Schmidt number, ambient density does not have any effect on the error; but for the high level of Schmidt number, the error increases about 5% from using the low level to the high level of ambient density. Therefore, as concluded from the analysis of the main effect of the Schmidt number, it is proper to use a low value.

- BH, $\alpha_{k1} - \rho_g$: when using the low level of α_{k1}, ambient density barely affects the error; but for the high level of α_{k1}, the error increases about
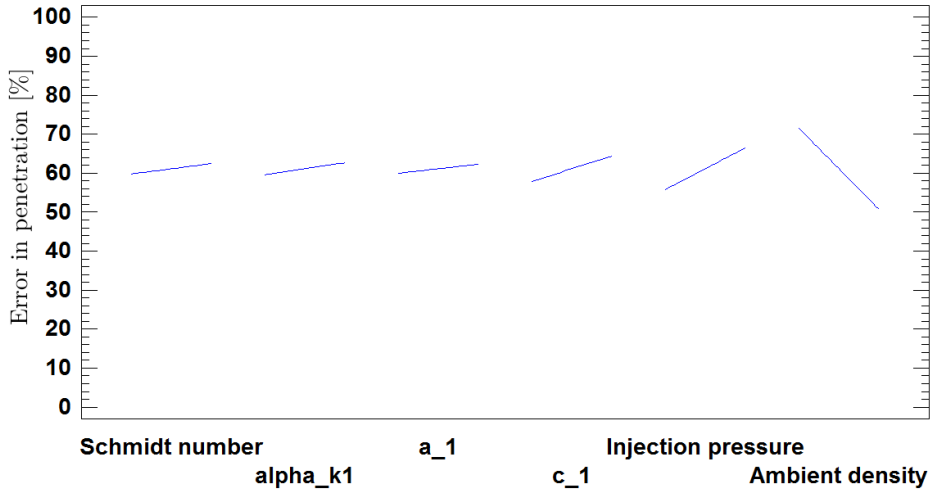
Figure 6.15: Main effects for the averaged error in the model parameters adjustment.
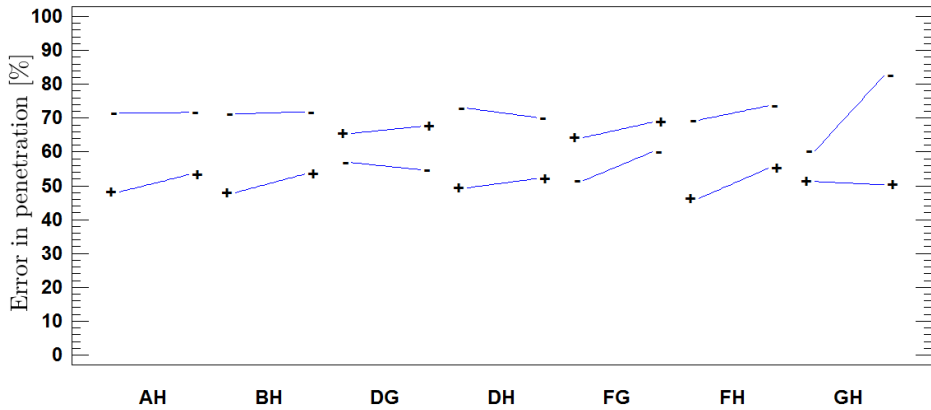
Figure 6.16: Interactions effects for the averaged error in the model parameters adjustment.

5% from using the low level to the high level of ambient density. Therefore, as concluded from the analysis of the main effect of α_{k1}, it is proper to use a low value.

- DG, $\beta^* - p_i$: though β^* main effect is not significant, its optimum value depends on injection pressure. When using the low level of β^*, the error slightly decreases from using the low level to the high level of injection pressure; but for the high level of β^* the error slightly increases.

- DH, $\beta^* - \rho_g$: though β^* main effect is not significant, its optimum value depends on ambient density too in the exact same way than depends on injection pressure. When using the low level of β^*, the error slightly decreases from using the low level to the high level of ambient density; but for the high level of β^* the error slightly increases.

- FG, $c_1 - p_i$: when using both the low and high level of c_1, the error increases about 8% from using the low level to the high level of injection pressure.

- FH, $c_1 - \rho_g$: again, when using both the low and high level of c_1, the error increases about 8-10% from using the low level to the high level of ambient density.

- GH, $p_i - \rho_g$: when using the high level of injection pressure, the level of ambient density barely modifies the error; however, when using the low level of injection pressure, the error increases more than 20% from using the low level to the high level of ambient density.

Despite all of this explanations, it seems that always one level of the model constants give a better value for both, high or low level of injection condition. Nonetheless, a bit of controversial is found. For example, a low level for c_1 is desired if only the combination with injection pressure is analyzed, but a high level is better if only combination with ambient density is considered. This means that, once constants are optimized, they should not be changed when boundary conditions are varied.

Finally, software Statgraphics can be used to obtain the optimum combination of parameters to minimize the averaged error. That combination is presented in Table 6.12, reduces the error more than 15%. Note that injection conditions and fuel properties are not depicted, simply because they are defined by the test point and were included in this statistical study only to check if they are related with the parameters of the model. Generally, low levels are used. This means that turbulent kinetic energy production terms should be reduced in order to minimize the error, and therefore also its dissipation.

Factor	High level	Low level	Optimum level
Sc	1.5	0.5	0.5
α_{k1}	1.70068	0.42517	0.4229435
α_{k2}	2.0	0.5	0.844012
β^*	0.101	0.07	0.07
a_1	0.620	0.155	0.174982
c_1	20.0	5.0	5.0

Table 6.12: High, low and optimum values selected for the model parameters adjustment.

The most surprising value of those in Table 6.12 is the optimum Schmidt number, $Sc = 0.5$. This agrees with the work of Salvador et al. [11], who concluded that beyond approximately 3.5 or 4 mm, spray characteristics are properly reproduced by a Schmidt number of 0.5. Nonetheless, the same study proves that $Sc = 1$ is necessary for the right prediction of the intact core length. There has been always a bit of controversial in determining the Schmidt number value. The simplest way to do so is the Reynolds analogy[4], which yields a turbulent Schmidt number of 1. However, Reynolds analogy is valid for flows that are close to developed, for whom, changes in the gradients of field variables (velocity and temperature) along the flow are small [12]. Thus, even if an optimum value of $Sc = 0.5$ has been obtained, a deeper and more focused study is necessary to confirm or reject that result. The variable of interest in such study could be the error in spray angle, though using the error in velocity or fuel concentration radial profiles seems a better option. This allows avoiding uncertainties in spray angle measurements (see Section §2.4.3).

6.4.3   Conclusions and recommendations

A multilevel factorial statistical study has been performed over: 6 constants that appear through the model (mainly on the turbulence model) injection conditions, and one fuel property. First order interaction between boundary conditions and model constants were considered.

---

[4]The main assumption in the Reynolds analogy is that heat flux (mass flux) in a turbulent system is analogous to momentum flux, which suggests that the ratio between these two fluxes must be constant for all radial positions.

Four constants (Sc, α_{k1}, a_1 and c_1) together with the injection conditions are statistically significant for the spray penetration error; and they cover 99% of the variability of the averaged error. This means that optimizing these four constants as function of injection conditions may allow a great reduction in the error. An optimum set of values within the range of variation (half and twice) for the six constants has been obtained. Nevertheless, this optimum need to be tested in a real Diesel spray case, including both internal and external flows.

6.5 Application of the adjustment

Previous studies have been performed in either a simplified spray case (Sections §6.2 and §6.3) or a reduced domain where only the near-field is considered (Section §6.4). Therefore, it is necessary to check if obtained conclusions apply to a real case, and how they modify some parameters which have not been analyzed.

6.5.1 Case description

In order to keep the same methodology followed so far, the problem case set-up, boundary conditions and turbulence model are the the ones used for the validation assessment, described in Section §5.3, where the parameters listed next have been modified according the results previously presented in this chapter:

- Constants α_0, α_1, C and $Sc_{\Sigma,coeff}$ of inter-facial surface density transport equation (Equation (4.24)) are given in Table 6.5.

- Inlet boundary condition is constant pressure instead of time varying velocity coefficient, simply because it improves the prediction of spray parameters (see Section §5.3.4).

- Constants α_{k1}, α_{k2}, β^*, a_1 and c_1 of the SST $k - \omega$ turbulence model are given in Table 6.12.

- Although the optimum Schmidt number obtained is 0.5, $Sc = 1$ has been employed to be able to accurately predict the break-up and intact core lengths, as discussed in Section §6.4.2.

Two points of the test matrix of Table 5.30 are taken: nozzle A, ambient density of $\rho_g = 40 \, \text{kg/m}^3$, and two different injection pressures, the highest value ($p_i = 130 \, \text{MPa}$) and the lowest ($p_i = 30 \, \text{MPa}$). These two different

injection pressures have been selected because it has been proved that the prediction accuracy is not the same for all injection conditions in the validation assessment of Section §5.3.6.

6.5.2 Results

Internal nozzle flow

Mass flow rate and momentum flux are presented in Figure 6.17. Note that two different experimental curves are plotted; each one corresponds to a different injection pressure. First clear difference is the one already commented in Section §5.3.4, constant pressure inlet boundary condition generates squared profiles of mass flow rate and momentum flux, without any oscillations in time and values slightly higher than in the experiments for low injection pressure conditions. This difference with experiments is due to the pressure head losses inside the injector body, negligible for high injection pressures but significant for low injection pressures [13]. In fact, the constant mass flow rate and momentum flux values matches maximum values obtained with the time varying inlet boundary condition.

Also commented before, the constant pressure boundary condition is much more accurate for high injection pressure, where the rising slope of mass flow rate and momentum flux are higher. Another interesting result concerns the oscillations obtained short time aSOI in the simulations, which seem to follow oscillations experimentally observed, but with a smaller amplitude. The only source of oscillations in the model is the compressibility of the liquid, which allow the pressure wave traveling up and down inside the nozzle. These oscillations are rapidly damped in the model whilst they extent for the whole injection duration in the mass flow rate measurement (see Figure 6.17a). However, very small or none oscillations are observed in the experimental momentum flux (Figure 6.17b), and the same is obtained with the simulations employing a constant pressure inlet boundary condition.

Dimensionless coefficients that describe the hydraulic behavior of the flow are depicted in Table 6.13. Clear over prediction in velocity coefficient and under-prediction of area coefficient, resulting in an increase in discharge coefficient, are obtained. This is because of the higher values of mass flow rate and momentum flux obtained, which can be explained through the velocity profile at the orifice exit, shown for all cases in Figure 6.18. For the low injection pressure case, the velocity is higher if the new configuration is used. This effect belongs to the change in the boundary condition. Furthermore, the parabolic part of the profile is reduced when proposed changes are applied. That means

(a) Mass flow rate.
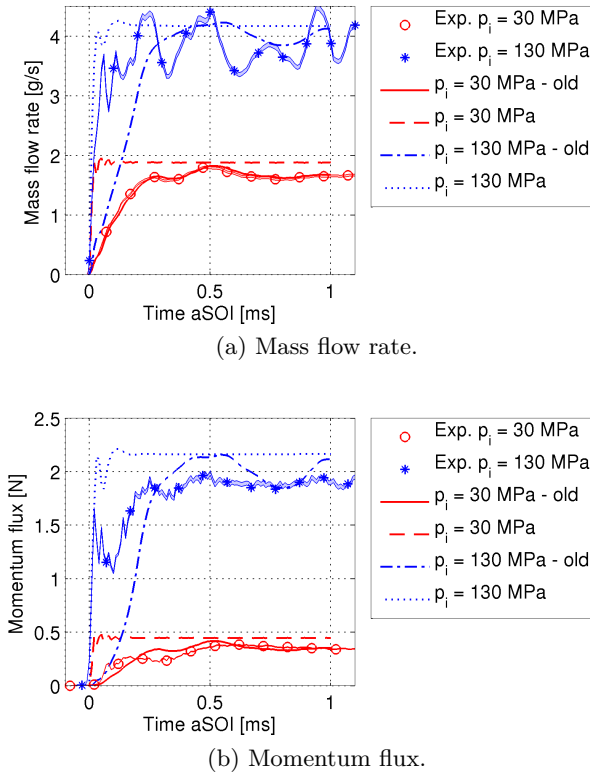
(b) Momentum flux.

Figure 6.17: Mass flow rate and momentum flux for the application of the adjustment cases.

a thinner boundary layer which seems to be the right solution, as discussed in Section §5.3.5. This second effect is associated to the change in the turbulence model constants (it means, reduction of the production of turbulent kinetic energy). Apparently, modifications on constants made in previous sections by simply considering only the spray penetration also improve the internal flow behavior.

In order to match experiments (values of dimensionless coefficients), a slightly lower pressure value than the nominal injection pressure has to be introduced at the inlet, specially at low injection pressures. A one-dimensional pressure losses model could be very interesting for that. Other possible solution is modeling the needle movement, then the mass flow rate is restricted at early stations of the injection process.

p_i [MPa]	C_d [-]	C_v [-]	C_a [-]
Exp. 30	0.85	0.89	0.95
30 old	0.80	0.82	0.98
30	0.90	0.95	0.95
Exp. 130	0.89	0.91	0.98
130 old	0.88	0.89	0.98
130	0.89	0.97	0.92

Table 6.13: Dimensionless coefficients that describe the hydraulic behavior for the application of the adjustment cases.
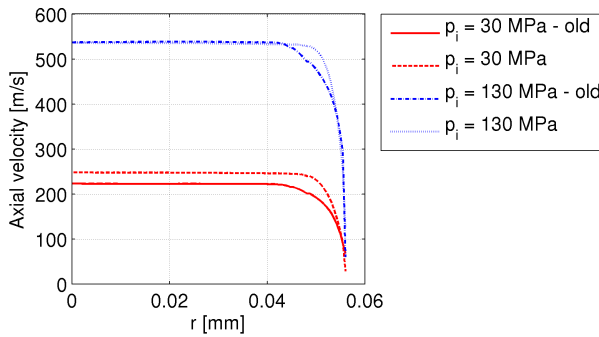
Figure 6.18: Velocity profile at the exit of the orifice for the application of the adjustment cases.

Spray evolution

Spray penetration and spray angle are plotted in Figure 6.19. In this case, unlike for the validation assessment, experimental penetration curves have not been moved in time. Although the high accuracy obtained if only the external flow is simulated (see Figure 5.22) is not present in this case, a great improvement in the prediction of spray penetration is observed. Still, the spray angle is under-predicted, nonetheless its value has increased with the modifications, getting closer to the experimental one.

However, differences between computations and experiments are better analyzed by the penetration curve slope, the $R - parameter$ (defined in the Appendix 5.A). Table 5.45 summarizes its value averaged in time for the whole injection duration. Modifications in the set-up of the case greatly change
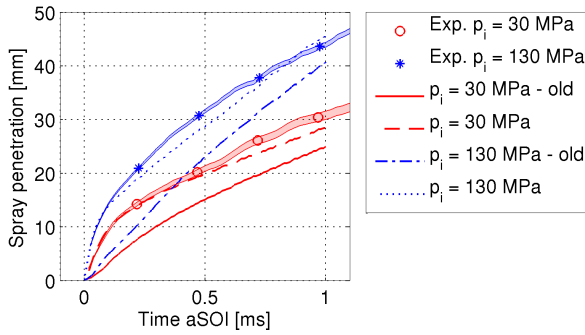
(a) Mass flow rate.
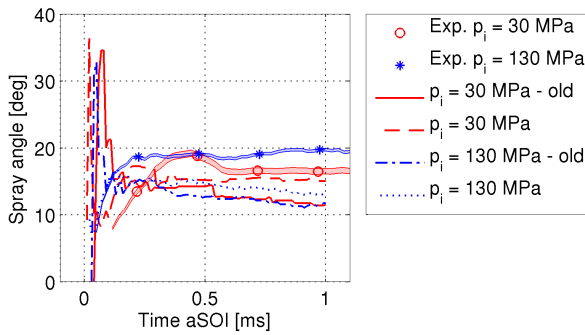
(b) Momentum flux.

Figure 6.19: Spray penetration and spray angle for the application of the adjustment cases.

$R - parameter$. With the old configuration, it is always under-predicted. With the new proposed constants, $R - parameter$ is under-predicted and the error is reduced for low injection pressures, but exactly the opposite happens for high injection pressures, $R - parameter$ is over-predicted and the error is increase.

p_i [MPa]	30	30	30	130	130	130
Set-up	Exp.	Old	Opt.	Exp.	Old	Op.
$R - parameter$ [m/ s$^{1/2}$]	0.98	0.65	0.78	1.86	1.73	2.03

Table 6.14: Steady state $R - parameter$ for the application of the adjustment cases.

For a better understanding of the spray behavior, time evolution of the $R - parameter$ is plotted in Figure 6.20. The behavior of the spray for low injection pressures is perfectly captured by the simulation, though a value 20% lower is obtained. Notwithstanding, for high injection pressure the obtained $R - parameter$ is not constant in time but grows linearly. The change on the configuration reduces the slope of the curve, but does not eliminate the time dependency. An even better optimization is needed for this case, either on boundary and initial conditions, or on constants values (values of constants β^* and c_1 are related to the injection pressure, as proved in the statistical analysis described in Section §6.4).
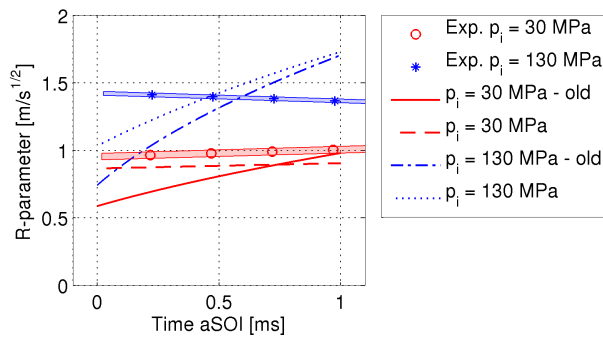
Figure 6.20: $R - parameter$ time evolution for the application of the adjustment cases.

So far, only the changes on turbulence model and boundary conditions have been analyzed because no microscopic parameter has been studied. Remember that the transport equation of inter-facial surface density is decoupled from the rest, and it is employed just to compute the droplet size. So changes proposed in Section §6.2 have to be analyzed through directly the surface density Σ or the droplet size SMD. Figure 6.21 shows the distribution of droplet size along the spray axis and the radial one at $x = 20\,\mathrm{mm}$. Differences between configurations observed in Figure 6.21a are mainly associated to differences in spray penetration, curves are barely the same but shifted in axial position. An interesting result is that differences are larger for low injection pressures, as clearly observed in Figure 6.21b, but also in in Figure 6.21a. In that last figure, the break-up length can be defined as the axial position where the droplet size drops from infinite (very large, no droplets but ligaments) to very small droplets, meaning that the break-up process is complete. That distance, with the change in the configuration of the case, increases from 5.32 to 6.13 mm

for the low injection pressure case and decreases from 6.78 to 6.29 mm for the
high injection pressure case.
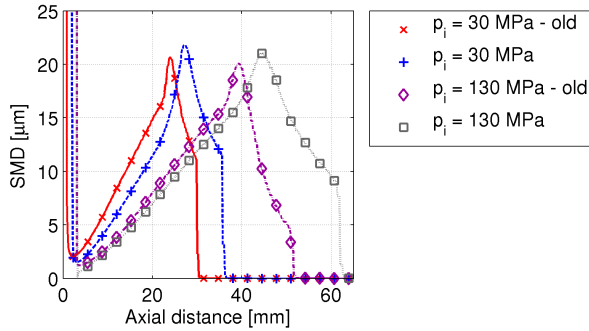
(a) Axial profile.
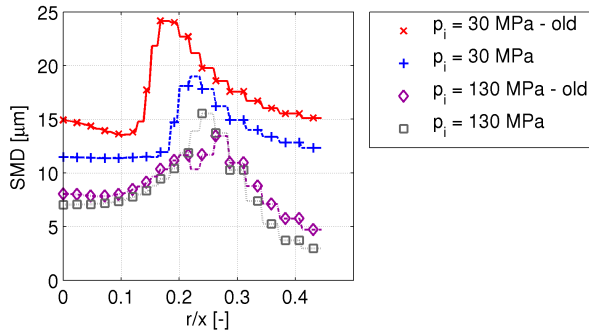
(b) Radial profile at $x = 20$ mm.

Figure 6.21: Distributions of Sauter Mean Diameter for the application of the
adjustment cases.

6.6 Summary

The model has been analyzed from the numerical point of view. Not only
different numerical schemes have been tested and compared with high accurate
solutions; also the effect of "arbitrary" constants used by the model has been
studied. The most relevant parameters that have a significant influence on
the prediction error have been identified.

First, constants that define source terms of the inter-facial surface density
transport equation have been varied. Values proposed by Vallet et al. [1]
turned out not to be the best ones for the present model. Nonetheless, just by

changing the inter-facial surface density diffusivity coefficient $Sc_{\Sigma,coeff}$ value, which is traditionally assumed equal to the mass fraction diffusivity coefficient Sc_t, the solution of the simulation can be adjusted to experimental or DNS results.

Regarding the linear solvers, no difference has been found in the solution but an increase in computational cost is obtained if other than the generally recommended ones are used. Central differencing first order discretization schemes have proved to be stable, fast and accurate enough for most terms of the transport equations. Only for gradient terms, a linear scheme with symmetric weighting gives best results than central differencing.

The effect of some other constants additional to those of inter-facial surface density transport equation have been also analyzed. Not all of them could be tested due to computational cost issues, but the six most relevant have, together with their relationships with injection conditions. Reducing the production of turbulent kinetic energy, in other words, lower values of the three most relevant constants of the SST $k - \omega$ turbulence model, reduces the error in predicting the spray penetration. Though optimum values for those constants have been given, a further analysis is needed because some of them fall to the minimum tested value, so maybe lower values allow reducing even more the error. A different discussion shall be done for the Schmidt number due to the controversial found in the literature. An optimization study only for this parameter should be performed if completive conclusions are desired. Nonetheless, now it is known that the Schmidt number value is related only to the ambient density, and not to the injection pressure, and this simplifies the future study.

Optimum parameters have been applied to a couple of the validation benchmark cases. A great improvement has been obtained for all the comparison metrics analyzed. Some important conclusions can be further drawn from this study. First, a constant pressure inlet boundary condition is better than the time varying velocity selected and employed in the validation assessment. Second, a time varying pressure inlet boundary condition is necessary to reproduce the experimental mass flow rate and then being able to accurately predict dimensionless coefficients (if needle movement is not simulated). Third, the spray behavior is now very well predicted by the model for low injection pressures; however, more work is necessary to adjust the model constants for high injection pressure cases.

References

[1] Vallet, A., A. A. Burluka, and R. Borghi. "Development of a Eulerian model for the "Atomization" of a liquid jet". *Atomization and Sprays*, vol. 11.6 (2001), pp. 619–642 (*cit. on pp. 270, 271, 276, 305*).

[2] Beheshti, N., A. A. Burluka, and M. Fairweather. "Assessment of $\Sigma - Y_{liq}$ model predictions for air-assisted atomisation". *Theoretical and Computational Fluid Dynamics*, vol. 21.5 (2007), pp. 381–397. DOI: `10.1007/s00162-007-0052-3` (*cit. on pp. 270, 278*).

[3] Demoulin, F. X., P. A. Beau, G. Blokkel, and R. Borghi. "A new model for turbulent flows with large density fluctuations: Application to liquid atomization". *Atomization and Sprays*, vol. 17.4 (2007), pp. 315–345. DOI: `10.1615/AtomizSpr.v17.i4.20` (*cit. on pp. 270, 287*).

[4] Montgomery, D. C. *Design and Analysis of Experiments*. Ed. by W. Anderson. Fifth edition. 605 3rd Avenue, 10158-0012, New York, New York, United States of America: John Wiley & Sons, Inc., 1997 (*cit. on pp. 271, 273–275, 286, 289, 291, 293*).

[5] Lebas, R., T. Ménard, P. A. Beau, A. Berlemont, and F. X. Demoulin. "Numerical simulation of primary break-up and atomization: DNS and modelling study". *International Journal of Multiphase Flow*, vol. 35.3 (2009), pp. 247–260. DOI: `10.1016/j.ijmultiphaseflow.2008.11.005` (*cit. on pp. 276, 278, 281*).

[6] Salvador, F. J., J. Martínez-López, M. Caballer, and C. de Alfonso. "Study of the influence of the needle lift on the internal flow and cavitation phenomenon in diesel injector nozzles by CFD using RANS methods". *Energy Conversion and Management*, vol. 66 (2013), pp. 246–256. DOI: `10.1016/j.enconman.2012.10.011` (*cit. on p. 279*).

[7] Ménard, T., S. Tanguy, and A. Berlemont. "Coupling level set/VOF/ghost fluid methods: Validation and application to 3D simulation of the primary break-up of a liquid jet". *International Journal of Multiphase Flow*, vol. 33.5 (2007), pp. 510–524. DOI: `10.1016/j.ijmultiphaseflow.2006.11.001` (*cit. on p. 281*).

[8] Martínez-López, J. "Estudio computacional de la influencia del levantamiento de aguja sobre el flujo interno y el fenómeno de la cavitación en toberas de inyección Diésel". PhD thesis. Camino de Vera, s/n, 46022, Valencia, Spain: Departamento de Máquinas y Motores Térmicos, Universitat Politècnica de València, 2013 (*cit. on p. 283*).

[9]   Payri, R., F. J. Salvador, J. Gimeno, and G. Bracho. "The effect of temperature and pressure on thermodynamic properties of diesel and biodiesel fuels". *Fuel*, vol. 90.3 (2011), pp. 1172–1180. DOI: `10.1016/j.fuel.2010.11.015` (*cit. on p. 287*).

[10] Secretary of Commerce on behalf of the U. S. A., U. S. *Dodecane.* English. National Institute of Standards and Technology. 2013. URL: `http://www.nist.gov/` (*cit. on p. 287*).

[11] Salvador, F. J., S. Ruiz, J. Gimeno, and J. de la Morena. "Estimation of a suitable Schmidt number range in diesel sprays at high injection pressure". *International Journal of Thermal Sciences*, vol. 50.9 (2011), pp. 1790–1798. DOI: `10.1016/j.ijthermalsci.2011.03.030` (*cit. on pp. 293, 298*).

[12] Mahulikar, S. P. and H. Herwig. "Fluid friction in incompressible laminar convection: Reynolds' analogy revisited for variable fluid properties". *European Physical Journal B*, vol. 62.1 (2008), pp. 77–86. DOI: `10.1140/epjb/e2008-00115-0` (*cit. on p. 298*).

[13] Garza de León, O. A. de la. "Estudio de los efectos de la cavitación en toberas de inyección diésel sobre el proceso de inyección y el de formación de hollín". PhD thesis. Camino de Vera, s/n, 46022, Valencia, Spain: Departamento de Máquinas y Motores Térmicos, Universitat Politècnica de València, 2012 (*cit. on p. 300*).

Chapter 7

Spray results

7.1 Introduction

Results presented in previous Chapter 6 were not available at the time other simulations needed to be run for obtaining more results concerning the Diesel spray. Therefore, the best numerical configuration is not used in this chapter. Instead, initial values used for validation in Section §5.3, which are mainly obtained from the literature, are selected. This means that there is still room for improvement of the results presented in this chapter.

A new and modern single-hole Bosch solenoid-activated, generation 2.4, injector is simulated in this chapter. This injector belongs to the research community Engine Combustion Network (ECN), so it is very well experimentally characterized and there is a lot of data to compare with. That allows further validation of the ESA model and also comparison with other computational approaches for both internal and external flows. But more interesting, ESA model is employed to obtain information of such new injector that would be highly complicated (expensive) or impossible with experiments, such spray structure changes when the fuel density is varied.

7.2 Engine Combustion Network: Spray A

The Engine Combustion Network (ECN) [1] started an international collaboration with the aim of obtaining high quality data and consistent results in the field of fuel injection and combustion. The work of the group lays

on several coordinated efforts in the Diesel research field, moving lately also to GDI: the complete definition of a standard condition, the use of nominal identical injectors (donated by Bosch) and the organic cross check of the data obtained by different facilities and through different techniques. Among the large ECN public research database, it can be found: detailed internal geometry characterization of ECN single-hole injectors, concretely of injector 210675 (obtained by Kastengren et al. [2]); definition of target injection and ambient conditions (named Spray A); and a deep experimental characterization of the Diesel spray [1, 3].

7.2.1   Spray A boundary conditions

Table 7.1 summarizes ECN Spray A operating conditions [1]. However, these conditions lead to an evaporative spray; and, as highlighted in Chapter 4, the present model does not include a third phase, fuel vapor. Therefore, ambient gas temperature is decreased to 303 K and ambient gas pressure is also decreased to 2 MPa. Reason why these values are selected is explained in next Section §7.2.2. Then, boundary conditions do not exactly match Spray A conditions, but they are the ones used for many types of experiments.

Although nominal characteristics of the injector are depicted in Table 7.1, nozzle internal geometry of several manufactured "identical" injectors was accurately measured employing X-ray tomography by Kastengren et al. [2]. Small differences with nominal conditions were found. Two particularities are: the orifice is not on the injector axis, there exists certain eccentricity that ranges from 20 to 53 μm (in the case of study is 37 μm); and the orifice cross-section is not exactly circular. Among the injectors that were characterized, the one used for the present work is coded as injector 210675, whose geometry can be seen in Figure 7.1. In this case, the orifice is considered circular, and only the eccentricity is taken into account. The mesh structure can also be seen in the figure. Mesh sensitivity study, similar to the one described in Section §5.3.3, was carried out by ECN collaborators and the final mesh is available on the website [1]. The discharge volume, not completely shown in Figure 7.1, is 10 mm in length and 7 mm in radius. At the end, the mesh consists of 2.25 million hexahedral cells with a minimum cell size of 1.5 μm near orifice walls and maximum cell size of 250 μm far from the nozzle exit.

Target conditions depicted in Table 7.1 give a Reynolds number of $Re = 27212$, an Ohnesorge number of $Oh = 0.0312$, Weber numbers of $We_g = 21000$ and $We_l = 722500$, and a density ratio of $\rho_g/\rho_f = 0.029$. Reynolds and Weber number are high enough to be considered infinite and then fulfill the

Parameter	Units	Value
Ambient gas temperature	K	900
Ambient gas pressure	MPa	6.0
Ambient gas density	kg/m^3	22.8
Ambient gas oxygen	% by volume	0 (non-reacting)
Ambient gas velocity	m/s	< 1, near-quiescent
Common rail fuel injector		Bosch solenoid 2.4
Nominal nozzle outlet diameter	µm	90
Nozzle *k-factor*	µm	1.5
Nozzle shaping		Hydro-eroded
Mini-sac volume	mm^3	0.2
Discharge coefficient	-	0.86
Number of holes		1 (single-hole)
Orifice orientation		Axial
Fuel injection pressure	MPa	150
Fuel		n-Dodecane
Fuel temperature at nozzle	K	363
Injection duration	ms	1.5
Injected mass	mg	3.5-3.7

Table 7.1: Specification for Spray A operating condition of the ECN.

assumptions of the model (see Section §4.2.1). This target condition can also be placed in Figure 5.20, falling inside the atomization regime.

Regarding the boundary conditions and numerical configuration, same than the ones used for the validation assessment and described in Section §5.3.1 are used, except for the inlet boundary condition. All ECN simulation collaborators must use the same boundary conditions (type and value) in order to be able to compare results. The change in the inlet boundary condition suggested by the ECN community is consistent with results obtained in the validation assessment, described in Section §5.3. Values of all field variables come from Table 7.1. Turbulence model is not established by the community, so SST $k - \omega$ turbulence model is selected (see Section §5.3.5) with default values for all of its constants. For inlet boundary condition, time varying pressure is employed. The time evolution of the pressure was measured in the rail during the mass flow rate experiment (data is available on-line [1]), and it is represented as function of time later in Figure 7.3. Reasons why this type of inlet boundary condition is employed by the ECN community
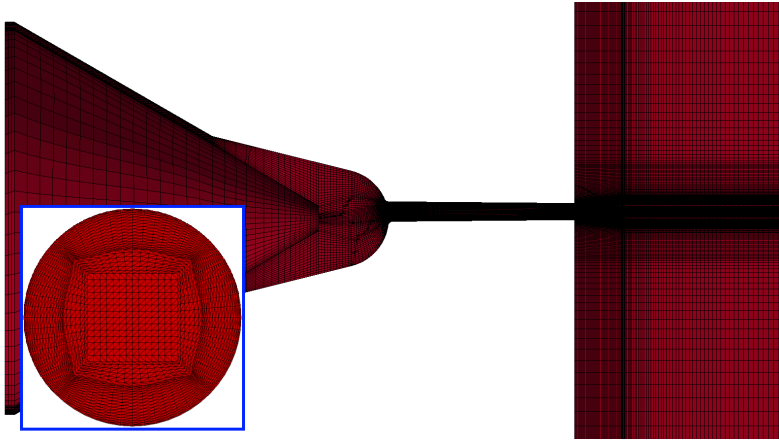
Figure 7.1: Image of the nozzle geometry of injector 210675. Detail of the mesh structure. Overall domain bounding box: (0 -0.006468 -0.006505) (0.013478 0.006542 0.006505) m.

are already explained in Section §5.3.4: better representation of the spray, it reproduces more or less well the mass flow rate for high injection pressure, and the rising slope of the mass flow rate can be also simulated when needle movement is considered.

7.2.2   Two-dimensional Spray A boundary conditions

A two-dimensional version of the case explained in the previous section, shown in Figure 7.2, is built to reduce the computational cost, and thus being able to perform larger number of simulations. Obviously, the eccentricity of the orifice cannot be considered.

Note that, for this two-dimensional domain, the discharge volume length is also short, 12 mm, much shorter than penetration values reached by the spray. This is done also to save computational cost, and it is allowed because the focus of the study is the near-field, only the first 10 mm. The mesh is built following results of the mesh sensitivity study previously performed and described in Section §5.3.3.

The ECN community decided to use the boundary conditions listed below. Boundary values differ from those on Table 7.1. The reason behind this is that results from simulations are compared to experimental data from X-ray measurements, where Spray A conditions could not be reached [4].
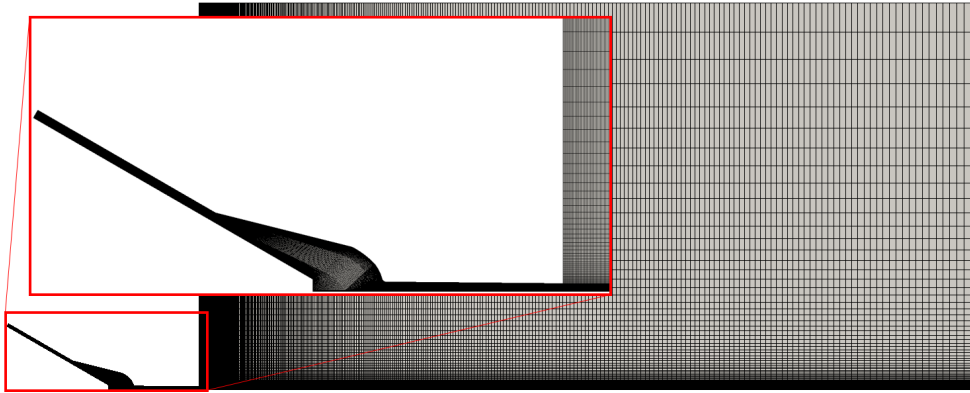
Figure 7.2: Two-dimensional injector 210675 domain for Spray A simulations. Overall domain bounding box: (0 -0.000262 0) (0.014987 0.000262 0.005994) m.

- Inlet boundary condition: time varying pressure with values obtained from experiments (available on the website [1]). Three nominal values for the injection pressure are used: 150, 100 and 50 MPa, all of them represented in Figure 7.3.

- Fuel temperature: 343 K.

- Constant temperature value at walls, equal to the fuel temperature.

- Ambient gas pressure: 2 MPa.

- Ambient gas temperature: 303 K.

7.2.3 Comparison metrics

From the point of view of internal nozzle flow simulations, the following parameters are analyzed and compared to experimental values, when it is possible:

- Mass and momentum flow rates and fluctuation distributions (turbulent kinetic energy) at the nozzle exit versus time.

- Dimensionless coefficients C_a, C_v and C_d.

- Axial slices showing contours of velocity, density, temperature and turbulent kinetic energy.
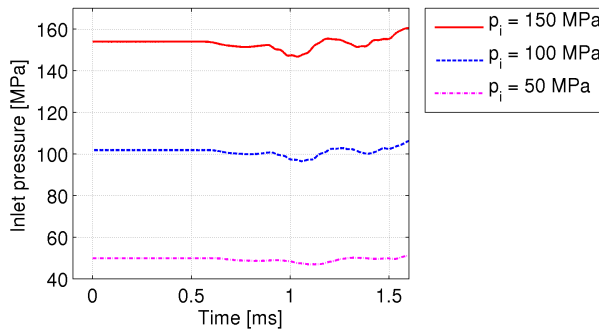
Figure 7.3: Value of pressure inserted at the inlet boundary condition for the two-dimensional ECN case.

- Transverse slices at the nozzle exit showing contours of velocity, density, temperature and turbulent kinetic energy.

From the point of view of spray simulations, focused on near-field, the following parameters are analyzed and compared to experimental values, again when it is possible:

- Fuel spray penetration versus time.
- Axial slices showing contours of projected density at 0.1 and 0.5 ms aSOI.
- Projected fuel density profiles at 0.5 ms aSOI and $x = 0.1, 0.6, 2$ and 10 mm downstream to nozzle exit.
- Transverse Integrated Mass (TIM) versus axial distance at 0.5 ms aSOI.
- Peak projected density and Full Width at Half Maximum[1] (FWHM) of distribution in intervals of 20 μs for the entire injection duration at $x = 0.1$ and 2 mm from the nozzle exit.

The experimental data shown in this entire chapter, obtained by the ECN collaborators, is available on-line [1]. Although many injection conditions have been tested by the ECN, only data for nominal injection conditions (Table 7.1) is represented. This is done to simplify the artwork, too many lines in the plots

---

[1]Full Width at Half Maximum is an expression of the extent of a function, given by the difference between the two extreme values of the independent variable at which the dependent variable is equal to half of its maximum value.

may confuse the analysis. Then, when the accuracy of the model is analyzed, comparison between simulations and experiments for the nominal case are done, but additional cases allow obtaining further conclusions about the flow structure and behavior. Furthermore, not all comparison metrics are available for all injection pressures, for example, X-ray tomography data is not available for low injection pressure.

7.2.4   Internal nozzle flow: two-dimensional results

Time dependent variables

First comparison metrics, mass flow rate and momentum flux, are presented in Figure 7.4. Note that only the first 0.5 ms have been calculated. Squared signals are obtained from simulations. As already observed in Section §5.3.4, a constant pressure inlet boundary condition does not capture the transient behavior without simulating the needle movement. Despite that, experimental steady state values are very well captured by the simulations. Comparing the different injection pressures, as expected, lower mass flow rate and momentum flux are obtained for lower injection pressures.

(a) Mass flow rate.   (b) Momentum flux.
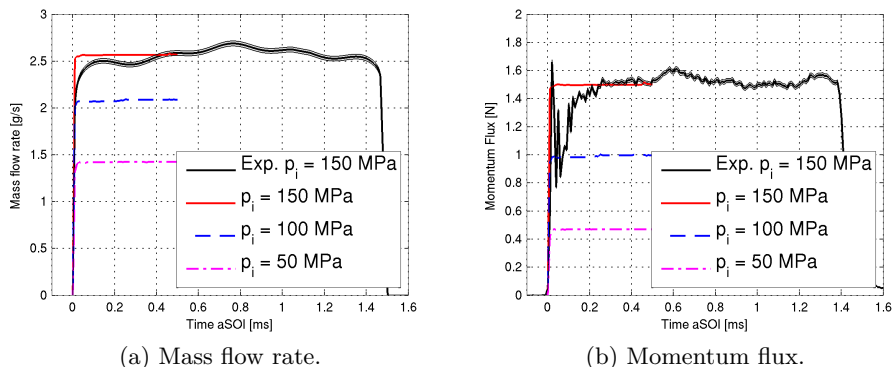
Figure 7.4: Mass flow rate and momentum flux for the two-dimensional ECN case.

The next comparison metric, fluctuation distributions, or in other words turbulent kinetic energy, at the orifice exit is one of the parameters that traditionally are exported from internal flow simulations to spray simulations [5, 6]. Although it is not constant in the radial direction, as shown later, a mass weighted average can be computed in order to check its time evolution, which is represented in Figure 7.5. After a short transient, the average turbulent

kinetic energy reaches a constant value. That value is proportional to the injection velocity, so larger for higher injection pressures. This result means that spray modelers may use a constant value for the turbulent kinetic energy of injected liquid droplets along the whole injection duration. The error is small and affects only to the first transient 0.05 ms.
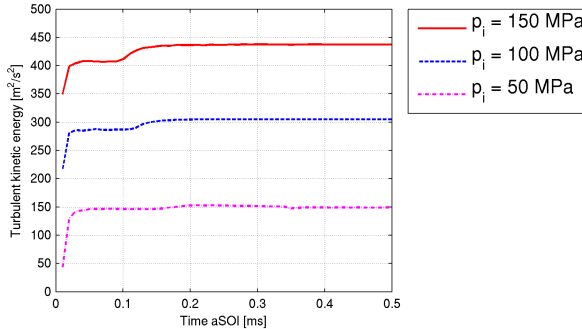
Figure 7.5: Turbulent kinetic energy time evolution at exit section for the two-dimensional ECN case.

Dimensionless coefficients

Values of all dimensionless coefficients that describe the hydraulic characterization of the nozzle (see Section §2.3.4) for this ECN case are depicted in Table 7.2. When simulations are compared to experiments, the highest difference is about 2%, found in the area coefficient. The reason of that is explained later, but is related to the turbulence model. Differences between the three injection pressures are very small, as expected, due to the differences in Reynolds number, also shown in the table, are also small. For all conditions, it is high enough to fall in the turbulent regime (see Figure 2.9).

Snapshots

Figure 7.6 shows the velocity field of the simulations. Very low velocity is found in the sac, as expected. Large acceleration is seen at the orifice inlet, from 0 to approximately 300-400 m/s, but the flow always remains attached. The boundary layer starts growing and reaches a significant width at the orifice exit, though this is better seen in the following analysis of turbulent kinetic energy.

p_i [MPa]	C_d [-]	C_v [-]	C_a [-]	Re [-]
Exp. 150	0.90	0.92	0.98	32211
150	0.88	0.91	0.96	32152
100	0.88	0.91	0.96	26403
50	0.86	0.90	0.95	18388

Table 7.2: Dimensionless coefficients that describe the hydraulic behavior of the two-dimensional ECN case.

(a) 150 MPa.

(b) 100 MPa.

(c) 50 MPa.
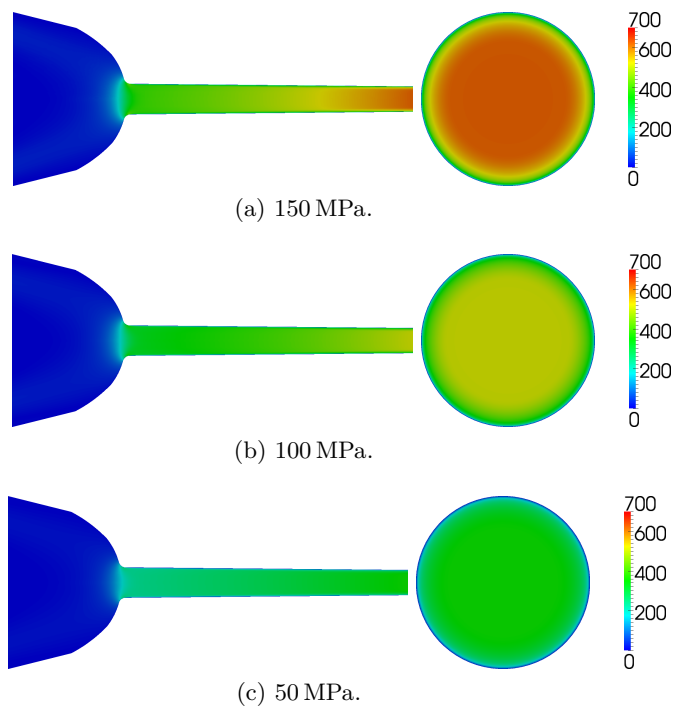
Figure 7.6: Contours of velocity field in m/s inside the nozzle and at the orifice outlet of the two-dimensional ECN case.

Turbulent kinetic energy field as a measure of fluctuations (turbulence) is observed in Figure 7.7. As commented before, turbulence is not the same along the orifice outlet section. Turbulence levels inside the nozzle are very low, except next to the walls, where the velocity gradient is higher and so the turbulent intensity. Boundary layer develops from the orifice inlet and reaches the exit, occupying a relevant part of the exit cross-section. It is known that RANS approach generates wider boundary layers than other approaches, for example LES [7], and this is the reason why the area coefficient is smaller than the experimental value. Nonetheless, a thinner boundary layer can be obtained simply by calibrating constants of the turbulence model, as proved in the optimization performed in Section §6.4.

(a) 150 MPa.

(b) 100 MPa.

(c) 50 MPa.
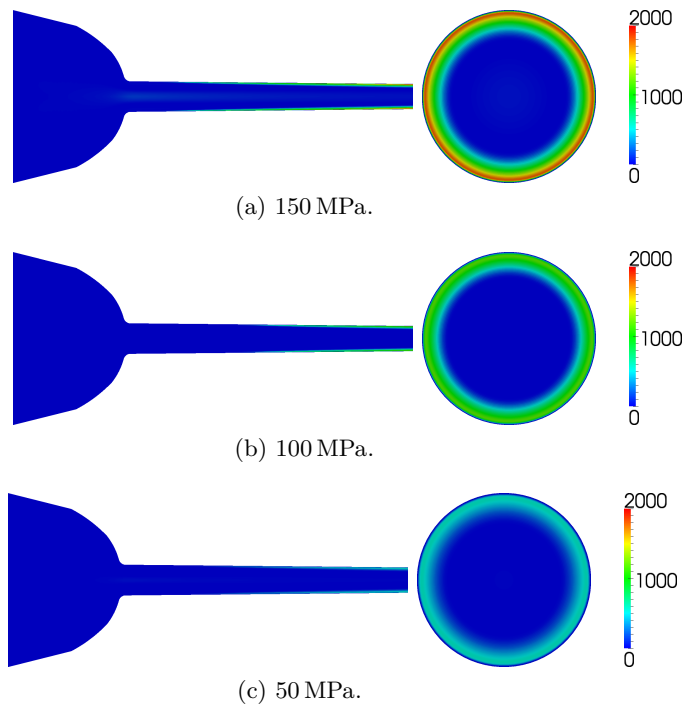
Figure 7.7: Contours of turbulent kinetic energy in $\mathrm{m^2/s^2}$ field inside the nozzle and at the orifice outlet of the two-dimensional ECN case.

Although it is barely visible in the images, at the center of the orifice inlet section, a small increase in turbulence level is obtained, but it is damped and disappears before reaching the mid section of the orifice.

Next variable to be analyzed is the density. This is commonly assumed constant (incompressible liquid), but in this case it depends on pressure and

temperature (see Section §4.4.2), both variables with strong gradients inside the nozzle, specially the pressure. As shown in Figure 7.8, large variations in density are obtained, up to 10%. This proves that liquid fuel should not be considered incompressible in Diesel engine simulations because that assumption is proper only when density variations are lower than 5% [8].

(a) 150 MPa.

(b) 100 MPa.

(c) 50 MPa.
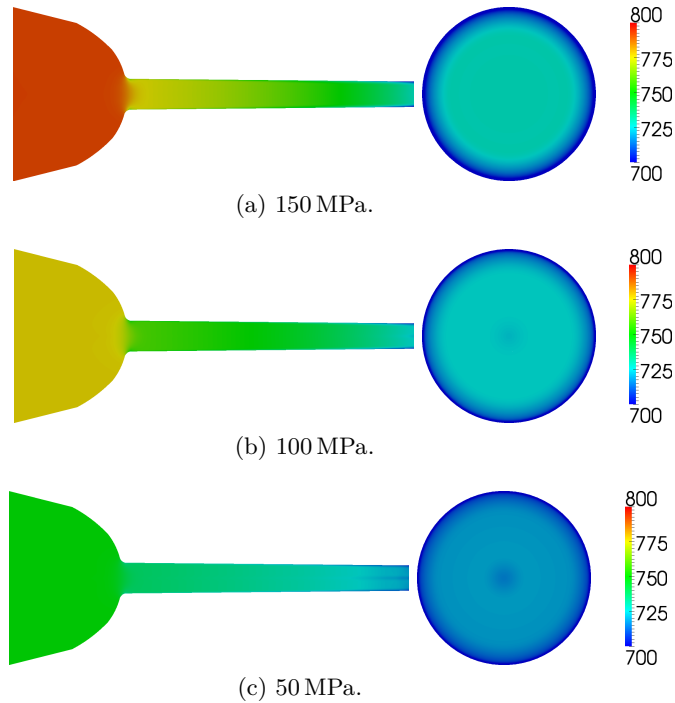
Figure 7.8: Contours of density field in $\mathrm{kg/m^3}$ inside the nozzle and at the orifice outlet of the two-dimensional ECN case.

Comparing different injection pressures, obviously larger density values at the nozzle sac are obtained for higher injection pressures. But more significant is that density variations are larger for higher injection pressures. That is related to temperature gradients, and it even leads to a lower fuel density at the orifice outlet section for higher injection pressures. So the hypothesis of incompressible fluid may be acceptable for low injection pressures, but definitely it is not right for high injection pressures.

Another interesting result is that viscous dissipation in the turbulent boundary layer raises the temperature and thus decreases density of the liquid next to the walls. Temperature contours are shown in Figure 7.9. That effect is clearly observed for the three injection pressures. Two additional comments

on Figure 7.9 can be made. First one is that a cooling of the liquid is obtained
due to the expansion process in the orifice. An average exit temperature of
about 325 K and a value of 323.3 K at the center of the orifice exit section
are obtained for the highest injection pressure case, when fuel temperature
is initially set to 343 K. If the expansion/acceleration from stagnated flow to
exit velocity is assumed one-dimensional and isentropic relationships are used
to compute the orifice exit temperature, a value of 324 K is obtained (NIST
n-Dodecane database [9] is used, where all thermal properties including the
enthalpy and the entropy are tabulated). This clearly means that the flow
inside the nozzle is isentropic. Thus, isentropic calculations are a good first
approximation to consider thermal effects inside the nozzle.

(a) 150 MPa.

(b) 100 MPa.

(c) 50 MPa.
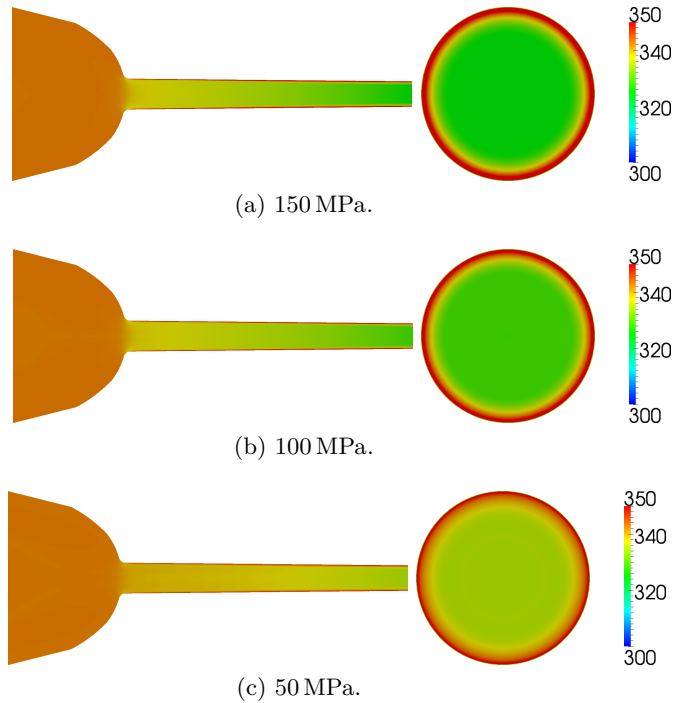
Figure 7.9: Contours of temperature field in K inside the nozzle and at the
orifice outlet of the two-dimensional ECN case.

Second comment regards the difference between the three injection pres-
sures. Temperature is higher for lower pressures because the cooling effect
is reduced by a lesser expansion. Furthermore, the thermal boundary layer
generated by viscous dissipation is thicker for lower injection pressures.

7.2.5 Near-field flow: two-dimensional results

Spray penetration

The first comparison metric of external flow is the spray penetration, as defined in Sections §2.4.3 and §5.3.1. Two different experimental values are considered: one obtained by Sandia National Laboratories through light extinction technique [3], and other obtained by Argonne National Laboratories employing a X-ray tomography technique [4]. Both are used because their values greatly differ and no agreement is found in which one is correct and which one is not.

Figure 7.10 shows the spray penetration. Simulation results agrees with measurements performed by Argonne National Laboratories. Nevertheless, the spray velocity in the first microseconds aSOI is higher than in the experiments because the transient part of the mass flow rate is not well reproduced, as previously shown in Figure 7.4a.
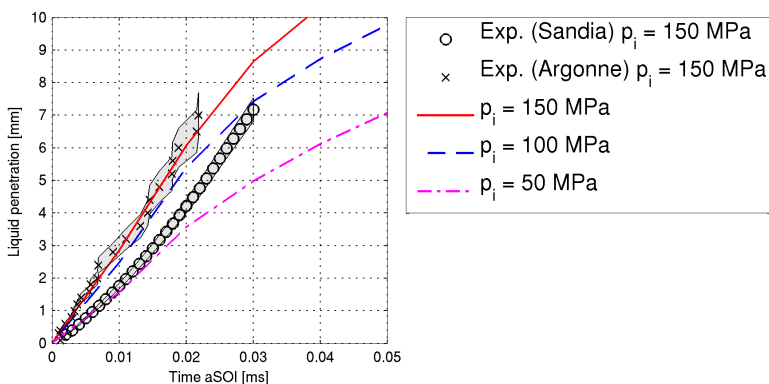
Figure 7.10: Spray penetration for the two-dimensional ECN case.

All three simulation curves follow the theoretical behavior of the penetration described in Section §2.4.3: a linear proportionality with time in the first millimeters, and a square root relation for longer times that t_b, the time needed for a complete break-up. That time is about $t_b = 0.03\,\mathrm{ms}$ in the simulations, whilst $t_b = 0.035\,\mathrm{ms}$ and $t_b = 0.032\,\mathrm{ms}$ are the values obtained with Equations (2.47) and (2.49), correspondingly. Experimentally this time was not observed due to a reduced visualization window size.

Snapshots

The magnitude used to study the fuel concentration in the spray is the projected density because is the one measured with X-ray tomography technique [4]. It could be converted into a mass or volume concentration, but then additional uncertainties would be added, i.e. the density of the liquid which is not exactly known in the spray. That is clearly observed in next Section §7.2.6.

Projected density contours are plotted in Figure 7.11. First comments are: simulations clearly over-predict liquid concentration at "long" distances from the outlet, and RANS model employed tend to be overly diffuse. The intact core length seems to be under-predicted, or at least the concentration on the axis is lower in the simulations. This suggests that the diffusivity coefficient employed in liquid mass fraction transport equation (Equation (4.9)) is too high, so turbulence model needs to be optimize or the diffusion model should be improved.

(a) Exp. 150 MPa at 0.1 ms aSOI.   (b) Exp. 150 MPa at 0.5 ms aSOI.

(c) 150 MPa at 0.1 ms aSOI.   (d) 150 MPa at 0.5 ms aSOI.

(e) 100 MPa at 0.1 ms aSOI.   (f) 100 MPa at 0.5 ms aSOI.

(g) 50 MPa at 0.1 ms aSOI.   (h) 50 MPa at 0.5 ms aSOI.
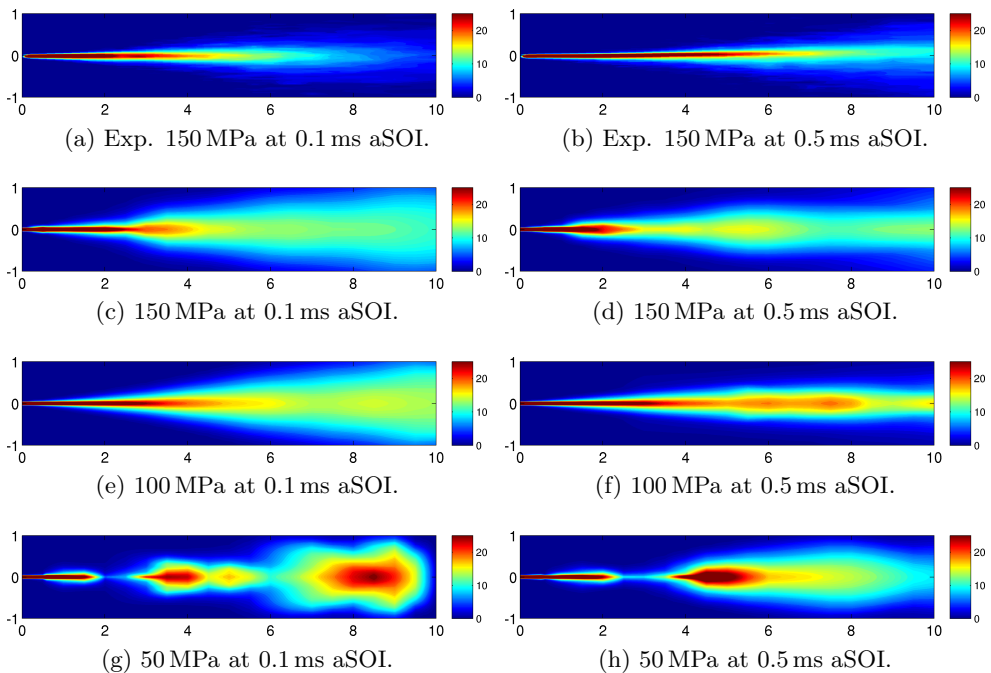
Figure 7.11: Contours of projected fuel density in µg/ mm^2 in the near-field region of the two-dimensional ECN case. Dimensions in millimeters.

Looking at Figures 7.11c and 7.11d it seems that the intact core length decreases with time, but this is not observed in the experiments. As checked

later, this is due to an oscillating nature of the model which should not occur in RANS simulations. These oscillations are associated to the definition of mixture compressibility, given in Section §4.4.2, which may be not correct for multiphase flows, and its relationship with pressure waves generated inside the nozzle and traveling up and down the full domain.

Liquid mass distributions

For a better analysis of the fuel concentration on the spray, projected density profiles are shown in Figure 7.12. First thing to notice is that the experimental curve is off-axis. This is due to the small eccentricity of the real nozzle geometry. The effect of this eccentricity is significant for distances shorter than 2 mm. For longer distances the projected density profiles is centered and almost symmetric.

(a) $x = 0.1$ mm.   (b) $x = 0.6$ mm.

(c) $x = 2$ mm.   (d) $x = 10$ mm.
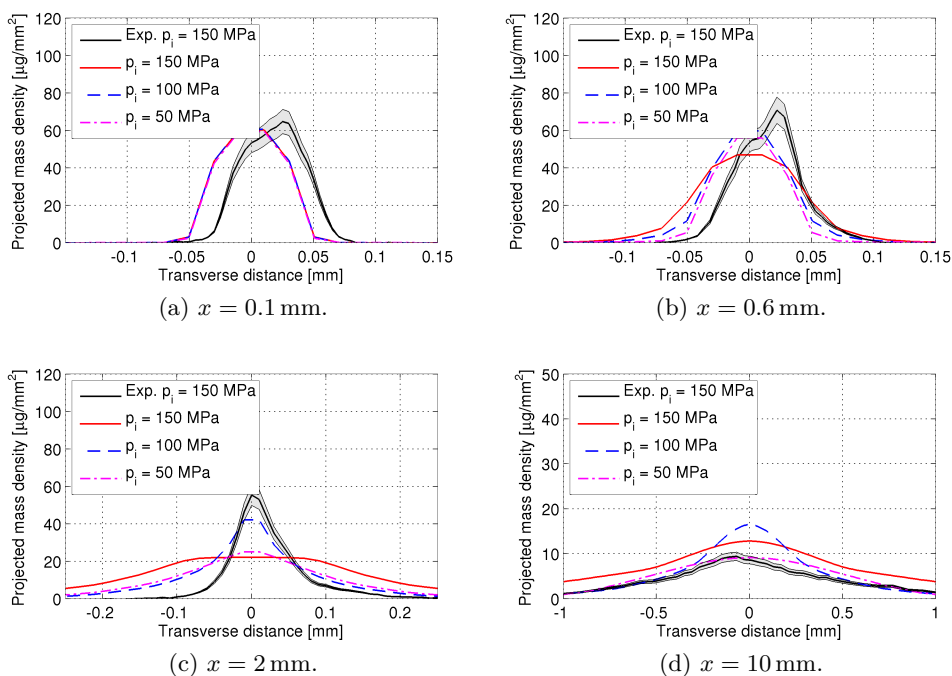
Figure 7.12: Radial profiles of projected fuel density of the two-dimensional ECN case.

When comparing simulation results to experiments, the already commented behavior is observed: for long distances, the spray is wider and the

concentration on the axis smaller, except for very long distances (longer than 10 mm) where the concentration of the simulations is higher than in the experiments.

According to the results shown in Figure 7.12, no much differences in fuel concentration are found for the two highest injection pressures tested. Right after the orifice exit in Figure 7.12a, profiles are exactly the same. Later on some differences are found in the peak values, but again they are associated to the oscillating nature of the solver. The lowest injection pressure provides a much wider spray, as previously shown in Figure 7.11. Nonetheless, this becomes clearer later in the analysis of the time evolution of peak values and FWHM.

Figure 7.13 represents the TIM versus the axial distance from the orifice outlet. TIM at nozzle exit corresponds with the mass flow rate of Figure 7.4a, and it increases with axial distance. Simulations capture this trend; however, they over-predict the TIM, which may be due to over dispersion in the radial direction. In this figure the oscillating nature of the model is obvious. Meanwhile the experimental curve is monotonic growing, the three simulation lines go up and down. In fact, for the lowest injection pressure the rise of the curve is quite large, result which can also be observed in Figure 7.11g and 7.11h. As already said, this behavior is probably associated to a not proper definition of the mixture compressibility. Nonetheless, the large difference found for the lowest injection pressure case may be related also to the time selected for comparison. Injection velocity for that case is lower, as it is the transient rising of the mass flow rate. So, maybe time steps selected of 0.1 and 0.5 ms are too short and steady state are not reached.
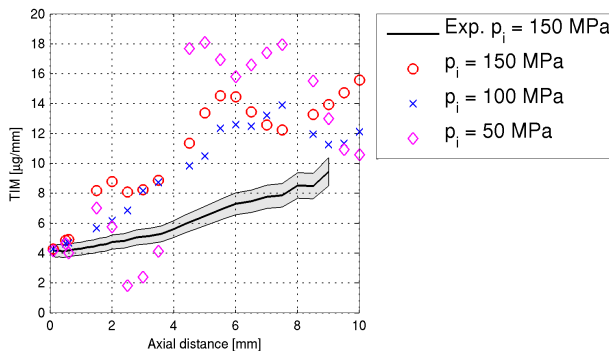
Figure 7.13: TIM versus axial distance for the two-dimensional ECN case.

To end the spray near-field analysis, time evolution of the peak projected density is plotted in Figure 7.14 for two different axial positions, and that of the FWHM is in Figure 7.15. Fluctuations were not expected. As previously observed in Figure 7.12, peak values and spray width are similar for the three injection pressures, and that happens not only at steady state conditions long time aSOI but also in the early stages of the injection. Thus, injection pressure effect on fuel mass distributions is small in the near-field of the spray.
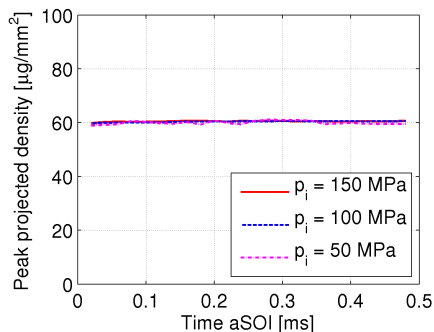
(a) $x = 0.1\,\mathrm{mm}$.
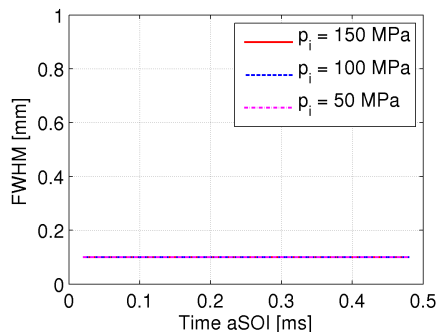
(a) $x = 0.1\,\mathrm{mm}$
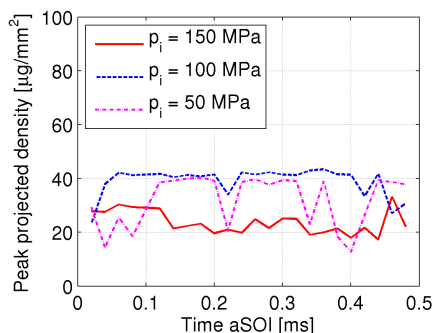
(b) $x = 2\,\mathrm{mm}$.
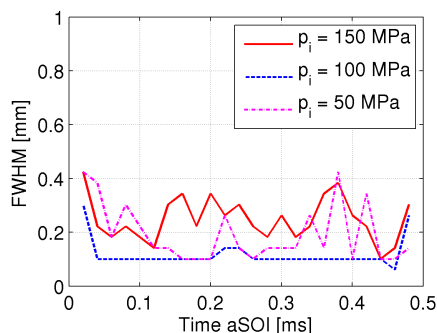
(b) $x = 2\,\mathrm{mm}$

Figure 7.14: Peak projected fuel density of the two-dimensional ECN case.

Figure 7.15: FWHM of the two-dimensional ECN case.

7.2.6   Three-dimensional effects

Two-dimensional domain of Spray A has been employed to study the basic structure of the flow, together with the effect of the injection pressure. However, as already commented in Section §7.2.1, the orifice of Spray A nozzle has a small eccentricity, and a three-dimensional domain is required to study

that (also some other effects, such a non-circular orifice outlet, which are not
considered in the present domain). Same analysis than the one performed in
previous Sections §7.2.4 and §7.2.5 can be done for the tree-dimensional case,
allowing to study the effect of the orifice eccentricity.

Internal nozzle flow

Time dependent variables mass flow rate and momentum flux are represented
in Figure 7.16. Note that not even the first 0.1 ms have been simulated due to
the high computational cost of three-dimensional cases. Still, some trends can
be obtained as additions to those comments already made in Section §7.2.4.
Lower mass flow rate and momentum flux than in the two-dimensional case
are obtained. That is associated to the small change in the nozzle geometry
upstream the nozzle sac, as shown in Figures 7.1 and 7.2. Larger part of
the needle is considered in the three-dimensional case, concretely until the
inlet becomes axial, whilst in the two-dimensional case the inlet follows the
direction of the needle cone. Therefore, inlet areas (which define inlet velocity)
and the development of boundary layers are different.

(a) Mass flow rate.   (b) Momentum flux.
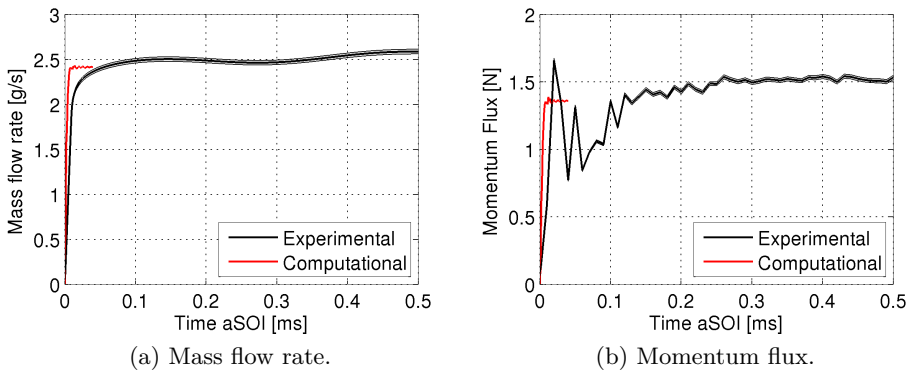
Figure 7.16: Mass flow rate and momentum flux for the three-dimensional
ECN case.

Speaking of turbulence, mass-weighted average of turbulent kinetic en-
ergy at the exit section is plotted in Figure 7.17. A steady value higher than
$500 \, \mathrm{m^2/s^2}$ is given by the three-dimensional simulation, but $435 \, \mathrm{m^2/s^2}$ is ob-
tained for the two-dimensional case. Even if boundary and initial conditions
are the same, the change in the domain generates a small change in turbulence
levels, which may be associated to a three-dimensional behavior of turbulent

eddies, longer walls or the orifice eccentricity, what leads to wider boundary layers.
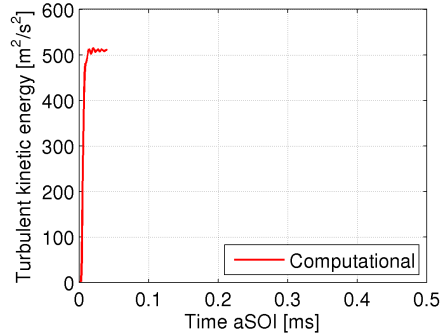
Figure 7.17: Turbulent kinetic energy time evolution at exit section for the three-dimensional ECN case.

Characteristic dimensionless coefficients of the nozzle are depicted in Table 7.3. A velocity coefficient lower than in the experiments is given by the simulation, consistent with lower mass flow rate shown in Figure 7.16a. This leads to an also lower discharge coefficient. However, the computational area coefficient almost matches the experimental value, which means that the real reduction of effective area is well simulated. Nevertheless, simulated time is yet not enough to reach truly steady state values, so that might enlarge observed errors.

p_i [MPa]	C_d [-]	C_v [-]	C_a [-]
Experimental	0.90	0.92	0.98
Computational	0.84	0.87	0.97

Table 7.3: Dimensionless coefficients that describe the hydraulic behavior of the three-dimensional ECN case.

To close the study of the internal flow, the effect of the orifice eccentricity needs to be analyzed. This is done by observation of the fields variables contours represented in Figure 7.18. Few differences are observed when comparing these with previous Figures 7.6-7.9. First concerns the orifice inlet, where gradients of all variables are blended instead of being axial due to the eccentricity. Fuel density and temperature at the lower part of the inlet (where

the turning angle of the flow is higher) are slightly lower than in the upper part. Second and more significant difference concerns turbulence. Turbulent kinetic energy levels are lower at the bottom of the orifice but the boundary layer there is thicker. That was expected because small fillet radius (sharp inlet edges) are prone to generate separated flow [10]. This difference in turbulence modifies the exit velocity profile [11], what can derive in modifications of atomization and so spray structure.

(a) Velocity in m/s.

(b) Turbulent kinetic energy in m²/s².

(c) Density in kg/m³.

(d) Temperature in K.
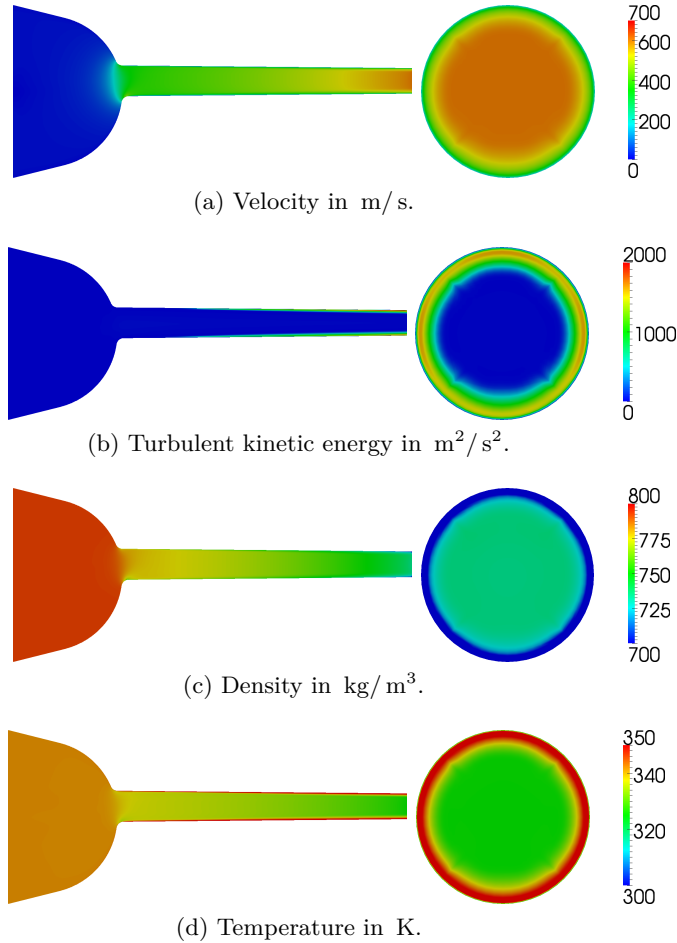
Figure 7.18: Contours of field variables inside the nozzle and at the orifice outlet of the three-dimensional ECN case.

In order to further assess the effect of orifice positioning, streamlines of the flow coming from the nozzle inlet are plotted in Figure 7.19. Looking at the

nozzle from the top (Figure 7.19a), geometry, internal flow (red background) structure and spray (blue background) are perfectly symmetric. However, looking at the domain from the side (Figure 7.19b), the eccentricity of the orifice is visible; and it generates an asymmetry on the internal flow pattern, moving the streamlines toward the nozzle upper part. This asymmetry is reflected on the spray structure: the velocity profile is not symmetric for the first 1-2 mm, and the spray axis seems to be slightly blended.

(a) Top view (no orifice eccentricity).

(b) Side view (small orifice eccentricity).
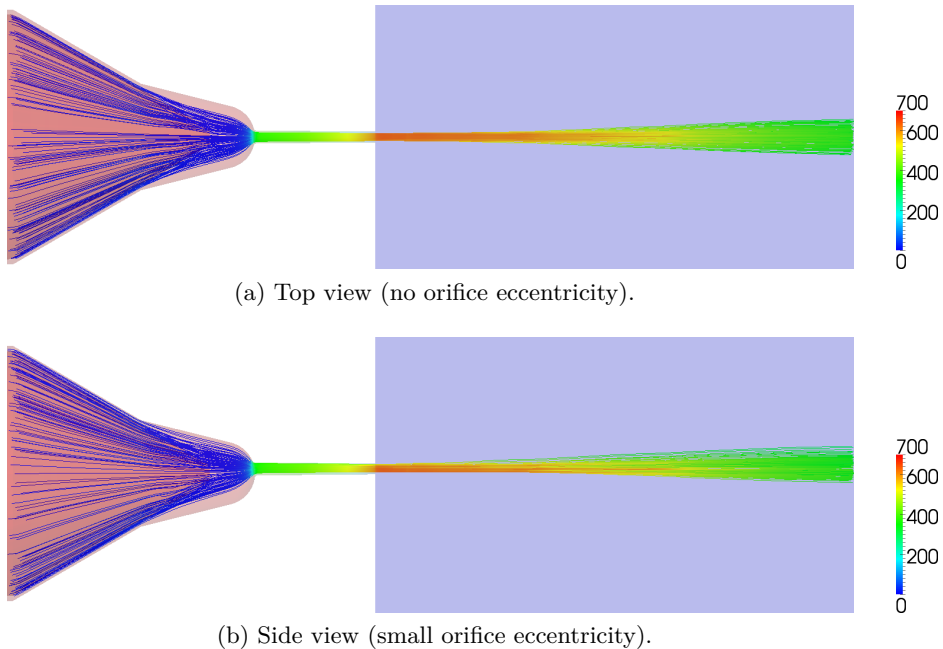
Figure 7.19: Flow streamlines, colored by velocity in m/s, coming out from the nozzle inlet for the three-dimensional ECN case.

Near-field flow

The effect of the orifice eccentricity on spray structure is better understood by looking at comparison metrics of the near-field. Firstly, spray penetration is shown in Figure 7.20. Computational results agree once more with experimental data obtained by Sandia National Laboratories [3].

Additionally, the intact core length has been plotted in the same figure. This magnitude has been defined in Section §2.4.3 as the distance between the orifice exit and the location where the first droplets appear due to the atomization process. In the simulation, this magnitude has been defined as
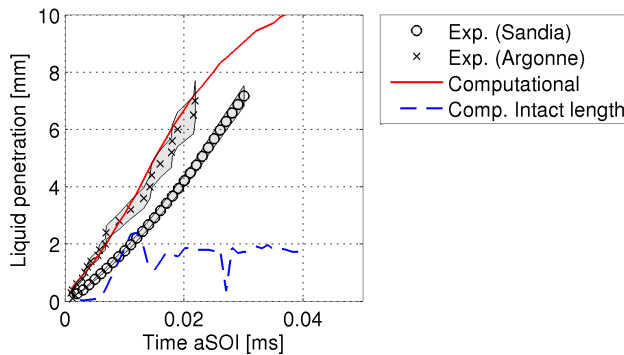
Figure 7.20: Spray penetration and intact core length for the three-dimensional ECN case.

the maximum distance from the orifice exit on the spray axis where the liquid volume fraction X_f is higher than 0.9. Liquid volume fraction is used instead of mass fraction to be consistent with experiments [12]. Different limiting values (such 0.95 or 0.99) have been tested, but average value did not change, only its time evolution, which was oscillating more. Figure 7.20 shows how the intact core is zero at very short time aSOI. This means that the liquid exiting from the nozzle is already atomized. Rapidly, the liquid vein appears and the intact core reaches its steady state value, which is 1.8 mm.

Intact core length has been experimentally measured by Pickett et al. [12] employing the tomography (X-ray) technique for the same injector and injection conditions than the ones simulated. They obtained that the liquid volume fraction drops below 1 after 2.4 mm, larger value than in the computations. However, they post-processed their experimental data assuming a constant fuel density value of $\rho_f = 720 \, \text{kg} / \text{m}^3$, which is based on the measured nozzle temperature. But in Figure 7.18c it is shown that the exit fuel density is slightly higher, around $735 \, \text{kg} / \text{m}^3$, what could slightly modify liquid volume fraction calculation and then the intact core length experimental value. Nevertheless, assuming that the error in the experiments would be small, larger experimental value than in the simulations means that the ESA model over-predicts the grade atomization and mixing, what was known from previous results of the validation assessment (Section §5.3) and the two-dimensional Spray A case (Section §7.2.5).

To assess the spray structure, in other words, the fuel distribution inside the spray, liquid volume fraction contour is employed instead of the previously

defined and used parameter, the fuel projected density. This is done because the fuel projected density is a 2D line-of-sight mass projection, while fuel mass or liquid data gives local 3D information [12]. In Figure 7.21 it is clear that the model over-predicts the grade of atomization. A possible source of errors is that the timing aSOI of experimental and computational images is not the same. For experiments, an average between 0.7 and 1.5 ms is shown whilst in the computations the time step shown is 0.040 ms. Nevertheless, the intact core length seems to reach its steady state value as soon as 0.015 ms aSOI in Figure 7.20, therefore no big changes in liquid volume fraction contours for more advanced time are expected.

(a) Experimental. (b) Computational.
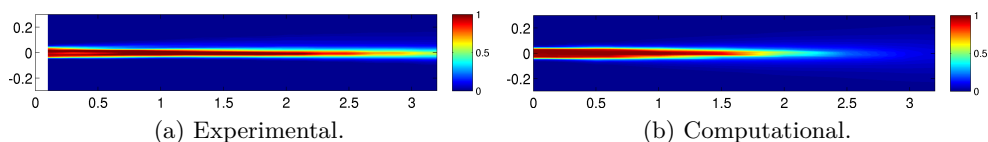
Figure 7.21: Contours of liquid volume fraction X_f in the near-field region of the three-dimensional ECN case. Side view (small orifice eccentricity). Dimensions in millimeters.

Transverse cuts of the spray are shown in Figure 7.22 for both experiments and simulations. Most important result is that, although it is said that mesh independence was reached, it was not. Gradients shown in Figure 7.22b clearly follow the grid structure inside the orifice, which is depicted in Figure 7.1. Regardless this dependency, axisymmetric results are obtained by the simulations because the orifice is a perfect circle, but in the experiments that is not true. Small imperfections in the orifice shape [2] generate asymmetric fuel distributions within the spray. A more detailed orifice geometry is required to capture this behavior.

Same conclusions are obtained if radial distribution of fuel concentration (liquid volume fraction) are compared with experiments, as done in Figure 7.23. Experimental values actually exceed one in some positions at the center. Barring a rapid cooling of the fuel spray to a low temperature, and hence a higher density than the $\rho_f = 720 \, \text{kg/m}^3$ used to post-process the data, it would be impossible for the liquid volume fraction to exceed one [12]. That higher value of fuel density which should be used is $\rho_f = 735 \, \text{kg/m}^3$, though it is variable along the radial direction.

Figure 7.23 shows how the spray width in terms of volume fraction is well captured by the model. All the same, differences in directions are not reproduced. Z-direction represents the direction of the eccentricity, and Y-direction

(a) Experimental.

(b) Computational.
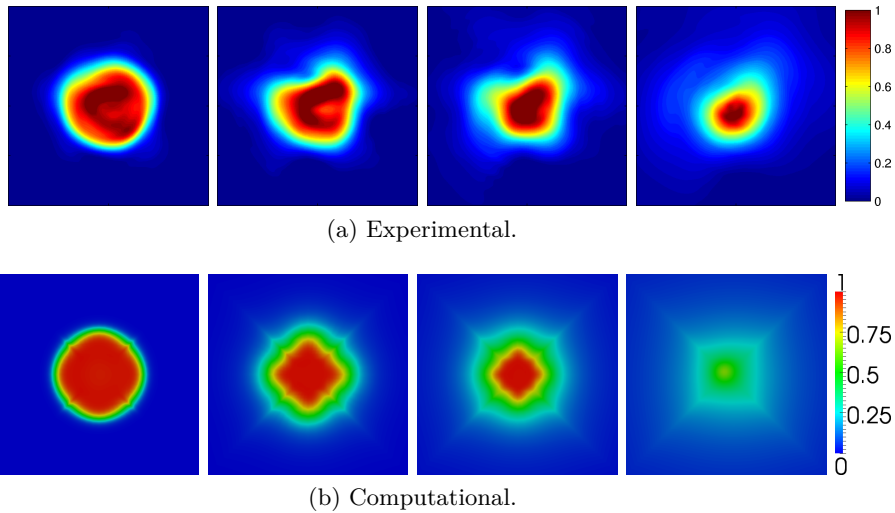
Figure 7.22: Transverse contours of liquid volume fraction X_f in the near-field region of the three-dimensional ECN case at different axial positions (from left to right): 0.1, 0.5, 1.0 and 2.0 mm. Shown box is a square whose side is 0.1 mm.

its perpendicular direction in a X-constant plane. These reference axis were defined by the ECN community [1]. In the simulations, no difference is found for both directions, meanwhile in the experiments a small effect of the orifice eccentricity is observed: the liquid distribution is slightly wider in the direction of the eccentricity. Nonetheless, this effect is negligible for axial distances larger than approximately 2 mm (as commented before in Section §7.2.5), it means, distances larger than approximately the intact core length.

7.3 Parametric studies

Strengths and weaknesses of the Eulerian Spray Atomization (ESA) model have been analyzed and presented in previous Chapter 5 and Section §7.2. Thus, the model can be used now to study the injection process itself. More concretely, to study how the internal flow and the spray change when some fuel properties are varied.

CFD simulations allow to change only a single property, either in the nozzle geometry or the fuel. This sometimes cannot be done in reality; for example, the only way to change fuel properties in experiments is by changing the fuel itself. This capability of the calculations is used to study the effect of single parameters in the spray evolution.
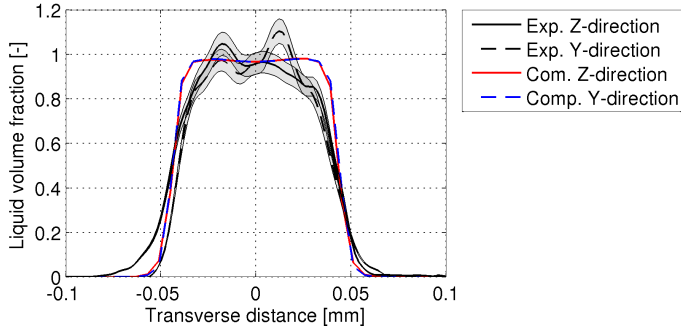
(a) $x = 0.1\,\text{mm}$.
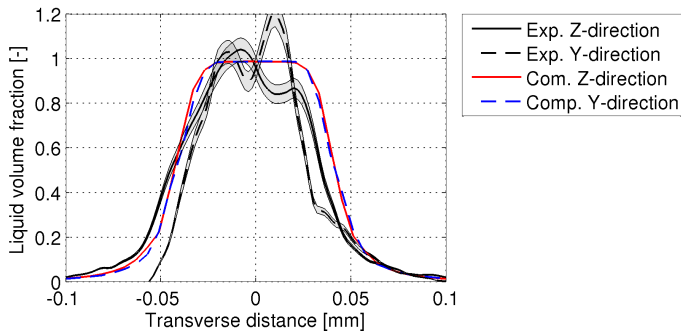
(b) $x = 0.6\,\text{mm}$.
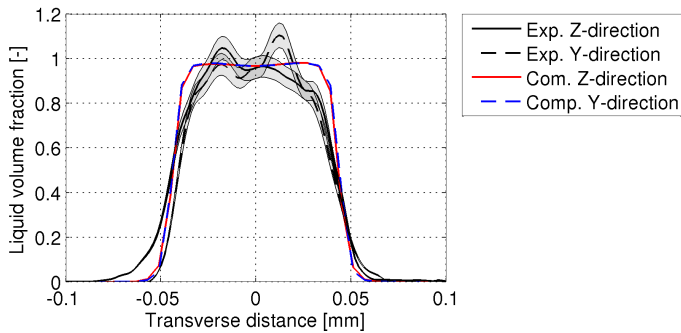
(c) $x = 1.0\,\text{mm}$.

Figure 7.23: Radial distributions of liquid volume fraction X_f in the near-field region of the three-dimensional ECN case.

There are many parameters that could be studied: $k - factor$, orifice out-
let diameter, sac volume, fuel temperature... and most of them can be ex-
perimentally studied. However, there are some which are difficult to change
individually, and those are the selected ones to break down in this chapter:

- Fuel density: as commented before, the only way to change the fuel
  density is by changing the fuel itself. Other possibility is to change the
  fuel temperature, but in that case some other properties (i.e. viscosity)
  vary too.

- Fuel viscosity: it is the same case than for the fuel density, if this prop-
  erty changes (different fuel or temperature) in the experiments, others
  change too. Although in Section §6.4 the liquid viscosity turned out
  to be a not a statistical significant parameter for the spray penetration
  error prediction, this fuel property may indeed change the internal flow
  pattern and so the spray.

Another fluid property which could be interesting to study is the fuel
surface tension. Surface tension is a thermodynamic property of a liquid
that depends on the temperature and other state variables such as chemical
composition and surface cleanliness. If the temperature differences are small,
the temperature dependence of σ can be linearized so that $\partial\sigma/\partial T$ is constant;
it is usually negative. When the temperature varies substantially along the
free surface, the gradient in surface tension results in a shear force that causes
fluid to move from the hot region to the cold region (capillary convection) [13].
However, the ESA model assumes that macroscopic parameters of the spray
are independent of this property. Thus, surface tension studies are dismissed
so far.

Simulation case and injection conditions selected for this kind of para-
metric studies are the two-dimensional version of Spray A, detailed in Sec-
tions §7.2.1 and §7.2.2, with the nominal injection pressure of $p_i = 150\,\mathrm{MPa}$.
This case is selected because of the large amount of experimental data available
in the literature [1], but also because its computational cost is reasonable.

In this whole section, only simulation results are shown and analyzed. As
already said, same studies could not be reproduced in experiments. Further-
more, the code has been already validated under several different injection
conditions.

7.3.1 Fuel properties: density

The fuel used by the ECN for Spray A conditions is n-Dodecane, whose density can be calculated through Equation (4.65) and corresponding coefficients of Table 4.15. Its density value at ambient conditions ($p_b = 2\,\text{MPa}$ and $T_b = 303\,\text{K}$) is $\rho_f = 741.23\,\text{kg/m}^3$; and at injection conditions ($p_i = 150\,\text{MPa}$ and $T_i = 343\,\text{K}$) is $\rho_f = 681.54\,\text{kg/m}^3$. The difference between these two conditions is 8.1%.

Larger differences are used for the present parametric study. A 30% lighter and a 30% heavier "fuels" (not real) are simulated. The rest of the fuel thermodynamic properties, such compressibility or specific heat capacity, are kept the same. The way of building these fuels is increasing or decreasing 30% the constant coefficient C_1 of Equation (4.65).

Internal nozzle flow

Mass flow rate and momentum flux are plotted in Figure 7.24. Squared signals are obtained, as in Sections §5.3.4 and §7.2.4. As expected, the lower the density, the lower the mass flow rate; however the momentum flux keeps almost constant. This is consistent with the theory.

(a) Mass flow rate. (b) Momentum flux.
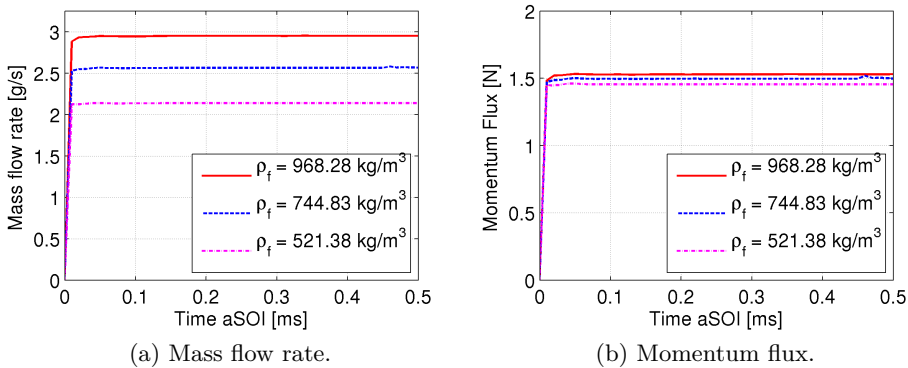
Figure 7.24: Mass flow rate and momentum flux of the fuel properties, density study.

Going back to Section §2.3.4, replacing Bernoulli's velocity (Equation (2.14)) into the theoretical definition of mass flow rate (Equation (2.13)),

Equation (7.1) is obtained, which shows that increasing the density, the mass flow rate also increases.

$$\dot{m}_{f,th} = A_o\sqrt{2\rho_f\Delta p} \tag{7.1}$$

The same replacement can be done in the definition of the momentum flux (Equation (2.26)), obtaining then Equation (7.2), which proves that the momentum flux is independent of the fuel density, it is related only with injection and geometrical conditions.

$$\dot{M}_{th} = 2A_o\Delta p \tag{7.2}$$

Another known effect of decreasing the fuel density is that the velocity increases. This is clearly shown later on in Figure 7.26. That increase in velocity implies an increase in fluctuations (turbulent kinetic energy) at the orifice outlet, as depicted in Figure 7.25, where the mass-weighted average turbulent kinetic energy is plotted versus time. This result suggests that light fuels may atomize faster than heavier ones.
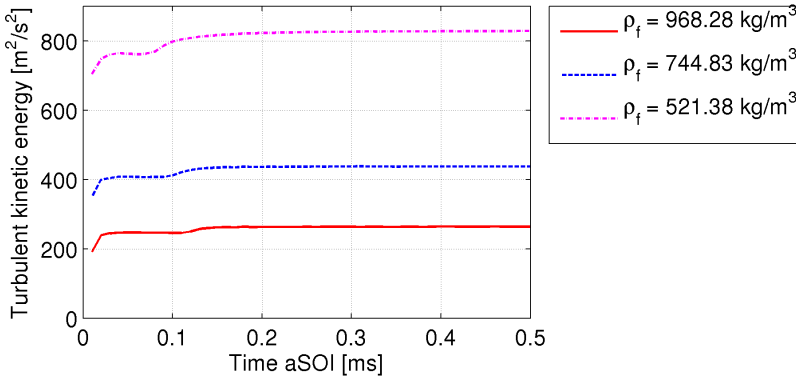
Figure 7.25: Turbulent kinetic energy time evolution at exit section of the fuel properties, density study.

Following the analysis of the internal nozzle flow, dimensionless coefficients that define the quality of the discharge process are summarized in Table 7.4. Although differences are very small, all values rise when density is increased. This is because turbulence levels decrease, so the discharge process seems more like an ideal one. As seen later in Figures 7.27 and 7.29, the boundary layer is

thinner for higher fuel densities (lower Reynolds numbers). This counters the well known trend of thinner boundary layer for higher Reynolds number [8]. Notwithstanding, the orifice length required to get developed flow grows with the Reynolds number (see Equation (2.10) for turbulent flows). Therefore, the increase in boundary layer width is related to a longer stabilization length after a sudden change of flow direction at the orifice inlet.

ρ_f [kg/ m^3]	C_d [-]	C_v [-]	C_a [-]	Re [-]
968.28	0.89	0.92	0.97	28305
744.83	0.88	0.91	0.96	32152
521.38	0.86	0.90	0.95	37845

Table 7.4: Dimensionless coefficients that describe the hydraulic behavior of the fuel properties, density study.

Commented rise in the velocity field is clearly shown in Figure 7.26. The effect of increasing the density is similar to decreasing the injection pressure (see Figure 7.6).

Turbulent kinetic energy field is observed in Figure 7.27. It has been already said that the boundary layer width grows as the fuel density decreases, also that level of oscillations increases. Nonetheless, turbulence levels inside the sac and in the center of the orifice are still very low. Care must be taken in interpreting this result because RANS approach tends to over-predict the size of the boundary layer, and then this strong effect of the density on the oscillations, in reality, could not be as important as shown here.

An interesting result regards the temperature of the fuel inside the nozzle. Even with exactly the same compressibility and heat capacity, a change in fuel density has a very strong effect in the temperature field inside the nozzle, what is shown in Figure 7.28. For light fuels, the cooling effect of the expansion process brings the temperature at the exit down to 290 K, which is a large temperature drop of about 50 K. As the density increases, that drop is reduced. Actually, a very small rise in temperature is obtained instead of cooling for high density fuels. This rise is produced by the viscous dissipation (the only energy source available if the heat flow through the walls is assumed negligible), which is able to heat up the fuel due to its low velocity. The same effect, to a lesser degree, is observed when the injection pressure is diminished (see Section §7.2.4).

For a better analysis of the temperature at the orifice exit, temperature distribution in radial direction for all fuel densities is plotted in Figure 7.29.

(a) $\rho_f = 968.28\,\mathrm{kg/m^3}$.

(b) $\rho_f = 744.83\,\mathrm{kg/m^3}$.

(c) $\rho_f = 521.38\,\mathrm{kg/m^3}$.

Figure 7.26: Contours of velocity field in m/s inside the nozzle and at the orifice outlet of the fuel properties, density study.

All results already commented can be seen: thicker boundary layer and lower temperature value for lower fuel densities. What is more interesting from this figure is the analysis of the maximum value of the temperature distribution, located as expected next to the orifice wall. Regardless the density, in other words, the mean velocity and turbulence level, the maximum value is found around 370-380 K. Thus, temperature rise due to viscous dissipation seems to be limited by the wall temperature. However, and going back to Section §7.2.4, when the injection pressure increases, the maximum value of the temperature also increases. Therefore, heating is also related to the total dynamic pressure.

Near-field flow

Figure 7.30 shows the spray penetration. A very small increase is observed when the density decreases. This effect was not expected because the spray penetration does not depend directly on the fuel density (see Equation (2.45)). It does depend on the momentum flux, and very small differences were found

(a) $\rho_f = 968.28 \, \mathrm{kg/m^3}$.

(b) $\rho_f = 744.83 \, \mathrm{kg/m^3}$.

(c) $\rho_f = 521.38 \, \mathrm{kg/m^3}$.
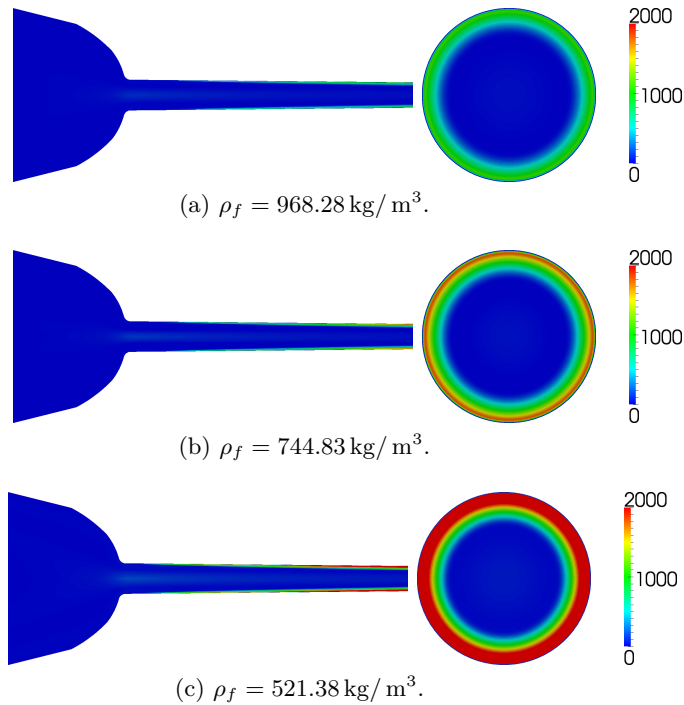
Figure 7.27: Contours of turbulent kinetic energy in $\mathrm{m^2/s^2}$ inside the nozzle and at the orifice outlet of the fuel properties, density study.

for it, as shown in Figure 7.24b. These differences in spray penetration are associated to differences in velocity and area coefficients (Table 7.4), as predicted by Equation (2.48). Actually, the slope of the initial part of the penetration depends on the spray velocity which at the same time depends on the fuel density, the higher it is, the lower the penetration slope gets, so computational results are once again consistent with theory and experiments.

Projected density contours are plotted in Figure 7.31. Intact core length, or at least very high concentration area, seems to decrease when fuel density is also decreased. This is consistent with the obtained higher velocity and higher turbulence level, and it confirms the previous hypothesis that light fuels atomize faster than heavier ones.

The width of the spray in the near-nozzle zone also seems to decrease for lower densities. This is consistent with the small increase in spray penetration observed in Figure 7.30. However, this result may be affected by the oscillating nature of the solver (a numerical issue that needs to be solved) that generates high concentration areas inside the spray. Lower density ratio ρ_g/ρ_f

(a) $\rho_f = 968.28\,\mathrm{kg/\,m^3}$.

(b) $\rho_f = 744.83\,\mathrm{kg/\,m^3}$.

(c) $\rho_f = 521.38\,\mathrm{kg/\,m^3}$.
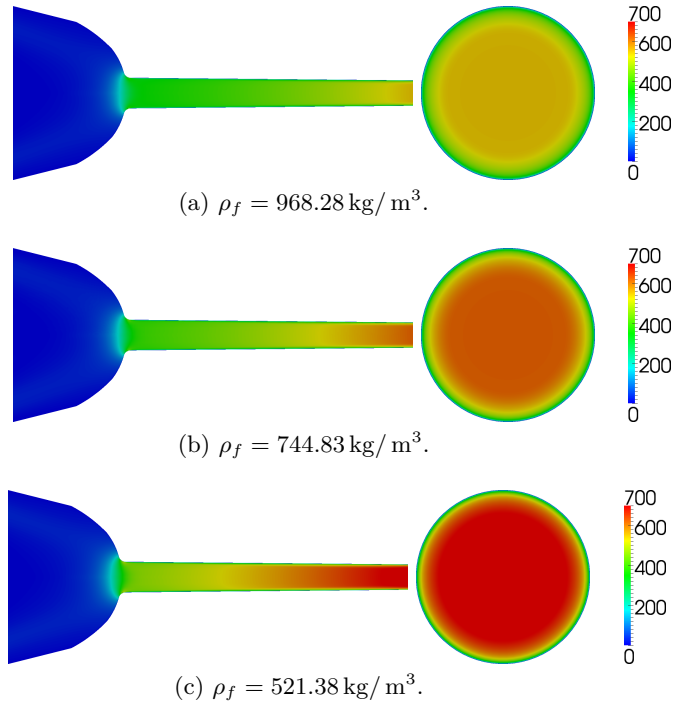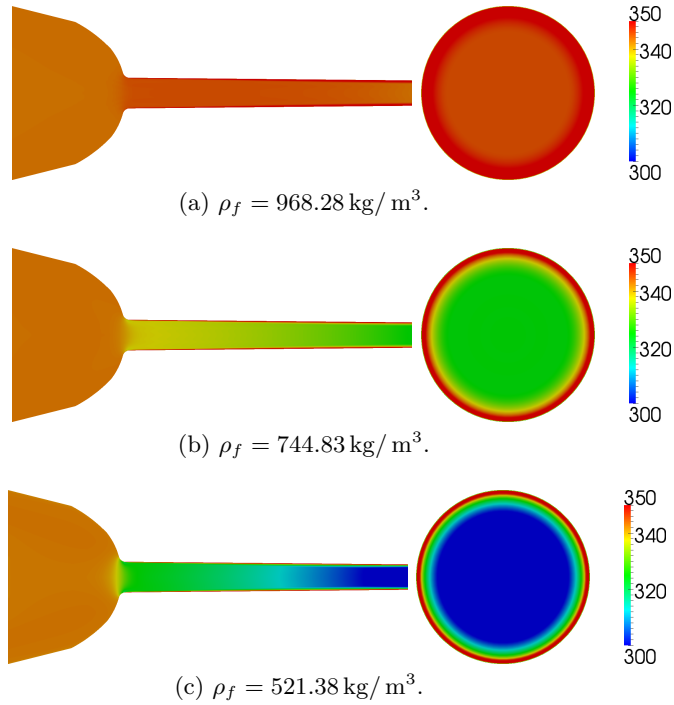
Figure 7.28: Contours of temperature field in m/s inside the nozzle and at the orifice outlet of the fuel properties, density study.
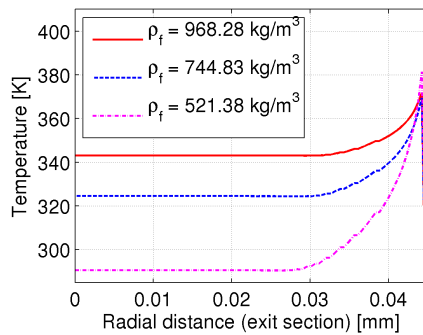
Figure 7.29: Temperature distribution in radial direction at the orifice exit of the fuel properties, density study.
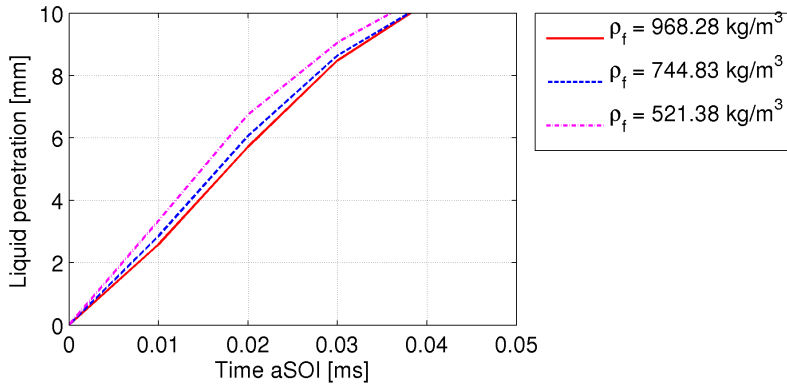
Figure 7.30: Spray penetration of the fuel properties, density study.

values somehow damp these oscillations, proved by the smoother contours of Figure 7.31e and 7.31f.

(a) $\rho_f = 968.28\,\mathrm{kg/\,m^3}$ at 0.1 ms aSOI.

(b) $\rho_f = 968.28\,\mathrm{kg/\,m^3}$ at 0.5 ms aSOI.

(c) $\rho_f = 744.83\,\mathrm{kg/\,m^3}$ at 0.1 ms aSOI.

(d) $\rho_f = 744.83\,\mathrm{kg/\,m^3}$ at 0.5 ms aSOI.

(e) $\rho_f = 521.38\,\mathrm{kg/\,m^3}$ at 0.1 ms aSOI.

(f) $\rho_f = 521.38\,\mathrm{kg/\,m^3}$ at 0.5 ms aSOI.
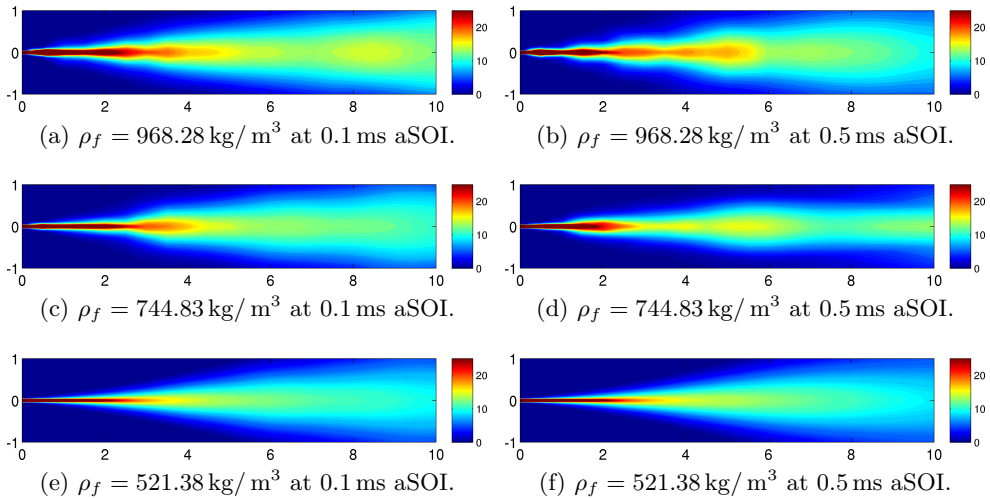
Figure 7.31: Contours of projected fuel density in $\mu\mathrm{g/\,mm^2}$ in the near-field region of the fuel properties, density study. Dimensions in millimeters.

This damping effect of low density values is also observed in Figure 7.32, which represents the TIM versus the axial distance from the orifice outlet. Additionally, it is observed how TIM values are lower as the fuel density decreases, except for long distances ($x > 6\,\mathrm{mm}$) where all three curves give

approximately the same value, despite the oscillations. In that area, air and fuel are already well mixed; in fact, low values of projected density are experimentally observed in Figures 7.11a and 7.11b.
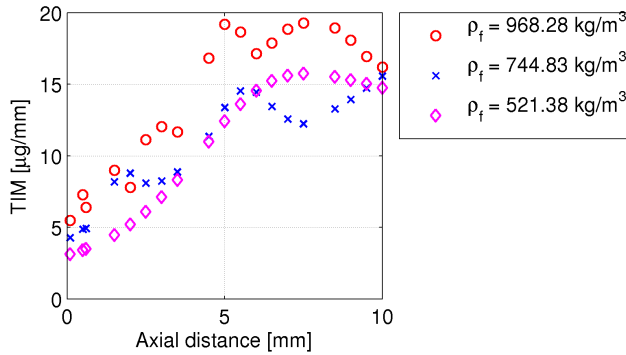
Figure 7.32: TIM versus axial distance of the fuel properties, density study.

7.3.2   Fuel properties: viscosity

Once more, the fuel used by the ECN for Spray A conditions is n-Dodecane, whose viscosity is obtained from the literature [9]. However, it can vary from $\mu_f = 0.0012796 \, \mathrm{kg/(\, m \, s)}$ at ambient conditions to $\mu_f = 0.00141 \, \mathrm{kg/(\, m \, s)}$ at injection conditions. That is a difference of 10%.

As before, larger differences are used for the present parametric study. A 30% more viscous and a 30% less viscous "fuels" are simulated. The rest of the fuel thermodynamic properties, such density or compressibility, are kept the same.

Internal nozzle flow

No big difference has been found in any of the comparison metrics defined in Section §7.2.3. Mass flow rate and momentum flux at orifice exit time evolutions, though they are not represented, are almost the same. Contours of velocity, density, temperature and turbulent kinetic energy also look similar. Maybe the best way of summarizing this result is by means of dimensionless coefficients, which are depicted in Table 7.5.

However, there is a large difference in Reynolds number (almost double), also shown in Table 7.5, due to the change in the viscosity. It suggests that there is a change in the development of the boundary layer, and then in the

$\nu_f \, [\, \mathbf{m^2/s}]$	C_d [-]	C_v [-]	C_a [-]	Re [-]
$2.339\ 10^{-6}$	0.869	0.905	0.960	24731
$1.799\ 10^{-6}$	0.876	0.909	0.964	32152
$1.259\ 10^{-6}$	0.877	0.907	0.977	45968

Table 7.5: Dimensionless coefficients that describe the hydraulic behavior of the fuel properties, viscosity study.

fluctuations (turbulent kinetic energy) at the orifice outlet. These fluctuations are plotted versus time in Figure 7.33. Even if area and velocity coefficients are equal for the three cases, in other words, the size of the boundary layer is the same regardless the liquid viscosity, the turbulence intensity increases for low viscous fuels. This can also be seen in Figure 7.34, which represents the contours of the turbulent kinetic energy field.
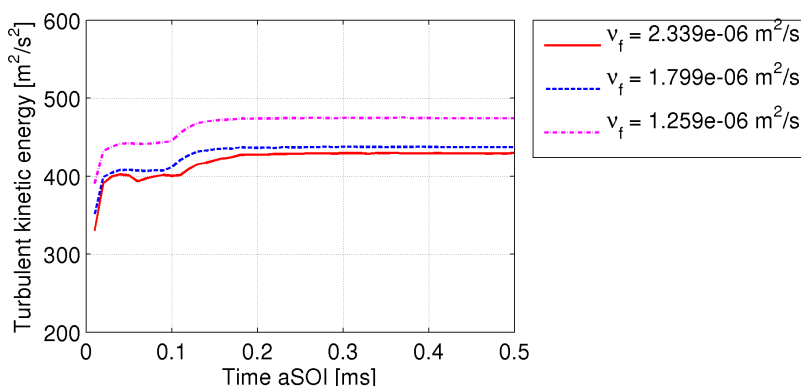
Figure 7.33: Turbulent kinetic energy time evolution at exit section of the fuel properties, viscosity study.

Near-field flow

Figure 7.35 shows the spray penetration. As predicted by the statistical study of Section §6.4, the liquid viscosity has no significant effect on spray penetration. This was kind of expected because one of the hypothesis of the model (see Section §4.2) is that large scale features of the multiphase flow must become independent of surface tension and viscosity. Further analysis of

(a) $\nu_f = 2.339 \ 10^{-6} \, \mathrm{m^2/s}$.

(b) $\nu_f = 1.799 \ 10^{-6} \, \mathrm{m^2/s}$.

(c) $\nu_f = 1.259 \ 10^{-6} \, \mathrm{m^2/s}$.
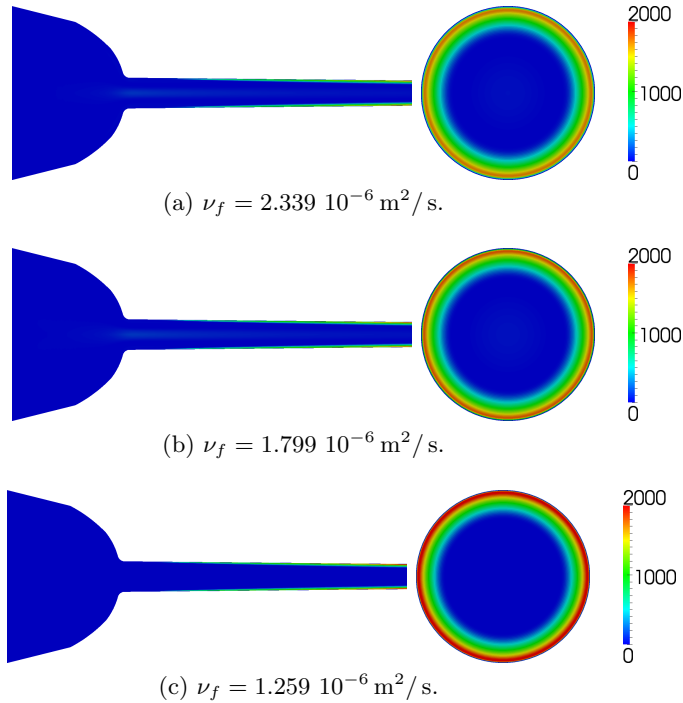
Figure 7.34: Contours of turbulent kinetic energy in $\mathrm{m^2/s^2}$ inside the nozzle and at the orifice outlet of the fuel properties, viscosity study.

other macroscopic parameters is not necessary (and does not give additional information) because of that.

On the contrary, small scale features such the mean size of liquid droplets are directly linked to the surface tension and dynamic viscosity. Though it is not included among the comparison metrics, Figure 7.36 represents the SMD of droplets along the spray axis and in radial direction at $x = 8 \, \mathrm{mm}$ position. Very small differences of about $0.5 \, \mathrm{\mu m}$ are obtained, and no clear trend (rise nor descent) is observed. This result is consistent with the employed model, described in Section §4.4.1, which does not consider the liquid viscosity in any of its equations, only the turbulent viscosity. In fact, none of the models found in the literature and also described in Section §4.4.1 take into account this variable [14–16]. Therefore, either the hypothesis of Vallet et al. [14] is not well formulated or models employed to obtain droplet size should be modified.

Figure 7.36a could be used to define the intact core length in a different way than in Section §7.2.6. Theoretically, it is defined as the distance between the orifice exit and the location where the first droplets appear due to the
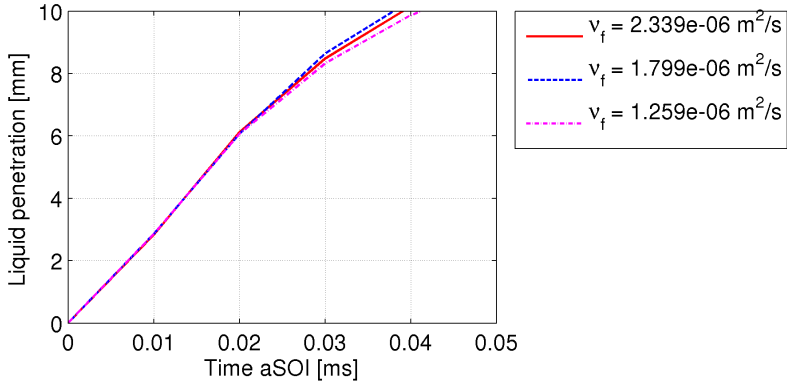
Figure 7.35: Spray penetration of the fuel properties, viscosity study..

(a) Axial distribution.

(b) Radial distribution.
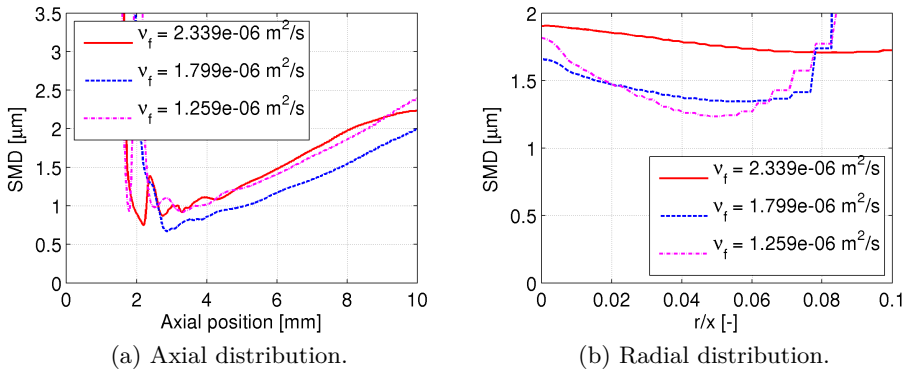
Figure 7.36: Sauter Mean Diameter (SMD) distributions on spray axis and in radial direction at $x = 8\,\text{mm}$ of the fuel properties, density study.

atomization process. It is clear in Figure 7.36a that first droplets appear around $x = 2\,\mathrm{mm}$, position which is close to the previous obtained value of $IL = 1.8\,\mathrm{mm}$ and the experimental value of $IL = 2.4\,\mathrm{mm}$.

7.4   Summary

The model has been successfully employed to simulate a different injector under different injection condition than in the validation assessment. Overall good agreement with experiments is obtained, and observed errors or miss-predictions (especially in projected density contours) are due to the nature of the model. In fact, other authors that use similar models also obtain similar errors [1].

The width of the boundary layer inside the injector is over-predicted due to the use of a RANS turbulence model. This provokes an error in the prediction of the discharge coefficient. Nonetheless, spray liquid penetration is very well captured, together with effects of varying injection pressure.

A novelty of this model is the calculation of fuel temperature variation inside the nozzle. Also outside, but due to the assumption of isothermal flow, there is not much to say about that. Mean temperature at the orifice outlet matches the isentropic value, which manifest the good capability of the model in considering thermal effects. Also the viscous dissipation heating effect is captured, though it is not highly relevant due to the transient nature of the injection process and the high flow velocities along the orifice.

Three-dimensional effect such orifice eccentricity has been investigated. It shows, in fact, a small impact on the internal turbulence levels pattern; however its effect on spray development and fuel concentration seems negligible. Other imperfections, i.e non-circular orifice shape, have a stronger effect on spray development. From the computational point of view, the mesh structure in the three-dimensional case has a large impact on the solution, and a further mesh sensitivity study is needed. However, large computational cost of three-dimensional cases suggests that two-dimensional cases should be used, specially taking under consideration the limited additional information that the three-dimensional domain pops out.

A parametric variation with a minimum of three different values has been performed for two fuel properties, density and viscosity. Some interesting results were obtained:

- Regarding the effect of fuel density, most of the analysis could be done theoretically with equations and explanations presented in Chapter 2.

The strong link found between the theory and the presented results given by the ESA model enhances the validation carried out in Section §5.3. One of the most interesting results is that light fuels atomize faster; so one possibility to increase the combustions efficiency is to increase the temperature of the fuel inside the injector, reducing its density and favoring the atomization but also the evaporation process.

- The effect of the fuel viscosity seems negligible. Only the turbulence level at the boundary layer is affected, and because this layer is thin, there is not significant influence on any of internal flow or spray parameters. Therefore, a mistake in the value of the viscosity is not relevant; furthermore, it is not necessary for this model to make the effort of obtaining the viscosity law as function of pressure and temperature.

References

[1] Pickett, L. M. *Engine Combustion Network*. English. Sandia National Laboratories. 2014. URL: http://www.sandia.gov/ecn/ (*cit. on pp. 309–311, 313, 314, 332, 334, 346*).

[2] Kastengren, A. L. et al. "Engine combustion network (ECN): Measurements of nozzle geometry and hydraulic behavior". *Atomization and Sprays*, vol. 22 (2012), pp. 1011–1052. DOI: 10.1615/AtomizSpr.2013006309 (*cit. on pp. 310, 331*).

[3] Bardi, M. et al. "Engine combustion network: Comparison of spray development, vaporization, and combustion in different combustion vessels". *Atomization and Sprays*, vol. 22.12 (2012), pp. 807–842. DOI: 10.1615/AtomizSpr.2013005837 (*cit. on pp. 310, 321, 329*).

[4] Kastengren, A. L. and C. F. Powell. "Spray density measurements using X-ray radiography". *Proceedings of the Institution of Mechanical Engineers, Part D: Journal of Automobile Engineering*, vol. 221.6 (2007), pp. 653–662. DOI: 10.1243/09544070JAUTO392 (*cit. on pp. 312, 321, 322*).

[5] Som, S. and S. K. Aggarwal. "Effects of primary breakup modeling on spray and combustion characteristics of compression ignition engines". *Combustion and Flame*, vol. 157.6 (2010), pp. 1179–1193. DOI: 10.1016/j.combustflame.2010.02.018 (*cit. on p. 315*).

[6]   Battistoni, M., C. N. Grimaldi, and F. Marianni. "Coupled Simulation of Nozzle Flow and Spray Formation Using Diesel and Biodiesel for CI Engine Applications". *SAE Technical Paper 2012-01-1267* (2012). DOI: 10.4271/2012-01-1267 (*cit. on p. 315*).

[7]   Payri, R., B. Tormos, J. Gimeno, and G. Bracho. "The potential of Large Eddy Simulation (LES) code for the modeling of flow in diesel injectors". *Mathematical and Computer Modelling*, vol. 52.7-8 (2010), pp. 1151–1160. DOI: 10.1016/j.mcm.2010.02.033 (*cit. on p. 318*).

[8]   Anderson, J. D. *Fundamentals of Aerodynamics*. Ed. by J. D. Anderson. Fourth edition. New York, New York, United States of America: McGraw Hill, 2007 (*cit. on pp. 319, 337*).

[9]   Secretary of Commerce on behalf of the U. S. A., U. S. *Dodecane*. English. National Institute of Standards and Technology. 2013. URL: http://www.nist.gov/ (*cit. on pp. 320, 342*).

[10] Payri, R., S. Molina, F. J. Salvador, and J. Gimeno. "A study of the relation between nozzle geometry, internal flow and sprays characteristics in diesel fuel injection systems". *KSME International Journal*, vol. 18.7 (2004), pp. 1222–1235 (*cit. on p. 328*).

[11] Kent, J. C. and G. M. Brown. "Nozzle exit flow characteristics for square-edged and rounded inlet geometries". *Combustion Science and Technology*, vol. 30.1-6 (1983), pp. 121–132. DOI: 10.1080/00102208308923615 (*cit. on p. 328*).

[12] Pickett, L. M., J. Manin, A. L. Kastengren, and C. F. Powell. "Comparison of Near-Field Structure and Growth of a Diesel Spray Using Light-Based Optical Microscopy and X-Ray Radiography". *SAE International Journal of Engines*, vol. 7.2 (2014), pp. 1044–1053 (*cit. on pp. 330, 331*).

[13] Ferziger, J. H. and M. Perić. *Computational Methods for Fluid Dynamics*. Ed. by J. H. Ferziger. Third edition. Heidelberg, Germany: Springer, 2002 (*cit. on p. 334*).

[14] Vallet, A., A. A. Burluka, and R. Borghi. "Development of a Eulerian model for the "Atomization" of a liquid jet". *Atomization and Sprays*, vol. 11.6 (2001), pp. 619–642 (*cit. on p. 344*).

[15] Beheshti, N., A. A. Burluka, and M. Fairweather. "Assessment of $\Sigma - Y_{liq}$ model predictions for air-assisted atomisation". *Theoretical and Computational Fluid Dynamics*, vol. 21.5 (2007), pp. 381–397. DOI: 10.1007/s00162-007-0052-3 (*cit. on p. 344*).

[16] Lebas, R., T. Ménard, P. A. Beau, A. Berlemont, and F. X. Demoulin. "Numerical simulation of primary break-up and atomization: DNS and modelling study". *International Journal of Multiphase Flow*, vol. 35.3 (2009), pp. 247–260. DOI: `10.1016/j.ijmultiphaseflow.2008.11.005` (*cit. on p. 344*).

Chapter 8

Conclusions and future work

8.1 Conclusions

Development of an atomization model is a major issue that remains open because of the complex interactions between the internal and external flow in the atomization processes. The presence of a dense and dispersed liquid phase and even, sometimes, the presence of a cavitation process, make it particularly difficult to capture experimentally all these interactions. Theoretical or numerical model are still under development however the model family (liquid surface density) and numerical methodology chosen by the author are among the most promising ones. A synthesis of the main ideas that have been assessed through out the development of such model in this Ph. D. Thesis is given in this last chapter. Most significant and/or original achievements of this investigation are highlighted.

This document and so this section have been divided in four different parts: literature review, development of the code, optimization, and use of the model. These four parts correspond to logical and general steps required for the creation of any new calculation methodology.

State of the art

All computational models and methodologies commonly used to simulate the fuel injection process into the combustion chamber have been investigated. The special feature of the liquid injection process is the multiphase nature of

351

the flow, and it turns out that the best computational methodology for that type of flows depends on the liquid concentration:

- For very dilute mixtures (liquid volume fraction lower than 10^{-6}) the effect of liquid particles is negligible and the corresponding single-phase model should be used. The particle path is calculated later by post-processing the results.

- For dispersed mixtures (liquid volume fraction lower than 0.1), DDM Eulerian-Lagrangian models have been successfully employed for many years despite the limitation in liquid concentration. Other main drawback of these models is the grid dependency.

- Interface tracking models work accurately when different phases can be clearly distinct, for example, the sea surface or a single liquid droplet. The computational cost for situations is excessive when there is a large amount of droplets.

- The same occurs for Eulerian multi-fluid models. They are useful to analyze transient phenomena, such wave propagations and flow regime changes, when the border between phases is simple; however these models become highly complicated if phases are strongly coupled.

- Homogeneous flow models have proved their good capability for simulating multiphase flows in the last years. Nonetheless, the assumption of local equilibrium must be fulfilled, otherwise the model lacks of physical sense and leads to wrong results.

Taking into account all the information collected in the literature review, the best approach to simulate at the same time the flow inside the nozzle and outside, in the combustion chamber, is the homogeneous flow model. In fact, these type of models already exist, for example those named ELSA or $\Sigma - Y$, but none of them has been used and optimized to study also the flow inside the nozzle. Therefore and just because of that, the present Thesis represents a step forward in the state of art of liquid injection simulation.

Development of the model

A new homogeneous flow model for simulating liquid sprays has been created and implemented in OpenFOAM ®. Guidelines and basics given in the first of this kind of models have been followed. In addition to the hypothesis of local equilibrium, that original model assumes (1) high Reynolds and Weber numbers so large scale features of the flow are independent of liquid viscosity

and surface tension; (2) the difference between the mean velocity of the liquid fluid and gaseous fluid particles can be calculated; (3) the dispersion of the liquid phase into the gas phase can be computed by a balance equation; and (4) the mean size of the liquid fragments can be calculated through the mean surface of the liquid-gas interface per unit volume.

Significant contributions to the original model have been made in the present investigation. Most important ones are listed below:

- A PIMPLE algorithm is used to improve the stability of the model. The main drawback that this algorithm entails is a large computational cost.

- A new flux update has been introduced into the sequence of equations. That change slightly reduces the computational cost and ensures consistency between liquid mass fraction and density fields, a problem found in the literature for similar models.

- The common pressure-velocity coupling is used to compute the pressure and correct fluxes. Other similar solvers use, directly, an equation of state or isentropic relationships to that end.

- Liquid density variations inside and outside the nozzle are calculated. The common hypothesis of incompressible flow lacks of validity specially for very high injection pressures. Density and speed of sound depend on thermodynamic variables (pressure and temperature) according to experimental data found in the bibliography.

- Computation of temperature field is enhanced. Instead of using a constant heat capacity, liquid enthalpy is directly obtained from thermodynamic variables. This leads to results that inside the nozzle are very close to isentropic one-dimensional calculations. Expansion cooling effects and viscous heating at walls are both accurately predicted. Large temperature drop inside the nozzle is obtained if alternative thermal models, the ones employed by other solvers, are used. This, firstly, has not been observed in the experiments, and secondly, it has no physical sense.

- In order to properly simulate the Diesel injection process, the SST $k - \omega$ turbulence model is selected as the best among the ones tested. Turbulence pattern inside the nozzle matches results obtained by Large Eddy Simulations. Additionally, spray structure matches experimental results but also computational results obtained by other authors who employed different models.

The forehead mentioned balance equation for the dispersion of the liquid into the gas phase (in other words, atomization and mixing processes) uses, by analogy with Fick's law of diffusion, a diffusion coefficient defined through the turbulent Schmidt number. Other possibilities have been investigated by other authors, but an agreement in the engine community is found with respect to the high performance of the Fick's law and its variants.

This new model, named Eulerian Spray Atomization (ESA), has been summited to verification and validation assessments. For verification, solutions given by the model have been compared with analytical and high accurate (i.e. DNS) solutions of simplified problems. Maximum and average errors for all 5 verification cases felt below previously imposed limits obtained from the literature. Therefore, the model can be considered verified.

For validation, a real Diesel injection problem has been simulated and compared with experiments. The problem consists of three different single-hole nozzles which are very well experimentally characterized. Large errors have been found in the early stages of the injection, associated to the boundary and initial conditions. Trends when changing injection conditions (i.e. injection pressure) or nozzle geometry (i.e. orifice exit diameter) are very well captured by the model qualitatively and quantitatively. When proper boundary conditions are used, errors in comparison metrics fall down to 5-10%. Therefore, the model can be considered validated.

Weaknesses of the computational code have been identified thanks to these verification and validation processes. Two examples are: high computational cost, and excessive spread of the fuel in the first millimeters after the nozzle outlet. Additionally, the relevance of the inlet boundary condition in the results has been investigated. Imposing the mass flow by a time varying velocity inlet allows reproducing the experimental mass flow rate if compressibility effects are corrected. However, due to the nozzle is filled with fuel but at zero velocity at the beginning, the momentum flux is lower than in the experiments short time after start of injection, and so it is the spray penetration. A constant or time varying pressure inlet solves this issue, but then the experimental mass flow rate is not well captured, specially at low injection pressures.

Optimization

Three different studies have been performed in order to optimize the ESA model: constants of the inter-facial area density transport equation, numerical schemes, and other constants of the model.

In the first study, results obtained by the ESA model are compared to Direct Numerical Simulations. It has been obtained that the constant $Sc_{\Sigma,coeff}$ is the one that reduces most the error in surface density predictions. A value of $Sc_{\Sigma,coeff} = 0.75$ gives accurate results close to the spray axis. However, no matter which combination of constants is employed, the inter-facial surface density is always over-predicted far from the axis, which is related to an over-prediction in spray width.

In the second study, discretization schemes and linear solvers are varied. Several options among the ones available in OpenFOAM ® libraries are tested. It turns out that generally suggested schemes (default ones) give a very accurate and fast solution; only the discretization scheme for gradient terms must be changed from linear to linear interpolation with symmetric weighting. This allows reducing the error in the prediction of fuel concentration along the spray axis.

In the last but not least study, five constants of the SST $k - \omega$ turbulence model, the Schmidt number and the liquid viscosity have been varied simultaneously in conjunction with injection conditions (injection pressure and ambient density). Several conclusions can be drawn from the statistical study performed to do that:

- Effect of liquid viscosity in spray penetration is negligible.

- The optimum Schmidt number is $Sc = 0.5$, value which agrees with some other models presented in the literature. Nonetheless, $Sc = 1$ is the value that properly represents the physics of a mixing process, and it is necessary to correctly predict the intact core length. That means that a deeper analysis is needed only for this variable.

- Modification of the value of turbulence model constants leads to an improvement in the spray penetration behavior. The error in the slope of the curve is reduced by diminishing the production of turbulent kinetic energy. Additionally, the boundary layer of the internal flow becomes thinner and the velocity profile at the orifice exit gets a rectangular shape.

Nozzle flow and spray analysis

The ESA model has been employed to study a modern research injector in the framework of the Engine Combustion Network (ECN). Internal nozzle flow and near-field spray have been deeply investigated and computational results have been compared with accurate and high quality experimental data:

- There is still uncertainty in the modeling of the internal nozzle plus the spray, i.e. the initial conditions. Whereas this kind of issues are not solved, more advanced and accurate techniques but also more expensive ones, i.e. Large Eddy Simulations, should be left apart for the future.

- The width of the boundary layer inside the injector is over-predicted due to the use of a RANS turbulence model. That induces a small error in the prediction of dimensionless coefficients that characterize the hydraulic behavior of the nozzle.

- Spray penetration during the first microseconds of the injection matches experimental data; the full computational curve falls inside the uncertainty of the experiments. Changes in spray behavior (macroscopic and microscopic parameters) when injection conditions are varied are well captured in both trend and magnitude.

- Two different additional weaknesses of the model have been identified:

  - Fuel mass distributions are over-predicted in both axial and radial directions. This is a common drawback of all homogeneous flow models available in the literature.
  - Highly oscillating time evolutions are obtained for some parameters of the spray related to mass distribution, i.e. fuel projected density contours. Those oscillations have been associated to pressure waves which are generated or amplified by a wrong definition of mixture compressibility.

- The effect of main fuel properties on the nozzle flow and spray behavior has been also studied with the aim of assessing how the spray changes if alternative fuels are used:

  - Fuel viscosity has a negligible influence in all comparison metrics. Therefore, a mistake in the value of this property is not relevant for spray studies.
  - Most effects of changing fuel density can be reasoned by employing theoretical and semi-empirical expressions available in the literature, but not all of them. Most significant result is that light fuels atomize faster, so increasing fuel injection temperature is recommended.

- Three-dimensional effects such orifice eccentricity are very well captured. However, it turned out that the effect of a small eccentricity is negligible at distances longer than 2 mm from the orifice exit. Imperfections in the orifice shape, though not simulated, based on experimental results, seem to have a stronger effect in the fuel mass concentration field.

8.2 Future work

There is still much more work to do in order to further improve the knowledge of the injection process, and the ESA model offers a wide range of new possibilities. Some future directions from the computational point of view are listed below:

- *Improvement of initial conditions.* So far, flow inside nozzle is initialized filled with stagnated liquid at injection conditions. However, in reality, when the liquid covers sac and orifice volumes, the flow already has certain velocity and turbulence levels. There are two options for taking that into account:

    - Perform a separate simulation considering only the internal flow, and then, after reaching convergence, mapping all fields to the real case. This methodology highly increases computational cost, and it demands an extra simulation, which was one of the old coupling requirements avoided by the use of the ESA model.
    - Initialize the nozzle partially filled with stagnated liquid. A new study is needed just to know which percentage of the nozzle needs to be filled with fuel. Actually, based on last experimental results where liquid and gas have been observed inside the nozzle prior the start of injection, part of the nozzle could be initialized with gas-fuel mixture.

- *Simulation of needle movement.* In order to properly simulate transients of the injection process (i.e. rising of the mass flow rate or end of injection phenomena), needle movement needs to be considered. Movement laws can be obtained from tomography (X-ray) measurements, but also from one-dimensional dynamic models of the whole injector. Implementation of mesh movement in OpenFOAM ® is complicated, though it has been improving for the last past years.

- *Addition of a third phase, fuel vapor, into the mixture.* Cavitation and evaporation are key phenomena in the fuel injection and combustion processes; they need to be included in the ESA model if that model is going to be used in practical cases. Separate cavitation and evaporation models already exists in the literature, but according to the literature reviewed they have not been applied together in the same solver.

- *Modeling turbulence by Large Eddy Simulations.* Resolving large scale turbulent eddies and modeling only small scales ones may improve the

prediction of discharge, velocity and area coefficients. That change in
turbulence modeling can also be beneficial for the prediction of mass
flow dispersion in the first two millimeters of the spray.

- *Study of non-circular orifices.* Flow pattern inside the nozzle, and then
  spray behavior too, are affected by the orifice cross-sectional shape.
  Therefore, it could be interesting to use this model to study, for ex-
  ample, an elliptical orifice, or a circular orifice with a nibble or a bump.

- *Improvement of mixture compressibility definition.* The employed ex-
  pression for the mixture compressibility, though widely used, is not cor-
  rect and generates artificial oscillations in other flow variables. This
  issue needs to be solved before any of the previously explain future work
  start.

- *Reduction of computational cost.* The focus of this Thesis has been the
  accuracy of the model and the stability of the solution. However, if this
  solver is going to be used by the automotive industry, computational
  cost (time required for performing simulations) needs to be decreased.
  This could be done by:

  - increasing the Courant number, which is possible thanks to using
    a PIMPLE algorithm, though the solver would be more unstable;
  - reducing the number of outer loops, in other words, use a PISO
    algorithm, though again the solver would be more unstable;
  - or using adaptive mesh refinement, allowing larger cell sizes where
    gradients of velocity and fuel concentration are low, and increasing
    the mesh resolution where needed. This last option needs to be
    carefully studied because the computational cost of creating and
    destroying cells is generally high.

- *Application to multi-hole nozzles.* Once the computational cost of the
  ESA model is reduced, it could be used to study multi-hole nozzles,
  the ones that are commonly found in the Diesel engine industry. For
  example, it may explain the relation between the flow pattern inside the
  nozzle and the bending between spray axis and orifice axis sometimes
  found in the experiments.

Bibliography

Abani, N. and R. D. Reitz. "Modeling subgrid-scale mixing of vapor in diesel sprays using jet theory". *Atomization and Sprays*, vol. 20.1 (2010), pp. 71–83. DOI: `10.1615/AtomizSpr.v20.i1.60`, (*cit. on: Chap.3-{97}*).

Abani, N. et al. "An Improved Spray Model for Reducing Numerical Parameter Dependencies in Diesel Engine CFD Simulations". *SAE Technical Paper 2008-01-0970* (2008). DOI: `10.4271/2008-01-0970`, (*cit. on: Chap.3-{97}*).

Abraham, J. "What is Adequate Resolution in the Numerical Computations of Transient Jets". *SAE Technical Paper 970051* (1997). DOI: `10.4271/970051`, (*cit. on: Chap.3-{95}*).

Abraham, J. and L. M. Pickett. "Computed and measured fuel vapor distribution in a diesel spray". *Atomization and Sprays*, vol. 20.3 (2010), pp. 241–250. DOI: `10.1615/AtomizSpr.v20.i3.50`, (*cit. on: Chap.3-{98,99}*).

Abramzon, B. M. and W. A. Sirignano. "Approximate theory of a single droplet vaporization in a convective field: effects of variable properties, Stefan flow and transient liquid heat". *Proceedings of the American Society of Mechanical Engineers / Japan Society of Mechanica Engineers. Thermal Engineering Joint Conference*. Ed. by P. J. Marto and I. Tanasawa. Honolulu, Hawaii, United States of America, 1987, (*cit. on: Chap.2-{56}*).

Adler, D. and W. T. Lyn. "The Evaporation and Mixing of a Liquid Fuel Spray in a Diesel Air Swirl". *Proceedings of the Institution of Mechanical Engineers*, vol. 184.10 (1969), pp. 171–180. DOI: `10.1243/pime_conf_1969_184_330_02`, (*cit. on: Chap.2-{66}*).

Alajbegovic, A., H. A. Grogger, and H. Philipp. "Calculation of Transient Cavitation in Nozzle Using the Two Fluid Model". *12th Annual Conference on Liquid Atomization & Spray Systems (ILASS Americas)*. Indianapolis, Indiana, United States of America, 1999, (*cit. on: Chap.3-{103,104}*).

Alajbegovic, A., G. Meister, D. Greif, and B. Basara. "Three phase cavitating flows in high-pressure swirl injectors". *Experimental Thermal and Fluid Science*, vol. 26.6-7 (2002), pp. 677–681. DOI: 10.1016/S0894-1777(02)00179-6, (*cit. on: Chap.3-{104,105}*).

Alajbegovic, A. et al. "Coupled Simulations of Nozzle Flow, Primary Fuel Jet Breakup, and Spray Formation". *Journal of Engineering for Gas Turbines and Power*, vol. 127.4 (2004), pp. 897–908. DOI: 10.1115/1.1914803, (*cit. on: Chap.3-{116}*).

Altieri, L. and A. Tonoli. "Piezoelectric Injectors for Automotive Applications: Modeling and Experimental Validation of Hysteretic Behavior and Temperature Effects". *Journal of Dynamic Systems, Measurement and Control, Transactions of the ASME*, vol. 135.1 (2013). DOI: 10.1115/1.4006627, (*cit. on: Chap.2-{25}*).

Anderson, J. D. *Fundamentals of Aerodynamics*. Ed. by J. D. Anderson. Fourth edition. New York, New York, United States of America: McGraw Hill, 2007, (*cit. on: Chap.2-{32,34}, Chap.4-{178,184}, Chap.5-{214}, Chap.7-{319,337}*).

Andriotis, A. and M. Gavaises. "Influence of vortex flow and cavitation on near-nozzle diesel spray dispersion angle". *Atomization and Sprays*, vol. 19.3 (2009), pp. 247–261. DOI: 10.1615/AtomizSpr.v19.i3.30, (*cit. on: Chap.2-{64}*).

Andriotis, A., M. Gavaises, and C. Arcoumanis. "Vortex flow and cavitation in diesel injector nozzles". *Journal of Fluid Mechanics*, vol. 610 (2008), pp. 195–215. DOI: 10.1017/S0022112008002668, (*cit. on: Chap.2-{43}*).

Araneo, L. and C. Tropea. "Improving Phase Doppler Measurements in a Diesel Spray". *SAE Technical Paper 2000-01-2047* (2000). DOI: 10.4271/2000-01-2047, (*cit. on: Chap.5-{232}*).

Arcoumanis, C., H. Flora, M. Gavaises, N. Kampanis, and R. Horrocks. "Investigation of Cavitation in a Vertical Multi-Hole Injector". *SAE Technical Paper 1999-01-0524* (1999). DOI: 10.4271/1999-01-0524, (*cit. on: Chap.2-{43}*).

Arcoumanis, C. and M. Gavaises. "Linking nozzle flow with spray characteristics in a diesel fuel injection system". *Atomization and Sprays*, vol. 8.3 (1998), pp. 307–347, (*cit. on: Chap.3-{115}*).

Arcoumanis, C., M. Gavaises, and B. French. "Effect of Fuel Injection Processes on the Structure of Diesel Sprays". *SAE Technical Paper 970799* (1997). DOI: `10.4271/970799`, (*cit. on: Chap.2-{36,52,53,54}*).

Arienti, M. and M. Sussman. "An embedded level set method for sharp-interface multiphase simulations of Diesel injectors". *International Journal of Multiphase Flow*, vol. 59 (2014), pp. 1–14. DOI: `10.1016/j.ijmultiphaseflow.2013.10.005`, (*cit. on: Chap.3-{94,118}*).

Arrègle, J. "Análisis de la estructura y dinámica interna de chorros diésel". PhD thesis. Camino de Vera, s/n, 46022, Valencia, Spain: Departamento de Máquinas y Motores Térmicos, Universitat Politècnica de València, 1998, (*cit. on: Chap.1-{4}*).

Arrègle, J., J. V. Pastor, and S. Ruiz. "The Influence of Injection Parameters on Diesel Spray Characteristics". *SAE Technical Paper 1999-01-0200* (1999). DOI: `10.4271/1999-01-0200`, (*cit. on: Chap.2-{66}*).

Ayoub, N. N. and R. D. Reitz. "Multidimensional Computation of Multicomponent Spray Vaporization and Combustion". *SAE Technical Paper 950285* (1995). DOI: `10.4271/950285`, (*cit. on: Chap.2-{56}*).

Bae, C., J. Yu, J. Kang, J. Kong, and K. O. Lee. "Effect of Nozzle Geometry on the Common-Rail Diesel Spray". *SAE Technical Paper 2002-01-1625* (2002). DOI: `10.4271/2002-01-1625`, (*cit. on: Chap.2-{30}, Chap.3-{83}*).

Baik, S., J. P. Blanchard, and M. L. Corradini. "Development of micro-diesel injector nozzles via MEMS technology and effects on spray characteristics". *Atomization and Sprays*, vol. 13.5-6 (2003), pp. 443–474. DOI: `10.1615/AtomizSpr.v13.i56.20`, (*cit. on: Chap.5-{232}*).

Bardi, M. "Partial needle lift and injection rate shape effect on the formation and combustion of the Diesel spray". PhD thesis. Camino de Vera, s/n, 46022, Valencia, Spain: Departamento de Máquinas y Motores Térmicos, Universitat Politècnica de València, 2014, (*cit. on: Chap.1-{4}, Chap.2-{44}*).

Bardi, M. et al. "Engine combustion network: Comparison of spray development, vaporization, and combustion in different combustion vessels". *Atomization and Sprays*, vol. 22.12 (2012), pp. 807–842. DOI: `10.1615/AtomizSpr.2013005837`, (*cit. on: Chap.2-{33,45,62}, Chap.5-{228}, Chap.7-{310,321,329}*).

Barrero, A. and M. Pérez-Saborid. *Fundamentos y aplicaciones de la mecánica de fluidos*. Ed. by A. Barrero. First edition. New York, New York, United States of America: McGraw Hill / Interamericana de España S. A., 2005, (*cit. on: Chap.2-{32}*).

Barroso, G., B. Schneider, and K. Boulouchos. "An Extensive Parametric Study on Diesel Spray Simulation and Verification with Experimental Data". *SAE Technical Paper 2003-01-3230* (2003). DOI: 10.4271/2003-01-3230, (*cit. on: Chap.3-{97}*).

Bataille, J. and J. Kesting. *Continuum modeling of two-phase flows*. Technical Report LA-UR-81-3325. Washington, District of Columbia, Washington, United States of America: Los Alamos National Laboratory, 1981, (*cit. on: Chap.3-{106}, Chap.4-{140,167,168}*).

Battistoni, M. and C. N. Grimaldi. "Numerical analysis of injector flow and spray characteristics from diesel injectors using fossil and biodiesel fuels". *Applied Energy*, vol. 97 (2012), pp. 656–666. DOI: 10.1016/j.apenergy.2011.11.080, (*cit. on: Chap.1-{5}, Chap.2-{29}, Chap.3-{104,110,117,118}, Chap.4-{137}, Chap.5-{229,240,241}, Chap.7-{315}*).

Battistoni, M., C. N. Grimaldi, and F. Marianni. "Coupled Simulation of Nozzle Flow and Spray Formation Using Diesel and Biodiesel for CI Engine Applications". *SAE Technical Paper 2012-01-1267* (2012). DOI: 10.4271/2012-01-1267.

Battistoni, M., S. Som, and D. Longman. "Comparison of Mixture and Multi-fluid Models for In-Nozzle Cavitation Prediction". *Journal of Engineering for Gas Turbines and Power*, vol. 136.6 (2014). DOI: 10.1115/1.4026369, (*cit. on: Chap.3-{109}*).

Baumgarten, C. *Mixture Formation in Internal Combustion Engines*. Ed. by D. Mewes and F. Mayinger. First edition. Heidelberg, Germany: Springer, 2006, (*cit. on: Chap.2-{54,55,56}*).

Béard, P. et al. "Extension of Lagrangian-Eulerian Spray Modeling: Application to High Pressure Evaporating Diesel Sprays". *SAE Technical Paper 2000-01-1893* (2000). DOI: 10.4271/2000-01-1893, (*cit. on: Chap.3-{97}*).

Beau, P. A., M. Funk, R. Lebas, and F. X. Demoulin. "Applying Quasi-Multiphase Model to Simulate Atomization Processes in Diesel Engines: Modeling of the Slip Velocity". *SAE Technical Paper 2005-01-0220* (2005). DOI: 10.4271/2005-01-0220, (*cit. on: Chap.3-{111}*).

Beck, J. C. and A. P. Watkins. "On the development of a spray model based on drop-size moments". *Proceedings of the Royal Society A: Mathematical, Physical and Engineering Sciences*, vol. 459.2034 (2003), pp. 1365–1394. DOI: `10.1098/rspa.2002.1052`, (*cit. on: Chap.3-{104}*).

Befrui, B., G. Corbinelly, M. D'Onofrio, and D. Varble. "GDI Multi-Hole Injector Internal Flow and Spray Analysis". *SAE Technical Paper 2011-01-1211* (2011). DOI: `10.4271/2011-01-1211`, (*cit. on: Chap.3-{91,117,119}*).

Befrui, B., G. Corbinelly, P. Spiekermann, M. Shost, and M. C. Lai. "Large Eddy Simulation of GDI Single-Hole Flow and Near-Field Spray". *SAE Technical Paper 2012-01-0392* (2012). DOI: `10.4271/2012-01-0392`, (*cit. on: Chap.3-{117}, Chap.5-{229}*).

Beheshti, N., A. A. Burluka, and M. Fairweather. "Assessment of $\Sigma - Y_{liq}$ model predictions for air-assisted atomisation". *Theoretical and Computational Fluid Dynamics*, vol. 21.5 (2007), pp. 381–397. DOI: `10.1007/s00162-007-0052-3`, (*cit. on: Chap.1-{5}, Chap.3-{113}, Chap.4-{142,169,173}, Chap.6-{270,278}, Chap.7-{344}*).

Belhadef, A., A. Vallet, M. Amielh, and F. Anselmet. "Pressure-swirl atomization: Modeling and experimental approaches". *International Journal of Multiphase Flow*, vol. 39 (2012), pp. 13–20. DOI: `10.1016/j.ijmultiphaseflow.2011.09.009`, (*cit. on: Chap.3-{113}*).

Benajes, J., J. V. Pastor, R. Payri, and A. H. Plazas. "Analysis of the influence of diesel nozzle geometry in the injection rate characteristic". *Journal of Fluids Engineering, Transactions of the ASME*, vol. 126 (2004), pp. 63–71. DOI: `10.1115/1.1637636`, (*cit. on: Chap.2-{30}*).

Benajes, J., R. Payri, S. Molina, and V. Soare. "Investigation of the Influence of Injection Rate Shaping on the Spray Characteristics in a Diesel Common Rail System Equipped with a Piston Amplifier". *Journal of Fluids Engineering, Transactions of the ASME*, vol. 127.6 (2005), pp. 1102–1110. DOI: `10.1115/1.2062767`, (*cit. on: Chap.2-{24}*).

Bergwerk, W. "Flow Pattern in Diesel Nozzle Spray Holes". *Proceedings of the Institution of Mechanical Engineers*, vol. 173.1 (1959), pp. 655–660. DOI: `10.1243/pime_proc_1959_173_054_02`, (*cit. on: Chap.2-{39,40,41}*).

Bermúdez, V., R. Payri, F. J. Salvador, and A. H. Plazas. "Study of the influence of nozzle seat type on injection rate and spray behaviour". *Proceedings of the Institution of Mechanical Engineers, Part D: Journal of Automobile Engineering*, vol. 219.5 (2005), pp. 677–689. DOI: `10.1243/095440705X28303`, (*cit. on: Chap.1-{5}*).

Bharadwaj, N. and C. J. Rutland. "A large-eddy simulation study of sub-grid two-phase interaction in particle-laden flows and diesel engine sprays". *Atomization and Sprays*, vol. 20.8 (2010), pp. 673–695. DOI: `10.1615/AtomizSpr.v20.i8.20`, (*cit. on: Chap.3-{101}*).

Bharadwaj, N., C. J. Rutland, and S. Chang. "Large eddy simulation modelling of spray-induced turbulence effects". *International Journal of Engine Research*, vol. 10.2 (2009), pp. 97–119. DOI: `10.1243/14680874JER02309`, (*cit. on: Chap.3-{101}*).

Bianchi, G. M., S. Falfari, M. Parotto, and G. Osbat. "Advanced Modeling of Common Rail Injector Dynamics and Comparison with Experiments". *SAE Technical Paper 2003-01-0006* (2003). DOI: `10.4271/2003-01-0006`, (*cit. on: Chap.2-{28}*).

Bianchi, G. M. et al. "Advanced Modelling of a New Diesel Fast Solenoid Injector and Comparison with Experiments". *SAE Technical Paper 2004-01-0019* (2004). DOI: `10.4271/2004-01-0019`, (*cit. on: Chap.2-{28}*).

Bicer, B., A. Tanaka, T. Fukuda, and A. Sou. "Numerical Simulation of Cavitating Phenomena in Diesel Injector Nozzles". *12th Annual Conference on Liquid Atomization & Spray Systems (ILASS Asia)*. Osaka, Japan, 2013, (*cit. on: Chap.3-{109}*).

Blessing, M., G. König, C. Krüger, U. Michels, and V. Schwarz. "Analysis of Flow and Cavitation Phenomena in Diesel Injection Nozzles and Its Effects on Spray and Mixture Formation". *SAE Technical Paper 2003-01-1358* (2003). DOI: `10.4271/2003-01-1358`, (*cit. on: Chap.2-{43}, Chap.3-{83}*).

Blokkel, G., B. Barbeau, and R. Borghi. "A 3D Eulerian Model to Improve the Primary Breakup of Atomizing Jet". *SAE Technical Paper 2003-01-0005* (2003). DOI: `10.4271/2003-01-0005`, (*cit. on: Chap.1-{5}, Chap.3-{111,112}, Chap.4-{168}*).

Bosch, W. "The Fuel Rate Indicator: A New Measuring Instrument For Display of the Characteristics of Individual Injection". *SAE Technical Paper 660749* (1966). DOI: `10.4271/660749`, (*cit. on: Chap.1-{3}*).

Brennen, C. "An oscillating-boundary-layer theory for ciliary propulsion". *Journal of Fluid Mechanics*, vol. 65.4 (1974), pp. 799–824. DOI: `10.1017/S0022112074001662`, (*cit. on: Chap.2-{51}*).

Brunneaux, G. "Liquid and vapor spray structure in high-pressure common rail diesel injection". *Atomization and Sprays*, vol. 11.5 (2001), pp. 533–556, (*cit. on: Chap.2-{45}*).

Buckingham, E. "Model experiments and the forms of empirical equations". *American Society of Mechanical Engineers Transcriptions*, vol. 37 (1915), pp. 263–296, (*cit. on: Chap.2-{48}*).

Cao, Z. M., K. Nishino, S. Mizuno, and K. Torii. "PIV measurement of internal structure of diesel fuel spray". *Experiments in Fluids*, vol. 29.Suppl. (2000), pp. 211–219. DOI: `10.1007/s003480070023`, (*cit. on: Chap.2-{67}*).

Çengel, Y. A. and M. A. Boles. *Thermodynamics: an engineering approach.* Ed. by Y. A. Çengel. Seventh edition. McGraw Hill Higher Education, 2011, (*cit. on: Chap.4-{180,182}*).

Chaves, H., M. Knapp, A. Kubitzek, F. Obermeier, and T. Schneider. "Experimental Study of Cavitation in the Nozzle Hole of Diesel Injectors Using Transparent Nozzles". *SAE Technical Paper 950290* (1995). DOI: `10.4271/950290`, (*cit. on: Chap.2-{40,43}, Chap.3-{108}*).

Chávez Cobo, M. d. J. "Modelado CFD Euleriano-Lagrangiano del chorro diésel y evaluación de su combinación con modelos fenomenológicos y unidimensionales." PhD thesis. Camino de Vera, s/n, 46022, Valencia, Spain: Departamento de Máquinas y Motores Térmicos, Universitat Politècnica de València, 2013, (*cit. on: Chap.1-{4}*).

Chehroudi, B., S.-H. Chen, F. V. Bracco, and Y. Onuma. "On the Intact Core of Full-Cone Sprays". *SAE Technical Paper 850126* (1985). DOI: `10.4271/850126`, (*cit. on: Chap.2-{63}*).

Chen, J. L., M. R. Wells, and J. L. Creehan. "Primary Atomization and Spray Analysis of Compound Nozzle Gasoline Injectors". *Journal of Engineering for Gas Turbines and Power*, vol. 120.1 (1998), pp. 237–243. DOI: `10.1115/1.2818082`, (*cit. on: Chap.3-{115}*).

Chen, Y. and S. D. Heister. "Modeling cavitating flows in diesel injectors". *Atomization and Sprays*, vol. 6.6 (1996), pp. 709–726, (*cit. on: Chap.3-{107}*).

Chorin, A. J. "Flame advection and propagation algorithms". *Journal of Computational Physics*, vol. 35.1 (1980), pp. 1–11, (*cit. on: Chap.3-{90}*).

Chu, C. C. and M. L. Corradini. "One-dimensional transient fluid model for fuel/coolant interaction analysis". *Nuclear Science and Engineering*, vol. 101.1 (1989), pp. 48–71, (*cit. on: Chap.3-{96}*).

Colebrook, C. F. "Turbulent Flow in Pipes, with particular reference to the Transition Region between the Smooth and Rough Pipe Laws". *Journal of the Institution of Civil Engineers*, vol. 11.4 (1939), pp. 133–156, (*cit. on: Chap.2-{26,27,28}*).

Correas, D. "Estudio teórico-experimental del chorro libre diésel isotermo". PhD thesis. Camino de Vera, s/n, 46022, Valencia, Spain: Departamento de Máquinas y Motores Térmicos, Universitat Politècnica de València, 1998, (*cit. on: Chap.1-{4}*).

Crowe, C. T., J. D. Schwarzkopf, M. Sommerfeld, and Y. Tsuji. *Multiphase Flows with Droplets and Particles*. Ed. by C. T. Crowe. Second edition. 711 3rd Avenue, 10017, New York, New York, United States of America: CRC Press, Taylor & Francis Group, 1998, (*cit. on: Chap.3-{103}, Chap.4-{184}*).

Delacourt, E., B. Desmet, and B. Besson. "Characterisation of very high pressure diesel sprays using digital imaging techniques". *Fuel*, vol. 84.7-8 (2005), pp. 859–867. DOI: 10.1016/j.fuel.2004.12.003, (*cit. on: Chap.2-{61}*).

Delannoy, Y. and J. L. Kueny. "Two phase flow approach in unsteady cavitation modelling". *Proceedings of the American Society of Mechanical Engineerss. Fluids Engineering Division*. Vol. 98. Toronto, Canada, 1990, pp. 153–158, (*cit. on: Chap.3-{107}*).

Demoulin, F. X., P. A. Beau, G. Blokkel, and R. Borghi. "A new model for turbulent flows with large density fluctuations: Application to liquid atomization". *Atomization and Sprays*, vol. 17.4 (2007), pp. 315–345. DOI: 10.1615/AtomizSpr.v17.i4.20, (*cit. on: Chap.3-{112,113}, Chap.4-{169,170,187,188,191}, Chap.5-{220}, Chap.6-{270,287}*).

Demoulin, F. X. et al. "Toward using direct numerical simulationto improve primary break-up modeling". *Atomization and Sprays*, vol. 23.11 (2013), pp. 957–980. DOI: 10.1615/AtomizSpr.2013007439, (*cit. on: Chap.5-{200}*).

Dent, J. C. "A Basis for the Comparison of Various Experimental Methods for Studying Spray Penetration". *SAE Technical Paper 710571* (1971). DOI: 10.4271/710571, (*cit. on: Chap.2-{58}*).

Desantes, J. M., J. V. Pastor, J. M. García-Oliver, and J. M. Pastor. "A 1D model for the description of mixing-controlled reacting diesel sprays". *Combustion and Flame*, vol. 156.1 (2009), pp. 234–249. DOI: 10.1016/j.combustflame.2008.10.008, (*cit. on: Chap.3-{97}*).

Desantes, J. M., R. Payri, J. M. García, and F. J. Salvador. "A contribution to the understanding of isothermal diesel spray dynamic". *Fuel*, vol. 86.7-8 (2007), pp. 1093–1101. DOI: 10.1016/j.fuel.2006.10.011, (*cit. on: Chap.2-{39,66}*).

Desantes, J. M., R. Payri, F. J. Salvador, and A. Gil. "Development and validation of a theoretical model for diesel spray penetration". *Fuel*, vol. 85.7-8 (2006), pp. 910–917. DOI: `10.1016/j.fuel.2005.10.023`, (*cit. on: Chap.2-{66}*).

Desantes, J. M., R. Payri, F. J. Salvador, and J. Gimeno. "Prediction of Spray Penetration by Means of Spray Momentum Flux". *SAE Technical Paper 2006-01-1387* (2006). DOI: `10.4271/2006-01-1387`, (*cit. on: Chap.5-{256}*).

Desantes, J. M., R. Payri, F. J. Salvador, and V. Soare. "Study of the Influence of Geometrical and Injection Parameters on Diesel Sprays Characteristics in Isothermal Conditions". *SAE Technical Paper 2005-01-0913* (2005). DOI: `10.4271/2005-01-0913`, (*cit. on: Chap.1-{5}, Chap.2-{59,60,61,62}, Chap.3-{115}, Chap.4-{137}, Chap.5-{241}*).

Desjardins, O., J. O. McCaslin, M. Owkes, and P. T. Brady. "Direct numerical and large-eddy simulation of primary atomization in complex geometries". *Atomization and Sprays*, vol. 23.11 (2013), pp. 1001–1048. DOI: `10.1615/AtomizSpr.2013007679`, (*cit. on: Chap.1-{6}, Chap.3-{93}*).

Desjardins, O., V. Moureau, and H. G. Pictsch. "An accurate conservative level set/ghost fluid method for simulating turbulent atomization". *Journal of Computational Physics*, vol. 227.18 (2008), pp. 8395–8416. DOI: `10.1016/j.jcp.2008.05.027`, (*cit. on: Chap.3-{92}*).

Dirke, M. von, A. Krautter, J. P. Ostertag, M. Mennicken, and C. Badock. "Simulation of cavitating flows in diesel injectors". *Oil and Gas Science and Technology*, vol. 54.2 (1999), pp. 223–223, (*cit. on: Chap.3-{90}*).

Dohle, U., S. Kampmann, J. Hammer, T. Wintrich, and C. Hinrichsen. "Advanced Diesel Common Rail Systems for Future Emission Legislation". *International Conference on Automotive Technologies (ICAT)*. Ed. by A. M. Yildirim, C. Sorusbay, E. Tezer, B. Sanayo, and A. S. Ticaret. Hyatt Regency Hotel, Istanbul, Turkey, 2004, pp. 109–113, (*cit. on: Chap.2-{24}*).

Dombrowski, N. and W. R. Johns. "The aerodynamic instability and disintegration of viscous liquid sheets". *Chemical Engineering Science*, vol. 18.3 (1963), pp. 203–214, (*cit. on: Chap.3-{96}*).

Duke, D. J., A. L. Kastengren, F. Z. Tilocco, A. B. Swantek, and C. F. Powell. "X-ray radiography measurements of cavitating nozzle flow". *Atomization and Sprays*, vol. 23.9 (2013), pp. 841–860. DOI: `10.1615/AtomizSpr.2013008340`, (*cit. on: Chap.5-{229}*).

Dukowicz, J. K. "A particle-fluid numerical model for liquid sprays". *Journal of Computational Physics*, vol. 35.2 (1980), pp. 229–253. DOI: `10.1016/0021-9991(80)90087-X`, (*cit. on: Chap.3-{95}*).

Dumont, N., O. Simonin, and C. Habchi. "Numerical Simulation of Cavitating Flows in Diesel Injectors by a Homogeneous Equilibrium Modeling Approach". *CAV 2001: Fourth International Symposium on Cavitation*. California Institute of Technolog. Pasadena, California, United States of America, 2001, (*cit. on: Chap.4-{176,177}*).

Dung, K.-A. "The Eulerian-Lagrangian Spray Atomization (ELSA) model of the jet atomization in CFD simulations: evaluation and validation". PhD thesis. Camino de Vera, s/n, 46022, Valencia, Spain: Departamento de Máquinas y Motores Térmicos, Universitat Politècnica de València, 2012, (*cit. on: Chap.1-{4}*).

Duret, B., J. Réveillon, T. Ménard, and F. X. Demoulin. "Improving primary atomization modeling through DNS of two-phase flows". *International Journal of Multiphase Flow*, vol. 55 (2013), pp. 130–137. DOI: `10.1016/j.ijmultiphaseflow.2013.05.004`, (*cit. on: Chap.4-{174}*).

Echouchene, F., H. Belmabrouk, L. L. Penven, and M. Buffat. "Numerical simulation of wall roughness effects in cavitating flow". *International Journal of Heat and Fluid Flow*, vol. 35.5 (2011), pp. 1068–1075. DOI: `10.1016/j.ijheatfluidflow.2011.05.010`, (*cit. on: Chap.3-{109,110}*).

Elghobashi, S. "On predicting particle-laden turbulent flows". *Applied Scientific Research*, vol. 52.4 (1994), pp. 309–329. DOI: `10.1007/BF00936835`, (*cit. on: Chap.3-{84}*).

Espey, C., J. E. Dec, T. A. Litzinger, and D. A. Santavicca. "Planar laser Rayleigh scattering for quantitative vapor-fuel imaging in a diesel jet". *Combustion and Flame*, vol. 109.1-2 (1997), pp. 65–86. DOI: `10.1016/S0010-2180(96)00126-5`, (*cit. on: Chap.2-{67}*).

Fedkiw, R. P., T. Aslam, B. Merriman, and S. J. Osher. "A Non-oscillatory Eulerian Approach to Interfaces in Multimaterial Flows (the Ghost Fluid Method)". *Journal of Computational Physics*, vol. 152.2 (1999), pp. 457–492. DOI: `10.1006/jcph.1999.6236`, (*cit. on: Chap.3-{92}*).

Ferziger, J. H. and M. Perić. *Computational Methods for Fluid Dynamics*. Ed. by J. H. Ferziger. Third edition. Heidelberg, Germany: Springer, 2002, (*cit. on: Chap.3-{88,90}, Chap.4-{139,148,154,159,179}, Chap.5-{234}, Chap.7-{334}*).

Flaig, U., W. Polach, and G. Ziegler. "Common Rail System (CR-System) for Passenger Car DI Diesel Engines, Experiences with Applications for Series Production Projects". *SAE Technical Paper 1999-01-0191* (1999). DOI: `10.4271/1999-01-0191`, (*cit. on: Chap.2-{18}*).

Fox, T. A. and J. Stark. "Discharge coefficients for miniature fuel injectors". *Proceedings of the Institution of Mechanical Engineers. Part G: Journal of Aerospace Engineering*, vol. 203.17 (1989), pp. 75–78. DOI: `10.1243/pime_proc_1989_203_056_01`, (*cit. on: Chap.2-{35}*).

Friedrich, M. and B. Weigand. "Eulerian multi-fluid simulation of polydisperse dense liquid sprays by the direct quadrature method of moments". *10th International Conference on Liquid Atomization and Spray Systems (ICLASS)*. Kyoto, Japan, 2006, (*cit. on: Chap.3-{105}, Chap.5-{224}*).

Fullmer, W. D., M. A. L. de Bertodano, and X. Zhang. "Verification of a Higher-order Finite Difference Scheme for the One-dimensional Two-fluid Model". *Journal of Computational Multiphase Flows*, vol. 5.2 (2013), pp. 139–155. DOI: `10.1260/1757-482X.5.2.139`, (*cit. on: Chap.5-{200}*).

Fuster, D. et al. "Simulation of primary atomization with an octree adaptive mesh refinement and VOF method". *International Journal of Multiphase Flow*, vol. 35.6 (2009), pp. 550–565. DOI: `10.1016/j.ijmultiphaseflow.2009.02.014`, (*cit. on: Chap.2-{63}*).

García-Oliver, J. M. "Aportaciones al estudio del proceso de combustión turbulenta de chorros en motores de inyección directa". PhD thesis. Camino de Vera, s/n, 46022, Valencia, Spain: Escuela Técnica Superior de Ingenieros Industriales, Universitat Politècnica de València, 2004, (*cit. on: Chap.1-{4}, Chap.2-{16}*).

García-Oliver, J. M., X. Margot, M. L. Chávez, and A. Karlsson. "A combined 1D3D-CFD approach for reducing mesh dependency in Diesel spray calculations". *Mathematical and Computer Modelling*, vol. 54.7-8 (2011), pp. 1732–1737. DOI: `10.1016/j.mcm.2011.01.041`, (*cit. on: Chap.3-{97}*).

García-Oliver, J. et al. "Diesel spray CFD simulations based on the $\Sigma - Y$ eulerian atomization model". *Atomization and Sprays*, vol. 23.1 (2013), pp. 71–95. DOI: `10.1615/AtomizSpr.2013007198`, (*cit. on: Chap.1-{4,5,6}, Chap.3-{114}, Chap.4-{147,168}, Chap.5-{224,229,231,236}*).

Garza de León, O. A. de la. "Estudio de los efectos de la cavitación en toberas de inyección diésel sobre el proceso de inyección y el de formación de hollín". PhD thesis. Camino de Vera, s/n, 46022, Valencia, Spain: Departamento de Máquinas y Motores Térmicos, Universitat Politècnica de València, 2012, (*cit. on: Chap.2-{26,27}, Chap.5-{245}, Chap.6-{300}*).

Ghandhi, J. B. and D. M. Heim. "An optimized optical system for backlit imaging". *Review of Scientific Instruments*, vol. 80.5 (2009), pp. 1–3. DOI: 10.1063/1.3128728, (*cit. on: Chap.1-{3}*).

Ghia, U. et al. "The AIAA Code Verification Project - Test cases for CFD Code Verification". *48th AIAA Aerospace Sciences Meeting Including the New Horizons Forum and Aerospace Exposition*. 2010-0125. Orlando, Florida, United States of America, 2010, (*cit. on: Chap.5-{200,201,203,204,206,208,209,210,213}*).

Giannadakis, E., M. Gavaises, and C. Arcoumanis. "Modelling of cavitation in diesel injector nozzles". *Journal of Fluid Mechanics*, vol. 616 (2008), pp. 153–193. DOI: 10.1017/S0022112008003777, (*cit. on: Chap.3-{100}*).

Giannadakis, E., D. Papoulias, M. Gavaises, C. Arcoumanis, and C. Soteriou. "Evaluation of the Predictive Capability of Diesel Nozzle Cavitation Models". *SAE Technical Paper 2007-01-0245* (2007). DOI: 10.4271/2007-01-0245, (*cit. on: Chap.3-{100,101,108,109}, Chap.5-{209}*).

Gimeno, J. "Desarrollo y aplicación de la medida de flujo de cantidad de movimiento de un chorro Diésel". PhD thesis. Camino de Vera, s/n, 46022, Valencia, Spain: Departamento de Máquinas y Motores Térmicos, Universitat Politècnica de València, 2008, (*cit. on: Chap.1-{3,4}, Chap.2-{21,33,39,42,59}, Chap.5-{223,228,229,244,252,256}*).

Glassey, S. F., A. Stockner, and M. Flinn. "HEUI - A New Direction for Diesel Engine Fuel Systems". *International Congress & Exposition*. SAE International. Detroit, Michigan, United States of America: SAE Technical Paper, 1993. DOI: 10.4271/930270, (*cit. on: Chap.2-{24}*).

Grace, J. R. and F. Taghipour. "Verification and validation of CFD models and dynamic similarity for fluidized beds". *Powder Technology*, vol. 139.2 (2004), pp. 99–110. DOI: 10.1016/j.powtec.2003.10.006, (*cit. on: Chap.5-{200}*).

Grant, R. P. and S. Middleman. "Newtonian jet stability". *American Institute of Chemical Engineers Journal*, vol. 12.4 (1966), pp. 669–678. DOI: 10.1002/aic.690120411, (*cit. on: Chap.2-{47}*).

Gravensen, P., J. Branebjerg, and O. S. Jensen. "Microfluidics - a review". *Journal of Micromechanics and Microengineering*, vol. 3.4 (1993), pp. 168–182. DOI: 10.1088/0960-1317/3/4/002, (*cit. on: Chap.2-{34}*).

Gueyffier, D., J. Li, A. Nadim, R. Scardovelli, and S. Zaleski. "Volume-of-Fluid Interface Tracking with Smoothed Surface Stress Methods for Three-Dimensional Flows". *Journal of Computational Physics*, vol. 152.2 (1999), pp. 423–456. DOI: 10.1006/jcph.1998.6168, (*cit. on: Chap.3-{90}*).

Guildenbecher, D. R., C. López-Rivera, and P. E. Sojka. "Secondary atomization". *Experiments in Fluids*, vol. 46.3 (2009), pp. 371–402, (*cit. on: Chap.2-{52}*).

Habchi, C., N. Dumont, and O. Simonin. "Multidimensional simulation of cavitating flows in Diesel injectors by a homogeneous mixture modeling approach". *Atomization and Sprays*, vol. 18.2 (2008), pp. 129–162. DOI: 10.1615/AtomizSpr.v18.i2.20, (*cit. on: Chap.3-{108,110,117}*).

Hall, G. W. "Analytical Determination of the Discharge Characteristics of Cylindrical-Tube Orifices". *Journal of Mechanical Engineering Science*, vol. 5.1 (1963), pp. 91–97. DOI: 10.1243/jmes_jour_1963_005_013_02, (*cit. on: Chap.2-{36}*).

Han, J. H. and G. Tryggvason. "Secondary breakup of axisymmetric liquid drops. I. Acceleration by a constant body force". *Physics of Fluids*, vol. 11.12 (1999), pp. 3650–3667, (*cit. on: Chap.2-{52}*).

Hay, N. and P. L. Jones. "Comparison of the Various Correlations for Spray Penetration". *SAE Technical Paper 720776* (1972). DOI: 10.4271/720776, (*cit. on: Chap.2-{58}*).

Hayashi, K., S. Hosoda, G. Tryggvason, and A. Tomiyama. "Effects of shape oscillation on mass transfer from a Taylor bubble". *International Journal of Multiphase Flow*, vol. 58 (2014), pp. 236–254. DOI: 10.1016/j.ijmultiphaseflow.2013.09.009, (*cit. on: Chap.3-{88}*).

Hayashi, K. and A. Tomiyama. "Interface tracking simulation of mass transfer from a dissolving bubble". *Journal of Computational Multiphase Flows*, vol. 3.4 (2011), pp. 247–262. DOI: 10.1260/1757-482X.3.4.247, (*cit. on: Chap.3-{88}*).

Herrmann, M. A. "On simulating primary atomization using the refined level set grid method". *Atomization and Sprays*, vol. 21.4 (2011), pp. 283–301. DOI: 10.1615/AtomizSpr.2011002760Doc, (*cit. on: Chap.3-{93}*).

Hillamo, H., O. Kaario, and M. Larmi. "Particle Image Velocimetry Measurements of a Diesel Spray". *SAE Technical Paper 2008-01-0942* (2008). DOI: 10.4271/2008-01-0942, (*cit. on: Chap.1-{3}*).

Hinze, J. O. *Turbulence*. Ed. by J. O. Hinze. Second edition. New York, New York, United States of America: McGraw Hill, 1975, (*cit. on: Chap.4-{141}*).

Hiroyasu, H. and M. Arai. "Structures of Fuel Sprays in Diesel Engines". *SAE Technical Paper 900475* (1990). DOI: 10.4271/900475, (*cit. on: Chap.2-{58,61,63,64}*).

Hiroyasu, H., M. Arai, and M. Tabata. "Empirical Equations for the Sauter Mean Diameter of a Diesel Spray". *SAE Technical Paper 890464* (1989). DOI: 10.4271/890464, (*cit. on: Chap.2-{66}*).

Hirt, C. W. and B. D. Nichols. "Volume of fluid (VOF) method for the dynamics of free boundaries". *Journal of Computational Physics*, vol. 39.1 (1981), pp. 201–225, (*cit. on: Chap.3-{90}*).

Hohmann, S. and U. Renz. "Numerical simulation of fuel sprays at high ambient pressure: The influence of real gas effects and gas solubility on droplet vaporisation". *International Journal of Heat and Mass Transfer*, vol. 46.16 (2003), pp. 3017–3028. DOI: 10.1016/S0017-9310(03)00077-2, (*cit. on: Chap.3-{98}*).

Hossainpour, S. and A. R. Binsesh. "Investigation of fuel spray atomization in a DI heavy-duty diesel engine and comparison of various spray breakup models". *Fuel*, vol. 88.5 (2009), pp. 799–508. DOI: 10.1016/j.fuel.2008.10.036, (*cit. on: Chap.3-{98}*).

Hoyas, S., A. Gil, X. Margot, D. Khuong-Anh, and F. Ravet. "Evaluation of the Eulerian-Lagrangian Spray Atomization (ELSA) model in spray simulations: 2D cases". *Mathematical and Computer Modelling*, vol. 57.7-8 (2013), pp. 1686–1693. DOI: 10.1016/j.mcm.2011.11.006, (*cit. on: Chap.1-{6}, Chap.3-{114,115}, Chap.4-{168}, Chap.5-{241,249}*).

Hsiang, L.-P. and G. M. Faeth. "Near-limit drop deformation and secondary breakup". *International Journal of Multiphase Flow*, vol. 18.5 (1992), pp. 635–652, (*cit. on: Chap.3-{96}*).

Imagine.Lab, L. *AMESim v.4.2 user's manual*. 2004, (*cit. on: Chap.2-{37}*).

Irannejad, A. and F. Jaberi. "Large Eddy Simulation of Evaporating Spray with a Stochastic Breakup Model". *SAE Technical Paper 2013-01-1101* (2013). DOI: 10.4271/2013-01-1101, (*cit. on: Chap.3-{102}*).

Ishii, M. and T. Hinbiki. *Thermo-Fluid Dynamics of Two-Phase Flow*. Ed. by M. Ishii and T. Hinbiki. Second edition. Heidelberg, Germany: Springer, 1975. DOI: 0.1007/978-1-4419-7985-8_11, (*cit. on: Chap.3-{84,103,107}, Chap.4-{138,140,141,145,168,170,176,179}*).

Issa, R. I. "Solution of the implicitly discretised fluid flow equations by operator-splitting". *Journal of Computational Physics*, vol. 62.1 (1986), pp. 40–65. DOI: 16/0021-9991(86)90099-9, (*cit. on: Chap.4-{149}*).

Issa, R. I., B. Ahmadi-Befrui, K. R. Beshay, and A. D. Gosman. "Solution of the implicitly discretised reacting flow equations by operator-splitting". *Journal of Computational Physics*, vol. 93.2 (1991), pp. 388–410. DOI: 10.1016/0021-9991(91)90191-M, (*cit. on: Chap.4-{149}*).

Iyer, V. and J. Abraham. "An Evaluation of a Two-Fluid Eulerian-Liquid Eulerian-Gas Model for Diesel Sprays". *Journal of Fluids Engineering*, vol. 125.4 (2003), pp. 660–669. DOI: 10.1115/1.1593708, (*cit. on: Chap.3-{104}*).

Jasak, H. "Error Analysis and Estimation for the Finite Volume Method with Applications to Fluid Flows". PhD thesis. South Kensington Campus, SW7 2AZ, London, United Kingdom: Department of Mechanical Engineering, Imperial College of Science, Technology and Medicine, 1996, (*cit. on: Chap.4-{146,149,184}*).

Jicha, M., J. Jedelsky, J. Otahal, and J. Slama. "Influence of Some Geometrical Parameters on the Characteristics of Effervescent Atomization". *18th Annual Conference on Liqud Atomization & Spray Systems (ILASS Europe)*. Zaragoza, Spain, 2002, (*cit. on: Chap.2-{66}, Chap.3-{115}*).

Jin, J. D. and G. L. Borman. "A Model for Multicomponent Droplet Vaporization at High Ambient Pressures". *SAE Technical Paper 850264* (1985). DOI: 10.4271/850264, (*cit. on: Chap.2-{56}*).

Johnson, J. et al. "Correlations of Non-Vaporizing Spray Penetration for 3000 Bar Diesel Spray Injection". *SAE Technical Paper 2013-24-0033* (2013). DOI: 10.4271/2013-24-0033, (*cit. on: Chap.2-{20}*).

Jones, W. P. and C. Lettieri. "Large eddy simulation of spray atomization with stochastic modeling of breakup". *Physics of Fluids*, vol. 22.11 (2010), pp. 1–12. DOI: 10.1063/1.3508353, (*cit. on: Chap.3-{102}*).

Jung, S. K. and R. Myong. "A second-order positivity-preserving finite volume upwind scheme for air-mixed droplet flow in atmospheric icing". *Computers and Fluids*, vol. 86 (2013), pp. 459–469. DOI: 10.1016/j.compfluid.2013.08.001, (*cit. on: Chap.5-{200}*).

Kampmann, S., B. Dittus, P. Mattes, and M. Kirner. "The Influence of Hydro Grinding at VCO Nozzles on the Mixture Preparation in a DI Diesel Engine". *SAE Technical Paper 960867* (1996). DOI: 10.4271/960867, (*cit. on: Chap.2-{62}, Chap.3-{115}*).

Kärrholm, F. P., H. Weller, and N. Nordin. "Modelling Injector Flow Including Cavitation Effects for Diesel Applications". *Proceedings of the American Society of Mechanical Engineers / Japan Society of Mechanica Engineers. Fluids Engineering Summer Conference*. Vol. 2. San Diego, California, United States of America, 2007, pp. 465–474. DOI: `10.1115/FEDSM2007-37518`, (*cit. on: Chap.3-{108}*).

Kastengren, A. L. and C. F. Powell. "Spray density measurements using X-ray radiography". *Proceedings of the Institution of Mechanical Engineers, Part D: Journal of Automobile Engineering*, vol. 221.6 (2007), pp. 653–662. DOI: `10.1243/09544070JAUTO392`, (*cit. on: Chap.1-{2,3}, Chap.2-{45}, Chap.7-{312,321,322}*).

Kastengren, A. L. et al. "Engine combustion network (ECN): Measurements of nozzle geometry and hydraulic behavior". *Atomization and Sprays*, vol. 22 (2012), pp. 1011–1052. DOI: `10.1615/AtomizSpr.2013006309`, (*cit. on: Chap.2-{31,34}, Chap.7-{310,331}*).

Kent, J. C. and G. M. Brown. "Nozzle exit flow characteristics for square-edged and rounded inlet geometries". *Combustion Science and Technology*, vol. 30.1-6 (1983), pp. 121–132. DOI: `10.1080/00102208308923615`, (*cit. on: Chap.2-{35}, Chap.7-{328}*).

Khasanshin, T. S., V. S. Samuilov, and A. P. Shchemelev. "Determination of the thermodynamic properties of liquid n-hexadecane from the measurements of the velocity of sound". *Journal of Engineering Physics and Thermophysics*, vol. 82.1 (2009), pp. 149–156. DOI: `10.1007/s10891-009-0156-2`, (*cit. on: Chap.4-{177,178,181}*).

Khasanshin, T. S., A. P. Shchamialiou, and O. G. Puddobskij. "Thermodynamic Properties of Heavy n-Alkanes in the Liquid State: n-Dodecane". *International Journal of Thermophysics*, vol. 24.5 (2005), pp. 1277–1289, (*cit. on: Chap.4-{177,178}*).

Kim, S., S. W. Park, and C. S. Lee. "Improved Eulerian-Lagrangian spray simulation by using an enhanced momentum coupling model". *Proceedings of the American Society of Mechanical Engineerss. Internal Combustion Engine Division Fall Technical Conference*. Lucerne, Switzerland, 2009, pp. 433–442. DOI: `10.1115/ICEF2009-14079`, (*cit. on: Chap.3-{98}*).

Kolakaluri, R., Y. Li, and S.-C. Kong. "A unified spray model for engine spray simulation using dynamic mesh refinement". *International Journal of Multiphase Flow*, vol. 36.11-12 (2010), pp. 858–869. DOI: `10.1016/j.ijmultiphaseflow.2010.08.001`, (*cit. on: Chap.3-{98}*).

Kook, S. and L. M. Pickett. "Effect of ambient temperature and density on shock wave generation in a diesel engine". *Atomization and Sprays*, vol. 20.2 (2010), pp. 163–175. DOI: 10.1615/AtomizSpr.v20.i2.50, (*cit. on: Chap.5-{205}*).

Kösters, A. and A. Karlsson. "A Comprehensive Numerical Study of Diesel Fuel Spray Formation with OpenFOAM". *SAE Technical Paper 2011-01-0842* (2011). DOI: 10.4271/2011-01-0842, (*cit. on: Chap.3-{99,100}*).

Kristensson, E. et al. "Analysis of multiple scattering suppression using structured laser illumination planar imaging in scattering and fluorescing media". *Optics Express*, vol. 19.14 (2011), pp. 13647–13663. DOI: 10.1364/OE.19.013647, (*cit. on: Chap.2-{66}*).

Kubota, A., H. Kato, and H. Yamaguichi. "A new modelling of cavitating flows: a numerical study of unsteady cavitation on a hydrofoil section". *Journal of Fluid Mechanics*, vol. 240 (1992), pp. 59–96, (*cit. on: Chap.3-{107}*).

Laborda, J. M. M. "Engineering Large Eddy Simulation of Diesel sprays". PhD thesis. Camino de Vera, s/n, 46022, Valencia, Spain: Departamento de Máquinas y Motores Térmicos, Universitat Politècnica de València, 2014, (*cit. on: Chap.1-{4}*).

Lafaurie, B., C. Nardone, R. Scardovelli, S. Zaleski, and G. Zanetti. "Modelling Merging and Fragmentation in Multiphase Flows with SURFER". *Journal of Computational Physics*, vol. 113.1 (1994), pp. 134–147. DOI: 10.1006/jcph.1994.1123, (*cit. on: Chap.3-{90}*).

Launder, B. E. and B. I. Sharma. "Application of the energy-dissipation model of turbulence to the calculation of flow near a spinning disc". *Letters in Heat and Mass Transfer*, vol. 1.2 (1974), pp. 131–137, (*cit. on: Chap.4-{185}*).

Launder, B. E. "On the effects of a gravitational field on the turbulent transport of heat and momentum". *Journal of Fluid Mechanics*, vol. 67.3 (1975), pp. 569–581. DOI: 10.1017/S002211207500047X, (*cit. on: Chap.4-{169}*).

Lebas, R., G. Blokkel, P. A. Beau, and F. X. Demoulin. "Coupling Vaporization Model With the Eulerian-Lagrangian Spray Atomization (ELSA) Model in Diesel Engine Conditions". *SAE Technical Paper 2005-01-0213* (2005). DOI: 10.4271/2005-01-0213, (*cit. on: Chap.1-{5}, Chap.3-{112}, Chap.4-{168}*).

Lebas, R., T. Ménard, P. A. Beau, A. Berlemont, and F. X. Demoulin. "Numerical simulation of primary break-up and atomization: DNS and modelling study". *International Journal of Multiphase Flow*, vol. 35.3 (2009), pp. 247–260. DOI: `10.1016/j.ijmultiphaseflow.2008.11.005`, (*cit. on: Chap.1-{5}, Chap.2-{63}, Chap.3-{113,114}, Chap.4-{172,173}, Chap.5-{200,218,220,221}, Chap.6-{276,278,281}, Chap.7-{344}*).

Lee, C. H. and R. D. Reitz. "CFD simulations of diesel spray tip penetration with multiple injections and with engine compression ratios up to 100:1". *Fuel*, vol. 111 (2013), pp. 289–297. DOI: `10.1016/j.fuel.2013.04.058`, (*cit. on: Chap.1-{5}*).

Lee, W. G. and R. D. Reitz. "A numerical investigation of transient flow and cavitation within minisac and valve-covered orifice diesel injector nozzles". *Journal of Engineering for Gas Turbines and Power*, vol. 132.5 (2010), pp. 1–8. DOI: `10.1115/1.4000145`, (*cit. on: Chap.3-{110,117}*).

Lee, W.-K., K. Fezzaa, and J. Wang. "Metrology of steel micronozzles using x-ray propagation-based phase-enhanced microimaging". *Applied Physics Letters*, vol. 87.22 (2005). DOI: `10.1063/1.2034099`, (*cit. on: Chap.2-{31}*).

Lefebvre, A. H. *Atomization and Sprays.* Ed. by S. Tamburrino and M. Prescott. 711 3rd Avenue, 10017, New York, New York, United States of America: Taylor & Francis, 1989, (*cit. on: Chap.2-{47,50}*).

León, G. C. B. "Experimental and theoretical study of the direct Diesel injection process at low temperatures". PhD thesis. Camino de Vera, s/n, 46022, Valencia, Spain: Departamento de Máquinas y Motores Térmicos, Universitat Politècnica de València, 2011, (*cit. on: Chap.1-{4}*).

Lichtarowicz, A., R. K. Duggins, and E. Markland. "Discharge coefficients for incompressible non-cavitating flow through long orifices". *Journal of Mechanical Engineering Science*, vol. 7.2 (1965), pp. 210–219. DOI: `10.1243/jmes_jour_1965_007_029_02`, (*cit. on: Chap.2-{31,35,36}*).

Linne, M. "Imaging in the optically dense regions of a spray: A review of developing techniques". *Progress in Energy and Combustion Science*, vol. 39.5 (2013), pp. 403–440. DOI: `10.1016/j.pecs.2013.06.001`, (*cit. on: Chap.1-{2}, Chap.2-{45}*).

Linne, M., M. Paciaroni, and T. Hall. "Ballistic imaging of the near field in a diesel spray". *Experiments in Fluids*, vol. 40.6 (2006), pp. 836–846. DOI: `10.1007/s00348-006-0122-0`, (*cit. on: Chap.2-{33,45}*).

Liu, A. B., D. Mather, and R. D. Reitz. "Modeling the Effects of Drop Drag and Breakup on Fuel Sprays". *SAE Technical Paper 930072* (1993). DOI: 10.4271/930072, (*cit. on: Chap.2-{54}*).

Liu, B., M. Jia, and Z. Peng. "An Investigation of Multiple-Injection Strategy in a Diesel PCCI Combustion Engine". *SAE Technical Paper 2010-04-12* (2010). DOI: 10.4271/2010-01-1134, (*cit. on: Chap.2-{58}*).

López, J. J. "Estudio teórico-experimental del chorro libre diésel no evaporativo y de su interacción con el movimiento del aire". PhD thesis. Camino de Vera, s/n, 46022, Valencia, Spain: Departamento de Máquinas y Motores Térmicos, Universitat Politècnica de València, 2003, (*cit. on: Chap.1-{4}*).

Lucchini, T., G. D'Errico, and D. Ettorre. "Numerical investigation of the spray-mesh-turbulence interactions for high-pressure, evaporating sprays at engine conditions". *International Journal of Heat and Fluid Flow*, vol. 32.1 (2011), pp. 285–297. DOI: 10.1016/j.ijheatfluidflow.2010.07.006, (*cit. on: Chap.3-{98}*).

Lumley, J. L. "Modeling turbulent flux of passive scalar quantities in inhomogeneous flows". *Physics of Fluids*, vol. 18.6 (1975), pp. 619–621. DOI: 10.1063/1.861200, (*cit. on: Chap.4-{169}*).

Macián, V., V. Bermúdez, R. Payri, and J. Gimeno. "New technique for determination of internal geometry of a diesel nozzle with the use of silicone methodology". *Experimental Techniques*, vol. 27.2 (2003), pp. 39–43, (*cit. on: Chap.2-{31,32}, Chap.5-{224}*).

Macián, V., R. Payri, A. García, and M. Bardi. "Experimental evaluation of the best approach for diesel spray images segmentation". *Experimental Techniques*, vol. 36.6 (2012), pp. 26–34. DOI: 10.1111/j.1747-1567.2011.00730.x, (*cit. on: Chap.2-{62}*).

Macián, V., R. Payri, S. Ruiz, M. Bardi, and A. H. Plazas. "Experimental study of the relationship between injection rate shape and Diesel ignition using a novel piezo-actuated direct-acting injector". *Applied Energy*, vol. 118 (2014), pp. 100–113. DOI: 10.1016/j.apenergy.2013.12.025, (*cit. on: Chap.2-{20}*).

Mahulikar, S. P. and H. Herwig. "Fluid friction in incompressible laminar convection: Reynolds' analogy revisited for variable fluid properties". *European Physical Journal B*, vol. 62.1 (2008), pp. 77–86. DOI: 10.1140/epjb/e2008-00115-0, (*cit. on: Chap.6-{298}*).

Marcer, R. et al. "A Validated Numerical Simulation of Diesel Injector Flow Using a VOF Method". *SAE Technical Paper 2000-01-2932* (2000). DOI: 10.4271/2000-01-2932, (*cit. on: Chap.3-{90}*).

Marcer, R. et al. "Coupling 1D System AMESim and 3D CFD EOLE models for Diesel Injection Simulation". *23rd Annual Conference on Liqud Atomization & Spray Systems (ILASS Europe)*. Brno, Czech Republic, 2010, (*cit. on: Chap.3-{90}*).

Marchisio, D. L. and R. O. Fox. "Solution of population balance equations using the direct quadrature method of moments". *Journal of Aerosol Science*, vol. 36.1 (2005), pp. 43–73. DOI: `10.1016/j.jaerosci.2004.07.009`, (*cit. on: Chap.3-{104}*).

Marchisio, D. L., R. D. Vigil, and R. O. Fox. "Implementation of the quadrature method of moments in CFD codes for aggregation-breakage problems". *Chemical Engineering Science*, vol. 58.15 (2003), pp. 3337–3351, (*cit. on: Chap.3-{104}*).

Martínez-López, J. "Estudio computacional de la influencia del levantamiento de aguja sobre el flujo interno y el fenómeno de la cavitación en toberas de injección Diésel". PhD thesis. Camino de Vera, s/n, 46022, Valencia, Spain: Departamento de Máquinas y Motores Térmicos, Universitat Politècnica de València, 2013, (*cit. on: Chap.1-{4}, Chap.3-{110}, Chap.6-{283}*).

Masuda, R., T. Fuyuto, M. Nagaoka, E. von Berg, and R. Tatschi. "Validation of Diesel Fuel Spray and Mixture Formation from Nozzle Internal Flow Calculation". *SAE Technical Paper 2005-01-2098* (2005). DOI: `10.4271/2005-01-2098`, (*cit. on: Chap.3-{104,115}*).

Ménard, T., S. Tanguy, and A. Berlemont. "Coupling level set/VOF/ghost fluid methods: Validation and application to 3D simulation of the primary break-up of a liquid jet". *International Journal of Multiphase Flow*, vol. 33.5 (2007), pp. 510–524. DOI: `10.1016/j.ijmultiphaseflow.2006.11.001`, (*cit. on: Chap.3-{93,113}, Chap.5-{200,218}, Chap.6-{281}*).

Menter, F. R. *Improved Two-Equation $k - \omega$ Turbulence Models for Aerodynamic Flows*. Technical Report N93-22809. Ames Research Center, Moffett Field, California, United States of America: National Aeronautics and Space Administration, 1992, (*cit. on: Chap.4-{189}*).

Menter, F. R. "Two-equation eddy-viscosity turbulence models for engineering applications". *American Institute of Aeronautics and Astronautics Journal*, vol. 32.8 (1994), pp. 1598–1605. DOI: `10.2514/3.12149`, (*cit. on: Chap.4-{189}*).

Miesse, C. C. "Correlation of Experimental Data on the Disintegration of Liquid Jets". *Industrial & Engineering Chemistry*, vol. 47.9 (1955), pp. 1690–1701, (*cit. on: Chap.2-{50}*).

Mishra, C. and Y. P. Peles. "Cavitation in flow through a micro-orifice inside a silicon microchannel". *Physics of Fluids*, vol. 17.1 (2005), pp. 1–15. DOI: 10.1063/1.1827602, (*cit. on: Chap.2-{43}*).

Mishra, C. and Y. P. Peles. "Flow visualization of cavitating flows through a rectangular slot micro-orifice ingrained in a microchannel". *Physics of Fluids*, vol. 17.11 (2005), pp. 1–14. DOI: 10.1063/1.2132289.

Montgomery, D. C. *Design and Analysis of Experiments*. Ed. by W. Anderson. Fifth edition. 605 3rd Avenue, 10158-0012, New York, New York, United States of America: John Wiley & Sons, Inc., 1997, (*cit. on: Chap.6-{271,273,274,275,286,289,291,293}*).

Morena, J. de la. "Estudio de la influencia de las características del flujo interno en toberas sobre el proceso de inyección Diésel en campo próximo". PhD thesis. Camino de Vera, s/n, 46022, Valencia, Spain: Departamento de Máquinas y Motores Térmicos, Universitat Politècnica de València, 2011, (*cit. on: Chap.1-{4}, Chap.2-{40,42,45,51,64}, Chap.5-{244,251}*).

Mugele, R. A. and H. D. Evans. "Droplet Size Distribution in Sprays". *Industrial & Engineering Chemistry*, vol. 43.6 (1951), pp. 1317–1324. DOI: 10.1021/ie50498a023, (*cit. on: Chap.2-{65}*).

Naber, J. D. and D. L. Siebers. "Effects of Gas Density and Vaporization on Penetration and Dispersion of Diesel Sprays". *SAE Technical Paper 960034* (1996). DOI: 10.4271/960034, (*cit. on: Chap.2-{39,58,59,60,61,62,63,66}, Chap.5-{261}*).

Nakayama, Y. "Action of the Fluid in the Air-Micrometer (1st Report, Characteristics of Small-Diameter Nozzle and Orifice No. 1, In the Case of Compressibility Being Ignored)". *The Japan Society of Mechanical Engineers*, vol. 4.15 (1961), pp. 507–515. DOI: 10.1299/jsme1958.4.507, (*cit. on: Chap.2-{36}*).

Ning, W., R. D. Reitz, R. Diwakar, and A. M. Lippert. "An Eulerian-Lagrangian Spray and Atomization model with improved turbulence modeling". *Atomization and Sprays*, vol. 19.8 (2009), pp. 727–739. DOI: 10.1615/AtomizSpr.v19.i8.20, (*cit. on: Chap.1-{5}, Chap.3-{116}, Chap.4-{168}*).

Ning, W., R. D. Reitz, A. M. Lippert, and R. Diwakar. "Development of a Next-generation Spray and Atomization Model Using an Eulerian-Lagrangian Methodology". *20th Annual Conference on Liquid Atomization & Spray Systems (ILASS Americas)*. Chicago, Illinois, United States of America, 2007, (*cit. on: Chap.3-{113}, Chap.4-{142,146}*).

Ning, W., R. D. Reitz, A. M. Lippert, and R. Diwakar. "A Numerical Investigation of Nozzle Geometry and Injection Condition Effects on Diesel Fuel Injector Flow Physics". *SAE Technical Paper 2008-01-0936* (2008). DOI: `10.4271/2008-01-0936`, (*cit. on: Chap.3-{113,116}*).

Nurick, W. H. "Orifice Cavitation and Its Effect on Spray Mixing". *Journal of Fluids Engineering*, vol. 98.4 (1976), pp. 681–687. DOI: `10.1115/1.3448452`, (*cit. on: Chap.2-{40,41}*).

Oberkampf, W. L. and T. G. Trucano. "Verification and validation in computational fluid dynamics". *Progress in Aerospace Sciences*, vol. 38.3 (2002), pp. 209–272. DOI: `10.1016/S0376-0421(02)00005-2`, (*cit. on: Chap.5-{199,201,202,206,207,211,212,216,218,220,223}*).

Olsson, E. and G. Kreiss. "A conservative level set method for two phase flow". *Journal of Computational Physics*, vol. 210.1 (2005), pp. 225–246. DOI: `10.1016/j.jcp.2005.04.007`, (*cit. on: Chap.3-{92}*).

On type-approval of motor vehicles and engines with respect to emissions from heavy duty vehicles (Euro VI) and on access to vehicle repair and maintenance information and amending Regulation (EC) No 715/2007 and Directive 2007/46/EC and repealing Directives 80/1269/EEC and 2005/78/EC. English. Official Journal of the European Union. Regulation. Eurpoean Union, 2009, (*cit. on: Chap.1-{1}*).

O'Rourke, P. J. and A. A. Amsden. "The Tab Method for Numerical Calculation of Spray Droplet Breakup". *SAE Technical Paper 872089* (1987). DOI: `10.4271/872089`, (*cit. on: Chap.3-{96}*).

Osher, S. J. and R. P. Fedkiw. "Level Set Methods: An Overview and Some Recent Results". *Journal of Computational Physics*, vol. 169.2 (2001), pp. 463–502. DOI: `10.1006/jcph.2000.6636`, (*cit. on: Chap.3-{92}*).

Osher, S. J. and J. A. Sethian. "Fronts propagating with curvature-dependent speed: Algorithms based on Hamilton-Jacobi formulations". *Journal of Computational Physics*, vol. 79.1 (1988), pp. 12–49, (*cit. on: Chap.3-{91}*).

Park, S., H. K. Suh, and C. S. Lee. "Effect of cavitating flow on the flow and fuel atomization characteristics of biodiesel and diesel fuels". *Energy and Fuels*, vol. 22.1 (2008), pp. 605–613. DOI: `10.1021/ef7003305`, (*cit. on: Chap.2-{43}*).

Pastor, J. V., J. J. López, J. M. García, and J. M. Pastor. "A 1D model for the description of mixing-controlled inert diesel sprays". *Fuel*, vol. 87.13-14 (2008), pp. 2871–2885. DOI: `10.1016/j.fuel.2008.04.017`, (*cit. on: Chap.2-{62}, Chap.3-{97}*).

Pastor, J. V., R. Payri, J. M. García-Oliver, and J.-G. Nerva. "Schlieren Measurements of the ECN-Spray A Penetration under Inert and Reacting Conditions". *SAE Technical Paper 2012-01-0456* (2012). DOI: `10.4271/2012-01-0456`, (*cit. on: Chap.2-{60}*).

Pastor, J. V., R. Payri, J. M. Salavert, and J. Manin. "Evaluation of natural and tracer fluorescent emission methods for droplet size measurements in a diesel spray". *International Journal of Automotive Technology*, vol. 13.5 (2012), pp. 713–724. DOI: `10.1007/s12239-012-0070-z`, (*cit. on: Chap.4-{138}*).

Patankar, S. V. and D. B. Spalding. "A calculation procedure for heat, mass and momentum transfer in three-dimensional parabolic flows". *International Journal of Heat and Mass Transfer*, vol. 15.10 (1972), pp. 1787–1806. DOI: `10.1016/0017-9310(72)90054-3`, (*cit. on: Chap.4-{149}*).

Patterson, M. A. and R. D. Reitz. "Modeling the Effects of Fuel Spray Characteristics on Diesel Engine Combustion and Emission". *SAE Technical Paper 980131* (1998). DOI: `10.4271/980131`, (*cit. on: Chap.3-{96}*).

Payri, F., V. Bermúdez, R. Payri, and F. J. Salvador. "The influence of cavitation on the internal flow and the spray characteristics in diesel injection nozzles". *Fuel*, vol. 83 (2004), pp. 419–431. DOI: `10.1016/j.fuel.2003.09.010`, (*cit. on: Chap.2-{29,34,58}, Chap.3-{83,103}, Chap.5-{242,261}*).

Payri, F., J. M. Desantes, and et al. *Motores de combusitión interna alternativos*. Ed. by F. Payri and J. M. Desantes. First edition. Loreto 13-15, Local B, 08029 Barcelona, Spain: Editorial Reverté, 2011, (*cit. on: Chap.1-{1}, Chap.2-{15,17}*).

Payri, R., L. Araneo, J. S. Shakal, and V. Soare. "Phase doppler measurements: System set-up optimization for characterization of a diesel nozzle". *Journal of Mechanical Science and Technology*, vol. 22.8 (2008), pp. 1620–1632. DOI: `10.1007/S12206-008-0432-7`, (*cit. on: Chap.1-{3}, Chap.2-{66}, Chap.5-{231}*).

Payri, R., J. M. García, F. J. Salvador, and J. Gimeno. "Using spray momentum flux measurements to understand the influence of diesel nozzle geometry on spray characteristics". *Fuel*, vol. 84.5 (2005), pp. 551–561. DOI: `10.1016/j.fuel.2004.10.009`, (*cit. on: Chap.2-{35,37,38,42}, Chap.3-{83,115}*).

Payri, R., J. M. García-Oliver, M. Bardi, and J. Manin. "Fuel temperature influence on diesel sprays in inert and reacting conditions". *Applied Thermal Engineering*, vol. 35.1 (2012), pp. 185–195, (*cit. on: Chap.2-{62}*).

Payri, R., J. Gimeno, P. Martí-Aldaraví, and G. Bracho. "Study of the influence of the inlet boundary conditions in a LES simulation of internal flow in a diesel injector". *Mathematical and Computer Modelling*, vol. 57.7-8 (2013), pp. 1709–1715. DOI: `10.1016/j.mcm.2011.11.019`, (*cit. on: Chap.5-{240,246,247}*).

Payri, R., J. Gimeno, O. Venegas, and A. H. Plazas. "Experimental and computational study of the influence of partial needle lift on nozzle flowin diesel fuel injectors". *Atomization and Sprays*, vol. 22.8 (2012), pp. 687–714. DOI: `10.1615/AtomizSpr.2012005810`, (*cit. on: Chap.2-{25}, Chap.3-{115}*).

Payri, R., C. Guardiola, F. J. Salvador, and J. Gimeno. "Critical cavitation number determination in diesel injection nozzles". *Experimental Techniques*, vol. 28.3 (2004), pp. 49–52, (*cit. on: Chap.2-{31}*).

Payri, R., S. Molina, F. J. Salvador, and J. Gimeno. "A study of the relation between nozzle geometry, internal flow and sprays characteristics in diesel fuel injection systems". *KSME International Journal*, vol. 18.7 (2004), pp. 1222–1235, (*cit. on: Chap.2-{30,35,62}, Chap.3-{83}, Chap.7-{328}*).

Payri, R., S. Ruiz, F. J. Salvador, and J. Gimeno. "On the dependence of spray momentum flux in spray penetration: Momentum flux packets penetration model". *Journal of Mechanical Science and Technology*, vol. 21.7 (2007), pp. 1100–1111. DOI: `10.1007/BF03027660`, (*cit. on: Chap.5-{256}*).

Payri, R., F. J. Salvador, J. Gimeno, and G. Bracho. "The effect of temperature and pressure on thermodynamic properties of diesel and biodiesel fuels". *Fuel*, vol. 90.3 (2011), pp. 1172–1180. DOI: `10.1016/j.fuel.2010.11.015`, (*cit. on: Chap.4-{176,177,178}, Chap.5-{227}, Chap.6-{287}*).

Payri, R., F. J. Salvador, J. Gimeno, and A. García. "Flow regime effects over non-cavitating diesel injection nozzles". *Proceedings of the Institution of Mechanical Engineers, Part D: Journal of Automobile Engineering*, vol. 226.1 (2012), pp. 133–144. DOI: `10.1177/0954407011413056`, (*cit. on: Chap.5-{241,246,250}*).

Payri, R., F. J. Salvador, J. Gimeno, and J. de la Morena. "Macroscopic Behavior of Diesel Sprays in the Near-Nozzle Field". *SAE Technical Paper 2008-01-0929* (2008). DOI: `10.4271/2008-01-0929`.

Payri, R., F. J. Salvador, J. Gimeno, and J. de la Morena. "Effects of nozzle geometry on direct injection diesel engine combustion process". *Applied Thermal Engineering*, vol. 29.10 (2009), pp. 2051–2060. DOI: `10.1016/j.applthermaleng.2008.10.009`, (*cit. on: Chap.2-{33}*).

Payri, R., F. J. Salvador, J. Gimeno, and J. de la Morena. "Study of cavitation phenomena based on a technique for visualizing bubbles in a liquid pressurized chamber". *International Journal of Heat and Fluid Flow*, vol. 30.4 (2009), pp. 768–777. DOI: `10.1016/j.ijheatfluidflow.2009.03.011`, (*cit. on: Chap.2-{32}*).

Payri, R., F. J. Salvador, J. Gimeno, and R. Novella. "Flow regime effects on non-cavitating injection nozzles over spray behavior". *International Journal of Heat and Fluid Flow*, vol. 32.1 (2011), pp. 273–284. DOI: `10.1016/j.ijheatfluidflow.2010.10.001`, (*cit. on: Chap.5-{257,259}*).

Payri, R., F. J. Salvador, J. Gimeno, and V. Soare. "Determination of diesel sprays characteristics in real engine in-cylinder air density and pressure conditions". *Journal of Mechanical Science and Technology*, vol. 19.11 (2005), pp. 2040–2052. DOI: `10.1007/BF02916497`, (*cit. on: Chap.2-{60}*).

Payri, R., F. J. Salvador, J. Gimeno, and L. D. Zapata. "Diesel nozzle geometry influence on spray liquid-phase fuel penetration in evaporative conditions". *Fuel*, vol. 87.7 (2008), pp. 1165–1176. DOI: `10.1016/j.fuel.2007.05.058`, (*cit. on: Chap.1-{3}, Chap.2-{62}, Chap.3-{83}*).

Payri, R., F. J. Salvador, P. Martí-Aldaraví, and J. Martínez-López. "Using one-dimensional modeling to analyse the influence of the use of biodiesels on the dynamic behavior of solenoid-operated injectors in common rail systems: Detailed injection system model". *Energy Conversion and Management*, vol. 54 (2012), pp. 90–99. DOI: `10.1016/j.enconman.2011.10.004`, (*cit. on: Chap.2-{18,19,28}*).

Payri, R., B. Tormos, J. Gimeno, and G. Bracho. "The potential of Large Eddy Simulation (LES) code for the modeling of flow in diesel injectors". *Mathematical and Computer Modelling*, vol. 52.7-8 (2010), pp. 1151–1160. DOI: `10.1016/j.mcm.2010.02.033`, (*cit. on: Chap.5-{246,250,253}, Chap.7-{318}*).

Payri, R., B. Tormos, J. Gimeno, and Ga. "Large Eddy Simulation for high pressure flows: Model extension for compressible liquids". *Mathematical and Computer Modelling*, vol. 54.7-8 (2011), pp. 1725–1731. DOI: `10.1016/j.mcm.2010.12.001`, (*cit. on: Chap.5-{253}*).

Pereira, H̃. V. "Estudio del fenómeno de la cavitación en la inyección diésel mediante la visualización del flujo interno en orificios transparentes". PhD thesis. Camino de Vera, s/n, 46022, Valencia, Spain: Departamento de Máquinas y Motores Térmicos, Universitat Politècnica de València, 2014, (*cit. on: Chap.1-{3,4}, Chap.2-{43}*).

Pickett, L. M. *Engine Combustion Network*. English. Sandia National Laboratories. 2014. URL: http://www.sandia.gov/ecn/, (*cit. on: Chap.1-{2}, Chap.7-{309,310,311,313,314,332,334,346}*).

Pickett, L. M., J. Manin, A. L. Kastengren, and C. F. Powell. "Comparison of Near-Field Structure and Growth of a Diesel Spray Using Light-Based Optical Microscopy and X-Ray Radiography". *SAE International Journal of Engines*, vol. 7.2 (2014), pp. 1044–1053, (*cit. on: Chap.7-{330,331}*).

Pickett, L. M. et al. "Relationship Between Diesel Fuel Spray Vapor Penetration/Dispersion and Local Fuel Mixture Fraction". *SAE International Journal of Engines*, vol. 4.1 (2011), pp. 764–799. DOI: 10.4271/2011-01-0686, (*cit. on: Chap.2-{45}*).

Pilch, M. M. and C. A. Erdman. "Use of breakup time data and velocity history data to predict the maximum size of stable fragments for acceleration-induced breakup of a liquid drop". *International Journal of Multiphase Flow*, vol. 13.6 (1987), pp. 741–757, (*cit. on: Chap.2-{52}, Chap.3-{96}, Chap.4-{175}*).

Pinzello, A. "Analysis of fuel sprays and combustion processes in Diesel engines with a combined approach of CFD and phenomenological models." PhD thesis. Camino de Vera, s/n, 46022, Valencia, Spain: Departamento de Máquinas y Motores Térmicos, Universitat Politècnica de València and Dipartamento di Energetica, Politecnico di Torino, 2008, (*cit. on: Chap.1-{4}*).

Pope, S. B. "An explanation of the turbulent round-jet/plane-jet anomaly". *American Institute of Aeronautics and Astronautics Journal*, vol. 16 (1978), pp. 279–281. DOI: 10.2514/3.7521, (*cit. on: Chap.5-{230}*).

Post, S. L. and J. Abraham. "Modeling the outcome of drop-drop collisions in Diesel sprays". *International Journal of Multiphase Flow*, vol. 28.6 (2002), pp. 997–1019. DOI: 10.1016/S0301-9322(02)00007-1, (*cit. on: Chap.2-{54}*).

Premnath, K. N. and J. Abraham. "Lattice Boltzmann simulations of drop-drop interactions in two-phase flows". *International Journal of Modern Physics*, vol. 16.1 (2005), pp. 25–44. DOI: 10.1142/S0129183105006930, (*cit. on: Chap.5-{200}*).

Qian, J. and C. K. Law. "Regimes of coalescence and separation in droplet collision". *Journal of Fluid Mechanics*, vol. 331.25 (1997), pp. 59–80, (*cit. on: Chap.2-{54}*).

Qin, J. R. et al. "Correlating the Diesel Spray Behavior to Nozzle Design". *SAE Technical Paper 1999-01-3555* (1999). DOI: 10.4271/1999-01-3555, (*cit. on: Chap.3-{115}*).

Ranz, W. E. "Some experiments on orifice sprays". *The Canadian Journal of Chemical Engineering*, vol. 36.4 (1958), pp. 175–191. DOI: 10.1002/cjce.5450360405, (*cit. on: Chap.2-{50,61}*).

Reitz, R. D. "Atomization and other breakup regimes of a liquid jet". PhD thesis. 08544, Princeton, New Jersey, United States of America: Princeton University, 1978, (*cit. on: Chap.2-{46,49,50,63}, Chap.3-{95}*).

Reitz, R. D. and F. V. Bracco. "On the Dependence of Spray Angle and Other Spray Parameters on Nozzle Design and Operating Conditions". *SAE Technical Paper 790494* (1979). DOI: 10.4271/790494, (*cit. on: Chap.2-{61}*).

Reitz, R. D. and F. V. Bracco. "Mechanism of atomization of a liquid jet". *Physics of Fluids*, vol. 25 (1982), pp. 1730–1742. DOI: 10.1063/1.863650, (*cit. on: Chap.2-{46,48,49,50}*).

Reitz, R. D. and R. Diwakar. "Effect of Drop Breakup on Fuel Sprays". *SAE Technical Paper 860469* (1986). DOI: 10.4271/860469, (*cit. on: Chap.2-{50}, Chap.3-{96}*).

Reitz, R. D. and R. Diwakar. "Structure of High-Pressure Fuel Sprays". *SAE Technical Paper 870598* (1987). DOI: 10.4271/870598, (*cit. on: Chap.2-{50,54}*).

Ruiz, F. "Few useful relations for cavitating orifices". *Proceedings of the 5th International Conference on Liquid Atomization and Spray Systems*, vol. 813 (1991), pp. 595–602, (*cit. on: Chap.2-{50}*).

Ruiz, S. "Estudio teórico-experimental de los procesos de atomización y de mezcla en los chorros diésel D.I." PhD thesis. Camino de Vera, s/n, 46022, Valencia, Spain: Departamento de Máquinas y Motores Térmicos, Universitat Politècnica de València, 2003, (*cit. on: Chap.1-{4}*).

Saha, K., E. Abu-Ramadan, and X. Li. "Modified Single-Fluid Cavitation Model for Pure Diesel and Biodiesel Fuels in Direct Injection Fuel Injectors". *Journal of Engineering for Gas Turbines and Power*, vol. 135.6 (2013), pp. 1–8. DOI: 10.1115/1.4023464, (*cit. on: Chap.3-{111}*).

Salvador, F. J. "Estudio teórico experimental de la influencia de la geometría de toberas de inyección Diésel sobre las características del flujo interno y del chorro". PhD thesis. Camino de Vera, s/n, 46022, Valencia, Spain: Departamento de Máquinas y Motores Térmicos, Universitat Politècnica de València, 2003, (*cit. on: Chap.1-{3,4}, Chap.2-{35,37,39,40,42,51,62}, Chap.5-{225}*).

Salvador, F. J., J. Gimeno, J. de la Morena, and M. Carreres. "Using one-dimensional modeling to analyze the influence of the use of biodiesels on the dynamic behavior of solenoid-operated injectors in common rail systems: Results of the simulations and discussion". *Energy Conversion and Management*, vol. 54.1 (2012), pp. 122–132. DOI: `10.1016/j.enconman.2011.10.007`, (*cit. on: Chap.2-{28,29}*).

Salvador, F. J., J. Martínez-López, M. Caballer, and C. de Alfonso. "Study of the influence of the needle lift on the internal flow and cavitation phenomenon in diesel injector nozzles by CFD using RANS methods". *Energy Conversion and Management*, vol. 66 (2013), pp. 246–256. DOI: `10.1016/j.enconman.2012.10.011`, (*cit. on: Chap.2-{29,33}, Chap.4-{154}, Chap.5-{209}, Chap.6-{279}*).

Salvador, F. J., J. Martínez-López, J. V. Romero, and M. D. Roselló. "Influence of biofuels on the internal flow in diesel injector nozzles". *Mathematical and Computer Modelling*, vol. 54.7-8 (2011), pp. 1699–1705. DOI: `10.1016/j.mcm.2010.12.010`, (*cit. on: Chap.3-{109}*).

Salvador, F. J., A. H. Plazas, J. Gimeno, and M. Carreres. "Complete modelling of a piezo actuator last-generation injector for diesel injection systems". *International Journal of Engine Research*, vol. 15.1 (2014), pp. 3–19. DOI: `10.1177/1468087412455373`, (*cit. on: Chap.2-{26,27,28}*).

Salvador, F. J., S. Ruiz, J. Gimeno, and J. de la Morena. "Estimation of a suitable Schmidt number range in diesel sprays at high injection pressure". *International Journal of Thermal Sciences*, vol. 50.9 (2011), pp. 1790–1798. DOI: `10.1016/j.ijthermalsci.2011.03.030`, (*cit. on: Chap.6-{293,298}*).

Sames, P. C., T. E. Schellin, S. Muzaferija, and M. Perić. "Application of a two-fluid finite volume method to ship slamming". *Journal of Offshore Mechanics and Arctic Engineering*, vol. 121.1 (1999), pp. 47–52. DOI: `10.1115/1.2829554`, (*cit. on: Chap.3-{90}*).

Sato, K. and Y. Saito. "Unstable Cavitation Behavior in a Circular-Cylindrical Orifice Flow". *The Japan Society of Mechanical Engineers International Journal, Series B: Fluids and Thermal Engineering*, vol. 45.3 (2002), pp. 638–645. DOI: `10.1299/jsmeb.45.638`, (*cit. on: Chap.2-{40}*).

Sato, Y. and K. Sekoguchi. "Liquid velocity distribution in two-phase bubble flow". *International Journal of Multiphase Flow*, vol. 2.1 (1975), pp. 79–95. DOI: `10.1016/0301-9322(75)90030-0`, (*cit. on: Chap.3-{103}*).

Schlichting, H. and K. Gersten. *Boundary Layer Theory*. Ed. by H. Schlichting. Eighth edition. Heidelberg, Germany: Springer, 2000, (*cit. on: Chap.2-{33}*).

Schmidt, D. P., C. J. Rutland, and M. L. Corradini. "A fully compressible, two-dimensional model of small, high-speed, cavitating nozzles". *Atomization and Sprays*, vol. 9.3 (1999), pp. 255–276, (*cit. on: Chap.3-{108}*).

Schöppe, D. et al. "Delphi Common Rail System with Direct Acting Injector". *MTZ Worldwide*, vol. 69 (2008), pp. 32–38, (*cit. on: Chap.2-{25}*).

Secretary of Commerce on behalf of the U. S. A., U. S. *Dodecane*. English. National Institute of Standards and Technology. 2013. URL: `http://www.nist.gov/`, (*cit. on: Chap.4-{181,182,183}, Chap.6-{287}, Chap.7-{320,342}*).

Senecal, P. K., E. Pomraning, K. J. Richards, and S. Som. "Grid-convergent spray models for internal combustion engine CFD simulations". *Proceedings of the American Society of Mechanical Engineerss. Internal Combustion Engine Division Fall Technical Conference*. Vancouver, Canada, 2012, pp. 697–710. DOI: `10.1115/ICEF2012-92043`, (*cit. on: Chap.3-{100}*).

Senecal, P. K. et al. "Modeling high-speed viscous liquid sheet atomization". *International Journal of Multiphase Flow*, vol. 25.6-7 (1999), pp. 1073–1097. DOI: `10.1016/S0301-9322(99)00057-9`, (*cit. on: Chap.3-{96}*).

Settles, G. S. *Schlieren and shadowgraph techniques: visualizing phenomena in transparent media*. Ed. by Springer. First edition. Heidelberg, Germany: Springer, 2001, (*cit. on: Chap.1-{3}*).

Shuai, S., N. Abani, T. Yoshikawa, R. D. Reitz, and S. W. Park. "Simulating low temperature diesel combustion with improved spray models". *International Journal of Thermal Sciences*, vol. 48.9 (2009), pp. 1786–1799. DOI: `10.1016/j.ijthermalsci.2009.01.011`, (*cit. on: Chap.3-{98}*).

Siebers, D. L. "Liquid-Phase Fuel Penetration in Diesel Sprays". *SAE Technical Paper 980809* (1998). DOI: `10.4271/980809`, (*cit. on: Chap.1-{3}, Chap.2-{62,63}*).

Siebers, D. L. "Scaling Liquid-Phase Fuel Penetration in Diesel Sprays Based on Mixing-Limited Vaporization". *SAE Technical Paper 1999-01-0528* (1999). DOI: 10.4271/1999-01-0528, (*cit. on: Chap.2-{38,63}*).

Slater, J. W. *NPARC Alliance CFD Verification and Validation Web Site.* English. National Aeronautics and Space Administration. 2012. URL: http://www.grc.nasa.gov/WWW/wind/valid/archive.html, (*cit. on: Chap.5-{200,214,216,217}*).

Som, S. and S. K. Aggarwal. "Effects of primary breakup modeling on spray and combustion characteristics of compression ignition engines". *Combustion and Flame*, vol. 157.6 (2010), pp. 1179–1193. DOI: 10.1016/j.combustflame.2010.02.018, (*cit. on: Chap.1-{5}, Chap.3-{96}, Chap.4-{137}, Chap.5-{240,241}, Chap.7-{315}*).

Som, S., S. K. Aggarwal, E. M. El-Hannouny, and D. Longman. "Investigation of Nozzle Flow and Cavitation Characteristics in a Diesel Injector". *Journal of Engineering for Gas Turbines and Power*, vol. 134.4 (2010), pp. 1–12. DOI: 10.1115/1.3203146, (*cit. on: Chap.3-{110}*).

Som, S. et al. "A Numerical Investigation on Scalability and Grid Convergence of Internal Combustion Engine Simulations". *SAE Technical Paper 2013-01-1095* (2013). DOI: 10.4271/2013-01-1095, (*cit. on: Chap.3-{100}, Chap.5-{237,238,239}*).

Soteriou, C., R. Andrews, and M. Smith. "Direct Injection Diesel Sprays and the Effect of Cavitation and Hydraulic Flip on Atomization". *SAE Technical Paper 950080* (1995). DOI: 10.4271/950080, (*cit. on: Chap.2-{39,40,42,43,51}, Chap.3-{108}*).

Soteriou, C., M. Smith, and R. Andrews. "Diesel injection - laser light sheet illumination of the development of cavitation in orifices". *Institution of Mechanical Engineers Transactions*, vol. 4 (1998), pp. 137–158, (*cit. on: Chap.2-{42}*).

Sou, A., S. Hosokawa, and A. Tomiyama. "Effects of cavitation in a nozzle on liquid jet atomization". *International Journal of Heat and Mass Transfer*, vol. 50.17-18 (2007), pp. 3575–3582. DOI: 10.1016/j.ijheatmasstransfer.2006.12.033, (*cit. on: Chap.2-{43}*).

Spikes, R. H. and G. A. Pennington. "Discharge Coefficient of Small Submerged Orifices". *Proceedings of the Institution of Mechanical Engineers*, vol. 173.1 (1959), pp. 661–674. DOI: 10.1243/pime_proc_1959_173_055_02, (*cit. on: Chap.2-{41}*).

Sterling, A. M. and C. A. Sleicher. "The instability of capillary jets". *Journal of Fluid Mechanics*, vol. 68.3 (1975), pp. 477–495. DOI: `10.1017/S0022112075001772`, (*cit. on: Chap.2-{50}*).

Su, T. F., M. A. Patterson, R. D. Reitz, and P. V. Farrell. "Experimental and Numerical Studies of High Pressure Multiple Injection Sprays". *SAE Technical Paper 960861* (1996). DOI: `10.4271/960861`, (*cit. on: Chap.3-{96}*).

Subramaniam, S. "Lagrangian-Eulerian methods for multiphase flows". *Progress in Energy and Combustion Science*, vol. 39.2-3 (2013), pp. 215–245. DOI: `10.1016/j.pecs.2012.10.003`, (*cit. on: Chap.3-{97}*).

Suh, H. K. and C. S. Lee. "Effect of cavitation in nozzle orifice on the diesel fuel atomization characteristics". *International Journal of Heat and Fluid Flow*, vol. 29.4 (2008), pp. 1001–1009. DOI: `10.1016/j.ijheatfluidflow.2008.03.014`, (*cit. on: Chap.2-{42}*).

Sukumaran, S., S.-C. Kong, and N. H. Cho. "Modeling Evaporating Diesel Sprays Using an Improved Gas Particle Model". *SAE Technical Paper 2013-01-1598* (2013). DOI: `10.4271/2013-01-1598`, (*cit. on: Chap.3-{100}, Chap.5-{224}*).

Sussman, M., E. Fatemi, P. Smereka, and S. J. Osher. "An improved level set method for incompressible two-phase flows". *Computers and Fluids*, vol. 27.5-6 (1998), pp. 663–680. DOI: `10.1016/S0045-7930(97)00053-4`, (*cit. on: Chap.3-{92}*).

Sussman, M. and E. G. Puckett. "A Coupled Level Set and Volume-of-Fluid Method for Computing 3D and Axisymmetric Incompressible Two-Phase Flows". *Journal of Computational Physics*, vol. 162.2 (2000), pp. 301–337. DOI: `10.1006/jcph.2000.6537`, (*cit. on: Chap.3-{92}*).

Sussman, M., P. Smereka, and S. J. Osher. "A Level Set Approach for Computing Solutions to Incompressible Two-Phase Flow". *Journal of Computational Physics*, vol. 114.1 (1994), pp. 146–159. DOI: `10.1006/jcph.1994.1155`, (*cit. on: Chap.3-{91,92}*).

Tamim, J. and W. L. H. Hallett. "A continuous thermodynamics model for multicomponent droplet vaporization". *Chemical Engineering Science*, vol. 50.18 (1995), pp. 2933–2942, (*cit. on: Chap.2-{57}*).

Tanguy, S. and A. Berlemont. "Application of a level set method for simulation of droplet collisions". *International Journal of Multiphase Flow*, vol. 31.9 (2005), pp. 1015–1035. DOI: `10.1016/j.ijmultiphaseflow.2005.05.010`, (*cit. on: Chap.3-{92}*).

Tanguy, S., M. Sagan, B. Lalanne, F. Couderc, and C. Colin. "Benchmarks and numerical methods for the simulation of boiling flows". *Journal of Computational Physics*, vol. 264.1 (2014), pp. 1–22. DOI: `10.1016/j.jcp.2014.01.014`, (*cit. on: Chap.5-{200}*).

Tomiyama, A., I. Zun, H. Higaki, Y. Makino, and T. Sakaguchi. "A three-dimensional particle tracking method for bubbly flow simulation". *Nuclear Engineering and Design*, vol. 175.1-2 (1997), pp. 77–86. DOI: `10.1016/S0029-5493(97)00164-7`, (*cit. on: Chap.3-{100}*).

Tonini, S., M. Gavaises, and A. Theodorakakos. "Modelling of high-pressure dense diesel sprays with adaptive local grid refinement". *International Journal of Heat and Fluid Flow*, vol. 29.2 (2008), pp. 427–448, (*cit. on: Chap.3-{100}*).

Trask, N., D. P. Schmidt, M. Lightfoot, and S. Danczyk. "Compressible modeling of the internal flow in a gas-centered swirl-coaxial fuel injector". *Journal of Propulsion and Power*, vol. 28.4 (2012), pp. 685–693. DOI: `10.2514/1.B34102`, (*cit. on: Chap.3-{114}, Chap.4-{146,147}*).

Unverdi, S. O. and G. Tryggvason. "A front-tracking method for viscous, incompressible, multi-fluid flows". *Journal of Computational Physics*, vol. 100.1 (1992), pp. 25–37. DOI: `10.1016/0021-9991(92)90307-K`, (*cit. on: Chap.3-{88}*).

Vallet, A., A. A. Burluka, and R. Borghi. "Development of a Eulerian model for the "Atomization" of a liquid jet". *Atomization and Sprays*, vol. 11.6 (2001), pp. 619–642, (*cit. on: Chap.1-{5}, Chap.3-{111,118}, Chap.4-{141,142,146,148,168,169,170,173,176,191}, Chap.6-{270,271,276,305}, Chap.7-{344}*).

Varaksin, A. Y. *Turbulent Particle-Laden Gas Flows*. Ed. by A. Y. Varaksin. First edition. Heidelberg, Germany: Springer, 2007, (*cit. on: Chap.3-{84,86,87}*).

Vuorinen, V. A. et al. "Effect of droplet size and atomization on spray formation: A priori study using large-eddy simulation". *Flow, Turbulence and Combustion*, vol. 86.3-4 (2011), pp. 533–561. DOI: `10.1007/s10494-010-9266-3`, (*cit. on: Chap.3-{101}*).

Wakuri, Y., M. Fujii, T. Amitani, and R. Tsuneya. "Studies on the Penetration of Fuel Spray in a Diesel Engine". *Bulletin of the Japan Society of Mechanical Engineers*, vol. 3.9 (1960), pp. 123–130, (*cit. on: Chap.2-{58}*).

Wallis, G. B. *One-dimensional Two-phase Flow*. New York, New York, United States of America: Mcgraw-Hill, 1969, (*cit. on: Chap.4-{176}*).

Walther, J. "Quantitative Untersuchungen der Innenströmung in kavitieren-den Dieseleinspritzdüse". PhD thesis. Karolinenplatz 5, 64289 Darmstadt, Germany: TU Darmstadt, 2002, (*cit. on: Chap.1-{3}*).

Wang, Y., W. G. Lee, R. D. Reitz, and R. Diwakar. "Numerical Simulation of Diesel Sprays Using an Eulerian-Lagrangian Spray and Atomization (ELSA) Model Coupled with Nozzle Flow". *SAE Technical Paper 2011-01-0386* (2011). DOI: 10.4271/2011-01-0386, (*cit. on: Chap.2-{29}, Chap.3-{117}, Chap.4-{168}*).

Weller, H. G., G. Tabor, H. Jasak, and C. Fureby. "A Tensorial Approach to Computational Continuum Mechanics using Object Orientated Techniques". *Computers in Physics*, vol. 12.6 (1998), pp. 620–631. DOI: 10.1063/1.168744, (*cit. on: Chap.4-{138,142,149,191}*).

White, F. M. *Fluid Mechanics*. Ed. by M. Lange. Seventh edition. New York, New York, United States of America: McGraw-Hill Companies, Inc., 2011, (*cit. on: Chap.2-{33,34}, Chap.4-{178}*).

Wierzba, A. "Deformation and breakup of liquid drops in a gas stream at nearly critical Weber numbers". *Experiments in Fluids*, vol. 9.1-2 (1990), pp. 59–64. DOI: 10.1007/BF00575336, (*cit. on: Chap.2-{52,53}*).

Winklhofer, E., E. Kull, E. Kelz, and A. Morozov. "Comprehensive hydraulic and flow field documentation in model throttle experiments under cavitation conditions". *23rd Annual Conference on Liqud Atomization & Spray Systems (ILASS Europe)*. Ed. by B. Ineichen. Zurich, Switzerland, 2001, pp. 574–579, (*cit. on: Chap.1-{3}*).

Xue, Q., S. Som, P. K. Senecal, and E. Pomraning. "Large eddy simulation of fuel-spray under non-reacting IC engine conditions". *Atomization and Sprays*, vol. 23.10 (2013), pp. 925–955. DOI: 10.1615/AtomizSpr.2013008320, (*cit. on: Chap.2-{29}, Chap.5-{254}*).

Xue, Q. and S.-C. Kong. "Development of adaptive mesh refinement scheme for engine spray simulations". *Computers and Fluids*, vol. 38.4 (2009), pp. 939–949. DOI: 10.1016/j.compfluid.2008.10.004, (*cit. on: Chap.3-{98}*).

Xue, Q. and S.-C. Kong. "Multilevel dynamic mesh refinement for modeling transient spray and mixture formation". *Atomization and Sprays*, vol. 19.8 (2009), pp. 755–769. DOI: 10.1615/AtomizSpr.v19.i8.40, (*cit. on: Chap.3-{98}*).

Xue, Q., S.-C. Kong, D. J. Torres, Z. Hu, and J. Yi. "DISI Spray Modeling Using Local Mesh Refinement". *SAE Technical Paper 2008-01-0967* (2008). DOI: 10.4271/2008-01-0967, (*cit. on: Chap.3-{98}*).

Xue, Q. et al. "Eulerian CFD Modelling of Coupled Nozzle Flow and Spray with Validation Against X-Ray Radiography Data". *SAE International Journal of Engines*, vol. 7.2 (2014), pp. 1061–1072. DOI: `10.4271/2014-01-1425`, (*cit. on: Chap.3-{118}*).

Xue, Q. et al. "Three-dimensional Simulations of the Transient Internal Flow in a Diesel Injector: Effects of Needle Movement". *25th Annual Conference on Liquid Atomization & Spray Systems (ILASS Americas)*. Pittsburgh, Pensilvania, United States of America, 2013.

Yakhot, V. and S. A. Orszag. "Renormalization group analysis of turbulence. I. Basic theory". *Journal of Scientific Computing*, vol. 1.1 (1986), pp. 3–51. DOI: `10.1007/BF01061452`, (*cit. on: Chap.4-{186}*).

Yakhot, V., S. A. Orszag, S. Thangam, T. B. Gatski, and C. G. Speziale. "Development of turbulence models for shear flows by a double expansion technique". *Physics of Fluids A: Fluid Dynamics*, vol. 4.7 (1992), pp. 1510–1520. DOI: `10.1063/1.858424`, (*cit. on: Chap.4-{186}*).

Yue, Y., C. F. Powell, R. B. Poola, J. Wang, and J. K. Schaller. "Quantitative measurements of diesel fuel spray characteristics in the near-nozzle region using X-ray absorption". *Atomization and Sprays*, vol. 11.4 (2001), pp. 471–490, (*cit. on: Chap.1-{3}, Chap.2-{45}*).

Zhang, H., L. Zheng, V. R. Prasad, and T. Hou. "A curvilinear level set formulation for highly deformable free surface problems with application to solidification". *Numerical Heat Transfer, Part B: Fundamentals*, vol. 34.1 (1998), pp. 1–20, (*cit. on: Chap.3-{92}*).

Zhang, J., Q. Du, Y.-X. Yang, and J. Sun. "Study on cavitating flow in different types of diesel nozzle orifice". *Transactions of Chinese Society for Internal Combustion Engines*, vol. 28.2 (2010), pp. 133–140, (*cit. on: Chap.3-{103}*).

Zhuang, J., X. Qiao, J. Bai, and Z. Hu. "Effect of injection-strategy on combustion, performance and emission characteristics in a DI-diesel engine fueled with diesel from direct coal liquefaction". *Fuel*, vol. 121 (2014), pp. 141–148. DOI: `10.1016/j.fuel.2013.12.032`, (*cit. on: Chap.2-{20}*).